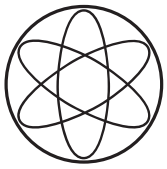

Searches for Supersymmetry in multi-leptonic and τ pair final states with the ATLAS experiment at the LHC at $\sqrt{s} = 13$ TeV

JOHANNES JOSEF JUNGGEBURTH

Dissertation

München 2020

TECHNISCHE UNIVERSITÄT MÜNCHEN
Fakultät für Physik

Max-Planck-Institut für Physik
(Werner-Heisenberg-Institut)

Searches for Supersymmetry in multi-leptonic and τ pair final states with the ATLAS experiment at the LHC at $\sqrt{s} = 13$ TeV

Johannes Josef Junggeburth

Vollständiger Abdruck der von der Fakultät für Physik der Technischen Universität München zur Erlangung des akademischen Grades eines

Doktors der Naturwissenschaften (Dr. rer. nat.)

genehmigten Dissertation.

Vorsitzender:

apl. Prof. Dr. Norbert Kaiser

Prüfer der Dissertation:

1. apl. Prof. Dr. Hubert Kroha
2. Prof. Lothar Oberauer

Die Dissertation wurde am 02.07.2020 bei der Technischen Universität München eingereicht und durch die Fakultät für Physik am 21.07.2020 angenommen.

Searches for Supersymmetry in multi-leptonic and τ pair final states with the ATLAS experiment at the LHC at $\sqrt{s} = 13$ TeV

Johannes Josef Junggeburth

Abstract

Supersymmetry (SUSY) is an attractive framework for extension of the Standard Model of particle physics providing answers for several open questions such as the nature of Dark Matter and the explanation of the value of the Higgs boson mass at the electroweak scale. It postulates for each Standard Model particle a superpartner with the same quantum numbers but differing in spin by half. None of these particles have been observed yet, leading to the conclusion that the superpartners are much heavier and SUSY must be broken. At the Large Hadron Collider (LHC), proton beams collide at a centre-of-mass energy of actually $\sqrt{s} = 13$ TeV in order to test the Standard Model and to search for new physics processes including supersymmetric particles.

In this thesis, two searches for Supersymmetry have been performed using data of the ATLAS experiment at the LHC at $\sqrt{s} = 13$ TeV with an integrated luminosity of 139 fb^{-1}. If R-parity is violated due to additional lepton number violating interactions, the lightest supersymmetric particle (LSP) which is assumed to be produced in pairs and electrically neutral, can decay into two charged leptons and a neutrino. A search for such SUSY scenarios exploits final states wit four or more charged leptons which are experimentally very clean with low background and high reconstruction efficiency. The low background contributions also allow for probing supersymmetric models with gauge mediated SUSY breaking where the LSP is a gravitino originating from higgsino decays together with a Z or Higgs boson. The measurements were in good agreement with the SM predictions and improved lower limits were set on the supersymmetric particle masses and their decay modes into SM particles in the framework of simplified signal models.

An essential prerequisite for searches in multi-leptonic final states is the precise knowledge of the lepton reconstruction efficiencies and of additional selection criteria. In this thesis, the muon reconstruction and identification efficiency as well as the efficiencies of a muon to originate from the primary collision vertex or to be isolated from hadronic activity in the detector have been estimated from data of $Z \to \mu\mu$ and $J/\psi \to \mu\mu$ decays with unprecedented precision of better than 0.1% using the so-called tag-and-probe method.

The second search presented in this thesis concerns the pair production of the supersymmetric partner of the τ lepton, the stau slepton. Light staus could reconcile the theoretical predictions with the measurements of the anomalous magnetic moment of the muon and also provide a mechanism for generating the Dark Matter relic density observed in the universe. The signature of such models consists of two τ leptons and missing transverse momentum from the two escaping LSPs and the neutrinos from τ decays. This final state is challenging at the LHC due to the large hadronic background. Hence, the limits on the stau mass from the LEP experiments prevailed until the end of the $\sqrt{s} = 13$ TeV data taking. Events in which both τ leptons decay hadronically are used to search for direct stau production. No excess above the SM expectation has been observed and lower limits are placed on the stau masses which significantly improve the previous results. Prospect studies for combination of these results using di-tau events where one of the τ leptons decay leptonically are also presented.

Acknowledgements
This thesis would not have been possible without the companionship and the support form various people, which I like to thank in the following. First, I express my gratitude to Prof. Hubert Kroha who gave me the opportunity to start working at such a great experiment when I was an undergraduate student and then accepted me as his PhD student. I greatly benefited from working at the Max Planck Institute and from the great atmosphere in the group and always felt supported in my concerns. Also, I am thankful to him for proof reading my thesis in a difficult era of Covid-19. Furthermore, I want to say thank you to Mike Flowerdew for being a great daily supervisor in the first days of my research experience. I profited a lot from his great knowledge and the fruitful discussions such that I was well prepared for my PhD.

I am also grateful to the four-lepton analysis team, especially, Zinonas Zinonos, Tina Potter, Matthew Klein and Gabriel Gallardo. I had a great joy with you to develop new ideas in the search. A great thanks belongs to Tina for her patient advice and for leading the team over all the years and also to Zinonas for keeping my back free in stressful times. I am also thankful to Alexander Mann, Clara Leitgeb, Stefan Guindon, and Mohamad Kassem Ayoub who exploited with me final states in a big traffic jam with large backgrounds.

Evenmore I am grateful for my experience to work in the Muon Combined Performance group. I would like to thank Massimilliano Bellomo, Stefano Rosati and Jochen Meyer for teaching me how to deal with unexpected behavior of the ATLAS software with great humor and fun. Further I am grateful to Federico Sforza and Stefano Zambito for providing a great atmosphere in which it was a pleasure to work. And here the biggest thank you belongs to Max Goblirsch and Nicolas Köhler for introducing me into the group, developing with me the various concepts, for giving the word cleaning a fully unprecedented and awesome meaning or for having fun at various activities like outreach guide or last aid courses. The fun I had with you was one of the greatest aspects during my PhD. Thank you. Thank you.

I do not want to forget the people here at the MPI group. I am grateful for the companionship of Phillipp Gadow, Rainer Röhrig, Andreas Hönle, Katharina Ecker, Bini Schmidt-Sommerfeld and Verena Walbrecht. I spent great times at the spring meeting, on castle Ringberg or at various free time activity. Thanks for Verena, Katha and Nico for cheering me up in periods of great despairness or for just spending time in the mountains. Another thanks goes to my students, Jonas Graw, Catriona Bruce, Patrick Selle or Makoto Teshima for being such patient with my great impatience. I also thank Michael Holzbock for working with me at the Muon Group over the past years and also for proof reading my thesis over the last three months.

I want to thank my friends outside physics. Yaschar, Fabian, Max, Pia, Guilia, Benni, Christian, Brian, David, Sophia and many more for distracting me from science and spending with me time at the mountains or just for being there. It is very well appreciated. Last but not least, I say thanks to my family, especially to my parents Marita and Josef for providing me the support and companionship on the path I have chosen in my life.

Table of Contents

INTRODUCTION

> Two things fill the mind with ever new and increasing admiration and awe, the oftener and the more steadily we reflect on them: the starry heavens above and the moral law within.
>
> *(Immanuel Kant – Critique of Practical Reason, 161–162)*

This quotation is from the German philosopher Immanuel Kant summarizes the two fundamental questions that people have been asking themselves for more than two millennia: How can one lead a virtuous life? And what are the constituents and the basic principles of all things in the world around us. To answer the second of these two questions, a theory has been developed in the second half of the last century which describes the phenomena from the microscopic to the largest scales of our universe with outstanding success, the Standard Model (SM) of particle physics together with Einstein's theory of gravity. According to the SM, all matter of the visible universe is made up of few elementary particles. In a plethora of experiments, the free parameters of the SM have been measured and the theoretical predictions have been tested with very high precision. In 2012, the last missing piece of the SM, the Higgs boson, has been found in proton-proton collisions at center-of-mass energies of $\sqrt{s}$ = 7 and 8 TeV by the ATLAS and CMS experiments at the Large Hadron Collider (LHC). The discovery of this boson is evidence for the mechanism of spontaneous electroweak symmetry breaking which gives masses to all elementary particles. Despite its great success, there are many reasons suggesting that the SM is not the ultimate theory of nature. For instance, while there were likely equal amounts of matter and antimatter in the early universe which eventually annihilated to radiation, the observable universe today is made up of matter only. The necessary amount of violation of the CP symmetry for this transition cannot be explained by the SM. Furthermore, astrophysical observations imply that the energy content of the universe consists to 95% of Dark Matter and Dark Energy which are not described by the SM. There are also many theoretical questions left open by the SM like the explanation of the mass values and the hierarchy of the fermionic matter constituents, the reason for exactly three generations of leptons and quarks, the equal magnitude of the electric charges of the

electron and proton, and the stabilization of the electroweak scale now studied at the LHC. For these reasons, the SM has to be extended.

Supersymmetry is one of the most promising candidates for an extension of the SM. It postulates the existence of superpartners for each particle in the SM differing in spin by half unit. This symmetry must also be spontaneously broken such that the masses of these new particles are much higher than the masses of their SM counterparts where the absolute values of the masses are unknown free parameters. The large parameter space allows for the construction of a large variety of supersymmetric models in which the supersymmetric particles decay into a vast number of different final states. If a discrete symmetry, called R-parity, is conserved, proton decay is prohibited and the lightest supersymmetric particle (LSP) must be stable, constituting an ideal candidate for Dark Matter, if it is also electrically neutral. It is usually identified with the lightest supersymmetric spin $\frac{1}{2}$ particle, the neutralino $\tilde{\chi}_1^0$. Searches for Supersymmetry have been performed at the LHC so far without finding any evidence for its existence at the energy scale accessible at the LHC.

In the period 2015–2018, the LHC continued with proton-proton collisions at an increased center-of-mass energy of $\sqrt{s} = 13$ TeV of which the ATLAS experiment recorded an integrated luminosity of 139 fb^{-1} to continue the search for new phenomena, in particular for supersymmetric particles. In this thesis, searches for three promising supersymmetric models have been performed, which could not be constrained sufficiently by previous studies. If R-parity is violated by lepton number violating interactions, the $\tilde{\chi}_1^0$ LSP decays into a pair of charged leptons and a neutrino. As the LSP is produced in pairs in the pp collisions, by R-parity conserving processes, the characteristic final state consists of four charged leptons, a signature which is well distinguishable from hadronic background. The four-lepton final state is also sensitive to supersymmetric models with R-parity conservation in which the gravitino, the superpartner of the graviton, is the LSP which is produced in the decay of a $\tilde{\chi}_1^0$ into a Z or a Higgs boson and the gravitino. Models in which the supersymmetric partner of the τ lepton, the stau slepton, has a mass of few hundred GeV, can explain the tensions between measurements and SM predictions of the anomalous magnetic moment of the muon as well as the observed Dark Matter relic density in the universe. If the stau is the only supersymmetric particle accessible by the LHC, it has to be directly produced in pairs. The resulting final state with two τ leptons is experimentally challenging due to the large backgrounds at he LHC such that limits on the stau mass prevailed from the era of the Large Electron Positron Collider (LEP) until now.

For the exploitation of rare final states like ones with four leptons at a hadron collider, precise knowledge of the lepton reconstruction and efficiencies is essential. Muon efficiency measurements have been carried out with unprecedented precision in this work which are a crucial input for many SM precision measurements and new physics searches by the ATLAS experiment.

The first part of the thesis introduces the concepts of the SM and its supersymmetric extensions, and

then describes the experimental setup with the LHC and the ATLAS experiment. In the second part, the reconstruction and identification of muons is discussed, followed by a detailed description of the extensive muon selection efficiency measurements. The third part of this thesis first introduces the supersymmetric models studied, and then presents the analysis and results of the search for Supersymmetry in four-lepton and di-tau final states.

In this thesis, plots annotated with an ”ATLAS Preliminary“ label have been peer-reviewed and approved by the ATLAS collaboration whereas ”ATLAS“ label plots are also reviewed by a scientific journal. Results without any label are at the stage of an internal review within the collaboration.

PART

I

Theoretical Framework and Experimental Setup

CHAPTER ONE

THE STANDARD MODEL OF PARTICLE PHYSICS

It has been a pending question since the beginning of mankind, what are the fundamental constituents of the universe. The present understanding is that the universe is made of point-like particles which interact through four fundamental forces, the electromagnetic, the weak, the strong and the gravitational force. The first three interactions are described with high precision by the Standard Model of Elementary

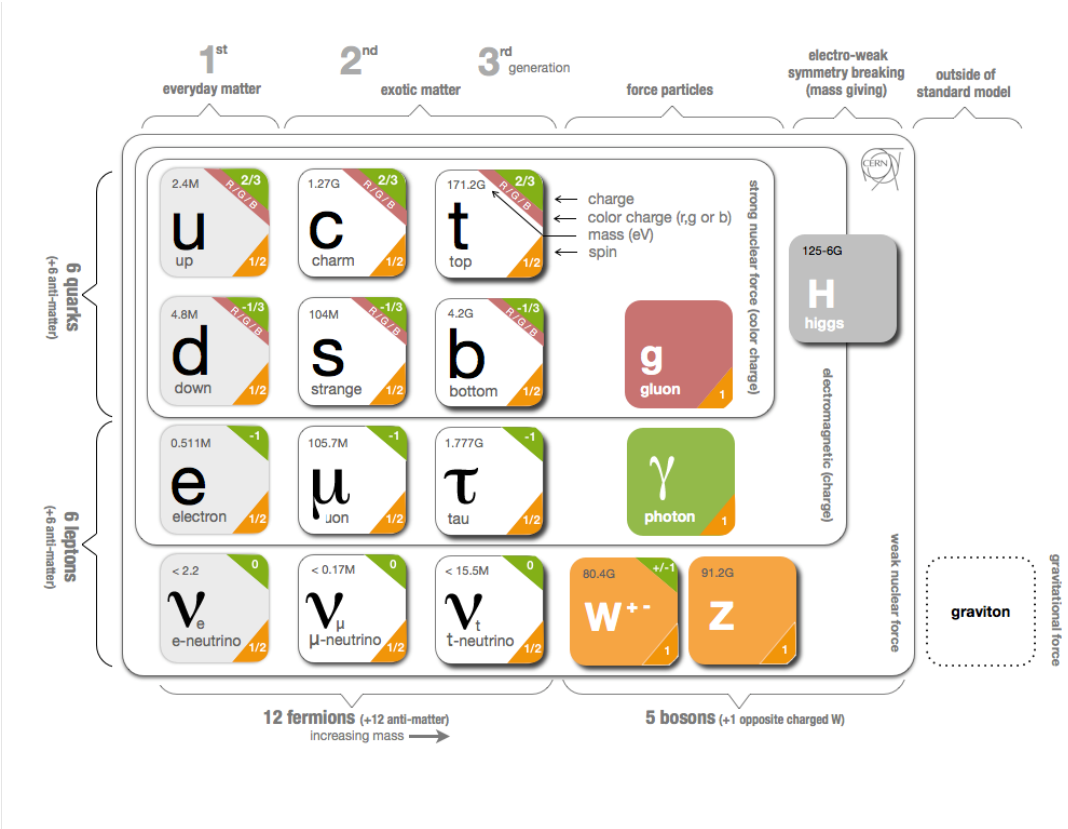

Figure 1.1: The particles of the Standard Model[1].

Particle physics (SM) [2–7]. The SM is a relativistic quantum field theory which describes the forces based on local gauge symmetries of the composite Lie-Group $\mathcal{G} = SU(3)_\mathrm{C} \times SU(2)_\mathrm{L} \times U(1)_\mathrm{Y}$.

1.1 Particle Content

The particle content of the Standard Model is shown in Figure 1.1. The particles are classified into two categories: fermions and bosons. Fermions are the constituents of matter carrying half-integer spin. The fermions in the SM are either *leptons* or *quarks* which quarks appear in three families with increasing masses but the same quantum numbers. The families contain the same number of quark and lepton states which appear in weak $SU(2)_\mathrm{L}$ doublets and singlets of charged lepton and neutrinos and of up- and down-type quarks. and are sorted by increasing mass. Thus all fermions interact through the weak force. The charged leptons are electrons, muons and taus which carry electric charge quantum number -1 and thus interact electromagnetically while the neutrinos are electrically neutral and massless in the SM [8]. Quarks interact electromagnetically and via the strong force carrying fractional electric charges, $\frac{+2}{3}$ for up-type quarks, (up, charm and top) and $\frac{-1}{3}$ for down-type quarks (down, strange and bottom). They have an extra degree of freedom in terms of the strong interaction, called color-charge and one of three so-called color quantum numbers of the $SU(3)_\mathrm{C}$ gauge group.

The mediators of the three gauge interactions are massless gauge bosons with spin 1 corresponding to the generators and charge operators of the gauge groups. There are three vector bosons W^i $(i = 1, 2, 3)$ of the weak isospin $SU(2)_2$ gauge symmetry, a gauge boson B of the weak hypercharge $U(1)_\mathrm{Y}$ and eight strong gauge bosons, called gluons, of the $SU(3)_\mathrm{C}$ color group. After spontaneous $SU(2)_\mathrm{L} \times U(1)_\mathrm{Y}$ symmetry breaking (cf. section 1.4), the electrically neutral weak states W^3 and B mix resulting in the mass eigenstates, the heavy Z^0 boson and the massless photon γ. The weak gauge bosons acquire masses and the Higgs boson is a scalar $SU(2)_\mathrm{L}$ doublet state resulting as massive excitation from the symmetry breaking scalar ground state with non-zero vacuum expectation value.

1.2 The Electroweak Interaction

The electromagnetic and the weak force are unified to the electroweak interaction with $SU(2)_\mathrm{L} \times U(1)_\mathrm{Y}$ gauge symmetry in the Glashow-Weinberg-Salam model [9–11]. After electroweak symmetry breaking (cf. Section 1.4), the group is broken down to the electromagnetic gauge symmetry $U(1)_\mathrm{em}$ with the photon (γ) as massless gauge boson. The third component of the weak isospin operator, I_3, the weak hypercharge Y and the electric charge operator Q are connected by the Gell-Mann-Nishijima relation

$$Q = I_3 + \frac{Y}{2}. \tag{1.1}$$

Table 1.1: Electroweak quantum numbers of the fermions in the Standard Model [13]

Particles	$SU(2)_{\mathrm{L}}$	$U(1)_{\mathrm{Y}}$	$U(1)_{\mathrm{em}}$
$Q_i = \begin{pmatrix} u_{\mathrm{L}} \\ d_{\mathrm{L}} \end{pmatrix}, \begin{pmatrix} c_{\mathrm{L}} \\ c_{\mathrm{L}} \end{pmatrix}, \begin{pmatrix} b_{\mathrm{L}} \\ t_{\mathrm{L}} \end{pmatrix}$	$\begin{pmatrix} 1/2 \\ -1/2 \end{pmatrix}$	1/3	$\begin{matrix} 2/3 \\ -1/3 \end{matrix}$
$u^i_{\mathrm{R}} = u_{\mathrm{R}}, c_{\mathrm{R}}, t_{\mathrm{R}}$	0	4/3	2/3
$d^i_{\mathrm{R}} = d_{\mathrm{R}}, s_{\mathrm{R}}, b_{\mathrm{R}}$	0	-2/3	-1/3
$L_i = \begin{pmatrix} \nu_e \\ e_{\mathrm{L}} \end{pmatrix}, \begin{pmatrix} \nu_\mu \\ \mu_{\mathrm{L}} \end{pmatrix}, \begin{pmatrix} \nu_\tau \\ \tau_{\mathrm{L}} \end{pmatrix}$	$\begin{pmatrix} 1/2 \\ -1/2 \end{pmatrix}$	-1	$\begin{matrix} -1 \\ 0 \end{matrix}$
$\ell^i_{\mathrm{R}} = e_{\mathrm{R}}, \mu_{\mathrm{R}}, \tau_{\mathrm{R}}$	0	-2	-1

As the weak force violates parity and charge conjugation[12], the left-handed leptons and quarks are arranged in weak isospin doublets,

$$L_i = \begin{pmatrix} \nu^i_L \\ \ell^i_L \end{pmatrix} \qquad \text{and} \qquad Q_i = \begin{pmatrix} u^i_L \\ d^i_L \end{pmatrix}, \tag{1.2}$$

of the fundamental representation of $SU(2)_{\mathrm{L}}$ and the right-handed charged leptons and quarks in weak isospin singlets

$$\ell^i_R \qquad \text{and} \qquad u^i_R, \qquad d^i_R. \tag{1.3}$$

As neutrinos are massless in the Standard Model, there are no right-handed neutrino states. The electroweak quantum numbers of the fermions are summarized in Table 1.1. The gauge covariant derivative of the electroweak theory is given by,

$$D_\mu = \partial_\mu - i g_{\mathrm{W}} \sigma_i W^i_\mu - i g_{\mathrm{B}} Y B_\mu, \tag{1.4}$$

where $\sigma_i = \frac{I_i}{2} (i = 1, 2, 3)$ are the weak isospin operators represented by the three Pauli matrices, and g_{W} and g_{B} are the coupling constants of the $SU(2)_{\mathrm{L}}$ and $U(1)_{\mathrm{Y}}$ group, respectively. The Pauli matrices are the generators of the $SU(2)_{\mathrm{L}}$ gauge group satisfying the commutation relation

$$\left[\sigma_i, \sigma_j\right] = i \epsilon_{ijk} \sigma_k, \tag{1.5}$$

with ϵ_{ijk} as the fully antisymmetric tensor providing the non-vanishing structure constants of the gauge group. The electroweak Lagrangian density $\mathcal{L}_{\mathrm{EW}}$ is given by

$$\mathcal{L}_{\mathrm{EW}} = \sum_f i \bar{\chi}_f \gamma^\mu D_\mu \chi_f - \frac{1}{4} W^i_{\mu\nu} W^{\mu\nu}_i - \frac{1}{4} B_{\mu\nu} B^{\mu\nu} \tag{1.6}$$

with the fermion spinor fields χ_f and the gauge field kinetic terms,

$$W^i_{\mu\nu} = \partial_\mu W^i_\nu - \partial_\nu W^i_\mu - g_{\mathrm{W}} \epsilon_{ijk} W^j_\mu W^k_\nu \qquad \text{and} B_{\mu\nu} = \partial_\mu B_\nu - \partial_\nu B_\mu . \tag{1.7}$$

The group structure constants lead to self-interactions between the heavy weak gauge bosons. Explicit mass terms for the fermions or for the gauge boson would break the gauge symmetry of the Lagrangian. Fermions and weak gauge bosons acquire their masses [14–19] by the Higgs mechanism discussed in Section 1.4.

1.3 Quantum Chromodynamics

The quarks are hold together in hadrons, e.g. proton and neutrons, by the strong interaction. It is described by quantum chromodynamics (QCD), a local gauge theory with $SU(3)_{\mathrm{C}}$ as gauge symmetry group [20]. Eight gluon fields G^a_μ are associated with the generators of the group, the operators of the associated color-charges. The quarks appear in three so-called color states, red(R), green (G) and blue (B) forming the fundamental representation of $SU(3)_{\mathrm{C}}$:

$$q = \begin{pmatrix} q_R \\ q_G \\ q_B \end{pmatrix}. \tag{1.8}$$

The covariant derivative applied to the quark states has to be augmented to

$$D_\mu = \partial_\mu - i g_{\mathrm{W}} \sigma_a W^a_\mu - i g_{\mathrm{B}} Y B_\mu - i g_{\mathrm{s}} \lambda_a G^a_\mu, \tag{1.9}$$

to achieve $SU(3)_{\mathrm{C}}$ gauge invariance, where λ_a are the generators of $SU(3)_{\mathrm{C}}$, represented by the Gell-Mann matrices, and g_{s} is the strong coupling constant. The free gluon fields are described by a kinetic term in analogy to Equation (1.6):

$$\mathcal{L}_{\mathrm{QCD}} = -\frac{1}{4} G^a_{\mu\nu} G^{\mu\nu}_a, \tag{1.10}$$

with the field strength tensors

$$G^a_{\mu\nu} = \partial_\mu G^a_\nu - \partial_\nu G^b_\mu - g_{\mathrm{s}} f_{abc} G^b_\mu G^c_\nu . \tag{1.11}$$

The non-vanishing structure constants f_{abc} of $SU(3)_{\mathrm{C}}$ and the self-interactions of the gluons under the strong forces give rise to the phenomenon of confinement of colored particles, quarks and gluons [21]. Quarks only occur in colorless bound states called hadrons. They are either quark-antiquark

pairs (mesons), or three-quark states (baryons). More complex states, like tetra- or pentaquarks are theoretically possible and have been recently discovered at the LHCb experiment [22–24]. Confinement is broken at sufficient high temperature. This state of matter with free quarks and gluons is called quark-gluon plasma which should have existed in the very early universe [25].

1.4 The Brout-Englert-Higgs Mechanism

The weak force-carriers $W^{\pm}$ and Z^0 are massive. However, an explicit mass term in the Lagrangian $\propto M^2 W_\mu W^\mu$ would break the $SU(2)_\mathrm{L}$ local gauge symmetry. Nevertheless, masses can be generated if the vacuum state does not respect the gauge symmetries of the Lagrangian density. These symmetries are then spontaneously broken giving rise to so-called massless Goldstone bosons for each broken symmetry generator [26]. The Brout-Englert-Higgs mechanism of spontaneous symmetry breaking [27–30] introduces a complex scalar field Φ

$$\Phi = \begin{pmatrix} \phi^+ \\ \phi^0 \end{pmatrix} \tag{1.12}$$

with $Y = 1$ which is a doublet of the weak isospin. The Lagrangian density of the Klein-Gordon field [31] is given by

$$\mathcal{L}_\mathrm{Higgs} = \left(D_\mu \Phi\right)^\dagger \left(D^\mu \Phi\right) - \underbrace{\mu^2 \Phi^\dagger \Phi - \lambda \left(\Phi^\dagger \Phi\right)^2}_{:= V\left(\Phi^\dagger \Phi\right)}, \tag{1.13}$$

where D_μ is the covariant derivative defined in Equation (1.4) and $V\left(\Phi^\dagger \Phi\right)$ is the self interaction potential of the field. The parameters λ and μ^2 are the dimensionless self-coupling and a mass parameter, respectively. If $\lambda > 0$ and $\mu^2 < 0$, the potential assumes an infinite set of minima with non-vanishing field value

$$|\Phi_0| = \sqrt{-\frac{\mu^2}{2\lambda}} =: \frac{v}{\sqrt{2}} \simeq 246 \text{ GeV}. \tag{1.14}$$

Choosing one particular ground state breaks the electroweak gauge symmetry spontaneously, leaving only $U(1)_\mathrm{em}$ unbroken. The scalar field can be expanded around this ground state according to

$$\Phi = \frac{1}{\sqrt{2}} \begin{pmatrix} 0 \\ v + H \end{pmatrix}, \tag{1.15}$$

with a massive excitation H, the Higgs field and where the three massless excitations to other ground states corresponding to Goldstone bosons have been transformed into longitudinal polarization states of

the weak gauge fields via local gauge transformations. Inserting Equation (1.15) into Equation (1.13) leads to mass terms for the W^i_μ and B_μ gauge boson fields. The mass eigenstates of the charged and neutral gauge bosons, $W^\pm_\mu$, Z_μ and of the massless photon field A_μ are obtained by unitary transformations

$$\begin{pmatrix} W^+_\mu \\ W^-_\mu \end{pmatrix} = \frac{1}{\sqrt{2}} \begin{pmatrix} 1 & -i \\ 1 & i \end{pmatrix} \begin{pmatrix} W^1_\mu \\ W^2_\mu \end{pmatrix}, \qquad \begin{pmatrix} A_\mu \\ Z_\mu \end{pmatrix} = \begin{pmatrix} \cos\theta_W & \sin\theta_W \\ -\sin\theta_W & \cos\theta_W \end{pmatrix} \begin{pmatrix} B_\mu \\ W^3_\mu \end{pmatrix}, \tag{1.16}$$

where $\cos\theta_W = \frac{g_\mathrm{W}^2}{\sqrt{g_\mathrm{W}^2+g_\mathrm{B}^2}}$ defines the so-called Weinberg angle. The masses of the $W^\pm$, Z^0 and the H bosons are then given by

$$m_W = \frac{g_\mathrm{W} v}{2}, \qquad m_Z = \frac{g_\mathrm{W} v}{2\cos\theta_W} \qquad \text{and} \qquad m_H = v\sqrt{2\lambda}, \tag{1.17}$$

respectively. The $W^\pm$ and Z^0 boson masses have been measured to $m_W = 80.370 \pm 0.019$ GeV and $m_Z = 91.1876 \pm 0.0021$ GeV [14, 15]. The Higgs boson was the last missing piece of the Standard Model until 2012 where was discovered by the ATLAS and CMS experiments at the Large Hadron Collider (LHC) [32, 33]. A recent measurement of the Higgs boson mass by the ATLAS experiment gives $m_H = 124.97 \pm 0.24$ GeV [34].

The mechanism of spontaneous symmetry breaking also allows for giving masses to the fermions by introducing Yukawa-type interactions of the fermions with the scalar field:

$$\mathcal{L}_\mathrm{Yukawa} = -\lambda_L^{ij} \ell^\dagger_{\mathrm{R}\,i} L_j \Phi - \lambda_u^{ij} u^\dagger_{\mathrm{R}\,i} Q_j i\sigma_2 \Phi^* - \lambda_d^{ij} d^\dagger_{\mathrm{R}\,i} Q_j \Phi + h.c. \tag{1.18}$$

with generation indices $i, j = 1, 2, 3$, where λ_L^{ij}, λ_u^{ij}, λ_d^{ij} are 3×3 complex matrices for the electroweak eigenstates of charged leptons, and up-type and down-type quarks, which are proportional to the complementary fermion mass matrices:

$$m_{ij}^{\ell,u,d} = \lambda_{ij}^{l,u,d} \frac{v}{\sqrt{2}}. \tag{1.19}$$

The λ_L^{ij}-matrix is diagonal, i.e. electroweak and mass eigenstates are equal, if the neutrinos are assumed to be massless. In the quark sector, the coupling and mass matrices have to be diagonalized to obtain the fermion mass eigenstates. The transformation leads to mixing of the fermion electroweak eigenstates via the complex unitary 3×3 Cabibbo-Kobayashi-Maskawa (CKM) matrix [35, 36] and correspondingly to charged electroweak transitions between the three fermion generations. The CKM matrix has a complex phase parameter which is responsible for the observed effects of CP violation in weak decays [37].

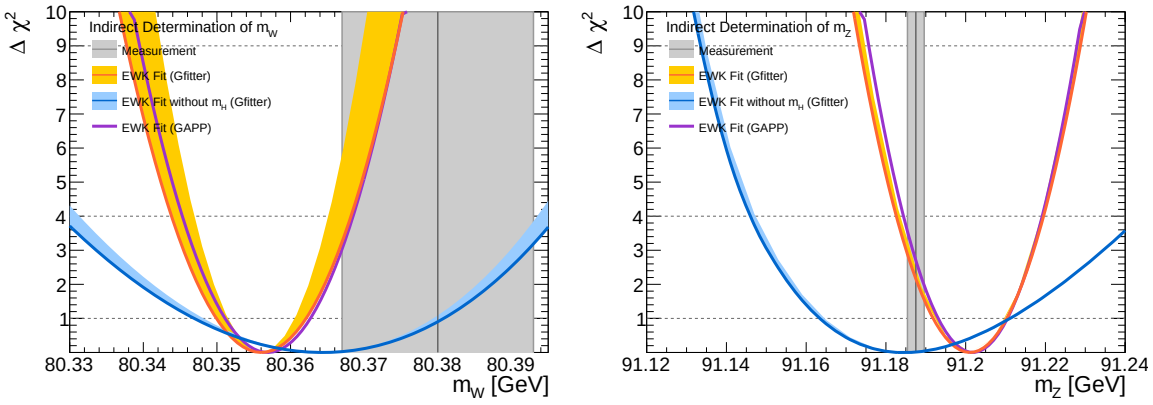

(a) (b)

Figure 1.2: Standard Model prediction of (a) the $W^{\pm}$ boson mass and (b) of the Z^0 boson with and without the Higgs mass constraint. The world average measured values are shown in grey [38].

1.5 Tests of the Standard Model

The Standard Model has 18 free parameters which have to be measured, the three gauge coupling constants, the six quark masses, the three charged lepton masses, the four free parameters of the CKM matrix, and the mass and the self-coupling constant of the Higgs field. The parameters have been measured at several colliders over the last decades [15–17]. The Higgs boson mass has been measured for the first time by the ATLAS and CMS experiments at CERN [32, 33]. The last missing parameter value is that of the Higgs self coupling constant, which will be constrained at future collider experiments like the HL-LHC.

The knowledge of the parameters allows for high-precision tests of the Standard Model as predictions in higher order perturbation can be compared with measured boson masses and coupling constants. The Next-to-Next-Leading-Order (NNLO) predictions of the Standard Model agree very well with the measurements [38]. An example is shown in Figure 1.2. Including the Higgs mass constraint, the W and Z boson masses are predicted to $m_W = 80.364 \pm 0.017$ GeV and $m_Z = 91.201 \pm 0.009$, which agree within one standard deviation with the measured values of $m_W = 80.380 \pm 0.013$ GeV and $m_Z = 91,188 \pm 0.002$ GeV.

The production cross sections (cf. Section 1.8) of numerous Standard Model processes have been measured in pp collisions at the LHC at three different center-of-mass energies $\sqrt{s}$ [39]. A summary is shown in Figure 1.3 with comparison to theoretical predictions which agree well within one standard deviation in most cases.

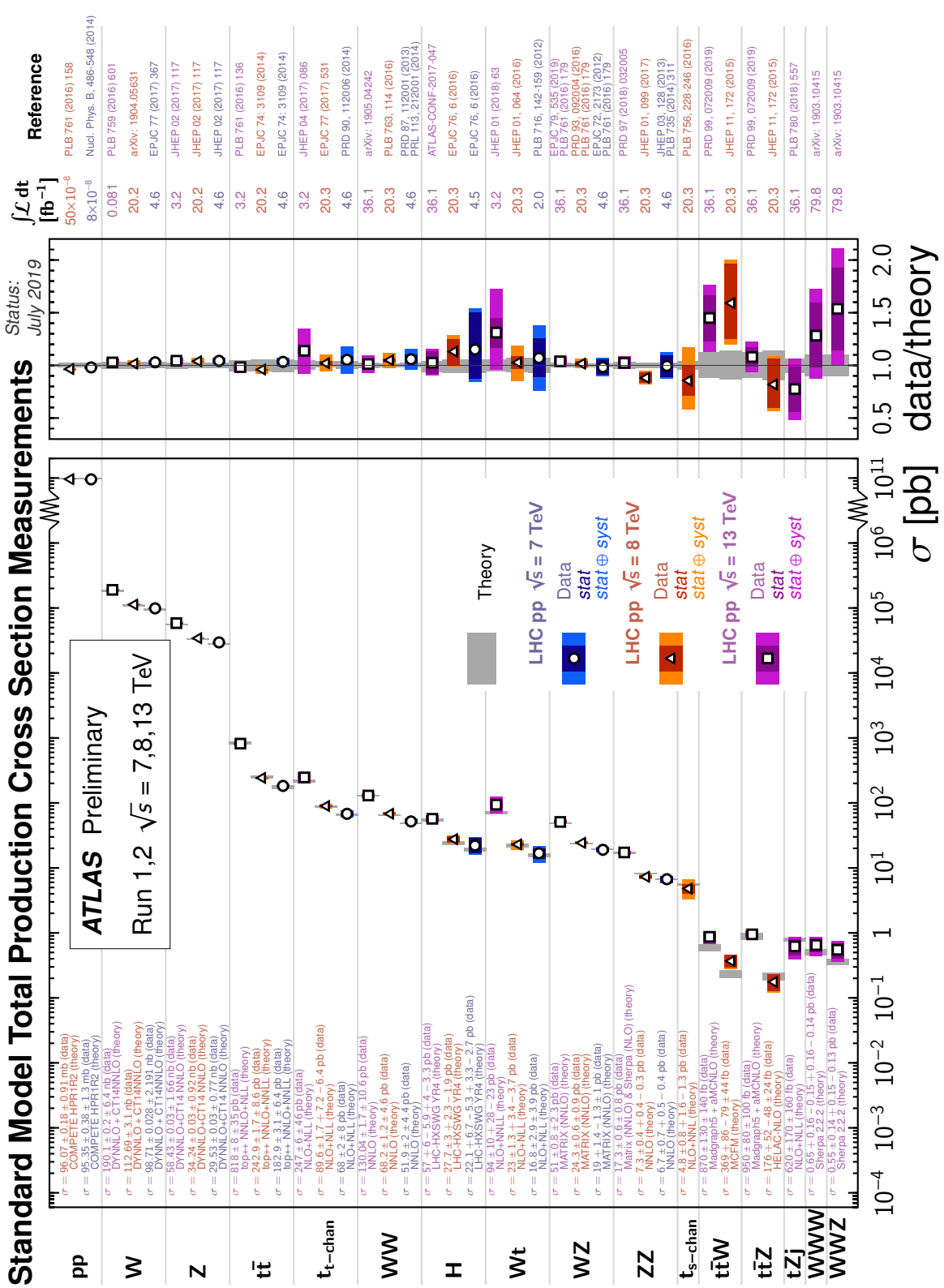

Figure 1.3: Summary of Standard Model cross section measurements by the ATLAS experiment at the LHC in comparison with theoretical expectations [39].

1.6 Limitations of the Standard Model

Despite its great success, the Standard Model (SM) has several shortcomings which lead to the belief that the theory has to be extended. A large variety of extensions has been proposed. Supersymmetry (cf. Section 1.7) is one of the theoretically most compelling ones. In the following, the most important shortcomings are briefly recapitulated.

Quantum description of gravity: The Standard Model describes only three fundamental forces, excluding gravity which is the dominant force on large scales in the universe described by Einstein's classical field theory of General Relativity [40]. At distances near the Planck length, gravity becomes as strong as the other forces such that quantum effects of gravity can no longer be neglected like shortly after the Big Bang [41]. Unfortunately, after one century of research no consistent quantization of gravity which can be combined with the Standard Model has been found yet [42, 43].

Dark Matter and Dark Energy: Astrophysical observations of galaxy rotation curves [44], merging galaxies, in the bullet cluster [45], gravitational lensing [46], temperature fluctuations in the cosmic microwave background radiation [47] and the large-scale structure of the universe [48] imply that only a small fraction of the energy content of the universe, namely 4.8%, consists of baryonic matter described by the SM [49]. Roughly 26% are Dark Matter and the largest part of 68% is due to the so-called Dark Energy, responsible for the observed accelerated expansion of the universe [50].

There are many models for Dark Matter particles. They are required to be massive electrically neutral and stable on the scale of the age of the universe. The most common group of models describes the Dark Matter particles as weakly interacting massive particles (WIMP) which allows for detecting them in underground laboratories [51–58]. The most prominent example is the lightest supersymmetric particle (cf. Section 1.7). Other possibilities to explain Dark Matter are sterile neutrinos, axions [59, 60], which could also solve the strong CP problem [59], Kaluza-Klein excitations in models with extra spatial dimensions [61] or particles predicted by so-called little Higgs models [62, 63].

Dark Energy can be described to good approximation by Einstein's cosmological constant. Recent models of Dark Energy proposed that Dark Energy might consist of a scalar field which could be produced at the Large Hadron Collider [64–66].

Matter-antimatter asymmetry: The matter-antimatter asymmetry problem addresses the question why essentially only matter is present in the visible universe today. In the very early universe, matter and antimatter, were produced and annihilated at the same rate in thermal equilibrium. This equilibrium broke down during the expansion of the universe. Still a mechanism with baryon or lepton

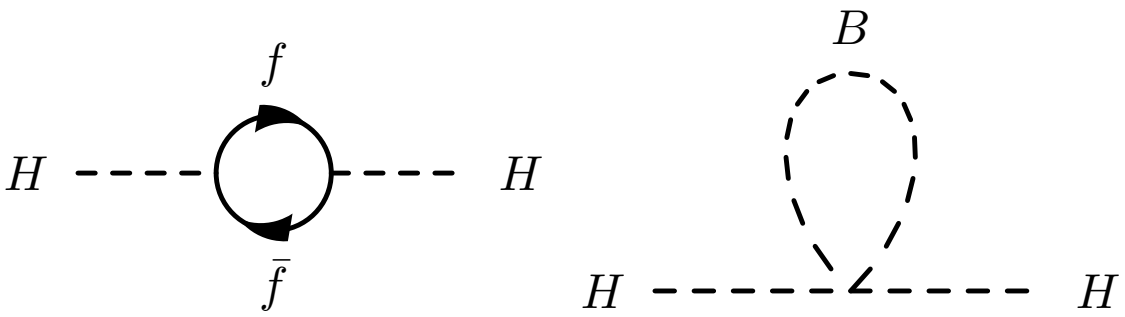

(a) Fermion (b) Boson

Figure 1.4: Leading-order Feynman diagrams of the quantum corrections to the Higgs boson propagator if a fermion (a) or a boson (b) couples to the Higgs boson.

number violation and with sufficiently strong CP violation is needed to explain the creation of an excess of matter. The Standard Model with the CKM mixing matrix does not provide sufficiently strong violation of the CP symmetry [67, 68].

Origin of neutrino masses: Neutrinos are assumed to be massless in the Standard Model. The observation of neutrino oscillations requires that at least two neutrino flavours are massive with mass splittings of $m_{12}^2 = O\left(10^{-5}\right)$ eV^2 and $m_{13} = O\left(10^{-3}\right)$ eV^2, respectively [69, 70], which implies the existence of right-handed neutrinos which are singlets with respect to the gauge groups of the SM. Additionally, the mass eigenstates do not coincide with the electroweak eigenstates. The transformation from mass to weak eigenstates is described by the Pontecorvo–Maki–Nakagawa–Sakata (PMNS) mixing matrix [71, 72]. Massive neutrinos could be their own anti-particle allowing for so-called Majorana neutrinos [51, 73]. Direct lepton number violation and extra CP violating phases in the PMNS matrix are implications for such neutrinos which and can be tested by experiments, like the search for the neutrinoless double β decay [74]. The mass splittings between the three neutrino generations and their mixing angles have been measured while only upper limits exist on the absolute mass values. The best current limit on the neutrino mass, $m_\nu < 1.1$ eV (at 90% CL.), has been recently set from a direct measurement by the KATRIN experiment [75]. Cosmological models imply indirect bounds on the sum of the neutrino masses to be $\sum m_{\nu_i} < 0.17$ eV (at 95% CL.) [76].

Naturalness problem: Although the Higgs mechanism provides a solution to the origin of massive particles in the SM, the large gap between the electroweak scale of about 100 GeV and the Planck scale of 10^{19} GeV give rise to the hierarchy problem. Like all other parameters in quantum field

theories, the mass of the Higgs boson is subject to radiative corrections,

$$m_H^2 = m_{\text{bare}}^2 + \Delta m_{\text{radiative}}^2, \tag{1.20}$$

where m_H^2 is the observed mass and m_{bare}^2 is the mass parameter in the Lagrangian. In contrast to fermions or gauge bosons, the masses of scalar particles are not protected by any (approximate) symmetry but can grow to arbitrarily large values [77]. The two leading-order diagrams contributing to $\Delta m_{\text{radiative}}^2$ are depicted in Figure 1.4 where fermions and scalar particles, like the Higgs boson itself, couple to the Higgs field with interaction strengths λ_f and λ_s, respectively. The leading loop corrections for the Higgs boson mass from fermions,

$$\Delta m_{\text{radiative,fermion}}^2 = -\frac{\left|\lambda_f\right|^2}{8\pi^2}\Lambda_{UV}^2 + \dots \tag{1.21}$$

and from bosons,

$$\Delta m_{\text{radiative,boson}}^2 = \frac{|\lambda_s|^2}{16\pi^2}\left(\Lambda_{UV}^2 - 2m_s^2 \ln\frac{\lambda_{UV}}{m_s}\right). \tag{1.22}$$

are quadratically divergent in the cutoff scale Λ_{UV} of the theory. If the Planck scale is the cutoff, these corrections become 30 orders of magnitude larger than the observed Higgs mass value of $m_H^2 \simeq (125\,\text{GeV})^2$ requiring an extreme fine-tuning between the parameters which seems quite unnatural. Additional contributions are expected from any unknown heavy particle appearing between the electroweak and the Planck scale, even if it couples only indirectly to the Higgs boson [54].

The divergence to the Higgs boson mass can be mitigated if for every fermion (boson) of the SM, there is a corresponding boson (fermion) with the same couplings to the Higgs boson an with masses not too far above the electroweak scale, because the fermionic and bosonic corrections leave opposite sign (cf. Equations (1.21) and (1.22)). This scenario is exactly provided by supersymmetric (SUSY) extensions of the Standard Model which will be discussed in the next section.

1.7 Supersymmetry

Supersymmetry [78–81] provides an elegant solution to the naturalness problem and it might in addition solve many of the other problems discussed in Section 1.6. A new fermionic operator Q transforms fermions into bosons and vice versa

$$Q\,|\text{boson}\rangle = |\text{fermion}\rangle\,, \qquad Q\,|\text{fermion}\rangle = |\text{boson}\rangle\,. \tag{1.23}$$

To manifest the operator Q as a symmetry of the theory, it has to satisfy the (anti-)commutation relations of the SUSY Lie-Algebra given by [54]

$$\left\{Q_\alpha, Q^\dagger_{\dot\alpha}\right\} = -2\sigma^\mu_{\alpha\dot\alpha}P_\mu, \tag{1.24a}$$

$$\left\{Q_\alpha, Q_\beta\right\} = \left\{Q^\dagger_{\dot\alpha}, Q^\dagger_{\dot\beta}\right\} = 0, \tag{1.24b}$$

$$[Q_\alpha, P^\mu] = \left[Q^\dagger_{\dot\alpha}, P^\mu\right] = 0, \tag{1.24c}$$

where P^μ is the generator of space-time translations, the four momentum generator. The fermions and bosons connected through the SUSY transformation Q are called superpartners. They have equal masses and belong to the same representations of the gauge groups, but differ in spin by half unit. SUSY has been proven to be the only viable non-trivial extension of the algebra of space-time translations, spatial rotations and Lorentz boosts, called the Poincare algebra [82, 83].

Superpartners form so-called supermultiplets of the SUSY algebra. There are two types of supermultiplets. One, called chiral supermultiplet, contains a Weyl spinor ψ and a complex scalar field referred to as sfermion (scalar fermion) and denoted by $\tilde\psi$. The second type of supermultiplets is called vector supermultiplet and contains a gauge field V^μ_a and again a Weyl spinor λ_a, referred to as gaugino denoted by $\tilde V_a$.

In supersymmetric theories interactions, between particles in chiral supermultiplets can be derived from the so-called superpotential which is a holomorphic function of the scalars $\tilde\psi_i$ in the theory and has the most general form of

$$W = \frac{M^{ij}}{2}\tilde\psi_i\tilde\psi_j + \frac{y^{ijk}}{6}\tilde\psi_i\tilde\psi_j\tilde\psi_k, \tag{1.25}$$

where M^{ij} have the dimension of mass and the y^{ijk} are dimensionless Yukawa couplings. The actual interaction terms between fermions and scalars as well as among the scalars are given by the first and second order derivatives of the superpotential with respect to the fields $\tilde\psi_i$:

$$\mathcal{L}_{\text{fermion–scalar}} = -\frac{1}{2}\frac{\partial^2 W}{\partial\tilde\psi_i\partial\tilde\psi_j}\psi_i\psi_j + h.c. = -\frac{1}{2}\left(M^{ij}\psi_i\psi_j + y^{ijk}\tilde\psi_k\psi_i\psi_j\right) + h.c \tag{1.26a}$$

$$\mathcal{L}_{\text{scalar–scalar}} = -\left(\frac{\partial W}{\partial \tilde{\psi}_k}\right)^* \left(\frac{\partial W}{\partial \tilde{\psi}_k}\right) \tag{1.26b}$$

$$= M^*_{ik} M^{kj} \tilde{\psi}^{*i} \tilde{\psi}_j + \tag{1.26c}$$

$$\left(\frac{1}{2} M^{in} y^*_{jkn} \tilde{\psi}_i \tilde{\psi}^{*j} \tilde{\psi}^{*k} + h.c.\right) + \tag{1.26d}$$

$$\frac{1}{4} y^{ijn} y^*_{kln} \tilde{\psi}_i \tilde{\psi}_j \tilde{\psi}^{*k} \tilde{\psi}^{*l}. \tag{1.26e}$$

To preserve supersymmetry in the case of gauge interactions between fermion and scalar fields, the following additional interaction terms have to be added for each gauge group:

$$\mathcal{L}^{\text{SUSY}}_{\text{gauge}} = -\sqrt{2} g \left(\tilde{\psi}^* T^a \psi\right) \lambda^a - \sqrt{2} g \lambda^{\dagger a} \left(\psi^\dagger T^a \tilde{\psi}\right) - g^2 \left(\tilde{\psi}^* T^a \tilde{\psi}\right) \cdot \left(\tilde{\psi}^* T^a \tilde{\psi}\right), \tag{1.27}$$

where T^a are the generators of the gauge group and λ^a are the corresponding gauge fermion fields.

1.7.1 The Minimal Supersymmetric Standard Model

The Minimal Supersymmetric Standard Model (MSSM) comprises the minimal possible particle content allowing for an extension of the Standard Model to a supersymmetric theory. The SM gauge bosons are grouped with their superpartners, the gauginos, called wino, bino and gluino, in vector supermultiplets (cf. Table 1.3). The leptons and quarks belong to chiral supermultiplets together with their superpartners, the sleptons and squarks, respectively, as listed in Table 1.2. The Higgs boson is also member of a chiral supermultiplet with the higgsino as superpartner. However, only one higgsino would break the gauge symmetry at quantum level, due to the chiral gauge anomaly [54, 84]. A second Higgs supermultiplet with opposite hypercharge is, therefore, needed for cancellation of this anomaly. The second Higgs field (H_u) gives masses to the up-type fermions and sfermions, while the first one, H_d, gives masses to down-type fermions and sfermions according to the superpotential terms

$$W_{\text{MSSM}} = -\lambda^u_{ij} \tilde{u}^* \tilde{Q}_j H_u - \lambda^d_{ij} \tilde{d}^*_i \tilde{Q}_j H_d - \lambda^e_{ij} \tilde{e}^* \tilde{L}_j H_d + \mu H_u H_d, \tag{1.28}$$

with Yukawa couplings $\lambda^{u,d,e}_{ij}$. After electroweak symmetry breaking, five Higgs boson mass eigenstates remain, two neutral scalars h and H, two charged bosons $H^\pm$ and one pseudoscalar A. The higgsinos and the superpartners of the electroweak gauge bosons, the winos and the bino, mix with each other resulting in four neutral mass-eigenstates $\tilde{\chi}^0{}_i$ (i=1,2,3,4 increasing with mass), called neutralinos, and two charged mass-eigenstates $\tilde{\chi}^\pm{}_i$ (i=1,2), called charginos.

Supersymmetry has to be spontaneously broken since no superpartner has yet been observed indicating that they are heavier than their SM partners. In this case, radiative corrections to the Higgs boson mass

Table 1.2: Chiral supermultiplets of the first fermion generation in the MSSM

Supermultiplet	$SU(3)_C$	$SU(2)_L$	$U(1)_Y$	particles
Q_L	3	2	$+\frac{1}{3}$	quarks (u_L, d_L) and squarks ($\tilde{u}_L$, $\tilde{d}_L$)
u_R	$\bar{3}$	1	$-\frac{4}{3}$	quarks (u_R) and squarks ($\tilde{u}_R$)
d_R	$\bar{3}$	1	$+\frac{2}{3}$	quarks (d_R) and squarks ($\tilde{d}_R$)
L_L	1	2	-1	leptons (e_L, ν_L) and sleptons ($\tilde{e}_L$, $\tilde{e}_L$)
e_R	1	1	$+2$	electron (e_R) and selectron ($\tilde{e}_R$)
H_u	1	2	-1	higgsinos and Higgs fields
H_d	1	2	$+1$	higgsinos and Higgs fields

Table 1.3: Vector supermultiplets in the MSSM

Supermultiplet		$SU(3)_C$	$SU(2)_L$	$U(1)_Y$	particles
G^i	(i=1,. . . ,8)	8	1	0	gluon (g) and gluino ($\tilde{g}$)
W^i	(i=1,2,3)	0	3	0	W and wino ($\tilde{W}$)
B		0	0	1	B and bino ($\tilde{B}$)

do not exactly cancel anymore. The remaining corrections to the Higgs boson mass have the form

$$\Delta m^2_{\text{H, broken SUSY}} = \frac{\lambda m^2_{\text{soft}}}{16\pi^2} \ln\left(\frac{\lambda_{UV}}{m_{\text{soft}}}\right) + \dots \tag{1.29}$$

where m_{soft} is the typical mass of the superpartners. For SUSY to still solve the hierarchy problem, its value should be in the range of few TeV which is accessible by the LHC (cf. Chapter 2). There are several mechanisms to break SUSY spontaneously [85–88], resulting in extra effective interaction terms of the form

$$\mathcal{L}_{\text{soft}} = -\left(\frac{1}{2} M_a \lambda^a \lambda^a \frac{a^{ijk}}{6} \tilde{\psi}_i \tilde{\psi}_j \tilde{\psi}_k + \frac{b^{ij}}{2} \tilde{\psi}_i \tilde{\psi}_j\right) + h.c. - m^2_{i,j} \tilde{\psi}^*_i \tilde{\psi}_j, \tag{1.30}$$

where M_a are gaugino masses and a^{ijk} and b^{ij} trilinear and bilinear sfermion coupling terms, respectively, and $m^2_{i,j}$ is the sfermion mass matrix. In the case of the MSSM, the number of soft SUSY-breaking parameters is 105 including three gaugino masses and masses and effective couplings of three generations of squarks and sleptons.

1.7.2 R-Parity

In the absence of chiral interactions, the SUSY operator Q has a continuous $U(1)_{\mathrm{R}}$ symmetry, called R-symmetry, which is explicitly broken by W_{MSSM} to a discrete symmetry called R-parity defined as,

$$P_R = (-1)^{B-L+2s}, \tag{1.31}$$

where B and L are the baryon and lepton number, respectively, and s is the particle spin. Thus each SM particle has positive R-parity, $P_R = 1$, and their superpartners $P_R = -1$. The conservation of R-parity has important phenomenological consequences:

- Interactions between chiral fermions mediated by sleptons or squarks are prohibited. Superpartners can only be produced in pairs from SM particle interactions.
- The lightest supersymmetric particle (LSP) is stable. Heavy supersymmetric particles decay in cascades to SM particles and the LSP.
- SM particles cannot mix with SUSY particles [89].
- Baryon and lepton number are conserved. Thus the proton remains stable.
- The LSP is an ideal candidate for Dark Matter provided it is electrically and color neutral. Usually it is identified with the lightest neutralino $\tilde{\chi}_1^0$ [90].

However, the most general superpotential may also contain R-parity violating (RPV) terms:

$$W_{\mathrm{RPV}} = \underbrace{\lambda_{ijk}\tilde{L}_i\tilde{L}_j\tilde{e}_k^* + \lambda'_{ijk}\tilde{L}_i\tilde{Q}_j\tilde{d}_k^*}_{\Delta L=1} + \underbrace{\lambda''_{ijk}\tilde{u}_i^*\tilde{d}_j^*\tilde{d}_k^*}_{\Delta B=1} + \underbrace{\kappa_i\tilde{L}_iH_u}_{\Delta L=1}, \tag{1.32}$$

where $\lambda_{ijk}^{(\prime,\prime\prime)}$ are dimensionless Yukawa couplings and κ_i is a bilinear mass parameter [54, 89]. The RPV terms violate either lepton number ($\Delta L = 1$) or baryon number ($\Delta B = 1$) conservation. Gauge symmetries imply that λ_{ijk} and λ''_{ijk} are antisymmetric in the first two and last two indices, respectively, resulting in 48 possible extra terms (9 λ_{ijk}, 27 λ'_{ijk}, 9 λ''_{ijk} and 3 κ_i). The RPV-terms change drastically the phenomenology of the model. Especially, the LSP can decay into SM particles. If baryon and lepton number violating couplings exist simultaneously, proton decay becomes possible through the exchange of virtual squarks as illustrated in Figure 1.5. The proton decay rate

$$\Gamma_{p\to e^+\pi^0} \propto \sum_k m_{\mathrm{proton}}^5 \frac{\left|\lambda'_{11k}\lambda''_{11k}\right|^2}{m_{\tilde{q}}^4} \tag{1.33}$$

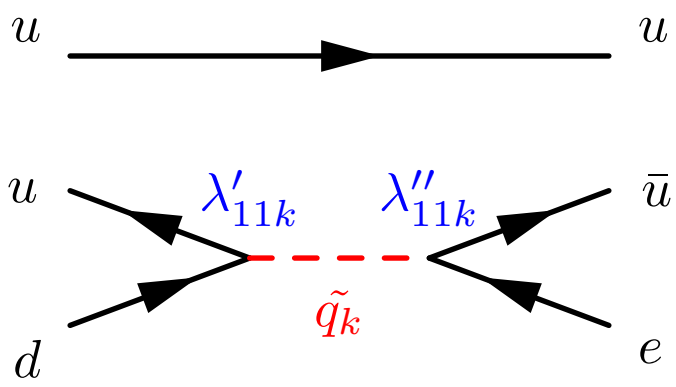

Figure 1.5: Feynman diagram of proton decay into a positron and a pion mediated by the simultaneous presence of lepton number violating λ'_{ijk} and baryon number violating λ''_{ijk} terms in the superpotential.

depends on the product of the RPV couplings λ'_{11k} and λ''_{11k} and the squark mass. From present searches at the LHC, the squark masses should be in the TeV range such that the coupling product must be extremely small to achieve a decay rate which is in accordance with current experimental limits on the proton life time of $\tau_{\text{proton}} > 10^{34}$ years [91]. R-parity conservation (RPC) is the most stringent way to prevent proton decay in supersymmetric extensions of the SM by forbidding all B and L violating couplings. But, proton decay is already prohibited if either lepton or baryon number is conserved while the other one can be violated opening a totally different phenomenology at collider experiments (cf. chapter 6.1). For instance, baryon number can be protected by imposing baryon triality symmetry [92].

1.8 Description of Proton-Proton Collisions

Experimental tests of the Standard Model require precise predictions of cross sections of the interesting processes. In the case of particle collider experiments like at the Large Hadron Collider (cf. chapter 2), the initial state consists of two colliding particles a and b with respective four-momenta $p_{a,b}$. If the incoming particles scatter inelastically, the final state can consist of an arbitrary number of particles f with four-momenta p_f forming a final state $|X\rangle$. According to Fermi's Golden Rule [2–5], the cross section of $|X\rangle$ is given by

$$\sigma_{ab\to X} = \frac{1}{4E_aE_b\,|\vec{v}_a - \vec{v}_b|} \int \prod_f \left(\frac{d^3p_f}{8\pi^3E_f}\right) |\mathcal{M}_{ab\to X}|^2\,(2\pi)^4\delta^4\left(\sum_f p_f - p_a - p_b\right). \tag{1.34}$$

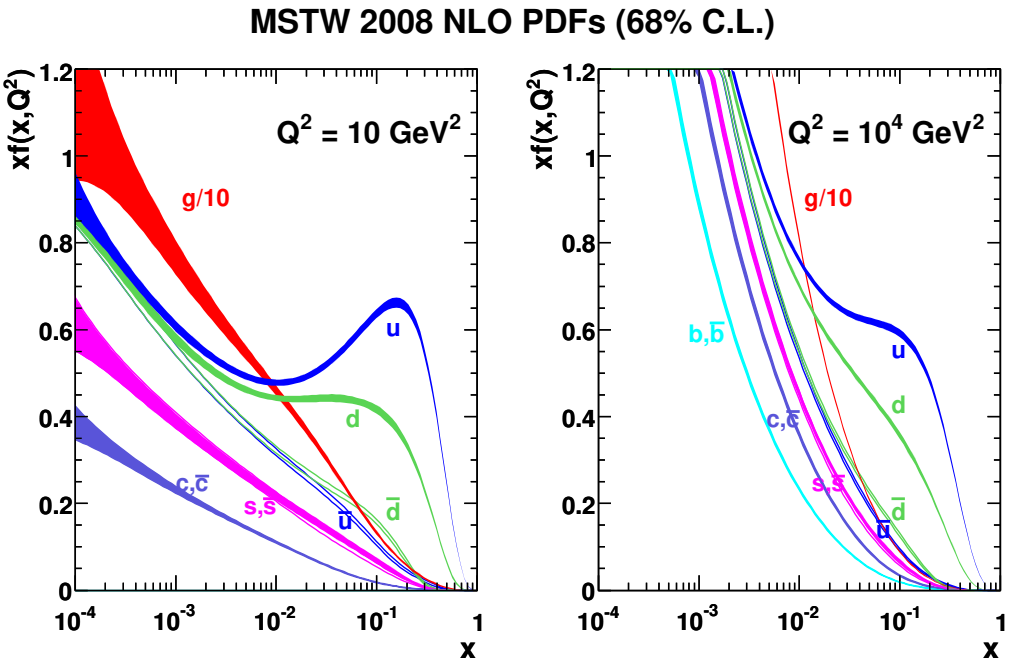

Figure 1.6: Parton density functions for low (left) and large (right) momentum transfers from inelastic proton-proton scattering [93].

The matrix element $\mathcal{M}_{ab\to X}$ comprises all possibilities allowed by conservation laws to reach $|X\rangle$. It has to be integrated over the available final-state phase-space $\left(\frac{d^3p_f}{8\pi^3E_f}\right)$ respecting energy-momentum conservation.

Typically a few hundred of particles are produced in a collision at the Large Hadron Collider (cf. chapter 2). Their production processes cover a wide range of energy scales, from the production of heavy particles, called hard scattering event, to the fragmentation of the final state quarks and gluons forming colorless hadrons which happens at rather low energies where α_s becomes large and perturbation theory breaks down. The factorization theorem allows to split the description of the processes happening at different energy scales. The hard scattering is described exploiting perturbation theory while for the fragmentation phenomenological models are employed. Both are then matched at the factorization scale μ_F [93, 94].

The collision of two composite particles, the partons, leads to an additional complication [95]. Only one parton (quark or gluon) of each proton, carrying the total proton momentum fraction of x, participates in the hard interaction. The cross section given in Equation (1.34) has to be averaged over

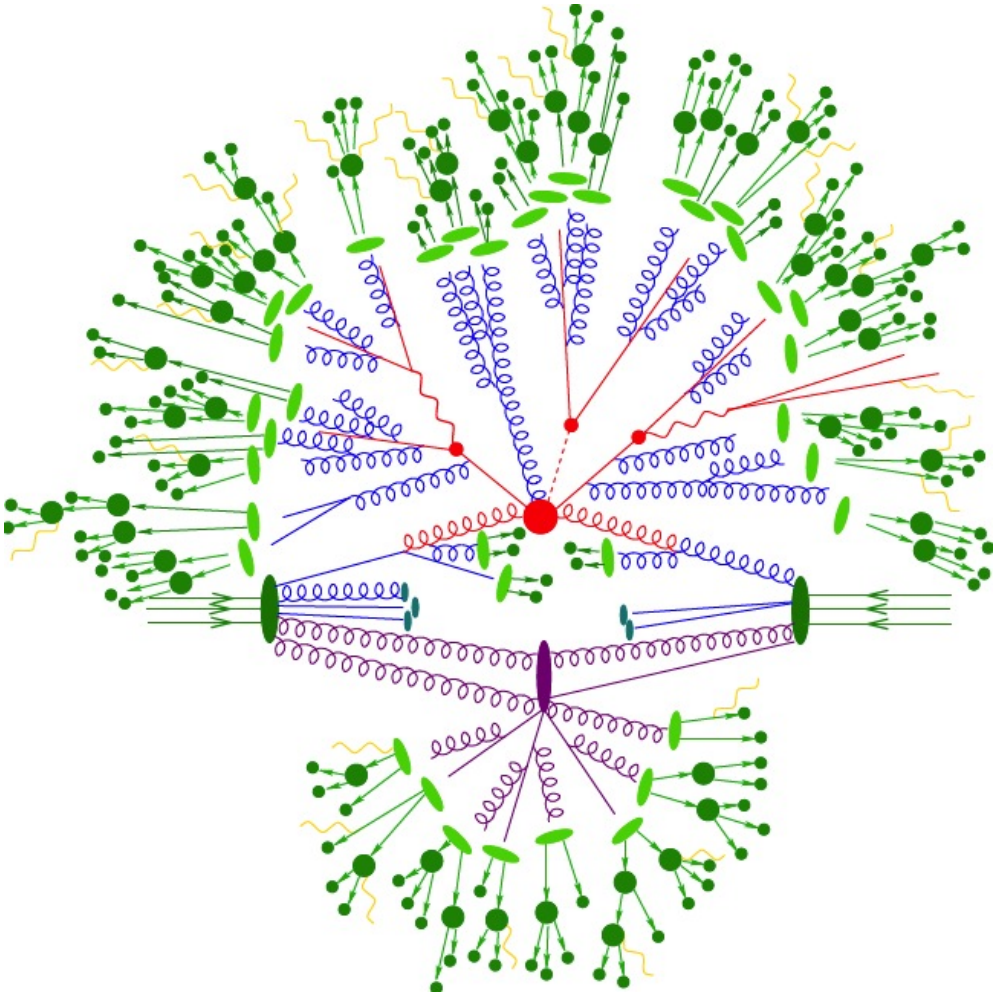

Figure 1.7: Schematic of the simulation of a pp collision [110].

all possible initial state configurations and momenta

$$\sigma_{pp\to X} = \sum_{ab} \int_0^1 dx_a dx_b f\left(x_a, \mu_F^2\right) f\left(x_b, \mu_F^2\right) \hat{\sigma}_{ab\to X}, \tag{1.35}$$

where $f\left(x, Q^2\right)$ is the parton density function (PDF) giving the probability that a parton carries the fraction x of the proton momentum for a given momentum transfer Q^2 between the colliding protons. The PDFs cannot be calculated from first principles, but have to be measured in $ep/pp/\bar{p}p$ collision data as a function of Q^2 [93, 96–105]. Their evolution in Q^2 is described by the Dokshitzer-Gribow-Lipatow-Altarelli-Parisi (DGLAP) equation [106–109]. Figure 1.6 shows the PDFs of the different parton types measured for $Q^2 = 10$ GeV^2 and their extrapolation to $Q^2 = 10^4$ GeV^2.

The wide range of energy scales of the considered processes, the large multiplicity of produced particles and the averaging over the initial-state PDFs do not allow for closed cross section formulas. Instead, the collision events are simulated by means of Monte Carlo methods. The simulations comprise the generation of events (final stats) according to the theoretical differential cross sections including the fragmentation of quarks and gluons, and the propagation of the generated particles through the detector (The detector simulation is described in chapter 3). Using the example of a $t\bar{t}H \rightarrow 3b\ell\nu jj$ event, Figure 1.7 illustrates the various aspects of the event generation which are discussed in more detail in the following.

- **Matrix element of the hard-scattering process (ME)**: The hard-scattering matrix element is evaluated in perturbation theory and then convolved with the PDFs and integrated over the phase-space using programs like Sherpa [111], MadGraph5 [112], PowHegBox [113] or aMCatNLO [114]. The occurring ultraviolet divergences in the loop diagrams in higher orders of perturbation theory are removed by a renormalization procedure which introduces a new parameter, the renormalization scale μ_R. This scale is usually chosen around the mass of produced heavy particles [96, 111–121].

- **Parton shower process**: The produced highly energetic partons radiate gluons which split into quark-antiquark pairs and soon, producing showers of secondary particles. The shower formation is described by iterative algorithms evaluating splitting kernels at each step and taking into account collinear and soft divergences. The evolved shower is then matched back to the parameters of the hard parton under the constraint of keeping the total hard-scattering cross section unchanged [117, 122–126].

- **Fragmentation and final-state radiation (FSR)**: The parton showering stops at an energy scale of O (1) GeV where the strong coupling constant becomes too large and the formation of colorless particles kicks in. The fragmentation process is modelled by phenomenological approaches with free parameters fitted to the data. Charged particles additionally radiate photons which are added in this step [127–130].

- **Multiple parton scattering and underlying event** The interactions of the remaining partons not taking part in the hard scattering process is referred to as the underlying event. At low momentum transfers and/or momentum fractions carried by the parton, multiple interactions can take place as well. These processes are also described by phenomenological models involving free parameters to be tuned [129].

The experimental cross section determination consists of counting the number of observed events N_X

for a given integrated luminosity $L = \int dt \mathcal{L}_{\text{inst}}$:

$$\sigma_{pp\to X} = \frac{N_x}{\epsilon_{\text{detector}} L}, \tag{1.36}$$

taking into account the detection efficiency, $\epsilon_{\text{detector}}$, which includes solid angle coverage, called acceptance, resolution effects and particle detection efficiencies, where $\mathcal{L}_{\text{inst}}$ is the so-called instantaneous luminosity which is discussed in chapter 2.

CHAPTER TWO

THE LARGE HADRON COLLIDER

The Large Hadron Collider (LHC) [131] is the world's largest particle accelerator, operated by the European Organization for Particle Physics (CERN). It is housed in a circular tunnel with a circumference of 26.7 km in which formerly the large electron-positron collider LEP was operated. The tunnel is located at a depth between 50–150 m crossing the border between France and Switzerland near Geneva Airport and the small town St Genis. The tunnel was drilled with an inclination of 1.4% towards the Jura mountains to ensure that all experimental caverns and the majority of the accelerator itself are surrounded by solid rock [132]. To have enough space for the acceleration cavities and to properly focus the beams at the interaction points, the tunnel has eight straight sections each around 528 m long. The four main experiments ATLAS [133], CMS [134], LHCb [135] and ALICE [136] are located in the sectors one, five, eight and two, respectively as shown in Figure 2.1. The two particle beams rotating in opposite directions are collimated by dedicated magnets in sections three and seven and accelerated by two superconducting radio frequency cavities in sector four. Finally, kicker magnets dump the beams into seven meter long graphite blocks when the collision run is terminated. The machine is designed to accelerate the proton beams up to an energy of 7 TeV and to collide them with an instantaneous luminosity of $\mathcal{L}_{\text{inst}} = 10^{34}\ \text{cm}^{-2}\text{s}^{-1}$. Operation with lead ion beams is also possible, which are collided with protons or lead ions with an energy of up to 2.76 TeV per nucleon [131].

Before injection into the LHC, the protons traverse a series of pre-accelerators as shown in Figure 2.2. The electrons are stripped from hydrogen atoms and the remaining protons which are then accelerated to 50 MeV energy in the linear accelerator, LINAC-2. Afterwards, the protons are transferred to the Proton Synchrotron Booster where the beam is split into four stacked beam pipes to form proton bunches which are accelerated to an energy of 1.4 GeV and then sent to the Proton Synchrotron where they are accelerated to an energy of 25 GeV and injected into the Super Proton Synchrotron (SPS). In the SPS, the proton bunches are accelerated to an energy of 450 GeV and are then injected into the LHC ring in clockwise or anti-clockwise direction. When the ring is completely filled with up to 2808 bunches with up to 10^{11} protons each, the beam energy is ramped up to the current maximum of 6.5 TeV. The accelerated beams collide every 25 ns at one of the four main interaction points where the

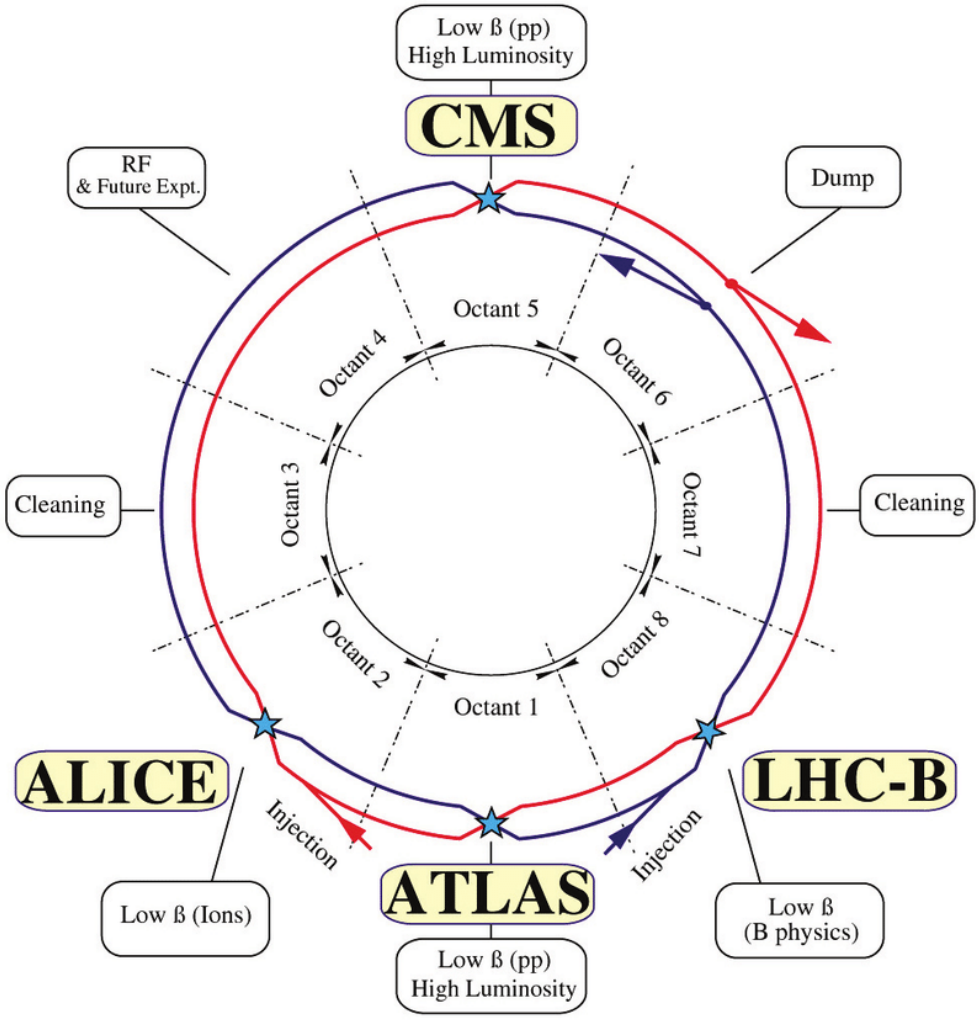

Figure 2.1: Layout of the LHC ring [131].

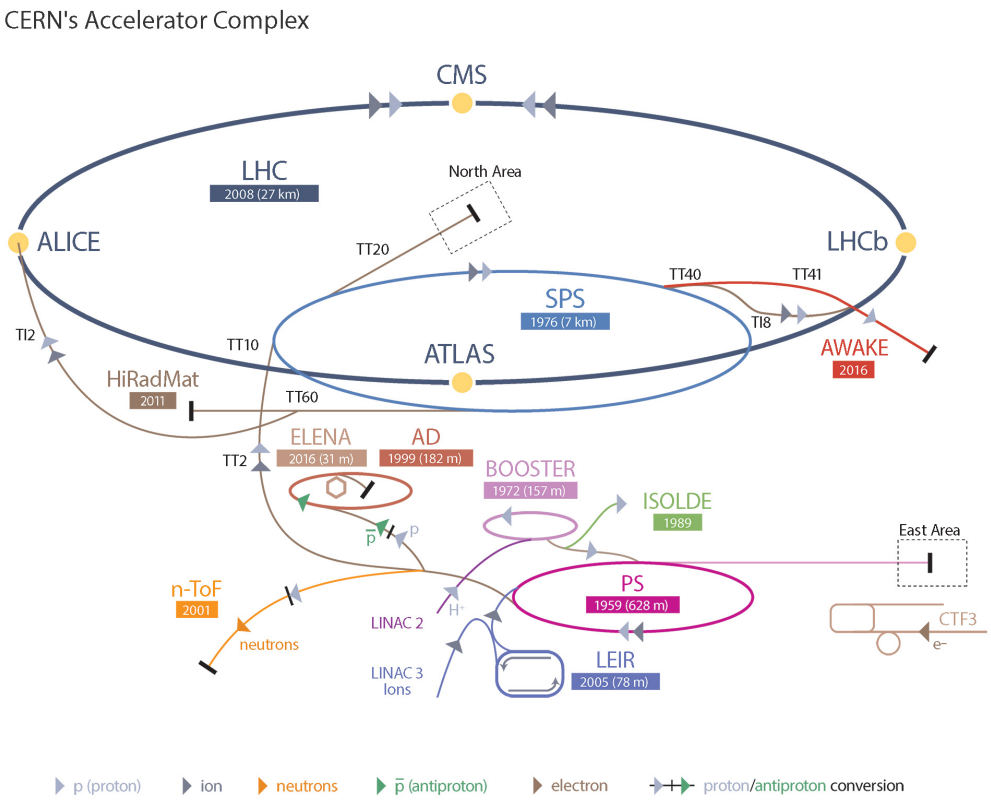

Figure 2.2: The accelerator complex of CERN [137].

experiments, ATLAS, CMS, LHCb and ALICE are located. ATLAS (cf. chapter 3) and CMS [134] are the two multi-purpose experiments, designed for the search for the Higgs boson, SM precision measurements, and for searches for new phenomena beyond the Standard Model. On July 4$^{\text{th}}$ 2012, both collaborations announced the observation of a new heavy boson at a mass of 125 GeV [32, 33], and with properties consistent with the Standard Model Higgs boson [138–146] which was the main goal of the LHC project. The LHCb experiment [135] investigates CP violation and other rare decays of charm and bottom mesons. Finally, the ALICE experiment [136] studies the properties of hot and dense nuclear matter and of the quark-gluon plasma in heavy ion collisions.

The LHC started operation in 2009 at a center-of-mass energy of $\sqrt{s}$ = 900 GeV with one year of delay caused by an incident where few of the magnets were destroyed due to faulty electrical connections [147]. In the years 2010 and 2011, the LHC was operated at center-of-mass energy $\sqrt{s}$ = 7 TeV, which was increased to $\sqrt{s}$ = 8 TeV in 2012. This completed the first data taking period of the LHC, called Run 1. In the next two years, the facility was shut down for upgrade and maintenance works. From June 2015, the collision program continued with the Run 2 of the LHC at

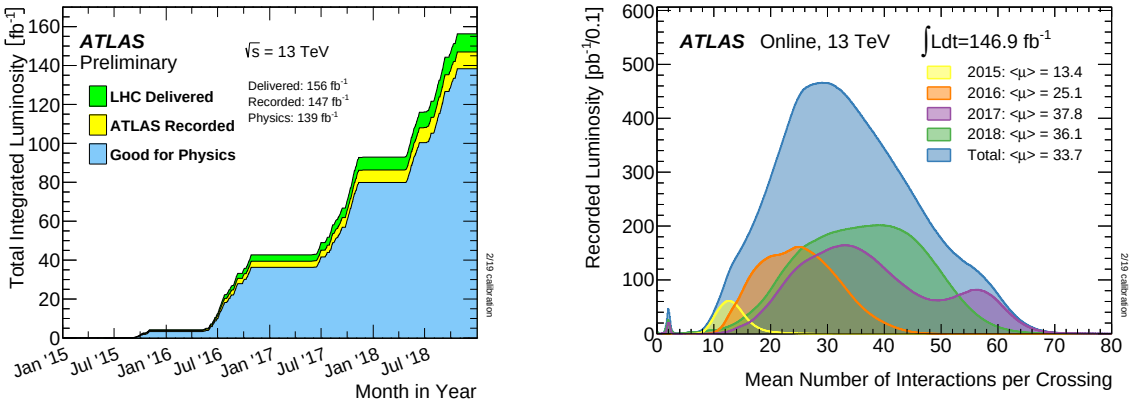

(a) (b)

Figure 2.3: Integrated luminosity versus time in Run 2 of the LHC (a) and the distribution of the average number of interactions per bunch crossing (b) for the different years of data taking with stable beams in 2015-2018 at a pp collision energy of $\sqrt{s}$ = 13 TeV [149].

an increased center-of-mass energy of $\sqrt{s}$ = 13 TeV until October 2018.

2.1 Luminosity and Pile-up

According to Equation (1.36), the expected number of events of a particular collision process is given by the product of the production cross section, $\sigma_{pp\to X}$ and of the integrated luminosity L,

$$L = \int dt \mathcal{L}_{\text{inst}}, \tag{2.1}$$

where $\mathcal{L}$ is the instantaneous luminosity which is the second main characteristic of a particle collider besides the center-of-mass energy. The rare processes studied at the LHC have cross sections on the order of pico to femto barns [39]. Thus large instantaneous luminosity is required to record enough data on a reasonable time scale. The instantaneous luminosity of a circular collider depends on the number of proton bunches, n_b in each beam, the number of protons per bunch, N_p, the revolution frequency, f, and the transverse beam spread, $\sigma^*_{x(y)}$, at the interaction point [148]:

$$\mathcal{L} = \frac{N_p^2 n_b f}{4\pi \sigma_x^* \sigma_y^*} F. \tag{2.2}$$

The factor F describes the geometric effect of a finite crossing angle on the luminosity. The collected luminosity in Run 2 is shown in Figure 2.3(a). In total, 147 fb^{-1} of data were recorded by ATLAS of

which 139 fb^{-1} passed the quality criteria of stable detector and beam conditions suitable for physics analysis [149]. The dataset of the first two years, 2015 and 2016, of 36.1 fb^{-1} is referred to as the early Run 2 data in this thesis. The maximum achieved instantaneous luminosity of $2.1 \cdot 10^{-34}$ cm^{-2}s^{-1} exceeded the LHC design value by a factor of two.

To achieve such high instantaneous luminosity values the beams have to be very strongly focused at the interaction points increasing the number of multiple proton-proton interactions per bunch crossing, causing the effect called event pile-up in the experiment. The number of pp interactions per bunch crossing, N_{bx}, can be estimated from the total inelastic proton-proton cross section, $\sigma_{\text{inelastic}}$, and from the instantaneous luminosity in Equation (2.2):

$$N_{bx} = \frac{\sigma_{\text{inelastic}}\mathcal{L}}{f n_b} = \frac{N_p^2 \sigma_{\text{inelastic}}}{4\pi\sigma_x^*\sigma_y^*}. \tag{2.3}$$

If the time resolution of the detector components is much larger than the bunch crossing time, collisions from adjacent beam crossings may overlay with the currently recorded event, an effect called *off-time* pile-up [150]. The pile-up was on average 33.2 interactions per bunch crossing and strongly varied from about 10–70 during the Run 2 data taking depending on the instantaneous luminosity (cf. Figure 2.3(b)). The unexpectedly large pile-up post severe challenges for the particle reconstruction software which will be discussed in Section 3.7.

2.2 The Worldwide Computing Grid

The four main LHC experiments produce a huge amount of data. For instance, the ATLAS experiment recorded up to 1500 events per second with an average size of 1.6 MB each during Run 2 (cf. Section 3.5 for a detailed discussion of the ATLAS data acquisition). To process and store such an amount of data, an unprecedentedly large computing infrastructure is required which could not be provided by CERN alone anymore. The Worldwide LHC computing grid (WLCG) was therefore created, a network of more than 170 high-performance computing centers in 72 countries around the world which provided the required computing resources [151, 152]. The centers are organized in Tiers as depicted in Figure 2.4.

The data of the experiments are sent to one of the two Tier-0 computing centers, one located at CERN and the other one in Budapest, to archive them and to run the initial event reconstruction and calibration. From the Tier-0 centers, the data are distributed to one of the 14 Tier-1 computing centers funded by the national particle physics communities, where backup copies are stored. At the Tier 1 sites, the full physics object reconstruction is performed (cf. Section 3.7), smaller derived datasets are created and distributed to the 170 Tier-2 computing centers which provide the infrastructure in

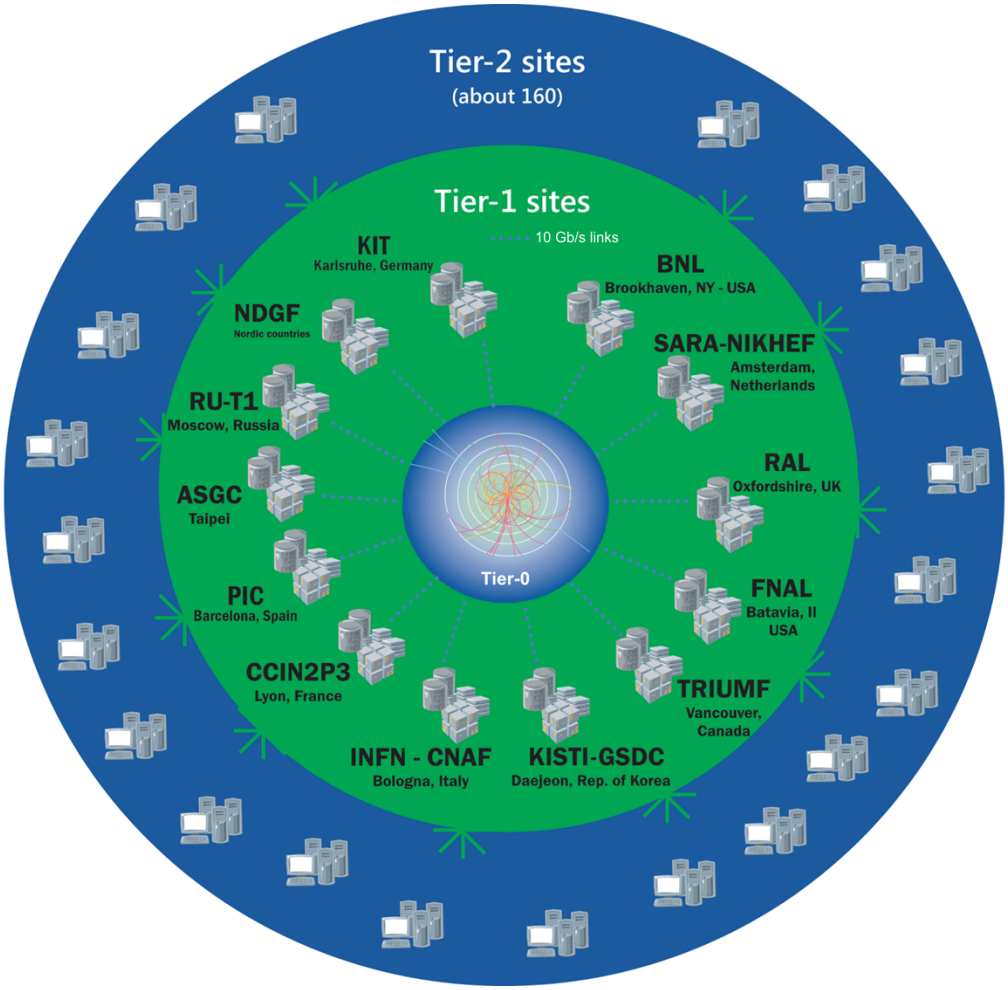

Figure 2.4: Computing structure of the WLCG [152].

the participating countries for data analysis and Monte-Carlo simulation. For long-term storage, data are sent back to the Tier-1 sites. The final layer of the WLCG are the Tier-3 sites, which are local computing clusters at the participating institutes and universities providing the access to the data for the 10000 LHC physicists distributed around the world. The WLCG stores currently more than 220 PB of simulated and recorded data and provides more than 450.000 CPUs for data-processing and analysis [153].

CHAPTER THREE

THE ATLAS EXPERIMENT AT THE LARGE HADRON COLLIDER

ATLAS (A Toroidal LHC ApparatuS) is the largest of the four main LHC experiments, located close to the CERN main site in Meryin near Geneva in Switzerland. It has a length of 44 m, a diameter of 25 m and a mass of about 7000 tons [133]. The ATLAS detector, illustrated in Figure 3.1, is cylindrical in shape with forward-backward symmetry with respect to the interaction point and covers almost the full solid angle. In the central region, called the barrel region, the detector elements are arranged in concentric cylinders while in the two endcap regions, the detectors are mounted on discs perpendicular to the beam axis. ATLAS consists of three main subsystems, the Inner Detector (ID), the Calorimeter System, and the Muon Spectrometer (MS). Two independent superconducting magnet systems provide the ID and the MS with a magnetic field.

3.1 Coordinate System

ATLAS uses a right-handed coordinate system with origin at the nominal interaction point. The z-axis points along the direction of the beam pipe, the x-axis points towards the center of the LHC ring and the y-axis points upwards. In the data analysis, spherical polar coordinates are used, where the polar angle, θ, is measured from the positive z-axis and the azimuthal angle, ϕ, in the transverse x–y plane with respect to the positive x-axis. The rapidity of a particle, y, is defined as

$$y = \frac{1}{2}\ln\frac{E + p_z}{E - p_z}, \tag{3.1}$$

which is equivalent to the pseudorapidity

$$\eta = -\ln\left(\tan\frac{\theta}{2}\right) \tag{3.2}$$

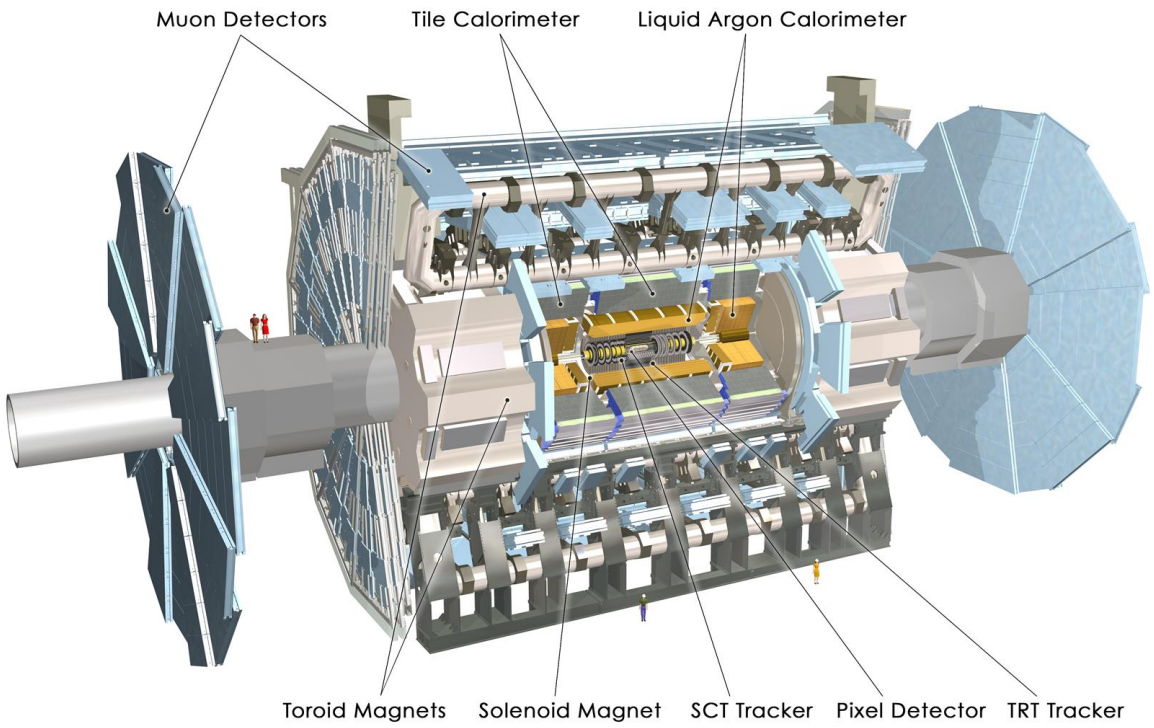

Figure 3.1: Cut-away view of the ATLAS detector [133].

in the ultra relativistic limit or for massless particles. The Lorentz invariant angular separations, ΔR and ΔR_y between two particles in the η–ϕ and in the y–ϕ plane, respectively, are defined as

$$\Delta R = \sqrt{(\eta_2 - \eta_1)^2 + (\phi_2 - \phi_1)^2} \tag{3.3}$$

and

$$\Delta R_y = \sqrt{(y_2 - y_1)^2 + (\phi_2 - \phi_1)^2}. \tag{3.4}$$

The transverse momentum, p_{T}, of a particle perpendicular to the beam axis is defined as

$$p_{\mathrm{T}} = \sqrt{p_x^2 + p_y^2} = \frac{|p|}{\cosh \eta} \tag{3.5}$$

and the transverse energy as

$$E_{\mathrm{T}} = \frac{E}{\cosh \eta}. \tag{3.6}$$

The distances of closest approach of charged particle tracks to the nominal interaction point or to a reconstructed vertex in the transverse plane and in the longitudinal direction are referred to as impact parameters d_0 and z_0, respectively.

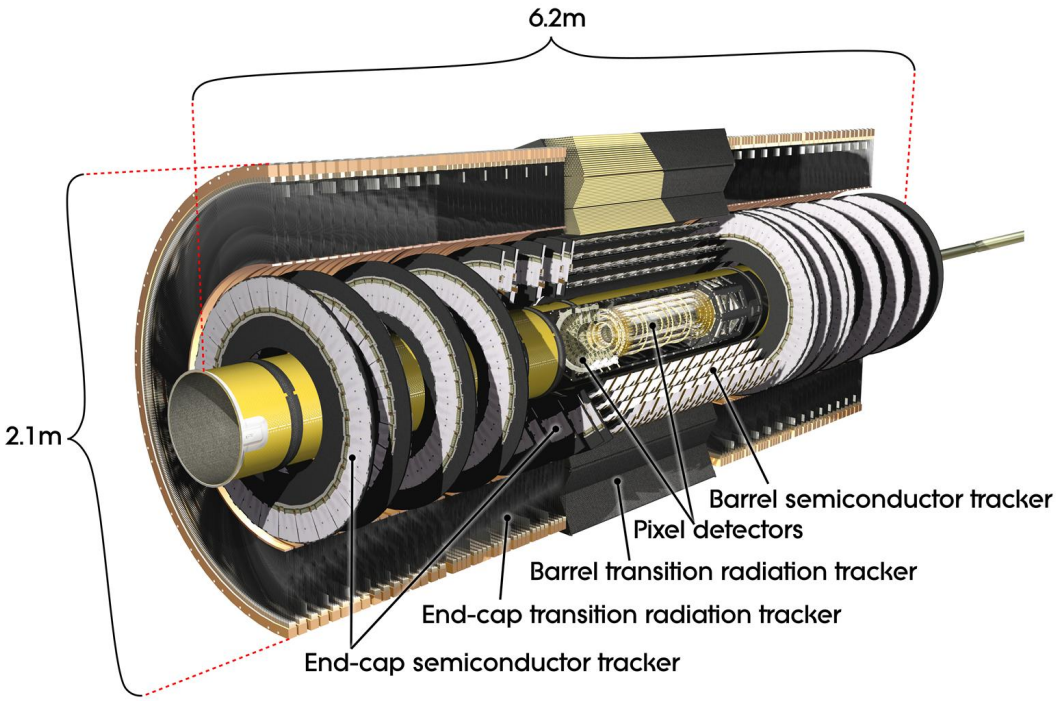

Figure 3.2: Cut-away view of the Inner Detector of ATLAS [133].

3.2 The Inner Detector

The Inner Detector (ID) is the first detector subsystem traversed by particles produced in the beam collisions. It is immersed in a 2 T solenoidal magnetic field oriented parallel to the z-axis and generated by a cylindrical superconducting coil. The ID covers the pseudorapidity region of $|\eta| < 2.5$ and measures the trajectories of charged particles curved in the magnetic field in order to determine the particle momenta. The tracks are extrapolated to the beam pipe to reconstruct the primary and pile-up collision vertices as well as secondary vertices from decays of long-lived particles like b-hadrons or τ leptons. An illustration of the ID is shown in Figure 3.2. It is divided into three subsystems, the pixel detector, the semi-conductor tracker (SCT) and the transition radiation tracker (TRT), described below [154–158].

3.2.1 The Pixel Detector

The pixel detector is the innermost part of the ID. It consists of silicon pixel sensors with high granularity, which is crucial to reconstruct the interaction and decay vertices with high precision. In

the barrel region, the pixel sensors are arranged in three concentric cylinders at radii of 51, 89 and 123 mm. In each endcap region, the pixel detectors are arranged in three discs, mounted at distances along z of ±495, ±580 and ±650 mm from the nominal interaction point. The pixel detector has 80 million pixels with a size of 50×400 μm each. The pixel detectors have a spatial resolution of 14 μm in the transverse plane and of 115 μm in the longitudinal direction. The pixel detector covers a pseudorapidity range of $|\eta| < 2.5$.

During the first long shutdown of the LHC, an additional pixel detector layer, the so-called insertable B-layer (IBL) [156, 157], was installed at a distance of 3.3 cm from the beam line. This adds another measurement to the tracks of the charged particles close to the interaction point, improving vertex reconstruction resolution and efficiency, especially for high levels of pile-up. b-jet tagging and τ lepton reconstruction are in particular benefiting from the IBL (cf. Section 3.7). The IBL consists of 14 staves of pixel sensors, each 64 cm long and 2 cm wide. The pixels have a size of 50 μm $\times$ 250 μm in the transverse and longitudinal direction, respectively. In order to cover the full azimuthal angle, the staves are tilted by 14° with respect to the tangential plane. The IBL covers the range $|\eta| < 2.9$.

3.2.2 The Semiconductor Tracker

The next subsystem traversed by outgoing particles is the semi-conductor tracker (SCT). It consists of four concentric cylinders in the barrel and nine discs in each endcap, equipped with silicon microstrip detectors [154, 155]. Each module is composed of strip sensors glued together back to back with a stereo angle of 40 mrad to determine the hit position also in the longitudinal coordinate. The barrel cylinders have radii of 299, 371, 443 and 514 mm. The endcap discs have distances from the origin between 853 mm and 2.72 m. The SCT measures hits with a resolution of 17 μm in the R–ϕ plane and of 580 μm in the non-bending direction [133] which allows for precise tracking in dense particle environment.

3.2.3 The Transition Radiation Tracker

The SCT is surrounded by the transition radiation tracker (TRT) which covers a smaller pseudorapidity range of $|\eta| < 2.0$ [158]. The TRT is made of straw drift tubes made of Kapton with a diameter of 4 mm which are filled with a $Xe/CO_2/O_2$ gas mixture. In the center of each straw there is a 30 μm diameter gold-plated tungsten anode wire. The straws in the barrel are 144 cm long and aligned parallel to the beam pipe while the straws in the endcaps are orientated radially and about 2 cm long. The position of hits of charged particles are measured with a precision of 130 μm per straw in the R–ϕ plane. The space between the straws is filled with carbon radiator material. Traversing electrons

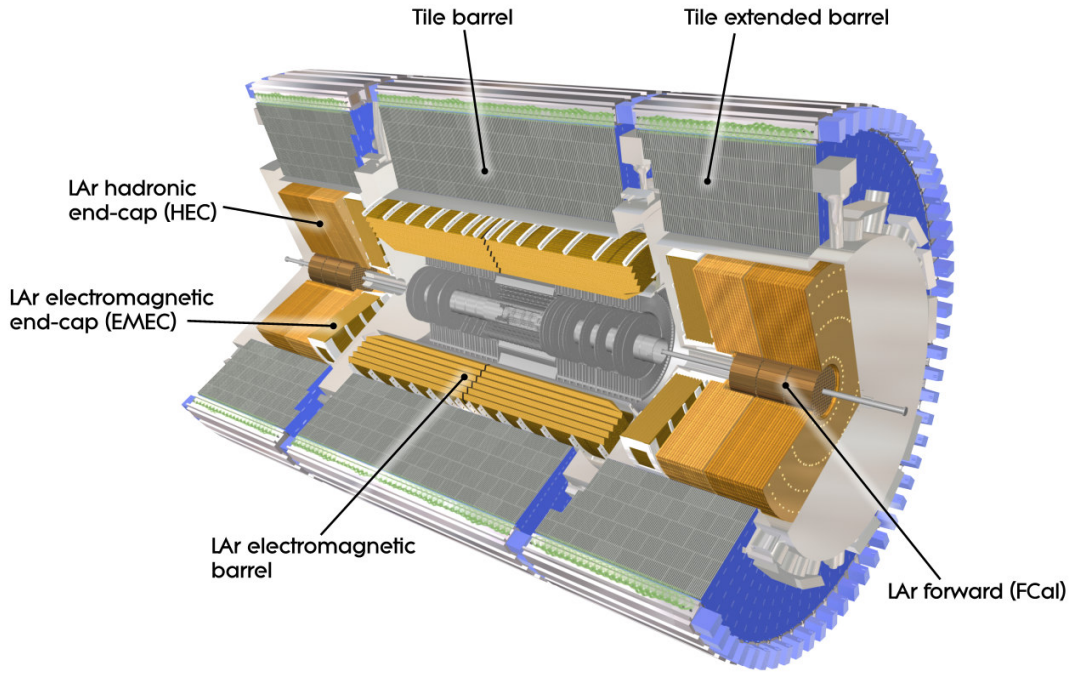

Figure 3.3: Illustration of the ATLAS calorimeter system [133].

emit transition radiation that is detected by the straw tubes allowing for additional identification of electrons (cf. Section 3.7.3).

3.3 The Calorimeter System

After having traversed the ID, the emerging particles enter the ATLAS calorimeter system shown in Figure 3.3. The calorimeter covers a pseudorapidity range of $|\eta| < 4.9$ and is divided into three main subsystems, the electromagnetic calorimeter, the hadronic calorimeter and the forward calorimeter [133, 159–162]. Electrons, photons and hadrons are interact in high-density absorber plates and their deposited energies in the form of secondary particles are measured in the active material in between. In addition, the calorimeters trigger events with highly energetic jets, electrons or photons, as well as events with large amounts of missing transverse momentum using reduced granularity of the readout electronics (cf. Section 3.7).

3.3.1 The Electromagnetic Calorimeter

The electromagnetic (EM) calorimeter is a sampling calorimeter consisting of alternating layers of accordion-shaped lead absorber plates and Kapton electrodes immersed in liquid argon as active medium. The electromagnetic showers produced in the absorber plates ionize the liquid argon in the gaps between them. The detector is segmented into three concentric layers with radially decreasing readout granularity and divided into a barrel part ($|\eta| < 1.475$) with a thickness of more than 22 interaction lengths and two endcaps ($1.375 < |\eta| < 3.2$) with a thickness of more than 24 interaction lengths. A presampling detector is installed in front of the innermost layer in the range $|\eta| < 1.8$ in the same cryostat as the solenoid magnet of the ID allowing for corrections for energy losses in the detector material upstream, especially in the solenoid coil. Due to the large space constraints, the EM calorimeter shares the same vessel with the Solenoid magnet. The $\Delta\eta \times \Delta\phi$ granularity of the calorimeter depends on the particular layer and the pseudorapidity range. In the second radial layer, where electrons deposit most of their energy, the granularity is 0.025×0.025 and 0.1×0.1 for $|\eta| < 2.5$ and $2.5 < |\eta| < 3.2$, respectively.

3.3.2 The Hadronic Calorimeter

The EM calorimeter is surrounded by the hadronic calorimeter system. Its purpose is to stop hadrons after they traversed the EM calorimeter and measure their energy. The hadronic calorimeter consists of a scintillating tile calorimeter in the barrel ($|\eta| < 1.7$) and of two liquid argon sampling endcap calorimeters in each endcap ($1.5 < |\eta| < 3.2$).

The tile calorimeter is made of alternating layers of steel absorber plates and scintillator tiles oriented perpendicular to the beam. It is subdivided into three, a 5.8 m long central part and two extensions at each side of 2.6 m length each. In radial distance, the barrels range between 2.28 m to 4.28 m. Each barrel is segmented into 64 modules in ϕ and three radial layers. At $|\eta| \sim 0$, the tile calorimeter has a thickness of 9.7 interaction lengths. The tiles are read out by two wavelength shifting optical fibres each coupled to photomultiplier tubes.

The two hadronic endcap calorimeters are located behind the EM calorimeter endcaps and use liquid argon as active material and copper plates as absorber. Each endcap consists of two wheels segmented into 32 ϕ-sectors and two sectors in the longitudinal direction. The inner wheel is with 24 layers liquid argon gaps more granular than the outer wheel which consists of 16 liquid argon gaps. The size of the readout cells is $\Delta\phi \times \Delta\eta = 0.1 \times 0.1$ for $|\eta| < 2.5$ and 0.2×0.2 for the remaining η-range.

3.3.3 The Forward Calorimeter

The two forward calorimeters (FCal) cover a pseudorapidity range of $3.1 < |\eta| < 4.9$. Each consists of three cylindrical modules. The inner module is made of a copper absorber with liquid argon holes filled which is optimized for EM calorimetry. The other two modules are designed for hadronic calorimetry and use tungsten as an absorber with holes filled with liquid argon as active material [133]. The FCal, HEC and the endcap ECal share the same cryostat.

3.4 The Muon Spectrometer

The Muon Spectrometer (MS), shown in Figure 3.4(a), is the outermost subsystem of ATLAS covering a pseudorapidity range of $|\eta| < 2.7$ [133, 163]. It measures with high precision the momenta of muons, which traverse the calorimeters only depositing small fractions of their energy and provides a first-level muon trigger (cf. Section 3.5). One barrel and two endcap superconducting magnet systems generate toroidal magnetic fields with average field strengths of 0.5 T and 1 T, respectively which bend the trajectories of the muons in the η-direction. Each magnet systems consists of eight superconducting coils arranged symmetrically in ϕ around the beam axis. The superconducting wires are an aluminium stabilised Nb/Ti/Cu alloy and are operated at a temperature of 40 K to sustain an electric current of 20.000 A. The barrel coils measure about 25 m in length and about 6 m in height. Three layers of rectangular muon chambers are mounted on the barrel coils, arranged in 16 ϕ sectors (cf. Figure 3.4(b)). Large and small-sector chambers alternate with partial overlap in ϕ allowing for relative alignment using straight muon tracks in the R–ϕ projection. The precision tracking chambers measure the crossing point of a muon track with 30–40 μm precision in the bending direction. The associated trigger chambers provide fast signals used by the first-level trigger. Monitored Drift Tube (MDT) chambers are used for precision tracking and Resistive Plate Chambers (RPC) for triggering. The eight coils in each of the endcaps are about 5 m long and 4.5 m in height embedded in a single cryostat. The trapezoidal-shaped muon chambers are mounted perpendicular to the beam axis on three large endcaps wheels with radii of about 7 and 11 m. The small wheels are mounted directly behind the FCal and in front of the endcap toroids, the middle big wheels are located at the ends of the barrel coils and the outer wheels are mounted to the cavern wall. The chambers are arranged in eight small and eight large ϕ sectors, which overlap. MDT chambers are used for high precision tracking, except in the most inner ring of the small wheel ($|\eta| > 2.$), where the high background rates require the use of Cathode Strip Chambers (CSC). Thin Gap Chambers (TGC) in the inner and middle layer are used for triggering covering the pseudorapidity range $|\eta| < 2.4$.

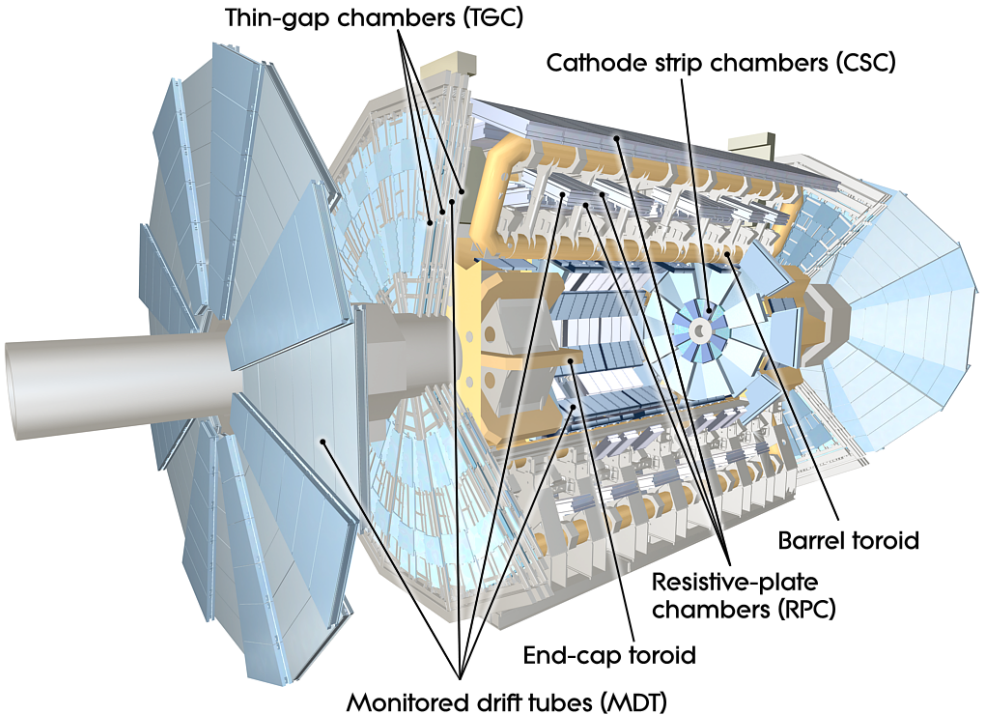

(a)

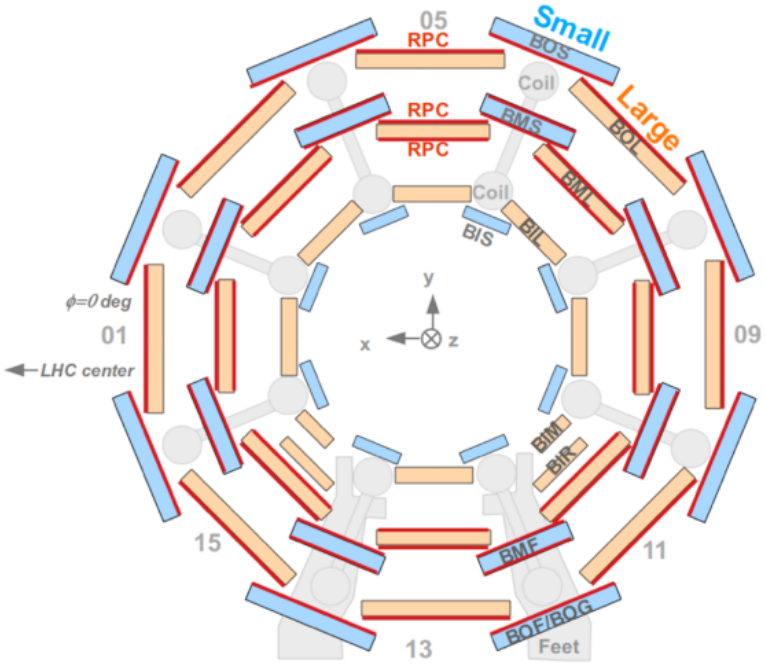

(b)

Figure 3.4: The ATLAS muon spectrometer with its air-core toroid magnets(a) and a cross section of the barrel spectrometer to illustrate the arrangement of the muon chambers in the large and small sectors [133, 164].

3.4.1 Precision Muon Tacking Chambers

Monitored Drift Tube (MDT) chambers form the majority of precision muon tracking chambers in ATLAS. They consist of six or eight layers of aluminium drift tubes with 30 mm diameter in two equal multilayers separated by an aluminium spacer frame. The tubes are filled with Ar/CO_2 (93/7) gas mixture and have a gold-plated tungsten-rhenium anode wire in the center which is at a potential of 3080 V relative to the tube wall. Traversing muons ionize the argon gas in the tubes. The electron-ion pairs are separated by the radial electric field. The primary ionizing electrons drift towards the wire with a maximum drift time from the tube wall of about 780 ns. The chambers are equipped with temperature sensors used for corrections to the space-to-drift time relation [165] and with an optical alignment system for the monitoring of mechanical deformations of the chambers under their own weight and due to temperature gradients. The spatial resolution of a MDT drift tube is 80 μm and the resolution of a six-layer chamber is 35 μm [165]. In the small bottom sectors of the barrel spectrometer, small-diameter drift tube (sMDT) chambers with 15 mm tube diameter are used which fit the small space inside the detector feet [166, 167].

Cathode Strip Chambers (CSC) are used in the the inner endcap layer for $|\eta| > 2$, where the background radiation rates are highest exceeding the rate capability of the MDT chambers. The CSCs are multi-wire proportional chambers with segmented-cathode readout. 16 CSC chambers are installed in each endcap forming projective towers with the MDTs in the middle and outer endcap layers. Each chamber consists of four layers of radially oriented anode wires each accompanied by two cathode layers with strips oriented parallel and perpendicular to the wires, respectively, providing the ϕ and η coordinates. The crossing point of the muon track is determined by interpolation between two neighbouring strips weighted with the induced charges resulting in a spatial resolution per layer of 60 μm [133].

The precision chambers are mounted in the MS with an accuracy of a few millimeters. However, the relative positions of the chambers in a tracking tower have to be known with an accuracy of 50 μm in order to achieve the required momentum resolution at high $p_T \simeq 1$ TeV. Therefore, the chambers are connected by an optical alignment system which measures the movements of the precision chambers with few μm precision during the data taking. The absolute values of the relative chamber positions are determined once per year using straight muon tracks while the toroid magnet is turned off.

3.4.2 Muon Trigger Chambers

The MDT chambers provide excellent spatial resolution, but their readout takes up to 780 ns. Thus they are too slow to detect the bunch crossing to which the muon belongs. They also only measure

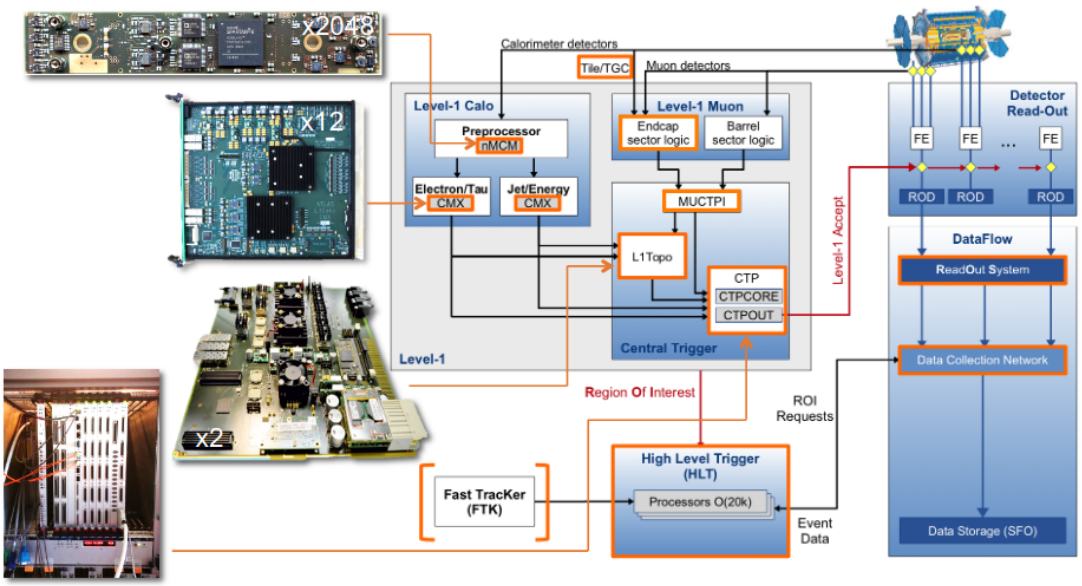

Figure 3.5: The ATLAS trigger system in Run 2 [168].

the η coordinate of the muons. Therefore, the precision chambers are complemented by fast trigger chambers which measure the second coordinate of the traversing muon, trigger the event, and identify the bunch crossing, and define regions-of-interest for the fast muon track reconstruction.

Resistive Plate Chambers (RPC) are installed in the middle and outer layers of the barrel MS (illustrated by the red bars in Figure 3.4(b)). They consist of high-pressure phenolic laminate electrode plates separated by a 2 mm wide gas gap over which a high voltage of 10 kV is applied. On either side of the gas gap, strip electrodes with orthogonal strip orientation for the η and ϕ coordinates are mounted to read out the induced signals of the avalanches created by the traversing muons in the gas gap with a time resolution of 5 ns.

Thin Gap Chambers (TGC) are installed as trigger chambers in the inner and middle layers of the endcaps. They are multi-wire proportional chambers with wires placed in a thin gas gap between two parallel resistive plates. Readout strip panels are glued to the outside of the cathode plates. Seven layers of readout panels are combined to measure the azimuthal angle of the track with a precision of 3 mrad providing a time resolution of <25 ns. Unlike the precision tracking chambers, they are arranged in 12 equal-sized ϕ-sectors without overlaps.

3.5 The Trigger System

At the LHC, the proton bunch crossing frequency is 40 MHz. Given that one event on average requires 1.6 MB of storage, about 40 TB of data had need to be recorded per second if every event were accepted which by far exceeds the computing and storage capacities of the WLCG. Most of the collision events are due to low-energy inelastic pp interactions and are hence not of interest for physics analysis. Thus, a highly selective trigger system is needed to reduce the total event rate to manageable levels while keeping most of the interesting events containing heavy SM particles, like the W/Z bosons, the top quark, the Higgs boson or new heavy particles produced in the collisions. During the Run 2 data taking, the ATLAS trigger system selected events in two stages (cf. the logic diagram in Figure 3.5), one hardware-based stage called Level 1 (L1) and one software-based stage called, High-Level-Trigger (HLT) [168–173].

The L1 trigger is implemented in the readout electronics of the calorimeters and of the muon trigger chambers. Highly energetic muons are selected by requiring spatial and temporal coincidence of hits in two consecutive or all three trigger chamber layers of the MS. In the calorimeter, the energies of the readout cells are summed up with reduced granularity to form topological clusters to detect energy deposits from energetic electrons, photons, and τ leptons or to identify a large imbalance in the transverse momentum. In both cases, the electronics defines regions of interest (RoI) around the trigger signals and sends the information for accepted events to the central trigger processor (CTP). Fast tracking algorithms in the ID supplement the information based on which the CTP accepts events at a rate of 100 kHz.

The accepted data is then sent to the second level of the ATLAS trigger, the HLT. The events are fully reconstructed in the RoIs and minimal kinematic and quality criteria are applied to the trigger objects using up to 40.000 CPUs. Certain event topologies like the Higgs boson produced via vector-boson fusion with two energetic jets in the forward directions are also selected. Events accepted by the HLT are sent to the WLCG at a rate of about 1.5 kHz. This bandwidth has to be shared by all triggers. Since the rate of individual triggers strongly depends on the instantaneous luminosity, triggers exceeding their rate limits are pre-scaled during data-taking at the L1 or the HLT stage, i.e. that only every i-th event from this particular trigger is actually written to the disk and reconstructed.

3.6 The ATLAS Detector Simulation

Monte Carlo simulations are the most fundamental tool in high energy physics to compare theoretical predictions of the SM to data. Further, they allow to understand the behaviour or the performance of each detector module and thus how the electrical signals are eventually reconstructed to physics objects,

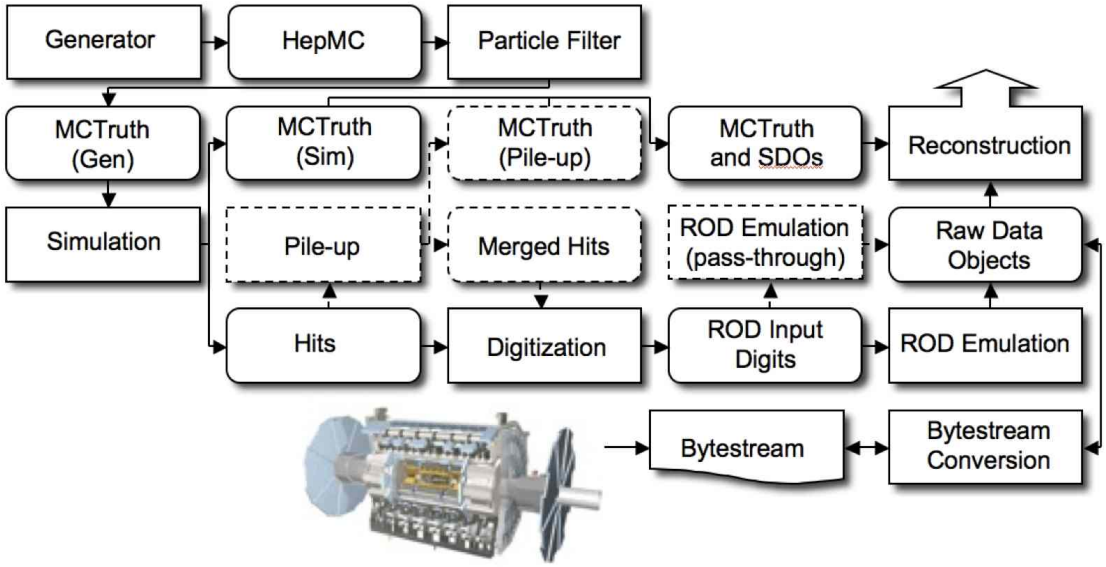

Figure 3.6: Workflow of the simulation framework and data processing in ATLAS [174].

like electrons or muons. Finally, their information forms the basis to develop algorithms separating e.g. a prompt electron from a quark jet leaving a similar signature in the detector. In ATLAS the simulation of collision events can be categorized into four big steps as illustrated in Figure 3.6: the event generation, describing the *pp* collision itself, the propagation of the produced particles through the detector system and its response to their energy deposits, called detector simulation, the processing of the simulated signals by the detector electronics, called digitization and finally the reconstruction of particles from the simulated electronic signals.

In the event generation step, the four-momenta as well as their potential decay chain of particles produced in the *pp* collisions are generated. This step is already described in full detail in section 1.8.

The generated particles propagate through the detector in the detector simulation. The interactions of the particles with the active sensors, the passive detector material, as well as their deflection in the magnetic field, are simulated in detail using the Geant4 toolkit [175, 176]. Two varieties of the ATLAS detector simulation are commonly used. The ATLAS detector simulation is using a full detector model in Geant4 (the so-called *full simulation*). However, most of the computing time is actually spent for the showering of the particles inside the calorimeters. Where the loss in precision is affordable, a parametrized model for the calorimeter response to electrons, photons and pions is used instead which is referred to as *fast simulation* [177].

After the detector simulation, additional simulated pile-up and soft proton interactions are added to the event. Then the merged hits are parsed to the digitization step which converts the simulated

energy deposition obtained from Geant4 into detector readout signals, taking into account the detector physics and modelling of the electronics response. Finally, these readout signals are piped to the reconstruction step (cf. Section 3.7) where the same algorithms are exploited as for the real recorded data. Additionally information about the corresponding generator-level particles causing the hits is added to the particles as well. All data is then saved to ROOT [178] files in the ATLAS event-data model (AOD) format [179].

3.7 Particle Identification with the ATLAS Detector

The correct and efficient reconstruction and identification of particles is the basis for all physics analyses. The identification is based on different interaction properties of each particle with the subsystems as nicely illustrated in Figure 3.7. Hadrons interact with the full calorimeter system, creating broad showers of secondary particles, while electrons and photons interact mainly with the EM calorimeter with similar narrower showers. Additional information from the ID classifies whether the showers belong to charged particles or not. Muons are reconstructed using mainly information from the MS and the ID. Finally, neutrinos do not interact with the detector at all leading to an imbalance of the total transverse momentum. The following section describes the algorithms to reconstruct ID tracks, electrons, photons, jets and τs. The muon reconstruction will be discussed in more detail in chapter 4. After the early Run 2 data-taking, some of the algorithms have been revised providing a better performance in terms of efficiency and rejection of falsely identified particles, commonly referred to as fakes. The 2015–2016 dataset has then been reprocessed using the updated ATLAS reconstruction software.

3.7.1 Charged Particle Tracks and Vertices

Trajectories of charged particles are reconstructed in the ID exploiting their deflection in the magnetic field. Two strategies are employed [181–184]: The *inside-out* and the *outside-in* strategy. In the first approach, track reconstruction is seeded from clusters of hits in the Pixel Detector and in the SCT. Hits in outer layers are added guided by a combinatorial Kalman filter [185]. The ambiguities of tracks sharing hits or badly reconstructed tracks are removed in the ambiguity resolving step based on the numbers of missing vs. expected hits, along the track and by exploiting a neural network to separate merged hits from two close-by energetic tracks [186]. Surviving track candidates are extrapolated to the TRT.

In the outside-in strategy, the track reconstruction starts from hits in the TRT. Tracks suffering from large energy losses due bremsstrahlung or from secondary displaced interaction vertices are

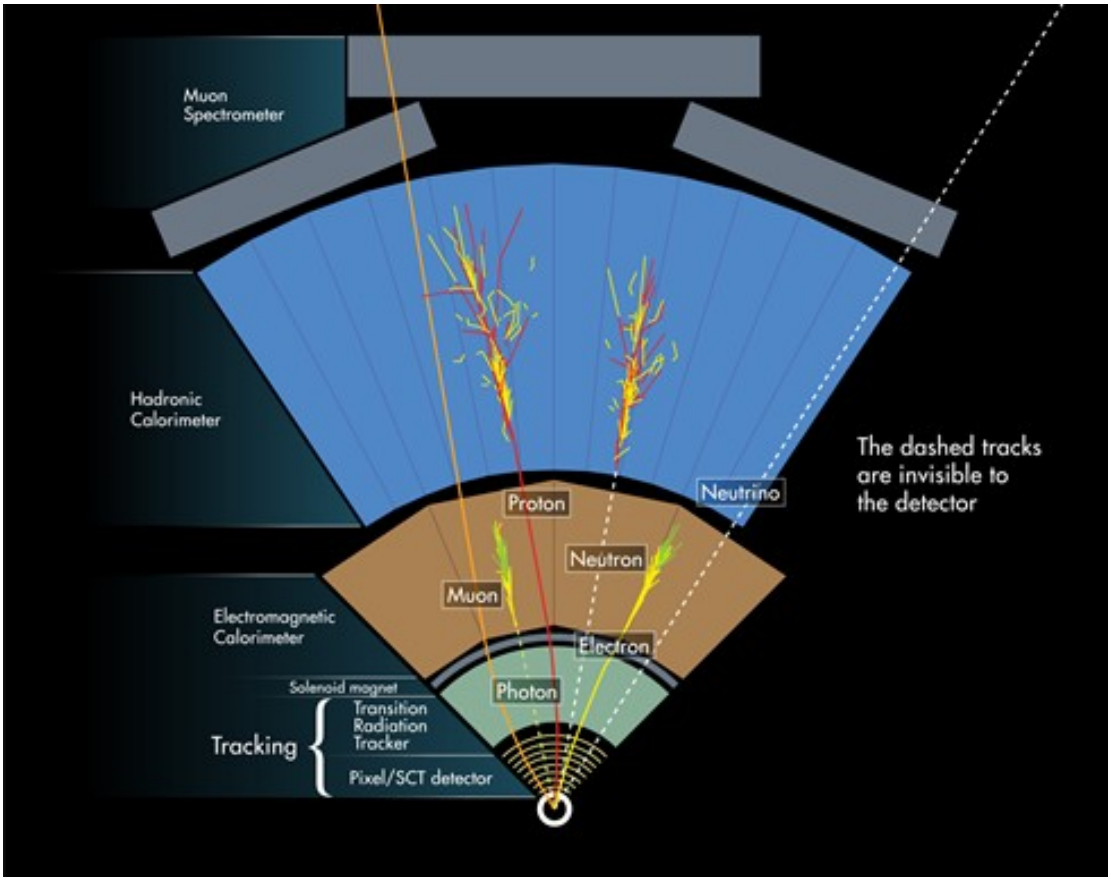

Figure 3.7: Illustration of the interactions of different particle types inside the ATLAS detector [180].

reconstructed more efficiently by this approach. The obtained tracks are used to reconstruct the interaction vertices by extrapolating them to common space-points [187, 188]. The longitudinal impact parameter, z_0, and the transverse impact parameter, d_0, are calculated with respect to the interaction vertex to which the tracks are assigned. The primary interaction vertex is defined to be the one with the highest $\sum p_{\mathrm{T}}^2$ of all associated tracks.

3.7.2 Topological Cluster Formation

Topological clusters are formed from the energy deposits in the calorimeters [189]. The cluster formation starts from calorimeter cells with signals of more than four standard deviations above the noise level. Neighbouring cells are iteratively added to the cluster if their signals exceed the noise level by two. When all close-by cells have been added, a final layer of cells is added to the cluster. Clusters with several topologically distinct seeds are split. The topological clusters obtained are calibrated with

respect to the electromagnetic scale and their position is calculated as the average of the cell positions weighted by their energy.

3.7.3 Electron Identification

The electron reconstruction starts with clusters of $\Delta\eta \times \Delta\phi = 0.025 \times 0.025$ cells in the EM calorimeter with a deposited energy above 2.5 GeV. In the early Run 2 data, the cluster search is performed using a sliding window of 3×5 cells. ID tracks belonging to an interaction vertex inside the beam pipe are refitted with the Gaussian Sum Filter (GSF) algorithm [191] to account for bremsstrahlung emitted by the particle [192–194]. The resulting tracks are extrapolated to the calorimeter and associated with energy clusters based on their distance in the η–ϕ plane. Seed clusters with at least one associated track are interpreted as electrons. Additional criteria are used to select the primary track from all associated tracks. The electron direction is determined from the primary track coordinates and the calibrated calorimeter cluster. The sign of its charge is determined from the primary track information [192]. In the later two years, the electron reconstruction uses topological clusters primarily build in the ECAL with subsequent track-matching. For electron candidates with at least 1 GeV, energy deposits from photons radiated in the ID are added if their cluster is within a window of $\Delta\eta \times \Delta\Phi = 0.125 \times 0.3$ around the electron candidate and the primary track of the electron suits to be the best matching track for that cluster as well. This method accounts for bremsstrahlung effects and delivers a more accurate description of the evolution of the particle shower in the calorimeter [195]. The reconstructed electrons are then calibrated using a Boosted Decision Tree [196] to extract the Monte Carlo correction factors accounting for the energy loss in the material upstream of the calorimeter and in neighbouring cells of the electron cluster. An additional in-situ data-calibration is applied to account for mismodelling and dead detector-modules exploiting $Z \rightarrow ee$ decays. The procedure is fully described in Ref. [190, 197].

Once electrons have been selected, additional multivariate identification algorithms are run in order to reject misidentified hadrons and converted photons. A likelihood discriminator is built based on the shapes of the energy deposits in each calorimeter layer, the quality of the primary track and the compatibility between the track and the electron cluster [190, 194]. Three working points are defined using this discriminator, called *LooseLH*, *MediumLH* and *TightLH*. For the LooseLH working point, an additional variant, called *LooseAndBLayerLH* is defined requiring additional hits in the IBL. The efficiencies of the first three working points are shown in Figure 3.8 for the first three years of Run 2 data-taking. On average, the identification efficiencies are approximately 93%, 88% and 80% for LooseLH, MediumLH and TightLH, respectively.

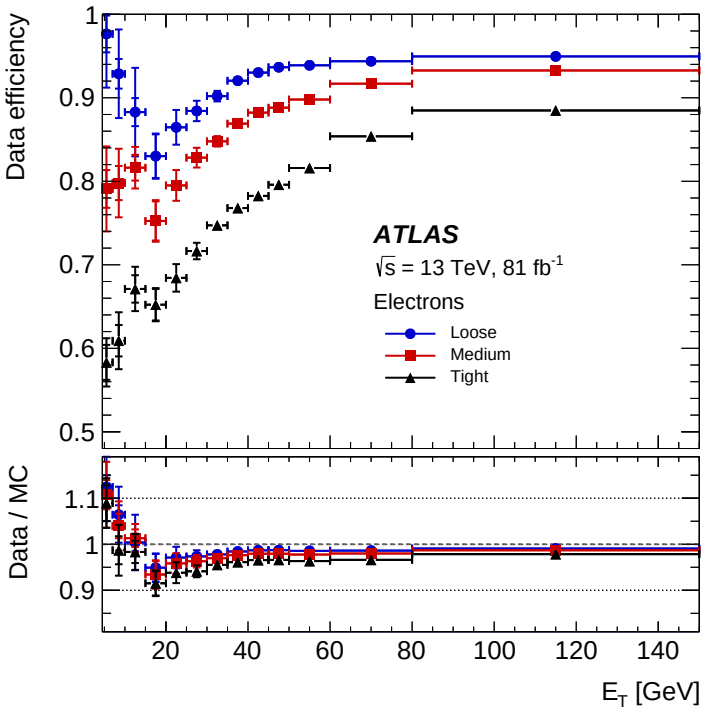

(a)

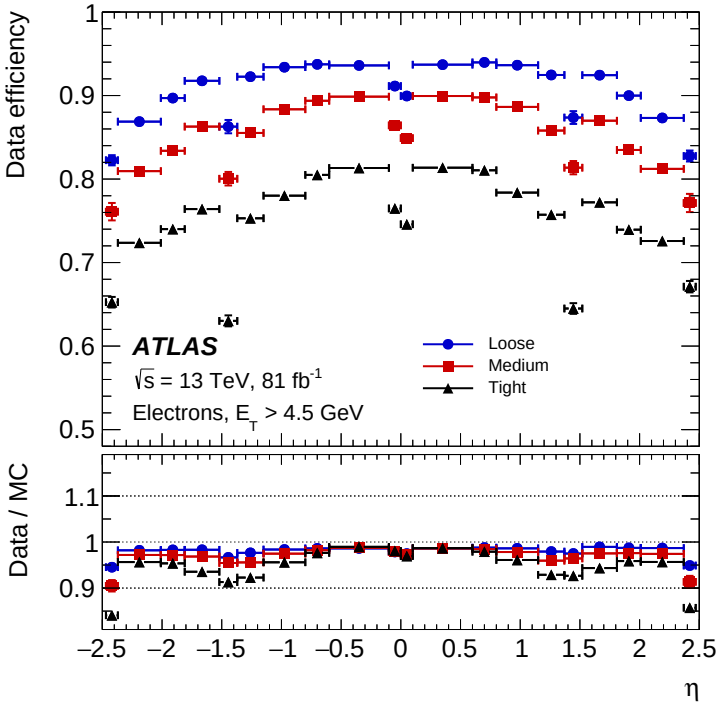

(b)

Figure 3.8: Electron identification efficiency as a function of the transverse energy E_T (a) and of the pseudorapidity η (b) measured in $Z \rightarrow ee$ events in the 2015-2017 dataset [190].

3.7.4 Photon Identification

The reconstruction of photons starts with the same cluster forming and track matching algorithm used for electron reconstruction (cf. Section 3.7.3). Energy clusters without a matching ID track are classified as energy deposits from photons [198]. If at least one track that originates from outside the beam pipe is associated with the cluster, it is classified as a converted photon. Converted photons are further distinguished by whether they have one or two matched tracks. Finally, the energy of the photons is calibrated in exactly the same way like for electrons and cross checked in radiative $Z \rightarrow ee\gamma$ events [190].

Photons are identified using a cut-based technique which provides two working points, *Loose* and *Medium*. Both working points exploit information about hadronic leakage and the shape of the energy deposits in the EM calorimeter. Loose is the default working point for triggering in the early Run 2 dataset while medium is used for the remaining years. The identification algorithms are optimized separately for unconverted and converted photons. During the Run 2 data-taking a third working point, *Tight* has been added which exploits multivariate techniques for a more efficient rejection against background π^0 decays [190].

3.7.5 Jet Reconstruction

Strongly interacting particles produce a bunch of secondary particles moving along the same direction because of the phenomenon of confinement. Since these aligned particles result from the same high-energetic parton, they are clustered to jets which also eases the comparisons with theoretical calculations. In ATLAS, jets are reconstructed from topological clusters using the anti-k_t jet algorithm with distance parameter $\Delta R = 0.4$ [199]. ID tracks are matched to the jet using the Ghost association technique [200]. The jets are calibrated from the calorimeter information only. At the first step, contributions from pile-up are subtracted from the jet momentum based on the jet-area and on the average pile-up density in the event [201]. The pile-up density is calculated from the median p_{T} density of jets using topological clusters within $|\eta| < 2$ which are formed to k_{T} jets with distance parameter $\Delta R = 0.4$. Extra correction factors are calculated in different $|\eta|$ bins to remove a residual dependence of the p_{T} on the in-time and out-time pile-up. In the second step, the energy and the η of the jet are calibrated to their true values based on MC correction factors accounting for energy losses from the material-hadron interactions and from insensitive detector material. Local energy fluctuations from the particle composition in a jet are corrected by a global sequential procedure exploiting five distinctive jet properties. At the last step, an in-situ calibration in data corrects for an imperfect description of the detector material and for a general mismodelling of material - jet interactions. The constants are extracted from balancing the jet-p_{T} against well known resonances,

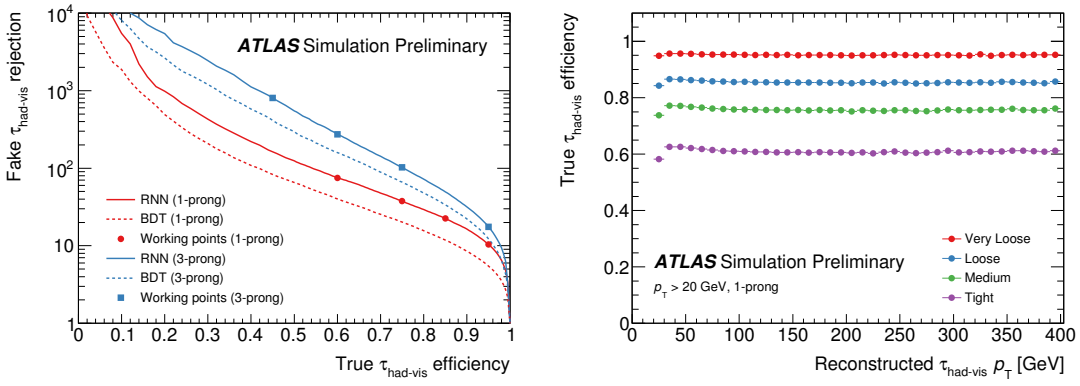

(a) (b)

Figure 3.9: Selection efficiency of reconstructed hadronic τ against the rejection power against particles falsely reconstructed as τ candidates scanning the requirement on the multivariate classification scores using the RNN classifier (solid lines) and the BDT classifier (dashed lines) and the signal τ selection efficiency of the RNN-identification working points against p_{T} [205].

like Z boson production, in data and MC [201]. Jets from pile-up interactions are further rejected by exploiting whether their associated tracks originate from the primary vertex [202].

B-tagging Jets containing b-hadrons are identified exploiting the long b-hadron lifetime of about 1.5 ps and the large particle multiplicity from their decays. Three low-level multivariate algorithms designed to classify b-jet candidates based on the impact parameters, based on the distribution of secondary vertices and finally based on the substructure of b-jets in the calorimeter, respectively, are combined in the MV2 algorithm [203, 204] which is a Boosted Decision Tree (BDT) trained on simulated $t\bar{t}$ and Z' events. The working point chosen for this work provides a selection efficiency of 85% with a rejection rate of 2.7, 6.1 and 21 for c-hadron jets, τ leptons and light-flavour jets, respectively.

3.7.6 τ Lepton Reconstruction

τ leptons have a proper decay length of $c\tau \approx 85$ μm and thus typically decay within the beam-pipe. Their decay channel can be either leptonically, i.e. electrons or muons, with a branching ratio of about 17.5% for each flavour or in the majority of the cases hadronically into an odd number of mesons, predominantly into pions. The hadronic decay modes are grouped according to their charged-meson multiplicity, referred to as prongs, which can either be one, three or five with a relative branching ratio of 77%, 23% and negligible small $\lesssim 0.1\%$, respectively. At hadron colliders, the leptonic decay

channel cannot be used for τ reconstruction, as the decay leptons are too similar to leptons from electroweak boson decays. Therefore, only the hadronic channel is used which is challenging due to the large abundance of pions from soft QCD interactions.

The reconstruction of τ leptons is seeded from jets calibrated to the local hadronic scale [206–208]. Only jets with $p_{\mathrm{T}} > 10$ GeV within the acceptance of the ID excluding the gap between the two barrel calorimeters ($1.37 < |\eta| < 1.52$) are considered. Associated tracks within $\Delta R < 0.2$ around the jet bary center are then used to construct the τ decay vertex. Tracks within the isolation annulus, $0.2 < \Delta R < 0.4$, are used to calculate the variables feeding the τ-identification. τ are then calibrated using a regression BDT correcting for detector responses and the amount of pile-up in the event.

tau leptons are identified using multivariate techniques exploiting the shower shapes in the calorimeter, the energy deposited in the core and in the isolation annulus, the track impact parameters and the similarity of the energies of the tracks to the jet-energy. The algorithm is optimized separately for one- and three-prong candidates. For the results based on the early dataset a BDT is employed. Three working points, referred to as *Loose*, *Medium* and *Tight*, are defined on the classifier output providing an identification efficiency of 70% (65%), 60% (55%) and 40% (35%), respectively, for 1-prong (3-prong) τ candidates. For the full dataset, the τ identification has been improved exploiting a Recurrent Neural Network (RNN) [205]. This algorithm advances in a two times better background rejection while retaining the same signal efficiency (cf. Figure 3.9(a)).

3.7.7 Missing Transverse Momentum

The momentum conservation implies that the momentum vectorial sum of all produced particles before and after the collisions is the same thus zero if only the transverse plane is considered. Weakly interacting particles like neutrinos do not interact with the subsystems of ATLAS leading to an apparent imbalance in the total transverse momentum, called missing transverse momentum, if the momenta of all detected particles are summed up [209]:

$$E_{x(y)}^{\mathrm{miss}} = -\sum_{\substack{i \in e,\mu,\tau, \\ \mathrm{jets}}} p_{x(y)}^{i} + E_{x(y)}^{\mathrm{miss,\,soft}}. \tag{3.7}$$

Only objects satisfying analysis' specific kinematic selection criteria and minimum quality requirements on the provided identification algorithms enter the sum in Equation (3.7). Energy deposits not associated with any physics object are accounted for in the second term which is called the soft-term [209]. It is calculated from ID tracks with $p_{\mathrm{T}} > 400$ MeV, a relative significance on the transverse impact parameter $\left|\frac{d_0}{\sigma(d_0)}\right| < 3$ and a maximum longitudinal distance to the primary vertex $|z_0 \sin\theta| < 3$ mm. This choice provides the best robustness against pile-up contributions. To avoid double counting of

tracks already associated with the selected physics objects an so-called, overlap removal procedure is applied. Further details can be found in Ref. [209]. The magnitude of the missing transverse momentum,

$$E_{\mathrm{T}}^{\mathrm{miss}} = \sqrt{\left(E_x^{\mathrm{miss}}\right)^2 + \left(E_y^{\mathrm{miss}}\right)^2}. \tag{3.8}$$

is commonly referred as missing transverse energy.

3.7.8 Isolation Criteria for Leptons and Photons

Leptons and photons from decays massive particles, like $Z \to \ell\ell$ or SUSY particle decays, are usually well separated from hadronic activity in the detector. In contrast, leptons from heavy flavour quark decays are usually accompanied by additional hadrons in their vicinity. This striking difference motivates the definition of isolation criteria measuring the energy deposited in the vicinity of the lepton. The isolation variables are either calculated from the transverse momenta of the ID tracks or from the transverse energies of the topological calorimeter clusters in a ΔR-cone around the lepton. There are two ways to define the maximum cone radius.

$$\Delta R_{\mathrm{Iso}X} = \frac{X}{100} \qquad \text{and} \qquad \Delta R_{\mathrm{Iso}X}^{\mathrm{Var}} = \min\left(\Delta R_{\mathrm{Iso}X}, \frac{10\ \mathrm{GeV}}{p_{\mathrm{T}}\,(\mathrm{particle})}\right), \tag{3.9}$$

where $X = 20, 30, 40$ defines the cone radius. In the second definition, the cone size shrinks with increasing lepton-p_{T}, which is optimal in boosted decay topologies, like a fast moving $t\bar{t}$ system, where the b-jet and the leptons of the decaying top quark start to overlap [210]. It is only used for track isolation because of the higher available granularity in ΔR. Tracks contributing to the track isolation variable $p_{\mathrm{T}}^{\mathrm{(Var)ConeX}}$ must fall within the corresponding cone and satisfy the following selection criteria [190, 193, 211]:

- The track has $p_{\mathrm{T}} > 1$ GeV
- The track is not associated with the lepton.
- The longitudinal impact parameter with respect to the primary vertex satisfies $|z_0 \sin\theta| < 3$ mm.
- The track satisfies the loose quality criteria described in Ref. [182].
- In analyses using the full Run 2 dataset, the track must originate from the primary vertex to mitigate efficiency losses from the higher pile-up.

Topological clusters within the isolation cone contribute to the $E_{\mathrm{T}}^{\mathrm{TopoCone}X}$ variable if they are within the cone radius $\Delta R_{\mathrm{Iso}X}$ and outside of the so-called core region, $\Delta R < 0.1(0.05)$ for electrons (muons), which defines the region of energy deposits associated with the lepton. The variables are then

corrected for pile-up contributions exploiting a similar method like the one used for the jet and τ energy calibration [193, 211].

Part

II

Muon Reconstruction and Efficiency Measurements

Muons are the only charged particles which fully reverse the calorimeters and are reconstructed in the muon spectrometer. Produced by the electroweak interaction, they are an essential component of many physics analyses. They provide final state signatures for precision measurements of the Higgs boson, W boson and top quarks [14, 212–216], for the flavour physics program [217, 218], or for searches for physics beyond the SM, like supersymmetric particle decays studied in this thesis (cf. chapter 7) or for additional gauge bosons decaying into muon pairs [219]. In addition, they are essential for analyses relying on the transverse momentum balance, e.g., data-driven techniques exploiting $Z \to \mu\mu$ events to determine the contribution of the $Z \to \nu\nu$ background in fully hadronic final states [220]. $Z \to \mu\mu$ and $J/\psi \to \mu\mu$ decays are used as "standard candle" for the energy calibration of the muon spectrometer itself or to study the performance and calibration of the missing transverse momentum [221]. Muons are also used in b-tagging algorithms and their calibration [204, 222].

After muon track reconstruction from the hits in the muon detector layers, the momenta of the muon tracks are determined and calibrated. Prompt muons are separated from hadronic background, also referred to as fake muons, e.g. from $\pi^{\pm} \to \mu^{\pm}\nu$ decays. The muon identification efficiency is evaluated in data and simulation. Scale factors are applied to the simulation as a function of the muon track three-momentum in order to match the efficiency in data. Chapter 4 summarizes the muon reconstruction, calibration and identification procedures. Chapter 5 describes the muon efficiency measurements performed in the context of this thesis.

CHAPTER FOUR

MUON RECONSTRUCTION AND IDENTIFICATION

Muon reconstruction starts with the conversion of the digital signals of the muon detectors into track constituents. The track segments in each detector layer are combined to curved muon tracks in the toroidal magnetic field. The transverse momenta of the tracks are calibrated using the precisely known masses of the Z and the J/ψ particles in $Z \to \mu\mu$ and $J/\psi \to \mu\mu$ decays. Muon candidates from semileptonic pion, kaon or B meson decays are separated from prompt muons originating from decays of electroweak bosons, top quarks or new particles beyond the Standard Model. The three steps are described in the following.

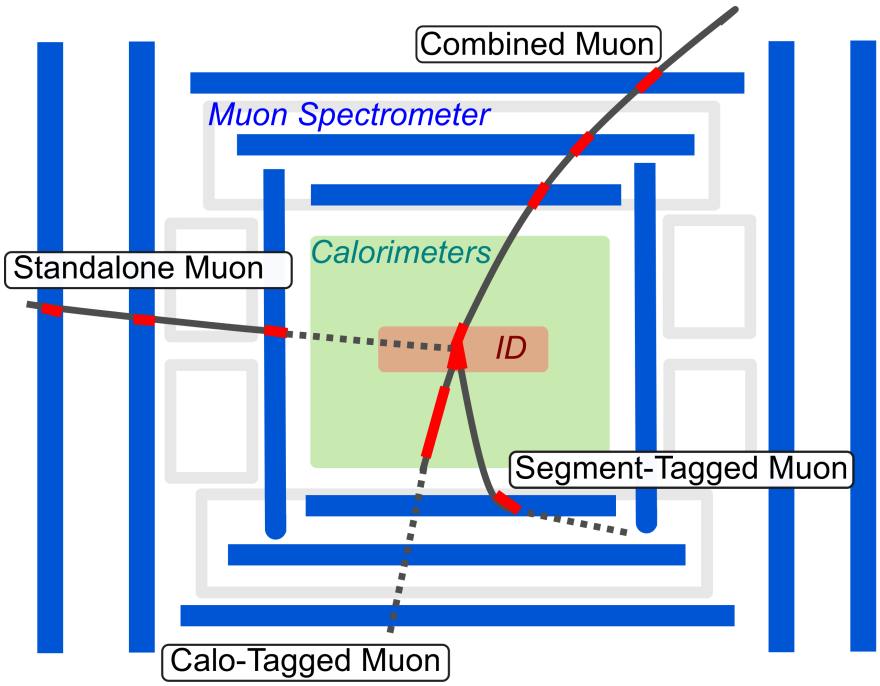

Figure 4.1: Schematic overview of the involved sub detector systems in the reconstruction of the different muon types.

4.1 Muon Reconstruction

The ATLAS muon spectrometer is designed to measure muon momenta at a precision of 2% for muons with $p_{\mathrm{T}} \simeq 10$–100 GeV and at 10% for muons with $p_{\mathrm{T}} \simeq 1$ TeV [163] relying solely on information from the MS. To achieve the maximum efficiency and momentum resolution, the muon reconstruction algorithms additionally exploit information from the ID and from the calorimeters. Four different types of muons are distinguished, namely *combined*, *calorimeter-tagged*, *segment-tagged* and *standalone/extrapolated* muons. These muon types correspond to different strategies for muon reconstruction (cf. Figure 4.1) and differ in the subsystems involved. This section briefly summarizes the algorithms to reconstruct each type. More detailed information on the algorithms can be found in Refs. [211, 223–225].

Standalone muons are only used outside the ID coverage, i.e. $|\eta| > 2.5$ and thus rely only on information from the MS. The reconstruction of MS tracks starts by combining the hits in the muon detectors into segments, which are short straight-line tracks projected to the reference plane of the chambers. The hits in three dimensions are projected into a two-dimensional Hough space [226]. Accumulation points of hits satisfying a minimum hit requirement are then combined to form segment candidates. Muon tracks are linearly extrapolated through the spectrometer, seeded by segments having a large hit multiplicity, to remove background induced segment candidates. Eventual overlap between the track candidates sharing the same hits is resolved by ranking the candidates based on the number of associated precision and trigger hits. MDT (CSC) segments are required to have at least four (two) hits in the chambers in order to be defined as a good precision layer. Final MS track candidates are then obtained by means of a global χ^2-fit taking into account the deflection of the muon by the magnetic field. Several algorithms are then executed to identify missing hits along the reconstructed track which could then potentially be recovered or to remove falsely included hits along the track. MS tracks with at least two associated precision layers are extrapolated to the interaction point and refitted taking into account the energy loss in the calorimeter. They are then called muon extrapolated tracks, *ME tracks*. Muons outside the ID coverage, for which single hits in the extended angular coverage of the IBL can be associated to the reconstructed trajectory of the muon, are referred to as silicon associated forward muons (SAF). SAF muons generally have a better resolution in the impact parameters than ME tracks due to the extra hit close to the beamline.

Combined muons (CB) are built from ID and ME tracks and are the most common muon type in ATLAS. In the first reconstruction step, possible ID–ME track combinations are collected together. Two different approaches are considered: The ME track is extrapolated to the ID looking for close-by ID tracks; or the ID track is extrapolated to the MS to search for close-by ME tracks. The latter

approach is usually applied for low-p_{T} muons as these muons barely reach a second MS layer if they are in the barrel. Then the hits of both tracks are combined to a single track using a global χ^2 fit, taking into account the energy loss in the calorimeters. Ambiguities between the track candidates are then resolved based on the quality of the fit and the compatibility of the two separate track momenta with each other as well as with the combined track momentum.

Segment tagged muons (ST) usually originate from very low energetic muons that consequently reach only the first stations of the MS before they are deflected by the magnetic field or stopped due to multiple scattering. ST muons are reconstructed by extrapolating ID tracks with $p_{\mathrm{T}} > 2$ GeV to the MS and matching them to single muon segments in the innermost layer of the MS.

Calorimeter tagged muons (CT) are used in the crack region of the detector ($|\eta| < 0.1$) where the MS is partially instrumented. They are reconstructed from ID tracks with $p_{\mathrm{T}} > 5$ GeV which are extrapolated to the calorimeters. Muons are minimal ionizing particles while they propagate through the calorimeter. Therefore muon identification is performed by requiring, that each of the associated energy deposits in the calorimeters must be smaller than a certain threshold depending on the muon p_{T}. Fake muons are removed by applying a loose isolation requirement using the $p_{\mathrm{T}}^{\mathrm{Cone40}}$ variable.

All muon types are built in parallel to each other. If the same muon is reconstructed by more than one algorithm, preference is given to CB over ST followed by CT muons.

4.2 Muon Momentum Calibration

The precision of the measured muon momentum depends, besides the intrinsic resolution of the precision chambers, on the knowledge of the magnetic field generated by the ATLAS magnet system, of the material traversed by the muon before entering the MS, on the multiple scattering of the muon inside the dense detector material upstream, and on the alignment of the chambers. The magnetic field is monitored by 800 Hall sensors distributed in the muon detector volume [133]. The alignment is determined by the optical alignment systems (cf. section 3.4) and special data taking runs with magnetic fields switched off providing straight muon tracks. The intrinsic resolution of the precision chambers also depends on the temperature, the humidity and the air pressure in the cavern. Hence calibration measurements on a daily basis are performed to determine the drift-time relation [165].

Simulated events are free from varying environmental conditions or chamber misalignment, but may be affected by imperfect modelling of the detector material and the multiple scattering, resulting in disagreement between the measured and simulated muon momentum distribution. Therefore,

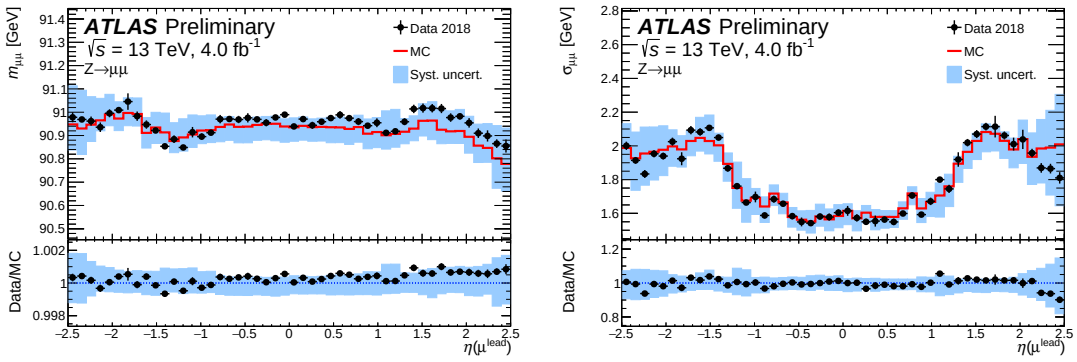

(a) (b)

Figure 4.2: Mass value (a) and mass resolution (b) from the fit of a Crystal Ball function convolved with a Breit-Wigner function plus Gaussian distribution to the invariant di-muon mass spectrum in $Z \to \mu\mu$ events from simulation (red curve) and the early 4 fb^{-1} of 2018 data (black dots) as a function of η of the leading muon. The blue uncertainty band is derived from $\pm 1\sigma$ variations of the calibration smearing parameters in the denominator of Equation (4.1) [227].

the reconstructed muon p_{T} in simulation is corrected for the intrinsic energy loss in the upstream material, parametrized by Δs_0, and bias in the non-uniform magnetic field, Δs_1 and then smeared using a Gaussian distribution, $\mathcal{G}(1, \sigma)$ with mean 1 and a width, σ to account for fluctuations in the energy loss, Δr_0, multiple scattering, Δr_1 and the intrinsic resolution of the precision chambers and misalignment, Δr_2:

$$p_{\mathrm{T}} \to \frac{\Delta s_0 + (1 + \Delta s_1)\, p_{\mathrm{T}}}{\mathcal{G}\left(1, \sqrt{\left(\frac{\Delta r_0}{p_{\mathrm{T}}}\right)^2 + \Delta r_1^2 + (\Delta r_2 p_{\mathrm{T}})^2}\right)} \tag{4.1}$$

The corrections are performed separately for ID, ME and CB tracks. The correction parameters depend on p_{T} and η, and, in the case of ME tracks, additionally on ϕ. They are determined by an iterative fit to data exploiting the mass and width of well known resonances decaying into muons, like $Z \to \mu\mu$ and $J/\psi \to \mu\mu$. Both provide an abundant source of muons in the intermediate p_{T}-range of $p_{\mathrm{T}} \simeq 15$–100 GeV and in the complementary low p_{T}-range of $p_{\mathrm{T}} \simeq 3$–20 GeV. They are selected by requiring exactly two combined muons with opposite charge and an invariant mass around the respective resonance mass [211]. The calibration procedure is validated using a fit of a Crystal Ball function [228, 229], that is convolved with a Breit-Wigner function plus a Gaussian function, to the simulated and recorded di-muon invariant mass $m_{\mu\mu}$ distributions in $Z \to \mu\mu$, $J/\psi \to \mu\mu$ and $\Upsilon \to \mu\mu$ events. The Crystal Ball function describes the position of the resonance, losses from final state radiation and the intrinsic detector resolution. The Breit-Wigner function accounts for the intrinsic width of the resonances and the Gaussian for secondary effects affecting the resolution. In the

fit to data, a falling exponential function is added to model the non-resonant backgrounds. Figure 4.2 shows the result of the validation for $Z \to \mu\mu$ events recorded in the early 2018 dataset as a function of the pseudorapidity of the higher p_{T} muon in the pair. The calibration reproduces the Z boson mass in data and simulation within an agreement at permille level. The mass resolution obtained is 2 GeV and 1.6 GeV in the endcaps and in the barrel, respectively. The agreement between data and MC is better than 10% over almost the full η range. For $\eta > 2$, the agreement degrades to about 15%, mainly caused by non-working CSC chambers in the data taking. The validation results for the Υ and J/ψ resonances can be found in Refs. [211, 230].

4.3 Muon Selection

Not only muons from heavy particles, like electroweak boson decays, but also from $\pi^{\pm}$, $K^{\pm}$, or semi leptonic heavy hadron decays are reconstructed by the ATLAS detector. The latter are effectively rejected by applying quality criteria to the muon candidates, comprised in five working points. Three of them, called *Loose*, *Medium* and *Tight*, are designed to be generic over the whole p_{T} spectrum. In contrast, the *low-p_T* and *high-p_T* working points are optimized for the eponymous p_{T} regions. In the following, each of the working points is briefly discussed. More detailed information is given in Refs. [211, 231].

Loose working point muons are a compromise between a high muon selection efficiency while maintaining the contamination from non-prompt muons at an acceptable level. It is the most inclusive working point meaning that any muon satisfying another of the four remaining working points is also a Loose muon. Muon candidates within the full MS η coverage and with $p_{\mathrm{T}} > 3$ GeV are accepted. Muons within $|\eta| < 2.5$ must be combined muons with at least two associated muon segments. The MS is partially instrumented in the region $|\eta| < 0.1$ to make room for supply lines to the calorimeters and to the ID. In order to recover efficiency, the CB muons are allowed to have only one associated MS segment with the restriction that at most one expected segment is missing in this region. Additionally, CT and ST muons are accepted for $|\eta| < 0.1$ as well. The ID tracks associated to the CB muon must have at least one hit in the Pixel detector and at least five hits in the SCT and must not miss more than two expected hits in each of the two silicon detectors. Muons from in flight decays of charged pions or kaons often have a kink in their track at the location of the meson decay leading to a worse compatibility between the ID, the MS and the combined track. The *q/p significance*,

$$Z\left(\frac{q}{p}\right) = \frac{\left|\left(\frac{q}{p}\right)_{\mathrm{ID}} - \left(\frac{q}{p}\right)_{\mathrm{ME}}\right|}{\sqrt{\sigma\left(\frac{q}{p}\right)^2_{\mathrm{ID}} + \sigma\left(\frac{q}{p}\right)^2_{\mathrm{ME}}}}, \tag{4.2}$$

where q is the muon charge, p is the momentum of the muon, and $\sigma\left(\frac{q}{p}\right)$ is the respective uncertainty, provides a good rejection of such muons. Combined muons with $Z\left(\frac{q}{p}\right) > 7$ are discarded as background. To improve the identification efficiency of low-p_{T} muons in the barrel, muons with $p_{\mathrm{T}} < 7$ GeV and only one associated MS segment are also selected within $|\eta| < 1.3$. Extrapolated muons are accepted outside of the coverage of the ID ($2.7 > |\eta| > 2.5$) if they have associated hits in all three stations of the MS.

Medium working point muons are most commonly used in ATLAS physics analyses. The working point comprises all Loose criteria, excluding CT and ST muons and the exception for low-p_{T} muons in the barrel. Medium muons provide a better purity in prompt muons than Loose muons leading to smaller systematics in the efficiency calibrations and thus in the SM precision measurements.

Tight working point muons provide the best rejection power against hadronic background at the cost of a loss in the selection efficiency. Only combined muons satisfying the Medium requirements with at least two associated track segments are accepted. To exploit further the kink in the track for hadronic backgrounds, the χ^2 divided by the number of degrees of freedom of the track fit must not exceed eight. Additionally, the variable,

$$\rho' = \frac{p_{\mathrm{T}}^{\mathrm{ID}} - p_{\mathrm{T}}^{\mathrm{ME}}}{p_{\mathrm{T}}^{\mathrm{CB}}}, \tag{4.3}$$

is used to evaluate the compatibility of the transverse momenta of the three tracks. η dependent cuts on ρ' and on $Z\left(\frac{q}{p}\right)$ are applied to maximize the background rejection at a selection efficiency of 95% for $p_{\mathrm{T}} > 15$ GeV [211].

High-p_{T} identification criteria mark a compromise between a high selection efficiency for muons with p_{T} beyond 100 GeV while simultaneously maintaining a good muon momentum resolution. Medium muons reconstructed in sectors with relatively large misalignment are vetoed. Additionally, high-p_{T} must have three associated track segments with an exception in the barrel ($|\eta| < 1.3$), where muons without hits in the inner layer are accepted as well.

Low-p_{T} muons with $p_{\mathrm{T}} \lesssim 7$ GeV in the barrel region also have a very low four momentum, as well. Therefore, they suffer more from multiple scattering than muons in the endcap regions which have about two to six times larger total momentum. Thus they barely reach the second layer of the MS. The low-p_{T} identification criteria maximize the identification efficiency for muons down to 3 GeV while retaining the same fake rejection power as for the Medium working point (cf. Figure 4.3). Two

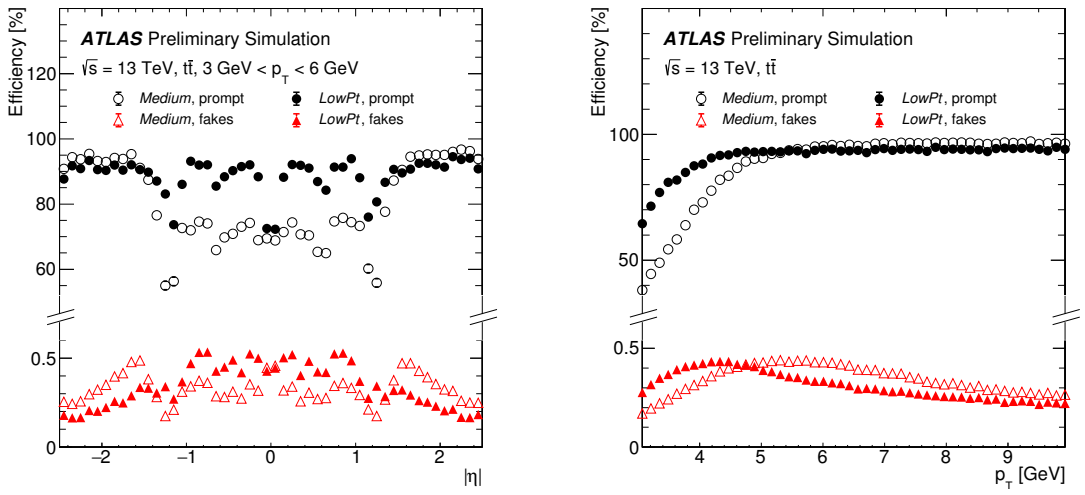

(a) (b)

Figure 4.3: Expected efficiency as a function of pseudorapidity (a) and transverse momentum (b) for muons fulfilling the Low-p_{T} (filled markers) and Medium (empty markers) requirements in simulated $t\bar{t}$ events. The efficiency is computed with respect to tracks reconstructed in the inner detector, and is shown separately for prompt (dots) and for fakes (triangles) muons [231].

versions of the working point are employed, one using a cut-based approach exploiting hit, scattering and track curvature information for $p_{\mathrm{T}} \in [3; 18]$ GeV, and another one, referred to as *low-p_T MVA* is based on a Boosted Decision Tree algorithm, combining the same variables, but resulting in a 3% higher selection efficiency at 10–20% better background rejection compared to the cut-based version. If the muon has $|\eta| > 1.55$, the muon has to satisfy the Medium selection criteria in addition and for muons with $p_{\mathrm{T}} > 18$ GeV the Medium selection criteria replace the ones described above.

CHAPTER FIVE

MUON EFFICIENCY MEASUREMENT

The muon momentum calibration following the changing data taking conditions (e.g. chambers that did not participate for a certain period in the data taking) is an essential prerequisite for the matching of the simulated events to the recorded data. Changing conditions and imperfect modelling of the detector also imply that the muon identification efficiency of the detector system is not perfectly described by the simulation and has to be corrected. The efficiency is measured in data and simulation by means of the so called tag-and-probe (T&P) method. $Z \rightarrow \mu\mu$ and $J/\psi \rightarrow \mu\mu$ events are exploited as an abundant source of muons which are easy to select. In addition, the efficiency calibration relies on the fact that for prompt muons the momentum of the ID track must be compatible with the MS track momentum. From the efficiency measurements in simulation and data, a so-called scale factor

$$sf = \frac{\epsilon^{\text{data}}}{\epsilon^{\text{MC}}}, \tag{5.1}$$

is calculated, which is then applied to each muon in the simulation to adjust the muon identification efficiency to the efficiency measured in the real data. In physics analyses, additional selection criteria are applied the muon track on top of the muon identification to reject background induced muon candidates. These criteria are in particular that the muon originates from the primary collision vertex, called track-to-vertex-association (TTVA) and that small energy is detected in the vicinity of the muon track, called muon isolation. Also the efficiencies of these two additional criteria may not coincide between data and simulation due to mismodelling and thus needs to be adjusted in simulation by dedicated scale-factor measurements. The T&P method using Loose muons as probes is also used for these measurements to derive the corresponding scale factors.

In this chapter, the muon efficiency measurements in $Z \rightarrow \mu\mu$ and $J/\psi \rightarrow \mu^+\mu^-$ events is described. The strategy to measure the reconstruction efficiency in $Z \rightarrow \mu\mu$ and $J/\psi \rightarrow \mu\mu$ decays by means of the tag-and-probe method is explained in section 5.1 followed by a description of the data and Monte Carlo event samples in section 5.2. The results of the identification efficiency measurements of $Z \rightarrow \mu\mu$ and the $J/\psi \rightarrow \mu\mu$ events are given in sections 5.3 and 5.4, respectively. A dedicated

measurement of the muon efficiency outside the ID coverage is discussed, where the T&P method cannot be applied and the so-called double ratio method is exploited instead (cf. section 5.5). The efficiency measurements for the additional muon selection criteria are presented in section 5.6. The results are summarized in section 5.7.

5.1 Muon Reconstruction Efficiency Measurement

The muon reconstruction efficiency measurement evaluates the basic performance of the ATLAS muon reconstruction to identify muons satisfying identification working point X (cf. Section 4.3) in simulation and real data. Discrepancies between both efficiencies, caused by, e.g., broken chambers during the data taking, by an imperfect description of the detector geometry and response leading to a mismodelling of the input variables entering the reconstruction and identification algorithms, are corrected by the scale factors derived from this measurement. This section explains the strategies used to measure the reconstruction efficiency in $Z \to \mu\mu$ and $J/\psi \to \mu\mu$ events focusing on combined muons which make up the vast majority of the muons used in ATLAS. First the so-called tag-and-probe (T&P) method is explained. The approach to measure the muon reconstruction efficiency used in the early iterations of this measurement [211, 223] is presented, together with a discussion of the limitations of the method and of improved strategies in the final analysis. The determination of the efficiency scale factor for SA muons with $|\eta| > 2.5$ is given in section 5.5.

5.1.1 The Tag-and-Probe Method

To successfully form a combined muon satisfying the identification working point X as described in section 4.3, three ingredients are needed, namely a reconstructed ID and MS track, and the algorithm combining the two tracks to a CB track. The total efficiency of such a muon can consequently be expressed as

$$\epsilon\,(\mathrm{X}) = \epsilon\,(\mathrm{ID} \wedge \mathrm{MS} \wedge \mathrm{combination})\,. \tag{5.2}$$

However, this formula is inapplicable experimentally as the total number of muons traversing the detector in data is a priori unknown. As explained in chapter 4, the four-momenta of the ID, MS, and CB of prompt muon tracks have to be compatible with each other. Di-muon resonances, like $Z \to \mu\mu$ and $J/\psi \to \mu\mu$, provide an abundant source of such muons in transverse momentum ranges above and below 10 GeV, respectively, which are easy to select due to the characteristic peak in the di-muon invariant mass spectrum and the opposite charges of the two produced muons. The tag-and-probe (T&P) method exploits each of these features. The independent reconstruction of the ID and MS tracks with compatible four-momenta allows for the testing of the performance of one of the two

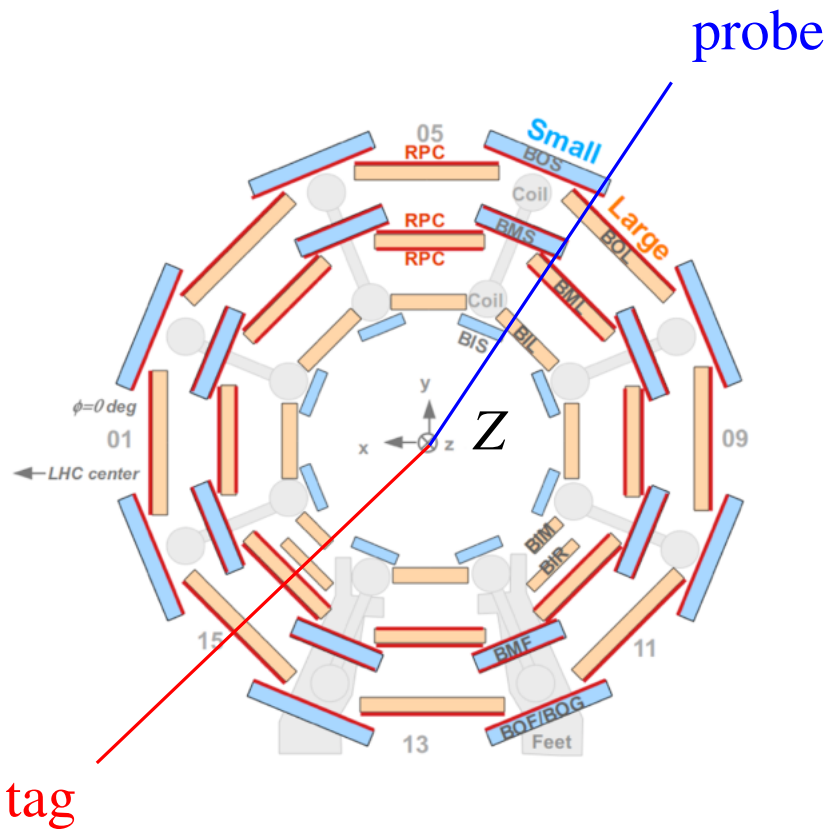

Figure 5.1: Illustration of a tag-and-probe muon pair from a Z decay in the ATLAS MS.

detector systems given that a the complementary track has been formed in the other system. Selecting di-muon resonances determines the total number of prompt muons in the sample. The T&P method is shown in Figure 5.1 where a Z boson decays into a pair of muons. One muon from the decay is required to be successfully reconstructed as Medium muon which triggered the event and is referred to as *tag* (the explicit criteria are discussed in sections 5.3.1 and 5.4.1). The second muon, called the *probe*, has opposite charge and forms together with the tag muon an invariant mass in the resonance peak. It has to be reconstructed in at least one of the two subsystems of the ATLAS detector, the ID or the MS, and is used to derive the efficiency of the muon reconstruction and of other selection criteria. The following reconstructed tracks are considered as probes:

- **MS tracks** to measure the ID track reconstruction efficiency,
- **CT/ST** muons to measure the MS track reconstruction and muon combination efficiency as explained later in this section,
- **ID tracks** passing the quality criteria employed for the Loose working point (cf. section 4.3) to

measure the MS track reconstruction efficiency or the full muon combination efficiency,

- **Two-track** probes, ID tracks with a close-by MS track within $\Delta R < 0.05$, to measure the combination efficiency as explained later in this section,

- **Loose muons** to measure the efficiency of selection criteria applied in addition of the five muon working points, e.g. isolation criteria.

The probe is called a *match* if the complementary muon track is within ΔR of the probe trajectory. For instance, if the Medium reconstruction efficiency is measured using ID tracks as probes, the ID track is defined is matched if the a Medium muon is found close-by. In cases of the measurements of the additional selection criteria, the probe track itself has to satisfy the corresponding criterion. The matching efficiency is the ratio of the number of matches to the number of probes:

$$\epsilon = \frac{\#\text{matches}}{\#\text{probes}}. \tag{5.3}$$

For the example given above, the muon reconstruction efficiency is given as the conditional efficiency that an ID track has already been reconstructed, whereas for the total muon reconstruction efficiency, the ID track reconstruction efficiency has also to be taken into account. Therefore Equation (5.2) has to be expanded.

$$\epsilon(X) = \epsilon(X|\text{ID}) \times \epsilon(\text{ID}) + \underbrace{\epsilon(X|\neg\text{ID})}_{=0} \times \epsilon(\neg\text{ID}) \tag{5.4a}$$

$$= \epsilon(X|\text{ID}) \times [\epsilon(\text{ID}|\text{MS}) \times \epsilon(\text{MS}) + \epsilon(\text{ID}|\neg\text{MS}) \times \underbrace{\epsilon(\neg\text{MS})}_{=1-\epsilon(\text{MS})}] \tag{5.4b}$$

$$\approx \epsilon(X|\text{ID}) \times \epsilon(\text{ID}|\text{MS}). \tag{5.4c}$$

The first line represents the situation described above. There, the second term is zero as all muon identification working points require the presence of an ID track for muons within $|\eta|$ <2.5. In the next step the ID track reconstruction efficiency has to be determined as well by means of T&P. This is achieved using reconstructed MS tracks as probes. Given that the two tracks are independently reconstructed from each other it is assumed that $\epsilon(\text{ID}|\text{MS}) \simeq \epsilon(\text{ID}|\neg\text{MS})$ which is then used to obtain the final formula. To summarize the combined muon reconstruction efficiency is determined in two steps. First the ID track efficiency is determined using MS tracks as probes and then the muon track reconstruction efficiency using ID tracks as probes in data and in simulation to derive the efficiency scale factor. To check the validity of this derivation, in simulation, the efficiency obtained by the T&P method is compared to the truth reconstruction efficiency which is defined as the number of generator-level muons matched to the reconstructed muon by $\Delta R < 0.05$ to the total number of

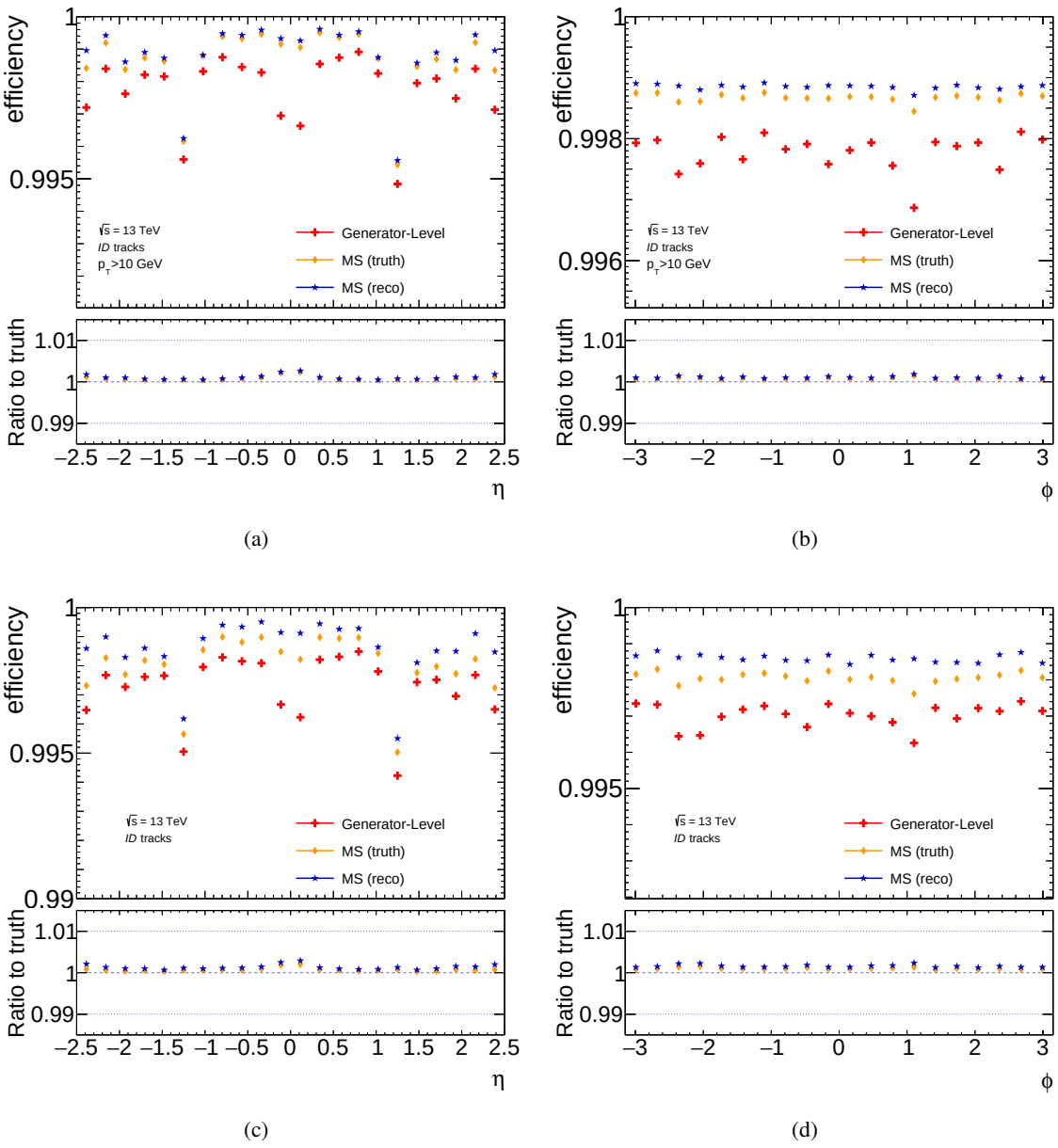

Figure 5.2: ID track reconstruction efficiency shown as a function of the probe pseudorapidity (left) and the azimuthal angle (right) in simulated $Z \to \mu\mu$ (top) and $J/\psi \to \mu\mu$ (bottom) events. The red markers show the truth efficiency, the orange markers show the truth efficiency obtained from generator-level muons matched to MS tracks in advance and the blue markers show the efficiency obtained by the T&P method using MS tracks as probes. Additional kinematic selections on the probe are indicated on each plot. The bottom panel shows the ratio between the latter two efficiencies to the truth efficiency.

generator-level muons. For the $Z \to \mu\mu$ and J/ψ resonances, the comparison is given in Figure 5.2

for the case of the ID reconstruction efficiency only and in Figure 5.3 for the full formula applied to the Medium (Low-p_{T}) identification working point in $Z \to \mu\mu$ ($J/\psi \to \mu\mu$) events. To assess whether a potential bias arises from the T&P selection itself or from the choice of the probe-track, both efficiencies are additionally compared to the truth efficiency where only generator-level muons which are matched in advance to the probe-track used in the corresponding T&P measurement are considered as probes. For the ID efficiency an excellent agreement between each of the efficiencies at a level of $O\left(10^{-1}\right)$ % is observed for both resonances. Exploiting the full formula agreement is almost as good for all muons, except for muons from $J/\psi \to \mu\mu$ decays in the crack region, $|\eta| < 0.1$ or with $p_{\mathrm{T}} < 5$ GeV. The disagreement there can be up to two percent. The reasons for this deviation are under investigation at the time of writing this document.

However, the usage of ID tracks as probes causes practical problems if the efficiency is measured in data. QCD processes lead to a large abundance of ID tracks in the event allowing to form fake T&P pairs if the tag muon originates from a W decay in W+jets events or is even a fake muon from a secondary quark decay and falsely passes the Medium identification working point. The contribution of those pairs needs to be properly estimated which is challenging due to their large number compared to the signal. To suppress the background, the advantage of the muon being a minimal ionizing particle is taken into account. ID probes are replaced by CT probes in Equation (5.4). However, this replacement comes along at the cost of introducing a bias to the measurement as calorimeter tagging is not necessarily independent from muon identification:

$$\epsilon(X) = \epsilon(X \wedge \mathrm{CT}) + \epsilon(X \wedge \neg\mathrm{CT}) \tag{5.5a}$$

$$= \epsilon(X|\mathrm{CT}) \times \epsilon(\mathrm{CT}) + \epsilon(\neg\mathrm{CT}|X) \times \epsilon(X) \tag{5.5b}$$

$$= \epsilon(X|\mathrm{CT}) \times \epsilon(\mathrm{CT}|\mathrm{ID}) \times \epsilon(\mathrm{ID}) + [1 - \epsilon(\mathrm{CT}|X)] \times \epsilon(X) \tag{5.5c}$$

$$\Rightarrow \epsilon(X) = \epsilon(\mathrm{ID}) \times \epsilon(X|\mathrm{CT}) \times \frac{\epsilon(\mathrm{CT}|\mathrm{ID})}{\epsilon(\mathrm{CT}|X)} \tag{5.5d}$$

$$\epsilon(X) \simeq \epsilon(\mathrm{ID}|\mathrm{MS}) \times \epsilon(X|\mathrm{CT}) \times \frac{\epsilon(\mathrm{CT}|\mathrm{ID})}{\epsilon(\mathrm{CT}|X)} \tag{5.5e}$$

In the first line the efficiency of the working point X is split into two terms according to whether the calorimeter tagging is passed or not. Next, the two terms are expressed in terms of conditional probabilities and the inefficiency is rewritten as the efficiency complement. In the next step, the terms are rearranged to obtain the final efficiency formula using the CT muons as probes. Equation (5.5e) is seen to differ from simply replacing ID tracks by CT muons as probes in Equation (5.4) by the third term, called the bias term. It reflects the fact that calorimeter tagging is more efficient for muons which have not undergone a very large energy loss in the calorimeter. Such muons are more likely to pass a successful combination and identification since their ID and MS track momenta are more compatible with each other. On the other side, muons with large energy losses beyond the expectations of the

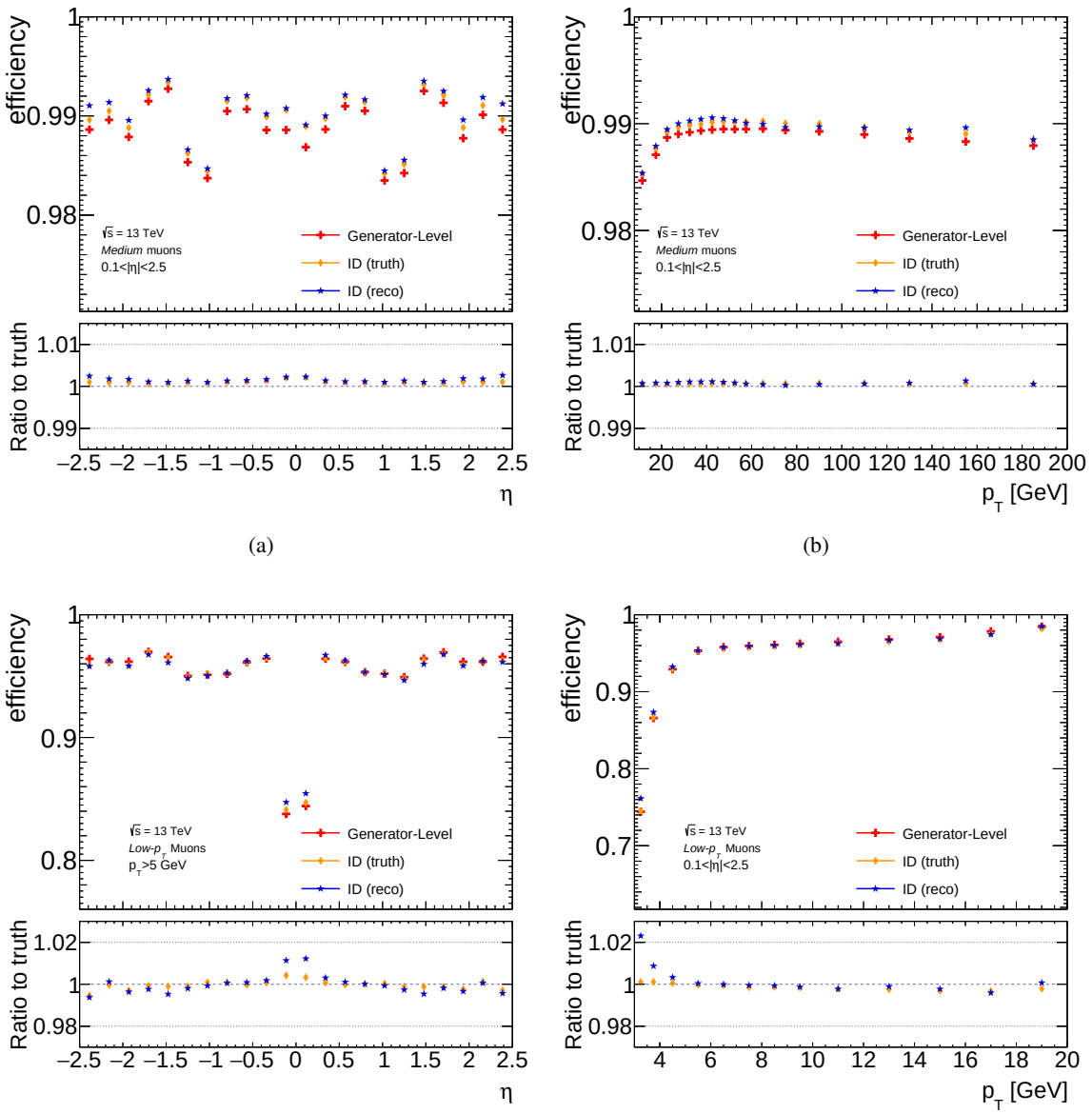

Figure 5.3: Reconstruction efficiency for the Medium identification working point in simulated $Z \rightarrow \mu\mu$ events (top) and for the Low-p_{T} working point in simulated $J/\psi \rightarrow \mu\mu$ (bottom) shown as a function of the probe pseudorapidity (left) and the transverse momentum (right). The red markers show the truth efficiency obtained from generator-level muons and the orange markers show the efficiency of those matched to an ID track in advance. The blue markers show the efficiency obtained by the full T&P method using ID tracks as probes. Additional kinematic selections on the probe are indicated on each plot. The bottom panel shows the ratio of the respective efficiencies to the truth efficiency.

applied reconstruction model are more likely to fail a successful combination, but these cases do not participate in the measurement from the beginning if CT muons are used as probes. For previous iterations of the measurement as performed in Refs. [211, 223], the third term in Equation (5.5e) has been neglected biasing the measurement by 0.5–1.5% independently from η for $p_{\mathrm{T}} > 10$ GeV, but showing a small dependency on the probe p_{T} (cf. Figure 5.4). Since the biases in data and simulation do not necessarily cancel each out in the scale factor, the half of the deviation is assigned as an intrinsic systematic uncertainty of the T&P method itself and called the truth closure uncertainty. However, full Run 2 Standard Model precision measurements with muons in the final state start to become limited by the systematic uncertainties assigned from the performance measurements [232]. In addition, the Low-p_{T} working point allows to access muons with p_{T} down to 3 GeV. However, calorimeter tagging is only provided for muons with $p_{\mathrm{T}} > 5$ GeV and hence the phase space between 3–5 GeV cannot be measured using CT muons introducing the problem of large backgrounds. Both limitations motivate to revise the strategy for the reconstruction efficiency measurements. The strategies are revised separately for the $Z \to \mu\mu$ and $J/\psi \to \mu\mu$ measurements as explained in the next section.

5.1.2 Strategy for Precision Measurement of the Muon Reconstruction Efficiency

As discussed in the previous section, the usage of CT muons as probes to measure the muon reconstruction efficiency causes a bias in the measurement as the inefficiency from muons with large energy losses in the calorimeter is not taken in to account. One possible solution to the problem would be to explicitly measure the bias term in Equation (5.5e) in data and simulation. However, calorimeter tagging strongly depends on the pseudorapidity and slightly on the transverse momentum. Therefore, the efficiencies have to be additionally parametrized as a function of these two variables resulting in large statistical uncertainties of the final result. In addition, this approach does not solve the problem that calorimeter tagging is only available for muons with $p_{\mathrm{T}} > 5$ GeV and that hence these probes cannot be used for momenta below that threshold.

Revised strategy for the measurement using $Z \to \mu\mu$ decays: Alternatively, the bias can be removed if Equation (5.2) is parametrized in a way such that the combination efficiency is not measured using CT muons as probes and the background is rejected at a comparable level. Both conditions are met for the vast majority of combined muons when ID tracks are used as probes to measure the combination efficiency with the additional requirement that a reconstructed MS track is within $\Delta R < 0.05$. These probe are referred to as *two-track probes*. However, the MS track reconstruction efficiency must be determined explicitly in this procedure. Using two-track probes, the formula for the

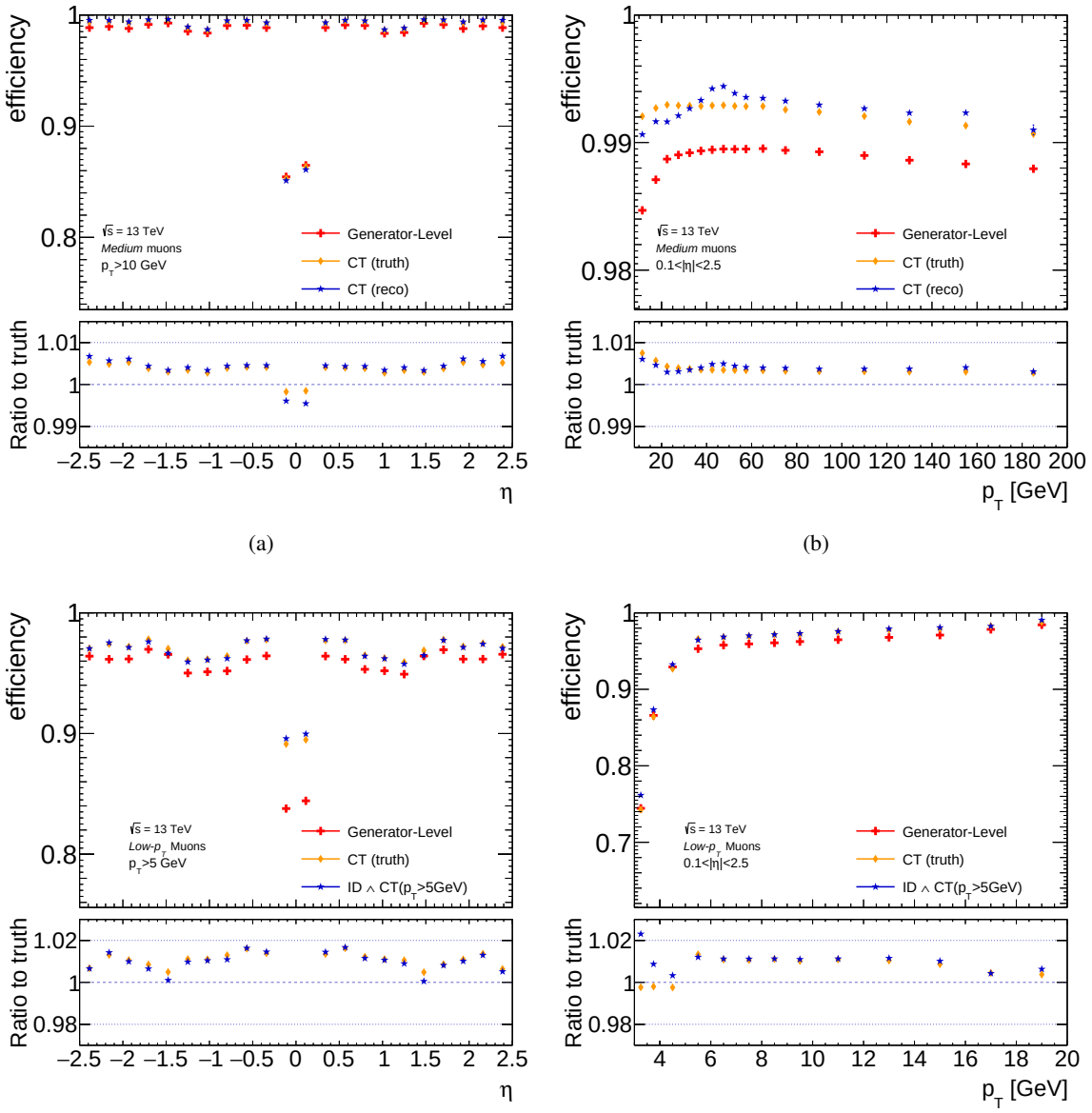

Figure 5.4: Reconstruction efficiency for the Medium identification working point in simulated $Z \rightarrow \mu\mu$ events (top) and for the Low-p_{T} working point in simulated $J/\psi \rightarrow \mu\mu$ (bottom) shown as a function of the probe pseudorapidity (left) and the transverse momentum (right). The red markers indicate the truth efficiency using generator level muons. The red markers show the truth efficiency obtained from generator-level muons and the orange markers show the efficiency of those matched to a CT muon in advance. The blue markers show the reconstruction efficiency obtained by employing the full T&P method using CT muons as probes. Additional kinematic selections on the probe are indicated on each plot. The bottom panel shows the corresponding ratios to the truth efficiency .

muon reconstruction efficiency can be approximated by

$$\epsilon\,(\mathrm{X}) \simeq \epsilon\,(\mathrm{ID}|\mathrm{MS}) \times [\epsilon\,(\mathrm{MS}|\mathrm{ID}) \times \epsilon\,(\mathrm{X}|\mathrm{ID} \wedge \mathrm{MS}) + \epsilon\,(\mathrm{X} \wedge \neg\mathrm{MS}|\mathrm{ID})]\,. \tag{5.6}$$

The first term approximates $\epsilon\,(\mathrm{ID})$, which is valid as discussed above. The second term and third term describe the MS track reconstruction efficiency and the combination efficiency of the two muons tracks, respectively. The last additive term is introduced adhoc to the formula. It accounts for the small fraction of muons without a full reconstructed MS track. These muons occur in the feet and in the crack region where the MS is partially instrumented. In the current form, the efficiency of the MS track reconstruction and of muons without a full MS track would be measured using ID tracks as probes raising the problem of a large background. MS track reconstruction and muon calorimeter tagging are independent from each other and thus this efficiency can be measured using CT muons as probes reducing the background significantly and without introducing a significant bias as illustrated in Figure 5.5. CT muons also have to be used for the last term to reduce the background at an acceptable level. The resulting efficiency parametrization takes the shape of

$$\epsilon\,(\mathrm{X}) \simeq \epsilon\,(\mathrm{ID}|\mathrm{MS}) \times [\epsilon\,(\mathrm{MS}|\mathrm{CT}) \times \epsilon\,(\mathrm{X}|\mathrm{ID} \wedge \mathrm{MS}) + \epsilon\,(\mathrm{X} \wedge \neg\mathrm{MS}|\mathrm{CT})]\,. \tag{5.7}$$

Following the discussion from above, the efficiency of those muons without full MS tracks is biased as well. However, their total contribution to the sample is small such that the net effect becomes negligible. The reconstruction efficiency for the Medium, Tight, Low-p_{T} and High-p_{T} identification criteria can be directly measured using this Equation (5.7). For the Loose criteria however, it can only be applied for the muons which are not primarily a CT muon. The efficiency for the latter is measured separately using MS tracks as probes.

To verify that Equation 5.7 provides a more accurate measurement, Figure 5.6 shows the reconstruction efficiency for Medium muons using each of the probes discussed above, namely CT muons, ID tracks, and the newly introduced two-track probes. These results are shown as a function of the pseudorapidity and of the transverse momentum. The efficiency obtained from two-track probes agrees with the truth efficiency at a level comparable to the one obtained from using ID tracks as probes, across the entire η range. The exception is the crack region $|\eta| < 0.1$ where the additive term significantly contributes. It should be noted that even in this η-region an improvement in the bias is achieved arising from muons reconstructed in the ϕ-sectors with a fully equipped MS. Outside the crack region, no significant p_{T} dependence of the efficiency bias is observed (cf. Figure 5.6(b)).

Revised strategy for the measurement using $J/\psi \to \mu\mu$ decays: Muons from $J/\psi \to \mu\mu$ decays are used to evaluate the muon reconstruction efficiency if the muon p_{T} ranges between 3–15 GeV. Very soft muons suffer from large energy losses in the calorimeter and moreover they are then pulled out of

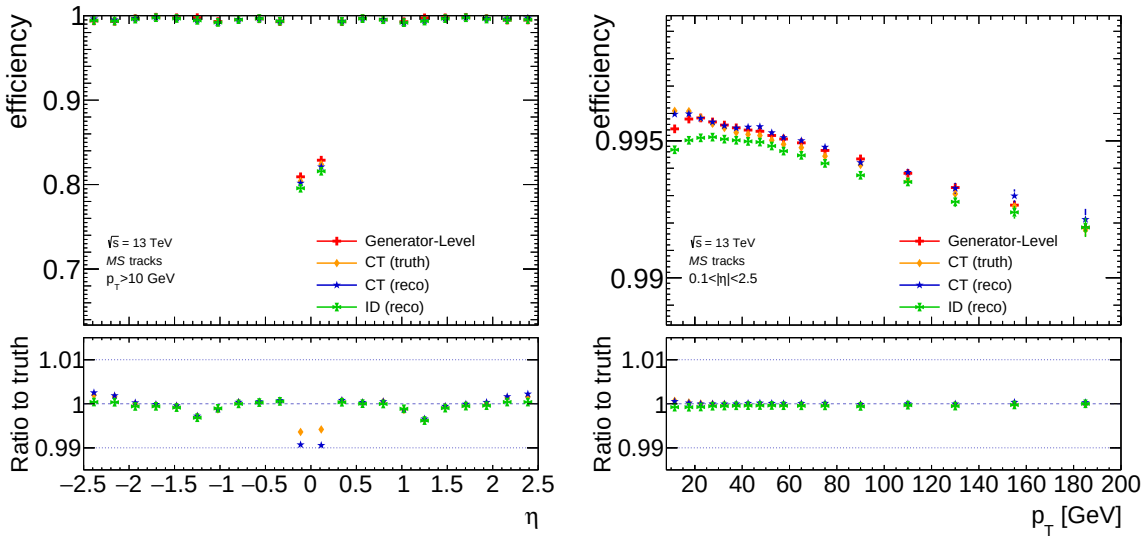

(a) (b)

Figure 5.5: Efficiency of the MS track reconstruction for muons within $0.1 < |\eta| < 2.5$ in simulated $Z \rightarrow \mu\mu$ events shown as a function of the muon pseudorapidity (a) and of the transverse momentum (b). The red markers show the truth efficiency obtained from generator-level muons and the orange markers show the efficiency of those matched to a CT muon in advance. The blue and green markers show the MS track efficiency determined by the T&P method using ID tracks and CT muons as probes, respectively. Additional kinematic selections applied on the probe are indicated on each plot. The bottom panel shows the ratio of each efficiency to the truth efficiency.

the MS by the magnetic field before they reach a second layer. Therefore, the MS track reconstruction efficiency significantly drops for muons with $p_{\mathrm{T}} < 5$ GeV (cf. Figure 5.7). A large fraction of muons does not have a full MS track and hence the additive term in Equation (5.7) significantly contributes. In addition, the problem arises that calorimeter tagging is only available for probes with $p_{\mathrm{T}} > 5$ GeV. For these two reasons, two-track probes have been found to be inappropriate to measure the muon reconstruction efficiency in $J/\psi \rightarrow \mu\mu$ decays with high precision. Muons reconstructed with the ST algorithm are available for any muon p_{T} and provide a good background suppression since additional information from the MS can be exploited. Likewise for the reconstruction efficiency using CT muons, a bias term needs to be added to the efficiency formula accounting for dependencies between the muon

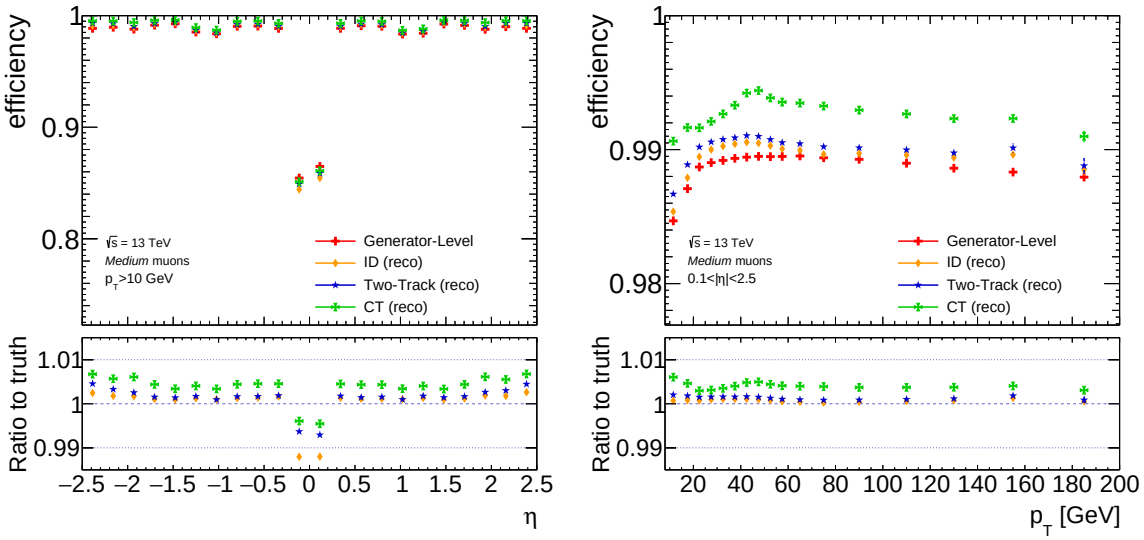

(a) (b)

Figure 5.6: Reconstruction efficiency for Medium muons in simulated $Z \to \mu\mu$ events shown as a function of the pseudorapidity (a) and the transverse momentum (b). The red markers show the truth efficiency. The yellow, blue and green markers show the efficiency obtained from using the full T&P method using ID tracks, two-track probes and CT muons as probes, respectively. Additional kinematic selections applied on the probe are indicated on each plot. The bottom panel shows the corresponding ratios to the truth efficiency.

combination and the ST muon reconstruction algorithm:

$$\epsilon\,(X) = \epsilon\,(\mathrm{ID}|\mathrm{MS}) \times \epsilon\,(X|\mathrm{ID}) \tag{5.8a}$$

$$\simeq \epsilon\,(\mathrm{ID}|\mathrm{MS}) \times \epsilon\,(X|\mathrm{ST}) \times \epsilon\,(\mathrm{ST}|\mathrm{ID}) \times \frac{1}{\epsilon\,(\mathrm{ST}|X)} \tag{5.8b}$$

$$\simeq \epsilon\,(\mathrm{ID}|\mathrm{MS}) \times \epsilon\,(X|\mathrm{ST}) \times \epsilon\,(\mathrm{ST}|\mathrm{ID} \wedge \mathrm{CT\ if}\ p_\mathrm{T} > 5\,\mathrm{GeV}) \times \frac{1}{\epsilon\,(\mathrm{ST}|X)}. \tag{5.8c}$$

From the second to the third line CT probes are imposed where possible to suppress the background. This does not introduce a significant bias as demonstrated in Figure 5.8(a) showing the ST muon reconstruction efficiency against the muon p_T using once purely ID tracks and once CT muons as probes. In contrast to the case using CT muons as probes, the ST efficiency given a muon passing working point X, $\epsilon\,(\mathrm{ST}|X)$ has been found to be compatible with unity within the statistical uncertainties in most cases. Although the usage of ID tracks as probes could not be avoided for muons between 3–5 GeV, the given decomposition of the muon reconstruction efficiency effectively splits up into three parts of which the ID and ST track reconstruction efficiencies are common for all muon identification working points and a third part which allows to assess discrepancies caused by mismodelling in the input variables used for the muon combination and identification algorithm with high precision due to

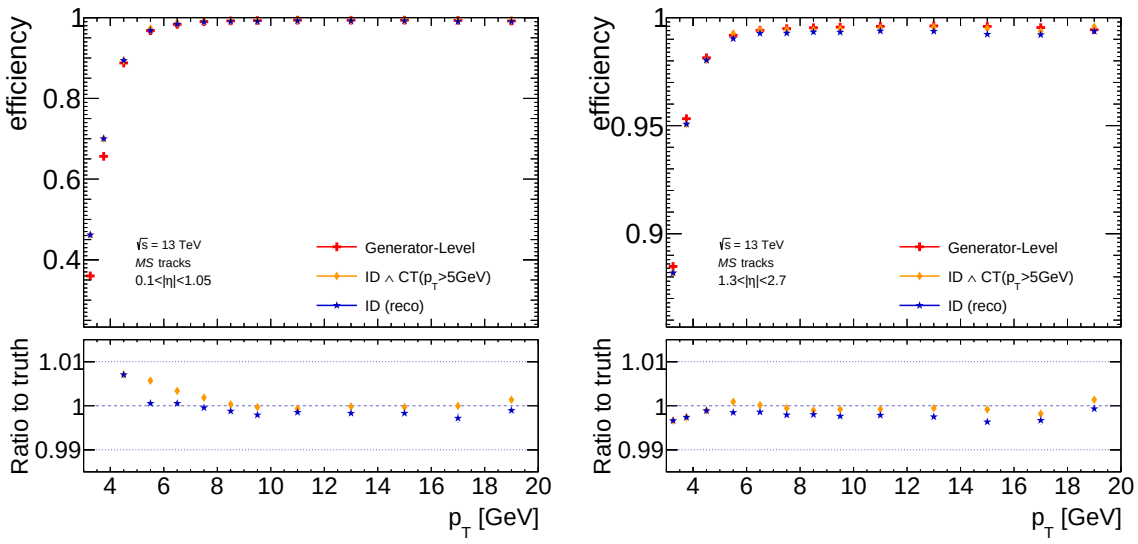

(a) (b)

Figure 5.7: MS reconstruction efficiency as a function of the probe transverse momentum in the barrel (a) and in the endcaps (b) of the ATLAS MS in simulated $J/\psi \rightarrow \mu\mu$ events. The red markers indicate the truth efficiency. The orange markers show the efficiency obtained by the T&P method using CT muons as probes for $p_{\mathrm{T}} > 5$ GeV and ID tracks otherwise. The blue markers show the efficiency using ID tracks as probes. The bottom panel shows the ratio of the respective efficiencies to the truth efficiency.

the low background. The validity of Equation (5.8(a)) is demonstrated in Figure 5.8(b) comparing the reconstruction efficiency for muons passing the Low-p_{T} identification criteria obtained by using ID tracks, CT muons for p_{T} and ST muons as probes to the truth efficiency as a function of the probe p_{T}. The efficiencies obtained from using ST muons or ID tracks excellently agree with the truth efficiency for muons with $p_{\mathrm{T}} > 5$ GeV, where in contrast the efficiency using CT muons as probes shows a bias of one percent, slightly decreasing with p_{T}, in the same p_{T} range. The discrepancy for the very low-p_{T} range is subject of ongoing research as already discussed above. The formula (5.8(a)) is employed to measure the efficiency of the Low-p_{T} (MVA), Loose excluding the CT muons, Medium, and Tight efficiency. Likewise in the $Z \rightarrow \mu\mu$ reconstruction measurement, the efficiency of Loose CT muons is measured using MS probes.

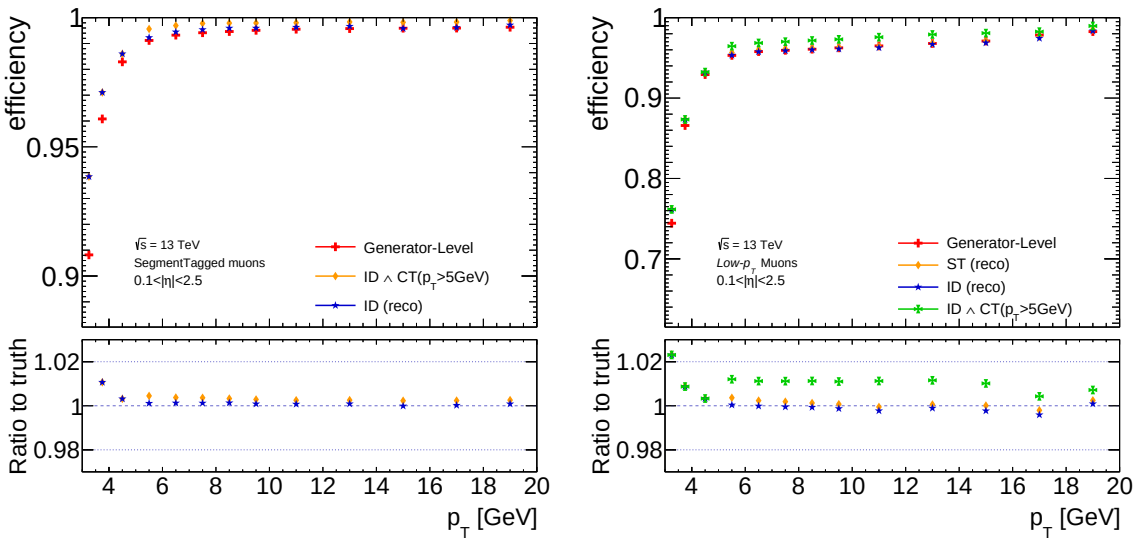

(a) (b)

Figure 5.8: Reconstruction efficiency for muons reconstructed with the ST algorithm (a) and for muons passing the Low-p_{T} identification criteria (b) shown as function of p_{T} in simulated $J/\psi \rightarrow \mu\mu$ events for muons within $0.1 < |\eta| < 2.5$. The red markers show the truth efficiency obtained using generator-level muons, the orange markers indicate the efficiency obtained by the T&P method using CT muons for $p_{\mathrm{T}} > 5$ GeV in (a) and ST muons in (b) and the blue markers using ID tracks as probes. The green markers in (b) show the Low-p_{T} reconstruction efficiency using CT muons for $p_{\mathrm{T}} > 5$ GeV as probes. The bottom panel shows the ratio of the respective efficiencies to the truth efficiency.

5.2 Simulated Samples and Selected Dataset

The results presented in the following are based on the $Z \rightarrow \mu\mu$ and J/ψ event samples in the full pp collision dataset recorded by the ATLAS experiment at $\sqrt{s} = 13$ TeV. Only events recorded under stable detector conditions are selected resulting in a total integrated luminosity of 139 fb^{-1} [149]. The data is compared to simulated events including all SM processes concerned. The $Z \rightarrow \mu\mu$ and $J/\psi \rightarrow \mu\mu$ events are referred to as signal. In the following, the Monte Carlo simulation programs used for each process are briefly described. More details can be found in Refs. [233–236].

The SM processes of $Z \rightarrow \mu\mu$, $Z \rightarrow \tau\tau$, $W(\rightarrow \mu\nu)$ and $Z^*/\gamma^* \rightarrow \mu\mu$, where the $*$ indicates the off-shell contributions to the final state, and diboson production are simulated using the Powheg-Box 2 generator [113] at NLO with the `CT10` PDF set [103] for the hard scattering process. For the parton showering, Pythia 8.186 [123] with the `CTEQ6L1` PDF set [102] and the AZNLO [237] underlying event tune are used. For comparison, $Z \rightarrow \mu\mu$ is additionally simulated with the Sherpa v2.2.1 generator [238] using the `NNPDF3.0nlo` PDF set [105]. The hard scattering process is calculated

Table 5.1: Overview of the simulations used for the SM processes in the $Z \to \mu\mu$ and $J/\psi \to \mu\mu$ T&P efficiency measurements. More details of the generator configurations can be found in [233–236]. For the simulation of diboson production, $WW \to \ell\nu\ell\nu$, $WZ \to \ell\nu\ell\ell$, $ZZ \to \ell\ell\ell\ell$, $ZZ \to \nu\nu\ell\ell$, $WZ \to qq\ell\ell$, $ZZ \to qq\ell\ell$ processes are considered. Samples marked by a † are only used for systematic studies and samples marked by a ‡ are additionally generated using the AFII detector simulation.

Process	Generator	Showering	PDF set	UE tune	Cross section order
$Z \to \mu\mu$‡	Powheg-Box 2	Pythia 8.186	CT10	AZNLO	NLO
$Z \to \mu\mu$†	Sherpa v2.2.1		NNPDF3.0nlo	Sherpa	NLO
$J/\psi \to \mu\mu$	Pythia 8B		CTEQ6L1	A14	LO
Drell–Yan	Powheg-Box 2	Pythia 8.186	CTEQ6L1	AZNLO	NLO
Diboson	Powheg-Box 2	Pythia 8.186	CTEQ6L1	AZNLO	NLO
$Z \to \tau^+\tau^-$	Powheg-Box 2	Pythia 8.186	CT10	AZNLO	NLO
$t\bar{t}$	Powheg-Box 2	Pythia 8.186	NNPDF3.0nlo	A14	NLO
$W(\to \mu\nu)$	Powheg-Box 2	Pythia 8.186	CT10	AZNLO	NLO
$b\bar{b}$	Pythia 8B		NNPDF2.3lo	A14	LO
$c\bar{c}$	Pythia 8B		NNPDF2.3lo	A14	LO

to NLO in perturbation theory with up to two additional jets, with up to four jets in LO using the Comix [239] and OpenLoops [121, 240] libraries. The jets are matched with the Sherpa parton shower [241] using the MEPS@NLO prescription [120, 242–244] with tuned parameters developed by the Sherpa authors. The prompt $J/\psi \to \mu\mu$ sample is generated using Pythia 8B with the CTEQ6L1 PDF set and the A14 underlying event tune [245]. PHOTOS++ [128] was used to simulate the effect of final state radiation of the muons. To optimize the statistics in the phase space accepted by the trigger, the leading muon is required to have a p_{T} larger than 6 GeV. SM $t\bar{t}$ production is generated using the Powheg-Box 2 generator at NLO with the NNPDF3.0nlo PDF set [105] while the parton showering is performed with Pythia 8.186, the NNPDF2.3lo PDF set [104] and the A14 underlying event tune. The simulation of heavy-flavour jet, $b\bar{b}$ and $c\bar{c}$ production, is performed using Pythia 8B [123] with the NNPDF2.3lo PDF set and the A14 underlying event tune. For all simulated samples except the multi-jet and J/ψ sample, the hadronization of b- and c-hadron decays is performed with EvtGen1.2.0 [125]. The event generators, the parton showering prescriptions, the parton distribution function sets, the underlying event parameters for all simulated processes are summarized in Table 5.1. All simulated events are passed through the full ATLAS detector simulation as described in section 3.6. A small fraction of the $Z \to \mu\mu$ events is also processed using the fast-simulation chain to study the impact of a parameterized calorimeter response on the efficiencies.

5.3 The Muon Reconstruction Efficiency in $Z \rightarrow \mu\mu$ Decays

$Z \rightarrow \mu\mu$ decays are used to measure the muon reconstruction efficiency for muons with $p_{\mathrm{T}} > 15$ GeV by means of T&P. In this section, the results of the muon reconstruction efficiency exploiting the strategy outlined in section 5.1 is presented. The section is structured as follows: First the selection criteria to obtain a sample pure in $Z \rightarrow \mu\mu$ events are described. The background estimation method as employed in Ref. [211] is presented together with an improved method developed in the course of this work resulting in smaller systematic uncertainties. The section continues with a discussion of the considered sources of systematic uncertainties and concludes with the presentation of the final results.

5.3.1 Tag and Probe Selection Criteria in $Z \rightarrow \mu\mu$ Events

To derive a sample pure in $Z \rightarrow \mu\mu$ events a set of selection criteria has to be applied on the T&P pairs. The criteria are summarized in Table 5.2 and explained in more detail in the following. The tag muon is required to satisfy the Medium identification criteria and have fired a single muon trigger. The available trigger vary based on the instantaneous luminosity conditions during the data taking. A requirement on the muon p_{T} to be five percent higher than the online trigger threshold removes the interval in which the trigger is not fully efficient. This trigger turn-on is challenging to model in simulation and hence may introduce a bias into the measurement. To suppress non prompt muons originating from jets, the muon must fulfill the *FCTight* isolation selection criteria as introduced in section 5.6.2. Further requirements on the tag impact parameters, $|d_0| / \sigma(d_0) < 3$ and $|z_0 \sin(\theta)| < 0.5$ mm ensure a maximum purity of tags originating from the primary interaction vertex. The three considered probe kinds, namely the two-track probes, CT muons and MS tracks, have to satisfy the specific track quality cuts listed in Table 5.2 and must have $p_{\mathrm{T}} > 10$ GeV and $|\eta| < 2.5$. Additional requirements on the impact parameters $|d_0| / \sigma(d_0) < 3$ and $|z_0| < 10$ mm are applied to reject background. A broad window of the T&P pair invariant mass of $m_{\mathrm{T\&P}} \in [61, 121]$ GeV selects events from the Z-resonance where the signal is accumulated in oppositely charged (OC) T&P muon pairs. Additional cuts on the probe track and calorimeter isolation need to be satisfied as reported in Table 5.2 for such pairs. In contrast, same charged (SC) pairs are expected to originate from QCD events and are used for the background estimate of the measurement. No isolation requirement is applied for those pairs to maximize the statistics and thus minimize the uncertainties in the background estimate.

Table 5.2: Selection criteria applied for the measurement of the muon reconstruction efficiencies exploiting $Z \to \mu\mu$ events

Tag selection			
Trigger	p_{T} threshold [GeV]	year	$\mathcal{L}_{\mathrm{inst}}$ [$\mathrm{cm}^{-2}\mathrm{s}^{-1}$]
	> 20	2015	—
	> 24	2016	$< 10^{-34}$
	> 26	2016	$\geq 10^{-34}$
	> 26	2017–2018	—
Kinematics	$p_{\mathrm{T}} > 1.05\times$ nominal trigger p_{T} threshold, $\lvert\eta\rvert < 2.5$		
Identification	Medium working point		
Impact parameters	$\lvert d_0\rvert / \sigma(d_0) < 3$, $\lvert z_0 \sin(\theta)\rvert < 0.5$ mm		
Isolation	*FCTight* isolation		
Probe selection			
Kinematics	$p_{\mathrm{T}} > 10$ GeV, $\lvert\eta\rvert < 2.5$		
Impact parameters	$\lvert d_0\rvert / \sigma(d_0) < 3$, $\lvert z_0\rvert < 10$ mm		
Isolation	requirements on $\frac{p_{\mathrm{T}}^{\mathrm{VarCone20}}}{p_{\mathrm{T}}} < 0.06$ and $\frac{E_{\mathrm{T}}^{\mathrm{TopoCone20}}}{p_{\mathrm{T}}} < 0.1$		
	Two-track probes	CT muon	MS tracks
Track requirements	ID track quality cuts described in Section 4.3		—
	Matched to a MS track $\Delta R < 0.05$	Passes CT cuts	
T&P pair requirements			
Invariant mass	$m_{\mathrm{T\&P}} \in [61; 119]$ GeV		
Electric charge	$q_{\mathrm{tag}} \cdot q_{\mathrm{probe}} < 0$		

5.3.2 Background Estimation

The selected simulated T&P pairs are automatically clean in $Z \to \mu\mu$ decays as these are considered as signal. In contrast, the T&P pairs recorded in data are contaminated by pairs where the probe is not a prompt muon. Their contribution needs to be estimated and subtracted each from the probe and matches before the data efficiency is calculated. In previous iterations of the measurement any T&P pair not originating from a $Z \to \mu\mu$ event was treated as background. This background can be divided into two categories: On the one hand there is the irreducible background, where both muons originate from primary particle decays, such as dileptonic $t\bar{t}$, or $Z \to \tau\tau$. The estimation for this kind is purely based on Monte Carlo. On the other hand, there is the reducible background where either the second muon is produced in meson decays as in $W \to \mu\nu$+jets events or even both muons originate from hadrons, referred to as multi-jet. As the muon identification criteria provide a rejection power of more

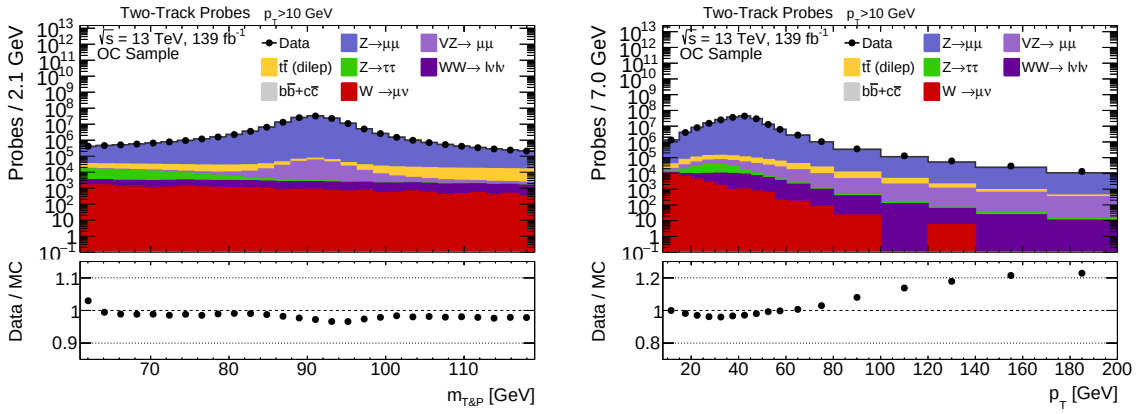

(a) (b)

Figure 5.9: Distribution of the of the invariant mass of the T&P pair (a) and of the transverse momentum of the two-track probes (b) in the recorded Run 2 dataset and simulated events passing the selection criteria listed in Table 5.2. Each background process shown is estimated entirely from simulation. The bottom panel shows the ratio of data to simulation.

than 98% against those non-prompt muons [211], the available Monte Carlo statistics is not sufficient to extract an estimate with reasonable small uncertainties. In addition, soft QCD processes are very challenging to model and therefore the estimate might be subject to a significant mismodelling. Hence, the reducible contribution is estimated in a data driven way. Two estimation techniques have been employed for the $Z \to \mu\mu$ T&P measurements. In the early Run 2 dataset the ABCD method was used which has been superseded by a background template fit method developed in the course of this thesis.

After applying the T&P selection, the purity of $Z \to \mu\mu$ decays in the probe distributions is about 99.9% (cf. Figure 5.9). The remaining 0.1% is comprised by diboson production involving $Z \to \mu\mu$ decays, irreducible contributions from $Z \to \tau\tau$ and $t\bar{t}$ as well as reducible contributions arising from $W \to \mu\nu$+jets and multi-jet events where probes are originating from secondary muons from pion, kaon or heavy-flavour decays. The modelling of the probe p_{T} shown in Figure 5.9(b) agrees with data at a level of 5% for $p_{\mathrm{T}} \lesssim 80$ GeV and deteriorates to a 20% level for momenta much beyond that threshold. The underlying reason for this discrepancy is an observed mismodelling of the Z-boson recoiling against high-p_{T} jets. It has been checked that a simulation based correction as outlined in Ref. [223] has negligible impact on the final results.

The ABCD background estimation method exploits the statistical independence of two uncorrelated variables and has been used in the previous iteration of the measurement [211]. The mass window is narrowed down to $m_{\mathrm{T\&P}} \in [81; 101]$ GeV for the sake of background suppression. The

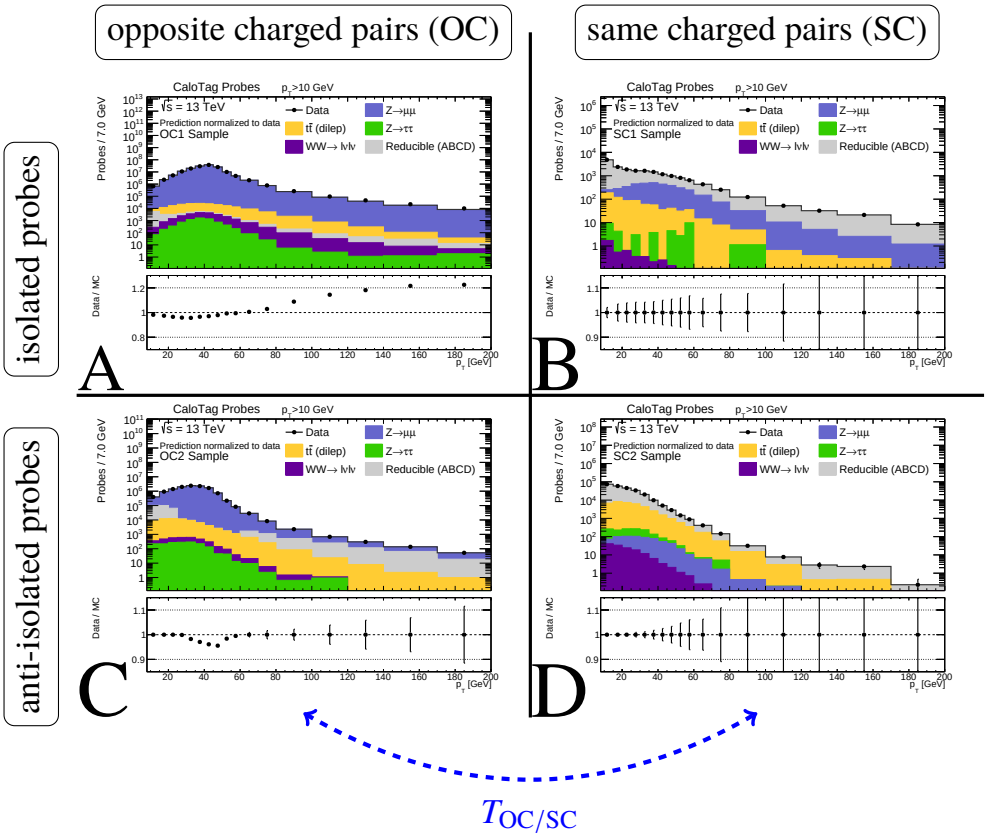

Figure 5.10: Sketch of the ABCD background estimation method used to estimate the reducible background in a data-driven way.

phase space is divided into four regions (visualized in Figure 5.10) using the charge product of the T&P pair and whether the probe is isolated in the ID and in the calorimeter. The signal accumulates in the isolated OC region. The shape of the reducible background is assumed to coincide between the isolated OC and SC region. Therefore, distributions of SC data are taken as shape template. To account for T&P pairs with same charge in simulation arising from irreducible background, such as diboson processes or charge-flips in $Z \to \mu\mu$ events, their contribution is estimated using simulation and subtracted from the template beforehand. The magnitude of the template needs to be corrected for the different rates of OC and SC T&P pairs from QCD by the so-called transfer factor $T_{\mathrm{OC/SC}}$. It is calculated from the ratio of the number of events between the anti-isolated OC and SC regions. The number of reducible background events in the OC region is then given by

$$N_{\mathrm{OC}}^{\mathrm{reducible}} = N_{\mathrm{SC,isolated}}^{\mathrm{data}} \times T_{\mathrm{OC/SC}} = N_{\mathrm{SC,isolated}}^{\mathrm{data}} = N_{\mathrm{SC,isolated}}^{\mathrm{data}} \times \frac{N_{\mathrm{OC,\ anti\text{-}isolated}}}{N_{\mathrm{SC,\ anti\text{-}isolated}}}. \tag{5.9}$$

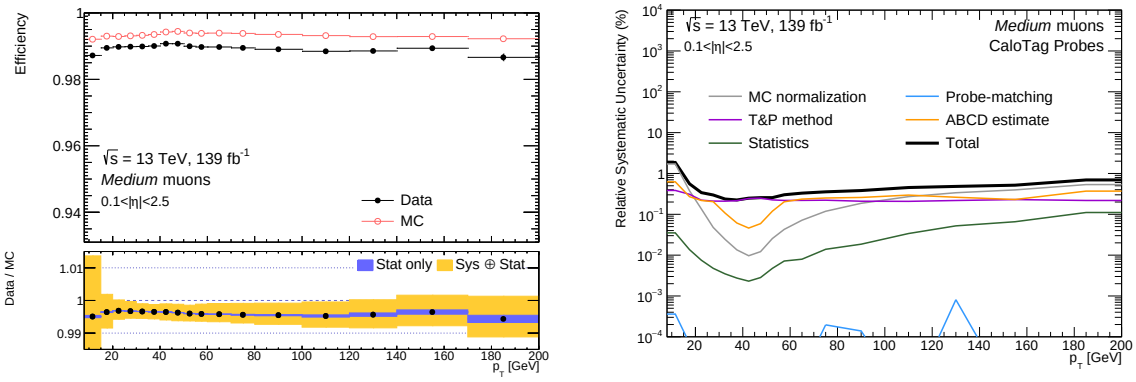

(a) (b)

Figure 5.11: Muon reconstruction efficiency (a) of the Medium identification criteria measured in simulated and reconstructed $Z \to \mu\mu$ events with $m_{\mathrm{T\&P}} \in [81; 101]$ GeV using CT muon within $0.1 < |\eta| < 2.5$ as probes as a function of the transverse momentum. The background is estimated from the ABCD method. The bottom panel shows the associated efficiency scale factor with the systematic and statistical uncertainties indicated by the yellow and blue error bands, respectively. The breakdown of the uncertainties is shown in (b).

Applying the same strategy as in the previous iteration of this measurement, i.e. using CT muons as probes and the ABCD method for the background estimation, the reconstruction efficiency for Medium muons in the full Run 2 dataset is measured to approximately 98.6%, shows only a small dependence on the muon transverse momentum (cf. Figure 5.11(a)). It agrees with the expected efficiency measured in simulation within $\lesssim 1\%$. These small differences can be mainly attributed to dysfunctional detector modules or misaligned muon chambers and will be discussed in more detail in section 5.3.4. However, this result has two major limitations. The first one is the size of uncertainty on the background estimation, which is comparable to the size of the already discussed truth closure uncertainty (cf. orange and purple lines in Figure 5.11(b)). Thus it poses a second limitation on the precision of the measurement. The second one is the break down of the method in cases of large background rates (e.g. at low p_{T} or in the ID efficiency measurement) that may sometimes result in unphysical efficiencies exceeding one which were in the past artificially truncated to unity. Consequently, to fully benefit from the improvements in precision by the revised strategy, a more accurate background estimation is required.

The template fit method: To overcome the drawbacks of the ABCD method, the template shape fit method has been developed for the Run 2 results. In each bin of the observable considered, such as p_{T} or η, a fit in the OC $m_{\mathrm{T\&P}}$ mass spectrum is performed using the *RooFit* toolkit [246], separately for probes and matches. This allows to separate the peaking signal of the $Z \to \mu\mu$ decays from the

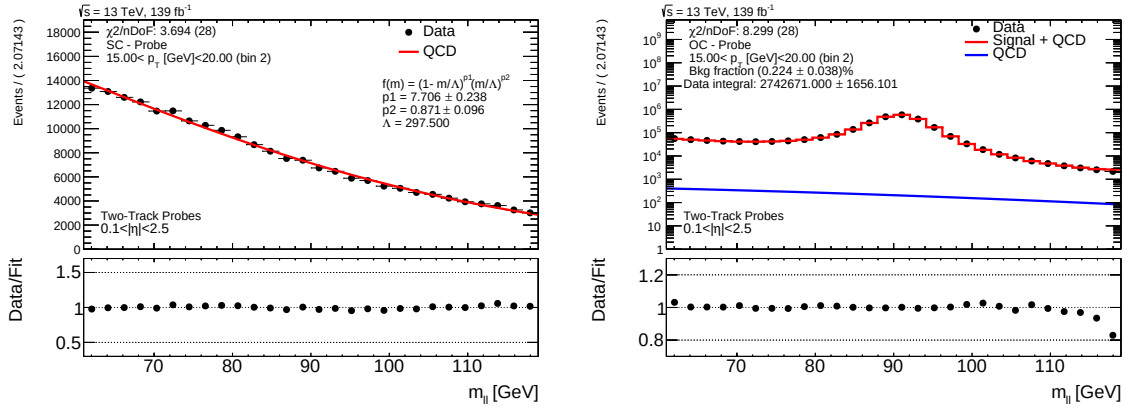

(a) (b)

Figure 5.12: Illustration of the two shape fits performed to estimate the reducible background in the $Z \to \mu\mu$ reconstruction efficiency measurement shown for two track probes with $p_{\mathrm{T}} \in [15; 20]$ GeV and $|\eta| \in [0.1; 2.5]$. In (a), the data points are replaced by the functional form given in Equation (5.10) by fixing its free parameters, p_1, p_2. The obtained function is then used to model the background in the fraction fit performed in (b). The shown fit functions are normalized to the number of data events. The bottom panel shows the ratio of the data to the prediction by the fit function.

smoothly falling background. As the background fraction is larger in the side bands of the Z-mass peak than underneath (cf. Figure 5.9(a)), the mass window is broadened up to $m_{\mathrm{T\&P}} \in [61; 119]$ GeV to precisely estimate its fraction. The signal template is constructed from simulation using any T&P pair where both particles originate from a hard process including the $Z \to \mu\mu$ signal and the irreducible background processes. Like in the ABCD method, the background template is taken from the $m_{\mathrm{T\&P}}$ distribution in SC-data events. To make the fit robust against fluctuations in the SC template, it is first approximated in an intermediate fit using the functional form

$$f(m_{\mathrm{T\&P}}) = \left(1 - \frac{m_{\mathrm{T\&P}}}{\Lambda}\right)^{p_1} \left(\frac{m_{\mathrm{T\&P}}}{\Lambda}\right)^{p_2}, \tag{5.10}$$

where p_1 and p_2 are free parameters and Λ is interpreted as the energy necessary to produce the di-muon pair [247]. In general, Λ is not constrained and can be allowed to float as well. However, cases where $\frac{m_{\mathrm{T\&P}}}{\Lambda} \simeq 1$ and p_1 is negative cause the fit to become highly unstable and unreliable. Therefore, Λ is fixed to be 2.5 times larger than the upper edge of the input mass distribution, i.e. $\Lambda = 2.5 \times 119$ GeV=297.5 GeV. In bins with poor SC data statistics, i.e. less than 16 events, the background is assumed to be a horizontal line across the mass spectrum. The extracted functional form with the fixed parameters, p_1 and p_2 is then fed into the final fit determining the background fraction (cf. Figure 5.12(b)). Finally, the obtained background fraction is subtracted from data and the efficiency is calculated.

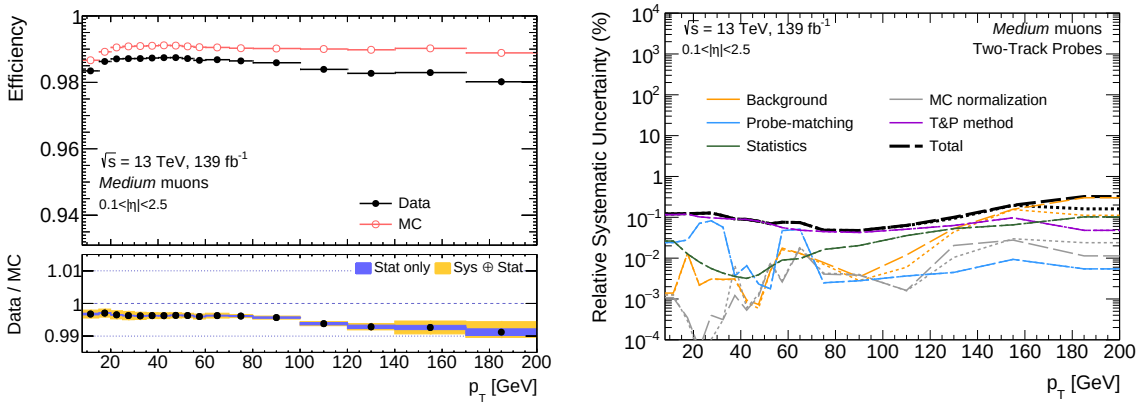

(a) (b)

Figure 5.13: Muon reconstruction efficiency for the Medium identification criteria using two-track probes in the region $0.1 < |\eta| < 2.5$ measured in simulation and the full Run 2 dataset (a). The bottom panel shows the associated efficiency scale factor with the systematic and statistical uncertainties indicated by the yellow and blue error bands, respectively. The breakdown of the uncertainties is shown in (b). The dashed (dotted) lines indicate the $+1\sigma$ (-1σ) variation of each nuisance parameter.

Figure 5.13 shows the Medium muon reconstruction efficiency obtained by using the two-track probes and the template shape fit method measured in the full Run 2 dataset and in simulation as a function of p_{T} together with the breakdown of the systematic sources. The reconstruction efficiency measured in simulation by using two-track probes is about $\sim 0.3\%$ lower than the efficiency obtained with the CT probes and shows a subtle increase at low p_{T}. Both observations are expected due to the intrinsic bias of CT muons predicting a too large efficiency as discussed in section 5.1.1. The efficiency scale factor obtained from the improved analysis is much flatter at p_{T} below 100 GeV than the one from the previous iteration. The size of the systematic error on the background estimate (a detailed discussion about the contributing sources is given in section 5.3.3) is evaluated to be $O\left(10^{-2}\right)$ % and the uncertainty on the T&P method is reduced from 0.5% to $\lesssim 0.1\%$.

5.3.3 Systematic Uncertainties in the $Z \rightarrow \mu\mu$ Reconstruction Measurement

The scale factor maps provided for the physics analysis, presented in section 5.3.4, are subject to systematic uncertainties as any measurement. Several sources of systematic uncertainties have been considered which are explained and their contribution to the total uncertainty is discussed below.

- **Statistics**: This category comprises the statistical uncertainty from the recorded dataset and the amount of generated Monte Carlo events. This source becomes dominant for muons with transverse momenta much beyond or below the peak of the p_{T} distribution located at around

50 GeV. As stated in section 5.3.4, the efficiency scale factors applied in the physics analysis are functions of the two muon angles split into each year of data taking. A binning common for all years is chosen such that the detector geometry is represented as precisely as possible and that the statistical uncertainty is well below 1% in each bin for the 2015 dataset which is the smallest one. The average contribution from the statistical uncertainty to total uncertainty is at the order of $O\left(10^{-2}\right)$ % outside the crack region and by a factor of four larger in the crack region.

- **T&P method**: The measurement strategy potentially introduces an efficiency bias (cf. the detailed discussion in Section 5.1). The T&P result on Monte Carlo is compared to the truth-level efficiencies using the same sample. While the bias is expected to affect both measured efficiencies in data and simulation in a similar way and thus may potentially cancel in their ratio, half of the observed deviation between the measured T&P and the truth efficiency in simulation is propagated to the scale factor uncertainty to conservatively account for dissimilarities in the biases. By using the two-track-probes the truth closure uncertainty is diminished from $\sim 0.5\%$ to $\lesssim 0.1\%$ (cf. Figure 5.13(b) and 5.11(b)).

- **Probe-matching**: The probe tracks are defined to be matched if the corresponding track, either a muon satisfying criteria X, a MS or ID track, is found within an angular cone with size $\Delta R < 0.05$. Alternatively, the probe can be defined as matched if the track itself has been used to form the final muon track. In collision events with a large activity many ID tracks are produced and more than one close-by probe track could be selected. The possible deviations in the efficiency between the two approaches are considered as systematic uncertainty. Its magnitude has been found to be of $O\left(10^{-3}\right)$ %.

- **Background**: Three different sources enter this category. The first one arises from the extracted parameters p_1 and p_2 in the SC fit. They are simultaneously varied by their respective $\pm 1\sigma$ uncertainty and the fit extracting the background fraction is then re-executed. The deviations on the final efficiency are fully propagated to the scale factor uncertainty. The variation also allows to estimate the impact from potential shape differences between the SC and OC region, at the same time. The size of this uncertainty has been estimated to be at the level of $O\left(10^{-3}\right)$ %. The second source also concerns the approximation of the reducible template by the power law given in Equation 5.10 where Λ is arbitrarily chosen to be 2.5 times of the upper edge in the mass spectrum to ensure a stable fit. Possible effects from this constraint on the background fit are estimated by lowering and lifting Λ to two and three, respectively. The changes in the scale factors are observed to be below $\lesssim O\left(10^{-3}\right)$ % due to this effect. Finally, the background-fractions for probes and matches are varied by their respective uncertainty to evaluate the effect on the data efficiency. This uncertainty has the largest contribution to the uncertainties considered for the background estimate with a magnitude at the order of $O\left(10^{-2}\right)$ %.

- **MC-normalization**: The MC simulations are normalized to their respective cross sections and then scaled to the luminosity of the respective dataset. Uncertainties on the cross section of each process change the composition of the signal template in the side bands of the peak and thus potentially affect the result in the fraction fit. For this reason, the normalization of each Monte-Carlo sample is varied by the measured cross section uncertainties reported in Refs. [248–250] affecting the final result at the order of $O\left(10^{-3}\right)$ %. The uncertainty on the total normalization of the dataset is expected to affect the SC data template where the contamination of real T&P pairs is subtracted using simulation. The total integrated luminosity is known at a precision of 2% [251]. Possible effects from this uncertainty are studied by varying the normalization of the whole simulation and are found to be at the same level.

- **p_{T}-flatness**: Even with the large dataset at $\sqrt{s} = 13$ TeV, the statistics is only sufficient to bin the scale factor maps in two observables. Given that the scale factor is almost flat in p_{T} (cf. Figure 5.13(a)) and that more pronounced observable dependencies are observed in the η–ϕ plane, the scale factor maps are provided as a function of these two variables. Nevertheless, to take into account this tiny dependency an extra systematic has been assigned. The scale factor is measured against p_{T} as shown in Figure 5.9(b). Relative deviations in the scale factor from the value given at the maximum of the probe p_{T} distribution ($p_{\mathrm{T}} \simeq 50$ GeV) are added in quadrature to the total systematic uncertainty. The deviations are shown in Figure 5.14(a) and have been evaluated to be at the level of $O\left(10^{-3}\right)$ % for muons with transverse momenta below 400 GeV and to be at level of 0.03 for muons around a TeV.

- **Limitations of the T&P method**: Muons carrying very high momenta are extremely rare such that the statistical uncertainty starts to significantly contribute for muons beyond 100 GeV and dominates for muons not much beyond that threshold. Extrapolations into this phase space are very challenging putting the reliability and applicability of the method in question. Furthermore, the muon reconstruction efficiency slightly degrades as the likelihood of a very high energy loss in the calorimeter increases with the muon energy. This may cause the successful reconstruction of a combined muon to fail and becomes a measurable effect for momenta beyond 200 GeV. When applying the resulting scale factor to muons above that threshold, an additional systematic uncertainty accounts for potential differences between simulation and collision data in the likelihood of such a catastrophic energy loss. For this purpose, the p_{T}-dependent efficiency loss in simulated high-mass Drell–Yan events is approximated by a linear fit for $p_{\mathrm{T}} > 200$GeV in three different η regions (cf. Figure 5.14(a)). The degradation of up to 7% per TeV in transverse momentum is applied as an additional conservative systematic uncertainty on the scale factor if the uncertainty on the p_{T}-flatness uncertainty exceeds the numerical value given by this uncertainty.

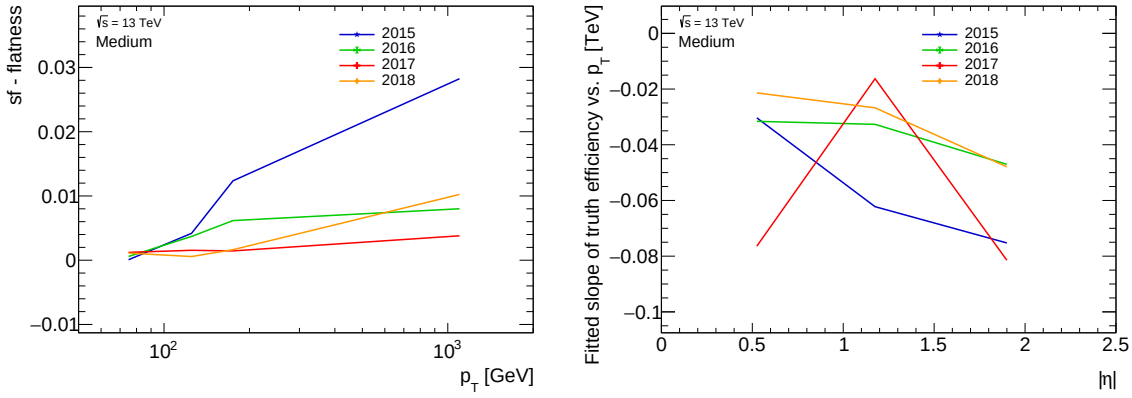

(a) (b)

Figure 5.14: Slope of the Medium muon reconstruction efficiency for muons with $p_{\mathrm{T}} > 200$ GeV per TeV in transverse momentum (b), evaluated in simulated Drell–Yan and $Z \rightarrow \mu\mu$ events and the deviation of the scale factor in each p_{T} bin from the bin containing the peak of the p_{T} distribution (a). The numbers are extracted for each year of data taking and are used to assign an extra uncertainty on the efficiency scale factor.

5.3.4 Results of the $Z \rightarrow \mu\mu$ Reconstruction Measurement

The reconstruction efficiencies for the Loose, Medium, and Tight identification criteria are compared against each other in Figure 5.15 as functions of the pseudorapidity and the transverse momentum of the probe. About 98% of the muons are identified as Loose across the considered η range. The efficiency of the Medium criteria matches with the Loose efficiency except in the crack region ($|\eta| < 0.1$) where a drop to 85% is observed due to the partially instrumented MS where no CB muons can be reconstructed. The Tight criteria accept about 95% of the muons with the largest dependence on p_{T} amongst the three working points. Both features arise from the p_{T} dependent selections on the ρ' and $Z\left(\frac{q}{p}\right)$ variable discussed in section 4.3. The measured data efficiencies agree with the simulated efficiencies at the one percent level depending mainly on the detector region with a slight deterioration at high p_{T}. It has been outlined that the muon reconstruction efficiency measurement aims to correct discrepancies between the simulated and measured efficiency caused by dysfunctional detector modules during the data taking. Hence the scale factor maps of the the Loose, Medium, Tight and Low-p_{T} (and its MVA variant) identification working point which are then used in the physics analysis are derived as functions of the azimuthal angle and the pseudorapidity. The maps for the High-p_{T} selection criteria are also derived as functions of the ϕ and η, but with a more granular binning in order to better represent the detector regions vetoed by the working point. To illustrate effects from dysfunctional detector modules on the total data efficiency, Figures 5.16 and 5.17, depict the reconstruction efficiency in data for the Medium and High-p_{T} identification working points together with their respective scale factor maps. As already mentioned the Medium muon reconstruction

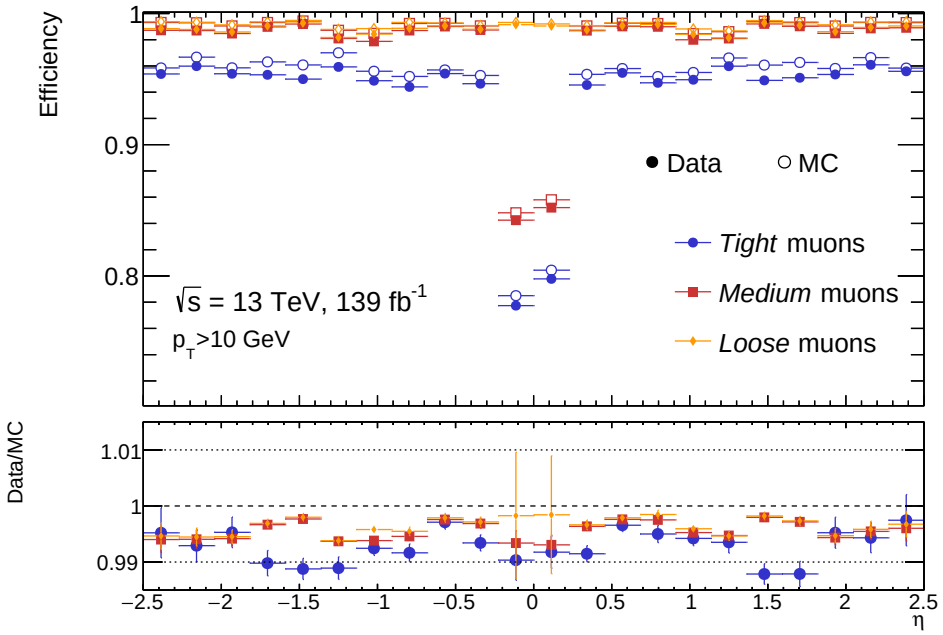

(a)

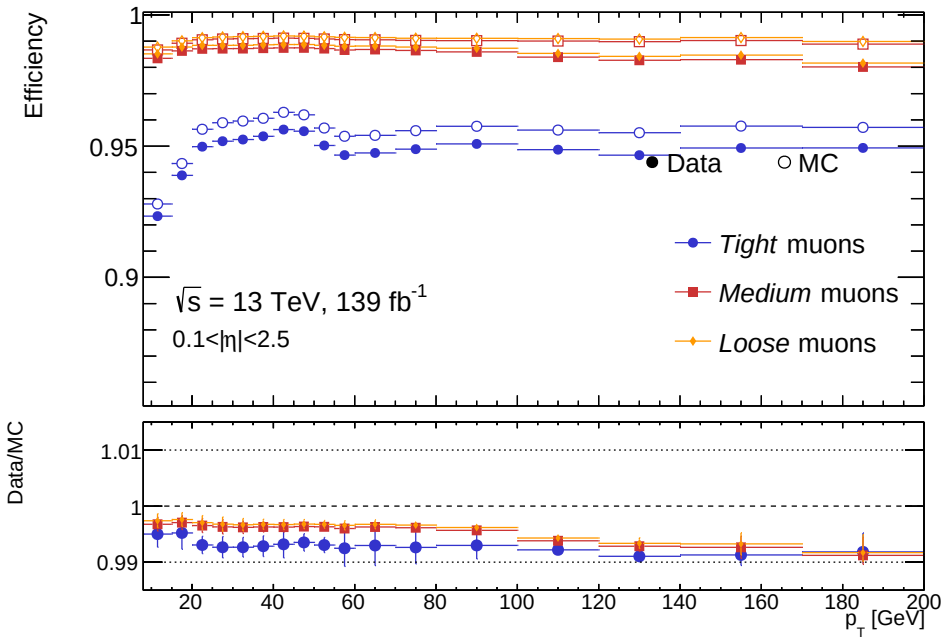

(b)

Figure 5.15: Measured muon reconstruction efficiencies for the Loose, Medium and Tight identification criteria in simulated $Z \rightarrow \mu\mu$ events and in the full Run 2 dataset in bins of the pseudorapidity (a) for muons with $p_{\mathrm{T}} > 10$ GeV and of the transverse momentum (b) in the region $0.1 < |\eta| < 2.5$. The bottom panel shows the associated efficiency scale factor. The error bars indicate the quadratic sum of statistical and systematic uncertainties.

efficiency exceeds 98.9% for a large fraction of the shown detector area. The drops in efficiency by 1% between $\eta \in [-1.5; 1.5]$ are caused the superconducting toroid coils which are along the path of the muons and excellently modelled in simulation. The largest drops in the efficiency are observed for the partially equipped ϕ sectors in the crack regions which also show the poorest modelling. Other locations with a relatively large scale factor, e.g., at $(\eta, \phi) \simeq (-1.3, -1.5)$ have been traced to poorly aligned MDT chambers, or at $(\eta, \phi) = (-2.5, -1)$ to malfunctioning CSC chambers in the 2017 dataset. The high-p_{T} working point shows the smallest efficiency of about 80% in average due to the more stringent requirement of three associated precision layers. Drops in the data-efficiency for $|\eta| < 2$ are associated to the veto of badly aligned chambers which are unacceptable to retain a good momentum resolution. In the CSC chamber located at the blind spot $(\eta, \phi) = (-2, 0)$, the reconstructed hits had insufficient quality.

To conclude this section, Figure 5.18 shows the Medium muon reconstruction efficiency as a function of the integrated luminosity interval of the full Run 2 dataset. The ATLAS MS maintained a constant, high reconstruction efficiency throughout its operation. Tiny steps in the efficiencies are observed at 36 $\mathrm{fb}^{-1}$and 79 fb^{-1}corresponding to the end of the data takings in the years 2016 and 2017, respectively where the system was shut over the winter and maintained. To better model these little differences caused by temporarily dysfunctional chambers in the corresponding years, the scale factor maps provided to the physics analysis are additionally split in each year of data taking. The maps for the other working points are given in Appendix A.1. The scale factors are applied in the physics analysis for every muon with $p_{\mathrm{T}} > 15$ GeV.

5.4 Reconstruction Efficiency for Muons with Low p_{T}

Muons stemming from a Z boson decay rarely have transverse momenta below 10 GeV limiting the available statistics to properly measure the muon reconstruction efficiency. However, $J/\psi \to \mu\mu$ resonance offers an abundant source of low-p_{T} muon pairs allowing to measure the reconstruction efficiency for such muons with sufficient statistics by means of T&P. In this section, the results of this measurement are presented using the strategy for $J/\psi \to \mu\mu$ decays as outlined in section 5.1. The section is structured as follows. First the T&P selection criteria to select a sample pure in J/ψ events are explained. Then the procedure to estimate the background is discussed followed by a description of the systematic uncertainties. The section concludes with the main results obtained.

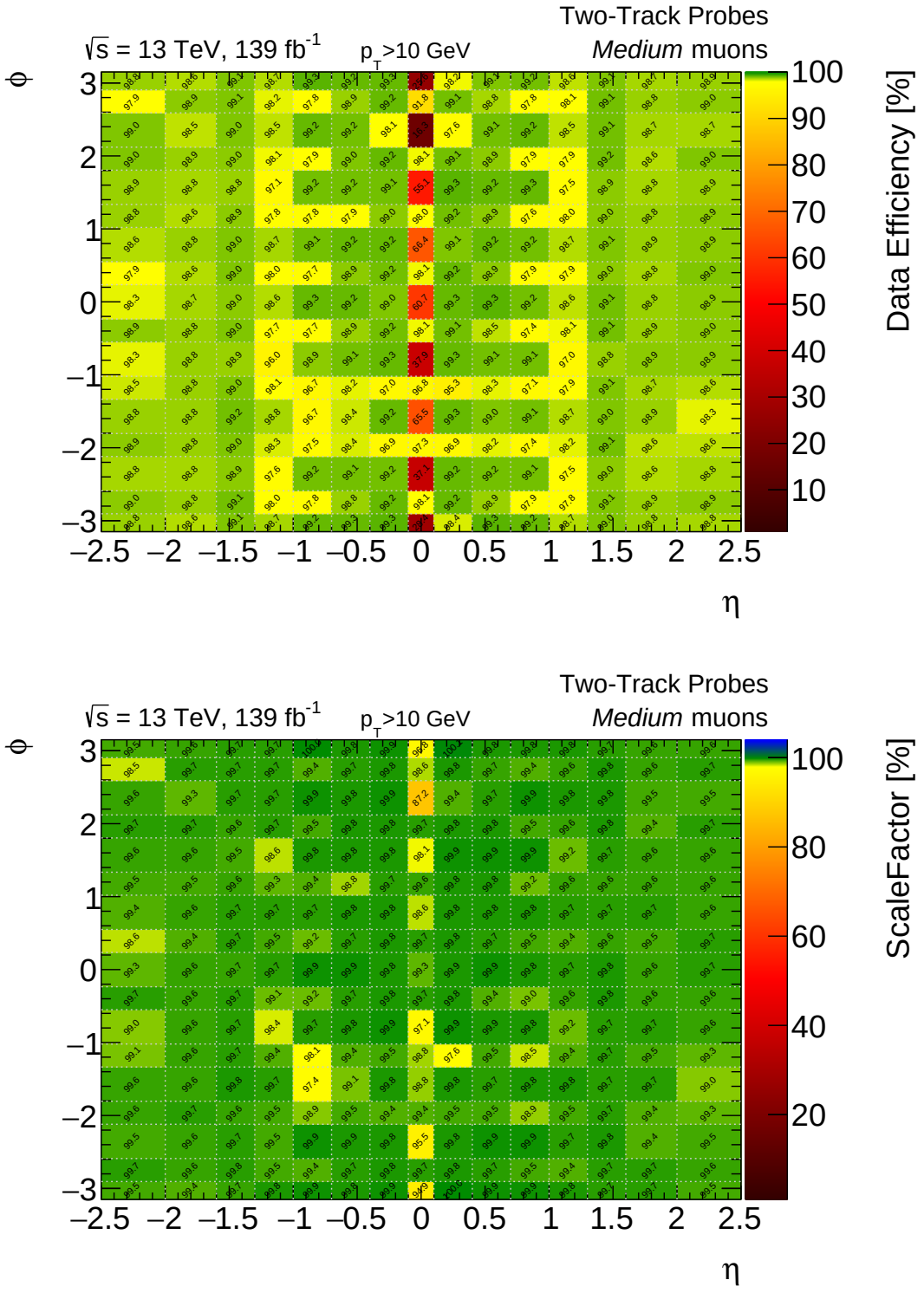

Figure 5.16: Reconstruction efficiency measured in the Run 2 dataset (top) and the efficiency scale factor for Medium muons shown as a function of the azimuthal angle and the pseudorapidity in $Z \to \mu\mu$ events.

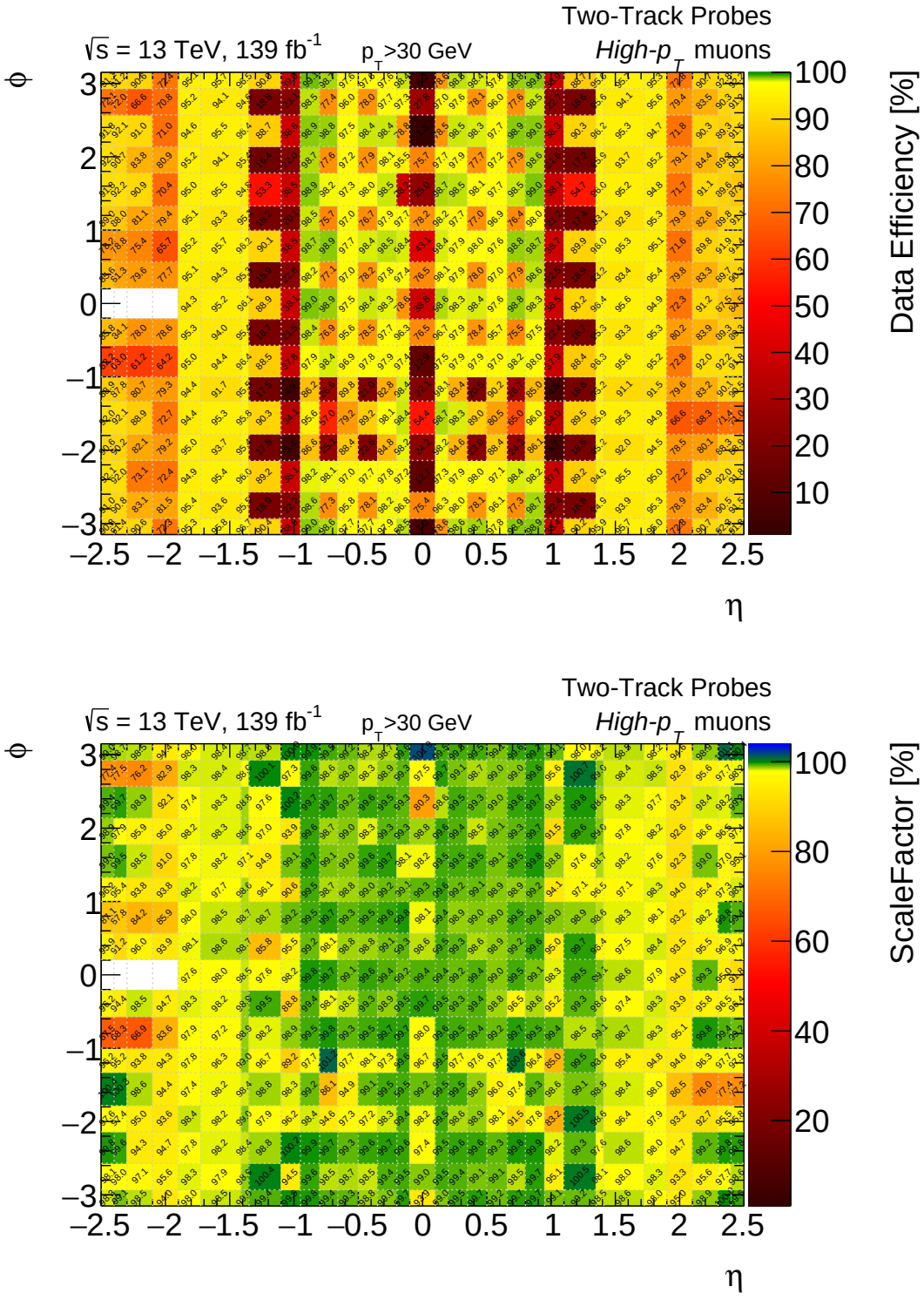

Figure 5.17: Reconstruction efficiency measured in the Run 2 dataset (top) and the efficiency scale factor for High-p_{T} muons shown as a function of the azimuthal angle and the pseudorapidity for muons with $p_{\mathrm{T}} > 30$ GeV in $Z \to \mu\mu$ events.

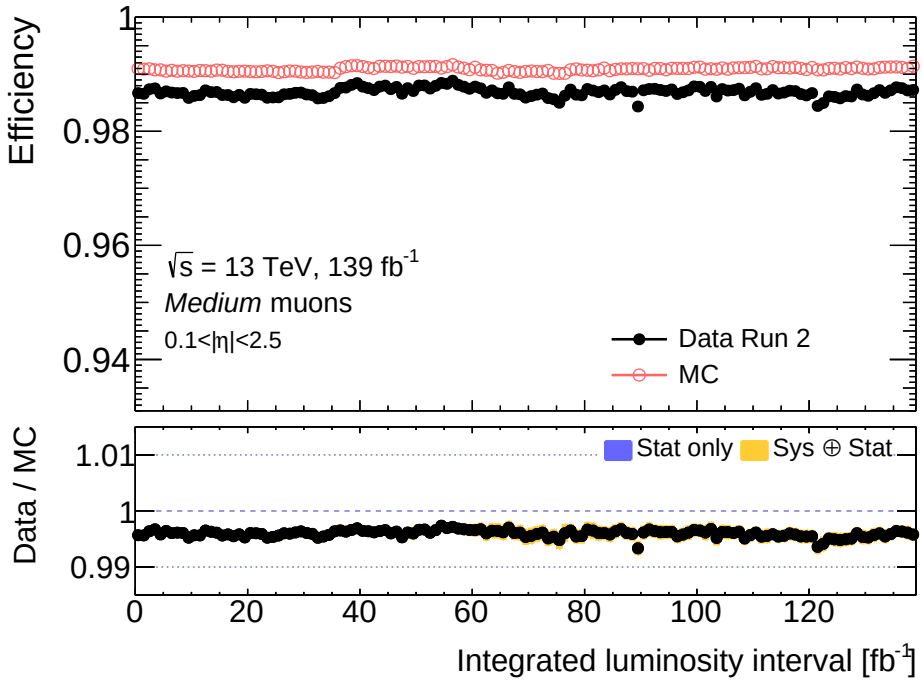

Figure 5.18: Muon reconstruction efficiency for the Medium identification algorithm measured in $Z \to \mu\mu$ events as a function of the integrated luminosity interval within $0.1 < |\eta| < 2.5$. Each data point corresponds to 1 fb^{-1} of collected data. The bottom panel shows the associated efficiency scale factor. The error bars in the bottom panel include the quadratic sum of statistical and systematic uncertainties.

5.4.1 Tag-and-Probe Selection Criteria in $J/\psi \to \mu\mu$ Events

To select a sample of T&P pairs pure in $J/\psi \to \mu\mu$ decays selection criteria have to be applied to the events which are summarized in Table 5.3 and explained in the following. The tag muon is required to have $p_{\mathrm{T}} > 6$ GeV and to satisfy the Tight identification criteria to reduce non-prompt muons with low p_{T} as efficiently as possible. The soft p_{T} of the tags necessitates to use extremely prescaled single muon triggers limiting the available statistics of the dataset. The prescale can be lowered by up to three orders of magnitude if an extra ID or MS track is required such that the invariant mass of the muon and the track is at least 2.5 GeV. In the later two years, a so-called *partial event building* (PEB) data stream has been set up, where detector signals of muons or in small cones around the muon are readout from the ATLAS detector by the data acquisition leading to a smaller event size. The smaller bandwidth enables to collect in 2018 1.6 times more J/ψ pairs per fb^{-1}recorded than in 2016. ID or MS tracks, or ST muons with $p_{\mathrm{T}} > 3$ GeV and $|\eta| < 2.5$ are selected as probes, if they are oppositely charged to the tag muon, both have an invariant mass in the window of $m_{\mathrm{T\&P}} \in [2.7; 3.5]$ GeV to select the J/ψ resonance, and if they satisfy the corresponding quality cuts reported in Table 5.3.

Table 5.3: Selection criteria applied for the measurement of the muon reconstruction efficiencies exploiting $J/\psi \to \mu\mu$ events

Tag selection			
Trigger	Combination of prescaled single μ and μ + track triggers with $p_{\mathrm{T}} > 4$ GeV		
Kinematics	$p_{\mathrm{T}} > 6$ GeV, $\lvert\eta\rvert < 2.5$		
Identification	Tight identification criteria		
Probe selection			
Pseudorapidity	$\lvert\eta\rvert < 2.5$		
Transverse momentum	$p_{\mathrm{T}} > 3$ GeV		
	MS tracks	ID tracks	ST muons
Track requirements	—	ID track quality cuts described in section 4.3	
		Matched to CT muon for $p_{\mathrm{T}} > 5$ GeV	Reconstructed by ST algorithm
Invariant mass	$m_{\mathrm{T\&P}} \in [2.7; 3.5]$ GeV		
Electric charge	$q_{\mathrm{tag}} \cdot q_{\mathrm{probe}} < 0$		
Impact parameters	$\left\lvert z_0^{\mathrm{tag}} - z_0^{\mathrm{probe}} \right\rvert < 1$ mm		
	$\left\lvert d_0^{\mathrm{tag}} - d_0^{\mathrm{probe}} \right\rvert < 0.8$ mm		
Angular separation	$\Delta R > 0.2$		

J/ψ mesons can also be produced in secondary pile-up interactions. To suppress random pairings of tracks originating from different interaction vertices, the difference in the impact parameters d_0 and z_0 of the two tracks must be smaller than 0.8 mm and 1 mm, respectively. The requirement on the angular separation of $\Delta R > 0.2$ avoids too collimated T&P pairs such that the tag muon would enter the matching cone of the probe or both tracks can be associated to the same trigger signature. In these cases it is impossible to distinguish which muon actually triggered the event.

5.4.2 Background Estimate in $J/\psi \to \mu\mu$ Events

The background in this measurement consists of T&P pairs from soft QCD processes and is estimated by a template fit method differing from the method applied in the $Z \to \mu\mu$ measurement (cf. section 5.3.2). As in the $Z \to \mu\mu$ measurement, the observable of interest, e.g. the probe p_{T} is additionally binned in the invariant mass of the T&P pair for probes and matches, as illustrated in Figure 5.19. The signal and background templates are modelled by smooth functions. The J/ψ peak is approximated by a Crystal Ball function, f_{signal}, where the free parameters between probes and matches are identical. Three different analytic models are used for the background using a first, second, or third order polynomial, respectively. For each of the three models, the background fraction

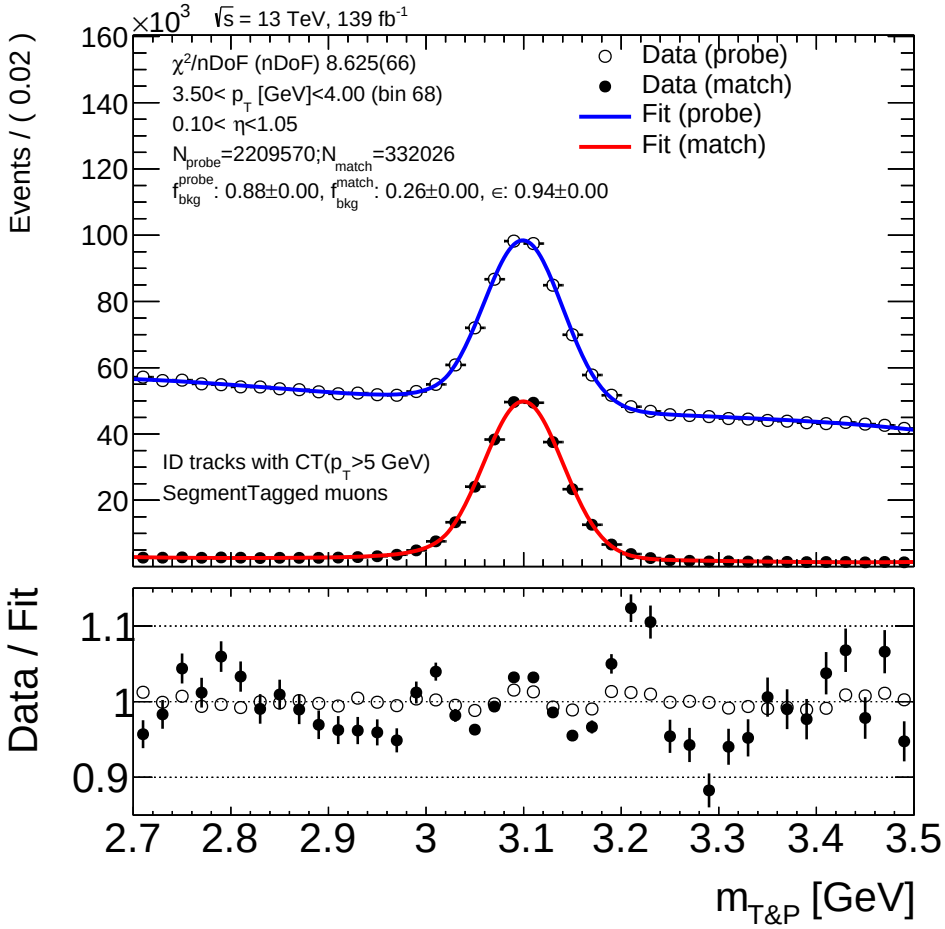

Figure 5.19: Illustration of the template fit method to determine the reconstruction efficiency of ST muons with $\eta \in [0.1, 1.05]$ and $p_{\mathrm{T}} \in [3.5, 4]$ GeV under the presence of ID tracks in the full Run 2 dataset. The open and closed circles show the recorded invariant mass distributions for probes and matches, respectively. The blue and red lines show the corresponding fit functions normalized to the respective number of recorded events in data. The shown labels, $f_{\mathrm{bkg}}^{\mathrm{probe}}$, $f_{\mathrm{bkg}}^{\mathrm{match}}$ and ϵ indicate the extracted background fractions for probes and matches and the final reconstruction efficiency. The bottom panel shows the ratio of the fit functions to the recorded data.

together with the free parameters of the Crystal Ball function are extracted from a simultaneous fit of the analytic signal and background shapes to the invariant mass distributions of probes and matches. Among the fitted models, the fit with the smallest reduced χ^2 is defined to describe the efficiency at the best. The extracted background fractions are then subtracted from the respective data distributions before the efficiency is calculated.

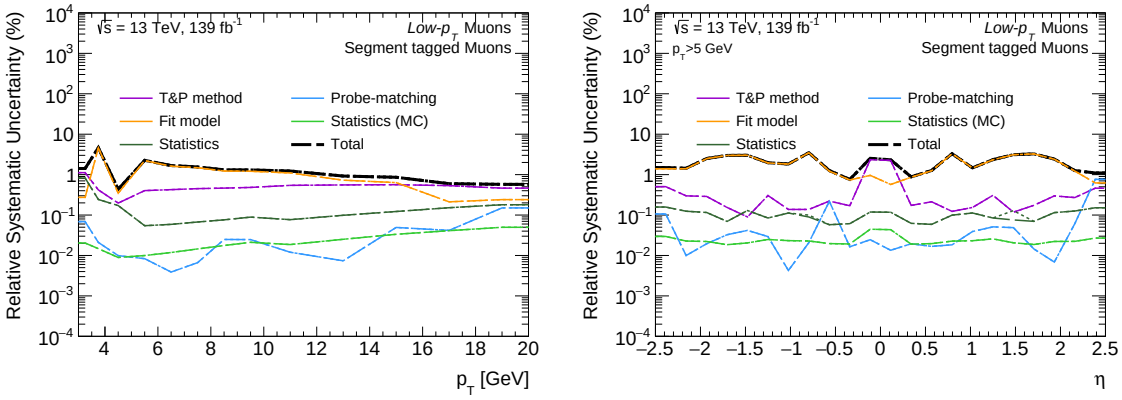

(a) (b)

Figure 5.20: Breakdown of the systematic of the Low-p_{T} reconstruction efficiency measured in $J/\psi \rightarrow \mu\mu$ events as a function of p_{T} for muons within $0.1 < |\eta| < 2.5$ (a) and of η for muons with $p_{\mathrm{T}} > 5$ GeV (b).

5.4.3 Systematic Uncertainties

The breakdown of the systematic uncertainties considered in this measurement is demonstrated in Figure 5.20 for the measurement of the Low-p_{T} working point. The precision of the measurement ranges is better than 1% for muons with $p_{\mathrm{T}} > 5$ GeV and increases up to 8% at $p_{\mathrm{T}} \simeq 3$ GeV. The following sources of uncertainty are contributing:

- **Fit model:** To check the capability of the Crystal Ball function to model the J/ψ signal peak, pseudo data is constructed. For this, the background shape extracted from the fit in data is added to the $m_{\mathrm{T\&P}}$ distribution from simulation such that the background fractions between data and simulation match. A fit is then performed using the same background hypothesis as in data and the background fraction obtained from this fit is subtracted to calculate the fitted Monte Carlo efficiency. Deviations from the nominal result are propagated as systematic uncertainties on the scale factor. This fit model uncertainty is the dominating source of uncertainty for large fraction of the phase space considered with a magnitude ranging between 1–8%.
- **T&P method:** This source of uncertainty is determined exactly the same way as for the $Z \rightarrow \mu\mu$ measurement (cf. section 5.3.3). It has been diminished from $\simeq 1\%$ to $\simeq 0.2\%$ by applying the revised measurement strategy outlined in section 5.1.
- **Probe-matching:** The source of the systematic uncertainty is explained in section 5.3.3 as well. It contributes minorly to the total uncertainty with a magnitude at the level of $O\left(10^{-2}\right)$ %.
- **Statistics:** The statistical uncertainty is driven by the available data statistics. It is $\simeq 1\%$ for muons with $p_{\mathrm{T}} = 3$ GeV and decreases to $O\,(0.1)$ % for muons with $p_{\mathrm{T}} > 5$ GeV.

5.4.4 Results

The muon reconstruction efficiencies as functions of the probe p_{T} and η for the Loose, Medium, Low-p_{T} and Tight working point are shown in Figure 5.21. For $p_{\mathrm{T}} > 5$ GeV, the efficiencies for the Loose and Low-p_{T} working points are stable at 99% while a slight (pronounced) increase in the efficiency for Medium (Tight) muons is observed. In the regime below 5 GeV, the Low-p_{T} and Loose working points recover a large fraction of muons and are 25–40% more efficient than the Medium working point. The Tight working point is only defined for muons with $p_{\mathrm{T}} > 4$ GeV and depends at the most on p_{T} as observed in the $Z \to \mu\mu$ measurement. In the endcaps, the data is more likely to pass the Tight criteria than in simulation by up to 10%. The $m_{\mathrm{T\&P}}$ distributions have been found to show discrepancies in the widths between probes and matches as the ρ' variable more likely removes muon tracks with poor resolution. This deviation is covered by the fit-model uncertainty. In the phase space $p_{\mathrm{T}} > 5$ GeV the Loose working point recovers selection efficiency in the crack region due to the accepted ST and CT muons and in the regions $|\eta| < 1.55$ due to the applied exception to select muons with one associated segment (cf. section 4.3). Overall the reconstruction efficiencies excluding the Tight working point are modelled better than 1% for $p_{\mathrm{T}} > 5$ GeV and better than 5–10% for the low p_{T} phase space.

Similarly to the $Z \to \mu^+\mu^-$ case, the reconstruction efficiency measurement using $J/\psi \to \mu\mu$ decays aims to correct mismodelling effects arising from dysfunctional chambers during the data taking or from mismodelled input variables. Given that a larger dependence of the efficiencies and hence on the scale factors on the probe p_{T} than on ϕ is observed, the efficiency scale factors applied in the physics analysis are provided as a function of η and p_{T}. To model the time dependence of the data efficiencies, the maps are additionally split into each year of data taking.

Figure 5.22 shows the data efficiency and the corresponding scale factor measured in $J/\psi \to \mu\mu$ decays for the Low-p_{T} identification working point. The reconstruction efficiency for muons with p_{T} below 5 GeV also strongly depends on η. Muons in the transition region, $|\eta| \in [1.05; 1.3]$, have the lowest reconstruction efficiency due to the overlap between the magnetic fields generated by the barrel and endcap toroids. The effect of the dysfunctional CSC chambers in the years 2017 and 2018 is most visible for muons with $p_{\mathrm{T}} < 5$ GeV resulting in scale factors down to 0.75. The largest scale factors are observed in the barrel for $p_{\mathrm{T}} < 5$ GeV, where the reconstruction efficiency measurement of ST muons has to cope with large backgrounds resulting in large uncertainties of $O(10)$ %. For higher p_{T}, the data efficiency agrees mostly with the simulated efficiency within 1%. The scale factor maps for the other working points and the maps for each year can be found in Appendix A.2.

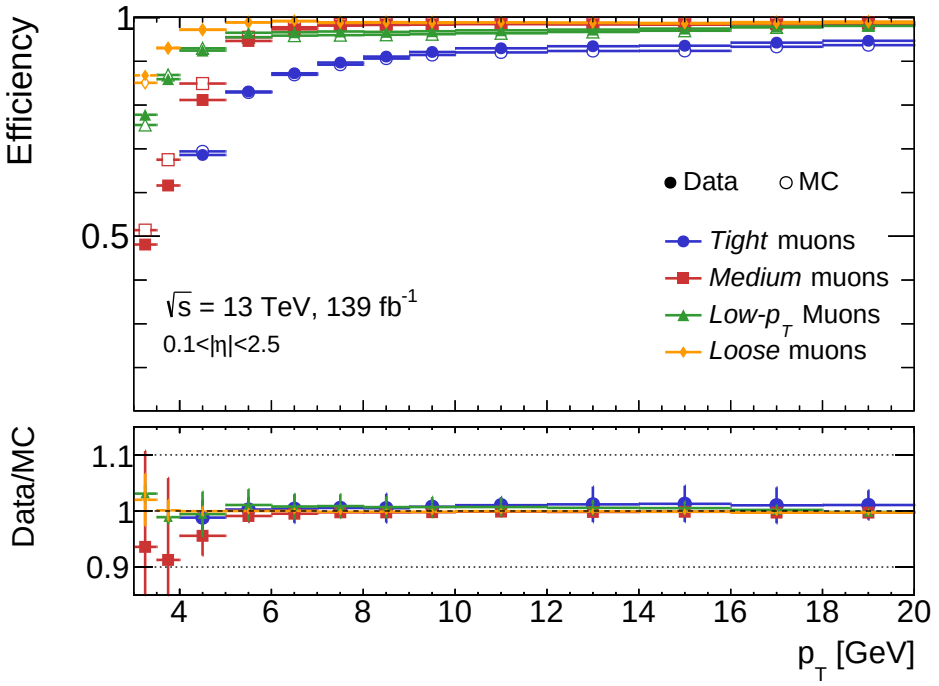

(a)

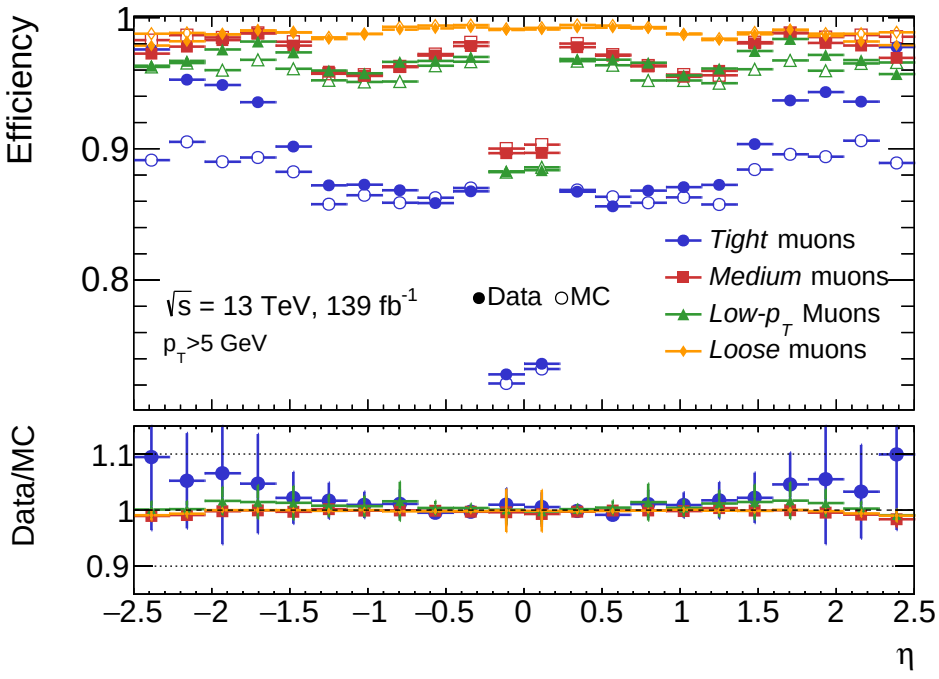

(b)

Figure 5.21: Measured muon reconstruction efficiencies for the Loose, Medium, Low-p_{T} and Tight identification criteria in simulated $J/\psi \rightarrow \mu\mu$ events and in the full Run 2 dataset as a function of the transverse momentum for muons within $0.1 < |\eta| < 2.5$ (a) and of the pseudorapidity for muons $p_{\mathrm{T}} > 5$ GeV (b). The bottom panel shows the efficiency scale factors. The error bars indicate the quadratic sum of statistical and systematic uncertainties.

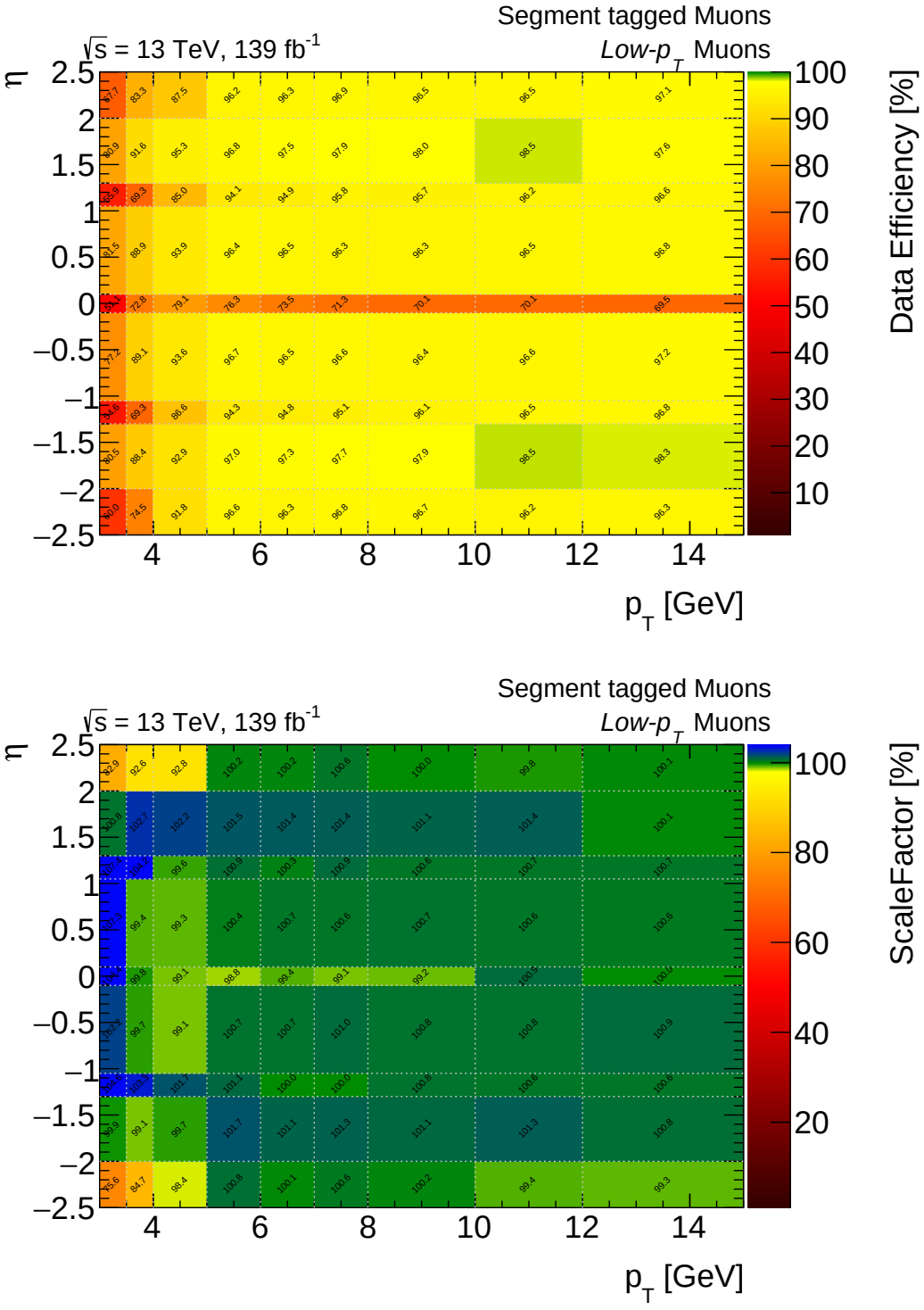

Figure 5.22: Reconstruction efficiency measured in the Run 2 dataset (top) and the efficiency scale factor for Low-p_{T} muons shown as a function of the transverse momentum and the pseudorapidity in $J/\psi \rightarrow \mu\mu$ events.

5.5 Muon Efficiency Scale Factors for Forward Muons

The T&P method is not applicable for muons beyond the ID coverage, i.e. $|\eta| \in [2.5; 2.7]$, since there is no independent subsystem available to reconstruct a second track which would then allow to measure the efficiency analogously to Equation 5.4. By comparing the agreement of a muon observable between data and simulation in $Z \to \mu\mu$ events in the very forward detector region, i.e. $|\eta| > 2.5$, to the one in more central detector region, i.e. $2.2 < |\eta| < 2.5$, an efficiency scale factor can be approximated using the so-called double-ratio method. One muon from the Z boson decay is required to pass the same selection criteria as the tag muon in the $Z \to \mu\mu$ T&P analysis and is henceforth also called the *tag*. The second muon, also called *probe*, is then used to determine the agreement between data and simulation. The number of probes from $Z \to \mu\mu$ decays for which the probe populates a certain η-region, for data or simulation, can be expressed as

$$N^X\left(\eta - \text{region}\right) = N^X_{\text{tot}} \cdot \epsilon^X_{\text{event}} \cdot \epsilon^X_{\text{probe}}\left(\eta - \text{region}\right) \cdot \mathcal{A}^X\left(\eta - \text{region}\right), \tag{5.11}$$

where $X \in \{\text{data}, \text{MC}\}$, N^X_{tot} is the product of total the total $Z \to \mu\mu$ cross section and integrated luminosity, $\epsilon^X_{\text{event}}$ is a global efficiency factor accounting for trigger and tag reconstruction efficiencies, $\epsilon^X_{\text{probe}}$ is the probe reconstruction efficiency and $\mathcal{A}^X\left(\eta - \text{region}\right)$ is the probability for the probe to fall in the given η-region. The ratio of the number of probes in data to simulation,

$$r\left(\eta - \text{region}\right) = \frac{N^{\text{data}}\left(\eta - \text{region}\right)}{N^{\text{MC}}\left(\eta - \text{region}\right)} = sf_{\text{rate}} \cdot sf_{\text{event}} \cdot sf_{\text{probe}}\left(\eta - \text{region}\right) \cdot \frac{\mathcal{A}^{\text{data}}\left(\eta - \text{region}\right)}{\mathcal{A}^{\text{MC}}\left(\eta - \text{region}\right)}, \tag{5.12}$$

is the product of two global scale factors accounting for the differences in the normalization and event efficiencies times the scale factor for the probe and a fourth factor describing the agreement in the shape of the η distributions between data and simulation. For $|\eta|$ <2.5, the probe scale factor is eliminated by applying the scale factors presented in section 5.3 to the probe muons in simulation. To measure the efficiency scale factor for muons with $|\eta| > 2.5$, two detector regions are defined, one with $|\eta| \in [2.2; 2.5]$ where the muon reconstruction efficiency in simulation is corrected and the other with $|\eta| \in [2.5; 2.7]$. By dividing the data to simulation ratios for the two regions to obtain the so-called double-ratio, all factors except the scale factor for high-η muons cancel

$$sf = \frac{r\left(|\eta| \in [2.5; 2.7]\right)}{r\left(|\eta| \in [2.2; 2.5]\right)} = \underbrace{\frac{\mathcal{A}^{\text{data}}\left(|\eta| \in [2.5; 2.7]\right) \cdot \mathcal{A}^{\text{MC}}\left(|\eta| \in [2.2; 2.5]\right)}{\mathcal{A}^{\text{MC}}\left(|\eta| \in [2.5; 2.7]\right) \cdot \mathcal{A}^{\text{data}}\left(|\eta| \in [2.2; 2.5]\right)}}_{\simeq 1} \cdot sf_{\text{probe}}, \tag{5.13}$$

under the assumption that the shape mismodelling effect approximately cancel out for the two close-by η regions.

Table 5.4: Event selection criteria of the $Z \to \mu\mu$ high-η scale factor measurement

Tag selection			
Trigger	p_{T} threshold [GeV]	year	$\mathcal{L}_{\mathrm{inst}}$ [$\mathrm{cm}^{-2}\mathrm{s}^{-1}$]
	> 20	2015	—
	> 24	2016	$< 10^{-34}$
	> 26	2016	$\geq 10^{-34}$
	> 26	2017–2018	—
Kinematics	$p_{\mathrm{T}} > 1.05\times$ nominal trigger p_{T} threshold, $\lvert\eta\rvert < 2.5$		
Identification	Medium working point		
Impact parameters	$\lvert d_0\rvert / \sigma(d_0) < 3$, $\lvert z_0 \sin(\theta)\rvert < 0.5$ mm		
Isolation	*FCTight* isolation		
Probe selection requirements			
p_{T} [GeV]	>10		
Identification	*Medium*		
	Central region		Forward region
$\lvert\eta\rvert$	$\in [2.2; 2.5]$		$\in [2.5; 2.7]$
Impact parameters	$\lvert d_0\rvert / \sigma(d_0) < 3$, $\lvert z_0\rvert < 10$ mm		—
Invariant mass	$m_{\mu\mu} \in [81; 101]$ GeV		
Electric charge	Opposite charged muon pair		

Event selection: To select a sample pure in prompt muons, $Z \to \mu\mu$ is considered for this measurement and its selection criteria are reported in Table 5.4. The tag muon has to pass the same selection criteria as in the $Z \to \mu\mu$ T&P analysis. The other muon from the Z boson decay has to have $p_{\mathrm{T}} > 10$ GeV and to pass the Medium identification criteria. If the muon is in the central η region, which is denoted by η^{num} in the following, it also has to satisfy cuts on the impact parameters. This is not required if the muon is in the forward region, denoted by η^{den} in the following. The two muons in the pair must also have an invariant mass within the window of $m_{\mu\mu}$ [81; 101] GeV, which is smaller than for the T&P case to suppress background pairs.

Background estimation: The source of background are the same as for the $Z \to \mu\mu$ measurement. Muons from $t\bar{t}$, $Z \to \tau\tau$ or WW decays are considered and estimated from simulation. The reducible component in this measurement is neglected as a data-driven estimate for the reducible background has shown negligible impact on the result compared to other systematics considered.

Test of the double ratio method: The validity of Equation (5.13) is tested by defining two detector regions ranging between $\lvert\eta\rvert \in [1.5; 2]$ and $\lvert\eta\rvert \in [2; 2.5]$, respectively, and by applying then the scale factors derived from the T&P method to simulation in both regions. In this way, the probe scale

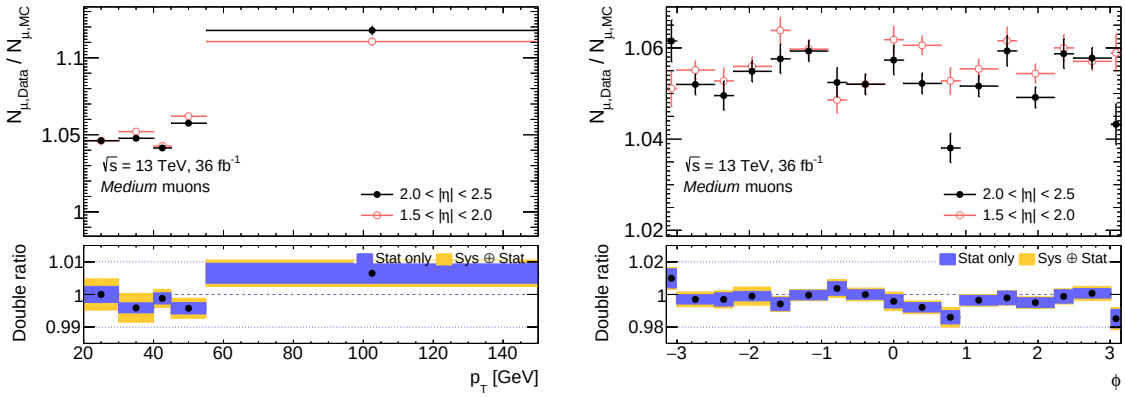

(a) (b)

Figure 5.23: Data to simulation ratio in $Z \to \mu\mu$ in two disjoint detector regions shown as a function of the muon transverse momentum (a) and of the azimuthal angle (b) in the 2015–2016 dataset. The simulated events are corrected by the muon reconstruction scale factors derived from the T&P method. The bottom panel shows the double ratio between the two regions. The yellow error bars indicate the quadratic sum of statistical and systematic uncertainties.

factor cancels as well and the double ratio is expected to be dominated by the acceptance factors, $\mathcal{A}$, allowing to test their cancellation to unity. For the 2015–2016 dataset, where the fewest cases of dysfunctional muon chambers are observed, the result is shown in Figure 5.23 as a function of the transverse momentum and of the azimuthal angle. In both cases, the double ratio is compatible with unity for the bulk of the considered phase space demonstrating the applicability of the method.

Results of the high-η measurement: The scale factor maps used in the later analysis are derived as functions of η and ϕ. As few CSC chambers in each year were switched off during the year, the scale factors are additionally split into the periods 2015–2016, 2017 and 2018. The results are shown in Figures 5.24, 5.25 and 5.26. The drop in the η^{den} ratio at $\phi \simeq -0.8$ in Figure 5.25(b) is caused by a dysfunctional CSC chamber in 2017. It is more pronounced at high η as the Medium muon selection requires hits in all three stations of the MS for SA muons while for combined muons one station can be missed. Also for the 2018 dataset, a drop in the high-η ratio at $\phi \simeq 3$ in Figure 5.26(a) is attributed to a dysfunctional chamber in this year. Apart from these localized inefficiencies the high-η ratio drops periodic in ϕ, which are stronger in the very forward $|\eta| > 2.6$ regions than for the $|\eta| \in [2.5, 2.6]$ regions, but are present in all years of data taking. This periodicity can be better visualized if the full interval of the azimuthal angle is projected by $\phi \to \tilde{\phi} = \phi \bmod \frac{\pi}{4}$ into the smaller interval $\tilde{\phi} \in \left[0; \frac{\pi}{4}\right]$ which is illustrated in Figure 5.27 for the 2018 dataset. In this projection, muons in the small and large sectors are folded into the intervals $0.13 \lesssim \tilde{\phi} \lesssim 0.66$ and $\tilde{\phi} \lesssim 0.38$ or $0.58 \lesssim \tilde{\phi} \lesssim \pi/4$, respectively.

At the edges of the large sectors, a drop down to 0.6 in the ratio for high η muons is observed but not for muons in the central region of the detector. Given that SA muons are required to pass a minimum requirement on the number of hits in all three stations, this drop is likely to be attributed to inefficiently operating detector modules in the MS. This will be further investigated in the course of this section.

Systematic uncertainties: The systematic uncertainties in the high-η scale factor measurement concern three different aspects: The phase space correlation between the tag and probe pairs; the validity of the assumption that the differences in the $\mathcal{A}$ between data and simulation cancel in the double ratio; Finally, the effect on the double-ratio from larger background contaminations; The first aspect is tested by raising the tag-p_{T} to 35 GeV which sculpts the p_{T} and η distribution of the probe muons due to the invariant mass requirement. Three detector regions for the denominator in the double ratio, denoted by CRi ($i = 1, 2, 3$), are defined with $\left|\eta^{\mathrm{den}}\right| \in [2; 2.2]$, $\left|\eta^{\mathrm{den}}\right| \in [2; 2.5]$, and $\left|\eta^{\mathrm{den}}\right| < 2.5$, respectively, probing localities in the mismodelling. More background events are accepted by omitting the cut on the probe impact parameters in the denominator region and the background is stronger rejected by additionally applying the *FCLoose* isolation on the probe muon. The overall achieved precision is at the level of $\simeq$ 2.5% where each component, except the requirement on the probe isolation, contribute to almost equal amount as shown in Figure 5.28.

Measurement of the hit efficiency of each MS layer: To investigate the reasons of the observed mismodelling at high η, the efficiency that a muon track has enough hits in a given layer of the MS is studied. The hit efficiency can be determined using muon tracks passing the hit requirements in the other two layers and checking whether the requirement is fulfilled in the third layer as well. A T&P method is exploited to select prompt muon tracks from $Z \to \mu\mu$ decays. The selection criteria largely follow the criteria used for the $Z \to \mu\mu$ reconstruction case with the exception that a probe muon is a muon track passing the hit requirement in the two complementary layers of the MS. It should be noted that this measurement cannot be used to determine the full Medium muon reconstruction efficiency at high-η as the measurement assumes a 2-layer probe track to be already have been reconstructed whose efficiency remains unknown. The background in this measurement is estimated in the same way as in the $Z \to \mu\mu$ reconstruction analysis using a template shape fit. The layer efficiencies are measured in the regions $|\eta| \in [2; 2.5]$, for cross checks, and $|\eta| > 2.5$. The results for the 2018 dataset are shown in Figure 5.29 as a function of $\tilde{\phi}$. In both considered regions, the hit efficiencies of the outer layer are rather flat across $\tilde{\phi}$ with the exception of two small bumps at $\tilde{\phi} \sim 0.2$ and $\tilde{\phi} \sim 0.55$ where the large and small sectors overlap (cf. Figures 5.29(a) and 5.29(b)). In both detector regions, the modelling is in general better than 1%. Also the layer hit efficiency in the middle layer shows the same trends as the outer layer hit efficiency. The drop of 8% at $\tilde{\phi} \in [0.4; 0.5]$ in the central region of the detector (cf.

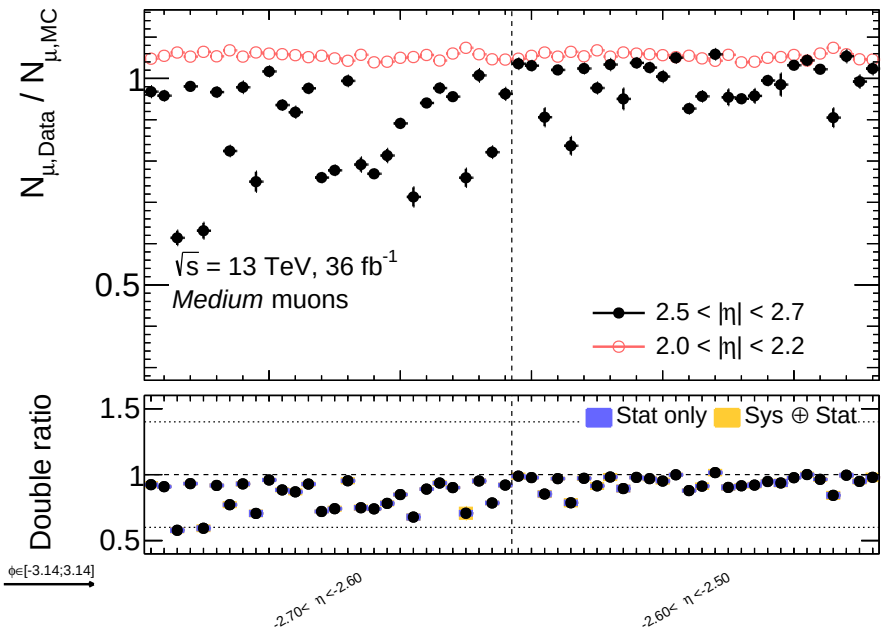

(a)

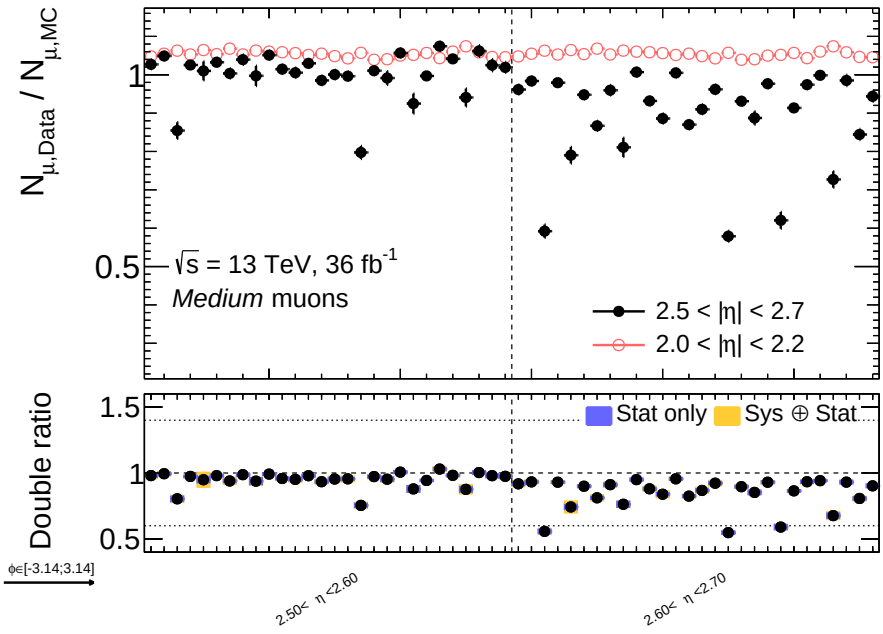

(b)

Figure 5.24: Data to MC ratio as a function of the muons azimuthal angle split into two bins for negative (top) and positive (bottom) η measured in $Z \rightarrow \mu\mu$ events recorded in the 2015–2016 dataset. The ratio is shown once for Medium muons in the forward regions of the MS (red) and once for Medium muons in the region $|\eta| \in [2.0; 2.2]$. For each η region the ratios are measured in 28 ϕ bins with edges at $|\phi| \in \{0, 0.24250, 0.50266, 0.59690, 0.90250, 1.02750, 1.32750, 1.38230, 1.81250, 2.11250, 2.54470, 2.60753, 2.79602, 2.95310, \pi\}$. The bottom panel shows the double ratio of the ratio in the forward region to the ratio in the central region of the detector. The yellow error bars indicate the quadratic sum of the systematic and statistical uncertainties.

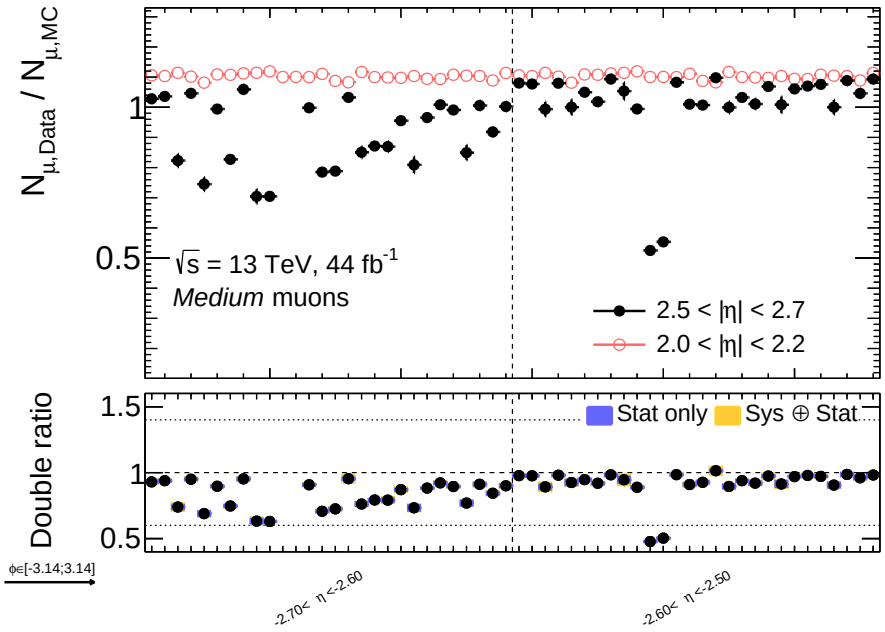

(a)

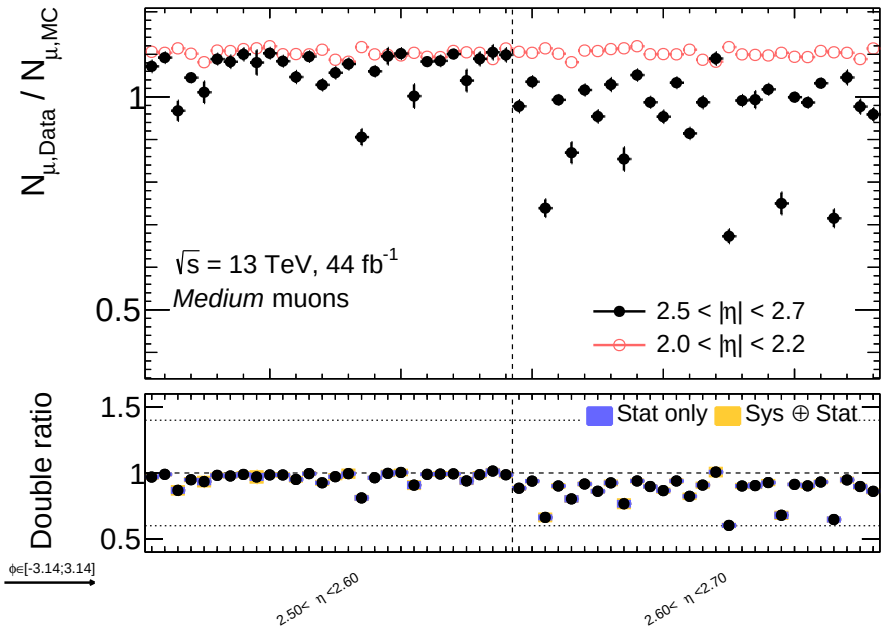

(b)

Figure 5.25: Data to MC ratio as a function of the muons azimuthal angle split into two bins for negative (top) and positive (bottom) η measured in $Z \rightarrow \mu\mu$ events recorded in the 2017 dataset. The ratio is shown once for Medium muons in the forward regions of the MS (red) and once for Medium muons in the region $|\eta| \in [2.0; 2.2]$. For each η region the ratios are measured in 28 ϕ bins with edges at $|\phi| \in \{0, 0.24250, 0.50266, 0.59690, 0.90250, 1.02750, 1.32750, 1.38230, 1.81250, 2.11250, 2.54470, 2.60753, 2.79602, 2.95310, \pi\}$. The bottom panel shows the double ratio of the ratio in the forward region to the ratio in the central region of the detector. The yellow error bars indicate the quadratic sum of the systematic and statistical uncertainties.

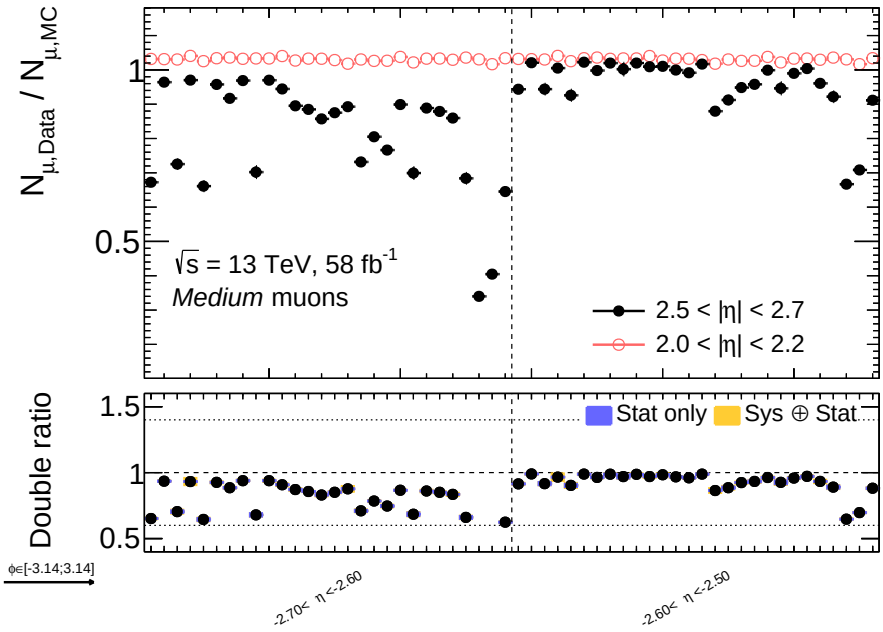

(a)

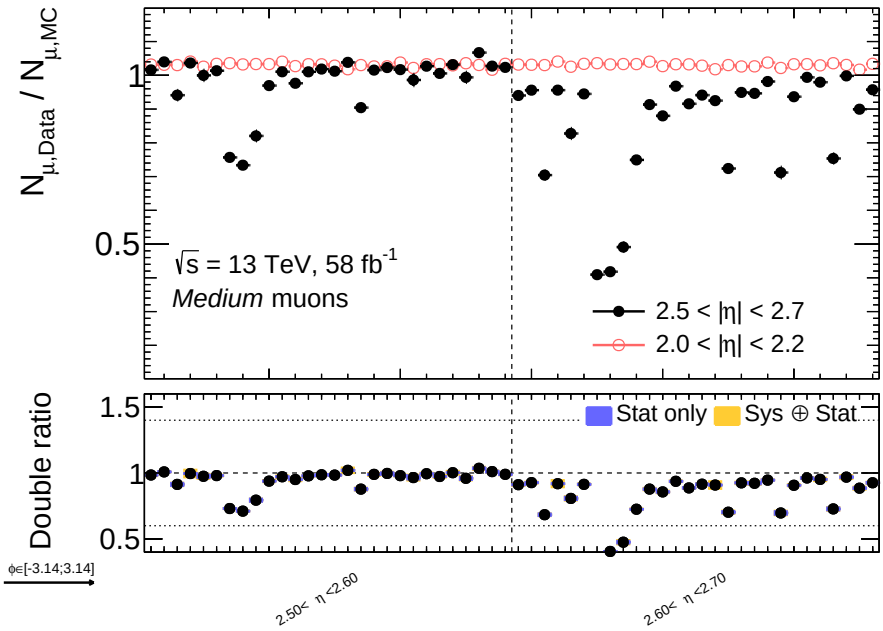

(b)

Figure 5.26: Data to MC ratio as a function of the muons azimuthal angle split into two bins for negative (top) and positive (bottom) η measured in $Z \rightarrow \mu\mu$ events recorded in the 2017 dataset. The ratio is shown once for Medium muons in the forward regions of the MS (red) and once for Medium muons in the region $|\eta| \in [2.0; 2.2]$. For each η region the ratios are measured in 28 ϕ bins with edges at $|\phi| \in \{0, 0.24250, 0.50266, 0.59690, 0.90250, 1.02750, 1.32750, 1.38230, 1.81250, 2.11250, 2.54470, 2.60753, 2.79602, 2.95310, \pi\}$. The bottom panel shows the double ratio of the ratio in the forward region to the ratio in the central region of the detector. The yellow error bars indicate the quadratic sum of the systematic and statistical uncertainties.

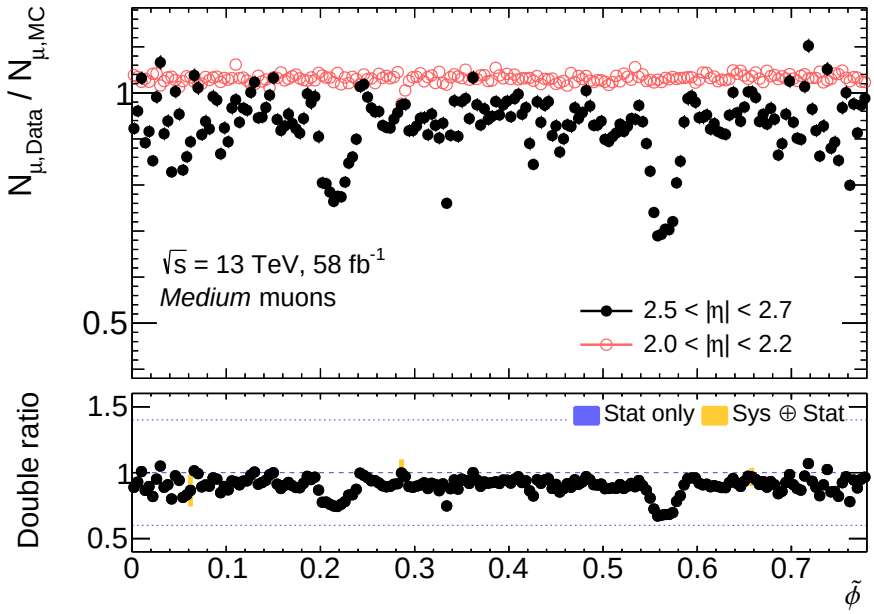

Figure 5.27: Data to MC ratio as a function of the muons azimuthal angle, projected by the mapping $\phi \rightarrow \tilde{\phi} = \phi \bmod \frac{\pi}{4}$ into the interval $\tilde{\phi} \in \left[0; \frac{\pi}{4}\right]$, measured in $Z \rightarrow \mu\mu$ events recorded in the 2018 dataset. The ratio is shown for Medium muons in the forward region of the MS (red) and for Medium muons in the region $|\eta| \in [2.0; 2.2]$. The bottom panel shows the double ratio of the ratio in the forward region to the ratio in the central region of the detector. The yellow error bars indicate the quadratic sum of the systematic and statistical uncertainties.

Figure 5.29(c)) is attributed to holes left in the chamber to make a free path for the alignment laser in the endcaps. In both detector regions an agreement in the modelling is observed at the level of 2–5% which is slightly worse than the modelling for the outer layer but not sufficiently large to explain the previously discussed modulation at high η. Instead, it is attributed to a drop in the data inner layer efficiency in the CSCs by up to 25% (Figure 5.29(f)). The inner layer efficiency is also predicted to drop by the simulation, but the location of the minimum is displaced by 0.04 radians compared to the observation in data. Also the drop is much narrower in simulation than in data. In the central detector region a drop in the data efficiency is also observed causing an additional disagreement in the simulated and measured layer hit efficiency by 5% (cf. Figure 5.29(e)). Nevertheless, this disagreement has a much weaker impact on the Medium muon reconstruction efficiency as combined muons with two associated MS stations are accepted by the working point selection.

Reconstruction studies in simulation: The periodic occurring of large muon reconstruction scale factors at high η is attributed to problems in the modelling and/or the reconstruction of hits in the CSC

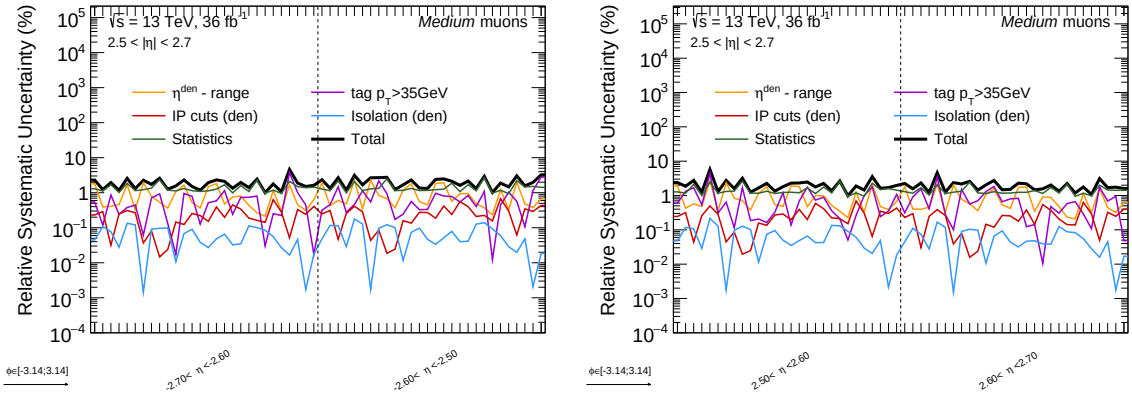

(a) (b)

Figure 5.28: Relative systematic uncertainty on the double ratio measured in the 2015–2016 dataset split into the contributing sources shown as a function of the azimuthal angle for the four η regions. For each η region the ratios are measured in 28 ϕ bins with edges at $|\phi| \in \{0, 0.24250, 0.50266, 0.59690, 0.90250, 1.02750, 1.32750, 1.38230, 1.81250, 2.11250, 2.54470, 2.60753, 2.79602, 2.95310, \pi\}$. The dashed (dotted) lines indicate the $+1\sigma$ (-1σ) variation of each nuisance parameter.

chambers located in the overlapping region between the large and small ϕ sectors. However, the largest background rates from the proton beams are also present in the CSC chambers. Hence, the observed features could be related to the high background. In order to study the muon reconstruction in an environment clean from background, simulated events with a single muon as the only particle escaping from the interaction point are generated and passed through the full detector simulation without the simulation of the pile-up overlay. The muon sample is uniform in $p_{\mathrm{T}} \in [20; 80]$ and in $\eta \in [2; 3]$ to ensure that potential effects from the kinematic range typical for a Z boson decay are avoided.

The results of the study are shown in Figure 5.30 illustrating the distribution of the single muons at different stages of the muon reconstruction. For $|\eta| < 2.5$, the muon reconstruction is fully efficient at a level of $\sim 99.8\%$. At nearly all times, a ME track is successfully associated to the muon. The reconstruction efficiency of MS tracks and muons passing the Medium selection is slightly worse by about 0.5%. For muons outside the ID coverage, the muon-track reconstruction efficiency slightly decreases to 99% at $|\eta| = 2.65$ and suddenly drops to 92% for the very last bin. The loss in efficiency is caused by the increasing contribution of the SA reconstruction algorithm and for the last bin, it is attributed to cases where muons are pulled out of the MS by the magnetic field. The Medium reconstruction efficiency sharply drops to a level of 96% at $|\eta| \simeq 2.55$. This drop is credited to the already observed loss in the inner layer hit efficiency at $\tilde{\phi} \simeq 0.2$ and $\tilde{\phi} \simeq 0.6$ (cf. Figure 5.30(b)). In most cases, the hits in the CSC chambers can be successfully combined to muon segments which are later used to reconstruct the full muon track (cf. Figure 5.30(c)). However, the association of the

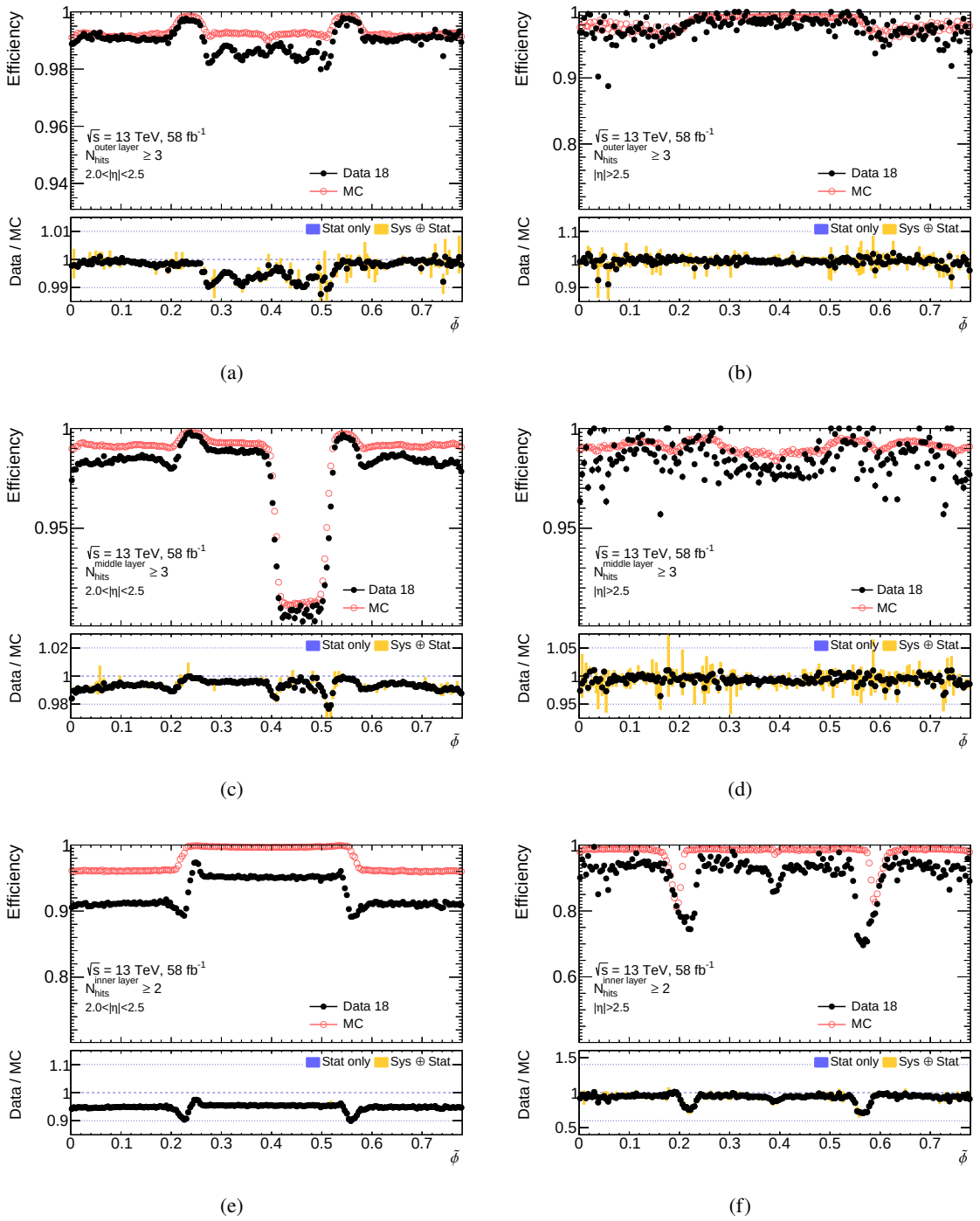

Figure 5.29: Outer (top), middle (middle) and inner (bottom) layer hit efficiency of reconstructed muons in the region $2 < |\eta| < 2.5$ (left) and $|\eta| > 2.5$ (right) measured in $Z \to \mu\mu$ decays recorded in the 2018 dataset as a function of the azimuthal angle, but projecting the full interval $\phi \in [-\pi; \pi]$ into $\tilde{\phi} \in \left[0; \frac{\pi}{4}\right]$ using the modulo operator. The bottom panel shows the efficiency scale factor. The yellow error bars indicate the quadratic sum of statistical and systematic uncertainties.

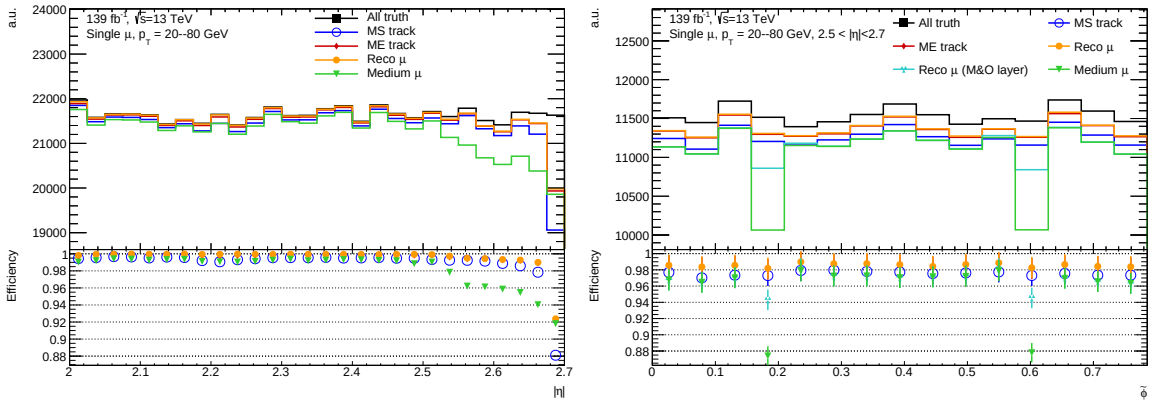

(a) (b)

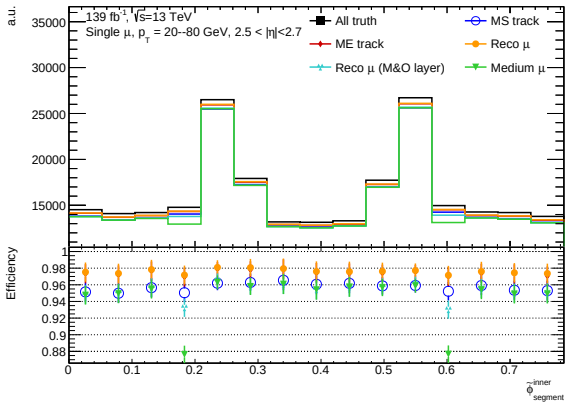

(c)

Figure 5.30: Comparison of generator-level muons at different stages of the muon reconstruction shown a function of $|\eta|$ (a) and $\tilde{\phi}$ (b) of the generator-level muon and as a function of $\tilde{\phi}$ of the inner segment reconstructed in the CSC chamber (c) in simulated single muon events. The black line shows the distribution for all generated muons, the blue and red lines for generator-level muons with associated MS and ME track, respectively. The orange and green line indicate the distributions for reconstructed muon tracks and the ones passing the Medium selection criteria. In (b) and (c), the bright blue line shows the distribution for reconstructed muons passing the hit requirements in the middle and outer layer and the muons have to be within $|\eta| \in [2.5; 2.7]$. The bottom panel shows the efficiency of the respective reconstruction stage and the error bars indicate the statistical uncertainties.

inner segments to the muon track more likely fails for these $\tilde{\phi}$ regions. In conclusion, the observed modulation of the muon reconstruction efficiency at high-η is likely attributed to a misbehaviour of the ATLAS reconstruction software in the endcap regions with CSC chamber overlap. This issue is under investigation at the time of writing this document.

5.6 Measurement of Additional Muon Selections using $Z \rightarrow \mu\mu$ Events

In the physics analysis, additional selections are applied to the muons on top of the working point selection to reject muons from secondary decays within jets, heavy-flavour decays and pile-up activity more effectively. These selections require either that the muon impact parameter is consistent with it originating from the primary vertex, called track-to vertex-association (TTVA) or that the muon is isolated from other close-by activity. As the input variables entering each criterion might be mismodelled, additional scale factors are needed to correct for selection biases between data and simulation. The tag and probe method makes it possible to measure not only the muon reconstruction efficiency in general but also the selection efficiency of these additional criteria. $Z \rightarrow \mu\mu$ decays with Loose muons as probes considered. In the following, the results of the TTVA and isolation efficiency measurements are presented.

5.6.1 Track-to-Vertex-Association Efficiency Measurement

In physics analyses, muons are typically required to originate from the primary vertex to suppress muons produced in the decay of hadrons. The track-to vertex-association (TTVA) is commonly achieved by applying cuts on the two impact parameters of the muon, namely $|z_0 \sin\theta| < 0.5$ mm and $|d_0| / \sigma_{d_0} < 3$ (cf. Section 7.2) on top of the identification working point selection. To correct for biases in the selection efficiencies between data and simulation, an additional scale factor is derived using a T&P method in $Z \rightarrow \mu\mu$ events [1]. The T&P pairs used to measure this scale factor are selected nearly in the same way as for the $Z \rightarrow \mu\mu$ reconstruction measurement. The only difference is that Loose muons are used within the full MS coverage under the constraint that muons within $2.5 < |\eta| < 2.7$ are SAF muons. SA muons are not considered for this measurement as they miss hits in the IBL leading to a worse resolution in the impact parameters. The usage of Loose probes purifies the sample sufficiently to permit a measurement using $Z \rightarrow \mu\mu$ evens at very low probe transverse momenta below 10 GeV. The background template fit method as described in section 5.3.2 is used to estimate the remaining contamination from non-prompt T&P pairs with the highest precision.

Figures 5.31 and 5.32 show the TTVA efficiency w.r.t muon p_{T} and $|\eta|$ and w.r.t. the luminosity interval during the data taking, respectively. The TTVA selection is efficient at a level of 98.5% for muons within $|\eta| < 2.5$ and drops down to 79% for SAF muons. Small dependencies of the efficiency on the transverse momentum and on the pseudorapidity, which occur likewise for positive and negative pseudorapidities, are observed. These dependencies can be attributed to a changing resolution of the ID in the impact parameters with the muon p_{T}. The TTVA efficiency slightly decays in the

[1] The production of J/ψ mesons in pile-up vertices, leads to a low TTVA acceptance for its decay muons making this resonance unsuitable for a proper measurement.

2016 dataset and at the end of the 2017 dataset (cf. the bins ranging between 60–80 in Figure 5.32) where unprecedented instantaneous luminosities were delivered by the LHC. Some fluctuations in the recorded efficiency are observed for the beginning of the 2018 data taking. They are caused by adjusting the detector parameters under the conditions of high pile-up. Overall the TTVA efficiency is modelled better than 1% in each case with slight dependencies on each variable.

The scale factors applied in the analysis are derived as functions of p_{T} and the absolute value of the pseudorapidity and split in addition into each year of data taking. The corresponding maps are given in Appendix A.3.

The achieved precision is better than 10^{-2}% which is dominated by the statistical uncertainty (cf. Figure 5.33). Uncertainties on the normalization of the Monte Carlo samples and uncertainties on the background estimate, both described in section 5.3.3, are considered as uncertainties. They are one magnitude smaller than the statistical uncertainties. To ensure that the efficiency scale factors actually improve the modelling of the TTVA efficiency, closure tests are performed. For these tests, the scale factors are applied to the matches in simulation and the obtained efficiency in simulation is compared to the measured data efficiency used to derive the scale factor. Deviations in this comparison from unity are assigned as an extra systematic uncertainty if they are not covered by the already existing uncertainties on the scale factor. The average size of this uncertainty has been evaluated to at the level of $O\left(10^{-2}\right)$ %. The corresponding plots are given in Appendix A.3.

5.6.2 Measurement of the Isolation Efficiency

Isolation requirements (cf. section 3.7.8) help to reject leptons from hadronic background. Similarly to TTVA, these requirements are not part any muon identification working point described in Section 4.3. Therefore, their selection efficiencies have to be calibrated by means of T&P in $Z \rightarrow \mu\mu$ decays. In contrast to TTVA, several isolation working points are defined, which represent different compromises between an optimal background rejection and a high prompt muon selection efficiency in boosted/generic decay topologies. Table 5.5 lists the defined isolation working points considered for the efficiency measurement. The same selection as for the TTVA efficiency measurement is applied, with the exception of dropping the isolation requirement on the probe and adding the following additional requirements: The probe needs to satisfy the TTVA selection criteria. It also needs to be separated from a jet with $p_{\mathrm{T}} > 20$ GeV by $\Delta R\left(\mu, \mathrm{jet}\right) > 0.4$. The latter requirement is not enforced if the overlapping jet has fewer than four associated ID tracks. To ensure that the tag does not contaminate the probe isolation, the muons in the T&P pair need to be separated from each other by $\Delta R\left(\mu_{\mathrm{tag}}, \mu_{\mathrm{probe}}\right) > 0.3$.

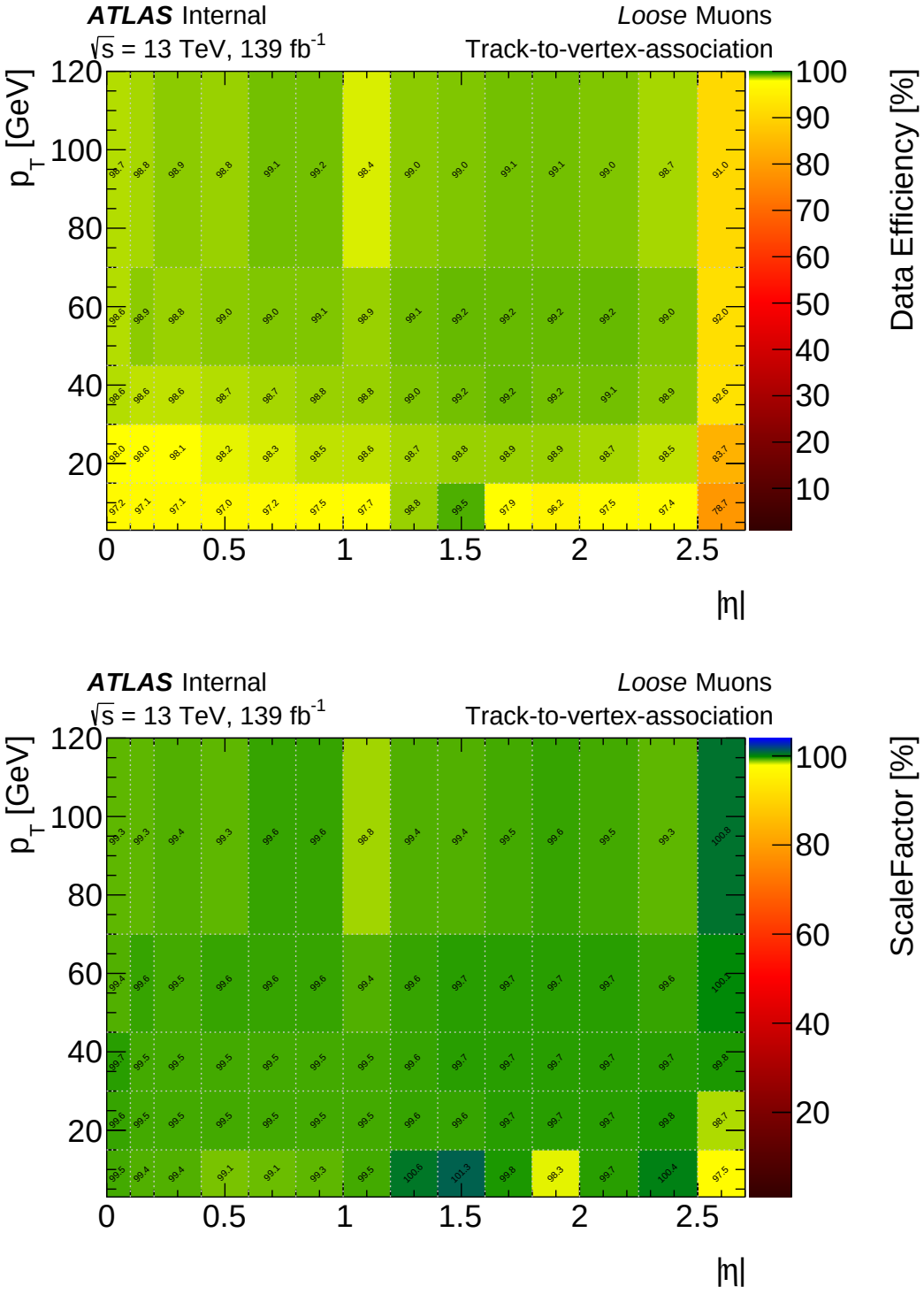

Figure 5.31: Selection efficiency for the TTVA selection measured in the full Run 2 dataset (top) and the efficiency scale factor (bottom) as a function of p_{T} and $|\eta|$ for Loose muons in $Z \to \mu\mu$ events.

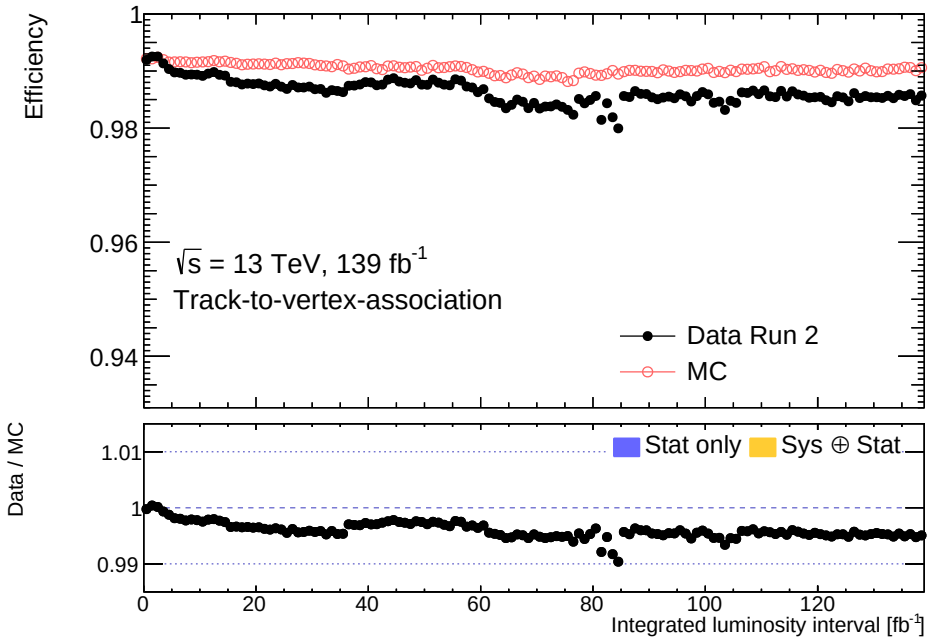

Figure 5.32: TTVA selection efficiency of Loose muons in $Z \rightarrow \mu\mu$ events shown as a function the integrated luminosity interval in the full Run 2 dataset. Each data point corresponds to 1 fb^{-1} of collected data. The bottom panel shows the efficiency scale factor. The yellow error bands indicate the quadratic sum of statistical and systematic uncertainties.

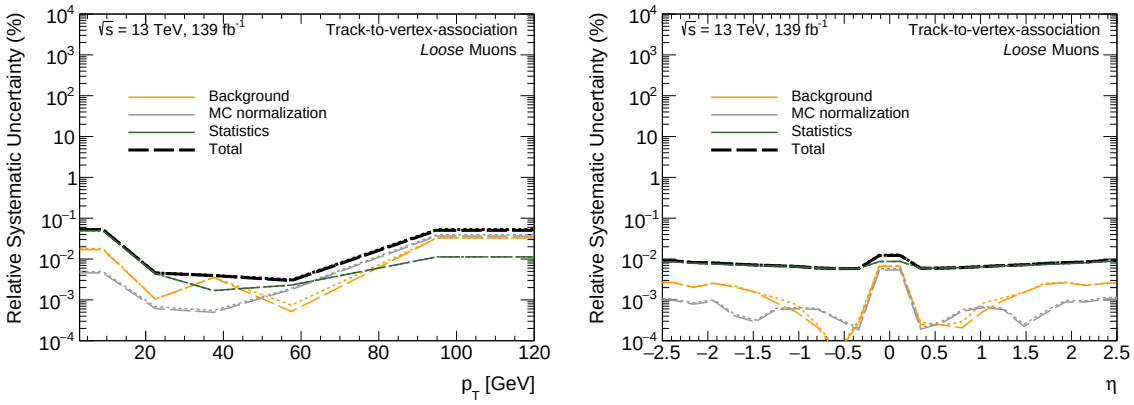

(a) (b)

Figure 5.33: Breakdown of the systematic uncertainties in the TTVA selection efficiency measurement shown as a function of the muon p_{T} (a) and η (b). The dashed (dotted) lines indicate the $+1\sigma$ (-1σ) variation of each nuisance parameter.

Table 5.5: Definitions of the muon isolation working points in terms of their requirements on the track- and calorimeter-isolation variables. (Var)Cone$\mathcal{X}$ denote that the p_{T} of any ID track or the E_{T} of any Topo-cluster within the cone as defined in Equation (3.9) is added to the isolation variable.

Working point	Track isolation $\frac{p_{\mathrm{T}}^{\mathrm{Cone}\mathcal{X}}}{p_{\mathrm{T}}}$			Calorimeter isolation $\frac{E_{\mathrm{T}}^{\mathrm{Topo20}}}{p_{\mathrm{T}}}$
FCLoose	VarCone30		<0.15	< 0.3
FCTight	VarCone30		<0.04	< 0.15
FCLoose (fixed ΔR)	VarCone30 Cone20	($p_{\mathrm{T}} < 50$ GeV) ($p_{\mathrm{T}} > 50$ GeV)	<0.15	<0.3
FCTight (fixed ΔR)	VarCone30 Cone20	($p_{\mathrm{T}} < 50$ GeV) ($p_{\mathrm{T}} > 50$ GeV)	<0.04	<0.15
FC high-p_{T}	Cone20		< 1.25 GeV	—
FCTight (track isolation, fixed ΔR)	VarCone30 Cone20	($p_{\mathrm{T}} < 50$ GeV) ($p_{\mathrm{T}} > 50$ GeV)	<0.06	—

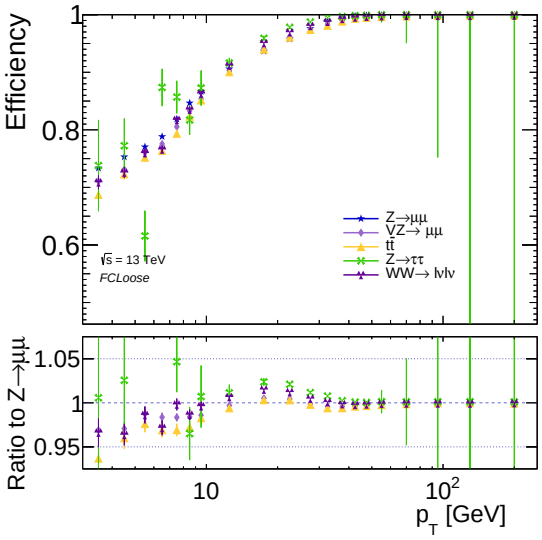

Figure 5.34: Selection efficiency of the FCLoose isolation working point shown as a function of the probe p_{T} in $Z \to \mu\mu$, $t\bar{t}$, VV and $Z \to \tau\tau$ simulated events. The lower pad shows the ratio of each efficiency to the efficiency in $Z \to \mu\mu$ events. The error bars indicate the statistical uncertainties.

Background estimation: The probability of whether a prompt muon satisfies the isolation criteria depends in the first place on the muon momentum and then on the additional hadronic activity in the event. Figure 5.34 depicts the isolation efficiency for probe muons originating from different SM processes. Deviations from the $Z \to \mu\mu$ efficiency of up to 5% are observed and hence prompt muons not coming from $Z \to \mu\mu$ decays are treated as irreducible background in contrast to the reconstruction and TTVA measurements. To account for the three contributing components, the data efficiency before background subtraction is decomposed into

$$\epsilon_{\text{data}}^{\text{measured}} = \epsilon_{\text{QCD}} f_{\text{QCD}} + \epsilon_{\text{irred.}} f_{\text{EWK}} + \epsilon_{\text{data}}^{Z\to\mu\mu} \underbrace{f_{Z\to\mu\mu}}_{=1-f_{\text{QCD}}-f_{\text{irred.}}} , \tag{5.14}$$

where $f_{\text{irred.}}$, f_{QCD} are the fractions of the irreducible and reducible background, respectively, and $\epsilon_{\text{irred.}}$ and ϵ_{QCD} are the corresponding isolation selection efficiencies. $\epsilon_{\text{data}}^{Z\to\mu\mu}$ is the isolation efficiency in $Z \to \mu\mu$ events. The two background fractions have to be determined first. In the previous iteration as performed in Ref. [211], the fractions were estimated exploiting a ABCD method which has been succeeded by a background template fit using the probes only. The templates are constructed and the fit determining the global contamination from non prompt muons, f_{QCD}, is performed in exactly the same way as described in section 5.3.2, where the sum of the irreducible background and signal is referred to as EWK template. To reduce the contamination from non-prompt muons, only T&P pairs within the window of $m_{\text{T\&P}} \in [81; 101]$ GeV are considered postfit to calculate the efficiencies and the corresponding process fractions. The efficiency of the irreducible background is calculated directly from OC T&P in simulation and the efficiency of the reducible component from the SC T&P pairs used to construct the QCD template. The fraction of the irreducible background is calculated from its relative contribution to the EWK template multiplied by the postfit complement of the QCD background fraction. By Reordering the terms in Equation (5.14), the efficiency for the $Z \to \mu\mu$ process in data is given by

$$\epsilon_{\text{data}}^{Z\to\mu\mu} = \frac{\epsilon_{\text{data}}^{\text{measured}} - f_{\text{QCD}}\epsilon_{\text{QCD}} - f_{\text{irred.}}\epsilon_{\text{irred.}}}{1 - f_{\text{QCD}} - f_{\text{irred.}}}. \tag{5.15}$$

Systematic uncertainties: Several sources of systematic uncertainties on the isolation scale factor are considered. The precision of the measurement strongly varies between the working point considered between ~0.2–1%. For each working point a strong dependence on the phase space interval is observed. Figure 5.35 shows the breakdown of the systematic uncertainties on the scale factor for the FCLoose isolation working point.

- **Mass window:** The narrowed mass window used to calculate the efficiency and the process fractions sculpts the kinematics of the decaying Z boson and hence the separation of the probe

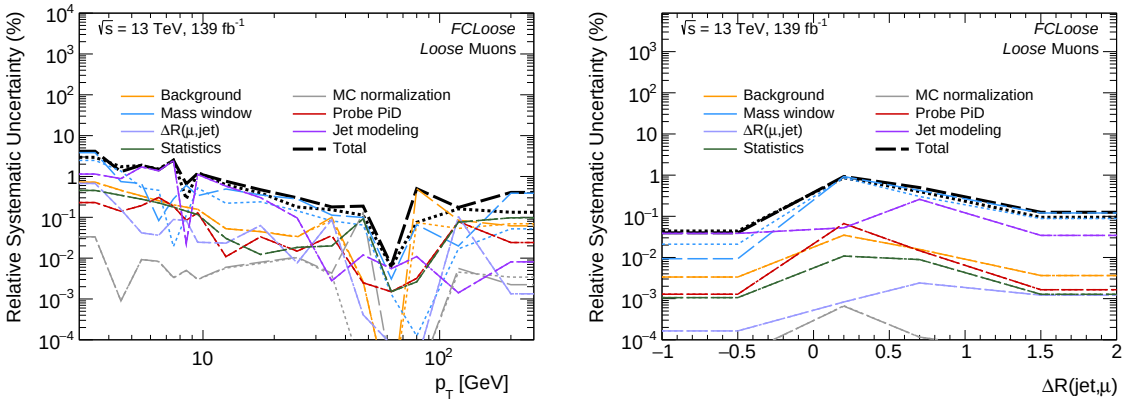

(a) (b)

Figure 5.35: Breakdown of the systematic uncertainties for the FCLoose isolation efficiency for muons measured in the full Run 2 dataset and shown as a function of the muon p_{T} (a) and the proximity to the next jet (b), where $\Delta R < 0$ corresponds events with no reconstructed jet. The dashed (dotted) lines indicate the $+1\sigma$ (-1σ) variation of each nuisance parameter.

to jets. To check the impact on the scale factor, the size of the window is varied once to $m_{\mathrm{T\&P}} \in [86; 96]$ GeV and once to $m_{\mathrm{T\&P}} \in [71; 111]$ GeV. The deviation can be as large as $5-6\%$ at low-p_{T} and is less than 1% for intermediate p_{T} making this uncertainty to the dominant contributor to the total uncertainty.

- **Jet modelling:** To probe the effect from differences in the jet modelling on the simulated efficiency and hence on the scale factor, the isolation efficiency in simulation is calculated from simulated $Z \to \mu\mu$ events generated by the Sherpa program. The overall deviation on the scale factor is found to be $\lesssim 0.1\%$.

- **Probe PiD:** The isolation scale factors are derived using Loose muons as probes. Nevertheless, the low-p_{T} or Tight identification working points have an intrinsic better background rejection and thus unisolated Loose muons may even tend to fail these criteria. This would spoil the applicability of the scale factor derived from Loose muons for other muon identification working points and hence require an efficiency measurement for all identification-isolation working point combinations. To test the applicability of the isolation scale factor, the measurement is repeated using muons passing the low-p_{T} criteria for p_{T} below 15 GeV and the Tight criteria for p_{T} above 15 GeV. Although the isolation efficiencies themselves vary by up to 12%, the scale factor is compatible with the nominal result at the 0.1% level.

- **Background:** This source of uncertainty is the same as for the reconstruction and TTVA efficiency measurement. It contributes to the total uncertainty by 0.05%.

- **MC normalization:** This uncertainty source is described in section 5.3.2 and its contribution to the total uncertainty has been found to be at the level of $O\left(10^{-3}\right)$ %.
- **$\Delta R\,(\mu, \text{jet})$:** In physics analyses, different overlap removal schemes are applied to resolve ambiguities between particles reconstructed from the same energy deposit in the detector. To estimate the impact from different schemes, an alternative μ jet overlap is considered where the probe muons is additionally required to pass cuts on the on the ratio of the muon p_{T} to the jet p_{T} and muon-p_{T} to the associated track p_{T} ratio of being > 0.5 and > 0.7, respectively. The overall contribution of this systematic is found to be $O\left(10^{-2}\right)$ %.
- **Statistics:** The statistical uncertainty varies between $O\left(10^{-2}\right)$ % for muons with $p_{\mathrm{T}} \simeq 50$ GeV well separated from jets and $\simeq 0.5\%$ for low p_{T} muons measured inside jets.

Isolation efficiency results: The isolation efficiencies measured for the FCLoose working point are illustrated in Figure 5.36 as functions of the muon transverse momentum and the separation to the closest-by jet with $p_{\mathrm{T}} > 20$ GeV. The isolation efficiency decreases for low-p_{T}, since even low energetic close-by tracks or energy deposits, which may not be associated with a jet having $p_{\mathrm{T}} > 20$ GeV, become more likely to cause the muon to fail the isolation criteria. For muons with p_{T} above 40 GeV, the isolation working point is fully efficient. For $p_{\mathrm{T}} > 10$ GeV, the obtained scale factor is compatible with unity within 1% which deteriorates down to an agreement of 5% for the lowest p_{T} bin. The isolation efficiency also depends on the proximity to jets. Muons reconstructed within a jet, i.e. $\Delta R < 0.4$, are by up to 4% less likely to pass the isolation selection criteria. To demonstrate the robustness of the isolation selection criteria against the amount of pile-up in the event, Figure 5.37 shows the FCLoose isolation efficiency w.r.t. this variable. A small dependence of the isolation efficiency on the pile-up of $\lesssim 0.5\%$ is observed. This robustness is achieved by only selecting tracks associated to the primary vertex for the calculation of the isolation variable as explained in section 3.7.8.

The scale factors applied in the physics analysis are provided as functions of p_{T} and $\Delta R\,(\mu, \text{jet})$. Likewise the other muon efficiency measurements presented in this document, the efficiencies are additionally split into the data taking period with the small difference that the 2015 and 2016 dataset are considers as a single period. The corresponding scale factor maps are given in Appendix A.4.

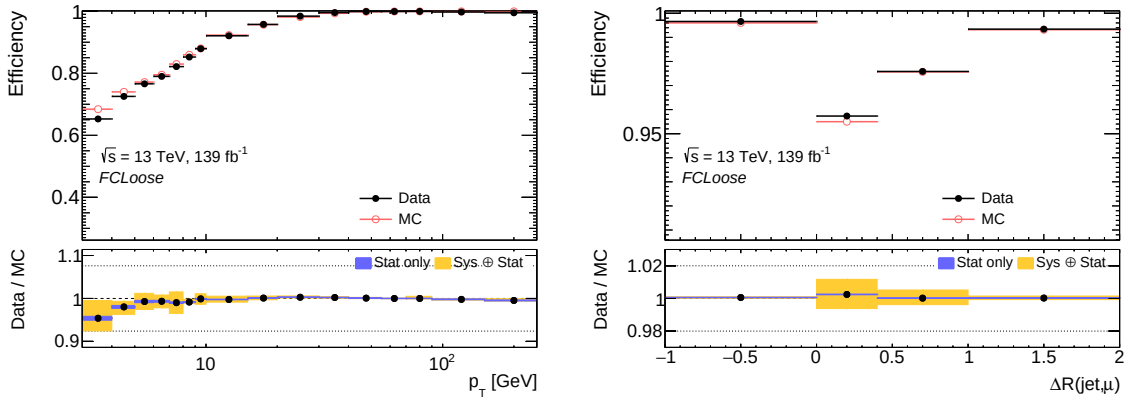

(a) (b)

Figure 5.36: FCLoose isolation efficiency for muons shown as a function of the muon p_{T} (a) and the proximity to reconstructed jets (b) in $Z \to \mu\mu$ events measured in the full run II dataset. The interval $\Delta R < 0$ in (b) corresponds to no jet events. The bottom panel shows the efficiency scale factor. The yellow error bands indicate the quadratic sum of statistical and systematic uncertainties.

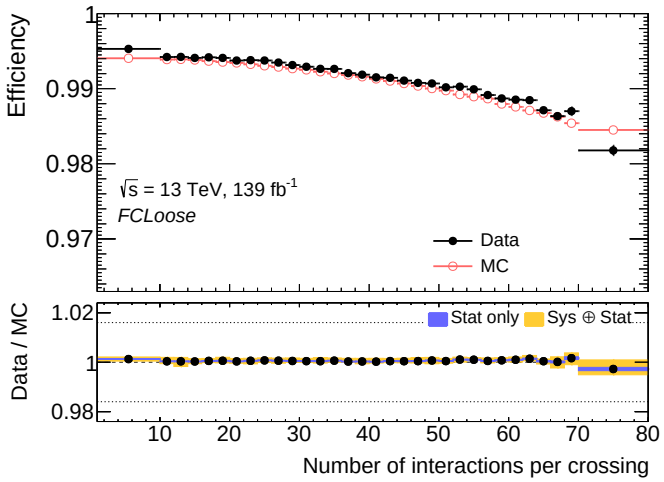

Figure 5.37: Isolation selection efficiency for the FCLoose working point shown against the event pile-up in $Z \to \mu\mu$ events measured in the full run II dataset. The bottom panel shows the efficiency scale factor. The yellow error bands indicate the quadratic sum of statistical and systematic uncertainties.

5.7 Summary of the Muon Efficiency Measurements

Muon reconstruction, track-to-vertex-association (TTVA) and isolation selection efficiencies have been measured in the full Run 2 dataset in $Z \to \mu\mu$ and $J/\psi \to \mu\mu$ events employing the T&P method. The improvement in precision in the muon reconstruction efficiency measurement is demonstrated in Figure 5.38 which shows the Medium reconstruction efficiency measured in $J/\psi \to \mu\mu$ and $Z \to \mu\mu$ events from a previous publication [211] compared to the measurement in this thesis. The efficiencies measured from $Z \to \mu\mu$ and $J/\psi \to \mu\mu$ decays agree very well with each other in the overlapping p_{T} range. The precision in the efficiency scale factor has been improved to better than 0.1% for $Z \to \mu\mu$ decays and to better than 0.5% for $J/\psi \to \mu\mu$ decays using a revised decomposition of the muon track into its parts and an improved background estimation method exploiting a template fit in the di-muon mass spectrum. TTVA efficiencies using muons from $Z \to \mu\mu$ decays with transverse momenta down to 3 GeV are determined for the first time and a precision of $O\left(10^{-2}\right)$ % is achieved. Isolation selection efficiencies have been measured with an precision of 0.2–1%. All results presented are used in every physics analysis of the $\sqrt{s} = 13$ TeV dataset published by the ATLAS collaboration.

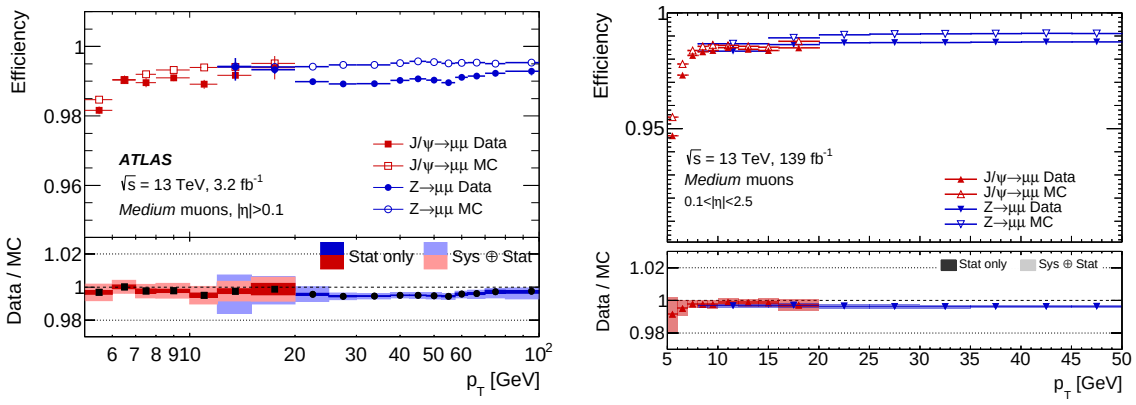

(a) (b)

Figure 5.38: Muon reconstruction efficiency for the Medium selection determined in $Z \to \mu\mu$ and $J/\psi \to \mu\mu$ events as a function of the muon p_{T} in the region $0.1 < |\eta| < 2.5$ at the beginning of the Run 2 data-taking (a) and at the end of the Run 2 data taking (b) with the improved methods developed in this thesis. The error bars on the efficiencies indicate the statistical uncertainty. The bottom panel shows the ratio of measured and predicted efficiencies with statistical and systematic uncertainties [211].

PART

III

Search for Supersymmetry in Multi-Lepton Events

Although Supersymmetry solves several outstanding problems of the Standard Model, the lack of any observation in collider experiments up to now leads to the conclusion that it has to be a broken symmetry. Another argument is given by the existence of oriented bondings in molecules created by electrons occupying p or d orbitals of the atomic shell which have higher energy than the s orbitals. If SUSY were unbroken, the superpartner of the photon, the photino, would also be massless. Hence, the electron at the higher energy levels could emit a photino and become then a selectron. Since the selection is a spin-0 boson, it could populate the lowest energy state together with other selectrons and thus no bondings would be created. The exact mechanism of spontaneous SUSY breaking is unknown. There are several popular models like gauge mediated SUSY breaking (GMSB) [86], locally supersymmetric grand unification (SURGA) [88] or anomaly mediated SUSY breaking (AMSB) [87]. The ignorance of the SUSY breaking mechanism is parametrized by considering all soft SUSY breaking terms in compliance with the gauge symmetries, adding more than 100 additional parameters to the effective MSSM Lagrangian with softly broken SUSY. This enormous parameter space opens a plethora of possibilities of how SUSY might be realized in nature and requires an extensive search program.

At the LHC, the first round of SUSY searches has been performed in Run 1 data at center-of-mass energies of $\sqrt{s} = 7$ and 8 TeV. No evidence for supersymmetric particle production was found but the SUSY mass limits were extended well beyond the electroweak energy scale. Final states with four or more leptons demonstrated unique sensitivity to SUSY scenarios with lepton number violation through R-parity violating (RPV) couplings in the superpotential or for scenarios with GMSB and light higgsinos [252, 253]. Di-τ final states are experimentally very challenging due to the large hadronic background but are sensitive to scenarios in which the supersymmetric partner of the τ lepton, the stau slepton, is relatively light. Such scenarios are theoretically attractive as they can solve the observed discrepancy between measurement and prediction of the anomalous magnetic moment of the muon [254, 255] and provide a mechanism to generate the observed Dark Matter abundance in the universe if the $\tilde{\chi}_1^0$ LSP is close in mass [58]. The results of the searches for such supersymmetric scenarios are presented in the following.

CHAPTER SIX

SEARCH FOR SUPERSYMMETRIC PARTICLES

Searches for new particles at hadron colliders follow a common scheme. The possible production modes of new particles in the pp collisions and their associated cross section and their decay cascades in SM particles have to be identified in order to develop a signal model. For different sets of the free model parameters and for the relevant Standard Model backgrounds Monte Carlo event samples are then generated. These samples are then used to design selection requirements, called signal regions, on the collision events in order to discriminate the beyond SM (BSM) signal from the background. Additional event selections are then defined to estimate the yields of each background from data and to extrapolate the yield to the signal region. The extrapolation has to be tested in phase space regions which are depleted in contributions from the signal, before the real data is compared to the background model in order to determine whether a new particle is found. The following chapter gives a basic overview over each of the concepts listed above. Section 6.1 describes the different supersymmetric particle production modes at the LHC and introduces the models considered. In section 6.2, the general search strategy for a new particle in the context of supersymmetry is explained. The Monte Carlo event samples used for the searches presented in this thesis are described in section 6.3.

6.1 Supersymmetric Particle Production at the LHC

As mentioned in the introduction of this part, the effective Lagrangian of the MSSM in the most general form of the description of spontaneous Supersymmetry breaking contains more than 100 additional free parameters compared to the SM. Many of these parameters are already constrained by previous tests of the Standard Model, like the $B_s^0 \to \mu^+\mu^-$ branching ratio measurement [256], the measurement of the anomalous magnetic moment of the muon [255], the observed amount of CP violation in the meson decays [257] or the observed Dark Matter relic density [258]. In each of the tests, the heavy SUSY particles would appear either indirectly as virtual particles in higher order loop corrections or directly for instance as Dark Matter particles. Based on theoretical assumptions and heuristic arguments [259], indirect constraints can be set on the free parameters and further

guidance is provided to identify promising channels for the search for SUSY at the LHC. The most important aspects for the design of a search for SUSY particles at the LHC are the types and masses of the kinematically accessible particles. Their production cross sections strongly depend on them (cf. Figure 6.1) and the decay cascades vary strongly with the mass differences. Squark-gluino production followed by gluino-pair production and then squark pair production [260–268] which are produced via the strong interaction at the LHC have the highest cross sections. Frequently, it is assumed that the first four squark flavours are mass degenerate and may be much heavier than the third-generation squarks as they couple less strongly to the Higgs fields and are affected more by radiative gluino corrections [54]. Masses of strongly interacting SUSY particles near the electroweak scale, i.e. in the range 100 GeV – 3 TeV, help to solve the hierarchy problem as the loop corrections from the quarks and squarks largely cancel (cf. section 1.6). The second class of supersymmetric particle production is the electroweak production where the colliding quarks first radiate electroweak bosons in order to produce SUSY particles. The direct production of electroweak gauginos typically has an order of magnitude smaller cross section compared to the strong production with slight variations depending on the particle type, i.e. whether a bino-, wino- or higgsino-like particle is produced [269–273]. The electroweak gauginos in most models are predicted to comprise the bottom of the SUSY mass spectrum [54, 259] where the $\tilde{\chi}_1^0$ usually is the LSP. Further arguments for light gauginos come from the measured anomalous magnetic moment of the muon [254] or that a small μ^2 parameter in the Higgs potential helps to solve the hierarchy problem [274, 275]. The direct production of slepton pairs has an even lower cross section by another two orders of magnitude smaller at a given particle mass [269, 271, 276–278]. Light sleptons might have played an important role in the development of the early universe since their co-annihilation with the lightest neutralino provides an excellent mechanism to correctly predict the observed Dark Matter density [58]. Sleptons also contribute in loop corrections to the anomalous magnetic moment of the muon [254].

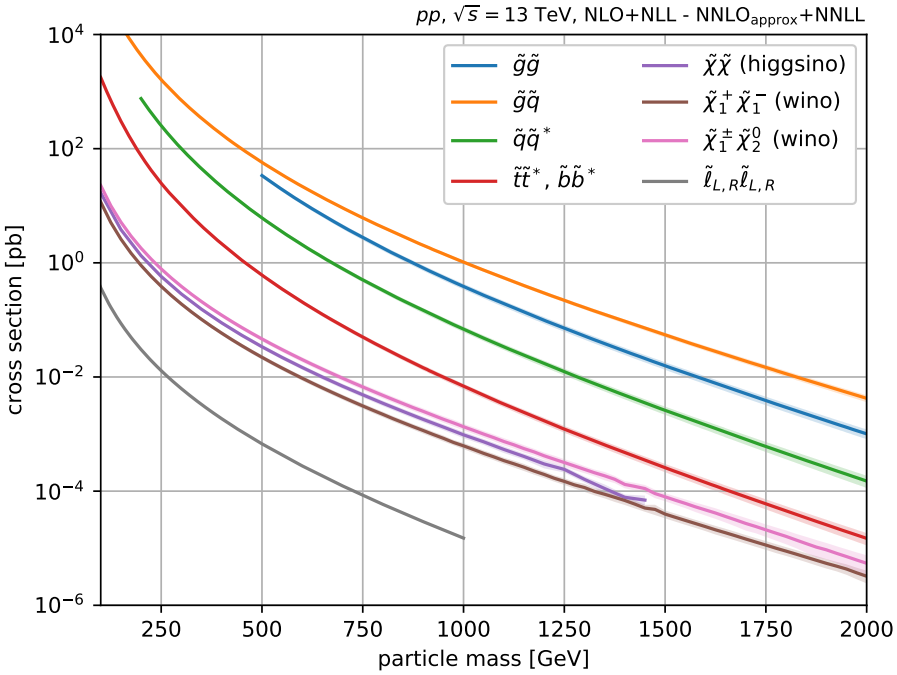

Figure 6.1: Cross sections for various supersymmetric particle production modes as a function of the particle mass at $\sqrt{s}$ = 13 TeV [279].

Simplified SUSY Models Even though the above theoretical considerations provide a guideline for the accessibility of SUSY particles at the LHC, practical search strategies cannot be based on the full range of SUSY decay modes allowed by the MSSM. The SUSY mass splittings and hence the decay modes branching ratios strongly depend on the SUSY breaking parameters. In many cases, different models predict the same final state and there can be no experimental preference for one or the other at the initial stage of a discovery. In order to perform more generic searches, simplified models are used [280, 281] which assume that only the next-to-lightest supersymmetric particle (NLSP) is produced in the *pp* collisions with subsequent decay into the LSP and SM particles via one or two different decay modes. The choice of the NLSP is inspired by the fully developed theory and the most dominant decay is assumed. The masses of the involved supersymmetric particles and the decay branching ratios are the free parameters of the simplified model reducing the number of free parameters drastically to only two or three. Signal points in the space of parameter combinations are selected and simulated to provide predictions for the signal selection. A crucial aspect for the design of a search for supersymmetry is whether R-parity conservation is assumed which has strong impact on the final states, in particular on the missing transverse energy due to the LSPs leaving the detector undetected (cf. section 1.7.2).

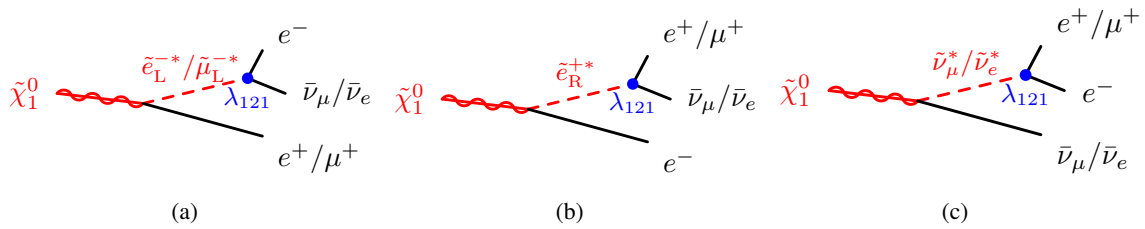

Figure 6.2: Examples of $\tilde{\chi}_1^0 \to \ell\ell\nu$ decays decays causes by a non-zero lepton number violating λ_{121} interaction term in the superpotential.

Table 6.1: $\tilde{\chi}_1^0$ decay modes due to non-vanishing $\lambda_{ijk}\tilde{L}_i\tilde{L}_j\tilde{e}_k$ terms in the superpotential. All decay modes are assumed to have the same branching ratio. The decay modes studied in this thesis are marked in blue (only electrons or muons in the final state) and orange (at least one τ lepton in the final state).

	$ij = 12$	$ij = 13$	$ij = 23$
$k = 1$	$ee\nu_\mu$ / $e\mu\nu_e$	$ee\nu_\tau$ / $e\tau\nu_e$	$e\mu\nu_\tau$ / $e\tau\nu_\mu$
$k = 2$	$e\mu\nu_\mu$ / $\mu\mu\nu_e$	$e\mu\nu_\tau$ / $\mu\tau\nu_e$	$\mu\mu\nu_\tau$ / $\mu\tau\nu_\mu$
$k = 3$	$e\tau\nu_\mu$ / $\tau\mu\nu_e$	$e\tau\nu_\tau$ / $\tau\tau\nu_e$	$\mu\tau\nu_\tau$ / $\tau\tau\nu_\mu$

Models with R-parity violation: If lepton number and hence R-parity are violated (RPV) by non-zero λ_{ijk} couplings in the superpotential (cf. Equation (1.32)), the LSP decays into a charged lepton pair and a neutrino – cf. for example Figure 6.2 for the case of a non-zero $\lambda_{121}\tilde{L}_1\tilde{L}_2\tilde{e}_1$ term – instead of escaping the detection. In this thesis, LSP decays mediated by such non-zero $\lambda_{ijk}\tilde{L}_i\tilde{L}_j\tilde{e}_k$ terms in the superpotential have been studied. The decays are assumed to be prompt such that the production and decay vertices of the LSP cannot be distinguished. This corresponds to typical lifetimes of the $\tilde{\chi}_1^0$ LSP of a few ps. The flavours of the final state leptons are determined by the choice of non-zero λ_{ijk} couplings where two decay modes are possible for each coupling (cf. Table 6.1). If only $\lambda_{121} \neq 0$ or $\lambda_{122} \neq 0$, the LSP exclusively decays into electrons or muons, referred to as light leptons in the following, while for $\lambda_{133} \neq 0$ or $\lambda_{233} \neq 0$ cases at least one of the decay leptons always is a τ lepton, in half of the cases or even both. These are the two extreme cases with rep sect to τ lepton multiplicity studied in this thesis (cf. Table 6.1).

As each pair-produced NLSP results in an LSP decaying leptonically, the experimental signatures of such processes are four charged leptons in conjunction with missing transverse momentum from the escaping neutrinos independent of the SUSY production mode (cf. Figure 6.3) and additional SM particles from the NLSP decay. Final states with high lepton multiplicities have the advantage of that they can be easily separated from the hadronic background allowing for high selection efficiency using lepton-based triggers with moderate transverse momentum thresholds on the order of only 20 GeV based on excellent momentum resolution. Also, this signature is rare in the SM and leading to very low

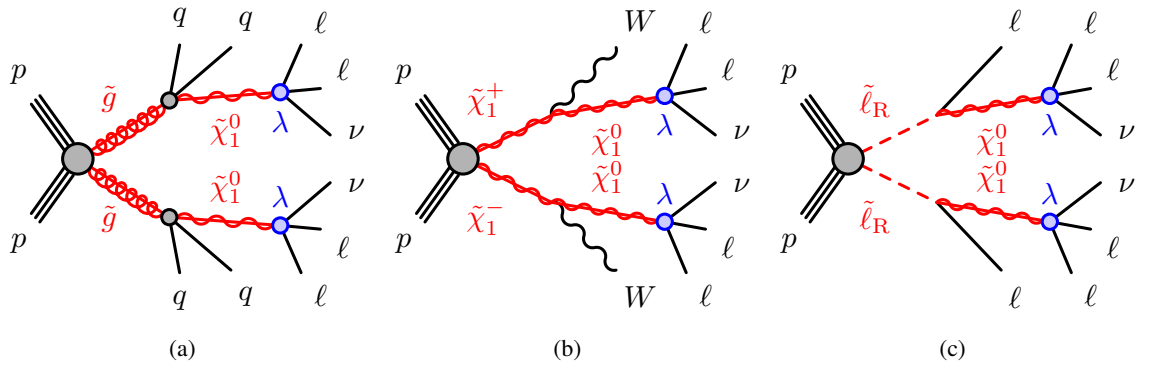

Figure 6.3: Representative diagrams of gluino (a), chargino (b) and slepton (c) pair production in simplified SUSY models with decays into SM particles and $\tilde{\chi}_1^0$ LSPs, which each further decays into a pair of charged leptons and a neutrino.

irreducible background (cf. section 7.1). Such a search has been performed with the Run 1 dataset at a center-of-mass energy of $\sqrt{s} = 8$ TeV with 20.1 fb^{-1}integrated luminosity [282]. Simplified models with either gluino, wino-like chargino or slepton NLSP were investigated. For each NLSP choice, four choices of the non-zero RPV λ_{ijk} couplings (marked in orange or blue in Table 6.1) were tested. No excess above the Standard Model expectation was observed allowing to derive 95% confidence level (CL) exclusion limits on the neutralino and NLSP masses depending on $\lambda_{ijk} \neq 0$ which are shown in Figure 6.4 for the gluino and wino NLSP model. For both models, the exclusion limits are stronger for the LSP decaying exclusively into light leptons than when τ leptons are in the final state, and have little dependence on the LSP mass with the exception of the low LSP mass region where the sensitivity decreases rapidly. The limits are also independent of whether the LSP decays into electrons or muons. Therefore, no distinction is made between λ_{121} (λ_{133}) and λ_{122} (λ_{233}) scenarios and they are collectively denoted by λ_{12k} (λ_{i33}) for the remainder of the thesis. Gluinos with masses up to 1.4 TeV (1.05 TeV) are excluded for non-zero λ_{12k} (λ_{i33}) couplings. The limits on the wino mass are weaker by roughly a factor of two due to the corresponding lower production cross section.

Efforts of reinterpretation of the Run 1 data analyses in terms of R-parity violating interactions demonstrated unique sensitivity of the four-lepton analysis to RPV models with low and moderate mass splittings between LSP and NLSP in scenarios with low τ multiplicities in the final state [252]. The increase in the center-of-mass energy from 8 TeV to 13 TeV in Run 2 of the LHC enhanced the production for even heavier particles, e.g. for gluinos with 1.7 TeV mass, for which the previous searches had no sensitivity, by increasing the production cross sections by up to two orders of magnitude (cf. Figure 6.5). Also the dataset from Run 2 is seven times larger than at $\sqrt{s} = 8$ TeV. Both aspects motivate the continuation of the search for supersymmetry at $\sqrt{s} = 13$ TeV, in particular for models with R-parity violation. The models considered are based on the ones used in [282]. They

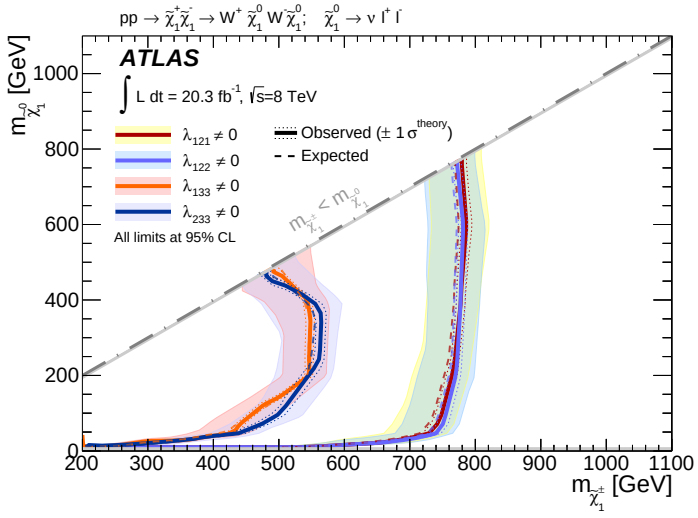

(a)

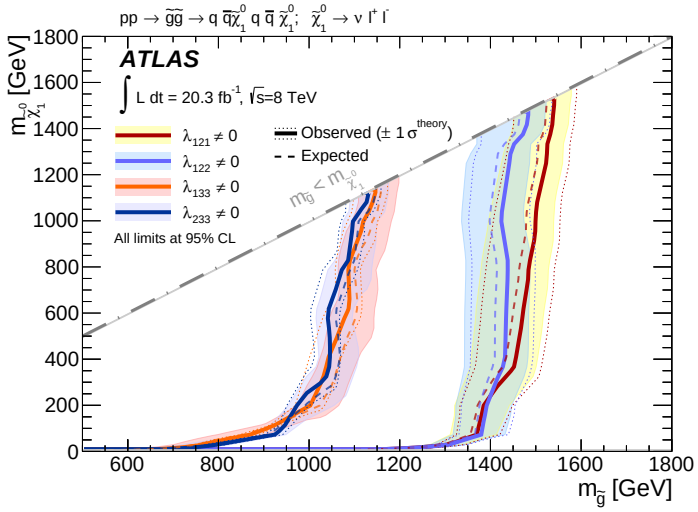

(b)

Figure 6.4: The observed (solid) and expected (dashed) 95% CL exclusion limit contours on the NLSP and LSP masses for simplified RPV models with $\tilde{\chi}_1^{\pm}$ NLSP (a) and $\tilde{g}$ NLSP (b) obtained from the Run 1 search for Supersymmetry in four-lepton events [282].

have been developed further in the course of this thesis.

The electroweak $SU(2)_{\mathrm{L}}$ gauge symmetry implies that the neutral component of the wino triplet is close in mass to the charged states [54]. In the wino model, the $\tilde{\chi}_1^+/\tilde{\chi}_2^0$ and $\tilde{\chi}_1^-/\tilde{\chi}_2^0$ production modes with $m_{\tilde{\chi}_1^{\pm}} = m_{\tilde{\chi}_2^0}$ and $\tilde{\chi}_2^0 \to \tilde{\chi}_1^0 V$ have been added (cf. Figure 6.6(a)). The V is either a Z or a Higgs boson where the latter is only possible if the mass splittings between NLSP and LSP allow for on-shell Higgs production. Left-handed charged sleptons are close in mass to the sneutrinos due to the same

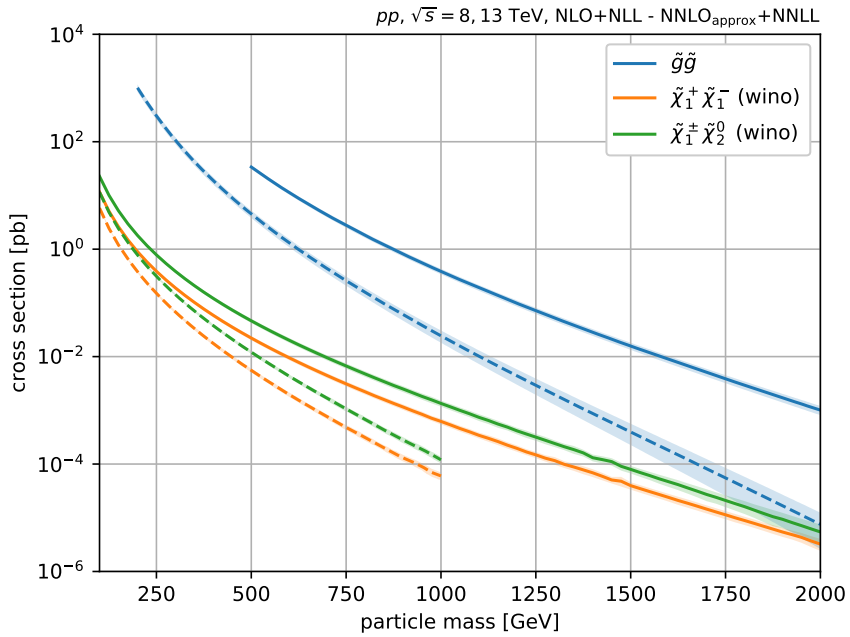

Figure 6.5: Comparison of the production cross sections of $\tilde{\chi}_1^+/\tilde{\chi}_1^-$, $\tilde{\chi}_1^\pm/\tilde{\chi}_2^0$ and $\tilde{g}\tilde{g}$ pairs at $\sqrt{s} = 8$ TeV (dashed lines) and at $\sqrt{s} = 13$ TeV (solid lines) as a function of the supersymmetric particle mass.

argument of $SU(2)_\mathrm{L}$ gauge symmetry. Hence, the sneutrino and slepton NLSP models in [282] have been combined into a single model where $\tilde{\ell}^\pm\tilde{\nu}$ production is considered as well (cf. Figure 6.6(b)). In each case, the slepton decays into its SM partner and the $\tilde{\chi}_1^0$ LSP. The three slepton flavours are assumed to be degenerated in mass. The gluino model is adopted from [282]. The pair produced gluinos each decay into a pair of quarks of any flavour except top[1] and the $\tilde{\chi}_1^0$. For each NLSP species, two RPV decay scenarios are considered. In the λ_{12k} scenario, the λ_{121} and λ_{122} couplings are both taken to be non-zero with equal magnitude while in the λ_{i33} scenario the λ_{133} and λ_{233} couplings are non-zero and equal. Details about the considered mass ranges and the generator programs used for the simulated signal samples are given section 6.3.

Supersymmetry with R-parity conservation: There is a broad variety of supersymmetric models assuming R-parity conservation (RPC). Analyses of the Run 1 collision data in terms of the phenomenological MSSM indicated that SUSY might be realized with light higgsinos which could not be excluded with the existing data [253]. Light higgsinos are also motivated by the hierarchy problem.

[1] The decay into top quarks is kinematically allowed for $m_{\tilde{g}} - m_{\tilde{\chi}_1^0} > 2m_t$ giving rise to additional leptons and jets from top decays such that these decay modes are more likely to be accepted by the selection criteria. They are not considered here to focus on the cases where the final state leptons originate from the $\tilde{\chi}_1^0$ decays.

A search for them as the lightest particles can be experimentally challenging since their mass spectrum is predicted to be compressed with mass splittings of few GeV at maximum [274, 283]. Higgsino masses below 92 GeV were already excluded by the LEP experiments in highly compressed scenarios where the particles were split in mass by only 0.1–3 GeV [284]. For moderate splittings of around 10 GeV the limits have been recently improved to 162 GeV by a dedicated ATLAS search [285]. The four-lepton final state can provide an excellent sensitivity if light higgsinos occur in General Gauge Mediated (GGM) SUSY breaking scenarios, where the fermionic superpartner of the graviton, the gravitino, $\tilde{G}$, serves as LSP and is almost massless [253, 286]. The neutral higgsinos then decay into V and the gravitino, where V is either a Higgs or a Z boson (cf. Figure 6.7). Simplified models with $\tilde{\chi}_1^0\tilde{\chi}_1^\pm$, $\tilde{\chi}_2^0\tilde{\chi}_1^\pm$, $\tilde{\chi}_1^0\tilde{\chi}_1^0$, $\tilde{\chi}_2^0\tilde{\chi}_2^0$ and $\tilde{\chi}_1^+\tilde{\chi}_1^-$ production have been considered where the mass of the $\tilde{\chi}_1^\pm/\tilde{\chi}_2^0$ triplet and the branching ratio of the $\tilde{\chi}_2^0/\tilde{\chi}_1^0$ to decay into a Z boson are the free parameters. To ensure prompt decays of the SUSY particles, the mass of the $\tilde{\chi}_1^0$ is set at 1 GeV below the mass of the $\tilde{\chi}_1^\pm/\tilde{\chi}_2^0$ triplet.

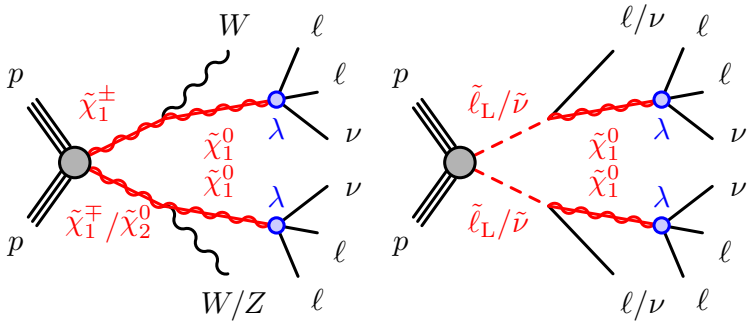

Figure 6.6: Simplified models of electroweak supersymmetric particle production and $\tilde{\chi}_1^0$ RPV decays studied in this thesis.

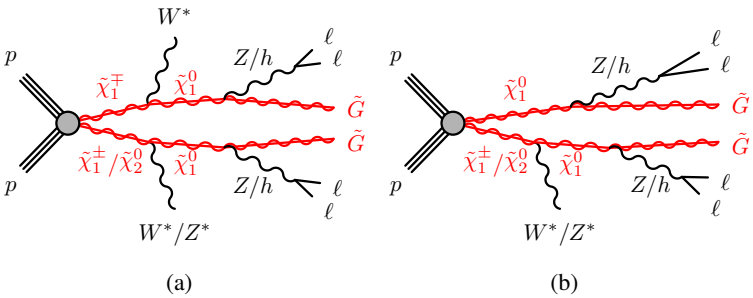

Figure 6.7: Diagrams of the processes in the SUSY RPC GGM higgsino models. The W^*/Z^* from $\tilde{\chi}_1^\pm/\tilde{\chi}_2^0$ decays are off-shell ($m_{V^*} \sim 1$ GeV) and their decay products are usually not reconstructed.

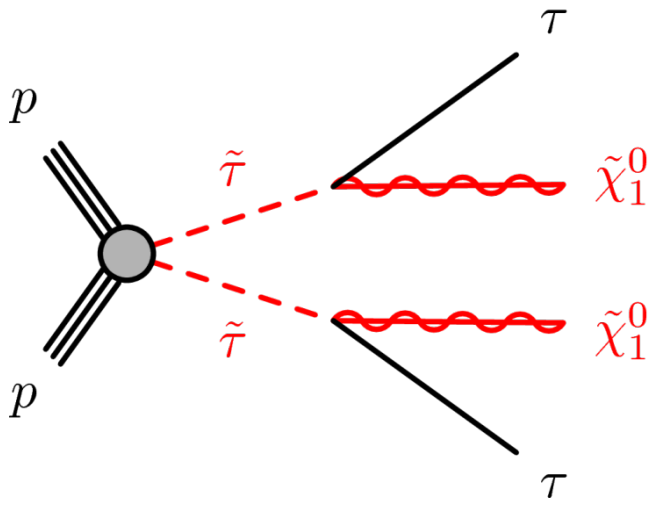

Figure 6.8: Diagram of direct stau production in pp collisions.

The third class of models investigated in this thesis are models in which the supersymmetric partner of the τ lepton, the stau slepton, is relatively light, i.e. $m_{\tilde{\tau}} \simeq 100$ GeV–1 TeV, and R-parity is conserved. These models are attractive as they could explain the observed discrepancy between the measured and predicted values of the anomalous magnetic moment of the muon [254, 255]. If the stau is the only supersymmetric particle kinematically accessible at the LHC it has to be produced directly in the pp collisions. A sketch of direct stau pair production in pp collisions is illustrated in Figure 6.8. Each produced stau decays into a τ lepton and the $\tilde{\chi}_1^0$ which is stable due to R-parity conservation and hence escapes detection. The signature for this search are two τ leptons with opposite charges and additional missing transverse momentum due to the two $\tilde{\chi}_1^0$. Both τ leptons decay inside the beam pipe either into hadrons and a tau-neutrino (τ_{had}) or into electron or muon and two neutrinos (τ_{lep}). The hadronic τ decays are identified with dedicated algorithms (cf. section 3.7.6). The three possible decay channels of the τ lepton pair, $\tau_{\text{had}}\tau_{\text{had}}$, $\tau_{\text{lep}}\tau_{\text{had}}$ and $\tau_{\text{lep}}\tau_{\text{lep}}$ channel, differ significantly in the efficiencies of the prompt lepton identification, in the rejection of fake leptons, in the rates and composition of the SM backgrounds, and in the precision in the reconstruction of the kinematic properties of the decaying stau-pair system as it will be discussed in more detail in section 8.1. The di-τ final state is experimentally very challenging due to the very large background rates and the tiny production cross section of the stau pairs. Hence, the best lower limits on stau mass, below 90 GeV at 95% confidence level (cf. Figure 6.9), prevailed from the era of LEP [287–291]. The search for direct stau pair production will be presented in chapter 8.

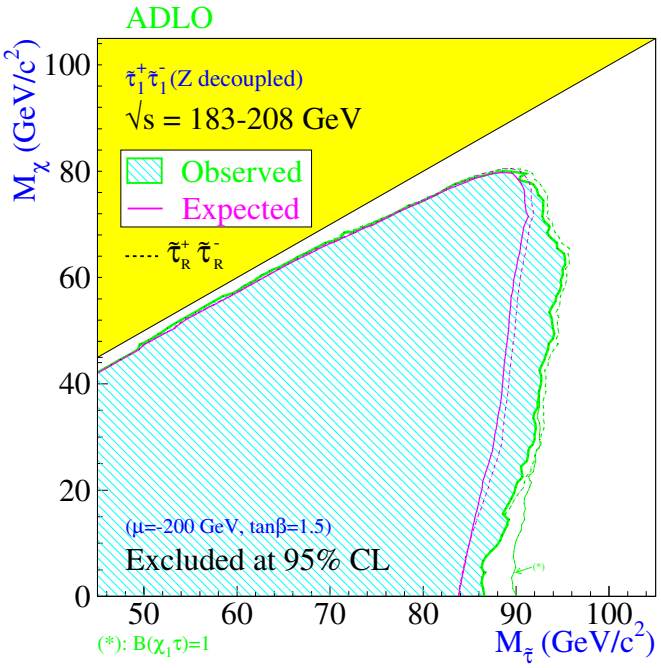

Figure 6.9: Expected (pink) and observed (green) exclusion contour in the stau and $\tilde{\chi}_1^0$ mass space from the LEP data at $\sqrt{s} = 186 - 203$ GeV recorded by the ALEPH, DELPHI, L3 and OPAL experiments. The yellow region is kinematically forbidden [287–291].

6.2 General Search Strategy

The strategy for the search for new physics beyond the SM is always guided by the predicted interactions of the new particles with the SM particles. For SUSY searches in pp collisions, the main consideration is the final state $|X\rangle$ expected from the decay cascade of the produced particles. The new particles contribute in the transitions from the initial state $\langle pp|$ to the considered final state $|X\rangle$ and hence probability for $|X\rangle$ to be produced in a pp collision. Supersymmetric particles increase the transition probability and an enhancement in the production cross section of $|X\rangle$ compared to the SM expectation is searched for. However, the production cross sections of new heavy particles are usually much smaller than the production cross sections of the SM particles decaying into the same final state. Therefore, the searched phase space of $|x\rangle$ is restricted to regions where even the small SUSY contribution is comparable to the SM contribution. This region with optimal signal to background ratio is selected using Monte Carlo simulation events. The general search procedure for new physics is illustrated in Figure 6.10. As first step, the phase space region with optimum signal to background ratio or expected signal significance is identified for each model, the so-called signal region (SR). For this purpose, signal and background Monte Carlo samples are generated at representative points in the signal model

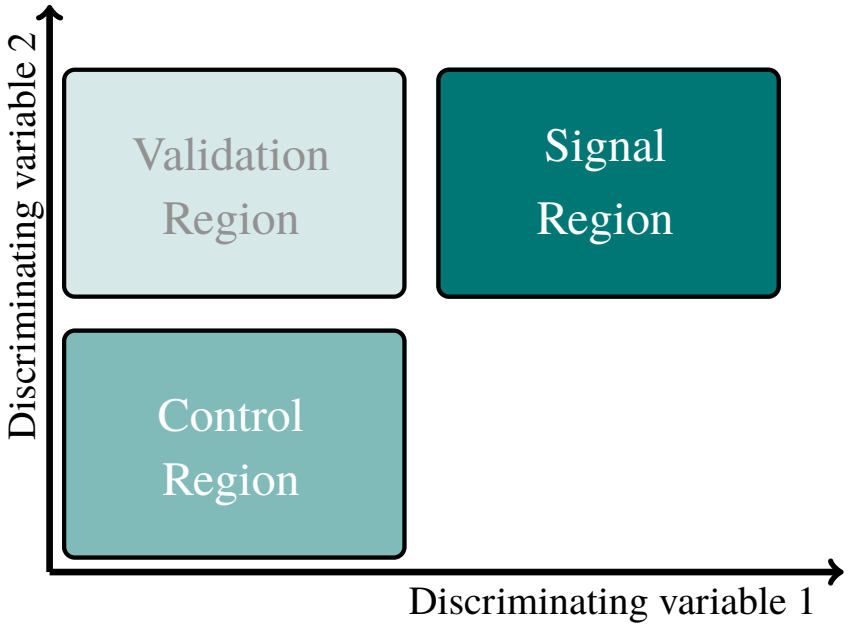

Figure 6.10: Illustration of the new physics search procedure. The signal region provides the largest sensitivity to the signal model. Control regions are used to estimate specific background contributions from data. The validation regions provide cross checks of the background estimates.

parameter space. However, some of the SM background processes at the LHC are difficult to model accurately. Therefore, the contributions of such processes are determined using data in so-called control regions (CR) which are enriched in the background and depleted in signal. The background predictions in the control control regions are extrapolated to the signal regions. In order to validate the extrapolation, so-called validation regions (VR) are chosen which are disjoint from the CR and SR and depleted in signal. If the background is modelled correctly in the VR, the signal selection can be applied to the data, called unblinding.

In the searches in this thesis, events are categorized according to their τ lepton multiplicity. Next, basic features of the event topology have to be exploited in order to discriminate the SM background against the SUSY signal. For example in the RPV model searches, all four leptons are expected to not originate from Z boson decays which are a frequent SM background. Hence, an initial reduction of the background is achieved by rejecting all four lepton events which contain oppositely charged di-electron or di-muon pairs, so-called Same Flavour Opposite Sign (SFOS) pairs, with invariant masses close to the rest-mass of the Z boson. After this basic pre-selection, cuts are applied on kinematic final state variables directly or they are combined in multivariate classifiers like Boosted Decision Trees (BDT) [292–294]. The optimum cuts are chosen by maximizing the expected signal significance [295]. For each cut value, the numbers of predicted signal and background events N_{sig} and N_{bkg} are evaluated.

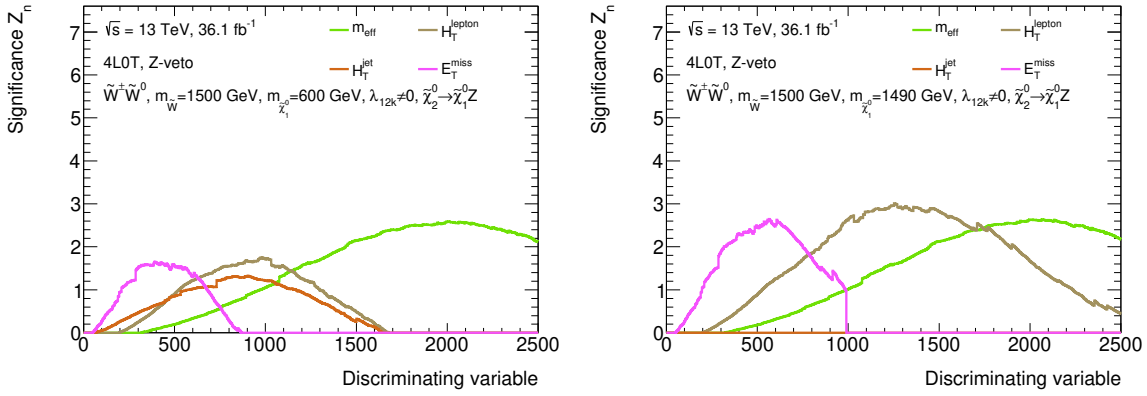

(a) (b)

Figure 6.11: Expected significance to two signal points in the wino model with $\tilde{\chi}_2^0 \rightarrow \tilde{\chi}_1^0 Z$ and $\lambda_{12k} \neq 0$ coupling in 36.1 fb^{-1} of data shown as a function of the lower threshold on various event variables considered in the analysis in events with four electrons and muons and applied Z-veto. The effective mass m_{eff} is defined as the scalar sum of p_{T} of the selected leptons and jets with $p_{\text{T}} > 40$ GeV and of $E_{\text{T}}^{\text{miss}}$ as described in section 7.2. The $H_{\text{T}}^{\text{lepton}}$ and $H_{\text{T}}^{\text{jet}}$ are the lepton and jet components of m_{eff}, respectively. Simulation is used to estimate the SM background.

A general systematic error on the background estimate of 30% is assumed. The p-value of testing the background-only hypothesis in presence of a signal is then determined. The probability distribution of observing $N_{\text{tot}} = N_{\text{sig}} + N_{\text{bkg}}$ events under the background-only hypothesis is modelled by a Gaussian with N_{bkg} as mean and the total error on N_{bkg} as standard deviation. The p-value is defined as the probability to observe at least N_{tot} events and allows for the determination of the number of standard deviations Z_n from the background-only hypothesis, the signal significance, according to

$$Z_n = \text{ierf}\,(1 - 2p)\,. \tag{6.1}$$

For the example of two signal model points in the four-lepton analysis containing electrons or muons only, Figure 6.11 shows the expected significance as a function of the lower thresholds on different event variables in 36.1 fb^{-1} of data. The optimal discriminating variable and corresponding threshold are chosen such that the significance is maximum over a large range of the parameter space of the investigated SUSY models. Commonly $Z_n \geq 3$ is required for evidence for a new process and $Z_n \geq 5$ for claiming a discovery. The procedure is repeated for other cuts for the events passing the previous cuts to arrive at the final signal region (SR). One signal region is usually not sufficient to cover the full parameter space. Hence multiple signal regions are defined. To allow for statistical combination of these signal regions, their selection criteria are chosen orthogonal such that the signal regions are disjoint

The dominant irreducible SM background contributions in the SR are normalized to data in dedicated control regions (CR) which are selected orthogonal to the SR and depleted in signal events by inverting at least one of the signal selection criteria while they need to be kinematically close to the SR, such that the uncertainties in the extrapolation to the SR are small and they are as pure as possible in the background processes which are normalized to them. The normalization factor is to first approximation given by

$$\mu_{\text{bkg}}^{\text{CR}} = \frac{N_{\text{data}}^{\text{CR}} - N_{\text{MC},\neg\text{bkg}}^{\text{CR}}}{N_{\text{MC, bkg}}^{\text{CR}}}, \tag{6.2}$$

where $N_{\text{MC, bkg}}^{\text{CR}}$ and $N_{\text{MC},\neg\text{bkg}}^{\text{CR}}$ are the expected numbers of events of the considered background and of the rest of the events selected in the CR, respectively, while $N_{\text{data}}^{\text{CR}}$ is the number of data events in the CR. In the final analysis, the normalization factor is obtained from a global maximum likelihood fit to the data which is explained in section 7.5.1.

Another aspect is the estimation of the reducible background. Since the particle identification algorithms are designed to minimize the fake lepton rate, a reliable simulation of the corresponding reducible background would require the generation of a very large number of MC events which is not practical. Furthermore, QCD processes with many confined particles are difficult to model. Therefore, this reducible background in the final analysis is estimated using control data containing lepton candidates discarded as background leptons by the particle identification algorithms. For initial optimization studies and for basic cross checks the simulation is used if not stated otherwise.

6.3 Simulated Event Samples

A summary of the used samples in this work is reported in Table 6.2. In the following, the generators used for each sample are briefly described based on the full documentation given in Refs. [233–236, 296].

Simulation of SM background: Electroweak single boson, diboson and triboson production is simulated with the Sherpa v2.2.1 or v2.2.2 [238] generator depending on the process, including off-shell effects of down to 4 GeV in boson mass and Higgs boson contributions where appropriate. At least one of the electroweak bosons is required to decay leptonically with $p_{\text{T}} > 2.5$ GeV. The production of V+jets ($V = Z, W$) is simulated using NLO-accurate matrix elements for up to two jets, and LO-accurate matrix elements for up to four jets calculated with the Comix [239] and OpenLoops [121, 240] libraries. Diboson processes (VV) are generated using matrix elements at NLO accuracy in QCD for up to one additional parton and at LO accuracy for up to three additional parton emissions. Samples for the loop-induced processes $gg \to VV$ and for the triboson processes

Table 6.2: Summary of the simulated SM background samples used in this analysis, where $V = W, Z$, and Z includes off-shell contributions. *Tune* refers to the set of tuned parameters used by the generator [129, 237, 245]. The used generators and PDF sets are documented in Refs. [111–114, 123, 124] and in Refs. [104, 105, 297], respectively. The cross sections are taken from Refs. [112, 233–236, 261–263, 271, 272, 277, 298–302]. The sample marked with a † is used for a cross check of yields and for studies of systematic uncertainties. Samples marked by ⋆ are only considered for the result based on the 36.1 fb^{-1}dataset while samples marked by ‡ are only used for the full Run 2 result.

Process	Matrix element	Showering	Full/fast sim. calculation	Cross section	Tune	PDF set
$ZZ \to 4\ell, WZ \to 3\ell\nu, VV \to \ell\ell\nu\nu$	Sherpa 2.2.2		Fullsim	NLO	Sherpa default	NNPDF3.0nlo
$WZ \to \ell\ell qq, WW \to \ell\nu qq, VVV$	Sherpa 2.2.1		Fullsim	NLO	Sherpa default	NNPDF3.0nlo
$VV^{\dagger}$	Powheg-Box 2	Pythia 8.186	Fullsim	NLO	AZNLO	CTEQ6L1
$ggH^{\star}$, VBF, $ggZH, t\bar{t}H^{\ddagger}$	Powheg v2	Pythia 8.186	Fullsim	NNLO+NNLL	AZNLO	CT10
ZH, WH	Pythia 8.186		Fullsim	NNLO+NNLL	A14	NNPDF2.3lo
$t\bar{t}H^{\star,\dagger}$	aMC@NLO 2.2.3	Pythia 8.186	Fullsim	NLO	A14	NNPDF2.3lo
$t\bar{t}Z^{\star}, t\bar{t}W^{\star}, t\bar{t}WW, t\bar{t}WZ$	MadGraph5_aMC@NLO 2.2.2	Pythia 8.186	Fullsim	NLO	A14	NNPDF2.3lo
$t\bar{t}Z^{\ddagger}, t\bar{t}W^{\ddagger}$	aMC@NLO 2.3.3	Pythia 8.186	Fullsim	NLO	A14	NNPDF2.3lo
$t\bar{t}Z^{\dagger}$	Sherpa 2.2.2		AF-II	NLO	Sherpa default	NNPDF3.0nlo
tWZ	aMC@NLO 2.2.3	Pythia 8.186	Fullsim	NLO	A14	NNPDF2.3lo
$tt\bar{t}(W), t\bar{t}t\bar{t}$	MadGraph5_aMC@NLO 2.2.2	Pythia 8.186	Fullsim	NLO	A14	NNPDF2.3lo
$t\bar{t}^{\star}$	Powheg v2	Pythia 6.428	Fullsim	NNLO+NNLL	Perugia2012	CT10
$t\bar{t}^{\ddagger}$	Powheg v2	Pythia 8.230	Fullsim	NNLO+NNLL	A14	NNPDF3.0nlo
Z + jets*, W + jets*	MadGraph5_aMC@NLO 2.2.2	Pythia 8.186	Fullsim	NNLO	A14	NNPDF2.3lo
Z + jets‡, W + jets‡	Powheg-Box 2	Pythia 8.186	Fullsim	NLO	AZNLO	CT10
Z + jets‡, W + jets‡	Sherpa 2.2.1		Fullsim	NLO	Sherpa default	NNPDF3.0nlo
SUSY signal	MadGraph5_aMC@NLO 2.2.2	Pythia 8.186	AF-II	NLO+NLL	A14	NNPDF2.3lo

(VVV) are generated using LO-accurate matrix elements with up to one additional parton emission. Electroweak diboson events in association with two jets ($VVjj$) are generated at LO accuracy. For all samples, the matrix element calculations are matched and merged with the Sherpa parton showering based on Catani-Seymour dipole [239, 241] using the MEPS@NLO prescription [120, 242–244]. The virtual QCD corrections are provided by the OpenLoops library [121, 240]. The NNPDF3.0nlo set of PDFs is used [105], along with the dedicated set of tuned parton-shower parameters developed by the Sherpa authors. Uncertainties from missing higher orders are evaluated [303] using seven variations of the QCD factorization and renormalization scales in the matrix elements by factors of 0.5 and 2 avoiding variations in opposite directions. Uncertainties on the nominal PDF set are evaluated using 100 eigenvector variations. Additionally, the results are cross checked using the central values of the CT14nnlo [304] and MMHT2014 NNLO [305] PDF sets. The uncertainty on the strong coupling constant α_S is assessed by variations of ±0.001. For cross checks and studies of theoretical uncertainties, diboson events generated as described in section 5.2 are used.

For the four-lepton search using the first 36.1 fb^{-1}dataset only, the MadGraph5_aMC@NLO v2.2.2 generator at LO with the NNPDF2.3lo set is used to model the production of $t\bar{t}Z$ and $t\bar{t}W$ events and has been replaced by the aMC@NLO v2.3.3 [112] generator at NLO with the NNPDF3.0nlo PDF [105] set for results based on the full Run 2 dataset. In the case of $t\bar{t}Z$, interference effects with γ^* and Z-boson and offshell gauge boson contributions for masses down to 1 GeV are included.

For the NLO samples, renormalization and factorization uncertainties are evaluated from their respective variation by factors of 2 and 0.5. PDF uncertainties are estimated by varying the 100 variations for the NNPDF3.0nlo set. MadGraph5_aMC@NLO v2.2.2 [112] generator at LO using the NNPDF2.3lo [105] PDF set is used to generate $t\bar{t}WW$, $t\bar{t}WZ$, three and four top production. Only on-shell boson contributions are considered. The production of tWZ and $t\bar{t}H$ events is modelled using the MadGraph5_aMC@NLO v2.3.3 [112] generator at NLO with the NNPDF3.0nlo [105] PDF set. Top quarks and Z bosons are decayed at LO using MadSpin [126, 306] to preserve spin correlations. Top quarks are decayed inclusively while Z bosons are set to decay to a pair of charged leptons. The five-flavour scheme is used where all the quark masses are set to zero, except the top quark. For each process described above, the events are interfaced to Pythia 8 [123] for showering and fragmentation of the quarks using the A14 tune [245] and the NNPDF2.3lo [105] PDF set. The decays of bottom and charm hadrons are simulated using the EvtGen v1.2.0 program [125].

For the full Run 2 result, the production of $t\bar{t}H$ events is modelled using the PowhegBox v2 generator [113, 118, 119, 307, 308] which provides matrix elements at next-to-leading order (NLO) in the strong coupling constant α_S in the five flavour scheme with the NNPDF3.0nlo [105] PDF set. The functional form of the renormalization and factorization scale is set to $\sqrt[3]{m_T(t) \cdot m_T(\bar{t}) \cdot m_T(H)}$. The events are interfaced to Pythia 8.230 [123] using the A14 tune [245] and the NNPDF2.3lo [105] PDF set. The decays of bottom and charm hadrons are performed by EvtGen v1.6.0 [125].

Higgs boson production via vector-boson fusion is generated with Powheg [113, 118, 119, 309] at NLO accuracy and interfaced with Pythia 8.186 [123] for parton showering and non-perturbative effects. The prediction is tuned to match calculations with effects due to finite heavy-quark masses and soft-gluon resummations up to NNLL. The PDF4LHC15 PDF set [101] and the AZNLO tune [237] of Pythia [123] are used. The Monte Carlo prediction is normalized to an approximate-NNLO QCD cross section with NLO electroweak corrections [310–312]. The normalization of all Higgs boson samples also accounts the decay branching ratio calculated with HDECAY [313–315] and PROPHECY4F [316–318].

$t\bar{t}$ events are generated with the Powheg-Box v2 [113, 118, 119, 307] generator at NLO using the NNPDF3.0nlo [105] PDF set and the h_{damp} parameter[2] set to 1.5 m_{top} [319]. For results based on 36.1 fb^{-1}of data, the events are interfaced to Pythia 6.428 [124] to perform the parton showering using the Perugia 2012 [129] set of tuned shower and underlying parameters. The CT10 PDF set is used for the matrix element calculations. The simulation is normalized to NNLO in perturbation theory [301, 302] including the resummation of soft gluon emission at NNLL accuracy [320] using Top++2.0[321]. For the full Run 2 result, the events are interfaced to Pythia 8.230 [123] to model the

[2] The h_{damp} parameter is a resummation damping factor and one of the parameters that controls the matching of Powheg matrix elements to the parton showering and thus effectively regulates the high-p_T radiation against which the $t\bar{t}$ system recoils.

Table 6.3: Decay modes and branching ratios for the $\tilde{\chi}_1^0$ LSP in the RPV models, where ν denotes neutrinos or antineutrinos of any lepton generation

Scenario	$\tilde{\chi}_1^0$ branching ratios		
λ_{12k}	$e^{\pm}e^{\mp}\nu$ (1/4)	$e^{\pm}\mu^{\mp}\nu$ (1/2)	$\mu^{\pm}\mu^{\mp}\nu$ (1/4)
λ_{i33}	$e^{\pm}\tau^{\mp}\nu$ (1/4)	$\tau^{\pm}\tau^{\mp}\nu$ (1/2)	$\mu^{\pm}\tau^{\mp}\nu$ (1/4)

parton showering, hadronization, and the underlying event, with parameter set according to the A14 tune [245] and using the `NNPDF2.3lo` set of PDFs [104]. The decays of bottom and charm hadrons are performed by EvtGen v1.6.0 [125].

In the result using 36.1 fb^{-1}of data, V+jets production is simulated using LO-accurate matrix elements (ME) with up to four final-state partons with MadGraph5_aMC@NLO 2.2.2 [112]. The ME calculation employs the `NNPDF3.0nlo` set of PDFs [105] (H_T-sliced) or the `NNPDF2.3lo` set of PDFs [104] (N_p-sliced). Events are interfaced to Pythia 8.186 [322] for the modelling of the parton showering, hadronization, and underlying event. The overlap between matrix element and parton showering emissions is removed using the CKKW-L merging procedure [323, 324]. The A14 tune [245] of Pythia is used with the `NNPDF2.3lo` PDF set [104]. The decays of bottom and charm hadrons are performed by EvtGen v1.2.0 [125]. The V+jets samples are normalized to NNLO prediction [325]. For the full Run 2 result, the same V+jets samples are utilized as in the $Z \to \mu\mu$ reconstruction efficiency measurement described in section 5.2.

If not stated otherwise in Table 6.2, the background samples are passed through the full ATLAS detector simulation as described in Section 3.6.

Signal simulation: For each signal model described 6.1, points with different sets of parameters are generated using MadGraph5_aMC@NLO v2.2.2 [112] for the ME calculation with up to two additional partons at LO accuracy using the `NNPDF2.3lo` PDF set [104]. The events are interfaced to Pythia 8.186 [322] for the modelling of the parton showering, hadronization, the decay of the produced SUSY particles and the underlying event using the A14 tune [245] parameter set. The decay of the bottom and charm hadrons is performed by the EvtGen v.1.2.0 program. The samples are normalized to NLO+NLL accuracy [261–263, 271, 272, 277, 298, 299]. The events are then passed through the AF-II detector simulation as described in section 3.6.

For the RPV models, two different sets of samples are generated with an active λ_{12k} and with active λ_{i33} coupling, respectively. The $\tilde{\chi}_1^0$ are decayed into $ee\nu/e\mu\nu/\mu\mu\nu$ and $e\tau\nu/\mu\tau\nu/\tau\tau\nu$, respectively, with equal branching ratio in order to minimize the statistical uncertainty of the sample. In the later analysis, the events are reweighted to match the physical branching ratios of 50% per decay mode for

each active coupling as listed in Table 6.3. Samples are generated with $\tilde{\chi}_1^0$ masses ranging between 10 GeV and $m_{\text{NLSP}} - 10$ GeV. Three different NLSP production modes are considered:

- **Gluino NLSP**: Pair produced gluinos decay into the $\tilde{\chi}_1^0$ under the emission of a quark-antiquark pair (cf. Figure 6.3(a)) which can be of any type except the top-quark. In scenarios with an active λ_{i33} coupling, gluino masses between 1 and 2 TeV are considered and in the case of non-vanishing λ_{12k} couplings the gluino masses range between 1.4 and 2.6 TeV for the 36.1 fb^{-1} publication. In the full Run 2 the mass ranges are 1.6–2.5 TeV and 2.2–2.8 TeV, respectively.
- **Wino NLSP**: Mass-degenerate wino like charginos or neutralinos are produced in $\tilde{\chi}_1^+\tilde{\chi}_1^-$ or $\tilde{\chi}_2^0\tilde{\chi}_1^\pm$ pairs (cf. Figure 6.6(a)). Both decay into the $\tilde{\chi}_1^0$ and their SM counterpart which is the W boson in the case of a $\tilde{\chi}_1^\pm$ and a Higgs or a Z boson for $\tilde{\chi}_2^0$. For signal grids that contain $\tilde{\chi}_2^0 \to H\tilde{\chi}_1^0$ decays, the upper limit on the $\tilde{\chi}_1^0$ mass is set to $m_{\text{NLSP}} - 130$ GeV to ensure on-shell Higgs production. To study possible acceptance differences two sets of samples are generated where the $\tilde{\chi}_2^0$ exclusively decays into one boson. Given that the 36.1 fb^{-1}result of the four-lepton search shows small differences between the two scenarios (cf. section 7.5.1), a single sample set is generated for the full Run 2 result, where the $\tilde{\chi}_2^0$ decays with equal branching ratio into each of the two bosons. Winos with masses between 600 GeV (1 TeV) and 1.1 (1.7) TeV are investigated for an active λ_{i33} (λ_{12k}) coupling in the 36.1 fb^{-1}iteration. In the full Run 2 iteration, the considered mass windows are 0.8–1.4 TeV and 1.3–1.9 TeV, respectively.
- **Slepton NLSP**: Left-handed charged sleptons ($\tilde{\ell}_{\text{L}}^\pm$) and sneutrinos ($\tilde{\nu}$) are considered to have equal mass and to be mass generated amongst the three generations. They are produced in $\tilde{\ell}_{\text{L}}^+\tilde{\ell}_{\text{L}}^-$, $\tilde{\nu}\tilde{\ell}_{\text{L}}^\pm$ or $\tilde{\nu}\tilde{\nu}$ pairs (cf. Figure 6.6(b)), where the sleptons decay into their SM counterpart and the $\tilde{\chi}_1^0$. Sleptons with masses between 400 GeV and 900 GeV (1.3 TeV) are considered in cases of an active λ_{i33} (λ_{12k}) coupling in the 36.1 fb^{-1}iteration. For the full Run 2 iteration, signal points with slepton masses of up to 1.1 TeV and 1.3 TeV are generated, respectively.

For the GGM model considered (cf. Figure 6.7), the free parameters are the branching ratio of the $\tilde{\chi}_1^0$ to decay into a Z or a Higgs boson and the mass of the higgsino triplet. Signal model points with masses ranging between 120 and 600 GeV have been generated for both iterations. In each case, an equal decay branching ratio of $\tilde{\chi}_1^0 \to Z\tilde{G}$ and $\tilde{\chi}_1^0 \to H\tilde{G}$ is considered and the simulated events are reweighted in the analysis to match the respective decay branching ratios.

Direct stau pair production is simulated considering mass degenerated left- and right-handed stau pairs. The decay of the stau lepton is performed using MadGraph5_aMC@NLO to preserve the spin information and polarization of the τ lepton decay. The mass of the stau lepton is varied between 80 and 440 GeV. For each stau mass, $\tilde{\chi}_1^0$ masses ranging between 1–200 GeV are considered where decay of the stau into the $\tilde{\chi}_1^0$ has always to be kinematically allowed in the chosen parameter pairs.

CHAPTER SEVEN

SEARCH FOR SUPERSYMMETRY IN FOUR-LEPTON EVENTS

Four-lepton events provide a clean signature and are rare in the Standard Model and hence are an excellent channel for the search for Supersymmetry as explained in chapter 6.1. The analysis presented here is inspired by the previous search performed with the LHC Run 1 data [282]. pp collision events with four or more leptons, of which up to two can be τ leptons, have been studied in this thesis. Results of the Run 2 search have been published in three iterations in the course of this thesis. Besides the increasing data statistics, the analysis procedures have been improved in each step with respect to the background estimation and additional signal models have been studied. The first publication [326] is based on the initial 13.1 fb^{-1}of $\sqrt{s}$ = 13 TeV data and considered only one RPV benchmark model with non-zero λ_{12k} coupling, i.e. without τ leptons in the final state. These results are superseded by Ref. [327] which is based on the 2015–2016 dataset and also τ leptons have been considered and the results were interpreted in additional simplified RPV models. Also a final state sensitive to the RPC GGM model described in chapter 6.1 was added. The final result is based on the full Run 2 data, and makes use of further improvements in the background estimation techniques [328]. In each iteration, the development of the RPV signal models, the optimization of the signal selection, the background estimate and its uncertainties have been achieved in the context of this thesis. The discussion here concentrates on the last two iterations which also include τ channels.

The chapter is structured as follows. In section 7.1, the SM background contributions are described. The object selection criteria are explained in section 7.2 and the optimization of the signal selection is presented in section 7.3. The background estimation strategy is described in section 7.4, highlighting the improvements between the iterations. The results and their interpretations in the context of different simplified models are discussed in section 7.5.

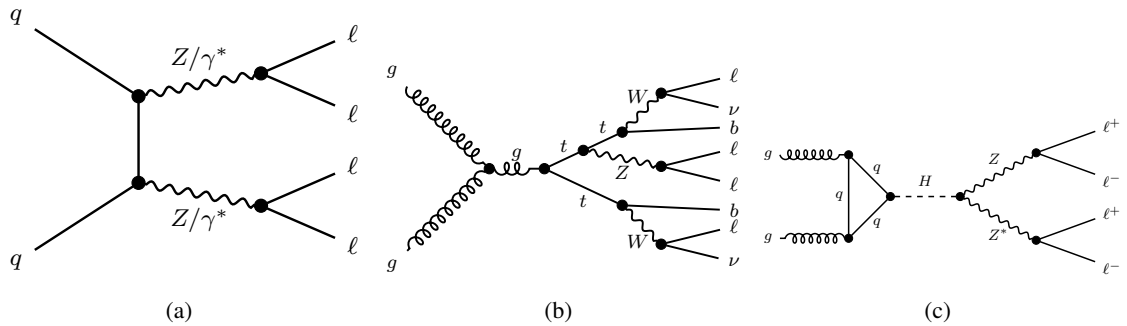

(a) (b) (c)

Figure 7.1: Diagrams of ZZ (a), $t\bar{t} + Z$ (b) and $H \rightarrow ZZ^*$ production (c), some of the main contributions to irreducible backgrounds in four-lepton searches.

7.1 Backgrounds in Four-Lepton Events

In the case of the RPV and GGM models presented in chapter 6.1, the common characteristic of the final states are at least four charged leptons. Hence, at the first stage of the analysis all events with four or more leptons passing the signal selection criteria described in section 7.2 are considered. In the RPV models, the flavor of the decay leptons is determined by the λ_{ijk} coupling considered. There are only light leptons for the λ_{12k} models and two to four τ leptons for the $\lambda_{i33} \neq 0$ scenarios. τ leptons can decay either leptonically or hadronically. As discussed in section 3.7, the first channel is reconstructed as a prompt light lepton and the other one is identified from the hadronic decay products of the τ lepton, denoted by τ_{had}, using multivariate analysis techniques.

The Standard Model background processes that give rise to four or more reconstructed leptons in the final state can be split into two categories: irreducible and reducible background. In the irreducible case, all leptons are prompt and originate from the decay of the primary produced particles in the collision. Examples of the most important processes of this type are shown in Figure 7.1. The most relevant processes are ZZ, $t\bar{t}V$ ($V = Z, WW, H$), triboson VVV ($V = W, Z$), four top, single top production in association with a Z boson (tWZ), as well as $H \rightarrow ZZ^*$ production via gluon fusion, vector boson fusion or in association with an electroweak gauge boson.

In reducible background processes, at least one of the four leptons originates from a hadron decay or has been misidentified. The latter lepton candidates are called fake leptons. The main reducible background sources are WZ and $t\bar{t}$+W events in which typically only one lepton is fake, and $t\bar{t}$ and Z + jets events with two fake leptons. Three or more fake leptons in an event, for instance in W + jets production, have been found to be sufficiently rare due to the high fake rejection of the lepton identification and are hence not considered in the following. Figure 7.2 shows examples of the three main reducible background processes. Irreducible processes generally dominate in events with at

least four light leptons where the prompt lepton selection efficiency and the fake lepton rejection are high whereas the reducible processes are dominant for events containing τ leptons because τ lepton identification is difficult at the LHC with significantly lower prompt lepton identification efficiency and much higher fake rates.

7.2 Object and Event Selection

In this section, the object and event selection criteria for the four-lepton search are presented. These criteria have been applied equally for all Run 2 results if not stated otherwise. The object selection is performed in three stages with increasing requirements. In the first stage, the particle preselection, minimal quality criteria are applied to the particles within the full acceptance of the ATLAS detector. Ambiguities arising from the fact that the same energy deposits in the calorimeter or the same ID tracks may be picked up in the reconstruction of different particles, are iteratively resolved in the second stage by a procedure, called overlap removal. Particles passing this step are referred to as baseline particles. In the final stage, the actual signal selection, the particles have to pass additional quality and tighter kinematic requirements and are labelled as signal objects. Leptons failing this selection are referred to as *loose* leptons.

Preselected electrons are required to pass the LooseAndBLayerLH criteria (cf. section 3.7.3) with $p_{\mathrm{T}} > 7$ GeV and $|\eta| < 2.47$. For the full Run 2 analysis, the p_{T} requirement has been softened to $p_{\mathrm{T}} > 4.5$ GeV. Preselected muons need to fulfill the Medium identification criteria as well as $p_{\mathrm{T}} > 5$ GeV and $|\eta| < 2.7$. For the full Run 2 analysis, the longitudinal impact parameter $|z_0 \sin(\theta)|$ of the preselected light leptons was in addition required to be less than 0.5 mm to suppress leptons from secondary vertices and to facilitate future combinations with other measurements by avoiding overlapping signal regions.

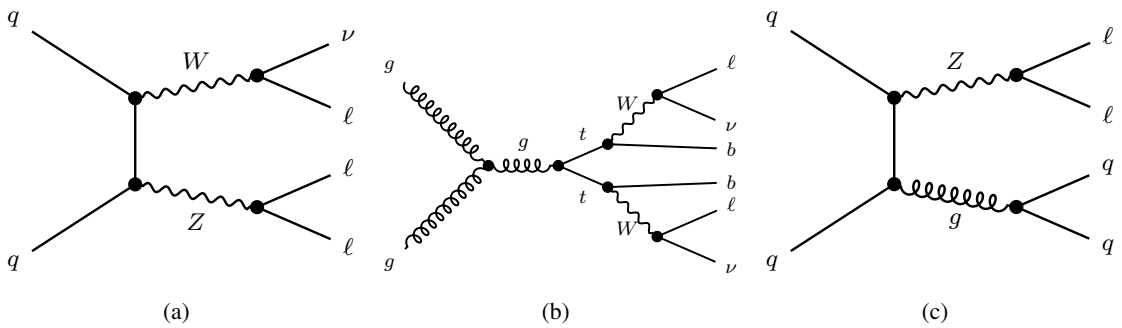

Figure 7.2: Diagrams of WZ (a), $t\bar{t}$ (b) and Z + jets (c) production which are the main reducible backgrounds in the four-lepton analysis.

Jets are reconstructed by the anti-k_t algorithm with radius parameter $\Delta R = 0.4$ (cf. section 3.7.5) and are preselected with $p_{\mathrm{T}} > 20$ GeV. Hadronic τ leptons with 1 or 3 associated ID tracks are required to have a visible transverse momentum of $p_{\mathrm{T}} > 20$ GeV and be within $|\eta| < 2.47$, excluding the calorimeter endcap gap regions $|\eta| \in [1.37; 1.52]$. For initial fake jet rejection, a loose cut on the τ identification classifier (cf. section 3.7.6), from a BDT algorithm for the 36 fb^{-1}result and from a RNN for the full Run 2 analysis, is applied.

The preselected objects are then passed through the iterative overlap removal which resolves ambiguities in the objects reconstruction according to the following scheme:

1. Preselected τ leptons overlapping with electrons or muons within $\Delta R < 0.2$ are removed.
2. Electrons sharing an ID track with muons are discarded in case the muon is not a CT muon. Otherwise the muon is removed.
3. Jets overlapping with electrons within $\Delta R < 0.2$ are removed.
4. To suppress electrons from heavy meson decays, electrons separated by less than $\Delta R < 0.4$ to a jet are discarded.
5. Jets overlapping with muons by $\Delta R < 0.2$ are discarded if the jet has less than three associated tracks with $p_{\mathrm{T}} > 500$ MeV.
6. Any surviving muon within $\Delta R < 0.4$ to a jet is removed.
7. Jets overlapping with preselected τ leptons passing the Medium identification working point within $\Delta R < 0.4$ are rejected.

The overlap removal procedure is completed by discarding any opposite-sign (OS) light lepton pairs with invariant mass less than 4 GeV and any same-flavor-opposite-sign (SFOS) pair with an invariant mass within $m_{\mathrm{SFOS}} \in [8.4; 10.4]$ GeV to remove lepton pairs from J/ψ and Υ decays, respectively.

Signal electrons need to satisfy the MediumLH identification criteria (cf. section 3.7.3). Light leptons which are not associated to the primary vertex are discarded if their longitudinal impact parameter is $|z_0 \sin(\theta)| > 0.5$ mm or the transverse impact parameter significance, $|d_0| / \sigma(d_0)$, exceeds three (five) in the case of electrons (muons). Leptons passing these two signal selection criteria are called identified leptons for the remainder of this chapter. Electrons and muons from hadronic background are further rejected by applying the *GradientLoose* isolation criteria [193, 211] which are replaced by the *FCLoose* criteria in the full Run 2 result. The isolation variables of the leptons are corrected for the contributions from other nearby identified leptons improving the sensitivity to boosted RPV decay topologies (cf. section 7.3). The pseudorapidity range of signal jets is narrowed down to $|\eta| < 2.8$. To reduce contamination from pile-up, jets with $p_{\mathrm{T}} < 60$, $|\eta| < 2.4$ and having a substantial fraction of

associated tracks from secondary vertices are discarded as signal. Signal τ leptons need to satisfy the Medium identification working point.

Candidate event selection: Candidate events are required to have at least one collision vertex with $\sum_{\text{tracks}} p_{\text{T}} > 400$ MeV and, in the case of real collision data, being recorded under stable beam and detector conditions [149]. Furthermore, preselected muons with $|d_0| > 0.2$ mm or $|z_0| > 1$ mm are likely from cosmic rays and hence the events are discarded. In order not to spoil the $E_{\text{T}}^{\text{miss}}$ resolution, events must not contain any badly measured jet [329] or any muon with a relative q-over-p significance of the CB track, $(q/p)/\sigma_{q/p} > 0.2$ or with an q-over-p significance ratio of the ID/ME track to the CB track of less than 0.8.

Events considered in the analysis must contain at least four baseline leptons. To distinguish between the different signal scenarios and given that the background composition looks different between τ-rich and τ depleted final states, the four-lepton events are classified according to their τ lepton multiplicity using the nomenclature $\mathcal{X}\text{L}\mathcal{Y}\text{T}$ where $\mathcal{X} \in \{2, 3, 4\}$ and $\mathcal{Y} \in \{0, 1, 2\}$ represent the numbers of light leptons and τ leptons in the final state, respectively as illustrated in Table 7.2. The 4L0T category also collects events with five or more light leptons. In the full Run 2 analysis, cases in which the additional leptons are τ leptons are also included in this category in order to be fully inclusive with respect to the lepton multiplicity. Due to the large expected SM background, and relatively low τ lepton identification efficiency, due to stringent p_{T} thresholds of the τ triggers [330], the 1L3T and 0L4T categories are not used. In each category, at least two of the light leptons must pass the signal selection criteria. The light leptons must also have triggered the event via single or di-lepton triggers (cf. Table 7.1). The di-lepton triggers serve as support if no single-lepton trigger fired or the p_{T} requirement of the single lepton trigger was not fulfilled. An extra 1 GeV (5%) is added to the online p_{T} requirement of the electron (muon) trigger to mitigate trigger turn-on effects. The applied scheme results in trigger selection efficiencies of 95–99% for the SUSY signal models considered. For the full Run 2 analysis, four-lepton events have been rejected if two light leptons are collimated with $\Delta R < 0.6$, where at least one lepton has $p_{\text{T}} < 30$ GeV. In this way, the fake background where two leptons originate from the semileptonic cascade decays of c- or b- quarks is strongly suppressed while retaining good efficiency for the RPV signal models at low $\tilde{\chi}_1^0$ masses.

The SUSY signal events studied are expected to contain at least four isolated signal leptons. Such events are used to design the signal and validation regions. For the first Run 2 analysis, the τ p_{T} threshold was raised to 30 GeV to mitigate the observed mismodelling in the validation regions (cf. section 7.4). The improved τ identification using a RNN-based discriminant allowed to resurrect the p_{T} cut of 20 GeV in the full Run 2 analysis. In contrast, events with one or two loose leptons are depleted in signal, while they are enriched in the reducible background. Such events are used to

Table 7.1: Triggers used to select the events for the four-lepton analysis. The offline p_{T} thresholds are required only for reconstructed charged leptons which match to the trigger signatures by $\Delta R < 0.05$. Trigger thresholds for data recorded in the years 2016–2018 are higher than in 2015 due to the increase in beam luminosity, and "or" denotes a move to a higher-threshold trigger during data-taking.

Trigger signature	Offline p_{T} threshold [GeV]		
	2015	2016	2017–2018
Single isolated e	25	27	27
Single non-isolated e	61	61	61
Single isolated μ	21	25 or 27	27
Single non-isolated μ	42	42 or 53	53
Double e	13, 13	18, 18	18, 18
Double μ (symmetric)	–	11, 11 or 15, 15	15, 15
(asymmetric)	19, 9	21, 9 or 23, 9	23, 9
Combined $e\mu$		8(e), 25(μ) or 18(e), 15(μ)	

define the loose lepton control regions (CR) and are utilized in the data-driven background estimate described in section 7.4.

Table 7.2: Categorization of the four-lepton events

label	N_ℓ	N_τ	
4L0T	≥ 4	$= 0$	36.1 fb^{-1} iteration
		≥ 0	Run 2 iteration
3L1T	$= 3$	≥ 1	
2L2T	$= 2$	≥ 2	

7.3 Signal Selection

In the following, the optimization of the selection criteria to the RPV and RPC signal models is described. The section starts with the description of the removal of the contamination of the isolation variables caused by two collimated leptons. Afterwards the optimization of the event selection criteria is presented, individually for the 36.1 fb^{-1} iteration and then for the full Run 2 result.

Isolation improvements: In the RPV signal model, the decaying $\tilde{\chi}_1^0$ become more boosted as the gap in mass between the NLSP decaying into the $\tilde{\chi}_1^0$ and the $\tilde{\chi}_1^0$ increases. This results in highly collimated decay leptons for the very low-mass $\tilde{\chi}_1^0$ scenarios (cf. Figure 7.3(a)). In scenarios with

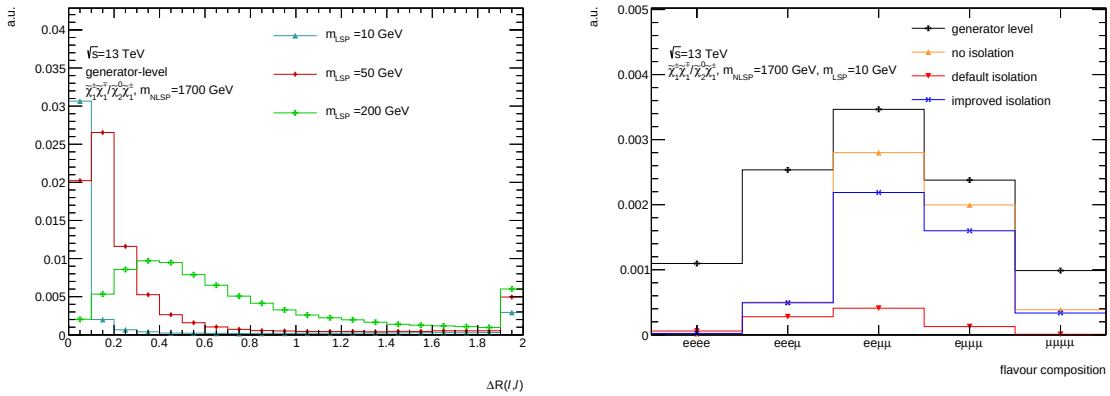

(a) (b)

Figure 7.3: Angular separation of the light leptons from a $\tilde{\chi}_1^0$ decay at generator level shown for three signal points of the Wino model with with non-zero λ_{12k} coupling and $m_{\tilde{W}} = 1.7$ TeV with different $\tilde{\chi}_1^0$ masses (a). For the signal point with $m_{\tilde{\chi}_1^0} = 10$ GeV, the flavor composition for events with four generator-level leptons (black), with four reconstructed identified leptons (orange), with four isolated signal leptons using the standard isolation variables (red) or the improved isolation variables (blue) is demonstrated in (b).

$m_{\tilde{\chi}_1^0} = 10$ GeV, the electron-muon and di-muon pairs can be successfully reconstructed such that the two leptons are identified leptons with efficiencies between 50–80% (cf. Figure 7.3(b)). If the $\tilde{\chi}_1^0$ decays into an electron pair, the electrons are highly collimated, with the result that their energy deposits in the calorimeter merge into a single cluster, causing reconstruction of the pair to fail. In any case, the identified leptons are eventually discarded by the object selection if the isolation requirement is applied, because the ID track and topo cluster associated to one lepton in the pair enter the isolation variable of the other lepton in the pair. This is exemplary illustrated for the muon track isolation in Figure 7.4(a) showing the angular separation of identified muons to the next identified light lepton against the isolation variable of the primary muon divided by the p_{T} of the close-by lepton. The accumulation at a contamination of $\simeq 1$ corresponds to the fact that the isolation variable of the muon is completely attributed to the close-by lepton. To efficiently mitigate the loss in the signal yield and hence to gain sensitivity to low-mass $\tilde{\chi}_1^0$ scenarios, the momenta of all ID tracks and topo clusters associated to the close-by lepton are removed from the isolation variable of the primary lepton if the close-by lepton is identified as well (cf. Figure 7.4(b)).

Using the improved isolation variables allows to select 75–85% of the events containing four identified leptons after imposing the isolation cut in signal scenarios with the lowest $\tilde{\chi}_1^0$ masses of 10 GeV (cf. Figure 7.5). Compared to the 10–15% signal selection efficiency this means an enhancement in the expected signal yields by a factor of five.

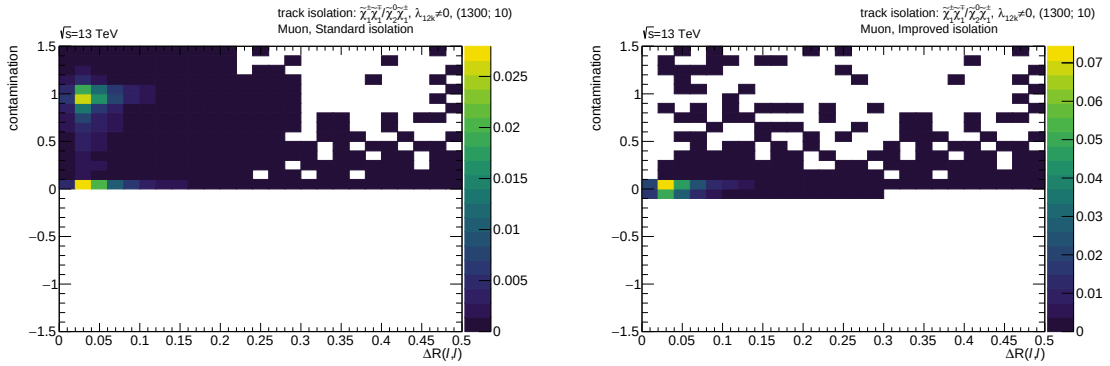

(a) (b)

Figure 7.4: Angular separation between an identified muon and the next identified light lepton against the isolation contamination, defined as the isolation variable of the primary muon divided by the p_{T} of the close-by lepton shown for the track isolation variable using the standard definition (a) and using the improved variable (b) for the wino model with $m_{\tilde{\chi}_1^{\pm}/\tilde{\chi}_2^0} = 1.3$ TeV, $m_{\tilde{\chi}_1^0} = 10$ GeV and $\lambda_{12k} \neq 0$.

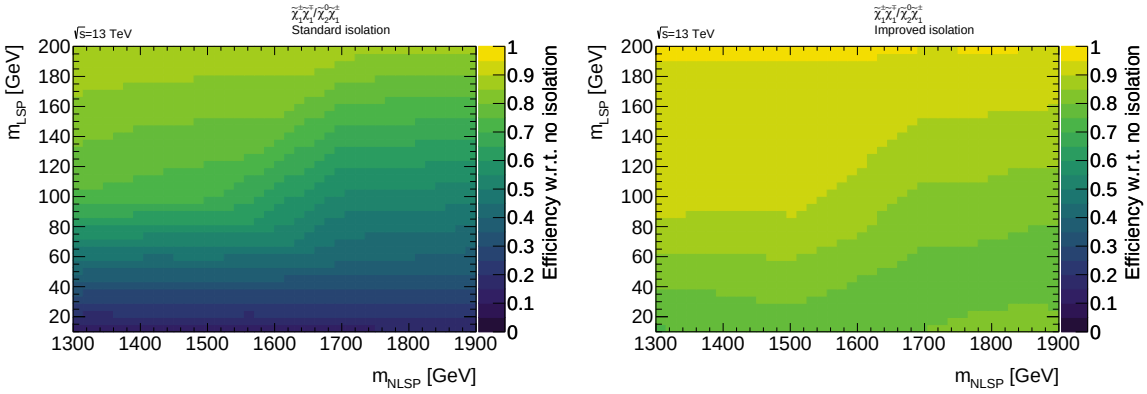

(a) (b)

Figure 7.5: Selection efficiency of events with four isolated light leptons with respect to four lepton events with identified leptons using the standard isolation variables (a) and the improved isolation variables (b) as a function of the NLSP and LSP mass shown for the wino model with $\lambda_{12k} \neq 0$.

Signal regions for 36.1 fb^{-1} of data: In each of the three categories introduced in section 7.2, additional selection criteria on the objects and events have to be found to increase the discrimination between the background and the signal models. First, basic features of the decay topology in the signal events are exploited. For instance in the RPV models, the signal leptons usually do not originate from Z boson decays, while in the majority of irreducible SM backgrounds at least one leptonic Z decay is involved. Hence, a Z-veto is applied to reject any four-lepton event where the invariant mass of a SFOS lepton pair, of a SFOS pair in combination with a third charged light lepton or of two SFOS pairs is within 10 GeV of the Z boson rest mass of $m_Z = 91.2$ GeV:

$$\begin{aligned} |m_{\text{SFOS}} - m_Z| &\geq 10\text{GeV} \\ |m_{\text{SFOS}+\ell^\pm} - m_Z| &\geq 10\text{GeV}. \\ |m_{\text{SFOS}+\text{SFOS}} - m_Z| &\geq 10\text{GeV} \end{aligned} \tag{7.1}$$

The three lepton component accounts for radiative $Z \to \ell\ell\gamma$ decays where the photon is misidentified as a lepton and the four lepton component for rare $Z \to \ell^\pm\ell^\mp\ell'^\pm\ell'^\mp$ decay modes. In the GGM model, the leptons result from Z boson or $H \to ZZ^*$ decays and thus a Z-veto would reject the signal events as well. Thus, a complementary ZZ selection is defined. Unlike the Z-veto, it accepts events containing two SFOS pairs, where the first pair has an invariant mass of 10 GeV around the Z boson mass. The window for the second pair has a lowered edge of 61.2 GeV to increase the acceptance for signal events in which a $\tilde{\chi}_1^0$ decays into a Higgs boson which then further decays via $H \to ZZ^* \to \ell^\pm\ell^\mp\bar{x}x$ ($x = \ell, q, \nu$) into a second lepton pair. The four leptons are combined into two distinct SFOS pairs, and a possible degeneracy in the assignment is resolved by minimizing the expression

$$\min_{\ell,\ell' \in \{\text{possible SFOS}\}} \{|m_{\ell^\pm\ell^\mp} - m_Z| + |m_{\ell'^\pm\ell'^\mp} - m_Z|\}\,. \tag{7.2}$$

The first pair is defined as the one which invariant mass is closer to m_Z.

To further enrich the selection in signal events, kinematic variables are defined whose distributions are different for signal and background and requirements on their thresholds are optimized as described in section 6.2. For the optimization to the RPV models, the effective mass

$$m_{\text{eff}} = E_{\text{T}}^{\text{miss}} + \sum_{i=e,\mu,\tau} p_{\text{T}}(i) + \sum_{\substack{\text{jets} \\ p_{\text{T}}>40\text{ GeV}}} p_{\text{T}}, \tag{7.3}$$

which is the scalar sum of the transverse momenta of the selected particles[1] and $E_{\text{T}}^{\text{miss}}$ is found to provide the best discrimination power regardless of the mass difference between NLSP and LSP and of the particle species. The variable is sensitive to the overall momentum transfer in the the event which

[1] Only jets with $p_{\text{T}} > 40$ GeV are considered to further reject contamination from pile-up jets

is significantly higher if particles with high masses are produced in the collision. The optimization on the minimal m_{eff} threshold is performed individually for the 4L0T, 3L1T, 2L2T category. For the optimization of the kinematic selection to the GGM model, only the 4L0T with applied ZZ selection is considered. Although the Z bosons from the $\tilde{\chi}_1^0$ decay also decay to τ leptons, the 3L1T and 2L2T categories are found to be insensitive due to the large contamination by Z + jets and ZZ events. As the ZZ selection does not discriminate against ZZ background which has the largest cross section among the SM backgrounds and given that the gravitinos carry a significant amount of the collision energy undetected out of the system, the missing transverse energy is found to provide a better discrimination power than the effective mass in the GGM scenario.

Models with active λ_{12k}-LLE terms usually do not result in final states with τ leptons and hence the 4L0T category is the most sensitive to them. In contrast, for cases of active λ_{i33} couplings, τ leptons are expected in the final state and thus the 3L1T and 2L2T categories are the most sensitive to these scenarios. The distributions of the expected number of events passing a minimum cut on the effective mass in each of the categories for the background and example signal points is illustrated in Figures 7.6(a), 7.6(b), and 7.6(c) together with the resulting significance of each signal point considered. In all three categories, the effective mass drops off faster for the SM background than for the SUSY signal. The optimal cut value is chosen for each category as a compromise between gaining the maximum significance across the considered model parameter space and to leave enough statistics for a reliable background estimation. The requirement to have at least one event has been found to provide enough MC statistics for the irreducible backgrounds and to leave enough room for a data-driven estimate from the loose lepton control regions (cf. section 7.4). An effective mass cut of 1100 GeV, 700 GeV and of 650 GeV for 4L0T, 3L1T and 2L2T events with applied Z-veto, respectively is found to simultaneously satisfy these three conditions. The constructed signal regions are called SR0B, SR1 and SR2 respectively. The numbers in the labels indicate the τ lepton multiplicity analogously to the general event categorization introduced at the beginning of this chapter. In Ref. [326], it has been shown that a larger sensitivity to RPV models with low-mass NLSP is achieved for moderate m_{eff} cuts. Hence an additional SR is defined for the 4L0T plus Z-veto category requiring $m_{\text{eff}} > 600$ GeV to target any physics scenario decaying into four light leptons where the produced particles are only moderately heavy and the coupling to the new particle is small.

The cumulative background and signal $E_{\text{T}}^{\text{miss}}$ distributions in 4L0T events with applied ZZ selection are given in Figure 7.6(d) together with the obtained significances for four reference points. For low higgsino masses, the significance peaks at values around 50 GeV while for larger higgsino masses cuts around 100 GeV are optimal. Therefore, two signal regions, called SR0C and SR0D, are defined requiring a lower $E_{\text{T}}^{\text{miss}}$ cut of 50 GeV and 100 GeV in 4L0T events with applied ZZ selection, respectively.

Table 7.3 summarizes the signal region definitions for the 36.1 fb^{-1} search. Figures 7.7, 7.8, and 7.9

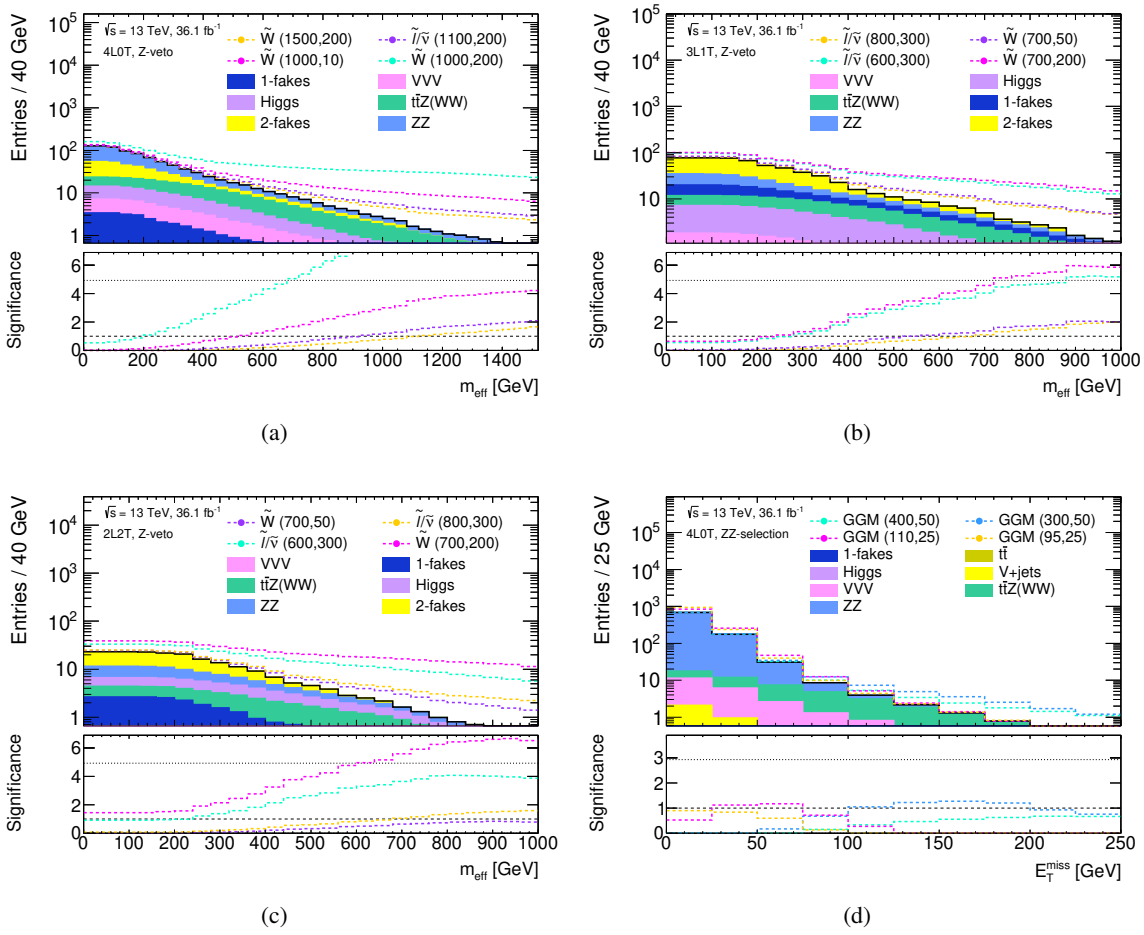

Figure 7.6: m_{eff} distribution in 4L0T (a), 3L1T (b), and 2L2T (c) events, respectively, with an applied Z-veto and $E_{\text{T}}^{\text{miss}}$ distribution in 4L0T events with an applied ZZ selection shown as a function of the expected number of events passing a lower threshold normalized to 36.1 fb^{-1}. In Figure (a), active λ_{12k} and in Figures (b) and (c) active λ_{i33} terms are assumed for the signal points shown. The numbers in brackets indicate the NLSP and LSP mass of each point. In Figure (d), GGM model points are shown and the numbers in brackets indicate the higgsino mass and $\mathcal{BR}\left(\tilde{\chi}_1^0 \rightarrow Z\tilde{G}\right)$, respectively. The bottom panel shows the significance to each signal point by applying the given threshold assuming a 30% overall uncertainty for the background. The predictions for all SM processes are taken from simulation.

depict the expected significance of the SR0B selection to the three λ_{12k}-RPV models, of the SR0D selection to the GGM model and of the SR1(SR2) selections to the three λ_{i33}-RPV models shown as a function of the free model parameters. The significances obtained by the SR0B selection show little dependence on the LSP mass with the exception of the low-mass region where the decay leptons become very collimated and hence the reconstruction efficiency drops as it has been discussed at the beginning of this section. Instead the expected significances depend on the considered NLSP and its

Table 7.3: Signal region definitions for the 36.1 fb^{-1} iteration of the four-lepton search. The $p_{\mathrm{T}}(\tau_{\mathrm{had}})$ column denotes the p_{T} threshold used for the τ lepton selection or veto. SR0B and SR0D are subsets of SR0A and SR0C, respectively, while SR1 and SR2 are completely disjoint [327].

Region	$N(e,\mu)$	$N(\tau_{\mathrm{had}})$	$p_{\mathrm{T}}(\tau_{\mathrm{had}})$	Z boson	Selection	Target
SR0A	≥ 4	$= 0$	> 20GeV	veto	$m_{\mathrm{eff}} > 600$GeV	General
SR0B	≥ 4	$= 0$	> 20GeV	veto	$m_{\mathrm{eff}} > 1100$GeV	RPV λ_{12k}
SR0C	≥ 4	$= 0$	> 20GeV	require 1$^{\mathrm{st}}$ & 2$^{\mathrm{nd}}$	$E_{\mathrm{T}}^{\mathrm{miss}} > 50$GeV	higgsino GGM
SR0D	≥ 4	$= 0$	> 20GeV	require 1$^{\mathrm{st}}$ & 2$^{\mathrm{nd}}$	$E_{\mathrm{T}}^{\mathrm{miss}} > 100$GeV	higgsino GGM
SR1	$= 3$	≥ 1	> 30GeV	veto	$m_{\mathrm{eff}} > 700$GeV	RPV λ_{i33}
SR2	$= 2$	≥ 2	> 30GeV	veto	$m_{\mathrm{eff}} > 650$GeV	RPV λ_{i33}

mass. A discovery sensitivity, i.e. $Z_n > 5$, to gluinos with up to 2 TeV, to winos with 1.1 TeV and to sleptons and sneutrinos with up to 800 GeV is achieved, if λ_{12k} couplings are exclusively active. The corresponding exclusion sensitivities are at around 2.3 TeV, 1.4 TeV and 1.1 TeV, respectively. For the GGM model, a discovery of higgsinos with masses between 120–270 GeV is possible if the $\tilde{\chi}_1^0$ decays in at least 80% of the cases into the Z boson, while higgsinos of up to 400 GeV show a 1.65σ significance if only Z decays are present. On the other hand, the branching ratio can be as low as 40% achieve the same significance for higgsinos with masses of around 200 GeV. The RPV models with active λ_{i33} couplings have lower expected significances than the λ_{12k}-RPV models and thus the potential to discover sleptons and sneutrinos is lowered to 500 GeV, 650 GeV for winos and in the case of gluinos to 1.3 TeV mass. The 1.65σ significance is achieved if the particles have masses of 750 GeV and 1.6 TeV, respectively. The lower τ identification efficiency and lower fake rejection provided by the τ identification algorithm (cf. section 3) are the main reasons for this difference. The significances depend stronger on the LSP mass as well, with the sensitivity notably breaking down at low masses as the τ leptons get collimated such that their hadronic decay products enter a single jet and cannot be separated from each other.

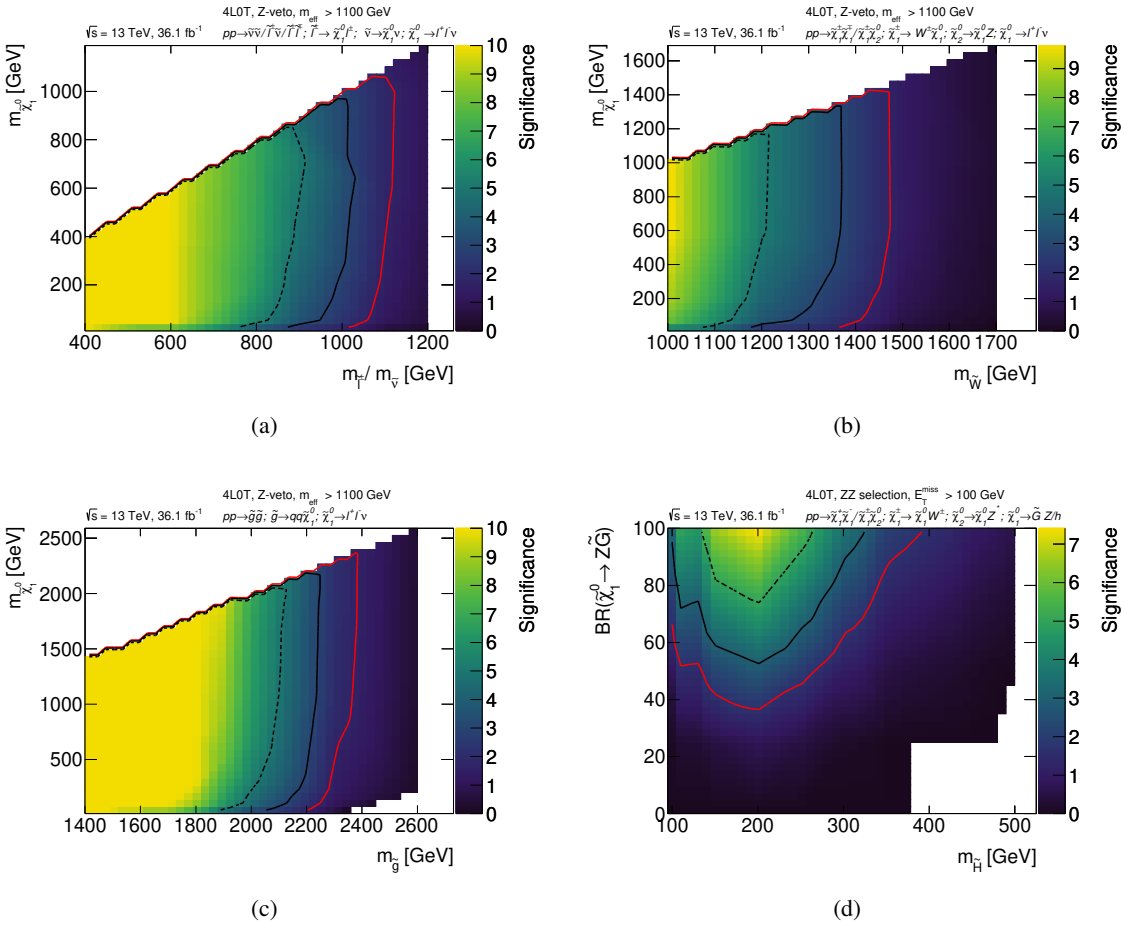

Figure 7.7: Expected significance for the λ_{12k} RPV models with slepton (a), wino (b), and gluino (c) NLSP in SR0B events and for the GGM model (d) in SR0D events for an integrated luminosity of 36.1 fb^{-1} shown as a function of the free model parameters. The event selection criteria are given in Table 7.3. The red, solid black and dashed black lines indicate the 1.68σ, 3σ and 5σ contours, respectively.

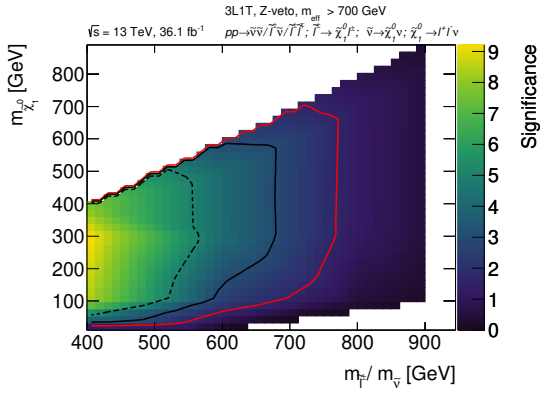

(a)

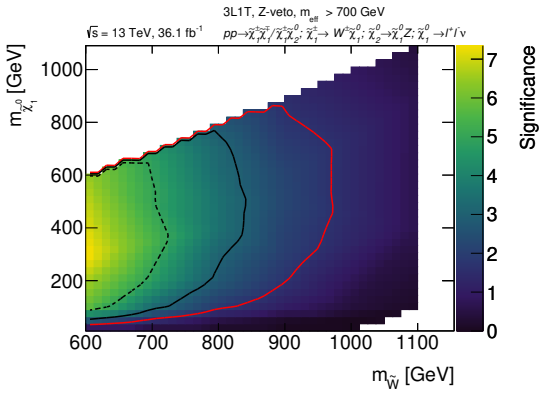

(b)

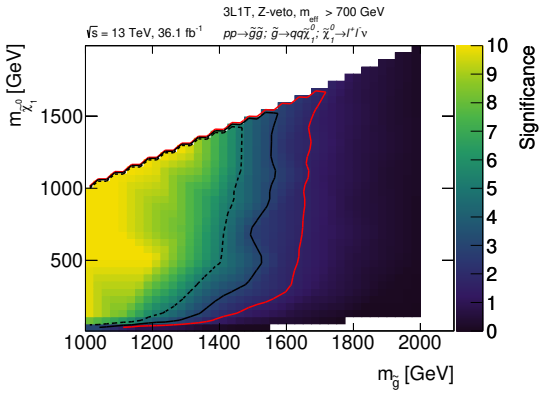

(c)

Figure 7.8: Expected significance for the λ_{i33} RPV models with slepton (a), wino (b), and gluino (c) NLSP in SR1 events for an integrated luminosity of 36.1 fb^{-1} shown as a function of the free model parameters. The event selection criteria are given in Table 7.3. The red, solid black and dashed black lines indicate the 1.68σ, 3σ and 5σ contours, respectively.

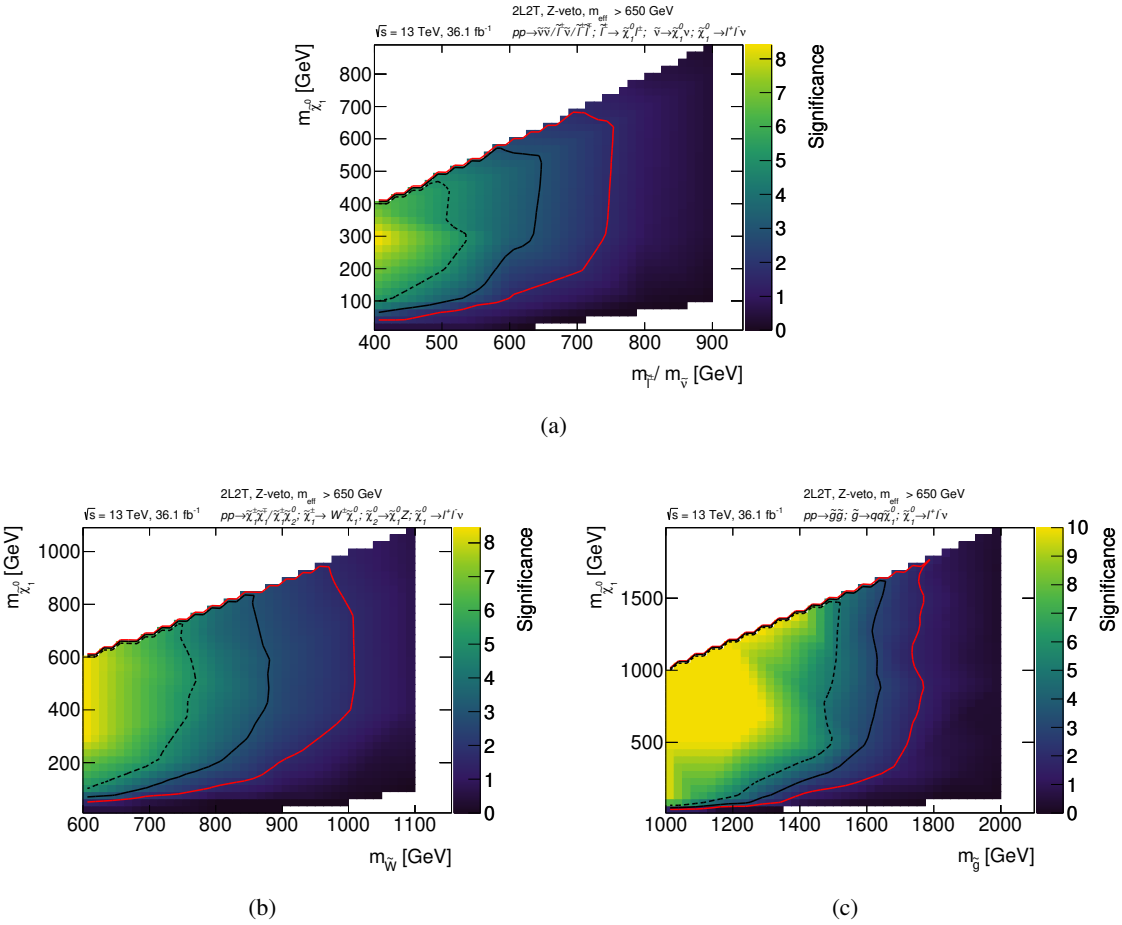

Figure 7.9: Expected significance for the λ_{i33} RPV models with slepton (a), wino (b), and gluino (c) NLSP in SR2 events for an integrated luminosity of 36.1 fb^{-1} shown as a function of the free model parameters. The event selection criteria are given in Table 7.3. The red, solid black and dashed black lines indicate the 1.68σ, 3σ and 5σ contours, respectively.

Revised signal regions for the full Run 2 dataset: The full Run 2 dataset has an increase in integrated luminosity of almost a factor of four. The background counts are expected to grow by the same amount. To gain sensitivity to the high-mass scenarios, the thresholds on the discriminating variables are reoptimized. Additionally, the events are split depending on the absence or presence of b-jets. In this way, the sensitivity can be tuned individually to scenarios where no or sometimes b-jets are expected from the decay of the heavy particles such like the gluinos or the Z boson in the wino model. This classification also facilitates the design of control and validation regions to estimate the ZZ and $t\bar{t}Z$ backgrounds in data (cf. section 7.4). To check how a small observed excess observed in the 36.1 fb^{-1} result (cf. section 7.5) evolves in a larger dataset, the SR0C and SR0D regions are reused in the full Run 2 iteration as well. In addition, two new regions are added to the analysis targeting the GGM scenario in order to improve the sensitivity to signal scenarios with high higgsino masses.

Table 7.4: Signal region definitions used in the full Run 2 iteration of the four-lepton search.

Region	$N(e,\mu)$	$N(\tau_{\text{had}})$	$N(b-\text{jets})$	Z boson	Selection	Target
$\texttt{SR0}^{\text{loose}}_{b-\text{veto}}$	≥ 4	≥ 0	$= 0$	veto	$m_{\text{eff}} > 600$ GeV	General
$\texttt{SR0}^{\text{tight}}_{b-\text{veto}}$	≥ 4	≥ 0	$= 0$	veto	$m_{\text{eff}} > 1250$ GeV	RPV λ_{12k}
$\texttt{SR0}_{b-\text{req}}$	≥ 4	≥ 0	≥ 1	veto	$m_{\text{eff}} > 1300$ GeV	RPV λ_{12k}
$\texttt{SR1}^{\text{loose}}_{b-\text{veto}}$	$= 3$	≥ 1	$= 0$	veto	$m_{\text{eff}} > 600$ GeV	General
$\texttt{SR1}^{\text{tight}}_{b-\text{veto}}$	$= 3$	≥ 1	$= 0$	veto	$m_{\text{eff}} > 1000$ GeV	RPV λ_{i33}
$\texttt{SR1}_{b-\text{req}}$	$= 3$	≥ 1	≥ 1	veto	$m_{\text{eff}} > 1300$ GeV	RPV λ_{i33}
$\texttt{SR2}^{\text{loose}}_{b-\text{veto}}$	$= 2$	≥ 2	$= 0$	veto	$m_{\text{eff}} > 600$ GeV	General
$\texttt{SR2}^{\text{tight}}_{b-\text{veto}}$	$= 2$	≥ 2	$= 0$	veto	$m_{\text{eff}} > 1000$ GeV	RPV λ_{i33}
$\texttt{SR2}_{b-\text{req}}$	$= 2$	≥ 2	≥ 1	veto	$m_{\text{eff}} > 1100$ GeV	RPV λ_{i33}
$\texttt{SR0-ZZ}^{\text{loose}}_{b-\text{veto}}$	≥ 4	≥ 0	$= 0$	require 1st & 2nd	$E_{\text{T}}^{\text{miss}} > 100$ GeV	higgsino GGM
$\texttt{SR0-ZZ}^{\text{tight}}_{b-\text{veto}}$	≥ 4	≥ 0	$= 0$	require 1st & 2nd	$E_{\text{T}}^{\text{miss}} > 200$ GeV	higgsino GGM
SR0C	≥ 4	≥ 0	≥ 0	require 1st & 2nd	$E_{\text{T}}^{\text{miss}} > 50$ GeV	higgsino GGM
SR0D	≥ 4	≥ 0	≥ 0	require 1st & 2nd	$E_{\text{T}}^{\text{miss}} > 100$ GeV	higgsino GGM

For the revision of the SRs sensitive to the GGM scenarios, it is exploited that no b-jets are expected from the signal. Hence, the basic 4L0T with ZZ requirement selection is additionally equipped with a b-veto suppressing the $t\bar{t}Z$ background in the tails of the $E_{\text{T}}^{\text{miss}}$ distribution (cf. Figure 7.10 (top)). Two individual requirements on $E_{\text{T}}^{\text{miss}}$ of 100 GeV and 200 GeV are found to provide a good balanced sensitivity across the GGM scenarios considered, defining the $\texttt{SR0-ZZ}^{\text{loose}}_{b-\text{veto}}$ and $\texttt{SR0-ZZ}^{\text{tight}}_{b-\text{veto}}$ selections, respectively (cf. Table 7.4).

In case of the RPV scenarios, the three Z-veto categories 4L0T, 3L1T and 2L2T, are split into SRs with and without a b-jet. Due to the additional suppression of $t\bar{t}V$ background by a b-veto, a larger sensitivity to the slepton model and to the compressed parameter space, i.e. $m_{\text{NLSP}} - m_{\tilde{\chi}_1^0} \leq 10$ GeV, is

achieved. However, b-jets may well occur in wino or gluino models where the mass splitting between the NLSP and the LSP leaves enough phase space to produce energetic b-quarks in up to 25% and up to 40% of the events, respectively. A b-veto therefore leads to a significant loss in sensitivity (cf. Figure 7.10 (middle) for the 4L0T case) to these models. This loss can be compensated by additionally optimizing the signal selection in four lepton events with b-jets. The chosen cut values on m_{eff} are reported in Table 7.4. The three signal regions $\texttt{SR0}^{\text{loose}}_{b-\text{veto}}$, $\texttt{SR1}^{\text{loose}}_{b-\text{veto}}$, and $\texttt{SR2}^{\text{loose}}_{b-\text{veto}}$ have moderate m_{eff} thresholds of 600 GeV each. As in the 36.1 fb^{-1} iteration, they are designed to pick up any new physics process decaying into four lepton without being too specific about the event topology.

To illustrate the boost in sensitivity achieved by the revised signal regions, Figures 7.11–7.14 depict the expected significances in the full Run 2 dataset from the SRs defined in the 36.1 fb^{-1} iteration against the significances obtained by the revised SRs to the GGM models, to the RPV models with λ_{12k} coupling and to the RPV models with λ_{i33} coupling, respectively. Using the optimized selection, it is possible to the 1.68σ significance to heavy higgsinos from 400 to 600 GeV if the $\tilde{\chi}^0_1$ purely decays to a Z boson (cf. Figure 7.11). Also the sensitivity towards lower decay branching ratios of the $\tilde{\chi}^0_1$ to the Z boson is improved from 40% to 30% for higgsinos with masses between 200 to 300 GeV. Moderate sensitivity improvements are achieved for the Wino model with $\lambda_{12k} \neq 0$ where the 1.68σ significance is extended by up to 80 GeV (cf. Figure 7.12). In cases of a gluino or slepton NLSP, the 1.68σ significance is improved by up to 200 GeV for a large fraction of the parameter spaces. In the τ-rich SRs targeting the RPV scenarios with $\lambda_{i33} \neq 0$, the 1.68σ significance is shifted by up to 300 GeV for a wino NLSP and up to 200 GeV for a gluino NLSP using the 3L1T and 2L2T selections (cf. Figures 7.13 and 7.14). The largest gain in sensitivity is observed for the slepton model, where the old criteria only allow to access a single point with $m_{\tilde{\ell}/\tilde{\nu}} = 700$ GeV. The revised 2L2T and 3L1T signal selections promise an 1.68σ significance for a large fraction of the area with $m_{\tilde{\ell}/\tilde{\nu}} \leq 900$ GeV and $m_{\tilde{\ell}/\tilde{\nu}} \leq 870$ GeV, respectively. The significances to each model obtained from the individual SRs are given in the Appendix B.1.

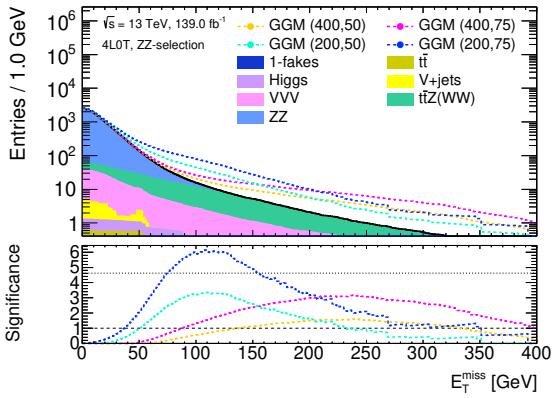

(a)

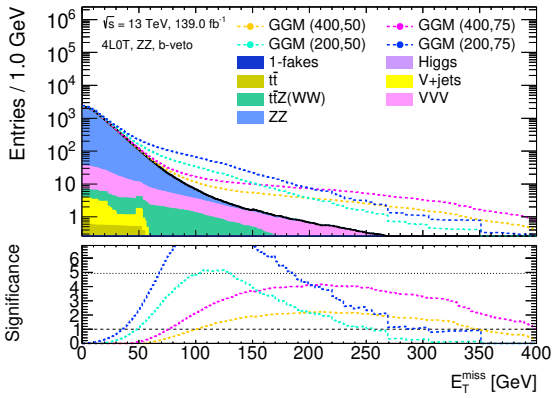

(b)

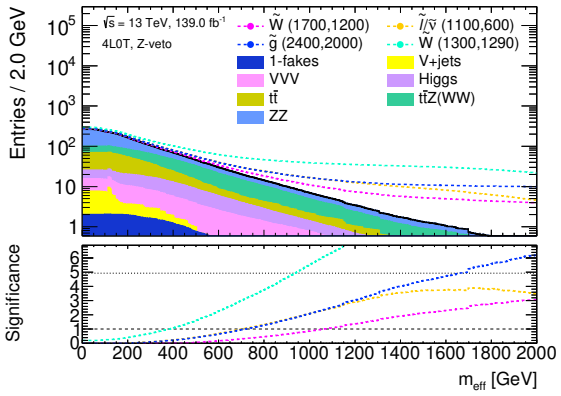

(c)

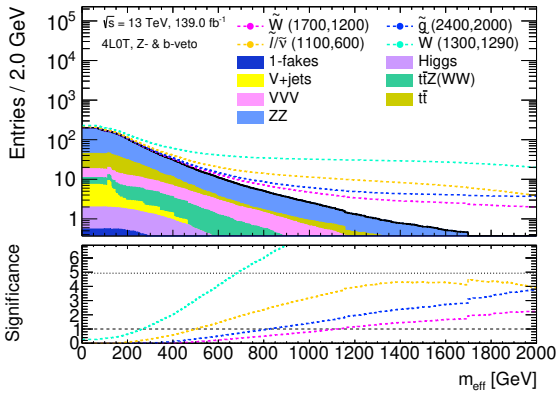

(d)

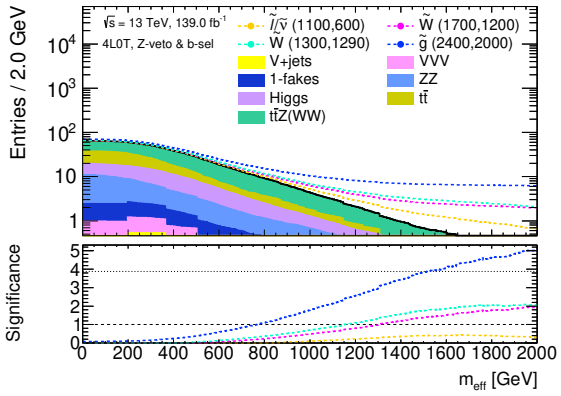

(e)

Figure 7.10: $E_{\mathrm{T}}^{\mathrm{miss}}$ in 4L0T events passing the ZZ selection (top) and m_{eff} in 4L0T events (middle) with an applied Z-veto shown as a function of a minimum threshold on the variable for the SM background and four signal points in 139 fb^{-1}of $\sqrt{s}$ = 13 TeV pp collision data. The left column is inclusive in b-jets, a b-veto is applied in the right column, and in (e) b-jets are explicitly required. The bottom panel depicts the statistical significance of each signal point for a given cut value assuming a background uncertainty of 30%.

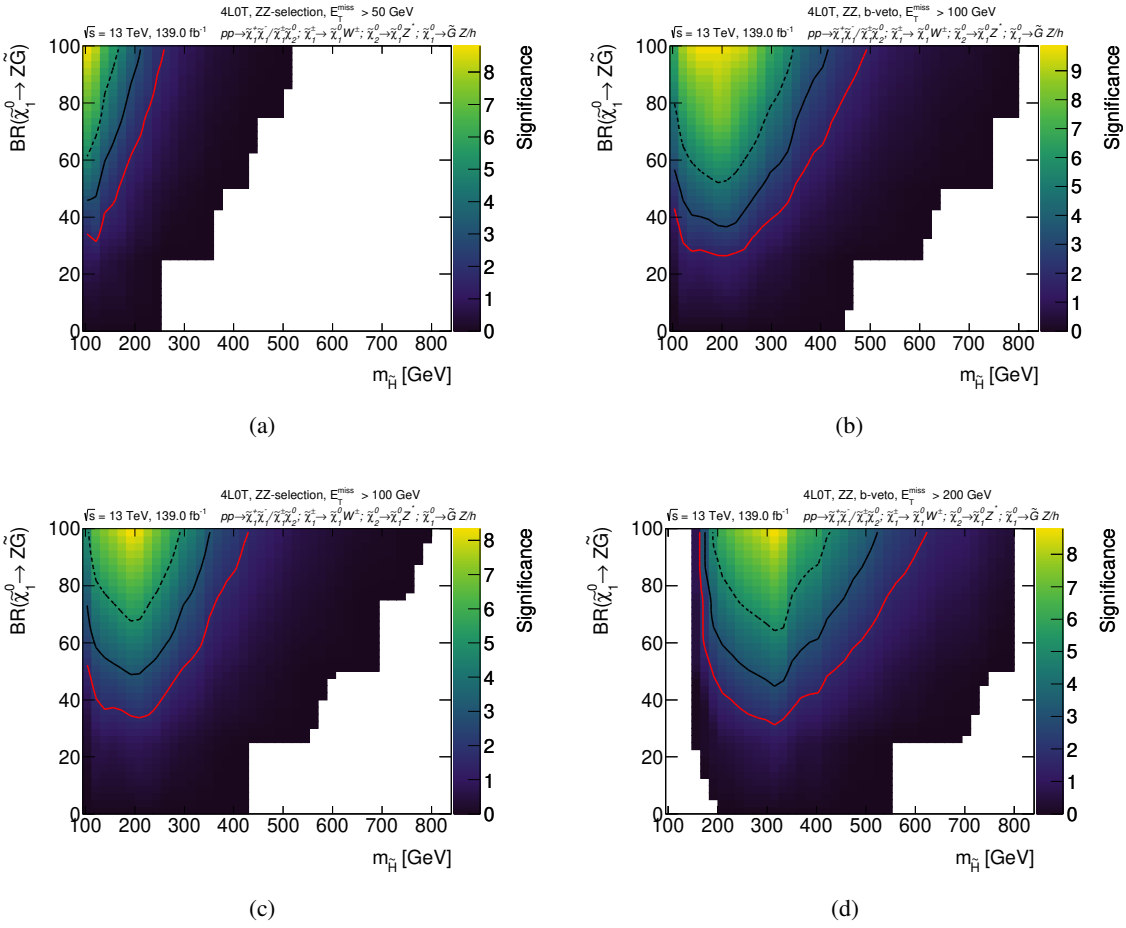

(a) (b) (c) (d)

Figure 7.11: Comparison of the sensitivity to the GGM models in the full Run 2 dataset, achieved with the SR0C and SR0-ZZ$^{\text{loose}}_{b-\text{veto}}$ (top), and the SR0D and SR0-ZZ$^{\text{tight}}_{b-\text{veto}}$ (bottom) selections. The red, solid black and dashed black lines indicate the 1.68σ, 3σ and 5σ contours, respectively.

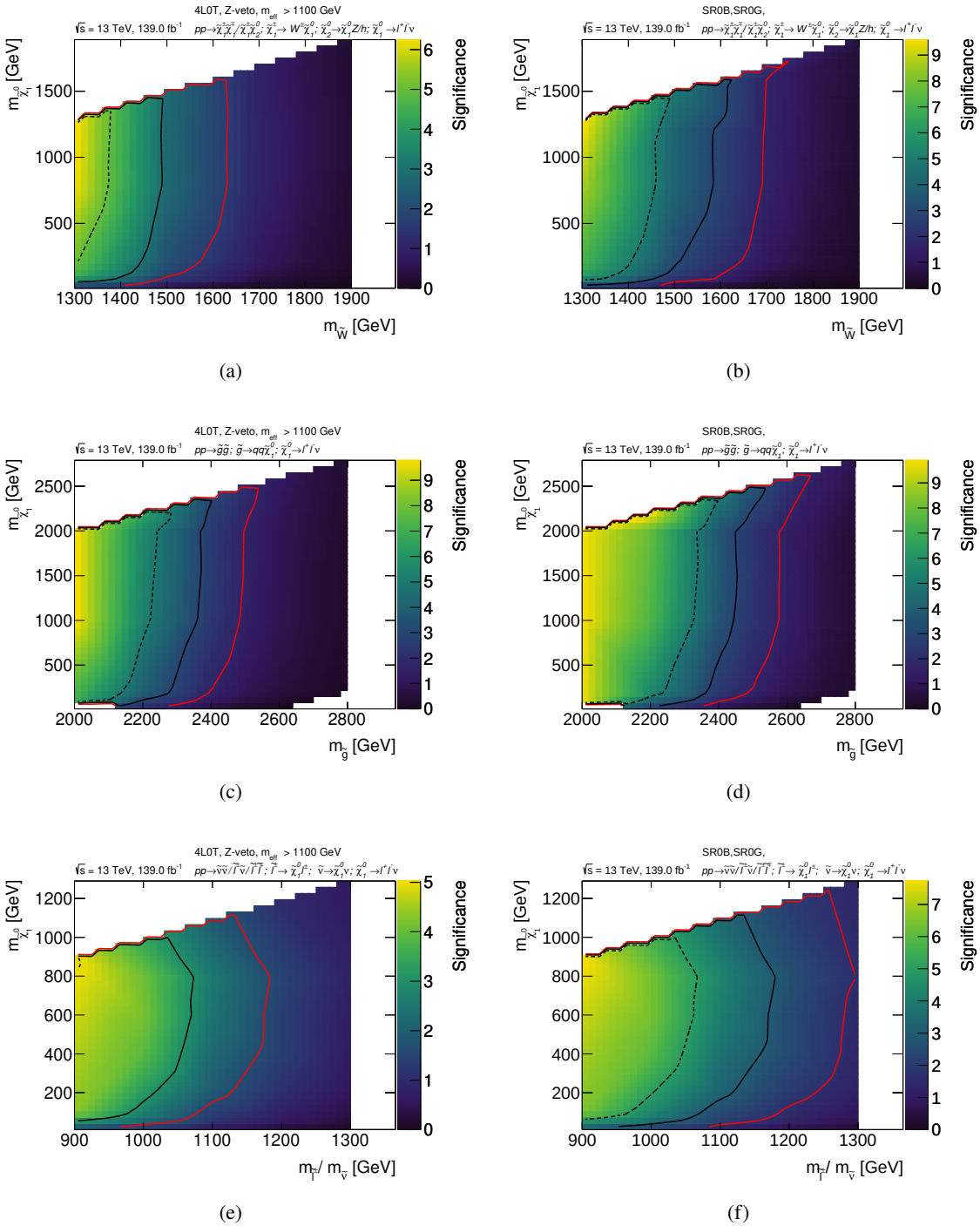

Figure 7.12: Comparison of the sensitivity obtained by the SR0B selection (left) and by the combination of the reoptimized $\mathtt{SR0}^{\text{tight}}_{b-\text{veto}}$ and $\mathtt{SR0}_{b-\text{req}}$ selections to RPV models with active λ_{12k} coupling and a wino (top), gluino (middle) and slepton (bottom) as NLSP in 139 fb^{-1} of $\sqrt{s}$ = 13 TeV pp collision data. The SR are combined by adding the expected significances in each SR in quadrature. The red, solid black and dashed black lines indicate the 1.68σ, 3σ and 5σ contours, respectively.

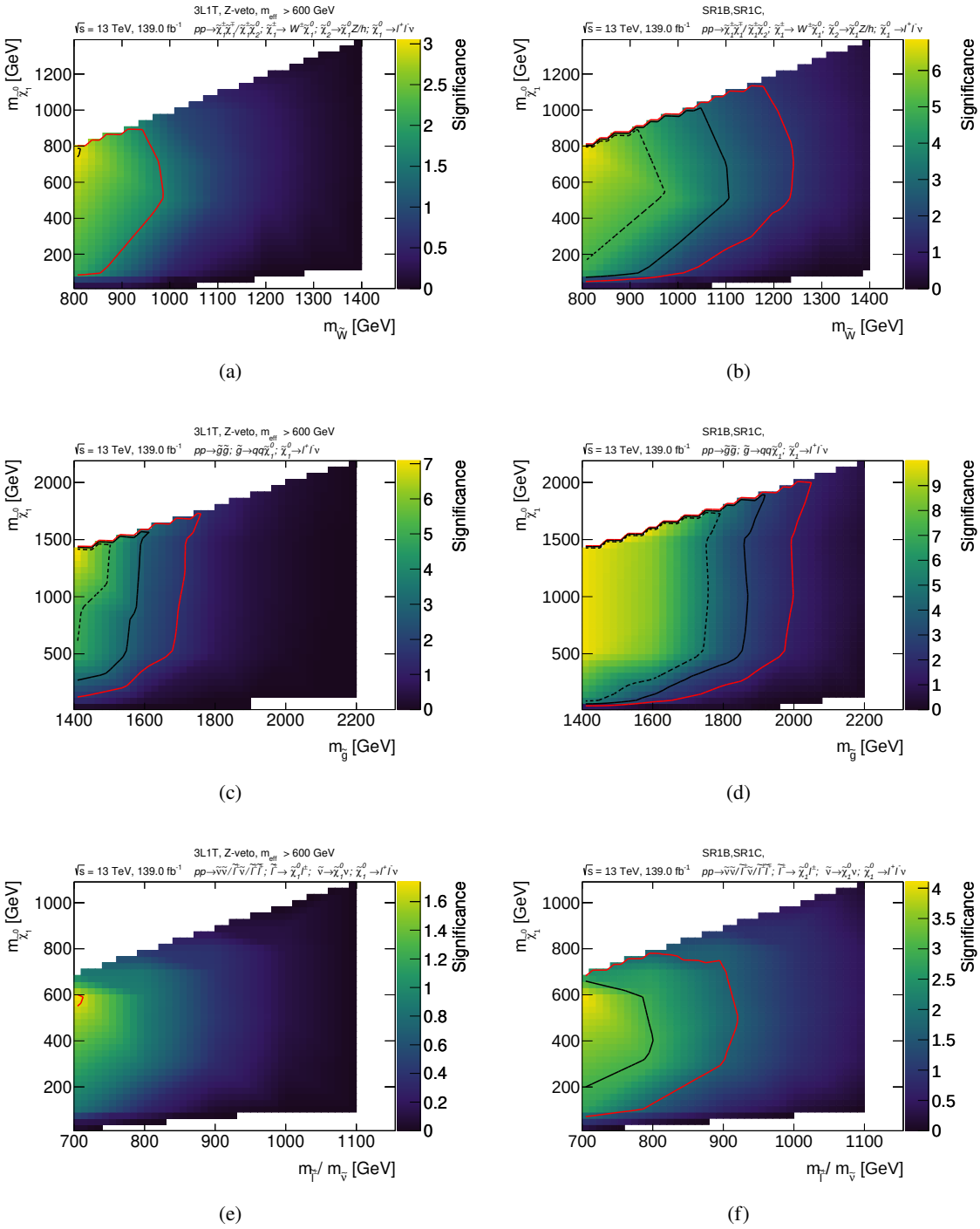

Figure 7.13: Comparison of the sensitivity obtained by the SR1 selection (left) and by the combination of the reoptimized $\mathrm{SR1}^{\mathrm{tight}}_{b-\mathrm{veto}}$ and $\mathrm{SR1}_{b-\mathrm{req}}$ selections to RPV models with active λ_{i33} coupling and a wino (top), gluino (middle) and slepton (bottom) as NLSP in 139 fb^{-1} of $\sqrt{s}$ = 13 TeV pp collision data. The SR are combined by adding the expected significances in each SR in quadrature. The red, solid black and dashed black lines indicate the 1.68σ, 3σ and 5σ contours, respectively.

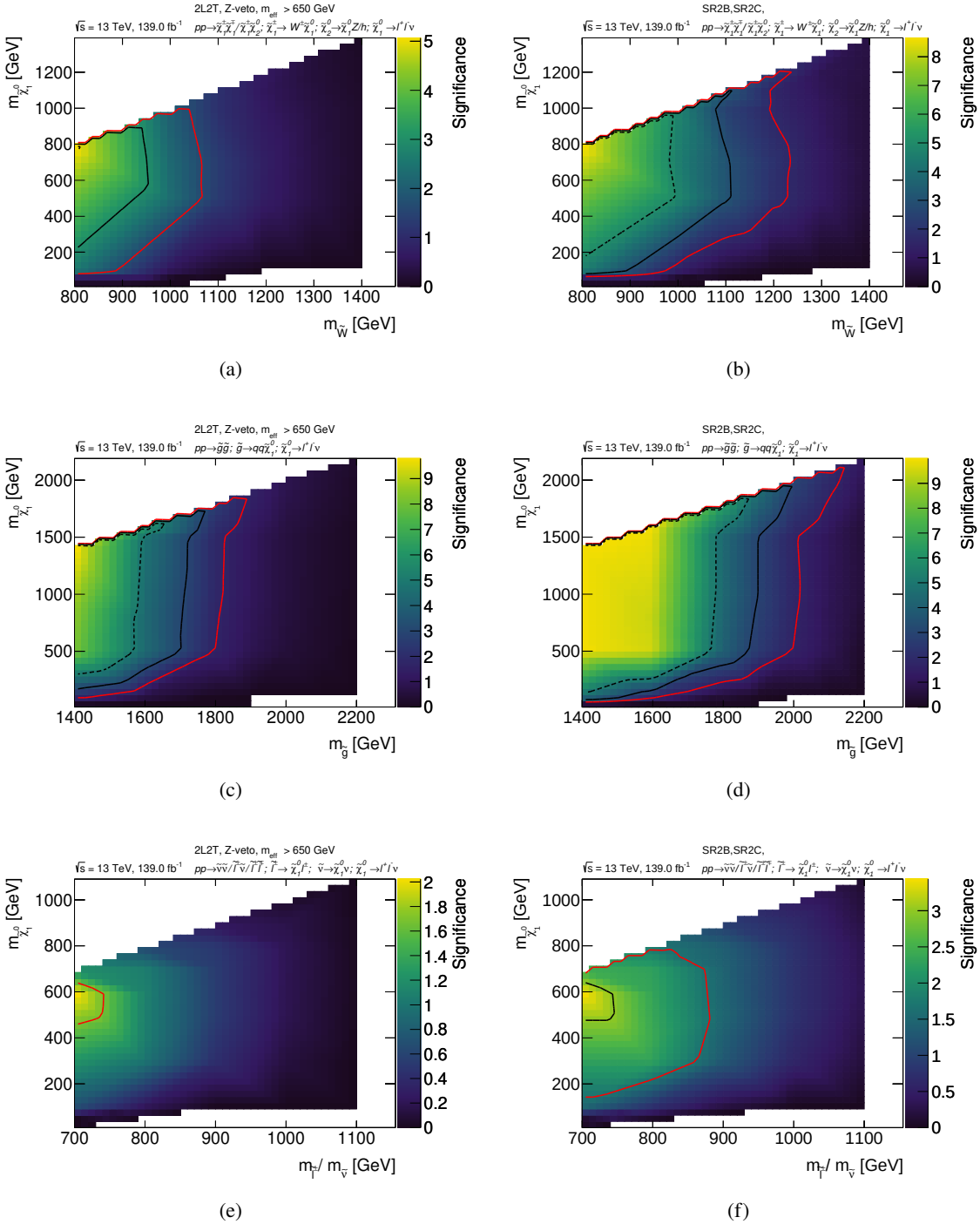

Figure 7.14: Comparison of the sensitivity obtained by the SR2 selection (left) and by the combination of the reoptimized $\mathrm{SR2}^{\mathrm{tight}}_{b-\mathrm{veto}}$ and $\mathrm{SR2}_{b-\mathrm{req}}$ selections to RPV models with active λ_{i33} coupling and a wino (top), gluino (middle) and slepton (bottom) as NLSP in 139 fb^{-1} of $\sqrt{s}$ = 13 TeV pp collision data. The SR are combined by adding the significances in each SR in quadrature. The red, solid black and dashed black lines indicate the 1.68σ, 3σ and 5σ contours, respectively.

7.4 Background Estimate in Four Lepton Events

After the signal selection is defined, the SM background in the signal regions is estimated. The irreducible component is determined using Monte Carlo simulation where errors are assigned from experimental uncertainties in the physics object calibration and from theoretical uncertainties on the cross section and on the acceptance of the selection. The reducible background is estimated using a data-driven method. The background estimation procedure is described in this section which is structured as follows: The reducible background estimate is explained in section 7.4.1. One of the improvements for the full Run 2 result is, that the normalization factors of the two major irreducible backgrounds ZZ and $t\bar{t}Z$ are extracted from a data CR which is discussed in section 7.4.2. The sources of systematic uncertainties are discussed in section 7.4.3. Validation studies for the background estimate are given in section 7.4.4.

7.4.1 Reducible Background Estimation

To estimate the reducible background, four-lepton control regions with one or two loose leptons are extrapolated into the signal regions using the so-called fake factor method [331]. In the following, the fake factor method is first described briefly. Then each component to obtain the reducible estimate is discussed for the example of the full Run 2 dataset.

The fake factor method: There are various processes in the Standard Model giving a four-lepton event signature in the detector. In the following discussion, these are divided into five different categories according to the number of fake leptons they contain. As previously denoted, the processes with 0-fakes are the irreducible background and the other ones are the reducible component. The ATLAS particle identification algorithms are designed to reject fake leptons as loose leptons (l) and to accept prompt leptons (also called real leptons) as signal leptons (L). The rates are dependent on the chosen selection criteria. The lepton selection criteria considered in this analysis provide a compromise between a high prompt lepton selection efficiency, ϵ, and a low fake rate, f. In the following, ϵ and f are defined as the probability that a prompt or fake baseline lepton is accepted by the signal selection criteria, respectively. Both differ for each lepton flavor and in the case of τ leptons also on the prongness of the τ leptons, i.e. the number of associated ID tracks. They generally depend on the lepton transverse momentum and pseudorapidity, the proximity of the lepton to other leptons or jets, or on event variables like $E_{\mathrm{T}}^{\mathrm{miss}}$ or $H_{\mathrm{T}}^{\mathrm{lep}}$. An additional dependence of the fake rate arises whether the fake leptons are produced in e.g. $t\bar{t}$ or Z + jets or WZ events. For each background processes, the fake rates also vary across the particular processes producing the fake lepton. Light-flavor quark (LF) jets, jets with bottom or charm quarks, called heavy flavor jets (HF) and photon conversion processes

(CONV) are the three main dominant processes producing fake light leptons. Fake τ leptons typically originate either from HF jets, LF, gluon jets (GJ), or from primary light leptons misidentified as τ leptons which are in the vast majority electrons (ELEC).

The reconstructed four-lepton events are classified according to their loose lepton multiplicity, denoted by CR$\mathcal{Y}$, where $\mathcal{Y} \in \{1, 2, 3, 4\}$ indicates the number of loose leptons in the event, followed by a sequence of four capital/small L or T letters to indicate whether a light lepton or a τ lepton is considered as loose lepton or not. For example, CR2_LLll denotes all events with four light leptons of which two leptons are loose. For the sake of simplicity in the discussion below, the four-lepton events with four signal leptons are denoted by SR and again followed by four letters indicating the flavor content, e.g. SR_LLLL. In the ideal case, it holds $\epsilon = 1$ and $f = 0$ meaning that the categorization of the physics process in terms of fake leptons exactly matches the reconstructed categories in terms of loose and signal lepton multiplicities. However, imperfections in the particle identification algorithms lead to $\epsilon < 1$ and $f > 0$. As a consequence, SR_LLLL events contain events with fake signal leptons and CR1_LLLl with prompt loose leptons. This mixing can be described by a linear mapping

$$\begin{pmatrix} N_{\text{CR4\_lll}} \\ N_{\text{CR3\_Lll}} \\ N_{\text{CR2\_LLl}} \\ N_{\text{CR1\_LLLl}} \\ N_{\text{SR\_LLLL}} \end{pmatrix} = \mathcal{I} \begin{pmatrix} N_{\text{4-fake}} \\ N_{\text{3-fake}} \\ N_{\text{2-fake}} \\ N_{\text{1-fake}} \\ N_{\text{0-fake}} \end{pmatrix}, \tag{7.4}$$

where $\mathcal{I}$ is the real-fake migration matrix and the N_X represent the number of events in each category. The real-fake migration matrix is constructed by starting from a SM background event with four baseline leptons which counts to e.g. the 2-fake category. For example, to contribute to the CR1_LLLl category, each lepton has to be multiplied by its corresponding prompt or fake lepton efficiency if the lepton is considered as signal or by the corresponding fake rejection and prompt lepton inefficiency, denoted by $\bar{f}_i = 1 - f_i$ and $\bar{\epsilon}_i = 1 - \epsilon_i$, respectively, otherwise. For a given CR1_LLLl event it cannot be distinguished whether the loose lepton is the softest lepton in p_{T} or actually is a prompt or fake lepton. Therefore, all possible combinations of fake rejections and prompt lepton efficiencies as well as of fake rates and prompt lepton inefficiencies have to be considered. This procedure results in combinatorial weights in the corresponding matrix entry. For the example of a 2-fake process in CR1_LLLl events, the entry is given by $\mathcal{I}^{\text{CR1\_LLLl}}_{\text{2-fake}} = 2f^2\epsilon\bar{\epsilon} + 2\epsilon^2 f\bar{f}$ accounting for the fact that either one of the two fake leptons is correctly discarded as loose or that one of the prompt leptons is rejected. The remaining matrix entries are obtained by applying the same procedure to the corresponding fake

processes and control region events such that the real-fake migration matrix is given by

$$\mathcal{I} = \begin{pmatrix} \bar{f}^4 & \bar{f}^3\bar{\epsilon} & \bar{f}^2\bar{\epsilon}^2 & \bar{f}\bar{\epsilon}^3 & \bar{\epsilon}^4 \\ 4f\bar{f}^3 & \epsilon\bar{f}^3 + 3\bar{\epsilon}\bar{f}^2 f & 2\epsilon\bar{\epsilon}\bar{f}^2 + 2\bar{\epsilon}^2 f\bar{f} & 3\epsilon\bar{\epsilon}^2\bar{f} + \bar{\epsilon}^3 f & 4\bar{\epsilon}^3\epsilon \\ 6f^2\bar{f}^2 & 3\epsilon f\bar{f}^2 + 3\bar{\epsilon}\bar{f}f^2 & \epsilon^2\bar{f}^2 + 4\epsilon f\bar{f}\bar{\epsilon} + \bar{\epsilon}^2 f^2 & 3\epsilon^2\bar{\epsilon}\bar{f} + 3\epsilon f\bar{\epsilon}^2 & 6\epsilon^2\bar{\epsilon}^2 \\ 4f^3\bar{f} & \bar{\epsilon}f^3 + 3\epsilon f^2\bar{f} & 2f^2\epsilon\bar{\epsilon} + 2\epsilon^2 f\bar{f} & 3\epsilon^2 f\bar{\epsilon} + \epsilon^3\bar{f} & 4\epsilon^3\bar{\epsilon} \\ f^4 & \epsilon f^3 & \epsilon^2 f^2 & \epsilon^3 f & \epsilon^4 \end{pmatrix}. \tag{7.5}$$

On the other hand, the background in the SR can be decomposed into the irreducible and reducible parts. To obtain the reducible component, the number of events in the SR needs to be subtracted by the number of 0-fake events

$$N^{\text{red.}}_{\text{SR\_LLLL}} = N_{\text{SR\_LLLL}} - \epsilon^4 N_{\text{0-fake}}, \tag{7.6}$$

where the latter has to be rewritten in terms of the yields in the CRs and in the SR. To do this, the real-fake migration matrix needs first to be inverted which is given in Appendix B.2. Using this result Equation (7.6) transforms into

$$\begin{aligned} N^{\text{red.}}_{\text{SR\_LLLL}} = N_{\text{SR\_LLLL}} - \frac{\epsilon^4}{(\epsilon - f)^4}[&\bar{f}^4 N_{\text{SR\_LLLL}} - f\bar{f}^3 N_{\text{CR1\_LLLl}} \\ &+ f^2\bar{f}^2 N_{\text{CR2\_LLll}} - f^3\bar{f} N_{\text{CR3\_Llll}} + f^4 N_{\text{CR4\_llll}}] \end{aligned} \tag{7.7}$$

$$\begin{aligned} \simeq N_{\text{SR\_LLLL}} - \frac{1}{(1 - f)^4}[&\bar{f}^4 N_{\text{SR\_LLLL}} - f\bar{f}^3 N_{\text{CR1\_LLLl}} \\ &+ f^2\bar{f}^2 N_{\text{CR2\_LLll}} - f^3\bar{f} N_{\text{CR3\_Llll}} + f^4 N_{\text{CR4\_llll}}] \end{aligned} \tag{7.8}$$

$$= F N_{\text{CR1\_LLLl}} - F^2 N_{\text{CR2\_LLll}} + F^3 N_{\text{CR3\_Llll}} - F^4 N_{\text{CR4\_llll}} \tag{7.9}$$

$$\simeq F N_{\text{CR1\_LLLl}} - F^2 N_{\text{CR2\_LLll}} + O\left(F^3\right). \tag{7.10}$$

In the first step, the prompt lepton efficiency is approximated by $\epsilon \approx 1$ as the signal lepton selection criteria of the light leptons have efficiencies around 98–99% (cf. chapter 5 for the case of muons and Ref. [193, 211] for the case of electrons). In the next step, a new quantity, called the fake factor, is introduced which is the ratio of the fake rate to the fake rejection or equivalently the ratio of the number of signal to loose leptons:

$$F = \frac{f}{1 - f} = \frac{N_{\text{signal}}}{N_{\text{loose}}}. \tag{7.11}$$

It is used to extrapolate the number of events in a loose lepton CR to the SR by applying it to each CR

event as many times as the CR contains loose leptons. The loose lepton CR event has to satisfy the same kinematic selection on the discriminating variables as for the corresponding SR (cf. Table 7.3 or 7.4) where the loose leptons enter the calculation of $H_{\mathrm{T}}^{\mathrm{lep}}$ and hence m_{eff}. The fake factors are typically much smaller than one and hence the contributions of the terms proportional to F^3 and F^4 are neglected. The negative sign between CR1 and CR2 events in Equation (7.10) reflects the removal of the double counting of the 2-fake processes in CR1 arising from the combinatorial weight as explained above. The discussion can be extended to the τ-rich categories giving the same relation.

For a data-driven estimate of the reducible background, the data events in the corresponding loose lepton CR (cf. Figure 7.15) are used for the extrapolation instead of the simulated events. The expected number of reducible background events for a given signal region is then given by

$$N_{\mathrm{SR}}^{\mathrm{red.}} = \left(N_{\mathrm{CR1}}^{\mathrm{data}} - N_{\mathrm{CR1}}^{\mathrm{irred.,\,MC}}\right) \times F - \left(N_{\mathrm{CR2}}^{\mathrm{data}} - N_{\mathrm{CR2}}^{\mathrm{irred.,\,MC}}\right) \times F \times F. \tag{7.12}$$

The data is corrected by the contribution of irreducible background events $N_{\mathrm{CR}\mathcal{Y}}^{\mathrm{irred.,\,MC}}$ estimated from MC to account for the fraction of cases in which the prompt lepton is rejected which is observed to be tiny.

The fake factor is determined from simulation as the weighted sum of the fake ratios, $f_{ij} = \frac{N^{\mathrm{signal}}}{N^{\mathrm{loose}}}$ for each fake type and reducible SM background, their respective process fractions, R_{ij}, measured in the CR2_LL$\mathcal{XY}$ ($\mathcal{X}, \mathcal{Y} \in \{\mathrm{l}, \mathrm{t}\}$) regions, and a fake process dependent scale factor sf_i:

$$F = \sum_{\substack{i \in \{\text{fake process}\},\\ j \in \{\text{reducible SM}\}}} f_{ij} \cdot R_{ij} \cdot sf_i. \tag{7.13}$$

The determination of each component is described in the following paragraphs.

Process fractions and fake ratios: In principle, all contributing processes need to be taken into account. In practice, however, the loose lepton CRs are dominated by Z + jets and $t\bar{t}$ background (cf. Figure 7.15). In addition, there is not enough Monte Carlo statistics available to calculate fake and process fractions with acceptable precision for the other processes. Thus only Z + jets and $t\bar{t}$ events have been considered to determine the fake ratios and process fractions. The plots shown in the following are based on the object definitions used for the analysis of the full Run 2 data. Improvements in the electron and τ reconstruction and identification as well as other object selection criteria lead to small differences between the results of the different analysis iterations. To illustrate the fake composition in the background contributions considered, Figures 7.16 and 7.17 show the fake lepton p_{T} distributions split with the contributions of the different fake processes, HF, LF and CONV (see above). Fake electrons produced in $t\bar{t}$ events mostly originate from HF fake processes (cf.

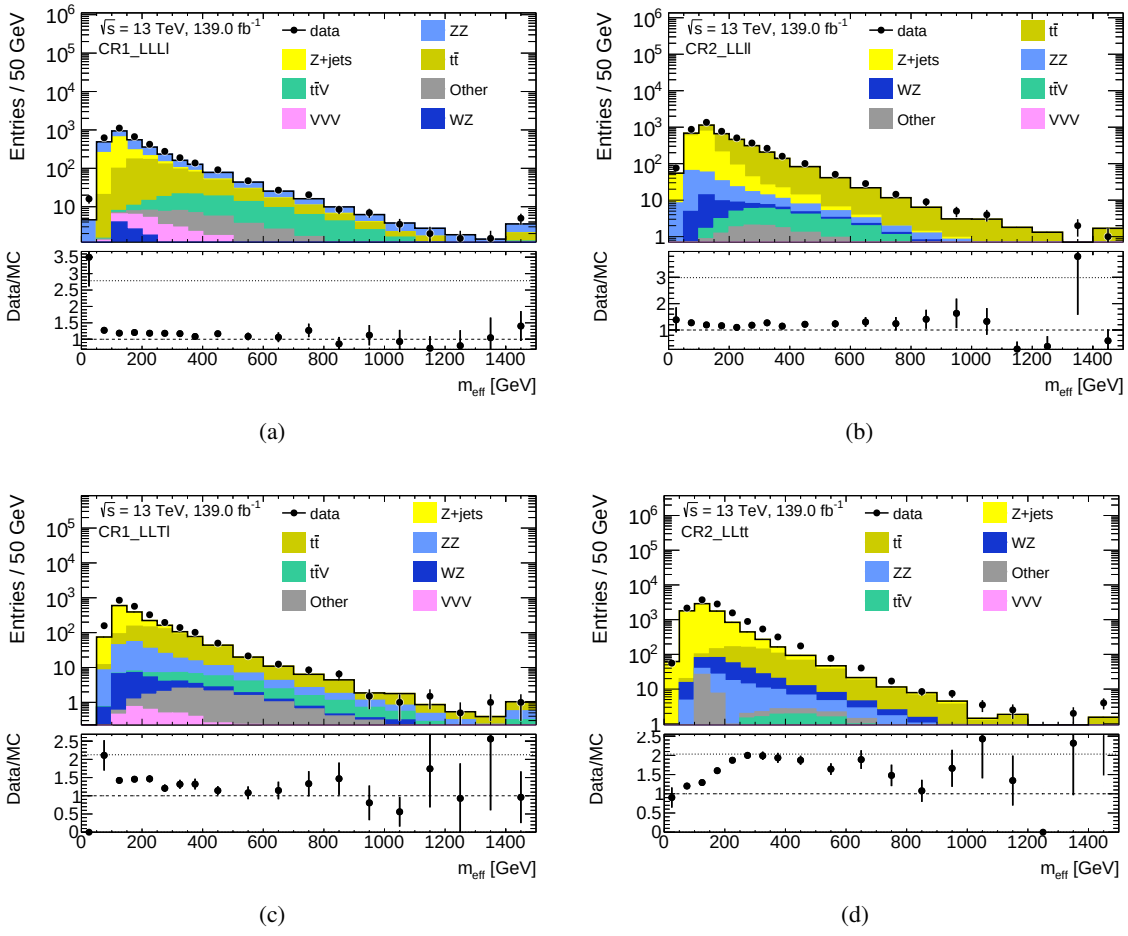

Figure 7.15: Distribution of the effective mass in CR1_LLLl (a), CR2_LLll (b), CR1_LLTt (c), and CR2_LLtt (d) events for simulation and 139 $fb^{-1}$of data. The bottom panel illustrates the ratio of the simulation to data. The error bars indicate the statistical uncertainties.

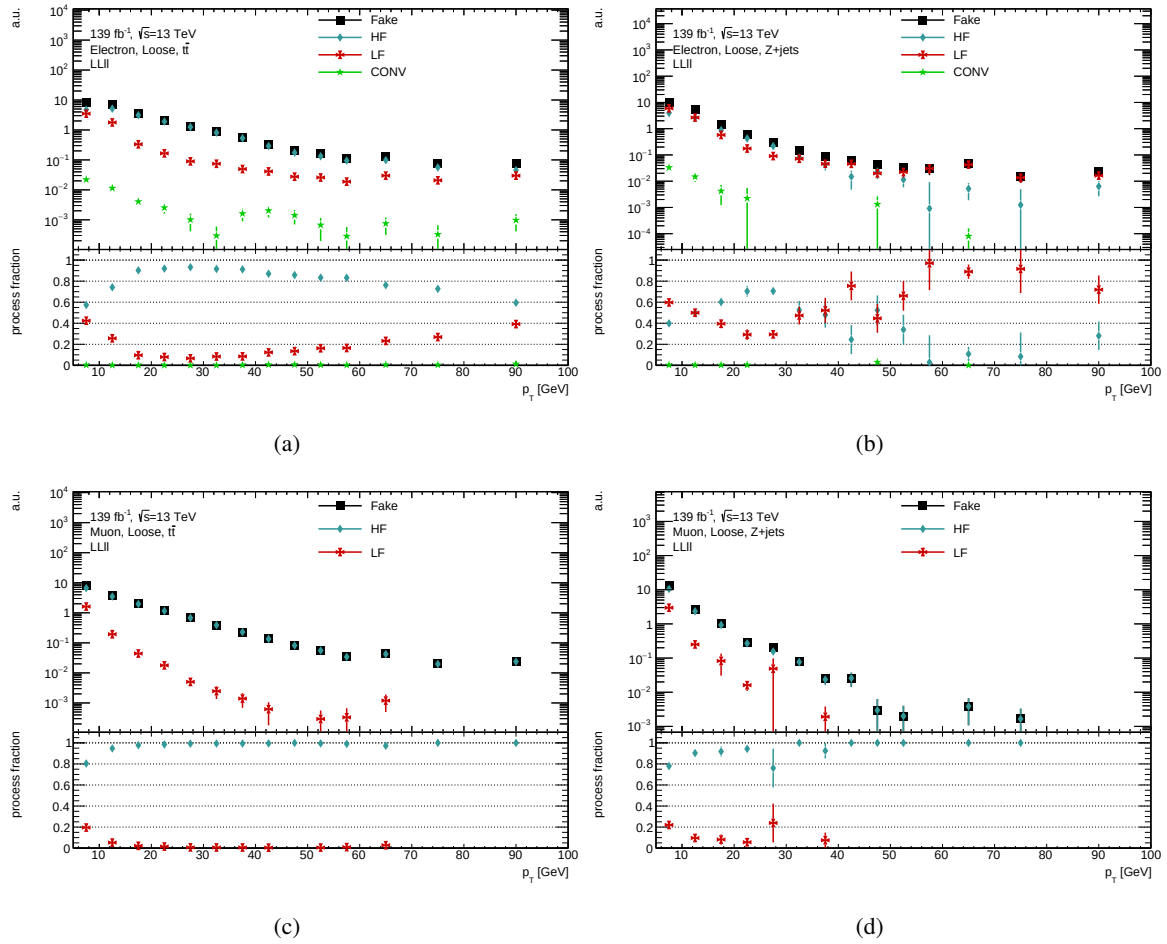

Figure 7.16: Distribution of the p_{T} of loose fake electrons (top) and muons (bottom) with the breakdown into the different fake processes for simulated $t\bar{t}$ (left) and Z + jets (right) CR2_LLll events. The bottom panel shows the process fraction of each fake process.

Figure 7.16(a)). LF fake electrons make up 40% and 20% of low and high p_{T} regions, respectively. In Z + jets events, the process fraction is more heterogeneous where HF and LF fake processes populate the sample to similar amounts (cf. Figure 7.16(b)). CONV fakes, by $\lesssim 1\%$, negligibly contribute for both backgrounds. In contrast, muons are almost exclusively from HF fake processes independent of the background process, with the exception at low p_{T} where LF sources contribute by 20% (cf. Figure 7.16). τ lepton fakes have more diverse contributions from fake processes (cf. Figure 7.17). In $t\bar{t}$ and Z + jets events, fake τ leptons are dominantly due to HF and LF processes, respectively. Differences in the purity of the dominating fake process by up 20% are observed between 1-prong and 3-prong τ leptons.

To obtain more accurate estimates, the process fractions considered in the analysis are additionally

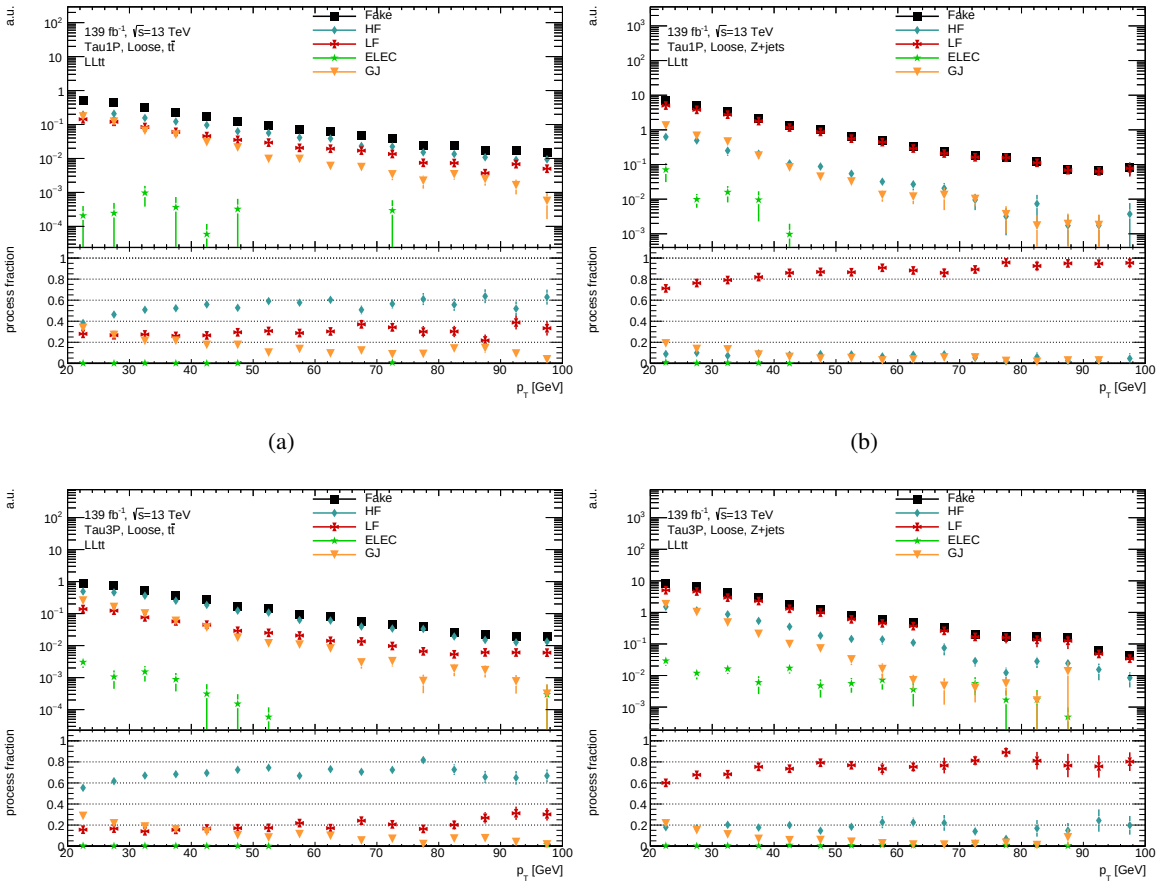

Figure 7.17: Distribution of loose 1-prong (top) and 3-prong (bottom) fake τ leptons together with the breakdown into the fake processes as a function of p_{T} for simulated $t\bar{t}$ (left) and Z + jets (right) CR2_LLtt events. The bottom panel shows the process fraction of each fake process.

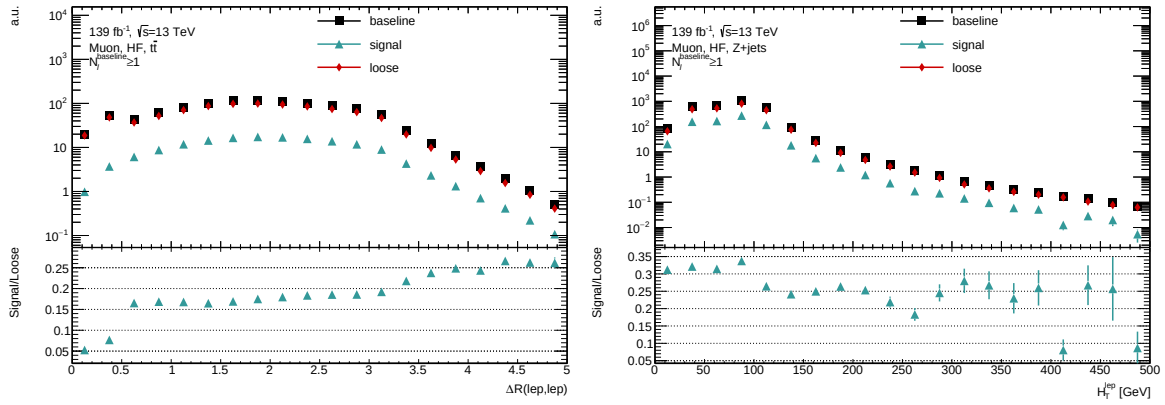

(a) (b)

Figure 7.18: ΔR distribution of HF muons to the next baseline lepton (a) in $t\bar{t}$ events and $H_{\mathrm{T}}^{\mathrm{lep}}$ distribution for HF muons (b) in Z + jets events shown for baseline, loose and signal muons. The bottom panel shows the ratio of the signal to the loose distribution. The error bars indicate the statistical uncertainties.

split according to their Z selection (i.e. Z-veto/selection or ZZ selection) and if necessary according to their b-jet selection as functions of the transverse momentum and the absolute pseudorapidity. No large dependence of the process fraction on the discriminating events variables such as m_{eff} or $E_{\mathrm{T}}^{\mathrm{miss}}$ was observed. In the full Run 2 analysis, the process fractions of light leptons are additionally parameterized as a function of the proximity to the next same-flavor or different-flavor light lepton.

The fake ratios, f_{ij}, are calculated using every baseline lepton of the given fake type in the simulated sample. They depend also on the transverse momentum and the absolute pseudorapidity but the larger statistics allow for using a finer segmentation of the bins. For the full Run 2 analysis, additional dependencies of the fake ratios for light leptons on the proximity of the lepton to another baseline light lepton in $t\bar{t}$ events and on $H_{\mathrm{T}}^{\mathrm{lep}}$ in Z + jets have been found and are considered. For the example of HF muons, these additional dependencies are depicted in Figure 7.18 which shows the angular separation to the next baseline lepton in $t\bar{t}$ events and the $H_{\mathrm{T}}^{\mathrm{lep}}$ distribution in Z + jets together with the respective fake ratios. A step in the fake ratio is visible at $\Delta R \sim 0.5$ for $t\bar{t}$ events (cf. Figure 7.18(a)). It is related to the fact that such collimated leptons in $t\bar{t}$ are likely to originate from the same cascade of a b-meson decay where a strong correlation whether both or no leptons in the pair pass the signal selection criteria has been observed. Simulated $t\bar{t}$ events in the SR are likely to have such a collimated lepton pair. The fake ratio maps derived in the p_{T}–$|\eta|$ plane vastly differ from the maps derived for such leptons only. Hence, a parametrization in the p_{T}–ΔR plane is used for $t\bar{t}$ events only if the closest lepton is within $\Delta R < 0.6$. A step in the fake ratio is also visible for $H_{\mathrm{T}}^{\mathrm{lep}} \sim 100$ GeV in Z + jets events (cf. Figure 7.18(b)) which corresponds roughly twice the typical p_{T} of a lepton from a Z boson decay. At leading order, the Z bosons are produced either in Drell–Yan, $q\bar{q} \rightarrow Z$, production with no

additional parton in the final state or in electroweak production where the additional parton recoils against the Z boson such as $gq \rightarrow Zq$. In the case of the latter, the fake lepton usually originates from the recoiling parton while in the former case, the lepton originates from a softer ISR parton. For $H_{\mathrm{T}}^{\mathrm{lep}} > 100$ GeV, a larger contribution from Drell–Yan production is observed resulting in different kinematics for the fake leptons and hence also in smaller fake ratios. Therefore, the fake ratios of the light leptons in Z + jets are additionally binned in this variable.

Closure test: To check that the obtained parametrizations for the fake ratios and process fractions capture the most crucial dependencies of the lepton fake factors in $t\bar{t}$ and Z + jets events, closure tests are performed. In these closure tests, the shape of the distributions in simulation in events passing the signal selection, e.g. SR_LLLL, are compared to the distributions obtained from the fake factor method by reweighting the CR events according to Equation (7.10). For the closure test, the process fractions are restricted to the sample on which the test is performed on.

Figure 7.19 shows the test results for the transverse momenta of the leptons in four-lepton events. An excellent closure is observed for the light leptons in the $t\bar{t}$ sample, where the p_{T} distribution from the direct estimate of the SR largely agrees with the estimate by the fake factor method. The τ p_{T} distributions well agree between the direct SR estimation and the extrapolation by the fake factor. However, the closure tests at high p_{T} suffer from low available Monte Carlo statistics that give rise to large statistical uncertainties. For the Z + jets sample, a good closure within the large statistical uncertainties is observed. To more thoroughly check the fake estimate in the Z + jets background, an additional closure test is performed in events with exactly three light leptons. The two associated loose lepton CR are analogously defined to the four-lepton case with CR1_LLl and CR2_Lll containing one and two loose leptons, respectively. The closure tests in three- and four light lepton events against the effective mass are shown in Figure 7.20. An excellent agreement between the predictions is observed for the closure tests in three lepton events and in four lepton events for the case of the $t\bar{t}$ sample. A good closure is observed for the Z + jets case in the low m_{eff} range where the statistics in the sample is sufficient. For the event selections requiring τ leptons, a non-closure at the level of 10–15% is observed.

Scale factor determination: The fake factors used for the closure test above are fully based on Monte Carlo. However, fake processes are very difficult to model at the LHC due to the soft QCD interactions in which they are produced. Therefore, the obtained fake rates might deviate from the actual fake rates in data. For the most important fake processes, the fake rates are corrected by a scale factor, sf_i to account for this potential mismodelling. The scale factors are obtained by the means of a tag-and-probe method (T&P). In the case of electrons and muons, the HF fake process is the

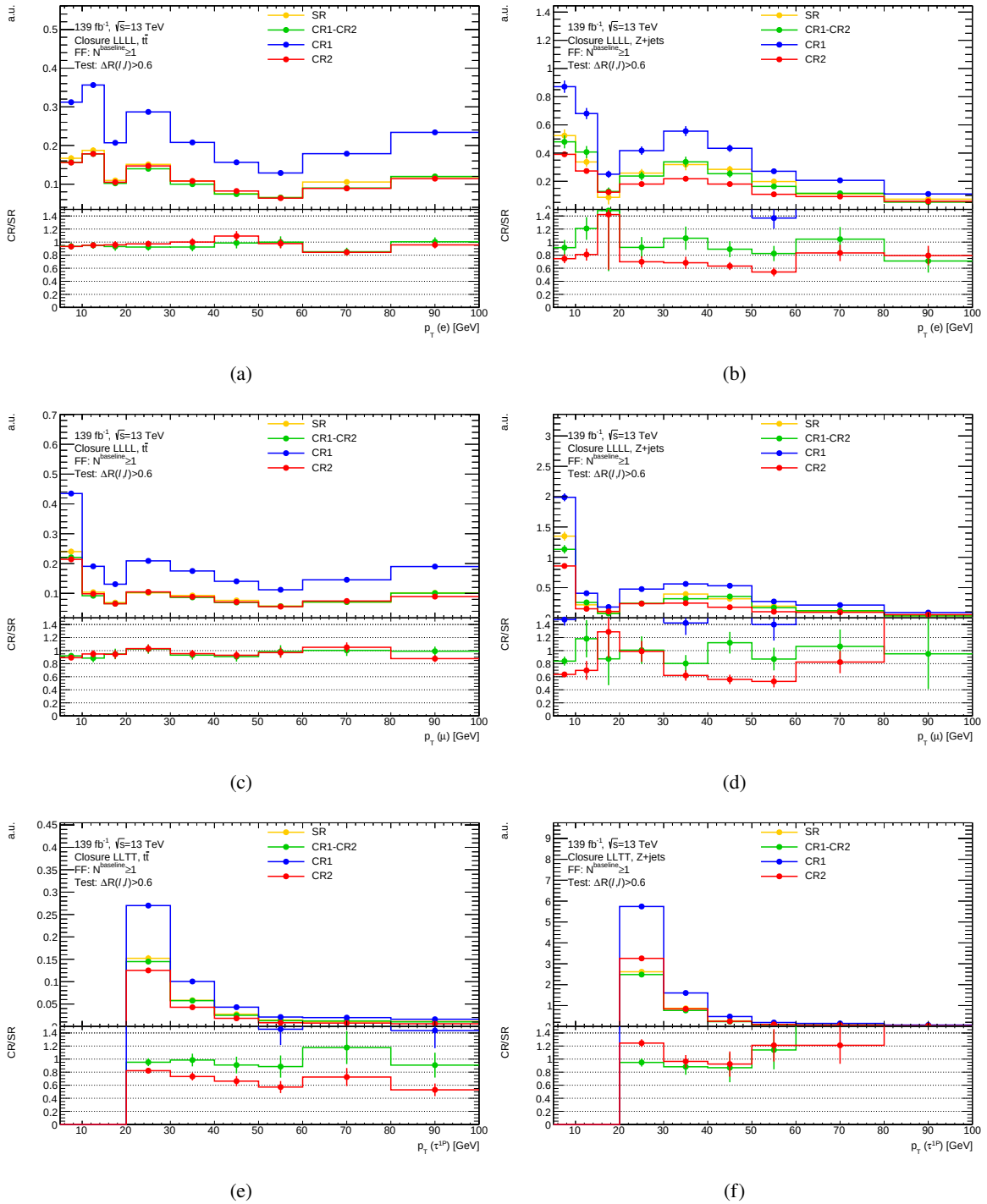

Figure 7.19: Closure test of the reducible estimate on the $t\bar{t}$ (left) and Z + jets (right) sample shown as a function of the electron p_{T} (top) and muon p_{T} (middle) in 4L0T events and of the 1-prong tau p_{T} (bottom) in 2L2T events. The yellow line shows the prediction for the signal region-like event selection, the blue and red lines demonstrate the estimate for the associated CR1 and CR2 regions weighted by the appropriate fake factors, respectively and the green line indicates the full reducible estimate which is the difference between the two. The bottom panel shows the ratio of the CRs to the signal region-like event selection.

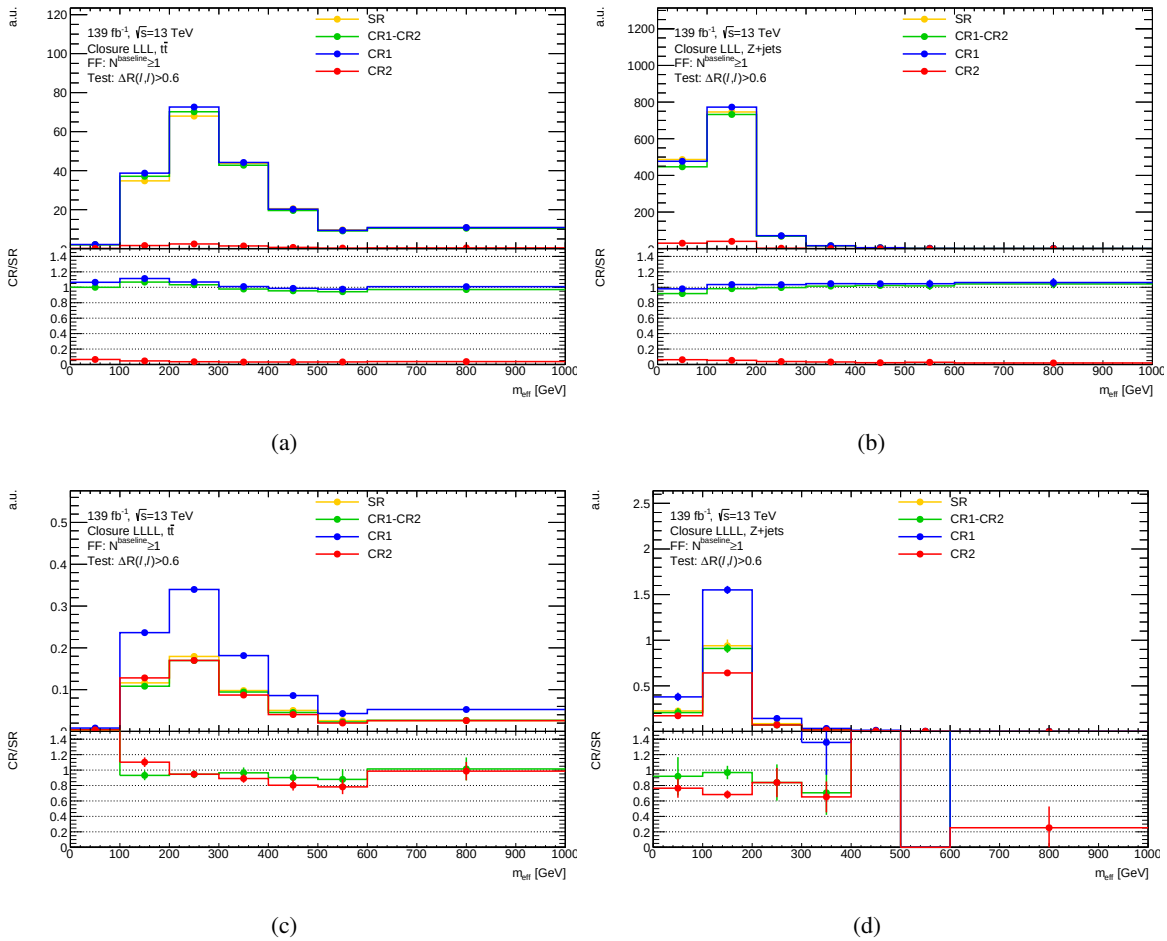

Figure 7.20: Closure test of the reducible estimate on the $t\bar{t}$ (left) and Z + jets (right) sample shown as a function of the effective mass in three-lepton (top) and four-lepton (bottom) events. The yellow line shows the prediction for the signal region-like event selection, the blue and red lines demonstrate the estimate for the associated CR1 and CR2 regions weighted by the appropriate fake factors, respectively and the green line indicates the full reducible estimate which is the difference between the two. The bottom panel shows the ratio of the CRs to the signal region-like event selection.

dominating source of fakes. Top quark pair production in association with a third lepton ($t\bar{t} + l$) events are found to be enriched in such fakes with the event selection as follows:

- Exactly three baseline light leptons of which the leading two leptons are a signal electron-muon pair with opposite charge. One lepton of the pair is required to have triggered the event following the same scheme given in Table 7.1.
- The event contains at least one b-tagged jet.
- The third light has to have the same charge as the corresponding lepton of the same flavor in the pair.

The electron-muon pair and the b-jet are the two characteristic features to select di-leptonic $t\bar{t}$ events. The third lepton is used to probe the HF fake rate. The same charge requirement efficiently reduces events in which two SFOS leptons originate from Z decays and the additional lepton is the highest in p_{T}. The probes are modelled within 20% accuracy for the bulk of the p_{T} spectrum (cf. Figure 7.21). The obtained sample is pure in HF fake muons. The electrons can be contaminated by up to 40% by prompt leptons and LF fakes (cf. Figure 7.22). This contamination is estimated from MC and subtracted from the data before the fake rate is calculated. Figure 7.23 depicts the HF fake rates of the probe leptons in data and simulation together with the scale factor. In both cases, the scale factor is in agreement with unity for the bulk of the spectrum. Both scale factors deteriorate for high p_{T} up to 2.2 and 1.7 in the cases of electrons and muons, respectively. In addition, the electron scale factor rises for transverse momenta below 10 GeV to 1.4.

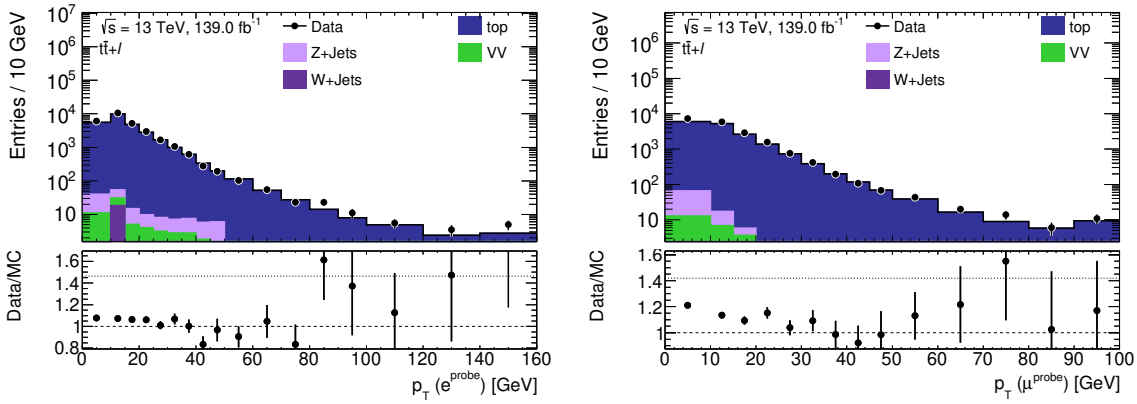

(a) (b)

Figure 7.21: p_{T} distribution of the probe electrons (a) and muons (b) in CR $t\bar{t} + l$ events for simulation and 139 fb^{-1}of data. The bottom panel shows the ratio of the simulation to the data. The error bars indicate the statistical uncertainties.

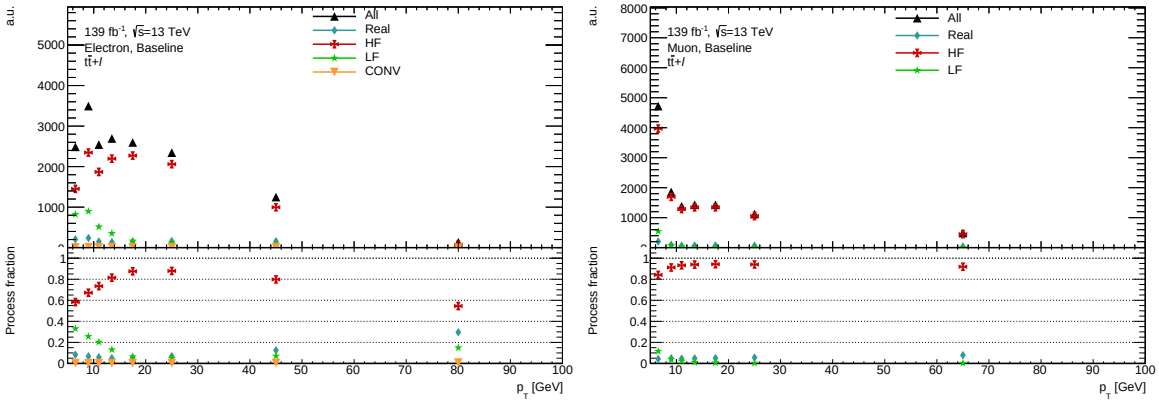

(a) (b)

Figure 7.22: Fake process fraction of the probe electrons (a) and muons (b) in simulated CR $t\bar{t} + l$ events shown as a function of the lepton p_{T}.

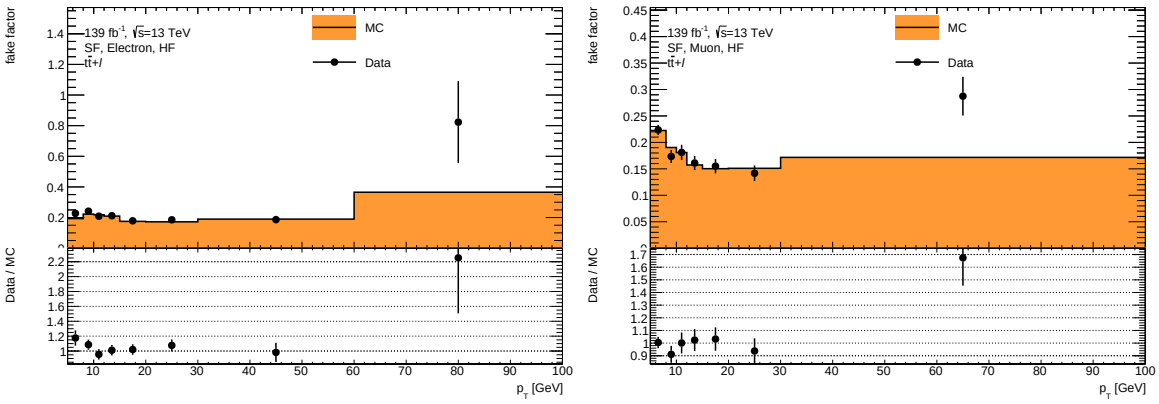

(a) (b)

Figure 7.23: Heavy flavor fake factors for electrons (a) and muons (b) as a function of p_{T} measured in $t\bar{t} + \ell$ events for simulation and data. The bottom panel shows the ratio of the simulated to the measured fake rate, i.e. the HF scale factor.

In the full Run 2 iteration of the analysis, W + jets production with a second baseline electron is found to provide a sample enriched in LF fake electrons. The following event selection criteria are applied to measure a LF electron scale factor by means of T&P:

- One electron-muon pair of same charge with the muon which satisfies the signal selection criteria, has triggered the event and $p_{\mathrm{T}} > 28$ GeV. The electron has to satisfy the baseline selection criteria.
- The electron must be separated in pseudorapidity from the muon by $|\Delta\eta| > 0.2$ and the two leptons needs to have an invariant mass of $m_{e\mu} > 20$ GeV to reject events in which the muon radiated a photon which is then misidentified as electron.
- To select $W \rightarrow \mu\nu$ decays, the event needs to have $E_{\mathrm{T}}^{\mathrm{miss}} > 30$ GeV and the transverse mass calculated from the muon and $E_{\mathrm{T}}^{\mathrm{miss}}$ needs to be $m_{\mathrm{T}} > 50$ GeV.
- The event contains at maximum three jets of which none is identified as b-jet to suppress $t\bar{t}$ background.

The obtained sample is about 80% pure in LF electrons (cf. Figure 7.24(a)). The modelling agrees with the recorded data better than 30% for p_{T} <100 GeV as shown in Figure 7.24(b). The obtained scale factor ranges between 1.05 and 1.4 (cf. Figure 7.24(c)).

The remaining fake processes causing fake light leptons, i.e. CONV electrons and LF muons, have been found to contribute only minorly to the fake background (cf. discussion above). Nevertheless, to account for a small mismodelling an additional flat 10% uncertainty is assigned to the fake ratios of these processes.

τ leptons have more heterogeneous process fractions. For the two dominating fake processes, LF and HF, scale factors are derived in $Z \rightarrow \mu\mu + \tau$ and $t\bar{t} + \tau$ control region events, respectively. The event selection for the $Z \rightarrow \mu\mu + \tau$ control region is given by:

- Exactly two signal muons with opposite charge and an invariant mass of $m_{\mu^{\pm}\mu^{\mp}} \in [61; 121]$ GeV. The muons need to trigger the record of the event.
- Veto of a third baseline light lepton.
- At least one baseline tau.

The $t\bar{t} + \tau$ event selection is the same as the $t\bar{t} + l$ selection with the difference that the third lepton is a baseline tau. The probe τ p_{T} distributions for the two CRs are shown in Figure 7.25. Each CR is almost pure in its respective SM background. A rising trend is observed for the data to simulation ratio from 10% at 10 GeV to 40% for τ leptons with $p_{\mathrm{T}} \sim 100$ GeV in $Z \rightarrow \mu\mu + \tau$ events. For the $t\bar{t} + \tau$ CR the modelling of the p_{T} distribution agrees at a level of 40% for low p_{T} and improves to

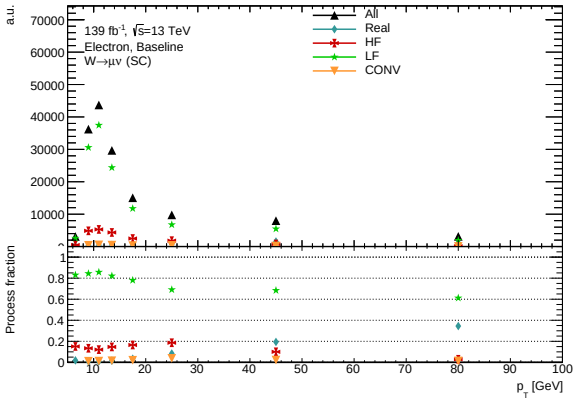

(a)

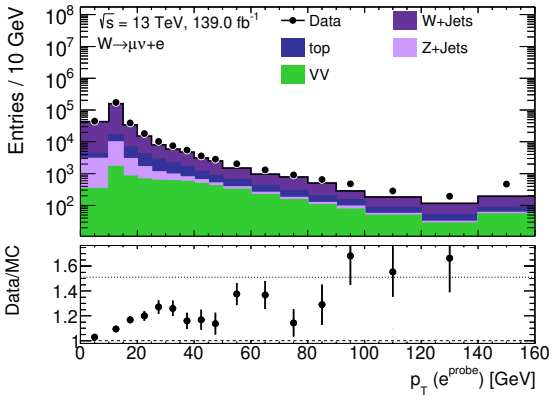

(b)

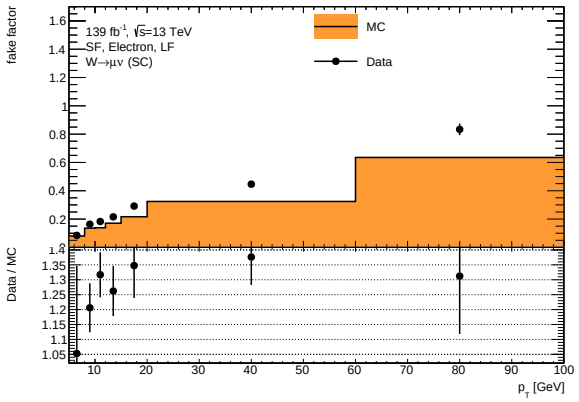

(c)

Figure 7.24: p_{T} distribution of baseline electrons in simulated W + jets events split into the fake sources (a) and compared to 139 fb^{-1}of recorded data (b), and p_{T} dependent LF electron fake factor in simulation and data (c). The bottom panel shows the process fraction (a), the ratio of data to simulation (b) and the LF scale factor (c). The error bars indicate the statistical uncertainties.

a good agreement for τ with p_{T} >40 GeV. The $t\bar{t} + \tau$ sample is pure in HF 1-prong and 3-prong τ leptons at a level of 50% and 70%, respectively (cf. Figure 7.26) and the $Z \rightarrow \mu\mu + \tau$ events are pure in LF fakes at a level of 80% for 1-prong and 3-prong τ leptons. Figure 7.27 shows the measured and simulated fake ratios in each sample as a function of p_{T} for 1-prong and 3-prong τ leptons. The HF scale factors are compatible with unity for τ leptons with p_{T} >30 GeV. For lower p_{T}, deviations of up to 25% are observed. The LF scale factors are about 5% below and above one for 1-prong and 3-prong τ leptons, respectively. Also in this case, the largest deviations in the scale factors are observed for low p_{T} τ leptons of up to 35%.

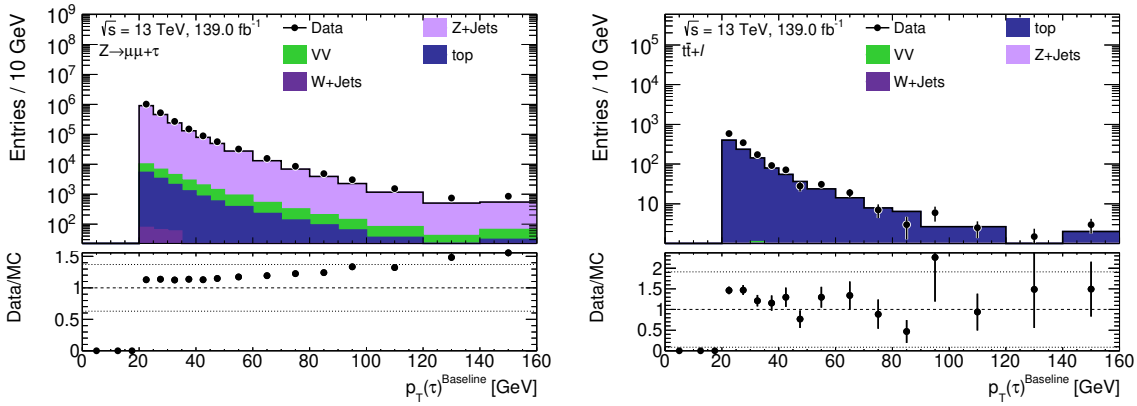

Figure 7.25: Baseline τ-p_{T} distribution in $Z \rightarrow \mu\mu + \tau$ (a) and $t\bar{t} + \tau$ (b) events shown for 139 fb^{-1}of data and simulation. The bottom panel indicates the data to simulation ratio and the error bars show the statistical uncertainties.

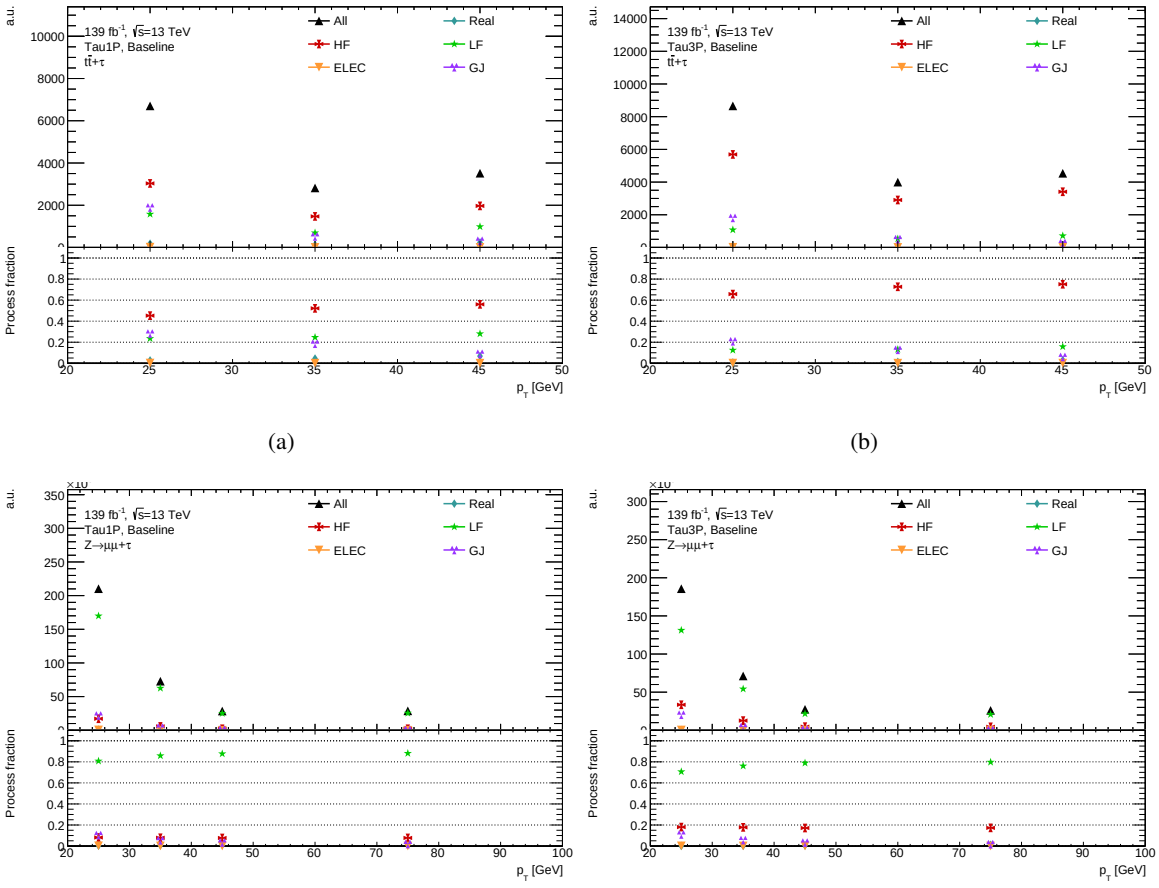

Figure 7.26: Fake process fractions of the probe 1-prong (left) and 3-prong (right) τ leptons in simulated $t\bar{t} + \tau$ (top) and $Z \rightarrow \mu\mu + \tau$ (bottom) events shown as a function of the lepton p_{T}.

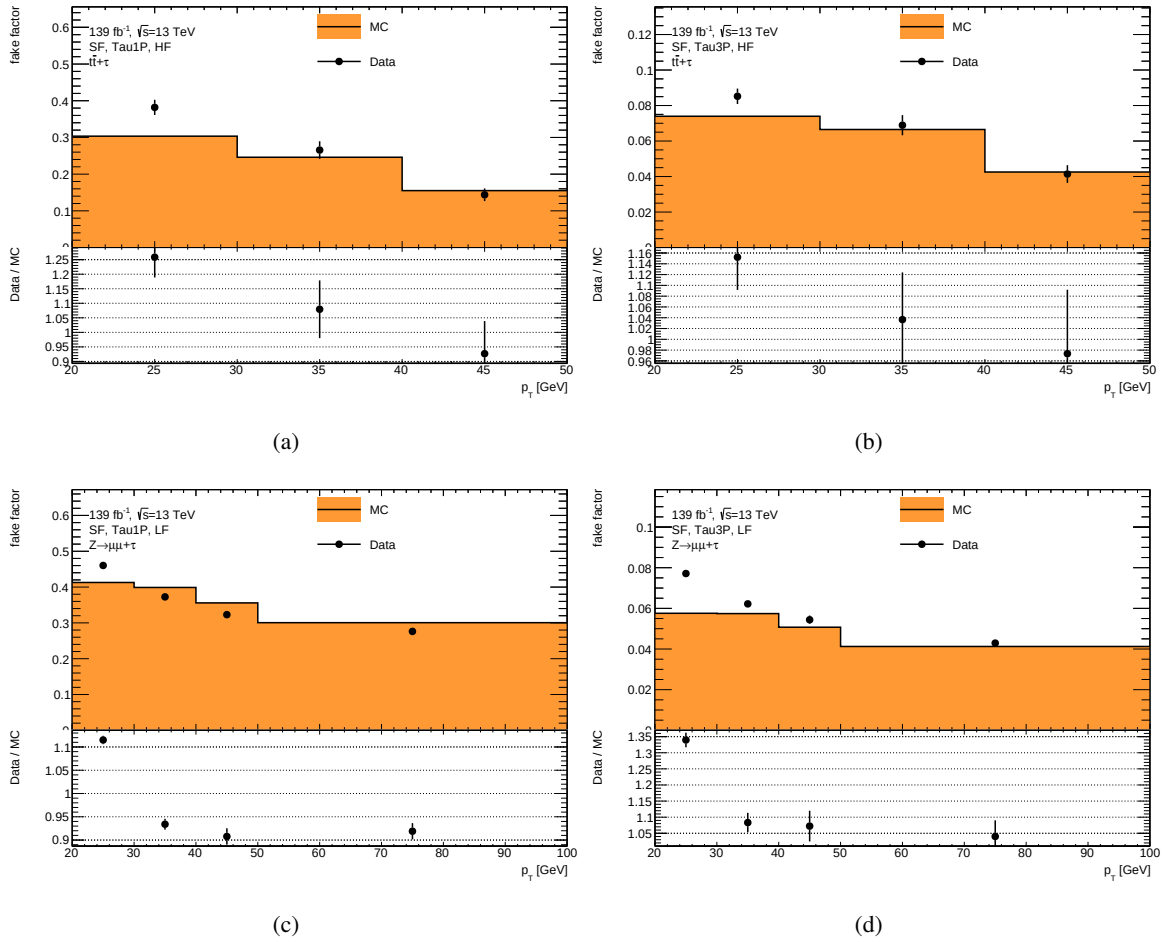

Figure 7.27: Heavy flavor (top) and light flavor (bottom) fake factors for 1-prong (left) and 3-prong (right) τ leptons shown as a function of p_{T} measured in $t\bar{t} + \tau$ and in $Z \rightarrow \mu\mu + \tau$ events, respectively, for simulation and data. The bottom panel shows the ratio of the simulated to the measured fake rate, i.e. the scale factor.

7.4.2 Data Control Regions for ZZ and $t\bar{t}Z$ backgrounds

The large size of the LHC Run 2 dataset opens the possibility to define event selections to measure the rates of rare Standard Model processes contributing to the four-lepton yield. In the course of the developments to improve the analysis between the 36.1 fb^{-1} and the full Run 2 iterations, two additional control regions have been designed to measure the normalization of the two major irreducible background processes, ZZ and $t\bar{t}Z$.

The selection criteria for the two CRs are summarized in Table 7.5. The CR_ZZ is constructed by inverting the requirement on $E_{\mathrm{T}}^{\mathrm{miss}}$ for the SR0E event selection (cf. Figure 7.28(a)). The CR_$t\bar{t}Z$ is constructed from 4L0T with exactly one Z boson candidate and at least one additional b-jet. An additional requirement on $E_{\mathrm{T}}^{\mathrm{miss}} > 100$ GeV significantly suppresses the contamination from ZZ (cf. Figure 7.28(b)). Table 7.6 lists the expected and observed number of events for both CR together with the particular purities. The CR_ZZ region has an excellent purity of 97% in ZZ production. The achieved purity for the $t\bar{t}Z$ background is 65% due to the lower production cross section than for the ZZ background and a larger contamination by fake backgrounds. The normalization factors are extracted from a simultaneous fit of the SM processes (cf. section 7.5.1) to data taking into account the full set of systematic uncertainties using the `HistFitter` framework [332]. The obtained normalization factors are $\mu_{\mathrm{CR}}^{ZZ} = 1.16 \pm 0.02$ and $\mu_{\mathrm{CR}}^{t\bar{t}Z} = 0.95 \pm 0.22$ which are in good agreement with the normalization factors obtained from the approximate calculation using Equation (6.2).

To check that the obtained normalization factors actually improve the modelling, two validation regions, one for each background, are defined whose selection criteria are listed in Table 7.5 as well. The VR_ZZ is orthogonal to the SRs due to requiring exactly one Z candidate in the event. The VR_$t\bar{t}Z$ region is disjoint from the other selections due the upper limit on m_{eff} in the 4L0T with applied Z veto and b selection category. The yields before and after the application of the respective $\mu_{\mathrm{bkg}}^{\mathrm{CR}}$ are also given in Table 7.6 and Figure 7.29 shows the m_{eff} and $E_{\mathrm{T}}^{\mathrm{miss}}$ distributions in VR_ZZ and VR_$t\bar{t}Z$ events, respectively, after the normalization factors are applied. A good agreement between data and simulation is observed for both cases.

Table 7.5: Selection criteria of the control and validation regions for the ZZ and $t\bar{t}Z$ backgrounds on top of the 4L0T requirement

Region	$N_{b-\mathrm{jets}}$	Z boson	Extra selection
CR_ZZ	0	1$^{\mathrm{st}}$ & 2$^{\mathrm{nd}}$ candidate	$E_{\mathrm{T}}^{\mathrm{miss}} < 50$GeV
CR_$t\bar{t}Z$	≥ 1	1$^{\mathrm{st}}$ candidate, veto 2$^{\mathrm{nd}}$	$E_{\mathrm{T}}^{\mathrm{miss}} > 100$GeV
VR_ZZ	0	1$^{\mathrm{st}}$ candidate, veto 2$^{\mathrm{nd}}$	—
VR_$t\bar{t}Z$	≥ 1	veto	$m_{\mathrm{eff}} \in [400; 1300]$ GeV

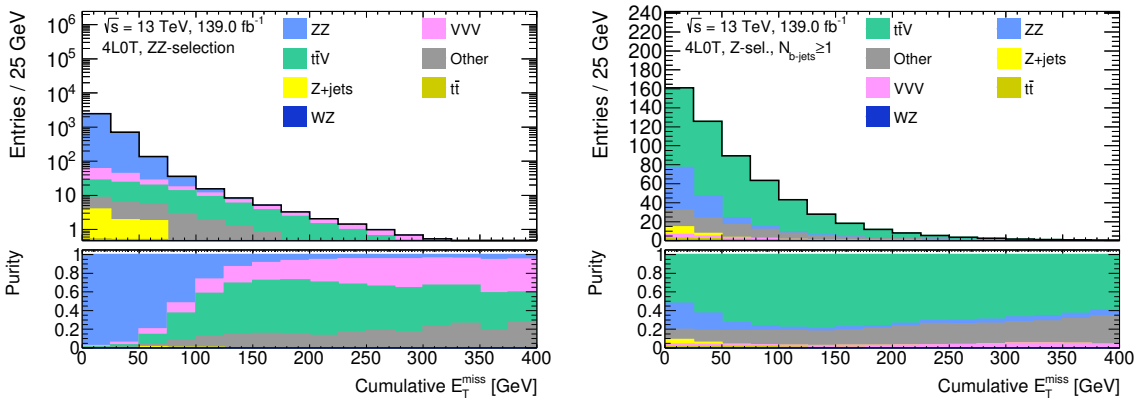

(a) (b)

Figure 7.28: Simulated $E_{\mathrm{T}}^{\mathrm{miss}}$ distribution in 4L0T events with additional ZZ selection (a) applied and with one Z boson candidate and at least one b-jet (b) shown as a function of the lower threshold. The bottom panel shows the contribution of each process to the total background.

Table 7.6: Expected and observed number of events for the control regions to estimate the ZZ and $t\bar{t}Z$ backgrounds and for the respective validation regions. The fake background is estimated using the fake factor method (cf. section 7.4.1) and none of the simulated backgrounds is constrained by a simultaneous fit (cf. section 7.5.1). "Other" is the sum of the tWZ, $t\bar{t}WW$, and $t\bar{t}t\bar{t}$ and Higgs backgrounds. In the case of the VRs, the numbers in brackets indicate the expected yield after the particular background is scaled by the respective $\mu_{\mathrm{bkg}}^{\mathrm{CR}}$. The quoted uncertainties include the experimental uncertainties for the irreducible background and the uncertainties on the fake factors for the reducible background combined each with the statistical uncertainty (cf. section 7.4.3).

	CR_ZZ	CR_$t\bar{t}Z$	VR_ZZ		VR_$t\bar{t}Z$	
ZZ	2153.75 ± 71.90	0.83 ± 0.11	672.82 ± 25.31	(773.74 ± 29.10)	2.41 ± 0.24	(2.77 ± 0.28)
$t\bar{t}Z$	0.46 ± 0.12	31.35 ± 1.24	4.97 ± 0.51	(4.72 ± 0.48)	15.57 ± 0.65	(14.79 ± 0.62)
Other	0.23 ± 0.08	6.92 ± 0.48	4.05 ± 0.31		8.46 ± 0.39	
VVV	21.30 ± 1.02	0.77 ± 0.10	25.64 ± 1.07		0.43 ± 0.06	
Reducible	51.22 ± 23.01	8.70 ± 2.74	76.33 ± 9.88		12.16 ± 3.35	
Total MC	2226.95 ± 76.17	48.56 ± 3.19	783.81 ± 28.42	(884.48 ± 28.46)	39.03 ± 3.52	(38.61 ± 3.52)
Data	2555	47	874		42	
Purity	0.97 ± 0.03	0.65 ± 0.05	0.86 ± 0.02		0.40 ± 0.04	
$\mu_{\mathrm{bkg}}^{\mathrm{CR}}$	1.15 ± 0.03	0.95 ± 0.24	—		—	

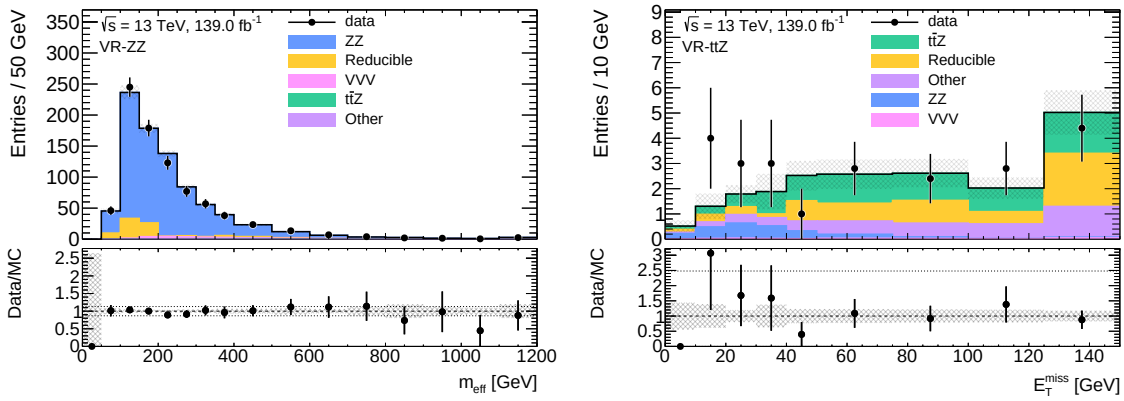

(a) (b)

Figure 7.29: m_{eff} distribution in CR_ZZ (a) events and $E_{\text{T}}^{\text{miss}}$ distribution in CR_$t\bar{t}Z$ (b) events for the full Run 2 dataset and simulation. The normalization factors are applied to the ZZ and $t\bar{t}Z$ backgrounds as listed in Table 7.6. "Other" is the sum of the tWZ, $t\bar{t}WW$, and $t\bar{t}t\bar{t}$ and Higgs backgrounds. The bottom panel shows the ratio of data to simulation. The error bars indicate the statistical uncertainties and the hatched areas indicate the quadratic sum of statistical and experimental uncertainties.

7.4.3 Systematic Uncertainties

Several sources of systematic uncertainties on the background estimate are considered for this analysis which can be divided into *theoretical*, *experimental*, *reducible background* and *statistical* uncertainties as illustrated in Figure 7.30 depicting the breakdown of the systematic uncertainties for both iterations. In the 36.1 fb^{-1} analysis, the sizes of the systematic uncertainties range between 20–32% depending on whether the SR contains τ leptons or not. For the full Run 2 analysis, the uncertainties on the background estimates in the SR range between 20–65%. Each uncertainty component is discussed briefly in the following.

Experimental uncertainties: The experimental uncertainties are evaluated for the irreducible background and each signal model point. They arise from the uncertainties on the calibrations of the momenta and efficiencies of the physics objects, i.e. electrons, muons, τ leptons, jets and $E_{\text{T}}^{\text{miss}}$, on the simulation of pile-up and on the measurement of the luminosity using the LUCID-2 detector [333]. The sources of each uncertainty are described in full detail in Refs. [190, 201, 204, 206, 209, 211] with the muon efficiency measurements being described also in chapter 5. For the 36.1 fb^{-1} iteration the experimental uncertainties related to the charged leptons are around 5% across all SRs. $E_{\text{T}}^{\text{miss}}$ and jet related uncertainties are few percent with the exceptions of the signal regions targeting the GGM scenarios where they rise up to 21%. The uncertainty on the luminosity measurement is evaluated to be 2.1% for the 36.1 fb^{-1} iteration which is improved to 1.7% in the full Run 2 result as described in

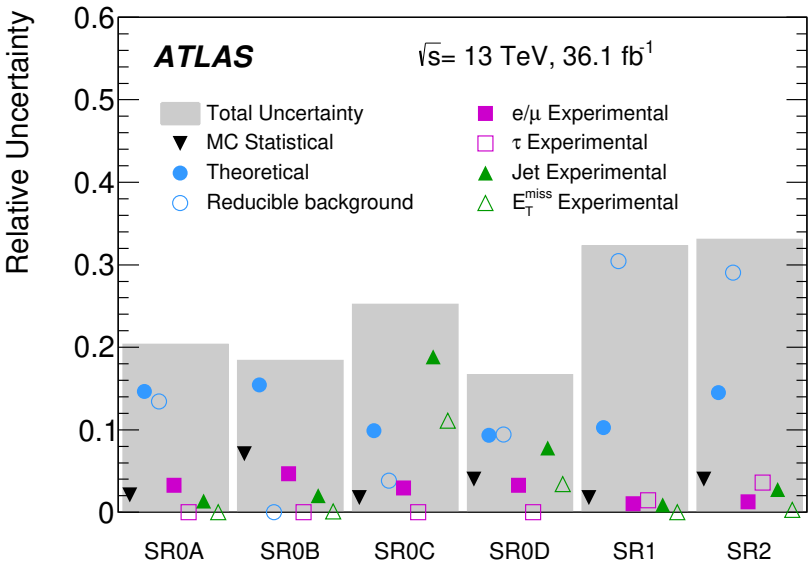

(a)

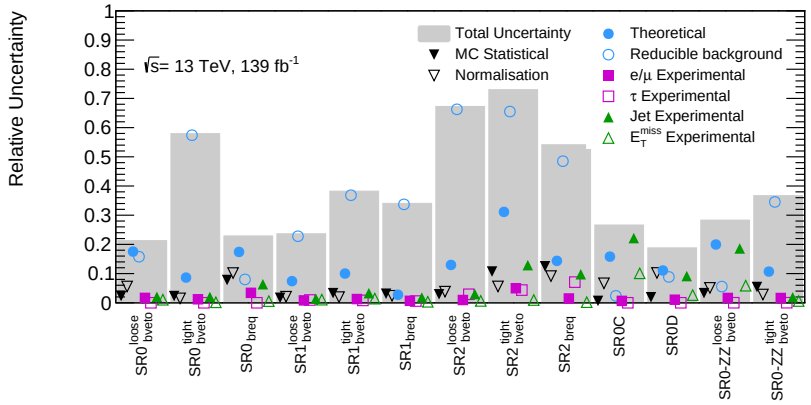

(b)

Figure 7.30: Breakdown of the dominant systematic uncertainties in the background estimates for the signal regions in the 36.1 fb^{-1} iteration (a) and the full Run 2 iteration (b). The individual uncertainties can be correlated, and do not necessarily sum in quadrature to the total background uncertainty [327, 328].

Ref. [334]. In the Run 2 iteration, the uncertainties related to the light leptons are slightly improved to a level of 2–3% for most of the signal regions except for the $\mathrm{SR2}^{\mathrm{tight}}_{b-\mathrm{veto}}$ region where the uncertainty is 5%. Uncertainties related to τ leptons contribute to a similar amount in the τ-rich SRs. Uncertainties on the jets are the dominant experimental uncertainties in the regions targeting the GGM models due to the requirements on $E_{\mathrm{T}}^{\mathrm{miss}}$ and $\mathrm{SR2}^{\mathrm{tight}}_{b-\mathrm{veto}}$.

Theoretical uncertainties: The theoretical uncertainties are calculated for the irreducible backgrounds and the signal models. For the 36.1 fb^{-1} iteration, the two dominant processes $t\bar{t}Z$ and ZZ are considered only. For the full Run 2 iteration, the Higgs, VVV and $t\bar{t}H$ background are included as well. Uncertainties on the total production cross section and on the acceptance of the event selection criteria are the two sources of theoretical uncertainties for a given simulated background. For the signal models, only uncertainties on the production cross section are considered. The former are taken from uncertainties on cross section calculations performed in higher orders of perturbation theory than the order provided by the Monte Carlo generator program. The theoretical uncertainties are the dominant uncertainties in the 36.1 fb^{-1} iteration for the two SR0A and SR0B regions which target the λ_{12k} RPV scenarios. In the full Run 2 iteration, they significantly contribute to the uncertainties in the 2L2T and 4L0T signal region selections.

Uncertainties on the acceptance arise if the shape of the distribution of the discriminating variables depends on the configuration of the Monte Carlo program or on free theory parameters appearing in the calculation such as the renormalization, factorization or resummation scale or on the parton showering model employed. Additionally, the choice on the PDF set or experimental uncertainties on the PDF set measurements or on the measurement of α_S may affect the simulated distributions. All acceptance uncertainties are calculated using generator-level events where the same kinematic selection cuts on the physics objects and on the discriminating variables are employed as on the fully simulated samples. The impact from the choice of the scales on the acceptance is estimated by regenerating the same events with each scale varied separately and/or simultaneously up and down by a factor of two. In a similar way the impact from the knowledge of α_S is assessed by regenerating the events with α_S varied by ± 0.001 from the nominal value. Differences between the expected number of events in the nominal and varied sample are then considered as 1σ uncertainty. Uncertainties originating from the choice on the PDF are estimated by generating dedicated samples using an alternative PDF set and assigning the largest deviation from the nominal sample among the generated variations as 1σ uncertainty. Systematic uncertainties originating from the K experimental uncertainties on the PDF set are estimated by a reweighting procedure of each Monte Carlo event and assigning the standard deviation of the deviations in the expected event yields as uncertainty [101]:

$$\sigma_{\mathrm{SR}}^{\Delta\mathrm{PDF}} = \sqrt{\frac{1}{K}\sum_{i=1}^{K} N_{\mathrm{SR}}^{\mathrm{nominal}} - N_{\mathrm{SR}}^{i^{\mathrm{th}}\ \mathrm{PDF\ variation}}}. \tag{7.14}$$

Table 7.7 summarizes for the irreducible background samples the considered sources of theoretical uncertainties. For the full Run 2 analysis, the uncertainties on the cross sections for the ZZ and $t\bar{t}Z$ backgrounds have been dropped in favour of a data-driven estimate of their normalization factors (cf. section 7.4.2). In the 36.1 fb^{-1} iteration, large uncertainties on the Higgs samples are assigned to

Table 7.7: Summary of theoretical uncertainties considered for the irreducible backgrounds. A "Y" denotes considered and applied, a "*o*" denotes considered but not applied, a "–" denotes not considered. Uncertainties on the cross sections are taken from Ref. [235, 236, 335]. Entries or values marked by † have been only considered for the 36.1 fb^{-1} iteration while ‡ is used to indicate the full Run 2 case.

Background	Cross section	Generator	PDF	α_S	Jet modelling	μ_F	μ_R	$\mu_R \wedge \mu_F$
ZZ	6%†	o	Y†	Y	$Y^{\ddagger}$	Y	Y	Y
$t\bar{t}Z$	12%†	Y†	$o^{\ddagger}$	–	–	Y‡	Y‡	Y
VVV	20%	–	$o^{\ddagger}$	$Y^{\ddagger}$	–	Y‡	Y‡	Y‡
$t\bar{t}H$	100%†/20%‡	o‡	$o^{\ddagger}$	–	–	Y‡	Y‡	Y‡
Higgs (non $t\bar{t}H$)	100%†/20%‡	–	$o^{\ddagger}$	$Y^{\ddagger}$	–	Y‡	Y‡	Y‡
$t\bar{t}WZ/WW$, tWZ	20%	–	–	–	–	–	–	–

conservatively cover not-considered uncertainties on the acceptance. and the nominal $t\bar{t}Z$ sample is compared to an alternative samples using Sherpa as event generator. Deviations between the two samples are considered as a conservative systematic uncertainty. The usage of improved $t\bar{t}Z$ and ZZ samples in the full Run 2 iteration allowed to assess effects from the choice on the renormalization and factorization scale separately and to assess jet modelling uncertainties, respectively. The jet modelling uncertainties are estimated by varying the resummation scale μ_Q and the jet merging scale in the parton showering (CKKW) [120, 244]. μ_Q is varied by factors of quarter and four and the jet merging scale is varied from 20 GeV to 15 GeV and 30 GeV. In addition, the impact of using an alternative recoil scheme for single particle emission in the Sherpa parton showering is estimated by comparing the nominal samples to alternative ones in which the CSS scheme is used (CSSKIN) [241]. In the full Run 2, iteration the uncertainties from the PDF sets are dropped as they are evaluated to be negligible compared to other sources. Also the comparison of two different generator programs are dropped as the alternative generators have been shown to describe data worse than the nominal chosen ones [215, 232, 336]. The uncertainties are separately calculated for each signal, validation and control region and for each background. The Tables for each category can be found in Appendix B.3. In the following, the results are summarized shortly. In the 36.1 fb^{-1} iteration, the uncertainties on the acceptance from the ZZ background are between 6–25% where 3–24% are attributed to scale variations and 5–6% to uncertainties in the PDF sets. For the $t\bar{t}Z$ background, the total uncertainty is between 7% to 21% where variations on the scales contribute by 1–11% and 6–19% arise from the comparison to an alternative generator. To illustrate the change in the uncertainties arising from using the improved NLO $t\bar{t}Z$ sample in the full Run 2 iteration, Figure 7.31 shows the m_{eff} distribution in 4L0T events with applied Z-veto. For the full Run 2 iteration, the uncertainties on the acceptance for the ZZ sample is found to range between 30% to 220%. Uncertainty values exceeding 100% have been found in SR with b-jet requirements or tight cuts on the discriminating variable. For the $t\bar{t}Z$ background, the uncertainties on the acceptance have been found to vary between 12% and 20% with

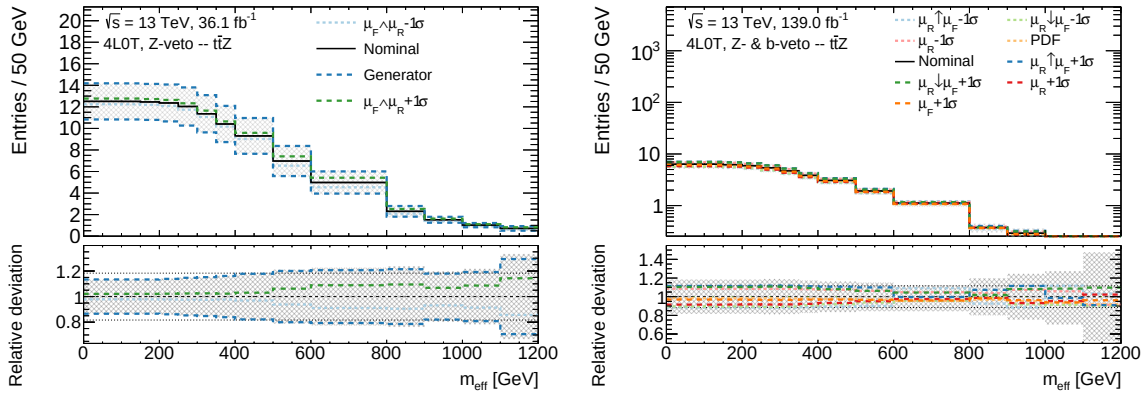

(a) (b)

Figure 7.31: Expected number of events at generator level shown as a function of the lower m_{eff} threshold in the 4L0T category with applied Z-veto using the LO sample $t\bar{t}Z$ sample for the 36.1 fb^{-1} iteration (a) and using the NLO sample for the full Run 2 iteration where a b-veto is additionally applied (b). The eight variations on the theory parameters resulting in the largest uncertainties are shown on the top panel. The lines in the bottom panel indicate the relative deviation of each variation from the nominal prediction. The hatched area shows the total uncertainty by adding all sources in quadrature.

the exception for the $\text{SR1}_{b-\text{req}}$ region where the uncertainty assigns 150%. For the Higgs and $t\bar{t}H$ backgrounds, the uncertainties on the acceptance vary between 30–40% and 14–45%, respectively. Finally, the uncertainties for the VVV background are found to be in the range between 14% and 25%.

Reducible background: for both analyses, the uncertainties on the reducible background dominantly arise from the observed counts in data in the respective loose lepton control regions. Additional sources of uncertainties originate from the statistical uncertainties on the fake and process fractions and on the measured scale factors. The fake factors are applied to data events with one signal lepton and three loose leptons to obtain a conservative estimate from the contribution of the neglected CR3 term in Equation (7.10). The obtained yield is then considered as systematic uncertainty. For the 36.1 fb^{-1} iteration, the neglected term is found to contribute by 0.14, 0.07 and 0.2 events to the total reducible estimate for the SR0A, SR1 and SR2 regions, respectively. For the full Run 2 result, non-vanishing contributions are calculated for the τ-rich signal regions with 0.42, 0.09, 0.03, 1.35 and 0.38 events in the $\text{SR1}^{\text{loose}}_{b-\text{veto}}$, $\text{SR1}^{\text{tight}}_{b-\text{veto}}$, $\text{SR2}^{\text{loose}}_{b-\text{veto}}$ and $\text{SR2}_{b-\text{req}}$ regions, respectively.

For the 36.1 fb^{-1}iteration the uncertainties on the reducible background are the most dominant uncertainties in the τ-rich signal regions and in the full Run 2 result they dominate the systematic uncertainties in most signal regions.

Normalization: This uncertainty is only present in the full Run 2 iteration of the analysis arising from data-driven estimate of the reducible ZZ and $t\bar{t}Z$ backgrounds. The uncertainty component generally has the size of 2–4% and is a subdominant source of the total systematic uncertainty except for the cases where $t\bar{t}Z$ majorly contributes to the background (e.g. in $\texttt{SR0}_{b-\text{req}}$ events). There the uncertainty can contribute as much as 10% to the total systematic uncertainty in the analysis.

Table 7.8: Validation region definitions in the two iterations of the four-lepton analysis. The p_{T} (τ_{had}) column denotes the p_{T} threshold used for the τ lepton selection or veto.

Validation Region	$N(e,\mu)$	$N(\tau_{\text{had}})$	$N(b-\text{jets})$	p_{T} (τ_{had})	Z boson	Selection	Target
36.1 fb^{-1} iteration							
VR0	≥ 4	$= 0$	≥ 0	> 20 GeV	veto	$m_{\text{eff}} < 600$GeV	$t\bar{t}$, Z + jets, ZZ
VR0Z	≥ 4	$= 0$	≥ 0	> 20 GeV	require 1$^{\text{st}}$& veto 2$^{\text{nd}}$	—	ZZ
VR1	$= 3$	≥ 1	≥ 0	> 30 GeV	veto	$m_{\text{eff}} < 700$GeV	$t\bar{t}$, Z + jets
VR2	$= 2$	≥ 2	≥ 0	> 30 GeV	veto	$m_{\text{eff}} < 650$GeV	$t\bar{t}$, Z + jets
Full Run 2 iteration							
$\texttt{VR0}_{b-\text{veto}}$	≥ 4	≥ 0	$= 0$	> 20 GeV	veto	$m_{\text{eff}} < 600$ GeV	$t\bar{t}$, Z + jets, ZZ
$\texttt{VR1}^{Z-\text{veto}}_{b-\text{veto}}$	$= 3$	≥ 1	$= 0$	> 20 GeV	veto	$m_{\text{eff}} < 600$ GeV	$t\bar{t}$, Z + jets
$\texttt{VR2}^{Z-\text{veto}}_{b-\text{veto}}$	$= 2$	≥ 2	$= 0$	> 20 GeV	veto	$m_{\text{eff}} < 600$ GeV	$t\bar{t}$, Z + jets
$\texttt{VR1}^{Z-\text{req}}_{b-\text{veto}}$	$= 3$	≥ 1	$= 0$	> 20 GeV	require 1$^{\text{st}}$	—	Z + jets
$\texttt{VR2}^{Z-\text{req}}_{b-\text{veto}}$	$= 2$	≥ 2	$= 0$	> 20 GeV	require 1$^{\text{st}}$	—	Z + jets

7.4.4 Background Model Validation

Before the data in the SR is unblinded, the full background estimation procedure needs to be validated. For this purpose, dedicated validation regions (VR) are defined which are close to the kinematic selections of the signal regions. For the two iterations of this analysis, Table 7.8 summarizes the selection criteria. The two regions used to validate the normalization of the ZZ and $t\bar{t}Z$ backgrounds have been discussed in section 7.4.2. The three VR0, VR1 and VR2 in the 36.1 fb^{-1} iteration and analogously the $\texttt{VR0}_{b-\text{veto}}$, $\texttt{VR1}^{Z-\text{veto}}_{b-\text{veto}}$ and $\texttt{VR2}^{Z-\text{veto}}_{b-\text{veto}}$ regions in the full Run 2 iteration are constructed by inverting the selection cuts of the SR targeting the RPV models. The VR0Z region is constructed by requiring two SFOS lepton pairs but vetoing the second pair to originate from a Z boson decay. The omitted selection on the $E_{\text{T}}^{\text{miss}}$ allows to test the validity of the background modelling in the high $E_{\text{T}}^{\text{miss}}$ phase space. In the full Run 2 iteration, the successor VR_ZZ is used to test the modelling of the ZZ background. For the τ-rich SR, two further VRs, called $\texttt{VR1}^{Z-\text{req}}_{b-\text{veto}}$ and $\texttt{VR2}^{Z-\text{req}}_{b-\text{veto}}$, are added with a Z boson requirement to thoroughly check the reducible background modelling across m_{eff}.

Validation for the initial analysis: The background validation results in terms of expected and observed yields are reported in Table 7.9. All four VR show a good agreement between the SM expectation and the observed data within the systematic uncertainties. For the τ-depleted regions, ZZ is the dominant background source followed by the reducible background, while for the τ-rich signal regions the reducible background contributes majorly. The slightly larger disagreement between data and prediction in VR1 is found to be attributed to an under fluctuation in data between $m_{\text{eff}} \in [200; 300]$ GeV. Figure 7.32 shows the distribution of the lepton p_{T} in VR0 and VR0Z, the invariant mass of the SFOS lepton pairs in VR0 and $E_{\text{T}}^{\text{miss}}$ in VR0Z events. The lepton p_{T} in VR0 has a decreasing trend in data which is at mostly attributed to the leading electron in the event. However, the high requirements on m_{eff} in the SRs make a significant impact on a mismodelling from a single electron unlikely. The small excess in the invariant mass distribution is found to be attributed to very low p_{T} electron pairs. A good modelling is observed for the variables shown in VR0Z. Figure 7.33 show the light lepton and τ p_{T} in VR1 and VR2 events. A good data to simulation agreement is observed for each of the variables shown.

Table 7.9: Expected and observed yields for 36.1 fb^{-1} in the validation regions. "Other" is the sum of the tWZ, $t\bar{t}WW$, and $t\bar{t}t\bar{t}$ backgrounds. Statistical and systematic uncertainties are included [327].

Sample	VR0	VR0Z	VR1	VR2
Observed	132	365	116	32
SM Total	123 ± 11	334 ± 52	91 ± 19	28 ± 6
ZZ	65 ± 7	234 ± 23	8.8 ± 1.0	3.4 ± 0.5
$t\bar{t}Z$	3.9 ± 0.6	10.5 ± 1.5	1.76 ± 0.25	0.60 ± 0.10
Higgs	5 ± 4	43 ± 37	3.2 ± 2.9	1.3 ± 1.2
VVV	2.9 ± 0.6	16.1 ± 3.4	1.23 ± 0.27	0.29 ± 0.07
Reducible	46 ± 7	28 ± 26	76 ± 19	22 ± 6
Other	0.40 ± 0.07	2.7 ± 0.5	0.34 ± 0.06	0.16 ± 0.04

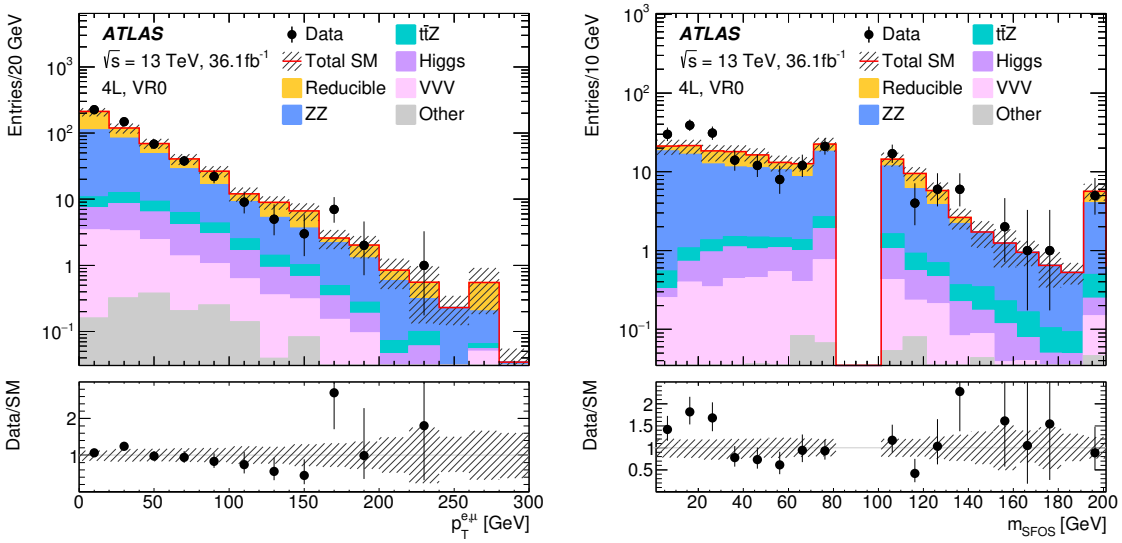

(a) (b)

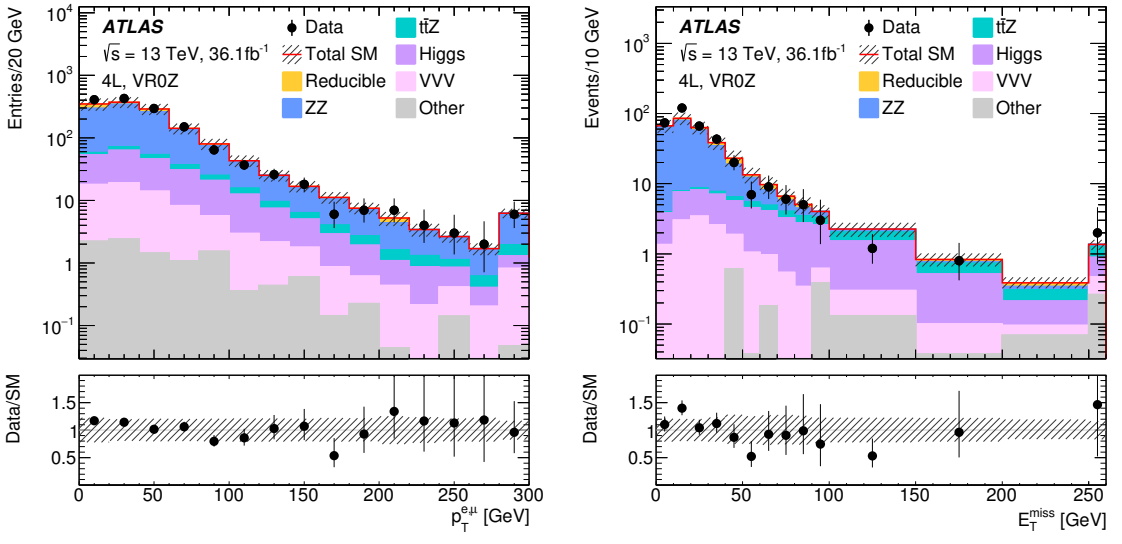

(c) (d)

Figure 7.32: The distributions for data and the estimated SM backgrounds in VR0 (top) and VR0Z (bottom) for the electron and muon p_{T} (left), the SFOS invariant mass (b), and the $E_{\mathrm{T}}^{\mathrm{miss}}$ (d).“Other” is the sum of the tWZ, $t\bar{t}WW$, and $t\bar{t}t\bar{t}$ backgrounds. The last bin includes the overflow. Both the statistical and systematic uncertainties in the SM background are included in the shaded band [327].

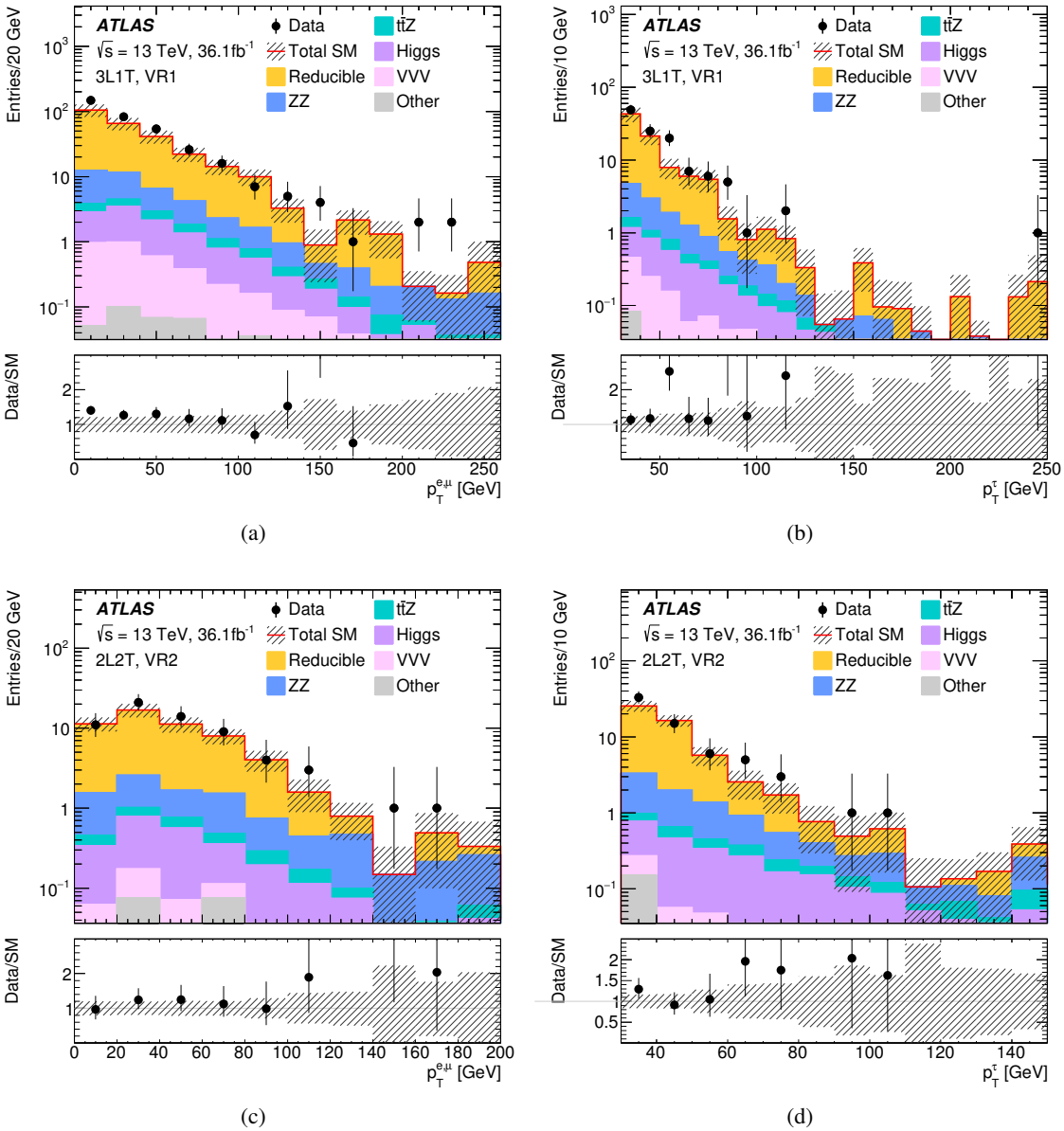

Figure 7.33: The distributions for data and the estimated SM backgrounds in VR1 (left) and VR2 (right) for the light lepton p_{T} (top), and the τp_{T} (bottom). "Other" is the sum of the tWZ, $t\bar{t}WW$, and $t\bar{t}t\bar{t}$ backgrounds. The last bin includes the overflow. Both the statistical and systematic uncertainties in the SM background are included in the shaded band [327].

Validation for the full Run 2 analysis: Despite the reducible estimate, the data-driven irreducible estimate for the ZZ and $t\bar{t}Z$ background is tested in the validation for the full Run 2 analysis as well. The expected and observed yields in the Run 2 validation regions are reported in Table 7.10. A good agreement between the prediction and observation is achieved for all regions considered, where the largest deviation of 1.5σ is seen for $\texttt{VR2}^{Z-\text{req}}_{b-\text{veto}}$.

Table 7.10: Expected and observed yields in the validation regions for the Run 2 dataset. The quoted uncertainties include the systematic and statistical uncertainties. The $t\bar{t}Z$ and ZZ background are constrained from a fit to data using the `HistFitter` framework [332]. The "Other" sample comprises the $t\bar{t}WW$,$t\bar{t}WZ$, $t\bar{t}t\bar{t}$, tZ and tWZ backgrounds.

Sample	$\texttt{VR0}_{b-\text{veto}}$	$\texttt{VR1}^{Z-\text{veto}}_{b-\text{veto}}$	$\texttt{VR1}^{Z-\text{req}}_{b-\text{veto}}$	$\texttt{VR2}^{Z-\text{veto}}_{b-\text{veto}}$	$\texttt{VR2}^{Z-\text{req}}_{b-\text{veto}}$
Observed	216	192	620	156	505
Total SM	229 ± 4	197.8 ± 2.1	613 ± 7	162.3 ± 1.3	472 ± 5
ZZ	160 ± 4	36.8 ± 1.1	200 ± 5	23.3 ± 0.8	119 ± 4
$t\bar{t}Z$	1.7 ± 0.4	0.75 ± 0.2	2.1 ± 0.5	0.3 ± 0.08	0.12 ± 0.03
Higgs	2.9 ± 0.4	0.79 ± 0.15	0.2 ± 0.03	0.42 ± 0.09	0.04 ± 0.01
VVV	5.4 ± 1.1	2.9 ± 0.6	8.7 ± 1.8	1.23 ± 0.25	1.52 ± 0.31
Other	0.43 ± 0.08	0.22 ± 0.05	0.97 ± 0.21	0.12 ± 0.03	0.06 ± 0.02
Reducible	58.8 ± 1.8	156.4 ± 1.8	401 ± 4	136.9 ± 0.8	350.9 ± 2.4

To illustrate the modelling quality achieved in the VRs, Figures 7.34 and 7.35 show the transverse momenta of the leptons in the validation regions targeting RPV scenarios as well as the m_{SFOS} distribution in $\texttt{VR0}_{b-\text{veto}}$ events and the m_{eff} distributions in the τ-rich validation regions requiring a Z boson. In each case, a good modelling of the respective variable shown is observed giving confidence in the reliability of the background model.

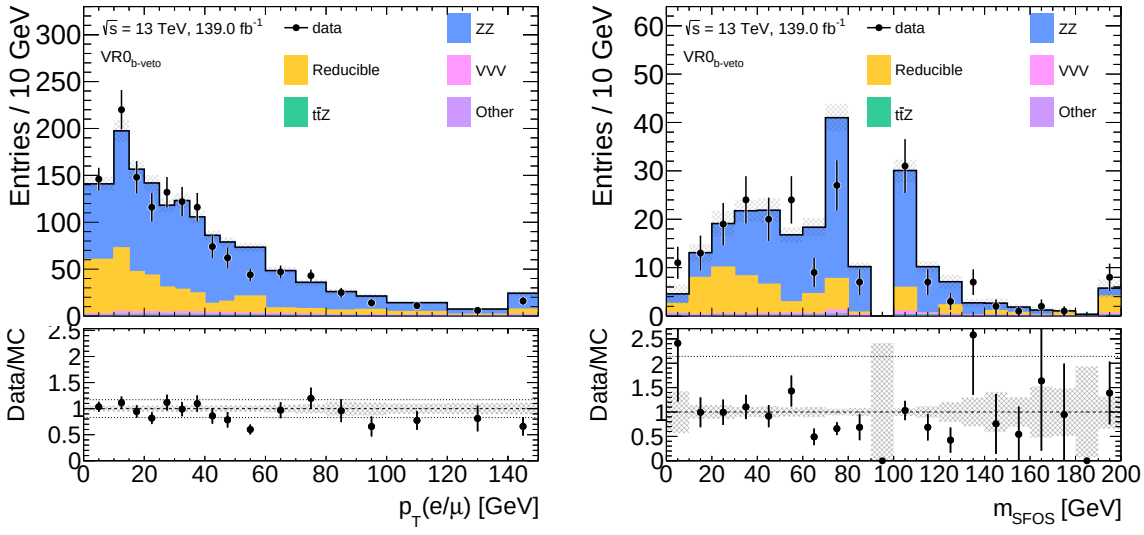

(a) (b)

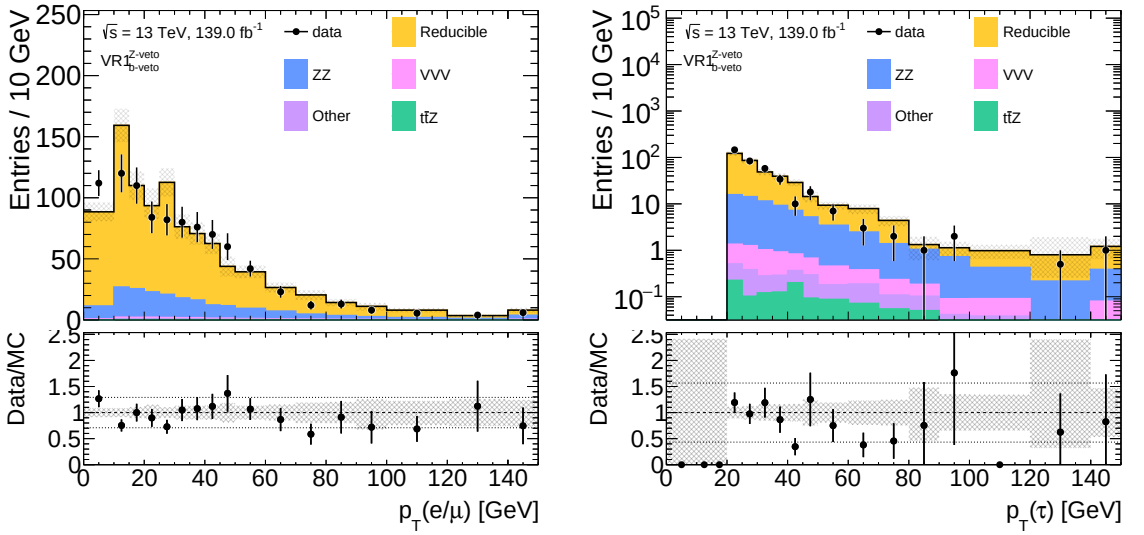

(c) (d)

Figure 7.34: p_{T} distribution of the light leptons (a) and invariant mass distribution of the lepton pair closer to the Z boson mass (b) in $\mathtt{VR0}_{b-\mathrm{veto}}$ events and p_{T} distribution of light leptons (c) and τ leptons (d) in $\mathtt{VR1}^{Z-\mathrm{veto}}_{b-\mathrm{veto}}$ events. "Other" is the sum of the tWZ, $t\bar{t}WW$, and $t\bar{t}t\bar{t}$ and Higgs backgrounds. The hatched bands indicate the quadratic sum of experimental and statistical uncertainties and the error bars indicate the statistical errors only. The bottom panel shows the ratio of data to simulation.

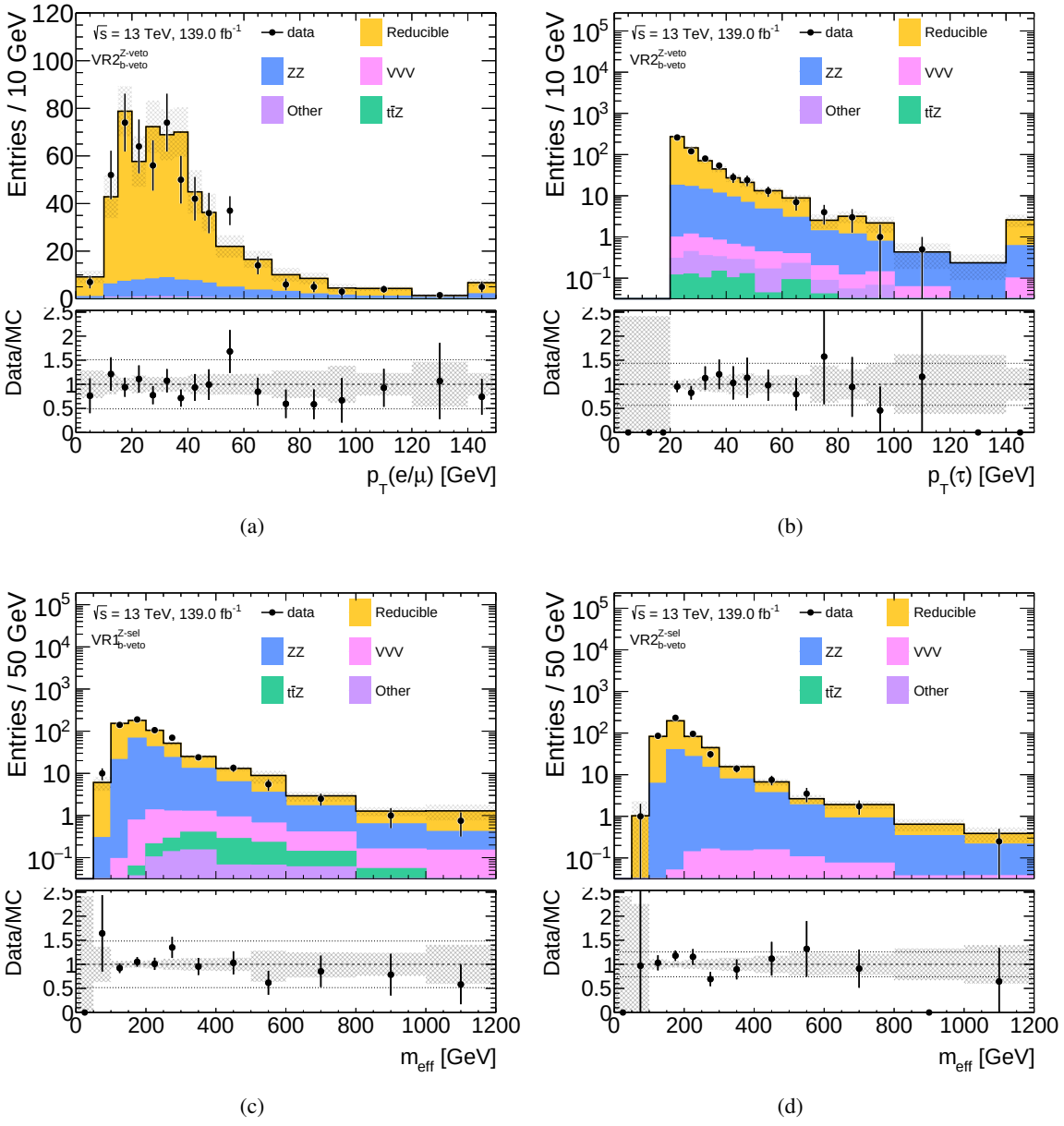

Figure 7.35: p_{T} distribution of the light leptons (a) and τ leptons (b) in $\mathtt{VR2}^{Z-\mathrm{veto}}_{b-\mathrm{veto}}$ events and m_{eff} distribution in $\mathtt{VR1}^{Z-\mathrm{req}}_{b-\mathrm{veto}}$ (c) and $\mathtt{VR2}^{Z-\mathrm{req}}_{b-\mathrm{veto}}$ (d). "Other" is the sum of the tWZ, $t\bar{t}WW$, and $t\bar{t}t\bar{t}$ and Higgs backgrounds. The hatched bands indicate the quadratic sum of experimental and statistical uncertainties and the error bars indicate the statistical errors only. The bottom panel shows the ratio of data to simulation.

7.5 Results of the Four-Lepton Search

The checks on the background modelling presented in the previous section demonstrated a good agreement between the estimates and the data in both iterations. Hence, the data in the signal regions can be unblinded. In this section, the results of the search for Supersymmetry in four-lepton events are presented for both iterations. The observations are interpreted in terms of the simplified models introduced in chapter 6.1. The section is structured as follows: First, the statistical methods to interpret the data are briefly described. Then the results in the 36.1 fb^{-1} iteration are presented together with its statistical interpretation. The section concludes with the discussion of the full Run 2 results.

7.5.1 Statistical Interpretation

The results presented in this thesis have to be statistically interpreted in order to judge whether the observations agree with the SM or evidence for the observation of new physics can be claimed. First, the agreement between the observed data and the SM background-only hypothesis is evaluated. In cases of confirmations of the SM, the signal-plus-background hypothesis is tested for each signal point in order to exclude parts of the free parameter space of the signal model considered. In both tests, the maximum likelihood ratio method [337, 338] is exploited which is discussed briefly in the following. The method and its implementation in the software packages used is documented in full detail in Refs. [246, 332, 339].

The statistical interpretation starts with the formulation of the likelihood function, which can be written in a simplified way as

$$\mathcal{L}\left(N_{\text{data}}|\mu,\boldsymbol{\theta}\right) = \prod_{i\in\text{SR}} \mathcal{P}\left(N^i_{\text{data}}|\lambda = N^{\text{exp}}_i\left(\mu,\boldsymbol{\theta}\right)\right) \prod_{\substack{j\in\text{systematic}\\ \text{uncertainties}}} \mathcal{G}\left(\theta_{ij}|\text{mean} = 0, \sigma = 1\right), \tag{7.15}$$

given the observation of N_{data} events spread across the considered signal regions. The likelihood function is composed of two parts. The first part is the product of the Poisson distributions, $\mathcal{P}\left(N^{\text{data}}_i|\lambda = N^{\text{exp}}_i\right)$, in each SR to model the likelihood of N^{exp}_i which are the expected number of events in each SR as a function of the data. N^{exp}_i is decomposed into the expected number of SM background $b_i\left(\theta\right)$ and of signal events $\mu s_i\left(\theta\right)$ for the signal model considered. Both depend on the nuisance parameter vector θ which takes the systematic and statistical uncertainties on the model into account. Moreover, the signal yield is scaled by the signal-strength parameter μ which is the parameter of interest (PoI) in the statistical interpretation. For $\mu = 0$, the expectation corresponds to the background-only hypothesis and for $\mu = 1$ to the signal-plus-background hypothesis for the particular signal model point. The second part of the likelihood is a product of Gaussian distribution functions with zero mean and unit width which are utilized to constrain the nuisance parameters in the

later fit. In order to evaluate the compatibility of the data with a given μ value the profile likelihood ratio [338],

$$q(\mu) = -2\ln\left(\frac{\mathcal{L}\left(N_{\text{data}}|\mu, \hat{\boldsymbol{\theta}}_\mu\right)}{\mathcal{L}\left(N_{\text{data}}|\hat{\mu}, \hat{\boldsymbol{\theta}}\right)}\right), \tag{7.16}$$

is considered where $\hat{\mu}$ and $\hat{\boldsymbol{\theta}}$ are the parameter values maximizing the likelihood globally, and $\hat{\boldsymbol{\theta}}_\mu$ is the conditional maximum likelihood estimator of $\boldsymbol{\theta}$ for a given μ. Large $q(\mu)$ values correspond to a poor agreement with the data. Depending on whether the background only hypothesis or of the background-plus-signal hypothesis is tested, two different definitions for the test statistic are defined.

For the background-only case, the test statistic is given by

$$t_0 = \begin{cases} q(0) & \text{if } \hat{\mu} \geq 0 \\ 0 & \text{otherwise} \end{cases}, \tag{7.17}$$

where the truncation to zero for $\hat{\mu} < 0$ ensures that downward fluctuations of the data do not serve as evidence to falsely reject the background-only hypothesis. In the current form, an upward fluctuation of the data much beyond the expectations from the signal-plus-background hypothesis would result in a large value of the test statistic and hence the signal hypothesis may be falsely rejected. In order to avoid such rejections, the test statistic used in the exclusion of the free model parameters is defined as

$$t_\mu = \begin{cases} q(\mu) & \text{if } 0 < \hat{\mu} \leq \mu \\ -2\ln\left(\frac{\mathcal{L}\left(N_{\text{data}}|\mu, \hat{\boldsymbol{\theta}}_\mu\right)}{\mathcal{L}\left(N_{\text{data}}|0, \hat{\boldsymbol{\theta}}_0\right)}\right) & \text{if } \hat{\mu} \leq 0 \\ 0 & \text{otherwise} \end{cases}. \tag{7.18}$$

The p-value measures the statistical compatibility of the observed test statistics, t_{obs}, with the tested null hypothesis. For the background-only hypothesis test to discover new particles, it is given by

$$p_b = P\left(t_{\text{obs}} \leq t\right) = \int_{t_{\text{obs}}}^{\infty} dt\, f\left(t|b\right), \tag{7.19}$$

and for the signal-plus-background test to exclude free model parameters by,

$$p_{s+b} = P\left(t_{\text{obs}} \leq t\right) = \int_{t_{\text{obs}}}^{\infty} dt\, f\left(t|s+b\right), \tag{7.20}$$

where $f(t)$ are the probability density functions of the test statistic considered obtained by sampling pseudo experiments. In the limit of a large sampling number, the $f(q)$ can be approximated by asymptotic formulas [338]. In the hypothesis tests for signal model exclusions a confidence level of 95% is commonly used, meaning that the corresponding p-value is below 5%. However, this approach

Table 7.11: Expected and observed yields for 36.1 fb^{-1} in the signal regions. "Other" is the sum of the tWZ, $t\bar{t}WW$, and $t\bar{t}t\bar{t}$ backgrounds. Statistical and systematic uncertainties are included [327].

Sample	SR0A	SR0B	SR0C	SR0D	SR1	SR2
Observed	13	2	47	10	8	2
SM Total	10.2 ± 2.1	1.31 ± 0.24	37 ± 9	4.1 ± 0.7	4.9 ± 1.6	2.3 ± 0.8
ZZ	2.7 ± 0.7	0.33 ± 0.10	28 ± 9	0.84 ± 0.34	0.35 ± 0.09	0.33 ± 0.08
$t\bar{t}Z$	2.5 ± 0.6	0.47 ± 0.13	3.2 ± 0.4	1.62 ± 0.23	0.54 ± 0.11	0.31 ± 0.08
Higgs	1.2 ± 1.2	0.13 ± 0.13	0.9 ± 0.8	0.28 ± 0.25	0.5 ± 0.5	0.32 ± 0.32
VVV	0.79 ± 0.17	0.22 ± 0.05	2.7 ± 0.6	0.64 ± 0.14	0.18 ± 0.04	0.20 ± 0.06
Reducible	2.4 ± 1.4	$0.000^{+0.005}_{-0.000}$	$0.9^{+1.4}_{-0.9}$	$0.23^{+0.38}_{-0.23}$	3.1 ± 1.5	1.1 ± 0.7
Other	0.53 ± 0.06	0.165 ± 0.018	0.85 ± 0.19	0.45 ± 0.10	0.181 ± 0.022	0.055 ± 0.012

has the shortcoming that signal model points with small yields are excluded although the analysis provides small sensitivity to them. To avoid such cases the CL_s technique is used [340] by taking the p-value of the background-only hypothesis also into account:

$$\mathrm{CL}_s = \frac{p_{s+b}}{p_b}. \tag{7.21}$$

The four-lepton search utilizes SRs which are subsets of a more inclusive SR, e.g. SR0D is a subset of SR0C. In order to avoid the usage of overlapping SRs in the statistical interpretation, several likelihoods have to be constructed using only one of the overlapping SR in each case. For each likelihood, the CL_s value is then determined as described above and the result with the most stringent CL_s is taken. In the full Run 2 iteration, the $t\bar{t}Z$ and ZZ backgrounds are normalized to data which is included into the fit by splitting up the expected number of background events in the SR i into the j contributing processes,

$$b_i = \sum_{j \in \text{SM backgrounds}} b_{ij}\, \mu_j^{\mathrm{CR}}, \tag{7.22}$$

and for each of the two irreducible background sources an additional signal strength parameter μ_j^{CR}. The likelihood has then to be extended to include the corresponding background CRs. These parameters are then simultaneously constrained by a fit of the data in all regions [332]. Expected exclusion limits are obtained by the same procedure but using the SM background prediction as data yield.

7.5.2 Observations in the Initial Analysis

The distributions of the discriminating variables used to construct the signal and validation regions in this analysis are shown in Figure 7.36. The lower parts of the three m_{eff} distributions represent

the validation regions for the phase space targeting the RPV models discussed above, where good agreement between the data and the SM prediction is observed. The regions with higher m_{eff} are the signal regions. Again, in all three cases the data follow the SM predictions and thus giving no evidence for a SUSY signal. In the case of the shown $E_{\text{T}}^{\text{miss}}$ distribution, the range $E_{\text{T}}^{\text{miss}} < 50$ GeV is not included in any of the validation regions used for the 36.1 fb^{-1} analysis and shown here only for the sake of completeness. Also in this kinematic regime, an excellent agreement of the data with the SM prediction is observed. The SR0C and SR0D regions generally show a good agreement between data and SM, except for small excesses in the bins with $E_{\text{T}}^{\text{miss}} > 100$ GeV. In order to better evaluate the compatibility between SM expectation and the data, the observed and expected number of events in the signal regions are summarized in Table 7.11. Overall, the deviations in the high $E_{\text{T}}^{\text{miss}}$ range in SR0C and SR0D result in a statistical discrepancy of 1 and 2.3 standard deviations, respectively.

Exclusion limits for the simplified models: Figures 7.37 and 7.38 show the exclusion contours obtained at 95% CL for the three RPV-models considered. For the wino model with active λ_{12k} couplings wino masses of up to $m_{\tilde{\chi}_2^0/\tilde{\chi}_1^\pm} \sim 1.46$ TeV are excluded. The SR0B region is found to usually give the most stringent exclusion limits with few exceptions at low wino masses. The limit is largely independent from whether the $\tilde{\chi}_2^0$ decays to a Higgs boson or a Z boson with the exception where $m_{\tilde{\chi}_1^\pm/\tilde{\chi}_2^0} - m_{\tilde{\chi}_1^0} < m_H$. In this parameter space only the decay into Z bosons of the $\tilde{\chi}_2^0$ is possible. The limit becomes notably weaker if the LSP is lighter than 200 GeV as the collimation between the leptons from the LSP decays becomes stronger leading to a reduced selection efficiency (cf. section 7.3). In the τ-rich RPV scenarios, wino models with masses up to 980 GeV are excluded. These limits are achieved by combining the two orthogonal SR1 and SR2 regions. Similarly to the λ_{12k} case, the limit becomes weaker for low LSP masses for the same reasons and no significant dependence on the $\tilde{\chi}_2^0$ decay mode is observed. The achieved limits improve the previous limits obtained from the four-lepton search on the $\sqrt{s} = 8$ TeV dataset by 400–750 GeV [282]. For RPV scenarios with slepton production, limits on the slepton mass of up to ~ 1.06 TeV and ~ 780 GeV are set if the $\tilde{\chi}_1^0$ decays via active λ_{12k} and λ_{i33} RPV couplings, respectively (cf. Figure 7.38(a)). Similar to the wino model, the limits become weaker if the decaying $\tilde{\chi}_1^0$ is very light compared to the slepton. The exclusion reach in terms of the slepton masses improved by 200–400 GeV compared to the $\sqrt{s} = 8$ TeV analysis [282]. The exclusion contours for RPV scenarios with gluino production are depicted in Figure 7.38(b). Gluinos with masses of up to ~ 2.25 TeV and ~ 1.65 TeV are excluded for the λ_{12k} and λ_{i33} RPV scenarios. This marks an improvement in the excluded mass range of 500–700 GeV compared to previous results [282]. The model-independent limits on the production cross sections are reported in Appendix B.4.

The SRs sensitive to the GGM model are SR0C and SR0D where a higher sensitivity to low higgsino masses is observed by the former and to heavy higgsinos by the latter region. Small excesses of 1σ

and 2.3σ are observed the two regions, respectively. Hence, the observed exclusion limit on the higgsino mass and the $\mathcal{BR}\left(\tilde{\chi}_1^0 \to Z\tilde{G}\right)$ notably differs from the expected limit shown in Figure 7.39. Higgsinos with masses up to 295 GeV are excluded for scenarios with exclusive $\tilde{\chi}_1^0$ decays into Z. The minimal excluded value on $\mathcal{BR}\left(\tilde{\chi}_1^0 \to Z\tilde{G}\right)$ is 58% for low higgsino masses of $\sim$ 120 GeV. The parameter space for scenarios where the $\tilde{\chi}_1^0$ decays more likely into a Higgs boson is covered by a search considering multiple b-jets in the final states [341].

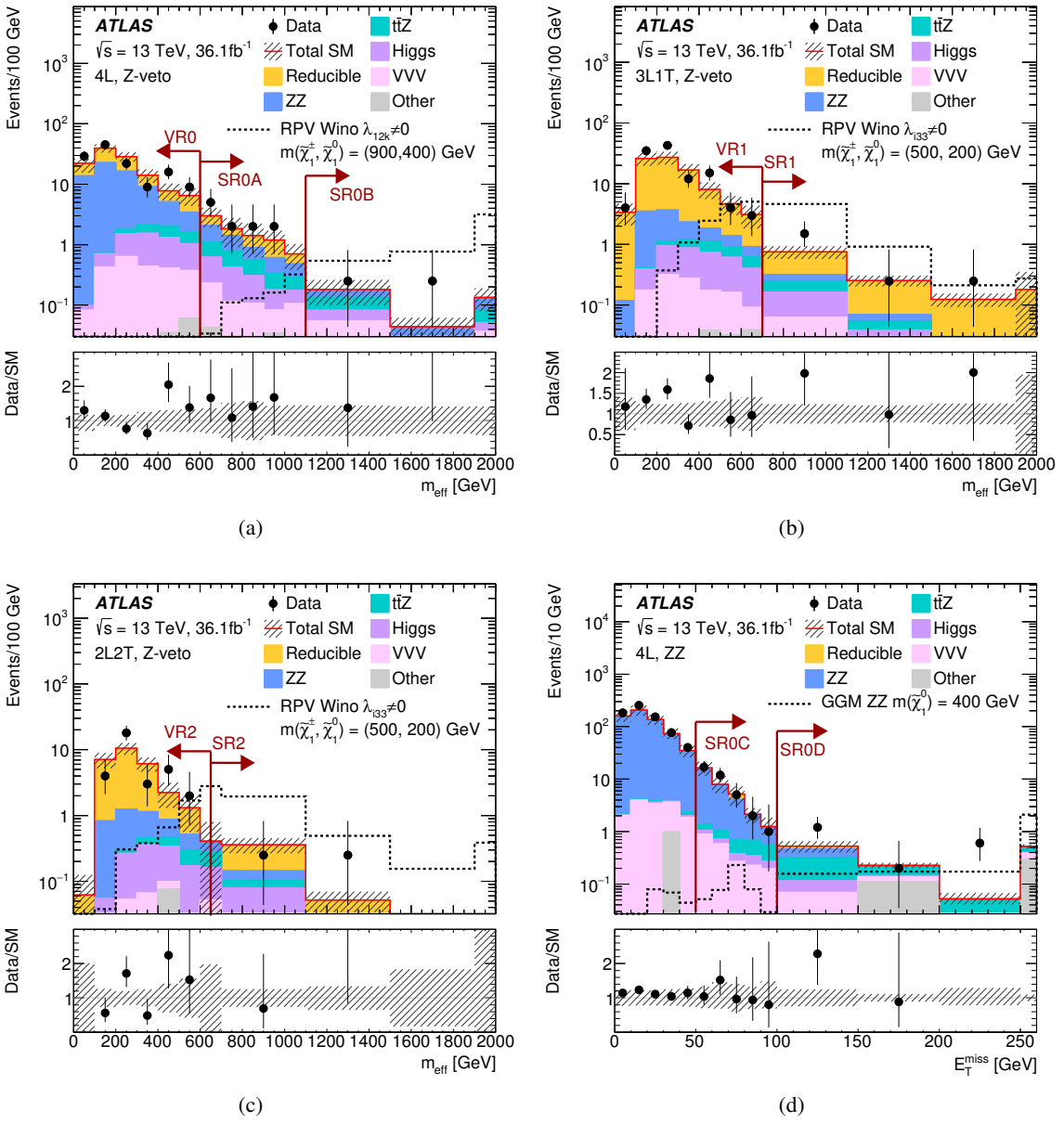

Figure 7.36: m_{eff} distributions in 4L0T (a), 3L1T (b) and 2L2T (c) events each with a Z-veto applied and $E_{\text{T}}^{\text{miss}}$ distribution in events passing the 4L0T and ZZ selection (d). Distributions for data, the estimated SM backgrounds, and an example SUSY scenario are shown. "Other" is the sum of the tWZ, $t\bar{t}WW$, and $t\bar{t}t\bar{t}$ backgrounds. Both the statistical and systematic uncertainties in the SM background are included in the shaded band. The red arrows indicate the m_{eff} or $E_{\text{T}}^{\text{miss}}$ thresholds of the signal and validation regions [327].

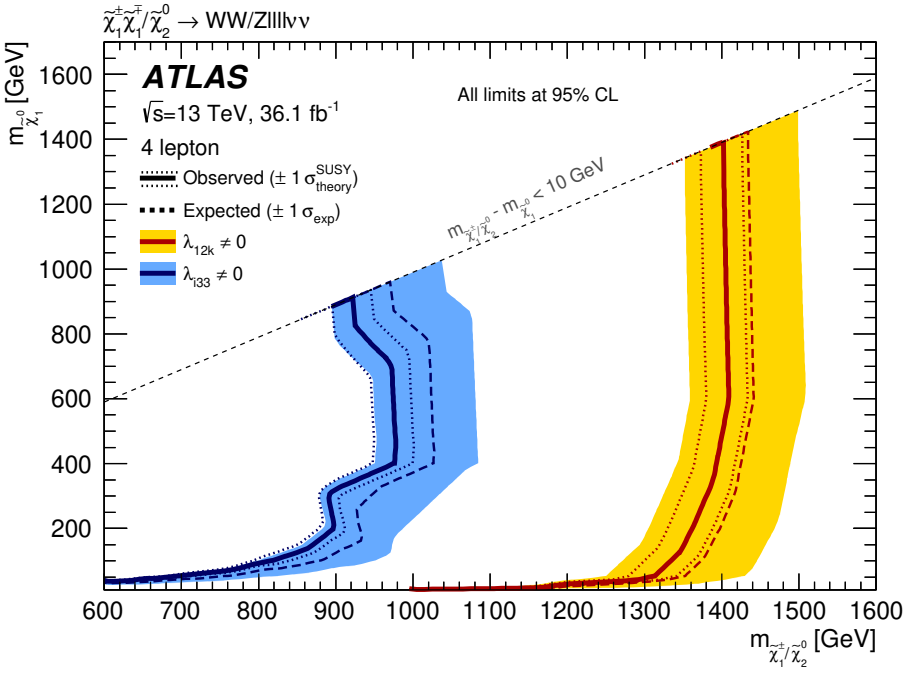

(a)

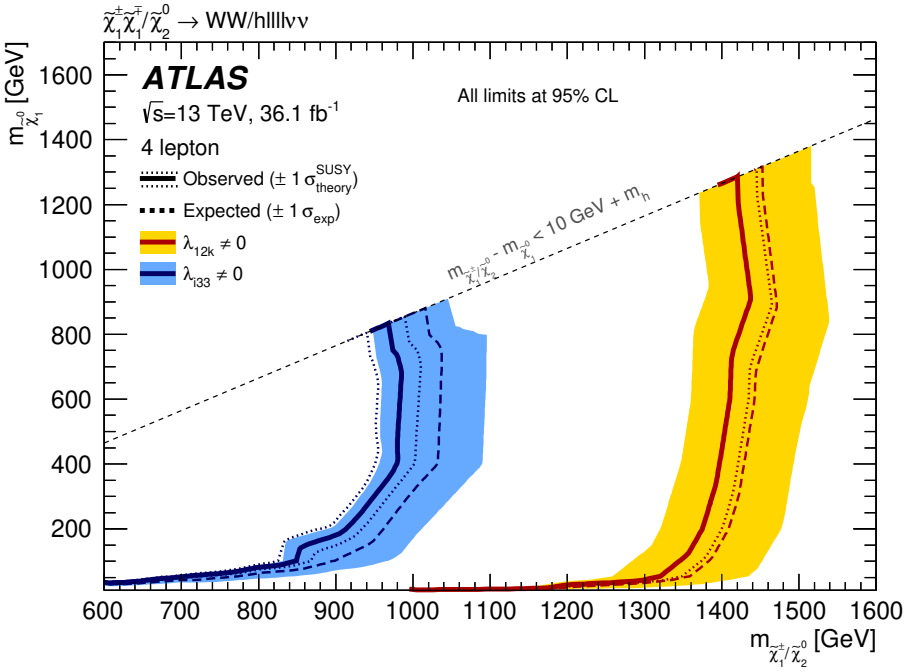

(b)

Figure 7.37: Expected (dashed) and observed (solid) 95% CL exclusion limits on Wino NLSP pair production with $\tilde{\chi}_2^0 \rightarrow \tilde{\chi}_1^0 Z$ (a) or $\tilde{\chi}_2^0 \rightarrow \tilde{\chi}_1^0 h$ (b) and with RPV $\tilde{\chi}_1^0$ decays via λ_{12k} (red) and λ_{i33} (blue) couplings for the initial analysis of 36.1 fb^{-1} of $\sqrt{s}$ = 13 TeV data. The limits are set using the statistical combination of disjoint signal regions. Where the signal regions are not mutually exclusive, the observed CLs value is taken from the signal region with the better expected CLs value [327].

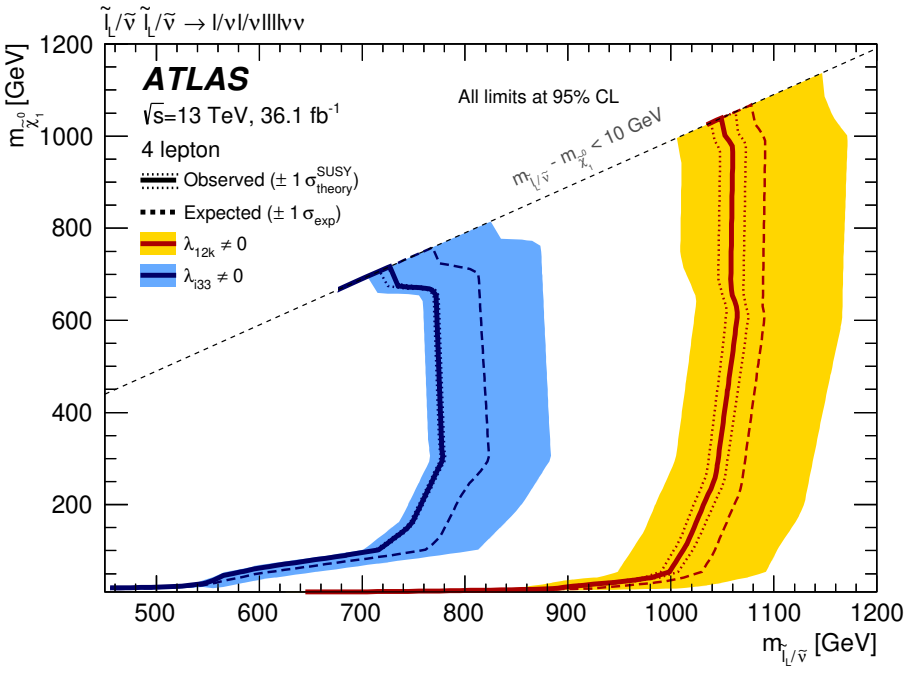

(a)

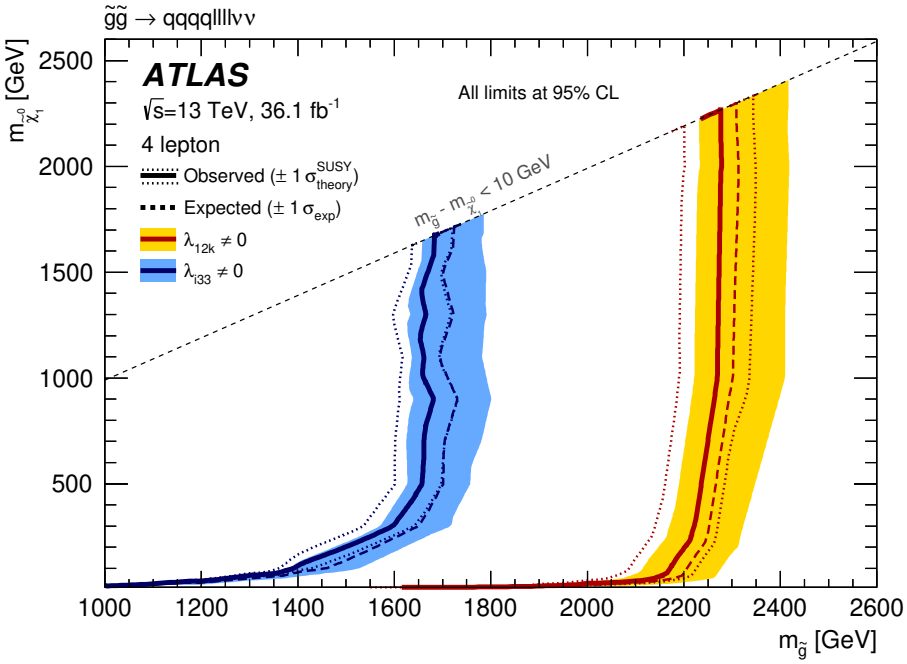

(b)

Figure 7.38: Expected (dashed) and observed (solid) 95% CL exclusion limits on $\tilde{\ell}/\tilde{\nu}$ NLSP (a), and $\tilde{g}$ NLSP (b) pair production with RPV $\tilde{\chi}^0_1$ decays via λ_{12k} (red) and λ_{i33} (blue) couplings for the initial analysis of 36.1 fb^{-1} of $\sqrt{s}$ = 13 TeV data. The limits are set using the statistical combination of disjoint signal regions. Where the signal regions are not mutually exclusive, the observed CLs value is taken from the signal region with the better expected CLs value [327].

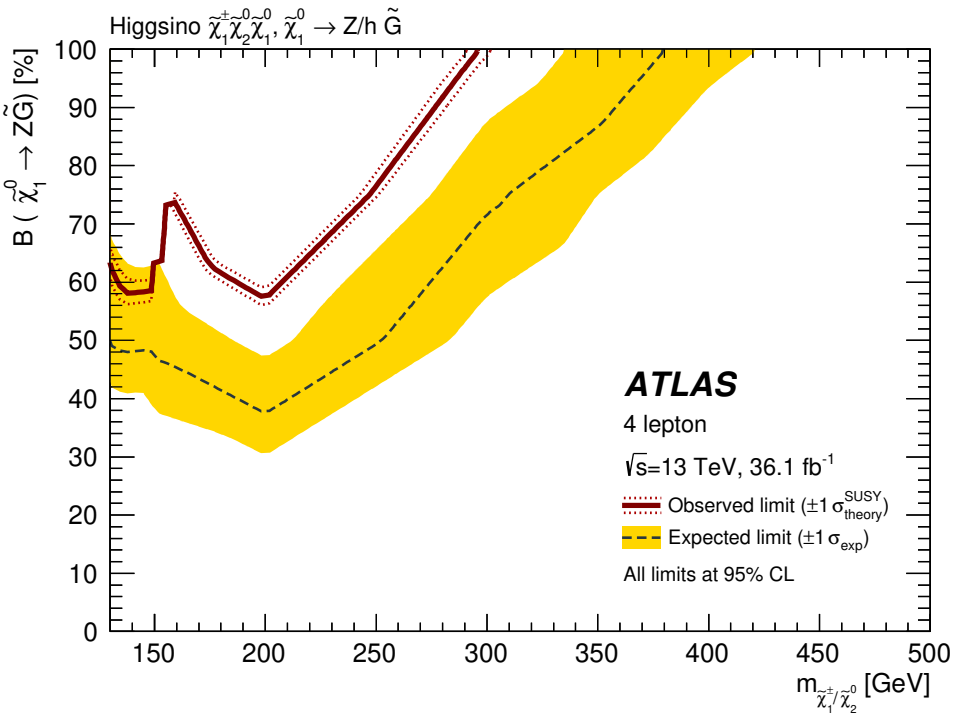

Figure 7.39: Expected (dashed) and observed (solid) 95% CL exclusion limits on the exclusion limits on the higgsino GGM model for the initial analysis of 36.1 fb^{-1} of $\sqrt{s}$ = 13 TeV data. The limits are set using the statistical combination of disjoint signal regions. Where the signal regions are not mutually exclusive, the observed CLs value is taken from the signal region with the better expected CLs value [327].

7.5.3 Observations in the Full Run 2 Analysis

Figures 7.41 and 7.40 show the distributions of the discriminating variables in the 14 signal regions considered in the full Run 2 iteration of the search for Supersymmetry in four-lepton events. As for the 36.1 fb^{-1} iteration, the m_{eff} range below 600 GeV in Figures 7.40(a), 7.40(c) and 7.41(a) and the m_{eff} range below 1300 GeV in Figure 7.40(b) are the adjacent validation regions where a good modelling between data and simulation is observed as discussed in the previous section. In Figures 7.41(b) and 7.40(d), the low m_{eff} range is not considered in any validation region in this analysis and just shown for completeness. In the 2L2T with applied Z veto and b-jet selection, a large mismodelling was observed in the low m_{eff} range attributed to τs with $p_{\text{T}} < 25$ GeV. Therefore, events containing τ leptons with $p_{\text{T}} < 25$ GeV are discarded for this plot. It has been confirmed that this threshold does not affect the background estimate or the observations in $\texttt{SR2}_{b-\text{req}}$. In the SR-like ranges of the m_{eff} the data generally follows the SM prediction. A small excess of two standard deviations is observed for $\texttt{SR2}^{\text{tight}}_{b-\text{veto}}$. In $\texttt{SR0}^{\text{tight}}_{b-\text{veto}}$, the data underfluctuates with one observed event while 3.5 are expected. No hint for Supersymmetry with R-parity violation is neither found in the full Run 2 dataset. The excesses observed earlier in SR0D corresponding to $E_{\text{T}}^{\text{miss}} > 100$ GeV in Figure 7.41(c) disappeared with more accumulated data. In the SR0C and SROC scenario, the data agrees well with the SM prediction across the entire $E_{\text{T}}^{\text{miss}}$ spectrum. Hence, no hint for higgsino production is found in the full Run 2 dataset. The observations for the full Run 2 dataset are summarized in Tables 7.12 and 7.13.

Table 7.12: Expected and observed yields in the 0-τ signal regions for the full Run 2 data. The quoted uncertainties include the systematic and statistical uncertainties. The $t\bar{t}Z$ and ZZ background are constrained from a fit to data using the `HistFitter` framework [332]. The "Other" sample comprises the $t\bar{t}WW$,$t\bar{t}WZ$, $t\bar{t}t\bar{t}$, tZ and tWZ backgrounds.

Sample	$\texttt{SR0}^{\text{loose}}_{b-\text{veto}}$	$\texttt{SR0}^{\text{tight}}_{b-\text{veto}}$	$\texttt{SR0}_{b-\text{req}}$	SR0C	SR0D	$\texttt{SR0-ZZ}^{\text{loose}}_{b-\text{veto}}$	$\texttt{SR0-ZZ}^{\text{tight}}_{b-\text{veto}}$
Observed	11	1	3	157	17	5	1
SM Total	11.4 ± 0.7	3.5 ± 0.7	1.16 ± 0.15	159 ± 19	17.4 ± 1.8	7.2 ± 0.8	1.1 ± 0.14
ZZ	7.65 ± 0.3	0.64 ± 0.07	0.19 ± 0.02	125 ± 19	4.5 ± 0.7	3.7 ± 0.7	0.05 ± 0.01
$t\bar{t}Z$	0.61 ± 0.16	0.02 ± 0.01	0.44 ± 0.11	13.2 ± 3.1	6.6 ± 1.6	0.78 ± 0.2	0.12 ± 0.03
Higgs	0.21 ± 0.04	0 ± 0	0.16 ± 0.04	0.47 ± 0.09	0.23 ± 0.04	0 ± 0	0 ± 0
VVV	1.61 ± 0.33	0.21 ± 0.05	0.08 ± 0.02	7.9 ± 1.6	2.4 ± 0.5	2.1 ± 0.4	0.44 ± 0.1
Other	0.12 ± 0.02	0.03 ± 0.01	0.28 ± 0.04	3.1 ± 0.6	1.63 ± 0.32	0.31 ± 0.07	0.04 ± 0.01
Reducible	1.2 ± 0.5	2.6 ± 0.7	0 ± 0	9.2 ± 1.7	2.1 ± 0.5	$0.17^{+0.2}_{-0.17}$	0.45 ± 0.08

Exclusion limits for the simplified models: The statistical agreement of the data in the signal regions is interpreted in terms of the simplified models considered. Figures 7.42 and 7.43(a) show the expected and observed exclusion limits for the three RPV models. The exclusion limit for the wino model can be improved to 1.65 TeV and 1.15 TeV for the scenarios with active λ_{12k} and λ_{i33}

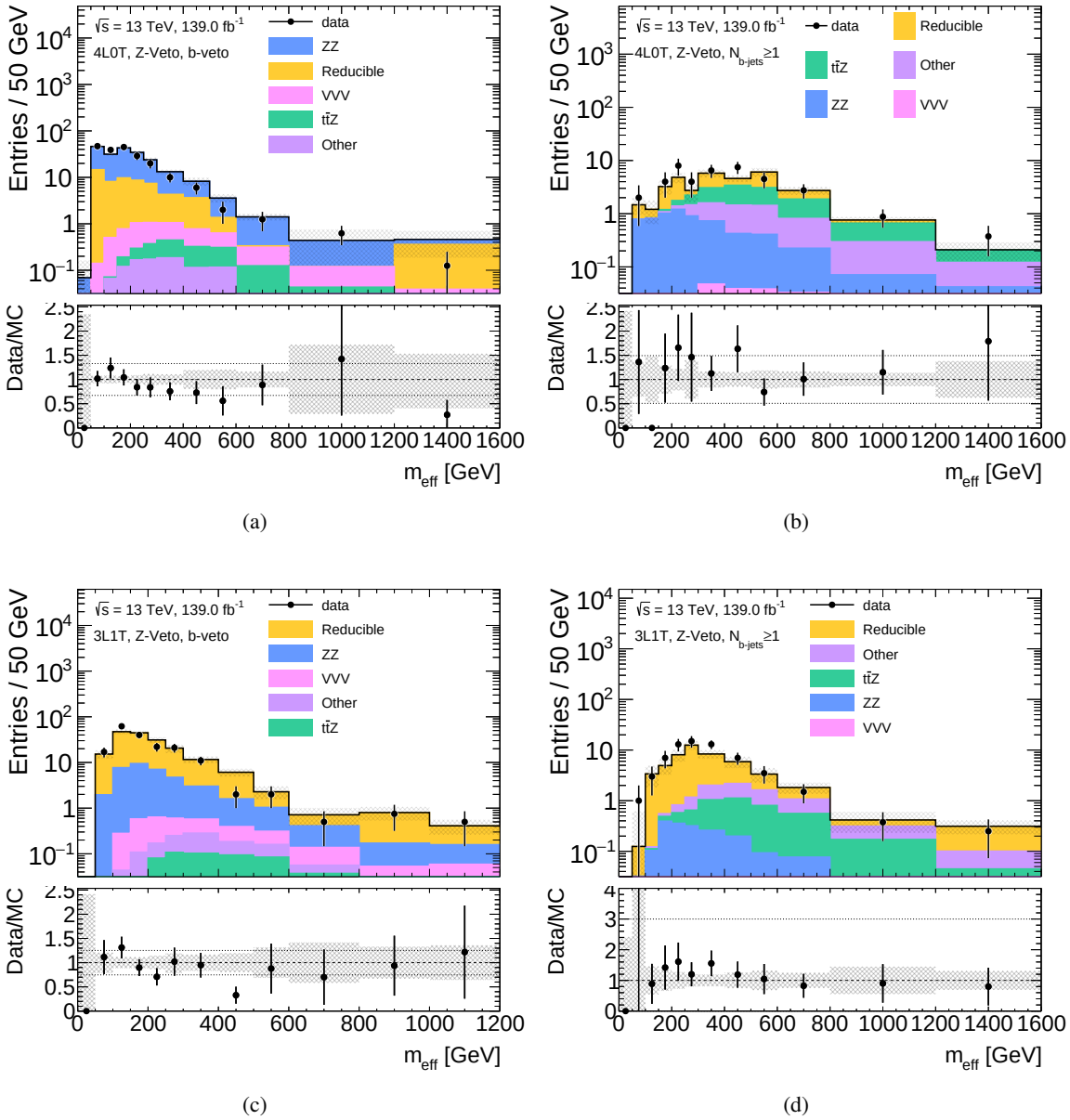

Figure 7.40: Distribution of the effective mass in 4L0T (top) and 3L1T (bottom) events with additional Z-veto once with b-jet veto (left) and once with b-jet selection (right) for the full Run 2 analysis. "Other" is the sum of the tWZ, $t\bar{t}WW$, and $t\bar{t}t\bar{t}$ and Higgs backgrounds. In (b), a τp_{T} threshold of 25 GeV is applied. The hatched bands indicate the quadratic sum of experimental and statistical uncertainties and the error bars indicate the statistical errors only. The bottom panel shows the ratio of data to simulation.

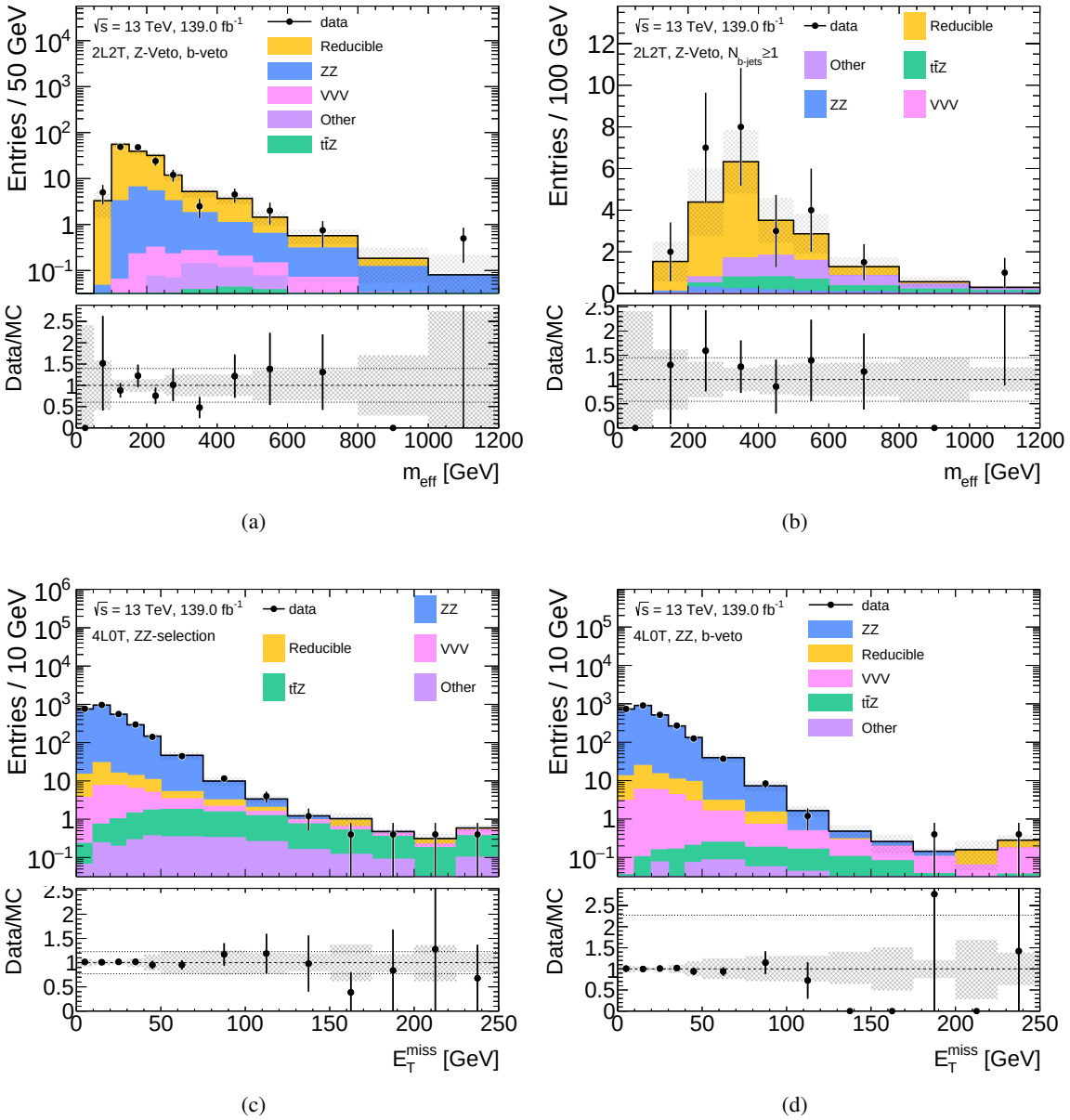

Figure 7.41: Distribution of the effective mass in 2L2T events with additional Z-veto requirement with b-jet veto (a) and with b-jet selection (b) and $E_{\mathrm{T}}^{\mathrm{miss}}$ distribution in 4L0T events with ZZ selection (bottom) and b-jet veto (d) for the full Run 2 analysis. "Other" is the sum of the tWZ, $t\bar{t}WW$, and $t\bar{t}t\bar{t}$ and Higgs backgrounds. The hatched bands indicate the quadratic sum of experimental and statistical uncertainties and the error bars indicate the statistical errors only. The bottom panel shows the ratio of data to simulation.

Table 7.13: Expected and observed yields in the 1–2 τ lepton signal regions for the full Run 2 data. The quoted uncertainties include the systematic and statistical uncertainties. The $t\bar{t}Z$ and ZZ background are constrained from a fit to data using the `HistFitter` framework [332]. The "Other" sample comprises the $t\bar{t}WW$,$t\bar{t}WZ$, $t\bar{t}t\bar{t}$, tZ and tWZ backgrounds.

Sample	$\texttt{SR1}^{\text{loose}}_{b-\text{veto}}$	$\texttt{SR1}^{\text{tight}}_{b-\text{veto}}$	$\texttt{SR1}_{b-\text{req}}$	$\texttt{SR2}^{\text{loose}}_{b-\text{veto}}$	$\texttt{SR2}^{\text{tight}}_{b-\text{veto}}$	$\texttt{SR2}_{b-\text{req}}$
Observed events	7	2	2	5	2	1
SM Total	7.7 ± 0.24	1.64 ± 0.1	2.17 ± 0.11	3.26 ± 0.22	0.33 ± 0.05	0.5 ± 0.09
ZZ	1.97 ± 0.11	0.39 ± 0.04	0.04 ± 0.01	1.54 ± 0.1	0.23 ± 0.03	0.06 ± 0.01
$t\bar{t}Z$	0.17 ± 0.04	0.03 ± 0.01	0.19 ± 0.05	0.04 ± 0.02	0 ± 0	0.17 ± 0.05
Higgs	0.16 ± 0.04	0.02 ± 0.01	0.14 ± 0.03	0.11 ± 0.03	0 ± 0	0.2 ± 0.05
VVV	0.66 ± 0.14	0.16 ± 0.04	0.02 ± 0.01	0.38 ± 0.08	0.08 ± 0.02	0.02 ± 0.01
Other	0 ± 0	0.02 ± 0.01	0.2 ± 0.03	0 ± 0	0 ± 0	0.05 ± 0.01
Reducible	4.73 ± 0.11	1.01 ± 0.07	1.58 ± 0.06	1.18 ± 0.15	0 ± 0	0 ± 0

coupling, respectively. The exclusion contour of the λ_{12K} scenarios is slightly stronger for small mass splittings between NLSP and LSP as the decay of $Z^* \to bb$ is significantly suppressed due to the small available decay phase space. It becomes weaker for $\tilde{\chi}^0_1$ masses below 200 GeV where the decay leptons become strongly collimated. The combination of the $\texttt{SR0}^{\text{tight}}_{b-\text{veto}}$ and $\texttt{SR0}_{b-\text{req}}$ selections gives the most stringent limits to this scenario. The observed exclusion limit for the λ_{i33} scenario is smaller than the expected exclusion limit due to the small observed excess in $\texttt{SR2}^{\text{tight}}_{b-\text{veto}}$. For the RPV models with slepton production the exclusion limits on the slepton masses can be extended to 1.25 TeV (900 GeV) for the λ_{12k} (λ_{i33}) scenario. The signal regions with b-jet requirements are insensitive to the model. For the λ_{i33} scenario, the observed exclusion limit is smaller than the expected limit for the same reason as for the wino model and becomes weaker for small mass splittings between the SUSY particles where the decay leptons from the $\tilde{\ell} \to \tilde{\chi}^0_1 \ell$ becomes too soft. In case of gluino production, gluinos with masses of up to 2.6 TeV and 2 TeV are excluded for the λ_{12k} and λ_{i33} RPV scenarios, respectively.

The observed and expected exclusion contour for the higgsino GGM model is shown in Figure 7.43(b). The exclusion limits in the full Run 2 iteration significantly improve the previous limits from the initial analysis. The exclusion is dominated by the $\texttt{SR0-ZZ}^{\text{loose}}_{b-\text{veto}}$ and $\texttt{SR0-ZZ}^{\text{tight}}_{b-\text{veto}}$ selections for light and heavy higgsinos, respectively. The exclusion reach for higgsinos is between 130–560 GeV if the $\tilde{\chi}^0_1$ decays purely into Z bosons and the gravitino. For $\mathcal{BR}\left(\tilde{\chi}^0_1 \to Z\tilde{G}\right) \simeq 50\%$, the exclusion is weaker covering higgsino masses with 130–400 GeV. The lowest excluded $\mathcal{BR}\left(\tilde{\chi}^0_1 \to Z\tilde{G}\right)$ is at 30% if the higgsino has masses between 130 GeV to 260 GeV.

Model independent limits on the production cross sections for each signal region are reported in Appendix B.4.

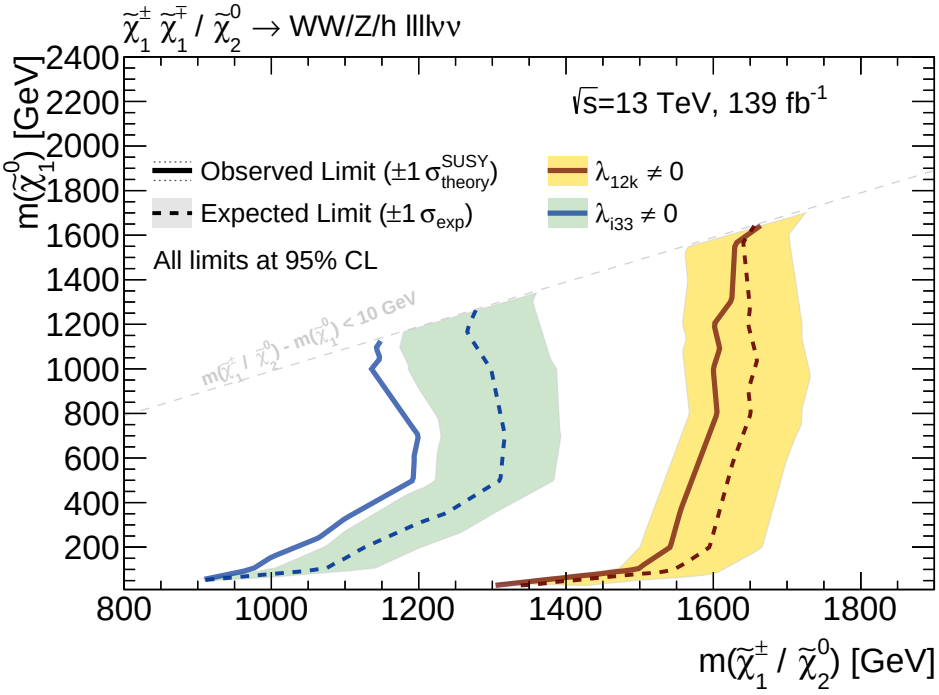

(a)

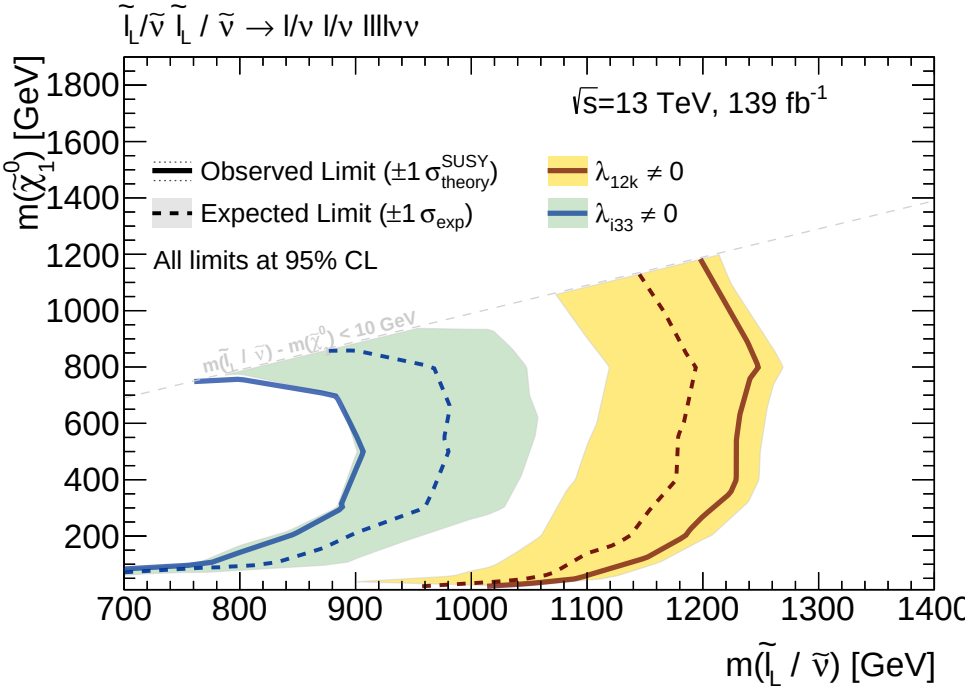

(b)

Figure 7.42: Expected (dashed) and observed (solid) 95% CL exclusion limits on wino (a) and $\tilde{\ell}/\tilde{\nu}$ (b) NLSP pair production with RPV $\tilde{\chi}_1^0$ decays via λ_{12k} (red) and λ_{i33} (blue) couplings for the full Run 2 analysis. The limits are set using the statistical combination of disjoint signal regions. Where the signal regions are not mutually exclusive, the observed CLs value is taken from the signal region with the better expected CLs value [328].

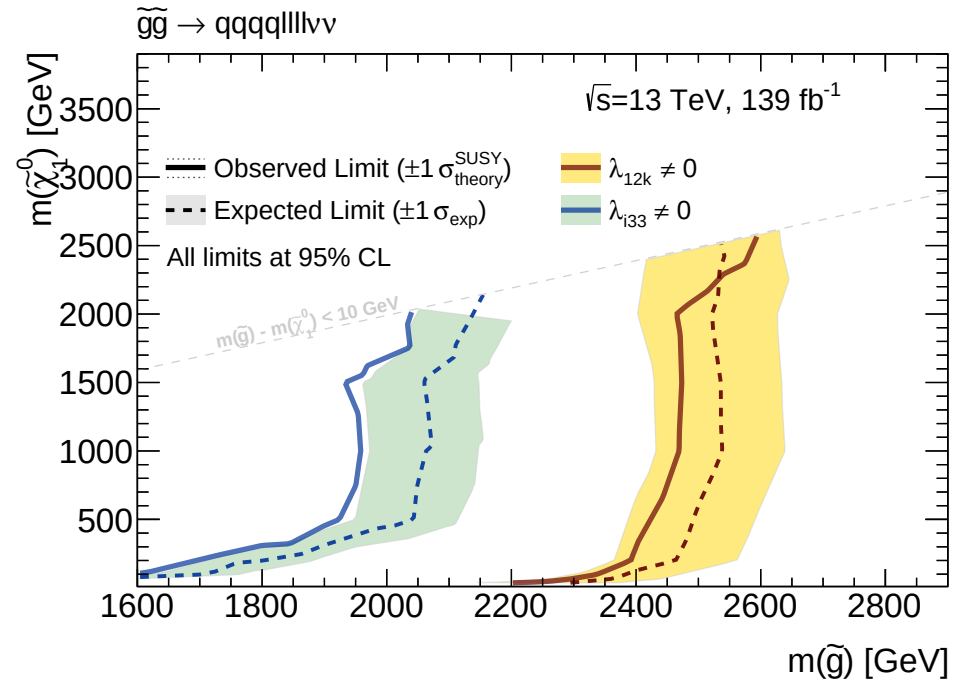

(a)

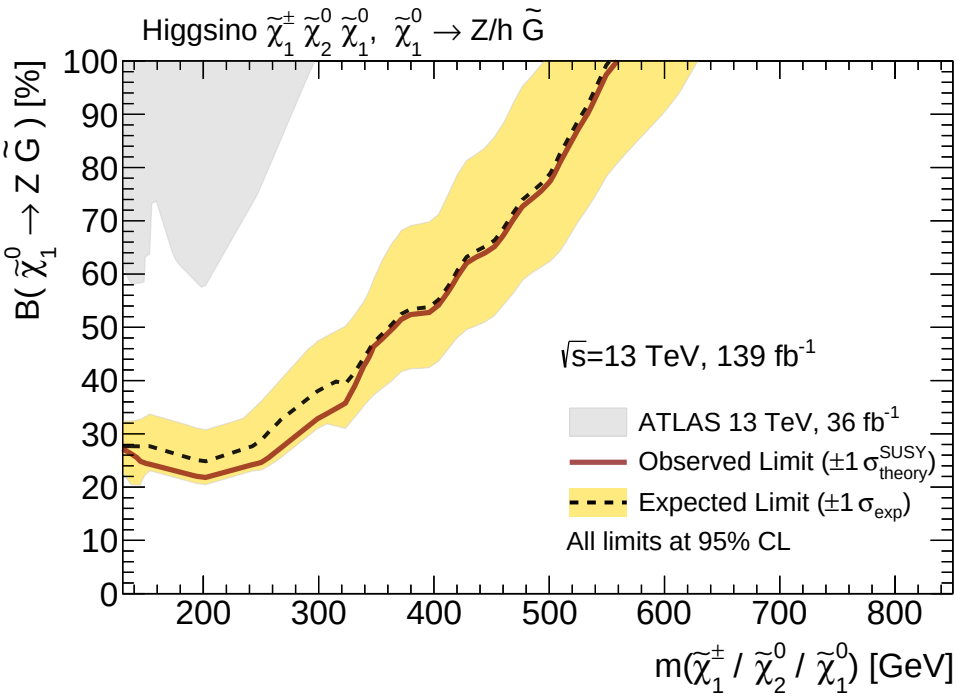

(b)

Figure 7.43: Expected (dashed) and observed (solid) 95% CL exclusion limits on $\tilde{g}$ NLSP pair production with RPV $\tilde{\chi}^0_1$ decays via λ_{12k} (red) and λ_{i33} (blue) couplings (a) and on the higgsino GGM model (b) for the full Run 2 analysis. The limits are set using the statistical combination of disjoint signal regions. Where the signal regions are not mutually exclusive, the observed CLs value is taken from the signal region with the better expected CLs value [328].

CHAPTER EIGHT

SEARCH FOR LIGHT STAU SLEPTONS

8.1 Backgrounds to Di-Tau Final States

As discussed earlier, the search for direct stau production is performed in events with two τ leptons. Figure 8.1 depicts Feynman diagrams of the most important Standard Model background processes giving rise to the same signature. The dominating irreducible SM background processes are Z + jets production with $Z \to \tau\tau$ and VV or VVV events ($V = W, Z$), called multi-boson background, where the vector bosons decay into two τ leptons like $WW \to (\tau\nu)(\tau\nu)$ decays or, $WZ \to (\tau\tau)(\mu\nu)$, where the additional leptons are not reconstructed. Di-leptonic $t\bar{t}$, single top and $H \to \tau\tau$ decays contribute only minorly as the additionally produced b-jets or the invariant mass of the decaying Higgs boson can be efficiently used for their suppression. The reducible background consisting of W + jets events where the jet is misidentified as τ lepton is found to be dominant. In the $\tau_{\text{had}}\tau_{\text{had}}$ channel, multi-jet production events, where both τ leptons are misidentified jets, is also a non-negligible background contribution.

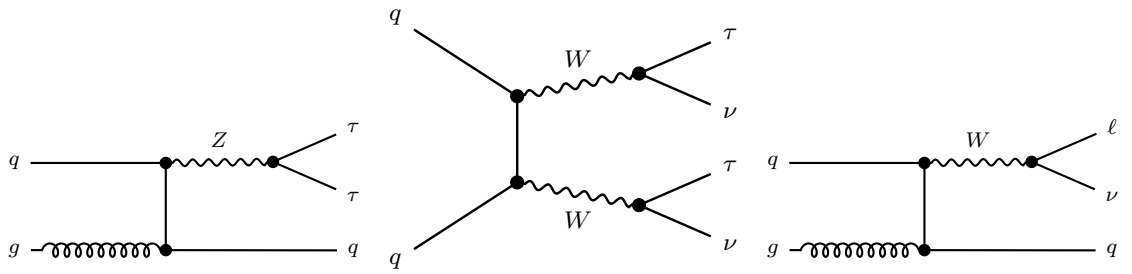

Figure 8.1: Diagrams of the dominant background processes of $Z \to \tau\tau$ (a), WW (b) and W + jets (c) production in the search for direct stau production.

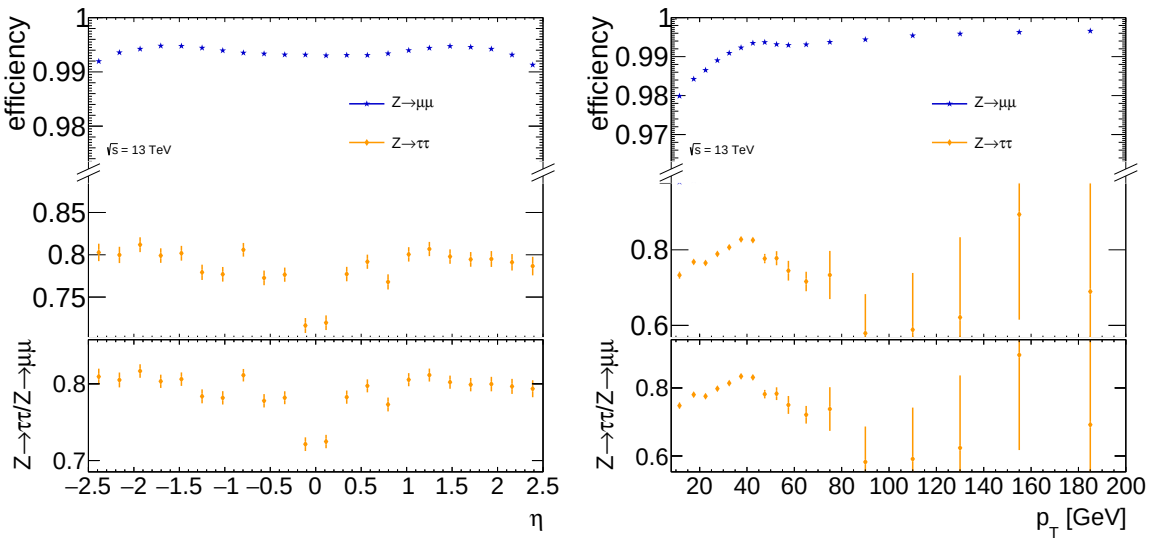

(a) (b)

Figure 8.2: Track-to-vertex-association (TTVA) efficiency in simulated $Z \to \mu\mu$ and $Z \to \tau\tau$ events where both τ leptons decay leptonically into muons using the tag-and-probe method described in chapter 5.6.1 shown as a function of the muon pseudorapidity (a) and the transverse momentum (b). The bottom panel shows the ratio of the TTVA efficiency in $Z \to \tau\tau$ to $Z \to \mu\mu$ events. The error bars indicate the statistical uncertainties.

The di-τ final states are classified according to the τ decay modes into $\tau_{\text{had}}\tau_{\text{had}}$, $\tau_{\text{lep}}\tau_{\text{had}}$ and $\tau_{\text{lep}}\tau_{\text{lep}}$. The background rates and thus the sensitivity differ vastly between these channels. The $\tau_{\text{had}}\tau_{\text{had}}$ channel has a branching ratio of 42%. The two τ-neutrinos produced from the hadronic τ lepton decays prevent a precise calculation of the invariant mass and the decay angles of the τ pair system used to discriminate against e.g. Z + jets background. Nevertheless, the limited mass and angular resolution combined with the fact that the backgrounds also contain hadronically decaying τ leptons or jets misidentified as τs provides enough discrimination power that the $\tau_{\text{had}}\tau_{\text{had}}$ channel is the most sensitive one for the search for direct stau production.

The $\tau_{\text{lep}}\tau_{\text{had}}$ channel has the largest branching ratio of 46%, but the additional neutrino produced in the leptonic τ decay further reduces the resolution in the di-τ mass as discriminant against SM background. In addition, the W + jets background with prompt light leptons from the W decays is larger than the W + jets background with $W \to \tau_{\text{had}}$ decays for the $\tau_{\text{had}}\tau_{\text{had}}$ channel. These electrons and muons have been found to pass the selection described in section 8.2 with higher rate than leptons from leptonic τ decays. The τ lepton has a proper decay length of about 90 μm. As a consequence, the τ decay vertex may be separated from the primary interaction vertex. Although, this decay vertex is not necessarily reconstructed, the impact parameters of the light leptons from the τ decays show larger tensions with the track-to-vertex-association (TTVA) selection. This effect is demonstrated

in Figure 8.2 which compares the TTVA selection efficiency for muons from $Z \to \mu\mu$ and $Z \to \tau\tau$ decays where both τ leptons decay into a muon, exploiting the tag-and-probe method described in section 5.6.1. Muons from leptonic τ decays only pass at a rate of 80% the TTVA selection criteria while the selection for prompt muons from Z is almost fully efficient at a rate of 99%. This drop in selection efficiency becomes larger with increasing lepton p_{T} due to the larger boost of the decaying τ lepton. Thus, the $\tau_{\mathrm{lep}}\tau_{\mathrm{had}}$ channel is affected by larger background rates than the $\tau_{\mathrm{had}}\tau_{\mathrm{had}}$ channel and therefore provides less sensitivity to the signal model. The $\tau_{\mathrm{lep}}\tau_{\mathrm{lep}}$ channel has the smallest branching ratio of 12%. It is contaminated with the largest background, namely from Z + jets and diboson production, such that the sensitivity to direct stau pair production the smallest.

The results presented in the following exclusively use the $\tau_{\mathrm{had}}\tau_{\mathrm{had}}$ channel for these reasons. The main contributions to the direct stau search is the development efficient software for the processing of the large amount of data from the whole Run 2 and validation efforts of the background estimation methods. In addition, multivariate analysis techniques have been developed to also make the $\tau_{\mathrm{lep}}\tau_{\mathrm{had}}$ channel accessible.

8.2 Object and Event Selection

In this section, the selection criteria of the direct stau search are described with focus on the $\tau_{\mathrm{had}}\tau_{\mathrm{had}}$ channel. The prospect studies for the $\tau_{\mathrm{lep}}\tau_{\mathrm{had}}$ channel presented in section 8.4 use slightly different criteria which are explicitly mentioned in the following. The object selection for the direct stau search is performed in three stages, preselection, baseline selection and final signal selection.

Preselected electrons must have $p_{\mathrm{T}} > 17(4.5)$ GeV and $|\eta| < 2.47$ and pass the TightLH (MediumLH) identification criteria [190] in the $\tau_{\mathrm{had}}\tau_{\mathrm{had}}$ ($\tau_{\mathrm{lep}}\tau_{\mathrm{had}}$) analysis. Medium muons are selected for the $\tau_{\mathrm{had}}\tau_{\mathrm{had}}$ channel if they have $p_{\mathrm{T}} > 14$ GeV and $|\eta| < 2.7$. In the $\tau_{\mathrm{lep}}\tau_{\mathrm{had}}$ channel, Loose muons with $p_{\mathrm{T}} > 3.5$ GeV are required at the preselection stage to ensure muons misidentified as τ leptons are maximally rejected at the baseline selection stage. Jets are reconstructed with the anti-k_t algorithm with radius parameter $\Delta R = 0.4$, and calibrated with respect to the electromagnetic energy scale (cf. section 3.7.5) are required to have $p_{\mathrm{T}} > 20$ GeV in the preselection. Hadronically decaying τ leptons with one or three associated ID tracks are required to have $p_{\mathrm{T}} > 20$ GeV and $|\eta| < 2.47$ excluding the calorimeter endcap gap regions $|\eta| \in [1.37; 1.52]$. A minimal cut is applied on the multivariate classifier from a Boosted Decision Tree (BDT) [206] used for the τ lepton identification to reject jet fakes in the $\tau_{\mathrm{had}}\tau_{\mathrm{had}}$ analysis. The development of the τ identification based on a Recurrent Neural Network (RNN) [205] was only completed after the publication of the $\tau_{\mathrm{had}}\tau_{\mathrm{had}}$ analysis. This RNN classifier provides twice the rejection power against jets faking τ leptons than the BDT method and is used for the $\tau_{\mathrm{lep}}\tau_{\mathrm{had}}$ analysis. The different preselected objects may geometrically overlap as they are

Table 8.1: Summary of the overlap removal steps in the direct stau analysis

Step	Remove	With	Condition	Comment
1	electron	electron	shared track	Remove the electron with lower p_{T}.
2	τ	electron	$\Delta R < 0.2$	
3	τ	muon	$\Delta R < 0.2$	
4	electron	muon	shared ID track	Remove the electron if muon is not CT otherwise the muon.
5	jet	electron	$\Delta R_y < 0.2$	
6	electron	jet	$\Delta R_y < 0.4$	
7	jet	muon	$\Delta R < 0.2$	If the jet has less than three associated tracks with $p_{\mathrm{T}} > 500$ MeV
8	muon	jet	$\Delta R_y < 0.4$	
9	jet	τ	$\Delta R_y < 0.2$	In the $\tau_{\mathrm{lep}}\tau_{\mathrm{had}}$ analysis, only the τ leading in p_{T} is considered.

reconstructed by independent particle identification algorithms. To resolve this ambiguity, an iterative overlap removal procedure is applied which is summarized in Table 8.1. All objects surviving the overlap removal are called baseline objects.

At the signal selection stage, additional kinematic requirements and tighter particle identification working points are applied to the objects to ensure a large purity of prompt leptons and best background rejection. The impact parameters of the signal light leptons must satisfy $|z_0 \sin(\theta)|$ <0.5 mm and d_0 <3 (5) for electrons (muons). In addition, the leptons need to pass the FCLoose isolation working point [190]. Signal τ leptons need to pass at least the Medium working point. In the $\tau_{\mathrm{lep}}\tau_{\mathrm{had}}$ analysis and in one of the signal regions in the $\tau_{\mathrm{had}}\tau_{\mathrm{had}}$ analysis, the τ leptons are additionally required to pass the Tight selection criteria which is discussed later. To reject τ candidates originating from pile-up interactions, the associated ID track with the largest p_{T} must satisfy $|z_0 \sin(\theta)|$ <0.75 mm in the $\tau_{\mathrm{lep}}\tau_{\mathrm{had}}$ analysis. Leptons not passing the signal selection are referred to as loose leptons for the remainder. Jets with $p_{\mathrm{T}} < 60$, $|\eta| < 2.4$ and having a substantial fraction of associated tracks from secondary vertices are discarded. Also signal jets must have $|\eta| < 2.8$. Signal jets from b-quark decays are identified using the MV2 algorithm described in section 3.7.5.

The same initial quality selection criteria as in the four-lepton analysis are applied to the candidate events to ensure that they do not contain any badly measured object and that they are recorded under stable beam and detector conditions (cf. section 7.2).

Event selection for the $\tau_{\mathrm{had}}\tau_{\mathrm{had}}$ channel: Candidate events in the $\tau_{\mathrm{had}}\tau_{\mathrm{had}}$ channel are required to have exactly two signal τs with oppositely signed charges (OS). The τ leptons are also required to

Table 8.2: Offline thresholds on the leading and subleading τ transverse momentum and on the $E_{\mathrm{T}}^{\mathrm{miss}}$ in order to match the trigger signatures to the reconstructed objects used in the $\tau_{\mathrm{had}}\tau_{\mathrm{had}}$ analysis

$p_{\mathrm{T}}\left(\tau^{\mathrm{lead}}\right)$ [GeV]	$p_{\mathrm{T}}\left(\tau^{\mathrm{sublead}}\right)$ [GeV]	$E_{\mathrm{T}}^{\mathrm{miss}}$ [GeV]	Year
di-τ + $E_{\mathrm{T}}^{\mathrm{miss}}$ trigger			
50 75	40	150	2015–2017 2018
Asymmetric di-τ trigger			
95	60 75	—	2015–2017 2018

Table 8.3: Selection criteria of $\tau_{\mathrm{lep}}\tau_{\mathrm{had}}$ candidate events. The symbol ℓ refers either to electrons or muons in the channel. For the counting of jets only signal jets with $p_{\mathrm{T}} > 60$ GeV are considered. The term preselection refers to the cuts shared between the 0 jet and 1-jet categories.

	0 jet	1-jet
$N_{\ell}^{\mathrm{signal}}$	=1	
$N_{\tau}^{\mathrm{signal}}$	=1	
$q_{\ell} \times q_{\tau}$	=-1	
Veto 2$^{\mathrm{nd}}$ τ, light lepton or any b-jet		
$m\left(\ell, \tau\right)$ [GeV]	>10	
$E_{\mathrm{T}}^{\mathrm{miss}}$ [GeV]	>15	
$\Delta R\left(\ell, \tau\right)$	<4.5	
$m_{\mathrm{T}}\left(\ell, E_{\mathrm{T}}^{\mathrm{miss}}\right)$ [GeV]	$\notin$ [60; 110]	
N_{jets}	0	≥ 1
$m_{\mathrm{T}}\left(\tau, E_{\mathrm{T}}^{\mathrm{miss}}\right)$ [GeV]	>75	>90
$m_{\mathrm{T}}\left(\ell, E_{\mathrm{T}}^{\mathrm{miss}}\right)$ [GeV]	>20	—

trigger the event. The large rates of background hadrons in the calorimeters necessitate the use of asymmetric di-τ triggers, where a tighter threshold on the p_{T} of the leading τ candidate is applied than on the subleading candidate, and of di-τ triggers in combination with a $E_{\mathrm{T}}^{\mathrm{miss}}$ trigger [330]. Additional thresholds, reported in Table 8.2, on the τ lepton p_{T} and $E_{\mathrm{T}}^{\mathrm{miss}}$ are applied at analysis level to ensure that the trigger is maximally efficient at a level of 75–80%. Due to changing instantaneous luminosity conditions during the data taking, triggers with a tighter τ lepton p_{T} threshold had to be used in 2018. Candidate events containing an additional signal τ or a signal light lepton are discarded. The signal model does not expect any b-jets in the final state. Hence, any event containing a b-jet is discarded to efficiently reduce $t\bar{t}$ background.

Table 8.4: Exploited triggers in the $\tau_{\text{lep}}\tau_{\text{had}}$ analysis. The offline p_{T} thresholds include the additional 1 GeV for electrons, 5% of the online trigger threshold for muons and 5 GeV for τs. Triggers denoted by "or" are used if the instantaneous luminosity exceeds $\mathcal{L} > 10^{-34}$ cm^{-2}s^{-1}. For the combined lepton-tau triggers, the lepton p_{T} must be below the threshold of the corresponding single lepton trigger.

Trigger signature	Offline p_{T} threshold light lepton [GeV]			Offline p_{T} threshold τ [GeV]
	2015	2016	2017–2018	
Isolated electron	25	27	27	—
Non-isolated electron	61	61	61	
Isolated muon	21	25 or 27	27	
Non-isolated muon	42	42 or 53	53	
Combined electron-tau	17	17	17	30
Combined muon-tau	15	15	15	40

Event selection for the $\tau_{\text{lep}}\tau_{\text{had}}$ channel: The candidate event selection is summarized in Table 8.3. Candidate events are required to contain exactly one signal light lepton and one baseline τ with opposite charge to the light lepton. The trigger scheme applied is reported in Table 8.4. The single lepton trigger is used if the p_{T} of the light lepton satisfies the minimum threshold. In order to gain acceptance to signal scenarios with low stau masses where the leptons are softer in p_{T}, the single lepton trigger is complemented by the lepton-tau trigger, if the light lepton does not match the corresponding single lepton trigger signature. Candidate events with an additional signal τ lepton or a baseline light lepton are discarded. Likewise in the $\tau_{\text{had}}\tau_{\text{had}}$ analysis, the event must not have a b-jet to efficiently suppress $t\bar{t}$ background. A loose cut on $E_{\text{T}}^{\text{miss}} > 15$ GeV provides an initial reduction of $Z \to \tau\tau$ background where the transverse momenta of the neutrinos balance to essentially zero missing transverse momentum. Requirements on $m(\tau, \ell) > 10$ GeV ($\ell = e, \mu$) and $\Delta R(\tau, \ell) < 4.5$ suppress multi-jet background. For the signal, it is not expected that energetic jets are produced in the collisions. Therefore, events are further split according to whether they contain energetic signal jets with $p_{\text{T}} > 60$ GeV. In both categories, additional cuts on m_{T} of the leptons are applied to facilitate the optimization of the signal selection using a multivariate classifier which will be discussed in section 8.4.

8.3 Search for Direct stau Production in the $\tau_{\text{had}}\tau_{\text{had}}$ Channel

As discussed in section 8.1, the $\tau_{\text{had}}\tau_{\text{had}}$ channel provides the best sensitivity to direct stau pair production. Hence the results published in Ref. [342] exploit this channel only. The main contributions to this result is the development of the data format and the implementation of the calculation of the variables used to perform this analysis. Further, assistance to validation efforts of the τ-promotion

method [343, 344] was provided. The results of this channel are presented in this section using a structure as follows. First, the signal selection together with the discriminating variables is discussed. The SM model background estimate is then presented afterwards. The validation of the background estimate and the associated systematic uncertainties are then described. The section concludes with the observations in the signal regions and the statistical interpretations of the results in terms of simplified signal models.

8.3.1 Signal Selection

Two signal regions are defined in the search for direct stau pair production, called SR-lowMass and SR-highMass, whose selection criteria are summarized in Table 8.5. The main difference between the two signal regions is the trigger considered. The asymmetric di-τ trigger has been found to provide a larger sensitivity to signal models with low stau masses as large portions of the energy available from the stau decay are already consumed by the requirement on the τ lepton p_{T} to satisfy the trigger selection and leading to smaller missing transverse momenta generated by the $\tilde{\chi}_1^0$. For the SR-lowMass region, both τ leptons have to pass the Tight working point rejecting the multi-jet and W + jets background significantly. For the SR-highMass region, only one τ lepton needs to be Tight as a compromise between a reduced selection efficiency for the SUSY signal and a good rejection against the reducible background. The minimum threshold on $E_{\text{T}}^{\text{miss}}$ to be greater than 75 GeV suppresses $Z \rightarrow \tau\tau$ background which is then further reduced by a cut on the invariant mass of the two τ leptons $m(\tau_1, \tau_2) > 120$ GeV. This requirement also eliminates all contributions from SM Higgs boson production. The requirements on the two angular variables $\Delta R(\tau_1, \tau_2)$, $|\Delta\phi(\tau_1, \tau_2)|$ provide a general rejection against all kinds of SM processes.

Table 8.5: Event selection requirements to define the two signal regions in the $\tau_{\text{had}}\tau_{\text{had}}$ channel of the direct stau search [342]

SR-lowMass	SR-highMass
asymmetric di-τ trigger	di-τ+$E_{\text{T}}^{\text{miss}}$ trigger
2 signal τs passing the Tight WP	2 signal τs , $\geq$ 1 Tight τ
$q_{\tau_1} \times q_{\tau_2} = -1$	
light lepton veto and 3$^{\text{rd}}$ signal τ veto	
b-jet veto	
$75 < E_{\text{T}}^{\text{miss}} < 150$ GeV	$E_{\text{T}}^{\text{miss}} > 150$ GeV
Z/H veto ($m(\tau_1, \tau_2) > 120$ GeV)	
$\|\Delta\phi(\tau_1, \tau_2)\| > 0.8$	
$\Delta R(\tau_1, \tau_2) < 3.2$	
$m_{\text{T2}} > 70$ GeV	

If heavy particles like the W boson decay into a lepton-neutrino pair, the neutrino escapes the detector

giving rise to a significant amount of missing transverse momentum in the event. The missing information about the longitudinal component of the neutrino four-momentum does not allow to fully reconstruct the mass of the W boson. In cases where the W is the only heavy particle decaying into invisible particles, the transverse mass

$$m_{\mathrm{T}}\left(\ell, E_{\mathrm{T}}^{\mathrm{miss}}\right) = \sqrt{2p_{\mathrm{T}}\left(\ell\right) E_{\mathrm{T}}^{\mathrm{miss}}\left[1 - \cos\Delta\phi\left(\ell, E_{\mathrm{T}}^{\mathrm{miss}}\right)\right]}, \tag{8.1}$$

between the lepton and the reconstructed missing transverse momentum is bounded by the W mass and matches if the lepton and neutrino are emitted at same rapidity. In topologies with two heavy particles decaying into one visible and invisible particle each, like the $\tilde{\tau}\tilde{\tau}$ initial state, the total missing transverse momentum is composed of the two transverse momenta of the two invisible particles. The transverse masses calculated from each visible particle, namely the τ leptons, and $E_{\mathrm{T}}^{\mathrm{miss}}$ are no longer bounded by the stau mass. Hence, little information about the initial topology of the stau pair system can be gained using this variable. If the transverse masses of both visible particles are simultaneously calculated where the total missing transverse momentum, $\mathbf{p}_{\mathrm{T}}^{\mathrm{miss}}$, is split into two branches $\mathbf{q}_{\mathrm{T}}$ and $\mathbf{p}_{\mathrm{T}}^{\mathrm{miss}} - \mathbf{q}_{\mathrm{T}}$, corresponding to the transverse momenta of each associated neutrino, there exists at least one non-trivial $\mathbf{q}_{\mathrm{T}}$ for which both transverse masses are smaller than the stau mass. This variable is called the stransverse mass [345, 346], given by

$$m_{\mathrm{T2}} = \min_{\mathbf{q}_{\mathrm{T}}}\left\{\max\left(m_{\mathrm{T}}(\mathbf{p}_{\mathrm{T},\tau_1}, \mathbf{q}_{\mathrm{T}}),\ m_{\mathrm{T}}(\mathbf{p}_{\mathrm{T},\tau_2}, \mathbf{p}_{\mathrm{T}}^{\mathrm{miss}} - \mathbf{q}_{\mathrm{T}})\right)\right\}. \tag{8.2}$$

To demonstrate the discrimination power of the m_{T2} variable, Figure 8.3 shows the background and signal distributions together with the expected significance by applying a minimal cut on this variable.

8.3.2 Background Estimation

Multi-jet background: It is very challenging to simulate multi-jet production accurately. Thus, this background component is estimated from data using an ABCD method as illustrated in Figure 8.4. In the ABCD method, requirements on two sets of largely uncorrelated variables are exploited. It is assumed that the shape of kinematic distributions in multi-jet background in the SRs does not differ significantly from distributions in selections with a same charged τ lepton pair or two loose τ leptons, but the total number of events due to a higher fake rejection rate and a different cross section. For each SR, a CR-A region is defined by applying the same kinematic selection criteria as in the SR, except that the τ pair is required to have either the same charge or to consist of two loose τ leptons. Background contributions from other SM processes than multi-jet are estimated from simulation and subtracted from data in order to obtain the multi-jet component. The purities in multi-jet background

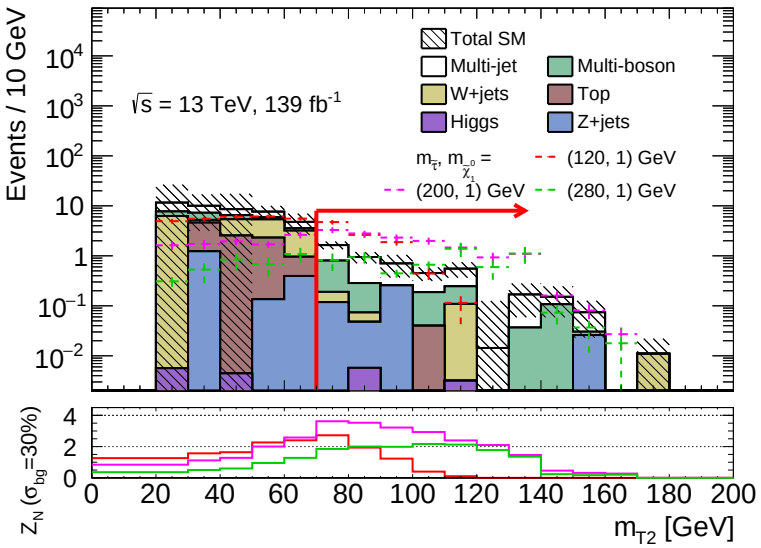

Figure 8.3: m_{T2} distribution in simulated SM background and in three signal reference models passing all event selection criteria listed in Table 8.5 except the criterion on m_{T2}. The bottom panel indicates the achieved significance to each signal model by placing a lower threshold on this variable assuming a background modeling uncertainty of 30%. The hatched areas indicate the statistical uncertainties [347].

are evaluated to 76% and 59% for the lowMass and highMass region, respectively. The multi-jet events are extrapolated by a transfer factor, $\mathcal{T}$, to the SR. For the determination of $\mathcal{T}$, two regions CR-B and CR-D are constructed in analogy to the SR and CR-A, respectively, but selecting events in a different range of m_{T2} and $E_{\text{T}}^{\text{miss}}$ as illustrated in Figure 8.4. In order to reduce the statistical uncertainties on $\mathcal{T}$, no cut on $\Delta R\,(\tau_1, \tau_2)$ is applied. The transfer factor is defined as the ratio of the number of multi-jet events in CR-D to CR-B. The validity of the transfer factor is tested in a phase space distinct from the phase spaces used by the four regions in the ABCD method. The regions VR-E and VR-F are constructed accordingly to CR-A and SR, respectively, with requirements on m_{T2} and $E_{\text{T}}^{\text{miss}}$ such that the selected phase space is adjacent to the phase space of the SR. The multi-jet background in VR-F is estimated by applying the transfer factor to VR-E multi-jet events. The results of the validation are shown in Figure 8.5, illustrating the $E_{\text{T}}^{\text{miss}}$ distributions in the two VR-F regions. In both cases, a good modelling of the data is achieved. The validation regions are also used to determine the systematic uncertainties on the transfer factor which will be later discussed. The multi-jet background obtained by the ABCD method is additionally cross checked against an estimate obtained by using a fake-factor method [348]. Both methods are found to agree with each other within the systematic uncertainties [342, 347].

***W* + jets background:** W + jets production with one misidentified τ lepton contribute to the total background in the signal regions at a level of 25%. This background component is estimated from

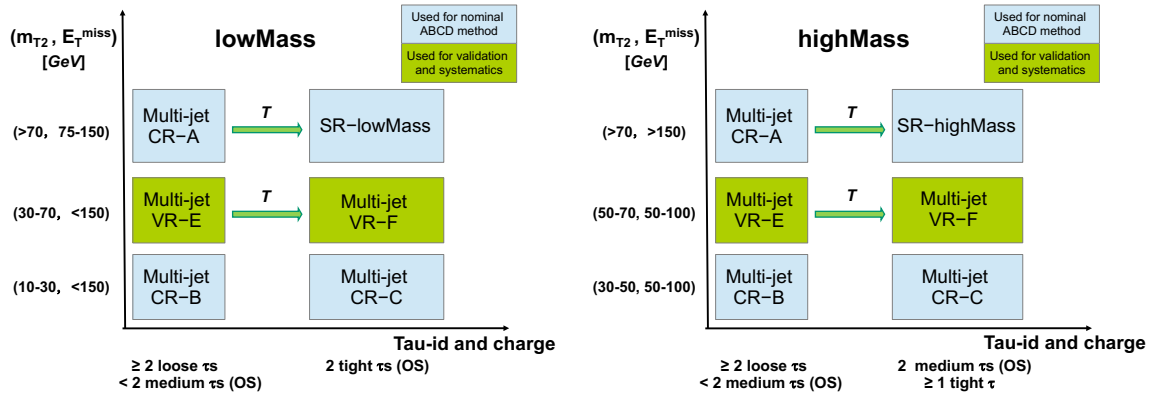

(a) (b)

Figure 8.4: Illustration of the ABCD method for the multi-jet background determination for SR-lowMass (a) and SR-highMass (b). The control regions A, B, C, and signal region D for the ABCD method described in the text (labeled as CR-A, CR-B, CR-C and SR-lowMass/SR-highMass) are drawn as light blue boxes. Shown in green and labeled as VR are the regions E and F, which are used to validate the ABCD method and to estimate the systematic uncertainty [342].

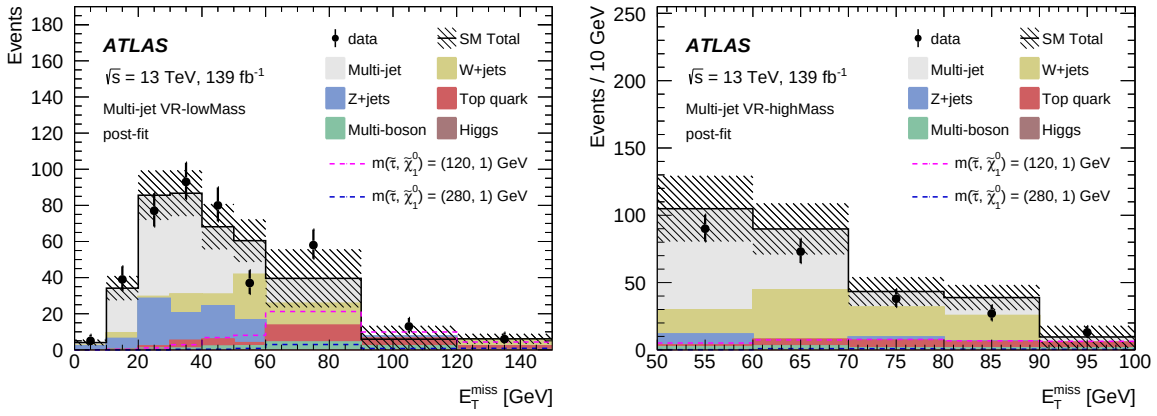

(a) (b)

Figure 8.5: $E_{\mathrm{T}}^{\mathrm{miss}}$ distribution in VR-F events corresponding to the lowMass (a) and highMass (b) signal regions shown for simulation and data. The multi-jet background is estimated by applying the transfer factor to the VR-E events as described in the text. The hatched error areas indicate the combined statistical and systematic uncertainty [342].

simulation using the τ promotion method and then normalized to data in a dedicated control region. The τ promotion method is documented in full detail in Refs. [343, 344] and briefly explained in the following.

In analyses with di-τ final states, W + jets production where the W decays into a hadronically decaying τ can significantly contribute to the SM background. Given that prompt τ leptons are identified at efficiencies ranging between 60–75% for the Medium working point [205] and that hadronic jets fake a τ lepton with a probability of few permille to percent, the production of sufficient simulated Monte-Carlo events to model this background with an acceptable statistical precision would require more computing and disk resources than available to the experiment, making such an estimate unfeasible. The τ promotion method makes better use of the available simulated events containing one prompt signal τ lepton and n fake τ leptons of which k pass the signal τ selection. At random, one of the loose τ leptons is picked and then promoted to be a signal lepton as well. However, this artificial promotion would destroy the normalization of the W + jets background as the fake rate, f, i.e. the probability that a fake τ lepton passes the signal identification requirement, is much smaller than one. Thus, in order not to spoil the normalization of the background, the promoted event has to be reweighted by the weight,

$$\omega = \frac{f}{1-f}\frac{n-k}{k+1} = F\frac{n-k}{k+1}, \tag{8.3}$$

which is the τ lepton fake factor, F, multiplied by the ratio of the number of loose τ lepton candidates before τ-promotion to the number of signal τ candidates after τ-promotion. In the direct stau analysis, the fake factors are parameterized as functions of the τ prongness, the transverse momentum and the missing transverse energy. To illustrate the reduction of the statistical uncertainties in the τ-promotion method, Figure 8.6 depicts the estimate of m_{T2} and $E_{\text{T}}^{\text{miss}}$ in W + jets once with and without using the method. The shape obtained by the τ-promotion method is much smoother and has smaller statistical uncertainties. In phase space regions which are well populated by W + jets containing two signal τ leptons, the agreement between two methods is observed to be at a level of 25% [343] which is considered as systematic uncertainty of the τ promotion method. The relative reduction in the statistical uncertainties is quantified to range between 5–15.

The W + jets estimate is normalized to data in a dedicated control region (WCR) and the normalization is then tested in the WVR validation region. The criteria of the two regions are summarized in Table 8.6. In both cases $W \to \mu\nu$ decays are utilized, where the muon triggered the event containing an additional signal τ lepton with opposite charge to the muon track. The cut on the muon transverse mass selects W decays and rejects Z + jets background. The latter is further reduced by placing minimal thresholds on the invariant mass of the *tau*–muon pair and on $E_{\text{T}}^{\text{miss}}$ of 70 GeV and 50 GeV, respectively. Multi-jet background is rejected by the cut applied on the angular separation between the leptons in the pair. $t\bar{t}$ production is efficiently suppressed by applying the b-veto and the *top-tagged*

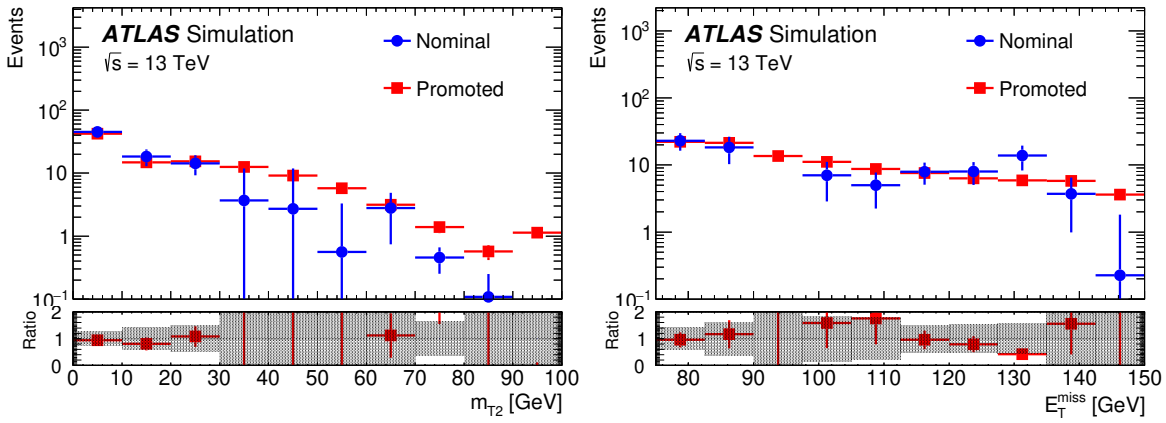

(a) (b)

Figure 8.6: m_{T2} (a) and $E_{\mathrm{T}}^{\mathrm{miss}}$ (b) distributions of simulated W + jets events passing the asymmetric di-τ trigger selection with two Tight τ leptons (Nominal) and with one fake τ lepton promoted as signal (Promoted). The bottom panels show the ratio of the Nominal to the Promoted prediction. The error bars indicate the statistical uncertainties and in the case of the Promoted sample an additional 25% systematic uncertainty [343].

Table 8.6: Summary of selection requirements for the W control (WCR) and validation (WVR) regions [342]

WCR	WVR
1 Medium τ and 1 isolated μ (OS)	
$p_{\mathrm{T}}(\tau) > 60$ GeV, $p_{\mathrm{T}}(\mu) > 50$ GeV	
single-muon trigger	
$m_{\mathrm{T}}\left(\mu, E_{\mathrm{T}}^{\mathrm{miss}}\right) \in [50; 150]$ GeV	
$m(\mu, \tau) > 70$ GeV	
$E_{\mathrm{T}}^{\mathrm{miss}} > 60$ GeV	
$\Delta R(\mu, \tau) \in [1; 3.5]$	
b-jet veto and top-tagged events veto	
$m_{\mathrm{T}}\left(\mu, E_{\mathrm{T}}^{\mathrm{miss}}\right) + m_{\mathrm{T}}\left(\tau, E_{\mathrm{T}}^{\mathrm{miss}}\right) > 250$ GeV	
$m_{\mathrm{T2}} \in [30; 70]$ GeV	$m_{\mathrm{T2}} > 70$ GeV

events veto [349, 350] which identifies events which are kinematically compatible with $t\bar{t}$ production exploiting the contra-transverse mass variable between two particles a and b given by

$$m_{\text{CT}}\left(p^a, p^b\right) = \sqrt{2p_{\text{T}}(a)\,p_{\text{T}}(b)\,[1+\cos\Delta\phi(a,b)]}. \tag{8.4}$$

Remaining processes containing top quarks are discarded by applying a cut on the sum of the transverse masses of the muons and the τ leptons to be greater than 250 GeV. The two regions then differ between each other by the selection on m_{T2}. The WCR and WVR are pure in W + jets events at a level of around 79% and 71%, respectively [347].

Table 8.7: Summary of selection requirements for top quark (TVR), Z+jets (ZVR) and multi-boson (VVVR) validation regions [342]

Selections	TVR -lowMass	ZVR -lowMass	VVVR -lowMass	TVR -highMass	ZVR -highMass	VVVR -highMass
	≥ 2 signal τs, ≥ 1 tight tau					
	≥ 1 b-jet	b-jet veto		≥ 1 b-jet	b-jet veto	
$m(\tau_1,\tau_2)$	–	< 70 GeV	< 110 GeV	–	< 60 GeV	< 110 GeV
$\Delta R(\tau_1,\tau_2)$	> 1.2	< 1	–	> 1.2	< 1	–
$m_{\text{T},\tau_1} + m_{\text{T},\tau_2}$	–	–	> 250 GeV	–	–	> 200 GeV
m_{T2}	> 60 GeV	< 60 GeV	> 60 GeV	> 60 GeV	< 60 GeV	> 60 GeV
Trigger	asymmetric di-τ trigger $60 < E_{\text{T}}^{\text{miss}} < 150$ GeV			di-τ+$E_{\text{T}}^{\text{miss}}$ trigger $E_{\text{T}}^{\text{miss}} > 150$ GeV		

Irreducible background: The irreducible processes Z + jets and $t\bar{t}$ make up together about 8% and 20% of the total background in the SR-lowMass and SR-highMass selections, respectively. Multi-boson processes are estimated to contribute to the background at a level of about 23–25%. All three processes are estimated using simulation. It is checked that the simulations accurately describe the data in dedicated validations regions, one for each background and signal region. The selection criteria are reported in Table 8.7. The ZVR and TVR are pure in the background processes they target to validate at a level of 83–96% and the purity of VVVR ranges between 41–71%. Figure 8.7 shows a summary of the expected and observed event yields for each VR and also for the WVR described previously. The data agrees with the prediction within the uncertainties in each case.

Systematic uncertainties: The relative size of the systematic uncertainties on the background estimate are evaluated to 28% and 32% for the SR-lowMass and SR-highMass selections, respectively. Table 8.8 reports a breakdown of the systematic uncertainty into the most relevant sources for the background and two signal points. Uncertainties from the statistics available for the simulated event

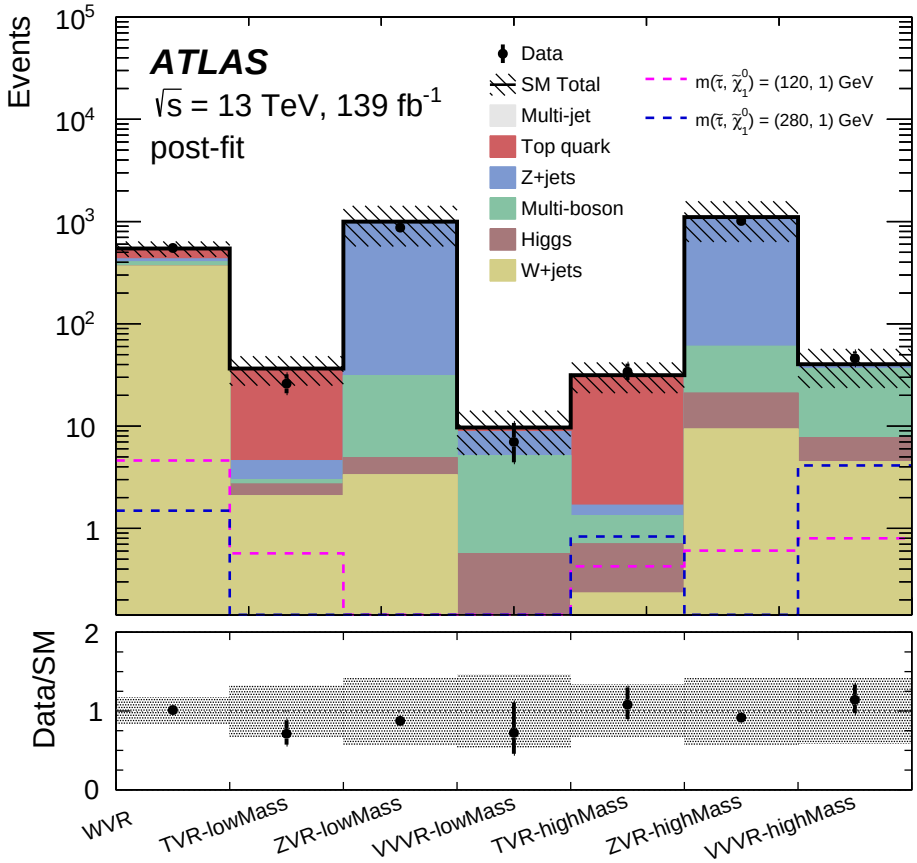

Figure 8.7: Yields in the WVR, TVRs, ZVRs and VVVRs defined in Table 8.7 after the W + jets and multi-jet backgrounds have been normalized to data by a simultaneous fit considering only the SM background. The hatched areas represent the combined statistical and systematic uncertainties. For illustration, the yields from two signal points are drawn as dashed lines. The bottom panel shows the ratio of data to simulation [342].

samples contribute by 11% and 21% to the total background uncertainty in SR-lowMass and SR-highMass, respectively, and they are the most dominant uncertainty source in the latter. Uncertainties on the energy and efficiency calibrations of the selected objects and the missing transverse energy are applied to simulation [190, 201, 204, 206, 209, 211]. The largest uncertainty source arises from the τ lepton calibration uncertainties contributing by 19% and 10% for the SR-lowMass and SR-highMass, respectively. Uncertainties from the jet energy scale and resolution and from $E_{\text{T}}^{\text{miss}}$ soft term (cf. section 3.7.7) are estimated to 5–8% and to 2%, respectively. Calibration uncertainties arising from the simulation of pile-up and from the measurement of the luminosity using the LUCID-2 detector [333] are also considered but found to contribute negligible. The relative uncertainties on the multi-jet background estimate are determined to 23% and 72%, whereas they contribute by 12% and 8% to the total background uncertainty for the SR-lowMass and SR-highMass regions, respectively [347]. Uncertainty sources on the multi-jet background arise from neglected correlations between the two sets of variables used in the ABCD method, from systematic uncertainties on the remaining background processes due to the calibration uncertainties on the selected objects, and from the available data statistics in each region. In order to estimate the effect from potentially correlated variables, the transfer factor is calculated from the ratio of the yield in VR-F to VR-E. Variations of the transfer factor by 8% and 34% are observed for the SR-lowMass and SR-highMass regions, respectively and considered as systematic uncertainty. Calibration uncertainties are propagated to the non multi-jet backgrounds which are subtracted from data to obtain the multi-jet component. The multi-jet background is found to change by 12% and 19%, respectively, due to these calibration uncertainties. The uncertainties from the available data statistics in CR-A are estimated to 19% and 66% for the extrapolations to SR-lowMass and SR-highMass, respectively. The remaining uncertainties on the background estimate are attributed to the theoretical uncertainties on the simulated backgrounds which are estimated using the same procedure as described in section 7.4.3. A 6% uncertainty is assumed for the cross section calculations of multi-boson and $t\bar{t}$ backgrounds and a 5% uncertainty for the Z + jets background.

For the two signal model points, the systematic uncertainties mainly arise from uncertainties on the τ lepton calibrations and from the available MC statistics.

Table 8.8: The post-fit relative systematic uncertainty (%) in the background estimate (signal reference points) in the SR-lowMass and SR-highMass regions from the leading sources at top (bottom). Uncertainties from different sources in the background estimate may be correlated, and do not necessarily add in quadrature to the total uncertainty [342].

Source of systematic uncertainty on background prediction	SR-lowMass [%]	SR-highMass [%]
Statistical uncertainty of MC samples	11	21
τ lepton identification and energy scale	19	10
Normalization uncertainties of the multi-jet background	12	8
Multi-jet estimation	4	10
Jet energy scale and resolution	5	8
Diboson theory uncertainty	5	6
W+jets theory uncertainty	2	3
$E_{\mathrm{T}}^{\mathrm{miss}}$ soft-term resolution and scale	2	2
Total	28	32
Source of systematic uncertainty on signal prediction	SR-lowMass [%]	SR-highMass [%]
m ($\tilde{\tau}$,$\tilde{\chi}_1^0$) [GeV]	(120, 1)	(280, 1)
τ lepton identification and energy scale	29	14
Statistical uncertainty of MC samples	6	10
Jet energy scale and resolution	3	2
Signal cross-section uncertainty	2	2
$E_{\mathrm{T}}^{\mathrm{miss}}$ soft-term resolution and scale	3	< 1
Total	31	17

8.3.3 Results in the $\tau_{\text{had}}\tau_{\text{had}}$ Channel

The W + jets and multi-jet backgrounds are normalized to data utilizing a combined fit in the WCR, in the two multi-jet CR-A and in the two SR similar to the fit exploited in the four-lepton search described in section 7.5.1. The extracted normalization factors for the W + jets and multi-jet backgrounds are 0.91 ± 0.12 and 1.03 ± 0.29, respectively. Figure 8.8 shows the m_{T2} distributions in both signal regions for data and simulation with normalization factors applied. In each case, the data is in good agreement with the SM prediction. Thus, no hint for supersymmetric particle production is neither observed in the $\tau_{\text{had}}\tau_{\text{had}}$ channel. Table 8.9 summarizes the expected and observed yields in the SRs and the CRs used in the combined fit.

Exclusion limits at 95% CL are derived for simplified model points with direct stau production in the $m_{\tilde{\tau}}$–$m_{\tilde{\chi}_1^0}$ plane. In each case, contaminations from the signal in the control regions are taken into account. Fits are derived considering combined left- and right-handed stau pair production and left-handed stau pair production only. Although it is observed that the acceptance for right-handed stau pair events is larger than for left-handed stau pairs, no exclusion contours on models with right-handed stau pairs only could be drawn due to the tiny cross section. The obtained exclusion contours are shown in Figure 8.9 for both cases. Stau masses from 120–390 GeV are excluded for scenarios with $m_{\tilde{\chi}_1^0} = 1$ GeV and combined left- and right-handed stau pair production. No exclusion could be achieved if the $\tilde{\chi}_1^0$ mass is heavier than ~ 0.4 times the stau mass as the τ leptons from the stau decay become softer with increasing $\tilde{\chi}_1^0$ mass. Considering only left-handed stau production, stau models with masses in the range between 155 GeV and 310 GeV are excluded for the case of a light $\tilde{\chi}_1^0$. These

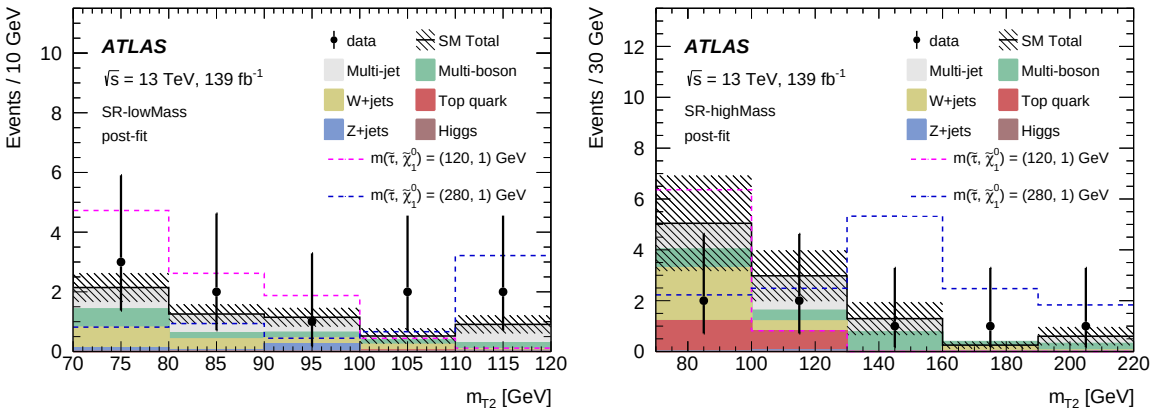

(a) (b)

Figure 8.8: m_{T2} distributions for SR-lowMass (a) and SR-highMass (b) in data and background. Distributions of two model points are shown as dashed lines. The hatched areas indicate the combined systematic uncertainties [342].

Table 8.9: Observed and expected numbers of events in the control and signal regions. The expected event yields of SM processes are given after the background-only fit. The entries marked as "–" are negligible. The uncertainties correspond to the sum in quadrature of statistical and systematic uncertainties. The correlation of systematic uncertainties among control regions and among background processes is fully taken into account [342].

	Multi-jet CR-A -lowMass	Multi-jet CR-A -highMass	WCR	SR -lowMass	SR -highMass
Diboson	1.4 ± 0.6	1.9 ± 1.0	63 ± 21	1.4 ± 0.8	2.6 ± 1.4
W+jets	13 ± 4	4^{+7}_{-4}	850 ± 70	1.5 ± 0.7	2.5 ± 1.8
Top quark	2.7 ± 0.9	3.3 ± 1.6	170 ± 40	$0.04^{+0.80}_{-0.04}$	2.0 ± 0.6
Z+jets	$0.25^{+1.43}_{-0.25}$	1.5 ± 0.8	13 ± 7	$0.4^{+0.5}_{-0.4}$	$0.05^{+0.13}_{-0.05}$
Multi-jet	55 ± 10	16 ± 6	–	2.6 ± 0.7	3.1 ± 1.4
SM total	72 ± 8	27 ± 5	1099 ± 33	6.0 ± 1.7	10.2 ± 3.3
Observed	72	27	1099	10	7

results extend significantly the limits on the stau mass achieved by the LEP experiments discussed in chapter 6.

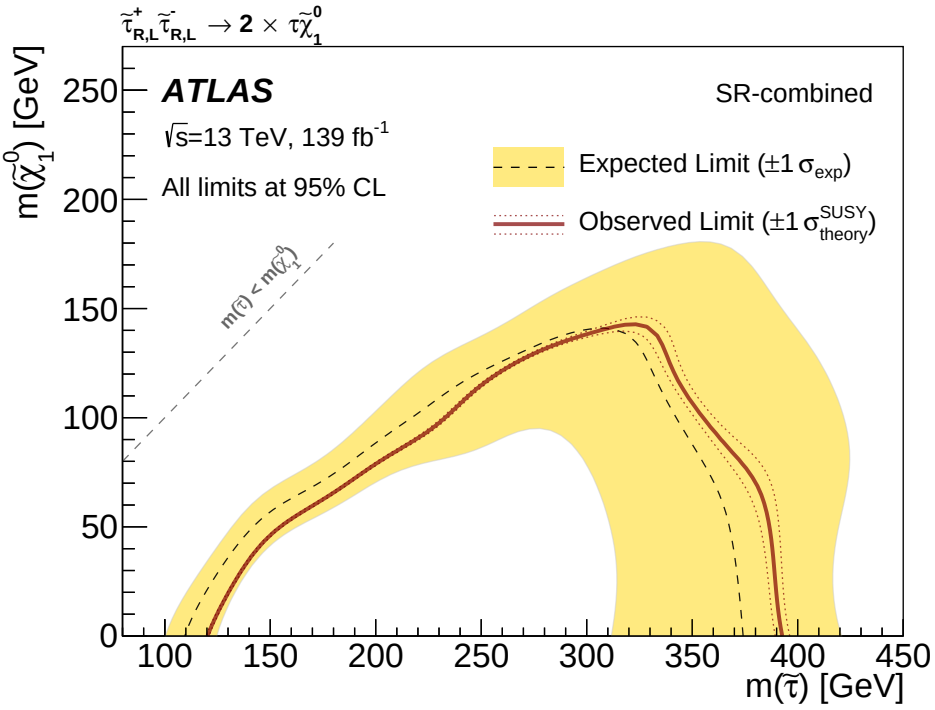

(a)

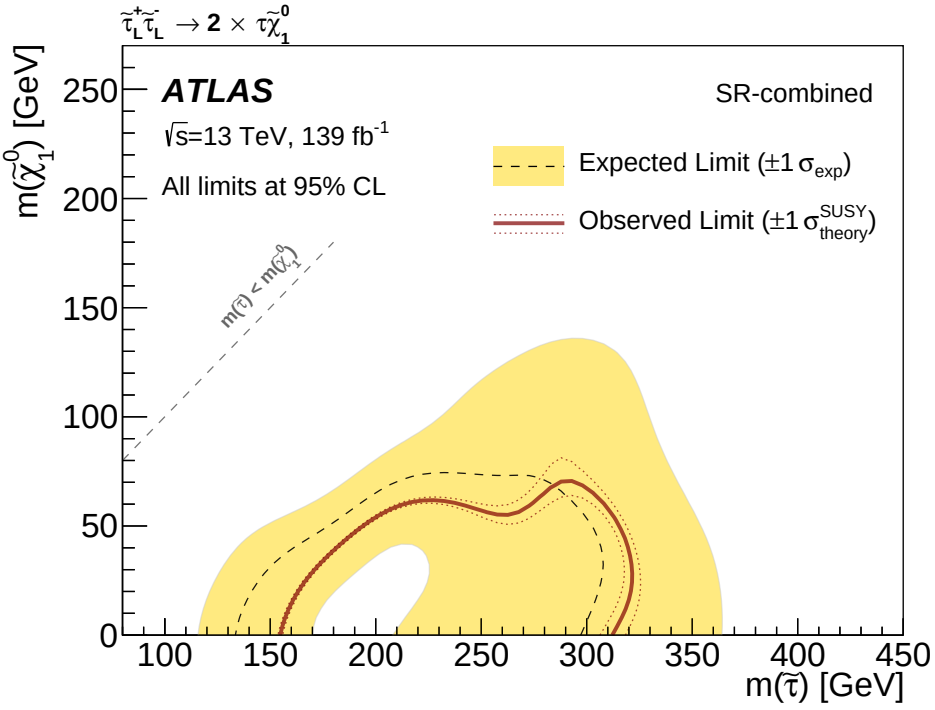

(b)

Figure 8.9: The 95% CL exclusion contours extracted from the combined SR-lowMass and SR-highMass regions for simplified model with direct stau production considering mass-degenerate left- and right-handed stau pairs (a) and left-handed stau pairs only (b) [342].

8.4 Prospect Studies for the $\tau_{\text{lep}}\tau_{\text{had}}$ Channel

Although the $\tau_{\text{lep}}\tau_{\text{had}}$ channel has the largest branching ratio among the three di-τ decay channels, the larger background rates from prompt $W \rightarrow \mu/e\nu$ decays in association with a hadron jet misidentified as τ lepton and the poorer resolution to reconstruct the initial state properties make this channel difficult to be used at the LHC. Given the small signal rates at $O\left(10^2\right)$ compared to the large background rates at $O\left(10^5\right)$, multivariate analysis techniques have to be exploited in order to design a signal selection. The following section presents preliminary prospect studies of the achievable expected significance using Boosted Decision Trees (BDT).

8.4.1 Background Estimation

The Standard Model backgrounds are estimated from simulation if they are irreducible processes and from using a fake factor method similar to the method described in section 7.4.1. Given the larger fake rates for τs than for light leptons, only τ leptons are considered in this analysis to originate from fake sources. Figure 8.10 shows the τ lepton p_{T} and the $E_{\text{T}}^{\text{miss}}$ distributions in simulated $\mu\tau$ events passing the 0 jet selection. The background is dominated at 70–80% by W + jets production followed by Z + jets and VV. Small dependencies of the background composition on the variables shown is observed. For the determination of the fake factor according to Equation (7.13), simulated W + jets are used together with $t\bar{t}$ and multi-boson events where the τ lepton originates from fake processes. The process fractions are calculated from the events satisfying the same kinematic selection criteria but

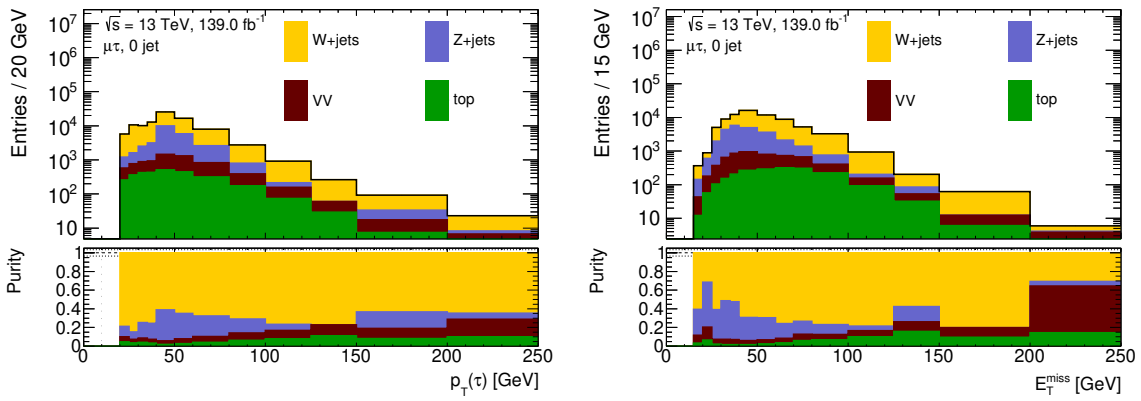

(a) (b)

Figure 8.10: τ lepton p_{T} (a) and $E_{\text{T}}^{\text{miss}}$ (b) in simulated $\mu\tau$ satisfying the 0 jet selection criteria. All backgrounds are estimated using simulation. The bottom panel shows the relative contribution of each background process to the total background.

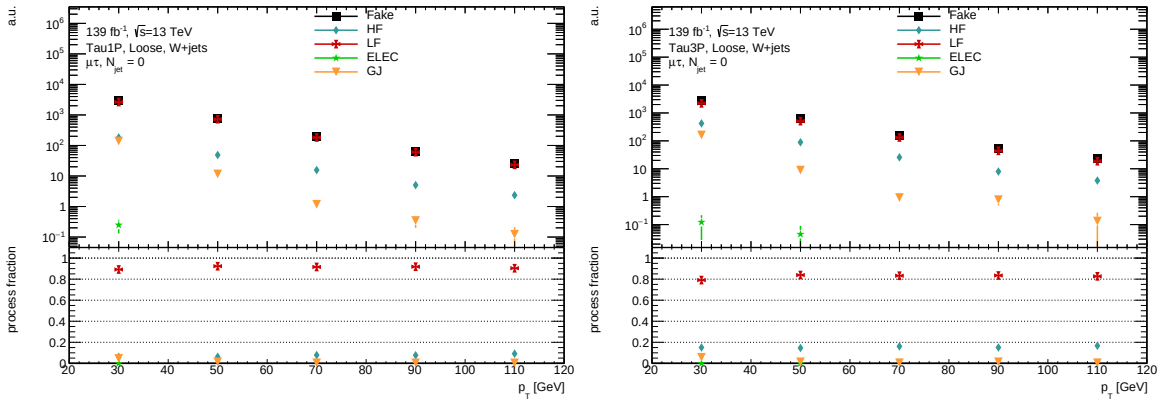

(a) (b)

Figure 8.11: p_{T} distribution of 1-prong (a) and 3-prong (b) loose τs in simulated W + jets events split into each fake process. The bottom panel shows the process fraction of each fake process to the total fake background. The error bars indicate the statistical uncertainties.

containing loose τs. The fake ratios are calculated from every simulated event with a τ-ℓ pair where the light lepton satisfies the signal selection, and the b-veto is applied on the event. For the W + jets case, Figure 8.11 illustrates the process fraction of fake τs for $\mu\tau$ events in the 0 jet category against p_{T} split into 1-prong and 3-prong τs. For both prongnesses, the τ lepton is faked by LF processes almost independent of the lepton p_{T}. Figure 8.12 shows the τ lepton p_{T} and m_{T} distributions for baseline, loose and signal τs together with the corresponding fake ratios. In the case of 1-prong τs, the fake ratio rapidly decreases until $p_{\text{T}} \sim 50$ GeV and then slightly increases again for even larger transverse momenta. Stepwise changes in the LF fake ratio of 1-prong τs are observed which could not be sufficiently described by fake-ratio parametrized against p_{T}. Hence, the fake ratios considered for 1-prong τs are parametrized as functions of p_{T} and m_{T}. For cases of 3-prong τs, the fake ratio is about one order of magnitude smaller than for 1-prong τs and much flatter against p_{T}. A subtle increase in the fake ratio at higher ranges of the p_{T} and m_{T} spectra are observed. For 3-prong τs a parametrization of the fake-ratios against p_{T} only has been found to sufficiently model the kinematic distributions using the fake factor method.

For the LF and HF processes, the fake factors are corrected by scale factors measured in Z + jets + τ and $t\bar{t}$ + τ events (cf. section 7.4.1), respectively. The corresponding scale factors are given in Appendix C.1 together with the fake ratios for the other fake processes in the W + jets sample.

Figure 8.13 shows the distributions of the most important variables used in the multivariate analysis discussed in section 8.4.2 for $\mu\tau$ events in the 0 jet channel. In each case, the modelled background distributions agree with the data at a level of 10–15%, which is sufficient to use the estimate for the

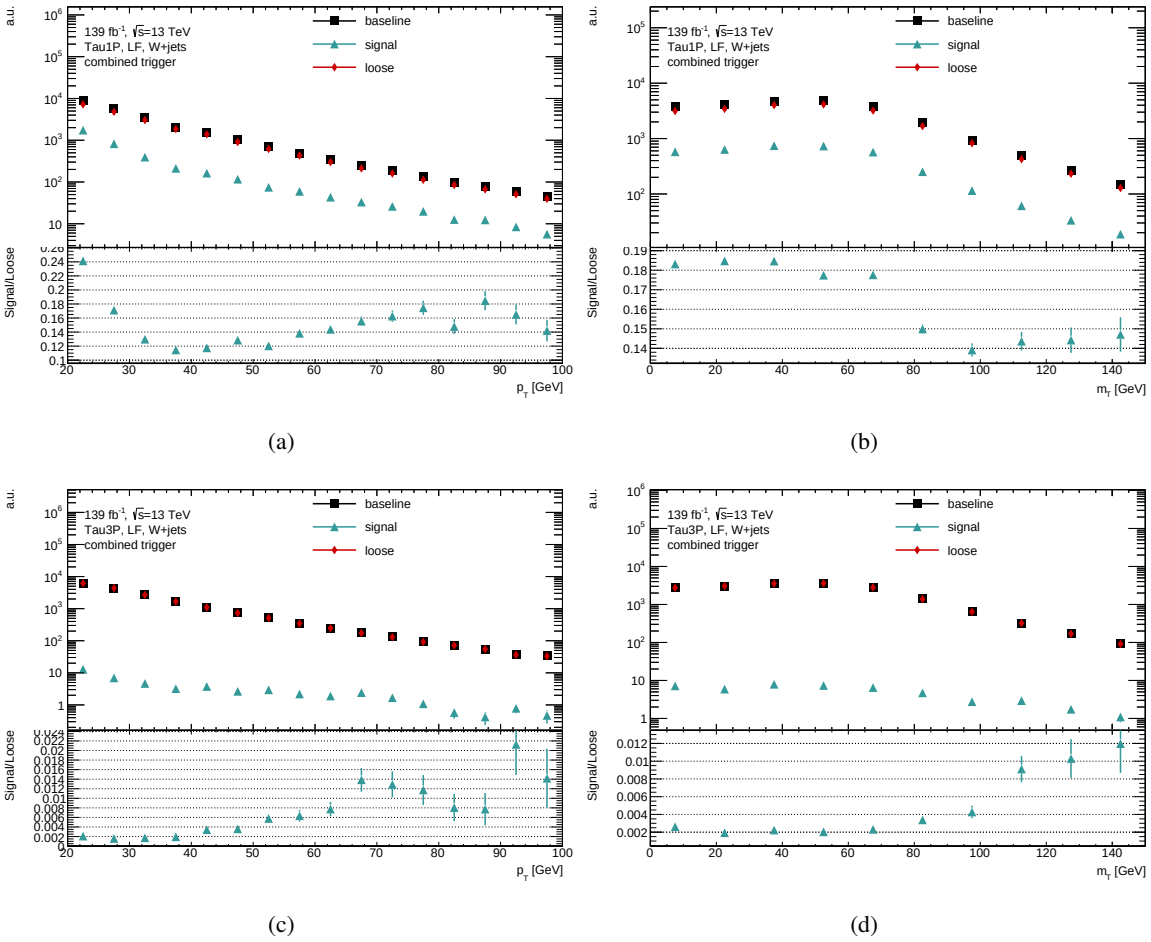

(a) (b)

(c) (d)

Figure 8.12: p_{T} (left) and m_{T} (right) distribution of LF 1-prong (top) and 3-prong (bottom) τs in simulated W + jets events shown for baseline, loose and signal τs. The bottom panel shows the ratio of the signal to the loose distribution. The error bars indicate the statistical uncertainties.

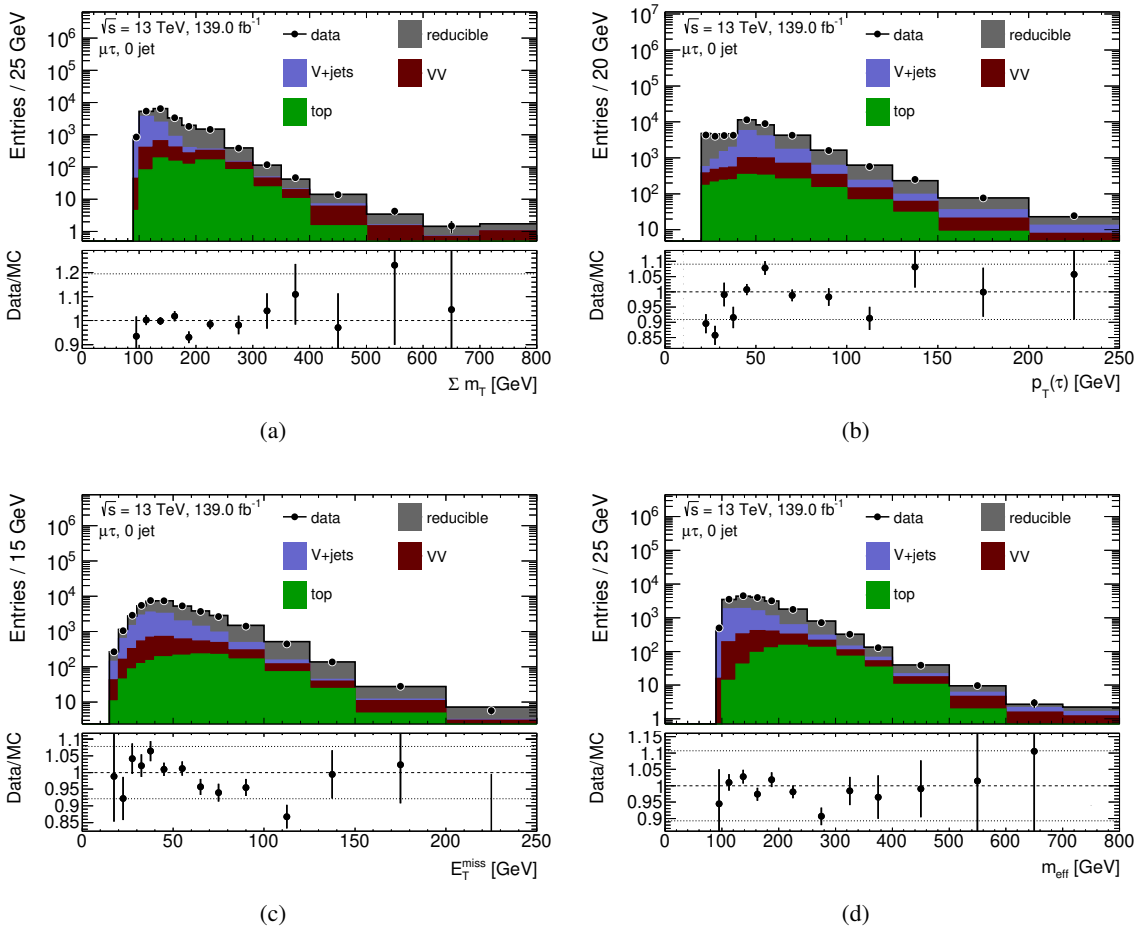

Figure 8.13: Distribution of $\Sigma m_{\text{T}} = m_{\text{T}}\left(\ell, E_{\text{T}}^{\text{miss}}\right) + m_{\text{T}}\left(\tau, E_{\text{T}}^{\text{miss}}\right)$ (a), the τ lepton p_{T} (b), $E_{\text{T}}^{\text{miss}}$ (c) and m_{eff} (d) in $\mu\tau$ events satisfying the 0 jet selection criteria. All backgrounds are estimated using simulation. The bottom panel shows the ratio of data to simulation and the error bars indicate the statistical uncertainties.

prospect studies presented in the following.

8.4.2 Signal Selection Studies

For the optimization of the signal selection in the $\tau_{\text{lep}}\tau_{\text{had}}$ channel, Boosted Decision Trees (BDT) [292, 293] provided by the SciKit-learn [294] framework. Like any multivariate classifier, a BDT has first to be trained using labeled signal and background events. In this step, the classification parameters of the BDT are adapted to discriminate between signal and background utilizing a combination of different kinematic variables. The trainings are performed separately in both jet channels using simultaneously $e\tau$ and $\mu\tau$ events. The variables considered in both trainings are listed in Table 8.10. In order to

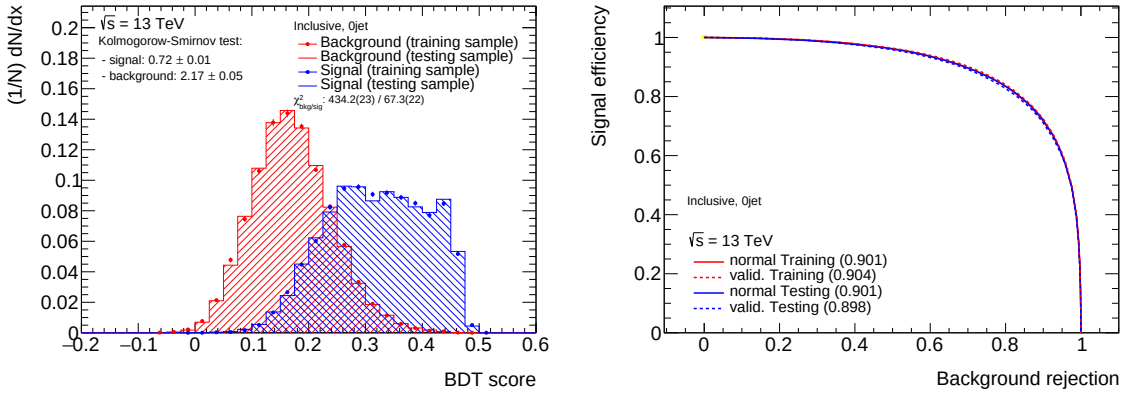

(a) (b)

Figure 8.14: Distribution of the multivariate classifier scores (a) and the corresponding ROC curve (b) for a BDT trained in 0 jet events for the Inclusive scenario. In (a), the distributions of the events from the training sample for background and signal are shown as blue and red hatched areas, respectively and from the test sample as data points. The χ^2 tests are calculated from the comparison of the respective training and testing datasets. In (b), the ROC curves in the training and testing datasets are shown for the nominal (solid line) and for the cross validation (dashed line) trainings. The numbers in brackets indicate the area under the ROC curve.

gain more training statistics for the signal and also to design a classifier which is not specifically optimized to a single stau–neutralino mass combination, several signal model points are combined into four configurations, called *LowMass*, *MidMass*, *HighMass* and *Inclusive*. Information about the composition of each configuration is given in Appendix C.2. The events from the fake estimate described in section 8.4.1 are taken in the training as background. In the second step, the trained classifier is applied to a second set of events not used in the training, called testing dataset, in order to assess whether the classifier "memorized the training events by heart", called over training, or whether it was able to identify the characteristic features of signal and background. In this thesis, the statistics of the two datasets are chosen to be equal. The events used in the training are later also used in the analysis to estimate the expected numbers of background and signal, respectively. In order to provide an independent classification of the training events and also to evaluate whether the training statistics are sufficient, a second BDT is trained using the testing datasets for training and vice versa. This procedure is called cross validation.

For the example of the Inclusive training in the 0 jet channel, Figure 8.14 shows the distributions of the classifier scores for signal and background in the training and testing datasets. For both datasets, the signal and background distributions have peaks at the right-hand and left-hand site of the plot with a small separation between. In order to quantify the separation power of the training, the Receiver Operating Characteristic (ROC) curve is used which is also shown in Figure 8.14. The curve is constructed by plotting the signal selection efficiency, ϵ_{sig}, against the background rejection,

Table 8.10: Description of the kinematic variables used in the training of the BDT in the particular jet channels. If the variable is marked in the third or fourth column by "X" it is used in the training for the corresponding channel.

Variable	Description	0 jet	1-jet
$p_{\text{T}}(\tau/\ell)$	Transverse momentum of the light lepton or τ	X	X
$E_{\text{T}}^{\text{miss}}$	Magnitude of the missing transverse momentum	X	X
$S_{E_{\text{T}}^{\text{miss}}}$	Object based $E_{\text{T}}^{\text{miss}}$ significance as described in Ref. [351]	X	
p_{T} (jet)	Transverse momentum of the leading jet		X
N_{jets}	Number of signal jets		X
$\lvert\Delta\phi(\text{jet},\tau)\rvert$	Azimuthal angle between the leading jet and τ lepton		X
$\lvert\Delta\phi(\tau,\ell)\rvert$		X	X
$\lvert\Delta\eta(\tau,\ell)\rvert$	Separation angles between the light lepton and τ lepton	X	X
$\Delta R(\tau,\ell)$		X	
$\Sigma\cos\Delta\phi$	Sum of the cosines of the angles between the light lepton and τ with the missing transverse momentum, respectively	X	X
$\cos\Delta\phi_{\text{min}}$	Cosine of the angle between the missing transverse momentum and the closest lepton	X	
$E_{\text{T}}^{\text{miss}}$ centrality	Centrality of the missing transverse momentum given by $\frac{A+B}{\sqrt{A^2+B^2}}$, where $A = \frac{\sin\Delta\phi(E_{\text{T}}^{\text{miss}},\ell)}{\sin\Delta\phi(\tau,\ell)}$, $B = \frac{\sin\Delta\phi(E_{\text{T}}^{\text{miss}},\tau)}{\sin\Delta\phi(\tau,\ell)}$		X
$\tau-\ell$ balance	The difference between the τ and light lepton p_{T} divided by their sum, i.e. $\frac{p_{\text{T}}(\tau)-p_{\text{T}}(\ell)}{p_{\text{T}}(\tau)+p_{\text{T}}(\ell)}$.	X	X
$\tau+\ell-E_{\text{T}}^{\text{miss}}$ balance	The difference between the sum of the light lepton and τ lepton p_{T} and $E_{\text{T}}^{\text{miss}}$ divided by the sum of the three, i.e. $\frac{p_{\text{T}}(\tau)+p_{\text{T}}(\ell)-E_{\text{T}}^{\text{miss}}}{p_{\text{T}}(\tau)+p_{\text{T}}(\ell)+E_{\text{T}}^{\text{miss}}}$.	X	X
$m_{\text{T}}(\tau, E_{\text{T}}^{\text{miss}})$	Transverse mass of the τ lepton with $E_{\text{T}}^{\text{miss}}$	X	
Σm_{T}	Sum of the transverse masses of the light lepton and τ each with $E_{\text{T}}^{\text{miss}}$	X	X
m_{CT}	Contra-transverse mass between the light lepton and the τ according to Equation (8.4)	X	X
$m(\tau,\ell)$	Invariant mass of the τ and light lepton	X	X
m_{eff}	Effective mass defined as scalar sum of $E_{\text{T}}^{\text{miss}}$ and the p_{T} of the light lepton, τ and jets	X	X

$\bar{\epsilon}_{\text{bkg}} = 1 - \epsilon_{\text{bkg}}$, as a function of a lower threshold on the classifier score. A perfect classification would correspond to a rectangular ROC curve, while a completely random classification, i.e. the algorithm cannot distinguish the background from the signal, would correspond to a straight line from $\left(\epsilon_{\text{sig}}, \bar{\epsilon}_{\text{bkg}}\right) = (1, 0)$ to $\left(\epsilon_{\text{sig}}, \bar{\epsilon}_{\text{bkg}}\right) = (0, 1)$. To assess the training quality, the area under the ROC curve (ROC-AUC) is used.

An important aspect of dealing with multivariate classifier is the tuning of its hyper parameters which define the flexibility of the classifier to recognize the relevant features. However, a too flexible classifier results in over training. The hyper parameters of the BDTs used in this analysis are the number of decision trees, N_{trees}, the maximum depth of each decision tree, the minimal amount of training events in each node of the decision trees, and the learning rate in the boosting [294]. The optimal set of parameters is determined from dedicated BDT trainings using preselected $\mu\tau$ events where two of the hyper parameters are simultaneously varied while the others are kept at the default settings [294]. The best training with the smallest amount of over training was selected in which the ROC-AUC for training events is at maximum but also the difference to the ROC-AUC for testing events is smallest which is achieved by maximizing the train quality given by

$$\text{ROC-AUC}^{\text{train}} \exp\left[-\left|\text{ROC-AUC}^{\text{train}} - \text{ROC-AUC}^{\text{test}}\right|\right]. \tag{8.5}$$

The setting with 450 decision trees where each node contains at least 3% of the training events and a learning rate of 1 was found to be optimal. Further information about the distributions of the training variables and about the constructed BDTs is given in Appendix C.2.

For the estimation of the expected signal significance, the 0 jet and 1-jet categories are further split according to the light lepton flavour. For each channel, the BDT distributions of the respective BDT classification scores are obtained for the signal model points and the SM backgrounds. In each bin of the distributions the expected significance of the signal model is calculated and then added in quadrature to the total significance of the channel. The highest significances in each channel are then combined to the total expected significance of the signal model. The result for the model points considered is shown in Figure 8.15 and compared to the expected significances from an improved $\tau_{\text{had}}\tau_{\text{had}}$ analysis which also exploits multivariate techniques and is currently developed by Clara Leitgeb and Anna Bertolini [352]. For the $\tau_{\text{lep}}\tau_{\text{had}}$ channel, the maximum signal significance achieved is 1.7σ for $\left(m_{\tilde{\tau}}, m_{\tilde{\chi}_1^0}\right) = (260, 1)$ GeV, where as a decent fraction of the parameter space up to $m_{\tilde{\tau}} = 260$ GeV is covered by a 1.6σ contour for the $\tau_{\text{had}}\tau_{\text{had}}$ channel. By combining the two channels, this coverage can be extended to $\tilde{\tau}$ masses with 300 GeV (cf. Figure. 8.15(c))

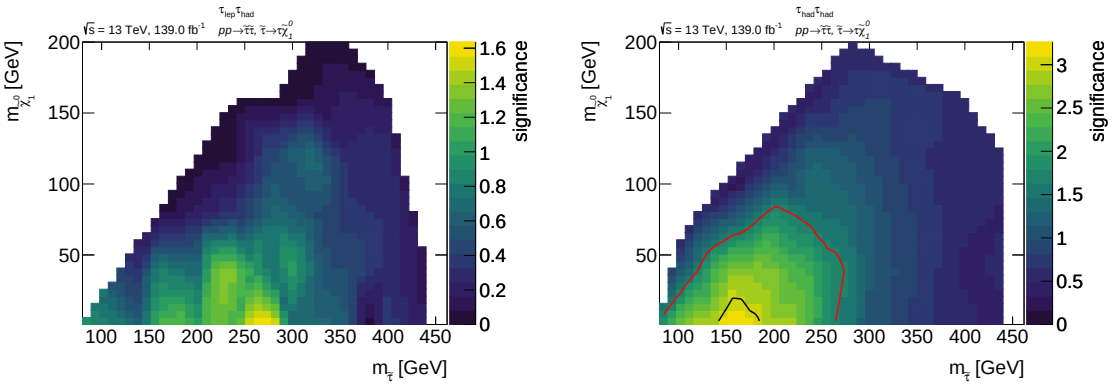

(a) (b)

(c)

Figure 8.15: Expected significance for the $\tau_{\text{lep}}\tau_{\text{had}}$ channel from combining the best classifier in the 0 jet and 1-jet categories (a) for each signal model point, for the $\tau_{\text{had}}\tau_{\text{had}}$ channel from using a multivariate analysis technique using the asymmetric di-τ trigger [352] and for the combination of the two channels (c) in 139 fb^{-1} of $\sqrt{s}$ = 13 TeV data. The red and the black lines indicate the 1.65σ and 3σ contours, respectively.

CHAPTER NINE

SUMMARY

Still here I am a stupid fool,
as wise as when I went to school!

(Johann Wolfgang von Goethe)

The evidence for the presence of Dark Matter and Dark Energy are compelling arguments that the Standard Model (SM) of particle physics cannot be the ultimate theory of the fundamental particles and their interactions. Supersymmetry (SUSY) is an attractive framework for the extension of the SM which also can solve the problem of explaining the small value of the Higgs mass observed at $m_H = 125$ GeV near the electroweak symmetry scale. It predicts for every SM particle a superpartner with equal quantum number but spin differing by half. As no superpartner have been observed so far, SUSY has to be spontaneously broken, leading to higher masses of the superpartners compared to the SM particles. The general parametrization of the unknown SUSY breaking mechanism introduces more than hundred additional free parameters. If R-parity is conserved, the lightest supersymmetric particle (LSP), which is either identified as the lightest neutralino $\tilde{\chi}_1^0$ or the gravitino, is stable and an ideal candidate for Dark Matter. In order to solve the hierarchy problem, the masses of the lightest superpartners should be in the range of few TeV which is well covered by the center-of-mass energy of $\sqrt{s} = 13$ TeV of the Large Hadron Collider (LHC) in Run 2.

In this thesis, searches for SUSY in final states with four charged leptons or two hadronically decaying τ leptons have been performed in proton-proton collisions at $\sqrt{s} = 13$ TeV at the LHC recorded by the ATLAS experiment. Four-lepton final states provide an excellent probe for supersymmetric particle production if R-parity is violated due to lepton number violating interactions, pair produced $\tilde{\chi}_1^0$ LSPs can decay into a charged lepton pair and a neutrino. The four-lepton final state also provides excellent sensitivity to supersymmetric models in which SUSY is broken with gauge mediated SUSY breaking and R-parity conservation where the LSP is an almost massless gravitino, pair produced from higgsino-like $\tilde{\chi}_1^0$ decays into the gravitino and a Z or Higgs boson.

In order to exploit signatures with multiple leptons in the final state, high lepton reconstruction and identification efficiency is crucial. In the context of this work, the muon reconstruction and selection

efficiency has been estimated from $Z \to \mu\mu$ and $J/\psi \to \mu\mu$ decays in data to exceed 95% with unprecedented precision of few permille. Calibration constants have been derived for correcting the simulation which are utilized for every measurement based on the $\sqrt{s}$ = 13 TeV ATLAS data. Four-lepton events with up to two hadronically decaying τ leptons have been used to search for the two supersymmetric models described above in two iterations with integrated luminosities of 36.1 fb^{-1}and 139 fb^{-1}, respectively. In all cases, the observations agreed with the SM expectation. Exclusion limits have been derived in the framework of simplified models on the masses of the primary supersymmetric particles produced in the pp collisions and on the mass of the LSP into which they decay. In the RPV models of pair produced, gluinos, winos and sleptons masses of up to 2.65 TeV, 1.65 TeV and 1.2 TeV have been excluded under the assumption that the $\tilde{\chi}_1^0$ only decays into electrons or muons. For scenarios with hadronically decaying τ leptons from the LSP decay, the limits are weaker at 2 TeV, 1.15 TeV, and 900 GeV, respectively, due to a lower τ lepton identification efficiency and larger background of hadrons misclassified as τ leptons. In both scenarios, the low $\tilde{\chi}_1^0$ mass range at 10–50 GeV is challenging, since $\tilde{\chi}_1^0$ decay leptons become increasingly collimated due to the increasing boost of the $\tilde{\chi}_1^0$ and cannot be separated anymore in the detector. For collimated electron-muon and di-muon pairs, algorithms have been developed which allow to recover 70–80% of such pairs and are also useful for other searches, for example for low-p_{T} leptons from decays of new particles with compressed mass spectra. New reconstruction methods for resolving di-τ and di-electrons pairs are still under development. Such techniques will significantly improve the sensitivity of future searches. The results achieved in this thesis improve the results of the previous search in Run 1 at $\sqrt{s}$ = 8 TeV by 600 GeV to 1.2 TeV. In the gauge mediated SUSY breaking model, higgsino-like $\tilde{\chi}_1^0$ with masses up to 560 GeV have been excluded for the case that the the higgsino exclusively decays into a Z boson. For branching ratios of $\tilde{\chi}_1^0$ decays into Higgs bosons of around 70%, higgsinos with masses in the range of 130–260 GeV are excluded. The latter model has been studied for the first time in ATLAS.

Di-τ final states have been investigated to search for the direct production of the supersymmetric partner of the τ lepton, the stau slepton. This final state is experimentally challenging as it shares the same signature with $Z \to \tau\tau$ production which has a several orders of magnitude larger production cross section. There is also a large background of events where hadronic jets are misidentified as hadronically decaying τ leptons. Thus, limits set from the experiments at the Large Electron Positron Collider prevailed until this new analysis. Events with two hadronically decaying τ leptons have been investigated because of the large branching ratios. No excess above the SM prediction has been found. Therefore, stau masses from 120 to 390 GeV have been excluded for $\tilde{\chi}_1^0$ with a mass of 1 GeV, extending by far the LEP limit of 96 GeV. In order to improve the sensitivity to direct stau production with the existing data, sensitivity studies in di-τ final states with one leptonically decaying τ lepton have been performed. This channel is even more difficult to use at the LHC due to the larger background rates. Boosted Decision Trees have been exploited to design a signal selection sensitive

to the signal model. Expected significances of around 1.7σ at maximum have been achieved which is about half of the size of the significances achieved in di-τ events with hadronically decaying τs. Combining the two channels, the 1.6σ significance contour can be extended by up to 50 GeV in stau mass. These results will be used in the next iteration of the direct stau search performed on the Run 2 data.

The results of the four-lepton search based on the initial 36.1 fb^{-1} dataset have been peer reviewed by the whole scientific community and are published in Ref. [327] whereas the full Run 2 result is at the stage of the internal reviewed by the ATLAS collaboration. A publication of these is planned in July or August 2020. The search for direct stau pair production with two hadronically decaying τ leptons is peer reviewed and published in Ref. [342]. The prospect studies for the di-τ final state with one leptonically decaying τ lepton are part of the efforts to improve the analysis and hence preliminary. For the muon reconstruction efficiency measurements, preliminary results have been published in terms of public plots August 2019 [353], whereas a comprehensive publication is currently in preparation which is planned to be released by July or August 2020.

Appendix

CHAPTER A

ADDITIONAL MATERIAL FOR THE MUON EFFICIENCY MEASUREMENTS

A.1 Muon Reconstruction Efficiencies Measured in $Z \rightarrow \mu\mu$ Decays

The reconstruction efficiencies measured in $Z \rightarrow \mu\mu$ decays in the *Run* 2 dataset and the corresponding scale factors for the Loose, Tight, Low-p_{T} and Low-p_{T} (MVA) selection criteria are reported in Figures A.1–A.4 as functions of the muon pseudorapidity and the azimuthal angle.

A.2 Muon Reconstruction Efficiencies Measured in $J/\psi \rightarrow \mu\mu$ Decays

The reconstruction efficiencies measured in $J/\psi \rightarrow \mu\mu$ decays in the *Run* 2 dataset and the corresponding scale factors for the Loose, Medium, Tight, and Low-p_{T} (MVA) selection criteria are reported in Figures A.5–A.8 as functions of the muon transverse momentum and the pseudorapidity.

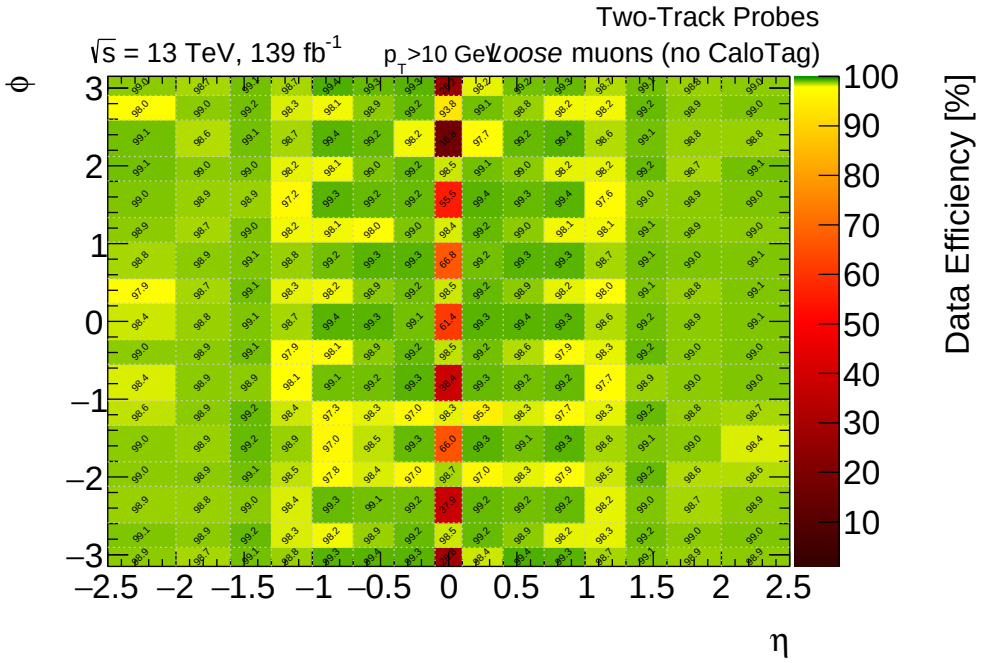

(a)

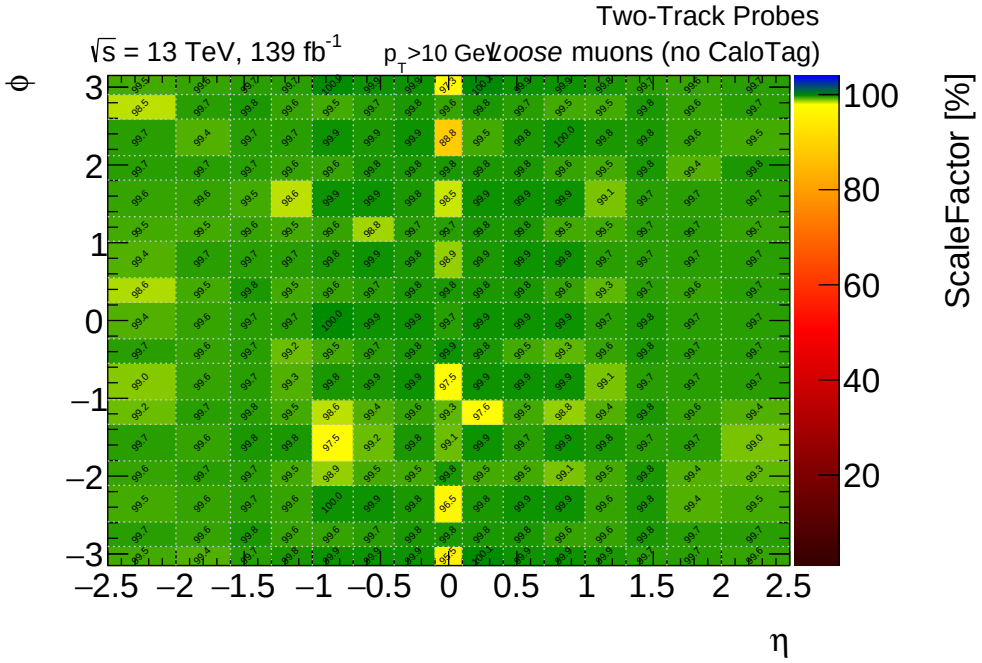

(b)

Figure A.1: Muon reconstruction efficiencies for the Loose identification algorithm excluding CT muons measured in $Z \to \mu\mu$ events (top) and the corresponding scale factor map (bottom) as a function of the muon pseudorapidity and the azimuthal angle for muons with $p_{\mathrm{T}} > 10$ GeV in the full Run 2 data.

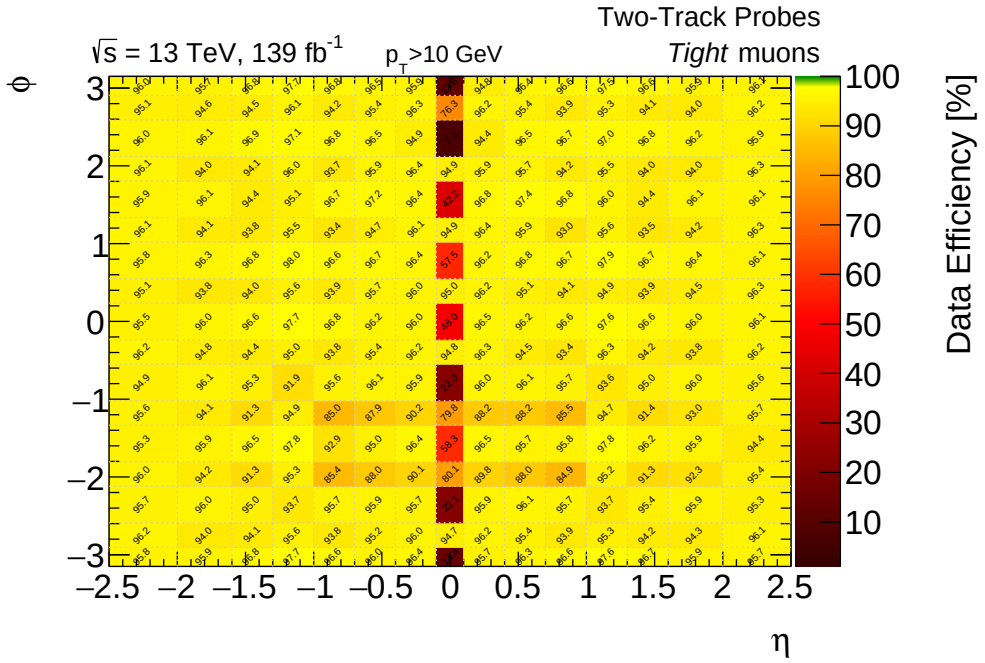

(a)

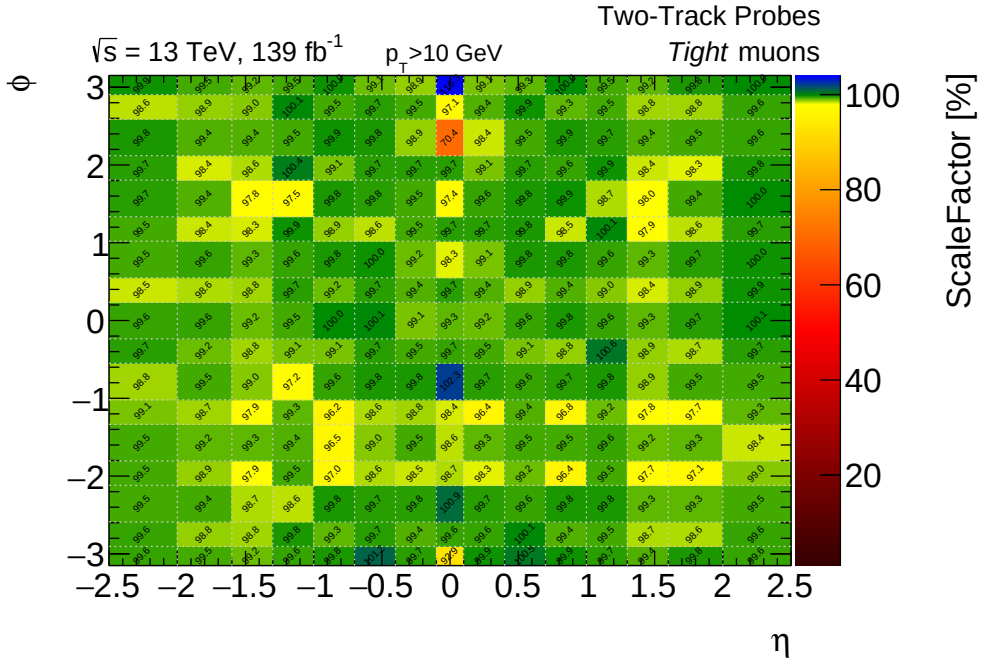

(b)

Figure A.2: Muon reconstruction efficiencies for the Tight identification algorithm measured in $Z \to \mu\mu$ events (top) and the corresponding scale factor map (bottom) as a function of the muon pseudorapidity and the azimuthal angle for muons with $p_{\mathrm{T}} > 10$ GeV in the full Run 2 data.

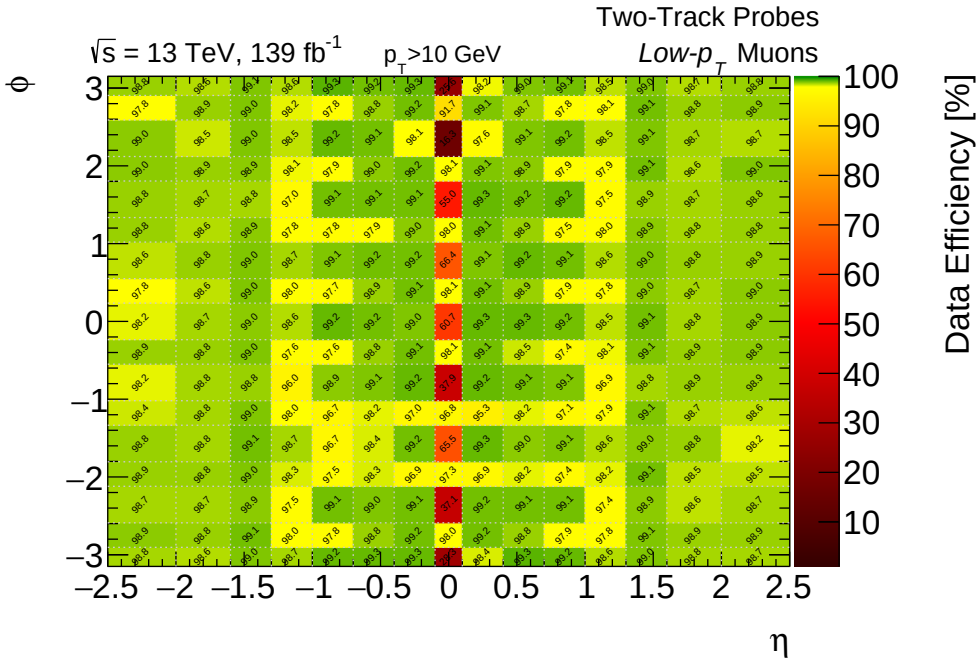

(a)

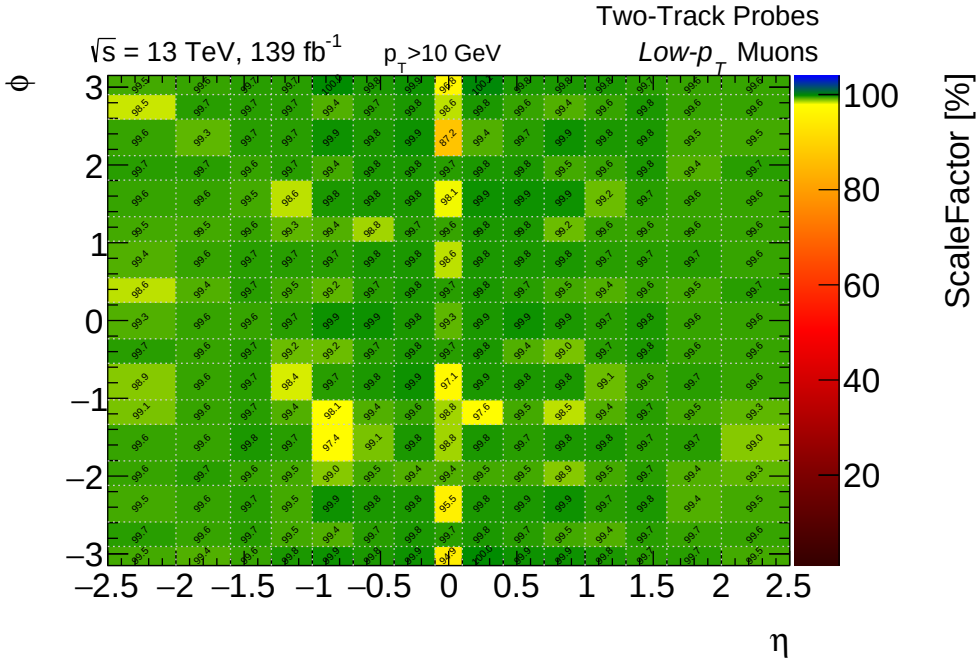

(b)

Figure A.3: Muon reconstruction efficiencies for the Low-p_{T} identification algorithm measured in $Z \rightarrow \mu\mu$ events (top) and the corresponding scale factor map (bottom) as a function of the muon pseudorapidity and the azimuthal angle for muons with $p_{\mathrm{T}} > 10$ GeV in the full Run 2 data.

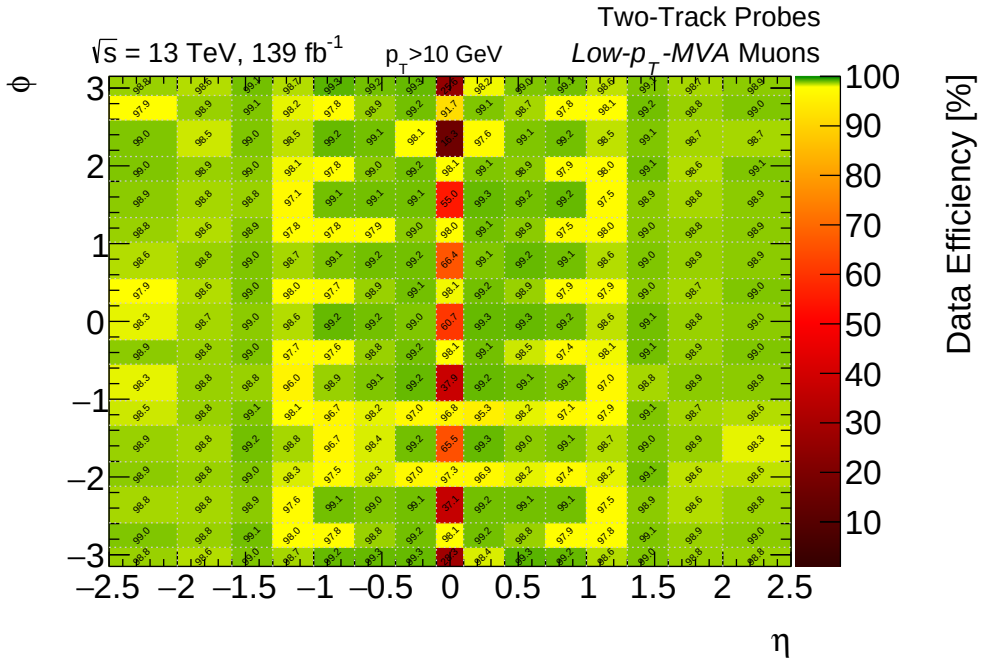

(a)

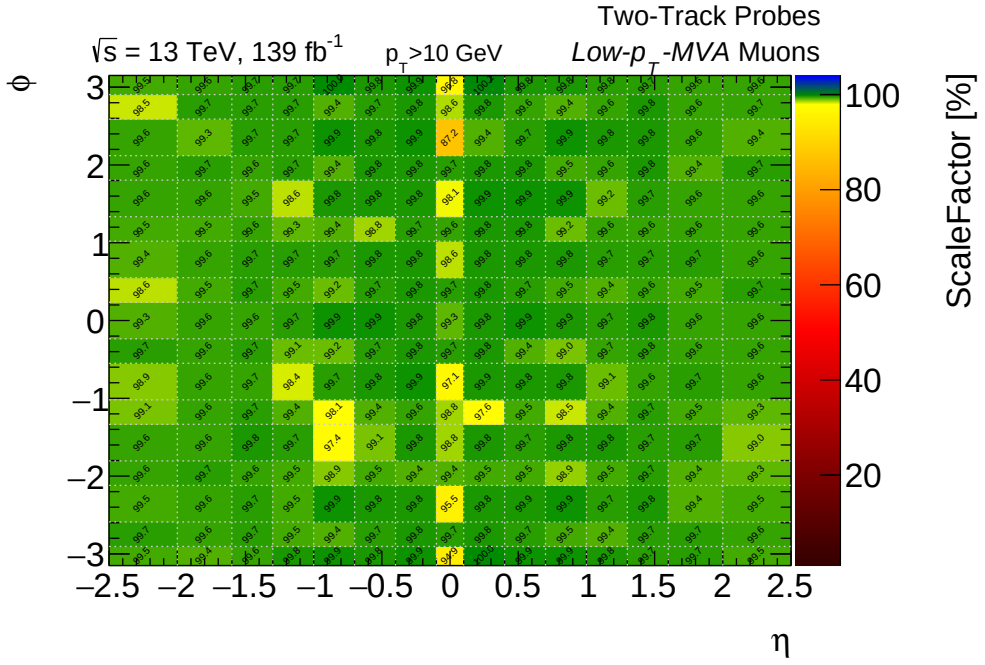

(b)

Figure A.4: Muon reconstruction efficiencies for the Low-p_{T} (MVA) identification algorithm measured in $Z \to \mu\mu$ events (top) and the corresponding scale factor map (bottom) as a function of the muon pseudorapidity and the azimuthal angle for muons with $p_{\mathrm{T}} > 10$ GeV in the full Run 2 data.

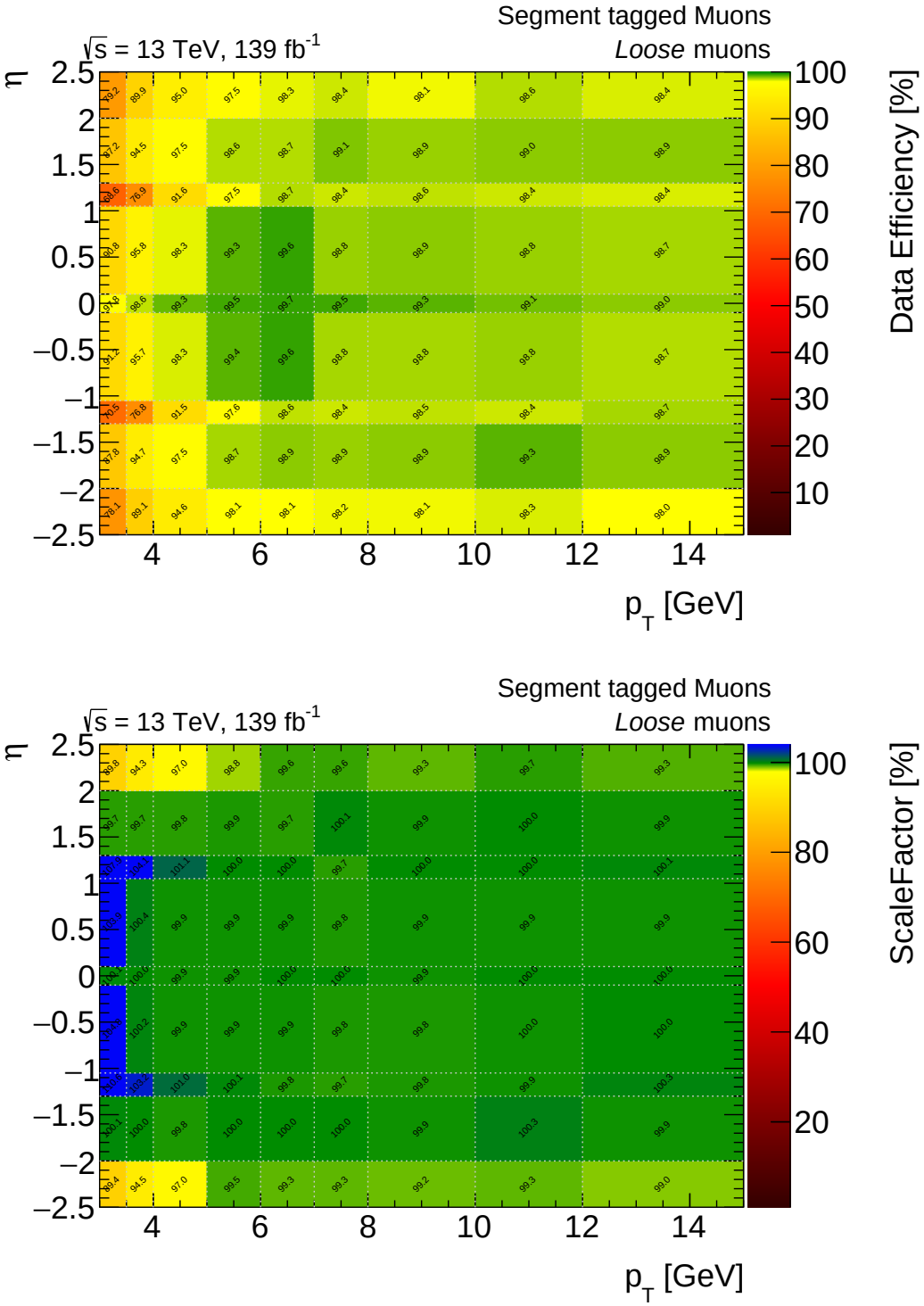

Figure A.5: Reconstruction efficiency measured in the Run 2 dataset (top) and the efficiency scale factor for Loose muons shown as a function of the transverse momentum and the pseudorapidity in $J/\psi \to \mu\mu$ events.

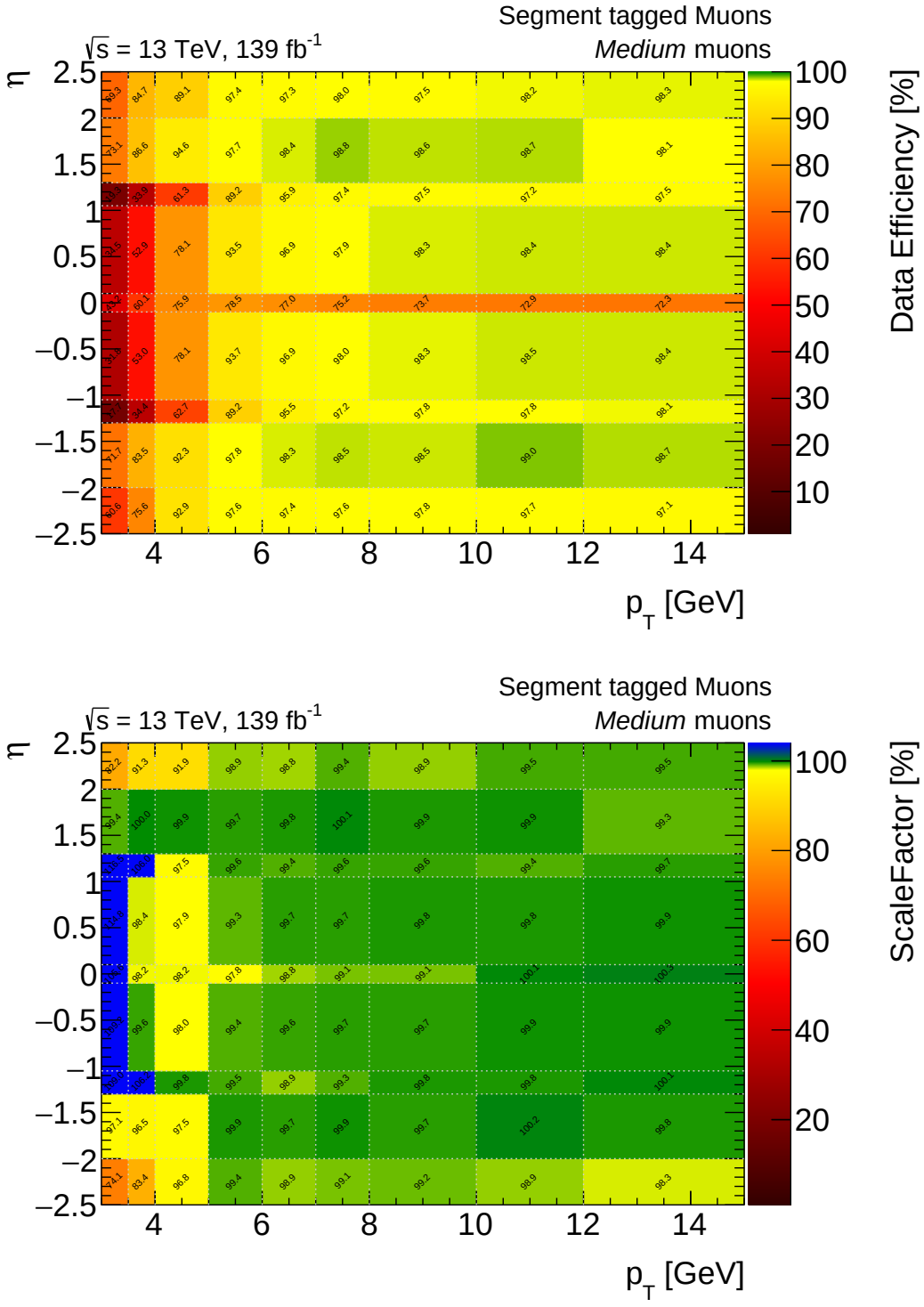

Figure A.6: Reconstruction efficiency measured in the Run 2 dataset (top) and the efficiency scale factor for Medium muons shown as a function of the transverse momentum and the pseudorapidity in $J/\psi \rightarrow \mu\mu$ events.

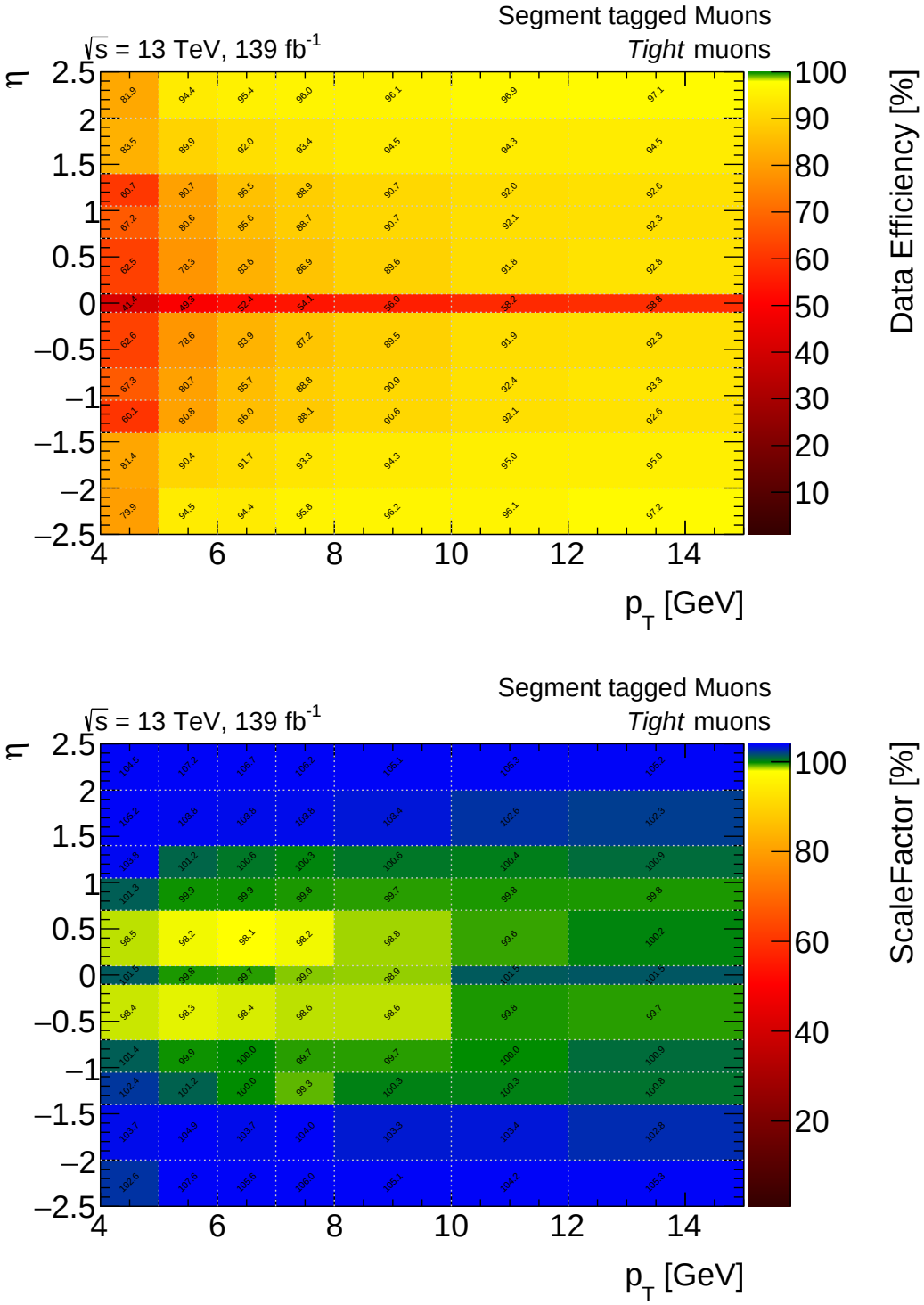

Figure A.7: Reconstruction efficiency measured in the Run 2 dataset (top) and the efficiency scale factor for Tight muons shown as a function of the transverse momentum and the pseudorapidity in $J/\psi \to \mu\mu$ events.

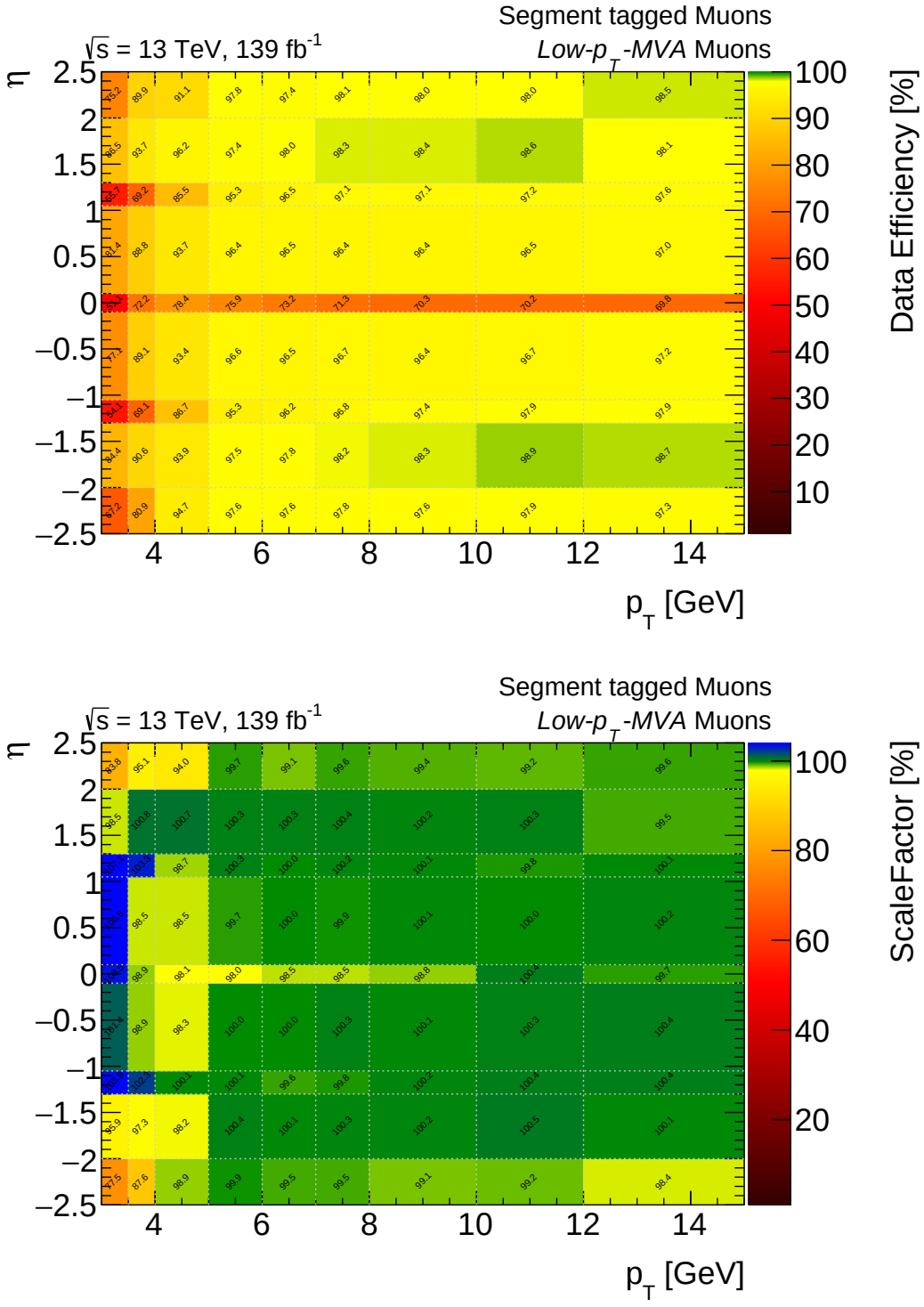

Figure A.8: Reconstruction efficiency measured in the Run 2 dataset (top) and the efficiency scale factor for Low-p_{T} (MVA) muons shown as a function of the transverse momentum and the pseudorapidity in $J/\psi \to \mu\mu$ events.

A.3 Non-Closure TTVA Uncertainty

For the muon TTVA selection efficiency measurement, an additional uncertainty is assigned to the provided scale factors. Therefore, a closure test of the scale factors is performed for each year of data taking by applying the derived scale factors to the matches in simulation. From comparing the corrected TTVA efficiency to the recorded efficiency in data, it is expected that the derived scale factor closes to unity. Deviations of the corrected scale factor from one are assigned as systematic uncertainty if they are not covered by the already existing uncertainties. The uncertainty maps for each year of data taking are given in Figure A.9. The uncertainties are found to be relatively large in the crack region, $|\eta| < 0.1$ and at low p_{T}.

A.4 Isolation Selection Efficiencies

The isolation selection efficiency as functions of the muon p_{T} and the separation to the next reconstructed jet with $p_{\mathrm{T}} > 20$ GeV are shown in Figure A.10 for three isolation selection working points. The corresponding systematic uncertainties are depicted in Figure A.11.

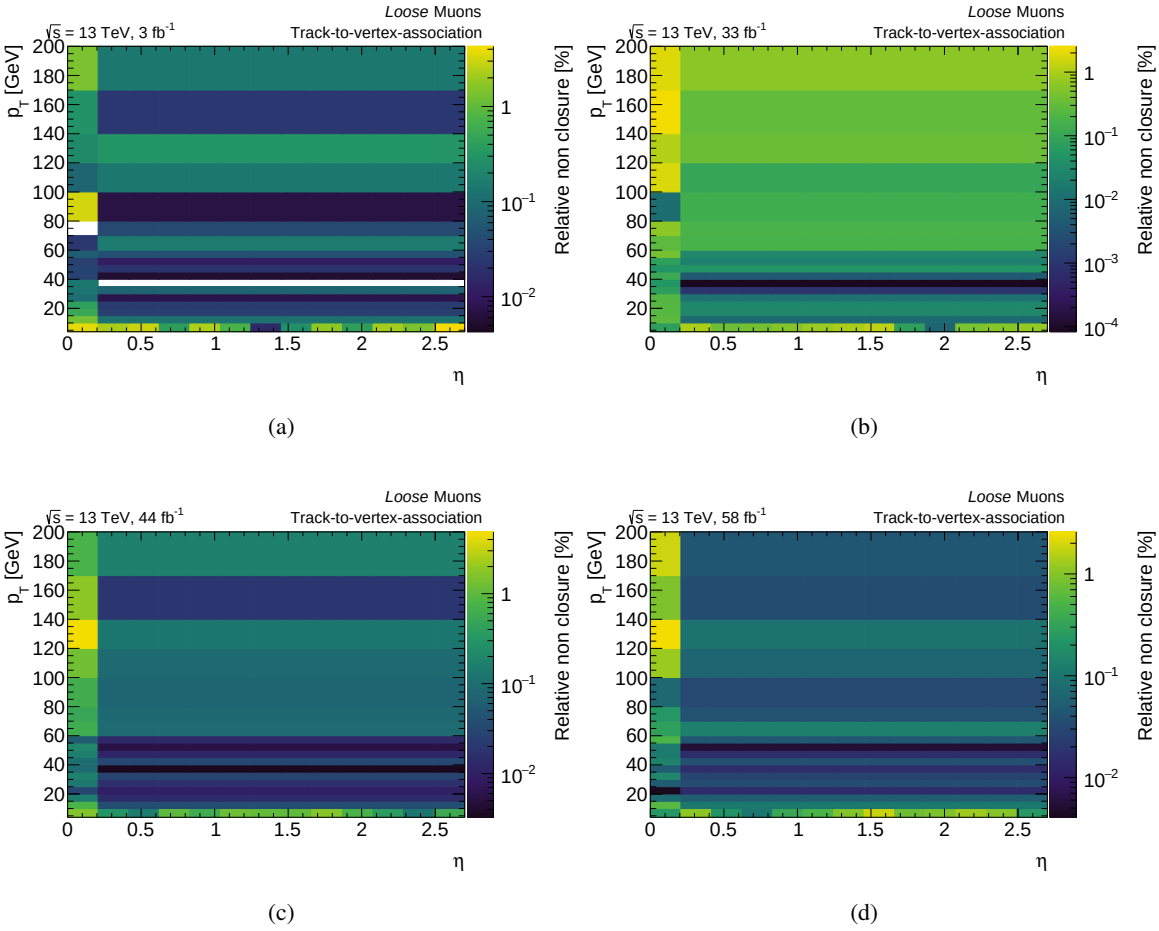

(a) (b)

(c) (d)

Figure A.9: Non-closure uncertainty on the TTVA efficiency scale factors.

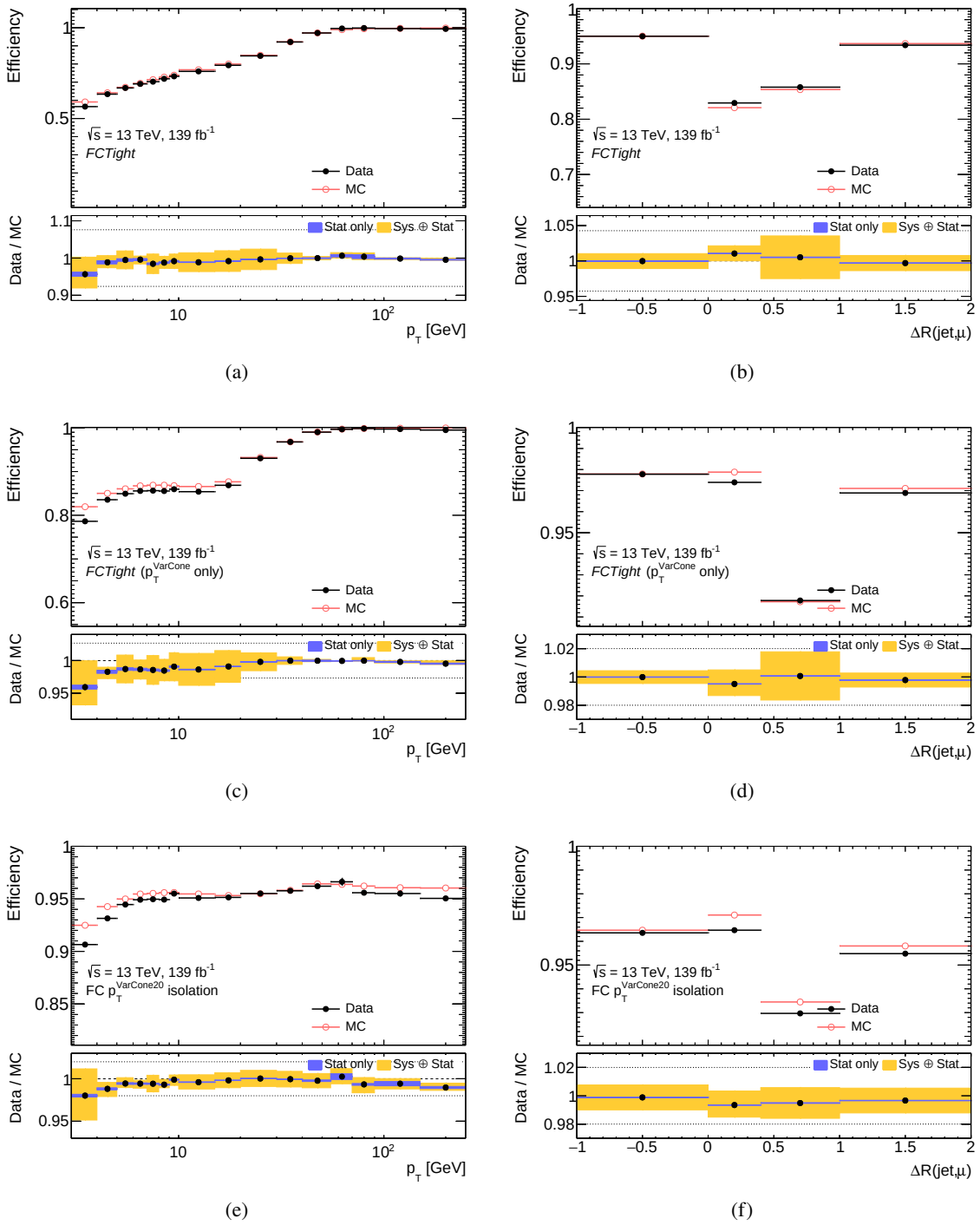

Figure A.10: FCTight (top), FC high-p_{T} (middle) and FCTight (bottom) considering only track isolation variable, isolation selection efficiencies for muons shown as a function of the muon p_{T} (left) and the proximity to reconstructed jets (right) in $Z \rightarrow \mu\mu$ events measured in the full run II dataset. The interval $\Delta R < 0$ in (b) corresponds to no jet events. The bottom panel shows the efficiency scale factor. The yellow error bands indicate the quadratic sum of statistical and systematic uncertainties.

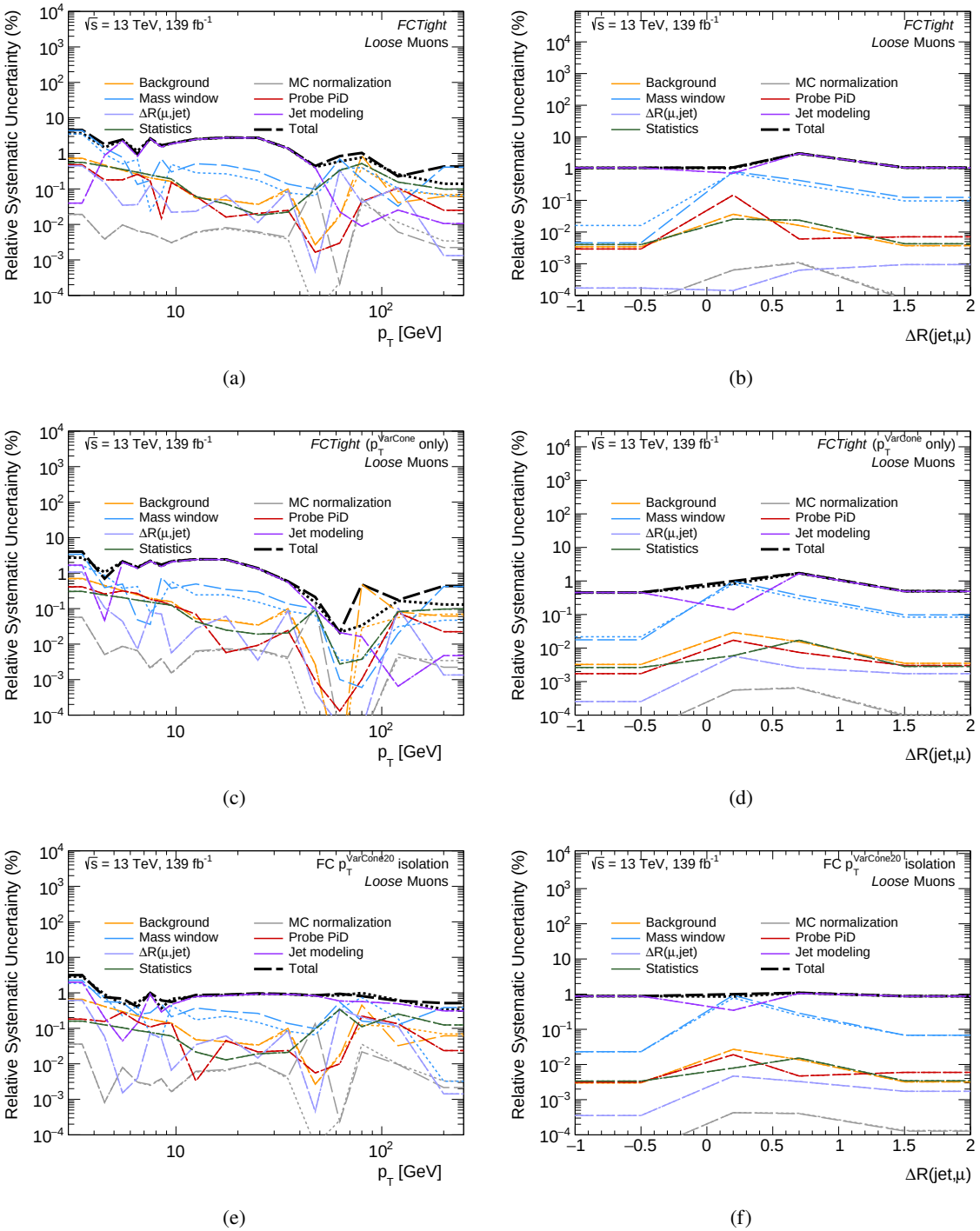

Figure A.11: Breakdown of the systematic uncertainties for the FCTight (top), FC high-p_{T} (middle) and FCTight (bottom) considering only track isolation variable, isolation selection efficiency efficiency for muons measured in the full Run 2 dataset and shown as a function of the muon p_{T} (left) and the proximity to the next jet (right), where $\Delta R < 0$ corresponds events with no reconstructed jet. The dashed (dotted) lines indicate the $+1\sigma$ (-1σ) variation of each nuisance parameter.

CHAPTER B

ADDITIONAL MATERIAL FOR THE FOUR LEPTON ANALYSIS

B.1 Expected Significances

Figure B.1 shows the simulated m_{eff} distribution in 3L1T and 2L2T events with applied Z-veto as a function of the lower threshold for the SM bckground and four RPV signal points in the scenario with $\lambda_{i33} \neq$ together with the expected significance. The expected significances in each RPV signal model achieved by the event selections in Table 7.4 are shown in Figures B.2–B.4.

B.2 Reducible Background Estimation

As explained in section 7.4.1, the real-fake migration matrix, $\mathcal{I}$, desribes the mixing of the expected number of events from SM backgrounds with fake lepton multiplicities ranging from zero to four in the reconstructed event categories with loose lepton multiplicities also ranging between zero to four. In order to estimate the contributions from the different fake processes, this matrix has to be inverted which is given by,

$$\mathcal{I}^{-1} = \frac{1}{(\epsilon - f)^4} \begin{pmatrix} \epsilon^4 & -\epsilon^3\bar{\epsilon} & \epsilon^2\bar{\epsilon}^2 & -\epsilon\bar{\epsilon}^3 & \bar{\epsilon}^4 \\ -4\epsilon^3 f & -4\epsilon^2(\epsilon f - \frac{1}{4}\epsilon - \frac{3}{4}f) & 4\epsilon\bar{\epsilon}(\epsilon f - \frac{1}{2}\epsilon - \frac{1}{2}f) & -4\bar{\epsilon}^2(\epsilon f - \frac{3}{4}\epsilon - \frac{1}{4}f) & -4\bar{\epsilon}^3\bar{f} \\ 6\epsilon^2 f^2 & 6\epsilon f(\epsilon f - \frac{1}{2}\epsilon - \frac{1}{2}f) & 6(\epsilon^2 f^2 - \epsilon^2 f + \frac{1}{6}\epsilon^2 - \epsilon f^2 + \frac{2}{3}\epsilon f + \frac{1}{6}f^2) & 6\bar{\epsilon}\bar{f}(\epsilon f - \frac{1}{2}\epsilon - \frac{1}{2}f) & 6\bar{\epsilon}^2\bar{f}^2 \\ -4\epsilon f^3 & -4f^2(\epsilon f - \frac{3}{4}\epsilon - \frac{1}{4}f) & 4f\bar{f}(\epsilon f - \frac{1}{2}\epsilon - \frac{1}{2}f) & -4\bar{f}^2(\epsilon f - \frac{1}{4}\epsilon - \frac{3}{4}f) & -4\bar{\epsilon}\bar{f}^3 \\ f^4 & -f^3\bar{f} & f^2\bar{f}^2 & -f\bar{f}^3 & \bar{f}^4 \end{pmatrix}. \quad \text{(B.1)}$$

B.3 Theoretical Uncertainties on the Background Estimate

As described in section 7.4.3, theoretical uncertainties on the irreducible backgrounds are evaluated using generator-level events for each event selection considered. Tables B.1 and B.2 report the summary of the theoretical uncertainties on the ZZ and $t\bar{t}Z$ background, respectively, for each event selection in the initial analysis of the search for Supersymmetry in four-lepton events. For the full

Table B.1: Summary of theoretical uncertainties and yields of the $t\bar{t}Z$ background. These are calculated for 36.1 fb^{-1}with generator-level events. The quoted scale uncertainty is the largest deviation from the nominal. The uncertainties are combined in quadrature to find the combined uncertainty.

Region	Nominal yield	Generator	$\mu_F \wedge \mu_R$	Total
SR0A	5.0 ± 0.1	20.7%	8.9%	22.5%
SR0B	0.7 ± 0.0	29.4%	14.3%	32.7%
SR0C	9.3 ± 0.2	0.1%	5.1%	5.1%
SR0D	4.7 ± 0.1	1.5%	2.6%	3.0%
VR0	7.5 ± 0.1	8.6%	2.4%	8.9%
VR1	11.6 ± 0.2	5.7%	2.7%	6.3%
VR2	7.9 ± 0.1	5.9%	5.5%	8.1%
VR0Z	44.2 ± 0.3	6.7%	3.6%	7.6%

Table B.2: Summary of theoretical uncertainties and yields of the ZZ background. These are calculated for 36.1 fb^{-1}with generator-level events. The quoted scale uncertainty is the largest deviation from the nominal. The uncertainties except the Generator uncertainty are combined in quadrature to find the combined uncertainty.

Region	Nominal yield	μ_R	Generator	PDF	PDF (alt.)	μ_F	$\mu_F \wedge \mu_R$	Total
SR0A	4.1 ± 0.1	16.9%	22.5%	5.7%	1.8%	4.1%	19.5%	26.8%
SR0B	0.6 ± 0.0	17.8%	31.8%	5.8%	1.7%	4.4%	21.0%	28.5%
SR0C	1.1 ± 0.1	13.0%	22.9%	5.9%	0.9%	4.7%	17.4%	23.0%
SR0D	0.3 ± 0.0	10.8%	4.7%	6.2%	1.6%	6.5%	16.7%	21.9%
VR0	185.3 ± 1.3	1.0%	7.2%	5.4%	0.4%	1.3%	2.6%	6.2%
VR1	106.0 ± 2.7	0.7%	2.6%	5.4%	0.4%	2.7%	3.1%	6.8%
VR2	96.3 ± 0.9	1.5%	2.0%	5.5%	0.5%	2.9%	3.9%	7.4%
VR0Z	422.5 ± 2.2	1.4%	5.3%	5.4%	0.4%	2.6%	3.6%	7.2%

Run 2 result, a summary of the theoretical uncertainties is given for the irreducible backgrounds in Tables B.3–B.7.

Table B.3: Summary of theoretical uncertainties and yields of the $t\bar{t}H$ background. These are calculated for 139fb^{-1} with generator-level events. The quoted scale uncertainty is the largest deviation from the nominal and the PDF uncertainties are calculated using the uncertainty envelope. The uncertainties except the PDF and Generator components are combined in quadrature to find the combined uncertainty.

Region	Nominal yield	α_S	μ_F	Generator	PDF	μ_R	$\mu_R \downarrow \mu_F$	$\mu_R \uparrow \mu_F$	Total
CR_ZZ	0.0 ± 0.0	4.7%	9.3%	105.0%	2.7%	8.5%	11.0%	10.2%	20.6%
CR_$t\bar{t}Z$	3.1 ± 0.0	2.0%	7.1%	3.8%	2.7%	7.4%	10.1%	4.6%	15.1%
$\texttt{SR0}^{\text{loose}}_{b-\text{veto}}$	0.3 ± 0.0	2.1%	10.6%	23.0%	2.9%	14.3%	14.1%	7.5%	24.4%
$\texttt{SR0}^{\text{tight}}_{b-\text{veto}}$	0.0 ± 0.0	1.4%	23.9%	116.6%	2.5%	39.2%	25.8%	11.8%	54.2%
$\texttt{SR0}_{b-\text{req}}$	0.4 ± 0.0	2.2%	19.0%	18.9%	3.2%	31.9%	22.2%	8.9%	44.5%
SR0C	0.9 ± 0.0	2.0%	6.9%	21.3%	2.6%	6.6%	9.6%	4.9%	14.2%
SR0D	0.5 ± 0.0	1.9%	7.3%	21.6%	2.7%	7.5%	10.1%	5.2%	15.4%
$\texttt{SR0-ZZ}^{\text{loose}}_{b-\text{veto}}$	0.0 ± 0.0	1.8%	7.8%	41.3%	3.0%	11.1%	11.5%	4.3%	18.6%
$\texttt{SR0-ZZ}^{\text{tight}}_{b-\text{veto}}$	0.0 ± 0.0	3.3%	12.7%	100.0%	3.1%	18.4%	16.6%	7.8%	29.5%
$\texttt{SR1}^{\text{loose}}_{b-\text{veto}}$	0.7 ± 0.0	1.5%	11.5%	13.9%	2.6%	16.6%	15.0%	7.5%	26.6%
$\texttt{SR1}^{\text{tight}}_{b-\text{veto}}$	0.2 ± 0.0	1.5%	19.5%	69.8%	3.0%	31.6%	22.0%	9.8%	44.6%
$\texttt{SR1}_{b-\text{req}}$	0.7 ± 0.0	1.7%	20.6%	9.2%	2.8%	34.5%	23.4%	9.7%	47.8%
$\texttt{SR2}^{\text{loose}}_{b-\text{veto}}$	0.9 ± 0.0	2.1%	11.6%	19.8%	2.8%	17.1%	15.2%	7.3%	27.0%
$\texttt{SR2}^{\text{tight}}_{b-\text{veto}}$	0.2 ± 0.0	1.6%	19.3%	17.5%	3.0%	31.8%	22.0%	9.5%	44.5%
$\texttt{SR2}_{b-\text{req}}$	1.8 ± 0.0	1.7%	17.0%	15.9%	2.9%	27.3%	20.1%	8.8%	39.2%
$\texttt{VR0}_{b-\text{veto}}$	1.3 ± 0.0	2.3%	6.2%	9.8%	2.5%	5.2%	9.0%	3.8%	12.8%
VR_ZZ	0.4 ± 0.0	2.1%	5.8%	1.7%	3.2%	4.1%	8.3%	3.5%	11.8%
VR_$t\bar{t}Z$	13.4 ± 0.1	2.1%	6.3%	0.6%	2.7%	5.2%	9.2%	4.1%	13.0%
$\texttt{VR1}^{Z-\text{veto}}_{b-\text{veto}}$	3.4 ± 0.0	2.3%	6.2%	10.6%	2.4%	4.8%	8.7%	4.1%	12.4%
$\texttt{VR1}^{Z-\text{req}}_{b-\text{veto}}$	0.6 ± 0.0	1.9%	7.0%	1.0%	2.5%	6.9%	9.8%	4.7%	14.5%
$\texttt{VR2}^{Z-\text{veto}}_{b-\text{veto}}$	4.1 ± 0.0	2.4%	6.0%	5.8%	2.5%	4.2%	8.4%	3.8%	11.9%
$\texttt{VR2}^{Z-\text{req}}_{b-\text{veto}}$	0.3 ± 0.0	1.1%	7.0%	50.8%	2.1%	8.0%	10.1%	4.1%	15.2%

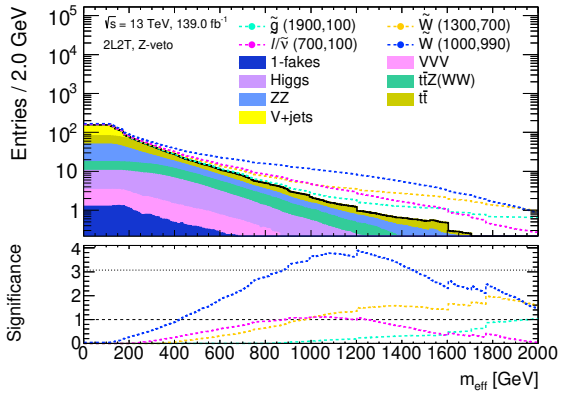

(a)

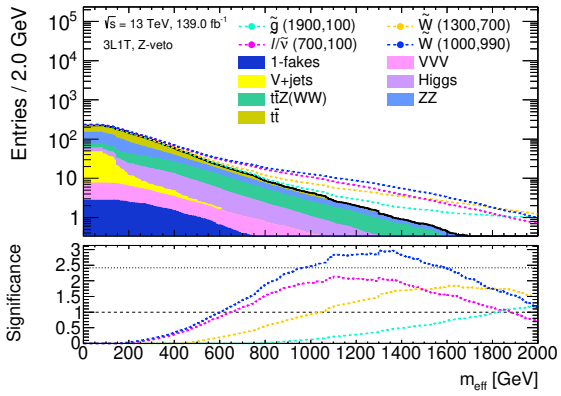

(b)

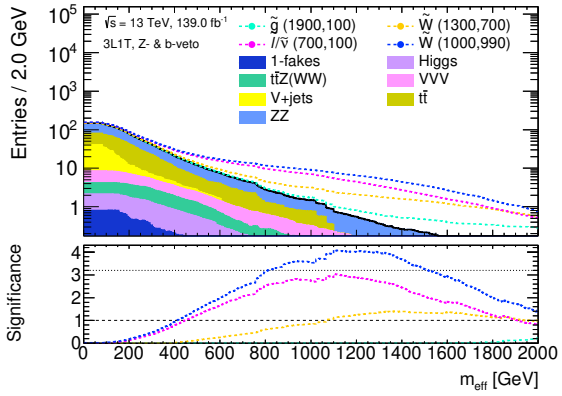

(c)

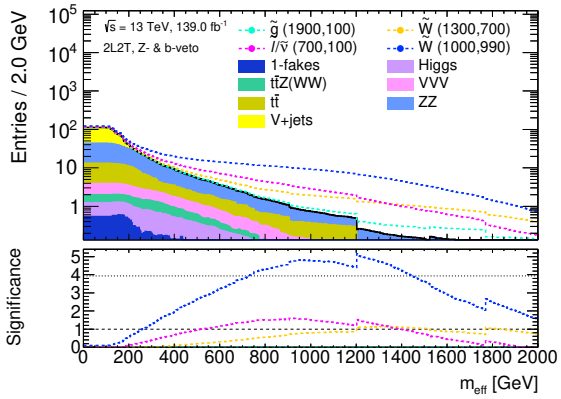

(d)

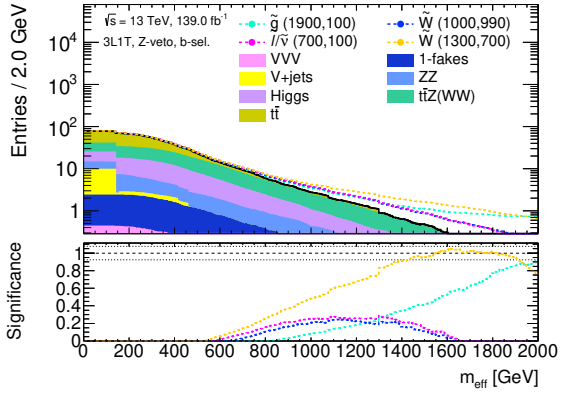

(e)

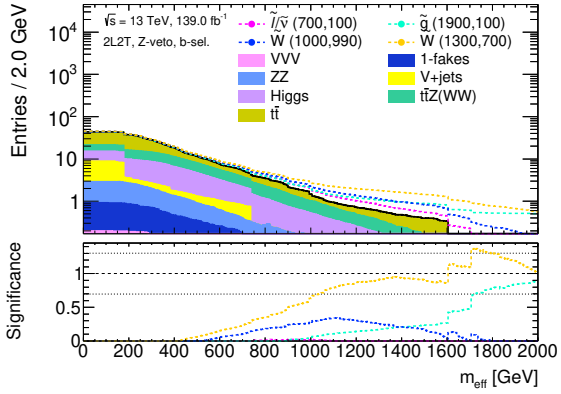

(f)

Figure B.1: m_{eff} in 3L1T (left) and 2L2T (right) events with an applied Z-veto shown as a function of a lower threshold for the SM background and four signal points. The top row is inclusive in b-jets, a b-veto is applied in the middle row and b-jets are required in the bottom row. The panel beneath depicts the expected signficance of each signal point in 139 fb^{-1} of data for a given cut-value assuming an relative uncertainty on the background of 30%.

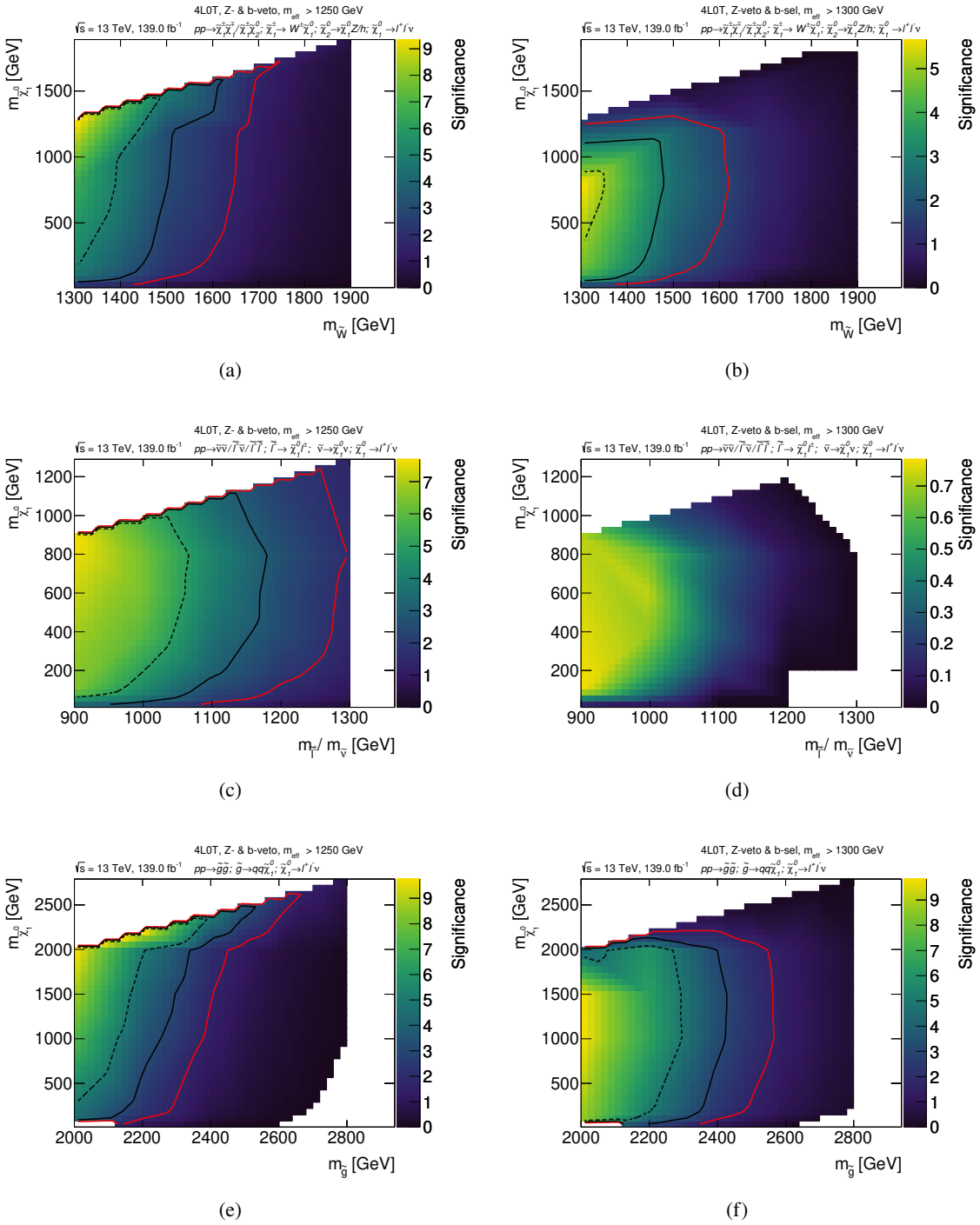

Figure B.2: Expected significance for the RPV models with $\lambda_{12k} \neq$ assuming wino (top), slepton (middle) and gluino (bottom) pair production in $\mathrm{SR0}\ell^{\mathrm{tight}}_{b-\mathrm{veto}}$ (left) and $\mathrm{SR0}\ell_{b-\mathrm{req}}$ (right) events for 139 fb^{-1} of data assuming a 30% uncertainty on the background. The red, solid black and dashed black lines indicate the 1.68σ, 3σ and 5σ contours, respectively.

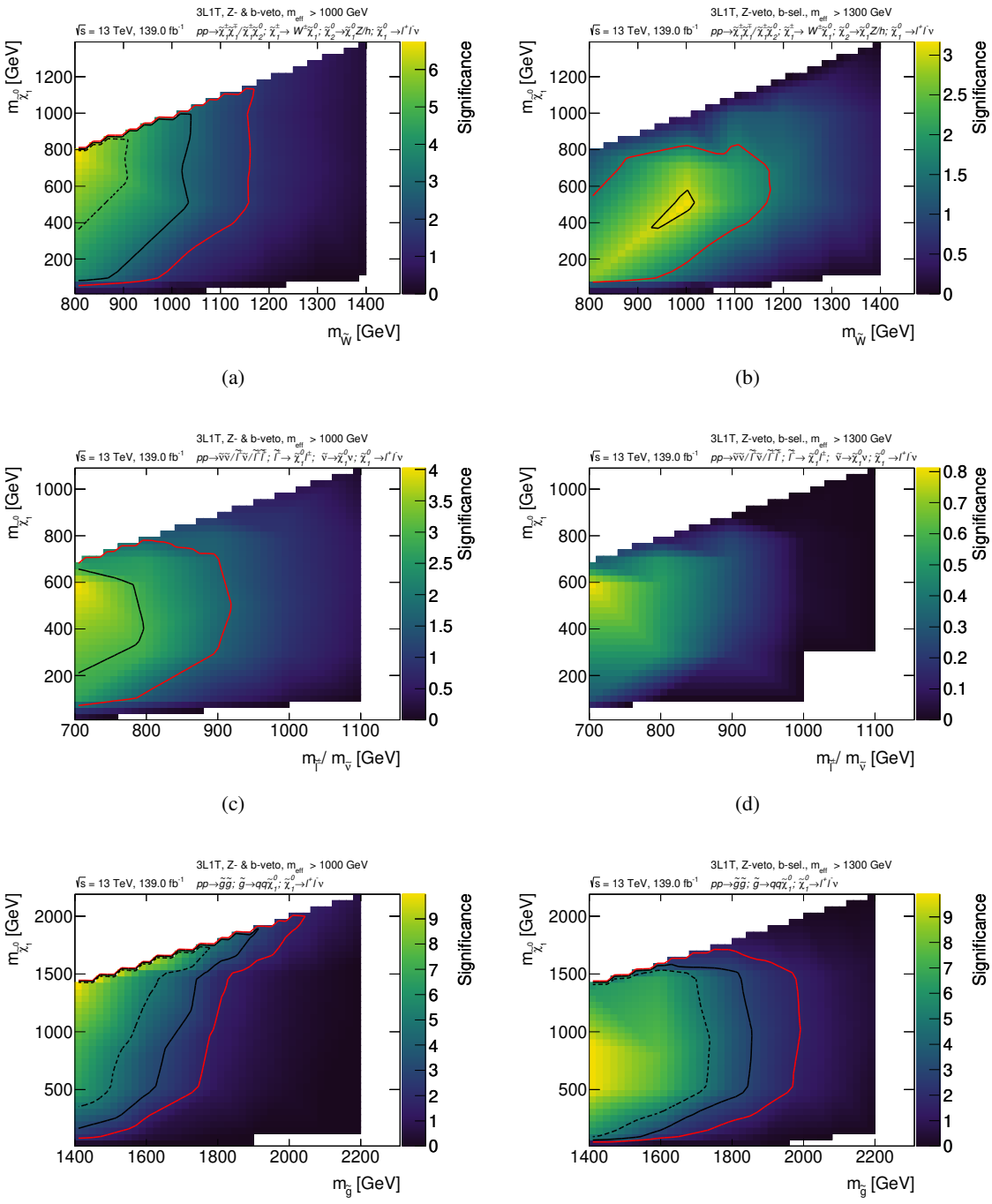

Figure B.3: Expected significance for the RPV models with $\lambda_{i33} \neq$ assuming wino (top), slepton (middle) and gluino (bottom) pair production in $\mathrm{SR1}^{\mathrm{tight}}_{b-\mathrm{veto}}$ (left) and $\mathrm{SR1}_{b-\mathrm{req}}$ (right) events for 139 fb^{-1} of data assuming a 30% uncertainty on the background. The red, solid black and dashed black lines indicate the 1.68σ, 3σ and 5σ contours, respectively.

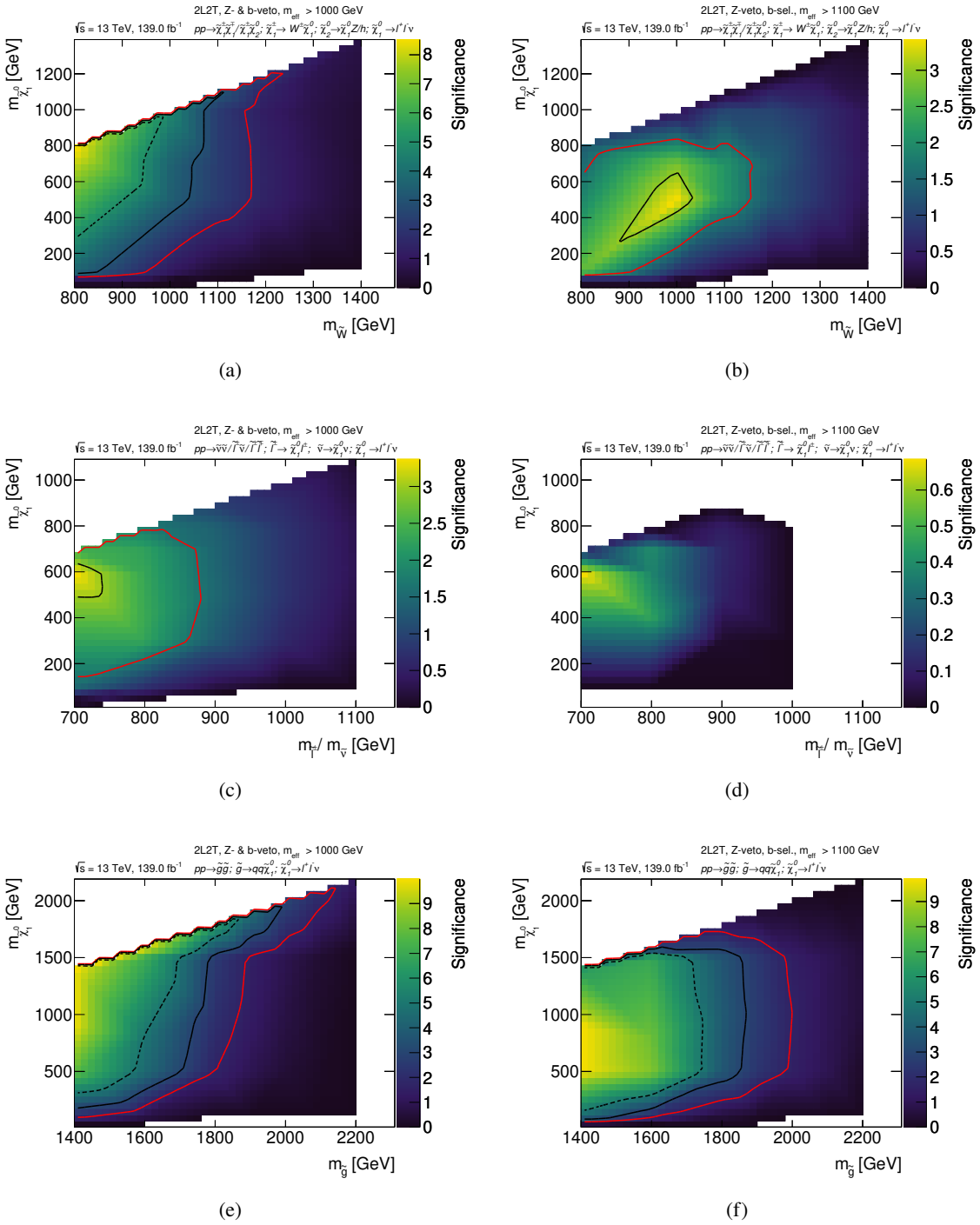

Figure B.4: Expected significance for the RPV models with $\lambda_{i33} \neq$ assuming wino (top), slepton (middle) and gluino (bottom) pair production in $\mathrm{SR2}^{\mathrm{tight}}_{b-\mathrm{veto}}$ (left) and $\mathrm{SR2}_{b-\mathrm{req}}$ (right) events for 139 fb^{-1} of data assuming a 30% uncertainty on the background. The red, solid black and dashed black lines indicate the 1.68σ, 3σ and 5σ contours, respectively.

Table B.4: Summary of theoretical uncertainties and yields of the VVV background. These are calculated for 139fb^{-1} with generator-level events. The quoted scale uncertainty is the largest deviation from the nominal and the PDF uncertainties are calculated using the uncertainty envelope. The uncertainties except the PDF components are combined in quadrature to find the combined uncertainty.

Region	Nominal yield	α_S	μ_F	PDF	PDF (alt.)	μ_R	$\mu_R \wedge \mu_F$	Total
CR_ZZ	50.8 ± 0.4	0.4%	3.9%	1.5%	2.5%	0.8%	4.7%	6.8%
CR_$t\bar{t}Z$	0.3 ± 0.0	1.1%	2.9%	1.3%	1.9%	10.0%	13.2%	17.0%
$\texttt{SR0}^{\text{loose}}_{b-\text{veto}}$	3.5 ± 0.1	0.6%	5.3%	1.4%	2.4%	6.7%	12.3%	15.3%
$\texttt{SR0}^{\text{tight}}_{b-\text{veto}}$	0.5 ± 0.0	0.7%	8.9%	2.0%	3.1%	7.0%	16.4%	20.3%
$\texttt{SR0}_{b-\text{req}}$	0.0 ± 0.0	1.7%	9.7%	5.2%	3.2%	8.0%	18.4%	23.2%
SR0C	8.3 ± 0.2	0.7%	1.4%	1.3%	2.2%	7.2%	8.6%	11.6%
SR0D	3.8 ± 0.1	0.7%	2.4%	1.3%	2.4%	7.9%	10.4%	13.6%
$\texttt{SR0-ZZ}^{\text{loose}}_{b-\text{veto}}$	3.7 ± 0.1	0.7%	2.4%	1.3%	2.5%	7.9%	10.4%	13.6%
$\texttt{SR0-ZZ}^{\text{tight}}_{b-\text{veto}}$	1.0 ± 0.1	0.6%	4.2%	1.4%	3.1%	8.3%	12.9%	16.3%
$\texttt{SR1}^{\text{loose}}_{b-\text{veto}}$	3.3 ± 0.1	0.6%	5.2%	1.4%	2.2%	6.4%	11.8%	14.6%
$\texttt{SR1}^{\text{tight}}_{b-\text{veto}}$	0.8 ± 0.1	0.4%	7.7%	2.1%	2.7%	6.0%	14.0%	17.4%
$\texttt{SR1}_{b-\text{req}}$	0.0 ± 0.0	0.7%	10.7%	1.9%	1.2%	7.3%	18.6%	22.7%
$\texttt{SR2}^{\text{loose}}_{b-\text{veto}}$	3.3 ± 0.1	0.4%	5.6%	1.4%	2.3%	6.0%	11.9%	14.7%
$\texttt{SR2}^{\text{tight}}_{b-\text{veto}}$	0.8 ± 0.1	0.5%	8.2%	1.8%	2.0%	5.4%	14.0%	17.3%
$\texttt{SR2}_{b-\text{req}}$	0.0 ± 0.0	0.3%	9.2%	2.9%	2.5%	4.1%	13.5%	17.3%
$\texttt{VR0}_{b-\text{veto}}$	13.3 ± 0.2	0.7%	0.7%	1.5%	2.3%	4.9%	4.2%	7.1%
VR_ZZ	60.4 ± 0.5	0.6%	0.9%	1.5%	2.4%	3.1%	3.7%	5.7%
VR_$t\bar{t}Z$	0.1 ± 0.0	0.8%	2.9%	1.4%	1.9%	7.6%	10.7%	13.7%
$\texttt{VR1}^{Z-\text{veto}}_{b-\text{veto}}$	17.2 ± 0.2	0.6%	0.6%	1.5%	2.3%	4.9%	4.3%	7.1%
$\texttt{VR1}^{Z-\text{req}}_{b-\text{veto}}$	35.4 ± 0.3	1.2%	1.6%	1.3%	2.5%	4.9%	6.4%	8.7%
$\texttt{VR2}^{Z-\text{veto}}_{b-\text{veto}}$	14.2 ± 0.2	0.7%	0.4%	1.6%	2.5%	4.5%	4.5%	7.1%
$\texttt{VR2}^{Z-\text{req}}_{b-\text{veto}}$	11.8 ± 0.2	0.4%	3.9%	1.5%	2.3%	2.1%	6.0%	8.0%

Table B.5: Summary of theoretical uncertainties and yields of the $t\bar{t}Z$ background. These are calculated for 139fb^{-1} with generator-level events. The quoted scale uncertainty is the largest deviation from the nominal and the PDF uncertainties are calculated using the uncertainty envelope. The uncertainties except the PDF and Generator components are combined in quadrature to find the combined uncertainty.

Region	Nominal yield	μ_F	Generator	PDF	μ_R	$\mu_R \downarrow \mu_F$	$\mu_R \uparrow \mu_F$	Total
CR_ZZ	0.9 ± 0.1	3.2%	17.2%	2.0%	8.8%	11.3%	11.7%	18.9%
CR_$t\bar{t}Z$	66.2 ± 0.7	3.0%	9.3%	1.6%	8.0%	9.4%	11.1%	16.9%
$\texttt{SR0}^{\text{loose}}_{b-\text{veto}}$	1.1 ± 0.1	4.0%	25.4%	4.4%	4.8%	4.4%	9.1%	12.5%
$\texttt{SR0}^{\text{tight}}_{b-\text{veto}}$	0.0 ± 0.0	2.6%	13.5%	10.1%	2.2%	3.4%	6.9%	13.2%
$\texttt{SR0}_{b-\text{req}}$	0.5 ± 0.1	4.6%	81.0%	5.1%	7.0%	9.0%	12.0%	17.9%
SR0C	26.4 ± 0.4	1.9%	3.6%	1.4%	8.3%	8.6%	10.4%	15.9%
SR0D	12.7 ± 0.3	2.5%	4.6%	1.6%	8.6%	9.8%	11.2%	17.5%
$\texttt{SR0-ZZ}^{\text{loose}}_{b-\text{veto}}$	1.5 ± 0.1	1.8%	27.6%	2.3%	9.6%	9.9%	11.4%	18.1%
$\texttt{SR0-ZZ}^{\text{tight}}_{b-\text{veto}}$	0.3 ± 0.0	2.8%	18.5%	3.2%	5.9%	4.8%	9.2%	12.6%
$\texttt{SR1}^{\text{loose}}_{b-\text{veto}}$	1.0 ± 0.1	0.6%	13.9%	2.2%	5.3%	6.3%	7.1%	10.3%
$\texttt{SR1}^{\text{tight}}_{b-\text{veto}}$	0.0 ± 0.0	24.1%	181.3%	10.7%	71.7%	121.1%	46.0%	150.4%
$\texttt{SR1}_{b-\text{req}}$	0.2 ± 0.1	6.5%	194.5%	7.4%	4.4%	6.1%	10.9%	15.1%
$\texttt{SR2}^{\text{loose}}_{b-\text{veto}}$	1.1 ± 0.1	2.8%	28.8%	2.7%	7.9%	8.4%	11.3%	16.6%
$\texttt{SR2}^{\text{tight}}_{b-\text{veto}}$	0.1 ± 0.0	6.1%	38.6%	15.0%	4.6%	6.5%	10.5%	19.7%
$\texttt{SR2}_{b-\text{req}}$	0.5 ± 0.1	1.0%	190.5%	3.2%	5.0%	11.3%	2.6%	13.1%
$\texttt{VR0}_{b-\text{veto}}$	5.2 ± 0.2	2.9%	37.9%	1.6%	9.8%	11.7%	12.1%	19.7%
VR_ZZ	9.7 ± 0.3	3.1%	18.6%	2.0%	8.3%	10.1%	11.4%	17.6%
VR_$t\bar{t}Z$	32.6 ± 0.5	2.9%	11.2%	1.5%	8.1%	9.3%	11.1%	16.8%
$\texttt{VR1}^{Z-\text{veto}}_{b-\text{veto}}$	5.3 ± 0.2	2.7%	18.5%	1.4%	8.5%	9.9%	11.2%	17.4%
$\texttt{VR1}^{Z-\text{req}}_{b-\text{veto}}$	10.3 ± 0.3	2.3%	13.8%	1.7%	8.3%	9.0%	10.9%	16.6%
$\texttt{VR2}^{Z-\text{veto}}_{b-\text{veto}}$	4.8 ± 0.2	3.3%	21.3%	1.7%	8.1%	10.0%	11.3%	17.4%
$\texttt{VR2}^{Z-\text{req}}_{b-\text{veto}}$	1.2 ± 0.1	0.6%	15.8%	2.1%	10.7%	12.6%	10.6%	19.8%

Table B.6: Summary of theoretical uncertainties and yields of the ZZ background. These are calculated for 139fb^{-1} with generator-level events. The quoted scale uncertainty is the largest deviation from the nominal and the PDF uncertainties are calculated using the uncertainty envelope. The uncertainties except the PDF and Generator components are combined in quadrature to find the combined uncertainty.

Region	Nominal yield	α_S	CKKW	CSSKIN	μ_F	Generator	PDF	PDF (alt.)	μ_Q	μ_R	$\mu_R \wedge \mu_F$	Total
CR_ZZ	3870.6 ± 7.4	1.4%	1.6%	0.4%	1.4%	8.2%	1.6%	2.6%	3.7%	6.1%	5.6%	9.8%
CR_$t\bar{t}Z$	0.8 ± 0.1	2.7%	31.1%	7.0%	0.7%	42.6%	2.4%	2.0%	37.1%	24.4%	26.4%	60.8%
$\texttt{SR0}^{\text{loose}}_{b-\text{veto}}$	11.6 ± 0.3	2.1%	14.4%	2.9%	0.7%	33.3%	1.3%	2.2%	4.5%	20.6%	19.7%	32.5%
$\texttt{SR0}^{\text{tight}}_{b-\text{veto}}$	1.0 ± 0.1	3.0%	17.4%	0.4%	1.6%	48.1%	1.9%	3.0%	33.1%	28.1%	29.4%	51.8%
$\texttt{SR0}_{b-\text{req}}$	0.0 ± 0.0	2.0%	12.8%	65.8%	2.2%	65.7%	2.3%	2.9%	88.5%	31.7%	34.9%	120.7%
SR0C	4.3 ± 0.2	2.0%	7.4%	3.0%	1.0%	28.4%	1.1%	1.3%	5.2%	17.6%	16.8%	26.2%
SR0D	0.9 ± 0.1	2.0%	14.2%	27.9%	0.3%	15.9%	1.4%	3.0%	37.4%	14.1%	13.7%	52.7%
$\texttt{SR0-ZZ}^{\text{loose}}_{b-\text{veto}}$	0.8 ± 0.1	1.8%	20.4%	26.3%	0.1%	9.6%	1.5%	3.6%	37.3%	11.4%	11.3%	49.3%
$\texttt{SR0-ZZ}^{\text{tight}}_{b-\text{veto}}$	0.1 ± 0.0	1.6%	67.0%	5.3%	3.4%	27.3%	4.8%	9.6%	207.7%	4.5%	6.5%	218.7%
$\texttt{SR1}^{\text{loose}}_{b-\text{veto}}$	9.2 ± 0.2	2.4%	10.0%	1.2%	0.3%	40.6%	1.3%	2.2%	4.1%	24.2%	23.2%	35.5%
$\texttt{SR1}^{\text{tight}}_{b-\text{veto}}$	1.7 ± 0.1	2.8%	18.8%	21.5%	0.4%	65.4%	3.2%	1.8%	12.2%	28.2%	27.7%	50.5%
$\texttt{SR1}_{b-\text{req}}$	0.0 ± 0.0	2.6%	51.5%	7.8%	0.4%	100.0%	2.8%	3.3%	159.1%	31.2%	28.7%	170.1%
$\texttt{SR2}^{\text{loose}}_{b-\text{veto}}$	11.5 ± 0.3	2.2%	4.2%	9.9%	0.3%	40.0%	1.5%	2.9%	9.9%	20.9%	20.4%	32.8%
$\texttt{SR2}^{\text{tight}}_{b-\text{veto}}$	2.3 ± 0.1	2.2%	20.2%	18.4%	0.1%	38.1%	2.3%	3.1%	37.6%	26.8%	26.6%	60.1%
$\texttt{SR2}_{b-\text{req}}$	0.1 ± 0.0	3.5%	69.4%	63.4%	3.6%	66.5%	2.7%	3.1%	33.0%	26.2%	28.5%	107.1%
$\texttt{VR0}_{b-\text{veto}}$	490.8 ± 2.8	1.2%	0.1%	0.0%	3.7%	16.0%	1.9%	1.8%	2.5%	5.3%	2.7%	7.4%
VR_ZZ	1389.5 ± 5.2	1.3%	3.1%	0.3%	2.0%	8.8%	1.7%	1.9%	2.1%	6.5%	5.6%	9.4%
VR_$t\bar{t}Z$	1.0 ± 0.1	2.6%	18.5%	1.0%	2.0%	73.7%	1.3%	0.3%	28.6%	25.2%	26.8%	44.8%
$\texttt{VR1}^{Z-\text{veto}}_{b-\text{veto}}$	278.9 ± 1.9	1.3%	4.4%	0.1%	2.1%	7.8%	1.7%	2.1%	3.8%	5.6%	4.6%	9.1%
$\texttt{VR1}^{Z-\text{req}}_{b-\text{veto}}$	813.9 ± 3.4	1.4%	1.4%	0.3%	1.3%	10.1%	1.6%	2.5%	2.6%	6.0%	5.5%	9.3%
$\texttt{VR2}^{Z-\text{veto}}_{b-\text{veto}}$	283.6 ± 2.2	1.4%	2.4%	0.1%	1.9%	3.5%	1.7%	2.2%	3.4%	6.1%	5.6%	9.8%
$\texttt{VR2}^{Z-\text{req}}_{b-\text{veto}}$	619.7 ± 3.0	1.4%	1.6%	1.3%	1.3%	9.4%	1.6%	2.7%	3.8%	6.1%	5.8%	10.0%

Table B.7: Summary of theoretical uncertainties and yields of the Higgs (non $t\bar{t}H$) background. These are calculated for 139fb^{-1} with generator-level events. The quoted scale uncertainty is the largest deviation from the nominal and the PDF uncertainties are calculated using the uncertainty envelope. The uncertainties except the PDF components are combined in quadrature to find the combined uncertainty.

Region	Nominal yield	α_S	μ_F	PDF	μ_R	$\mu_R \downarrow \mu_F$	$\mu_R \uparrow \mu_F$	Total
CR_ZZ	0.0 ± 0.0	—	—	—	—	—	—	—
CR_$t\bar{t}Z$	0.0 ± 0.0	6.6%	15.6%	2.1%	16.3%	15.8%	17.4%	33.4%
$\texttt{SR0}^{\text{loose}}_{b-\text{veto}}$	0.0 ± 0.0	8.0%	23.0%	4.6%	20.0%	19.6%	17.7%	41.4%
$\texttt{SR0}^{\text{tight}}_{b-\text{veto}}$	0.0 ± 0.0	9.9%	20.8%	2.7%	17.8%	19.6%	14.9%	38.2%
$\texttt{SR0}_{b-\text{req}}$	0.0 ± 0.0	—	—	—	—	—	—	—
SR0C	0.0 ± 0.0	—	—	—	—	—	—	—
SR0D	0.0 ± 0.0	—	—	—	—	—	—	—
$\texttt{SR0-ZZ}^{\text{loose}}_{b-\text{veto}}$	0.0 ± 0.0	—	—	—	—	—	—	—
$\texttt{SR0-ZZ}^{\text{tight}}_{b-\text{veto}}$	0.0 ± 0.0	—	—	—	—	—	—	—
$\texttt{SR1}^{\text{loose}}_{b-\text{veto}}$	0.0 ± 0.0	—	—	—	—	—	—	—
$\texttt{SR1}^{\text{tight}}_{b-\text{veto}}$	0.0 ± 0.0	—	—	—	—	—	—	—
$\texttt{SR1}_{b-\text{req}}$	0.0 ± 0.0	—	—	—	—	—	—	—
$\texttt{SR2}^{\text{loose}}_{b-\text{veto}}$	0.0 ± 0.0	—	—	—	—	—	—	—
$\texttt{SR2}^{\text{tight}}_{b-\text{veto}}$	0.0 ± 0.0	—	—	—	—	—	—	—
$\texttt{SR2}_{b-\text{req}}$	0.0 ± 0.0	—	—	—	—	—	—	—
$\texttt{VR0}_{b-\text{veto}}$	4.9 ± 0.0	4.9%	27.0%	4.9%	29.6%	14.2%	32.2%	53.7%
VR_ZZ	197.1 ± 0.2	4.9%	27.4%	4.9%	30.0%	14.3%	32.4%	54.4%
VR_$t\bar{t}Z$	0.0 ± 0.0	9.1%	22.2%	2.9%	20.5%	18.4%	19.4%	41.5%
$\texttt{VR1}^{Z-\text{veto}}_{b-\text{veto}}$	0.0 ± 0.0	—	—	—	—	—	—	—
$\texttt{VR1}^{Z-\text{req}}_{b-\text{veto}}$	0.0 ± 0.0	—	—	—	—	—	—	—
$\texttt{VR2}^{Z-\text{veto}}_{b-\text{veto}}$	0.0 ± 0.0	—	—	—	—	—	—	—
$\texttt{VR2}^{Z-\text{req}}_{b-\text{veto}}$	0.0 ± 0.0	—	—	—	—	—	—	—

B.4 Model Independent Limits

For each signal region, the expected and observed upper limits at 95% CL on the number of beyond-the-SM events (S^{95}_{exp} and S^{95}_{obs}) are calculated using the model-independent signal fit. The 95% CL upper limits on the signal cross section times efficiency ($\langle\epsilon\sigma\rangle^{95}_{\text{obs}}$) and the CL_b value for the background-only hypothesis are also calculated for each signal region. They are shown for both iterations of the four-lepton search for Supersymmetry in Tables B.8 and B.9.

Table B.8: Model-independent limits calculated from the signal region observations reported in Table 7.11; the 95% CL upper limit on (a) the visible cross section times efficiency ($\langle\epsilon\sigma\rangle^{95}_{obs}$), (b) the observed number of signal events(S^{95}_{obs}), and (c) the signal events given the expected number of background events (S^{95}_{exp}, $\pm1\sigma$ variations of the expected number) calculated by performing pseudo-experiments for each signal region. The last two rows report (d) the CL_b value for the background-only hypothesis, and finally (e) the one-sided p_0-value and the local significance Z (the number of equivalent Gaussian standard deviations) [327].

Sample	SR0A	SR0B	SR0C	SR0D	SR1	SR2
$\langle\epsilon\sigma\rangle^{95}_{obs}$ fb	0.32	0.14	0.87	0.36	0.28	0.13
S^{95}_{obs}	12	4.9	31	13	10	4.6
S^{95}_{exp}	$9.3^{+3.6}_{-2.3}$	$3.9^{+1.6}_{-0.8}$	23^{+8}_{-5}	$6.1^{+2.1}_{-1.3}$	$6.5^{+3.5}_{-1.3}$	$4.7^{+2.0}_{-1.3}$
CL_b	0.76	0.74	0.83	0.99	0.86	0.47
$p_{s=0}$	0.23	0.25	0.15	0.011	0.13	0.61
Z	0.75	0.69	1.0	2.3	1.2	0

Table B.9: Model-independent limits calculated from the signal region observations reported in Tables 7.12 and 7.13. Left to right: 95% CL upper limits on the visible cross section ($\langle\epsilon\sigma\rangle^{95}_{\text{obs}}$) and on the number of signal events (S^{95}_{obs}). The third column (S^{95}_{exp}) shows the 95% CL upper limit on the number of signal events, given the expected number (and $\pm 1\sigma$ excursions on the expectation) of background events. The last two columns indicate the CL_B value, i.e. the confidence level observed for the background-only hypothesis, and the discovery p-value ($p(s = 0)$).

	$\langle\epsilon\sigma\rangle^{95}_{\text{obs}}$[fb]	S^{95}_{obs}	S^{95}_{exp}	CL_B	$p(s = 0)$	Z
$\texttt{SR0}^{\text{loose}}_{b-\text{veto}}$	0.07	10.2	$10.3^{+4.6}_{-0.1}$	0.46	0.50	0.00
$\texttt{SR0}^{\text{tight}}_{b-\text{veto}}$	0.02	3.2	$5.0^{+2.7}_{-1.7}$	0.13	0.50	0.00
$\texttt{SR0}_{b-\text{req}}$	0.04	6.0	$3.6^{+2.3}_{-1.2}$	0.85	0.08	1.40
SR0C	0.31	43.1	$44.7^{+16.0}_{-12.2}$	0.47	0.50	0.00
SR0D	0.08	11.5	$11.5^{+7.4}_{-0.2}$	0.47	0.50	0.00
$\texttt{SR0-ZZ}^{\text{loose}}_{b-\text{veto}}$	0.04	5.1	$6.7^{+3.4}_{-2.1}$	0.23	0.50	0.00
$\texttt{SR0-ZZ}^{\text{tight}}_{b-\text{veto}}$	0.02	3.4	$3.5^{+2.3}_{-1.3}$	0.47	0.50	0.00
$\texttt{SR1}^{\text{loose}}_{b-\text{veto}}$	0.05	6.3	$6.9^{+3.3}_{-2.2}$	0.41	0.50	0.00
$\texttt{SR1}^{\text{tight}}_{b-\text{veto}}$	0.03	4.4	$4.0^{+2.4}_{-1.4}$	0.58	0.39	0.27
$\texttt{SR1}_{b-\text{req}}$	0.03	4.1	$4.3^{+2.5}_{-1.5}$	0.46	0.50	0.00
$\texttt{SR2}^{\text{loose}}_{b-\text{veto}}$	0.05	6.9	$5.0^{+2.8}_{-1.5}$	0.77	0.19	0.89
$\texttt{SR2}^{\text{tight}}_{b-\text{veto}}$	0.04	5.2	$2.7^{+2.0}_{-1.0}$	0.88	0.03	1.95
$\texttt{SR2}_{b-\text{req}}$	0.03	3.6	$2.9^{+2.0}_{-1.1}$	0.66	0.27	0.61

CHAPTER C

ADDITIONAL MATERIAL FOR THE $\tau_{\mathrm{LEP}}\tau_{\mathrm{HAD}}$ ANALYSIS

C.1 Fake Ratios and Scale Factors

Figures C.1 and C.2 show the p_{T} and m_{T} distributions of HF, GJ and ELEC fake τ leptons in simulated W + jets events together with the corresponding fake ratio.

Figure C.3 shows the measured fake ratios in $t\bar{t}+\tau$ and $Z \rightarrow \mu\mu+\tau$ events for the Tight τ identification criteria which are utilized in the search for direct stau production in the $\tau_{\mathrm{lep}}\tau_{\mathrm{had}}$ channel.

C.2 Multivariate Analysis for the $\tau_{\mathrm{lep}}\tau_{\mathrm{had}}$ Channel

Table C.1 reports the masses of the signal points used in each training scenario. The corresponding correlation matrices of the training variables in signal and background training events are given in Figures C.4 and C.5 for the 0 jet and 1 jet channels, respectively. Figures C.7–C.13 show the distributions of each training variable in the particular BDT training models. The distributions of the obtained classifier scores together with the corresponding ROC curves are illustrated in Figures C.16 and C.17. The rakning of each variable in terms of its relative usage to split a node in a decision tree is reported for each training in Figures C.14 and C.15.

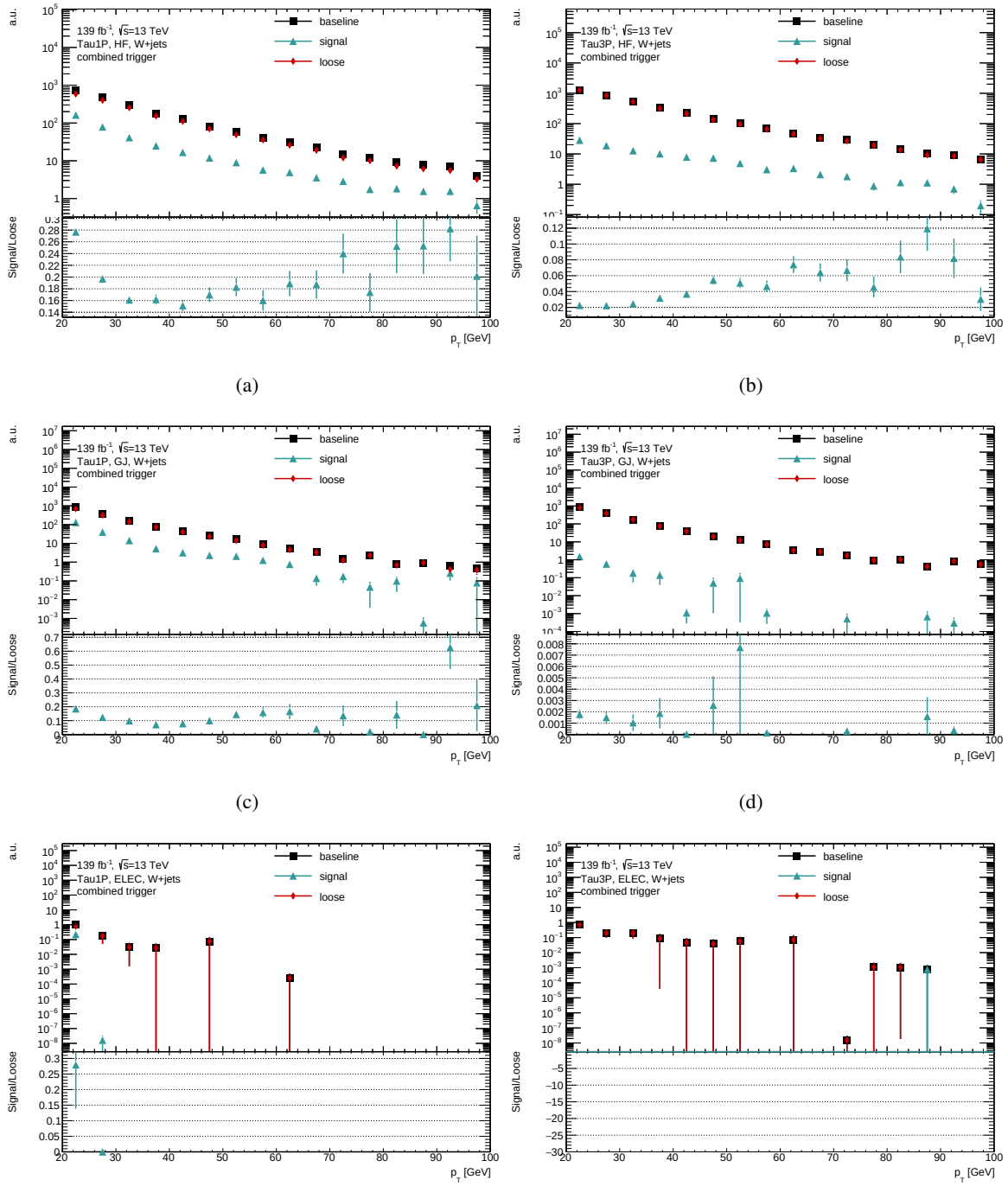

Figure C.1: p_{T} distribution of HF (top), GJ (middle) and ELEC (bottom) 1-prong (left) and 3-prong (right) fake τs in simulated W + jets events shown for baseline, loose and signal τs. The bottom panel shows the ratio of the signal to the loose distribution. The error bars indicate the statistical uncertainties.

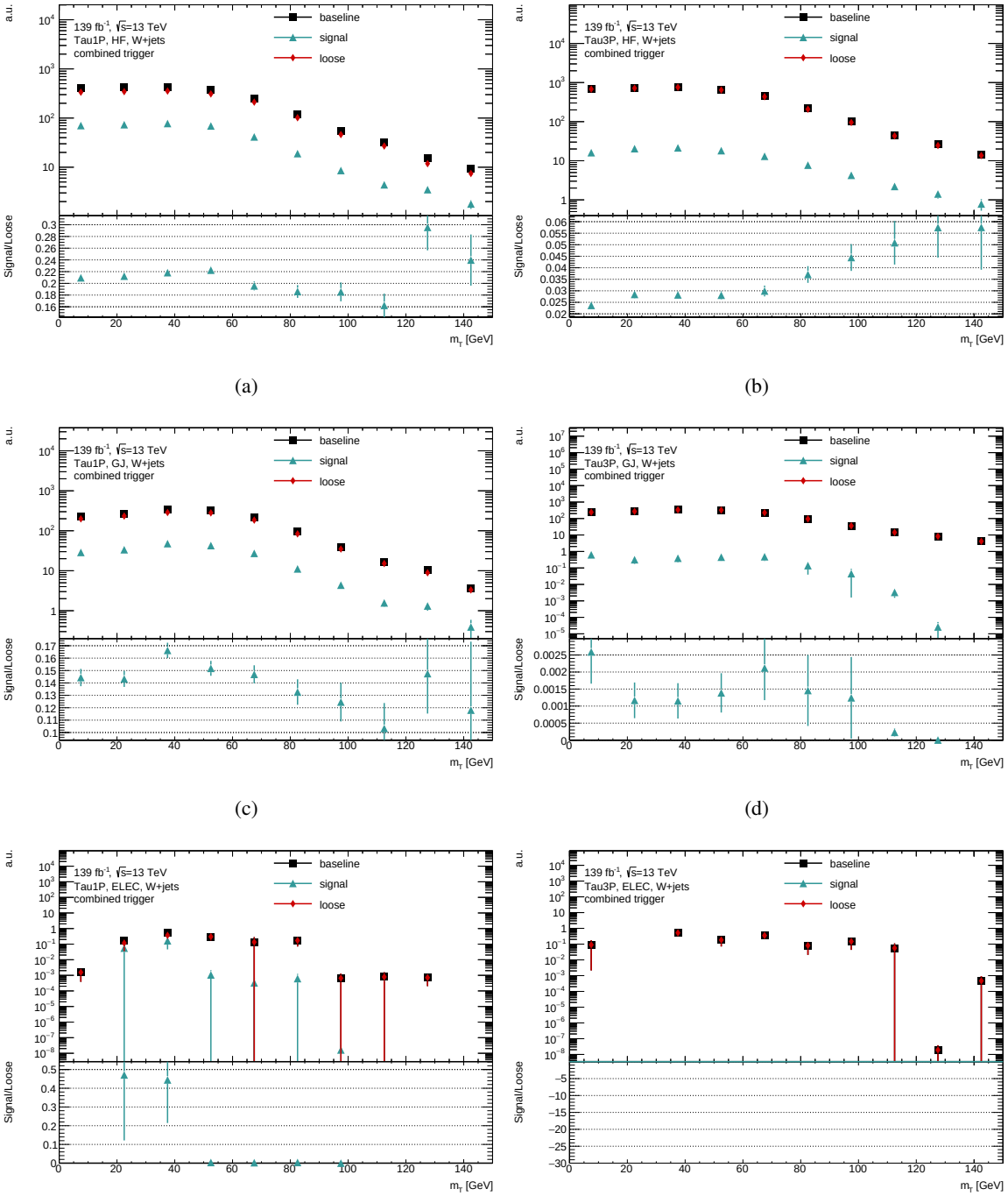

Figure C.2: m_{T} distribution of HF (top), GJ (middle) and ELEC (bottom) 1-prong (left) and 3-prong (right) fake τs in simulated W + jets events shown for baseline, loose and signal τs. The bottom panel shows the ratio of the signal to the loose distribution. The error bars indicate the statistical uncertainties.

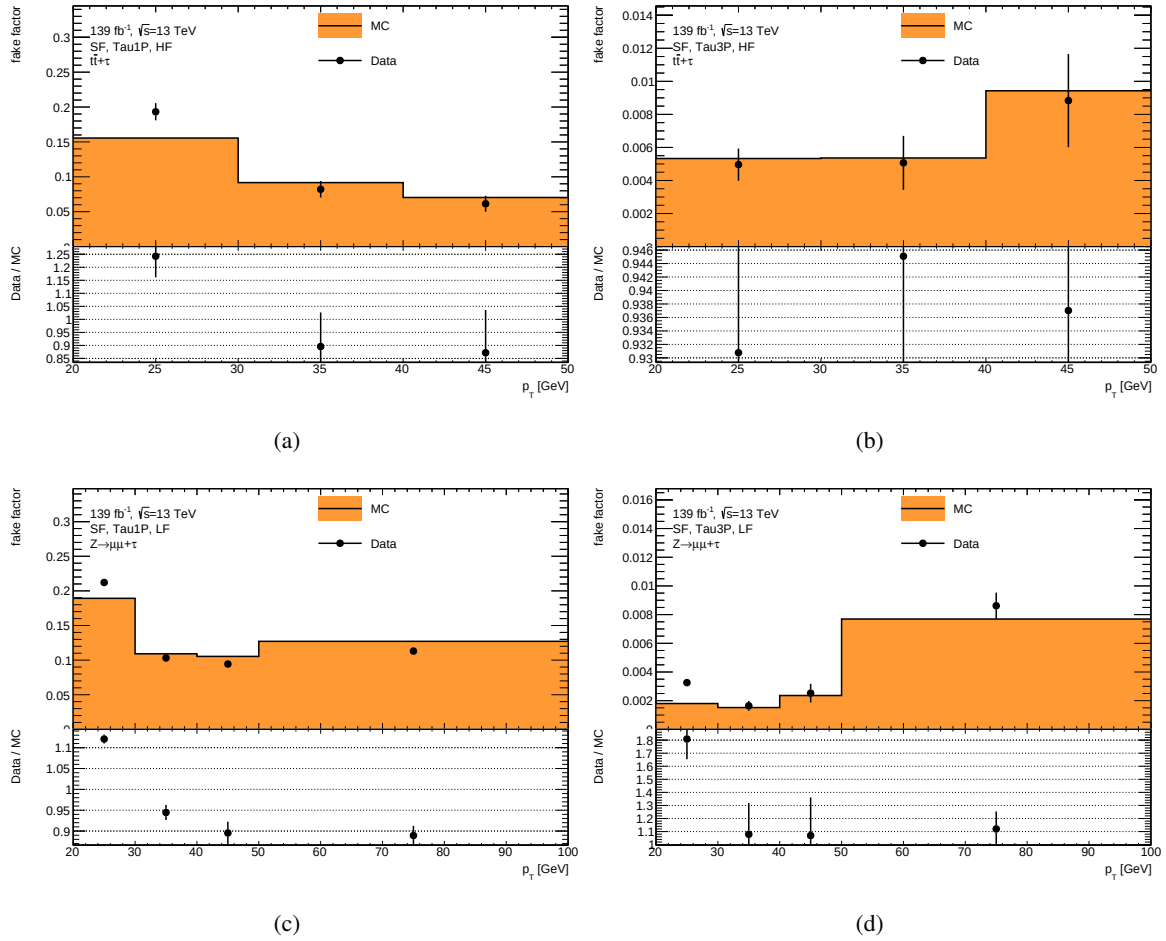

Figure C.3: HF (top) and LF (bottom) fake ratio for Tight 1-prong (left) and 3-prong (right) τ leptons shown as a function of p_{T}. The HF and LF fake ratios are measured in a $t\bar{t} + \tau$ and $Z \rightarrow \mu\mu + \tau$ CR as described in section 7.4.1. The bottom panel shows the coresponding scale factors. The error bars indicate the statistical uncertainties.

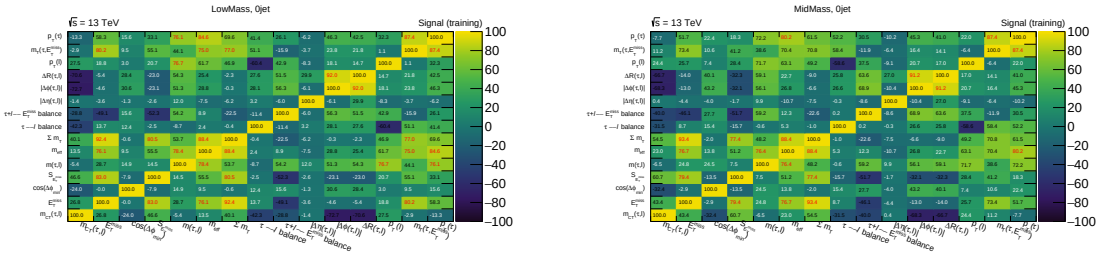

(a) (b) (c) (d) (e)

Figure C.4: Correlation Matrices of the used training variables for the four combinations of signal models (top four) and for the background (bottom) in the 0-jet category.

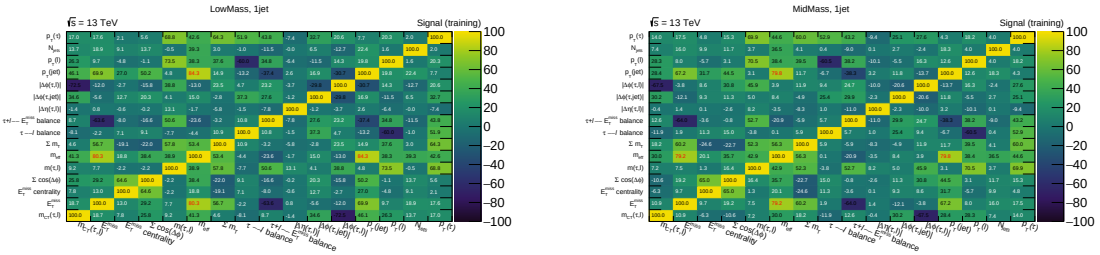

(a)

(b)

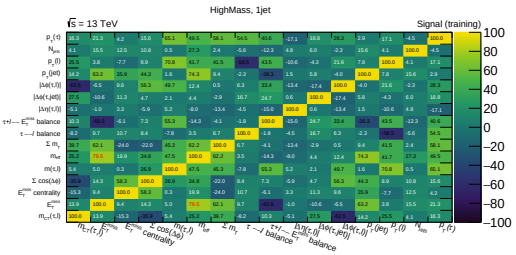

(c)

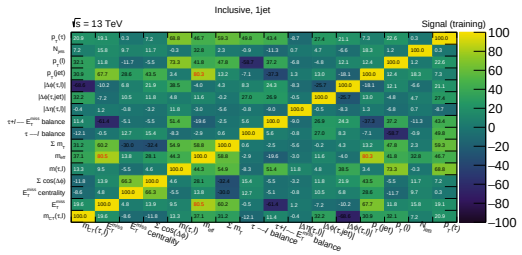

(d)

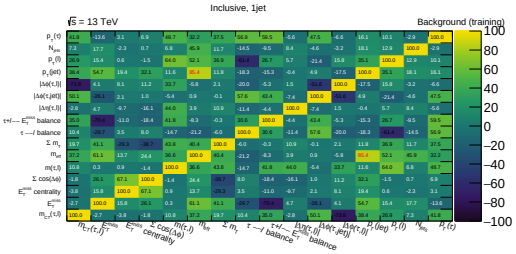

(e)

Figure C.5: Correlation Matrices of the used training variables for the four combinations of signal models (top four) and for the background (bottom) in the 1-jet category.

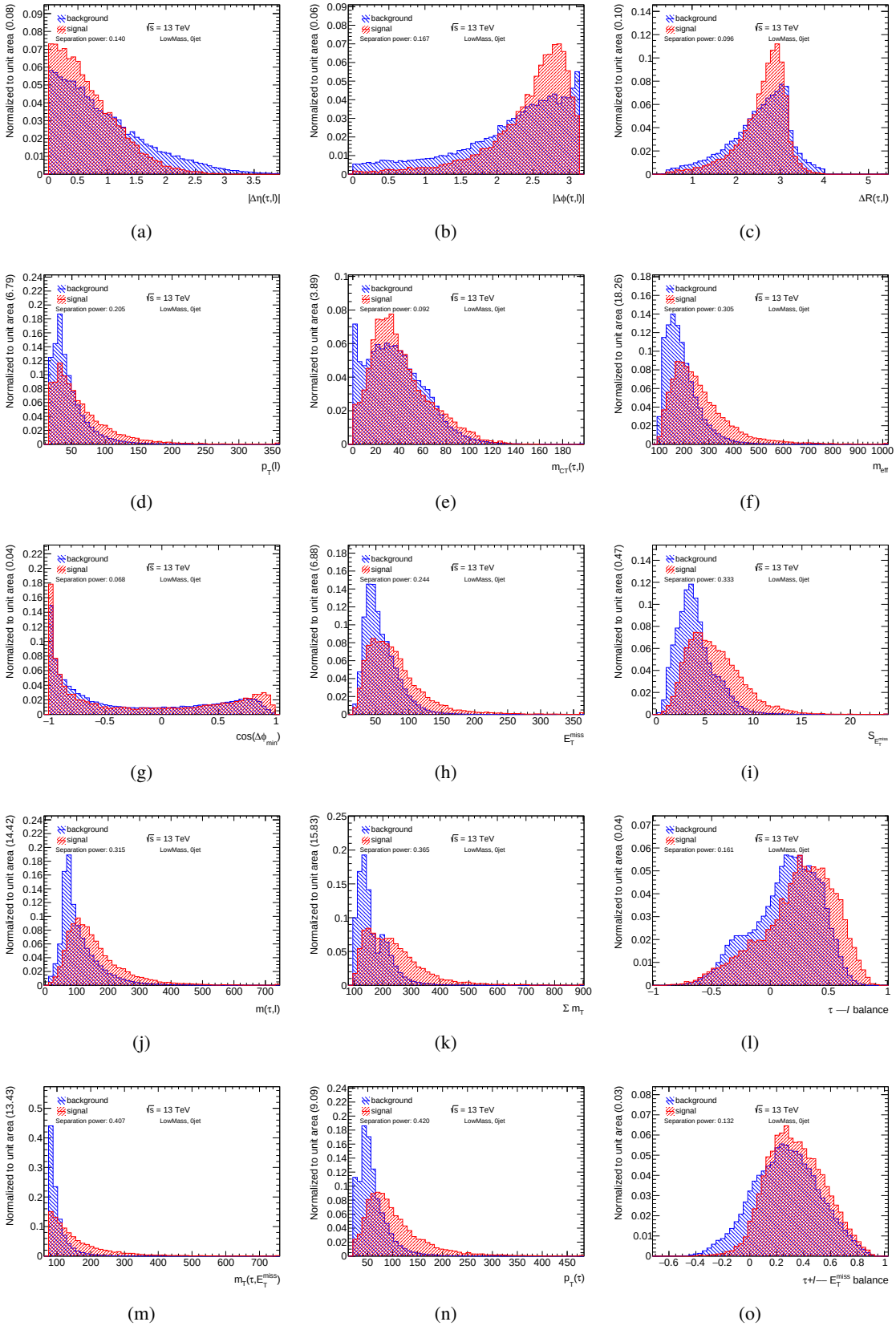

Figure C.6: Distributions of the training variables used in the LowMass 0-jet training.

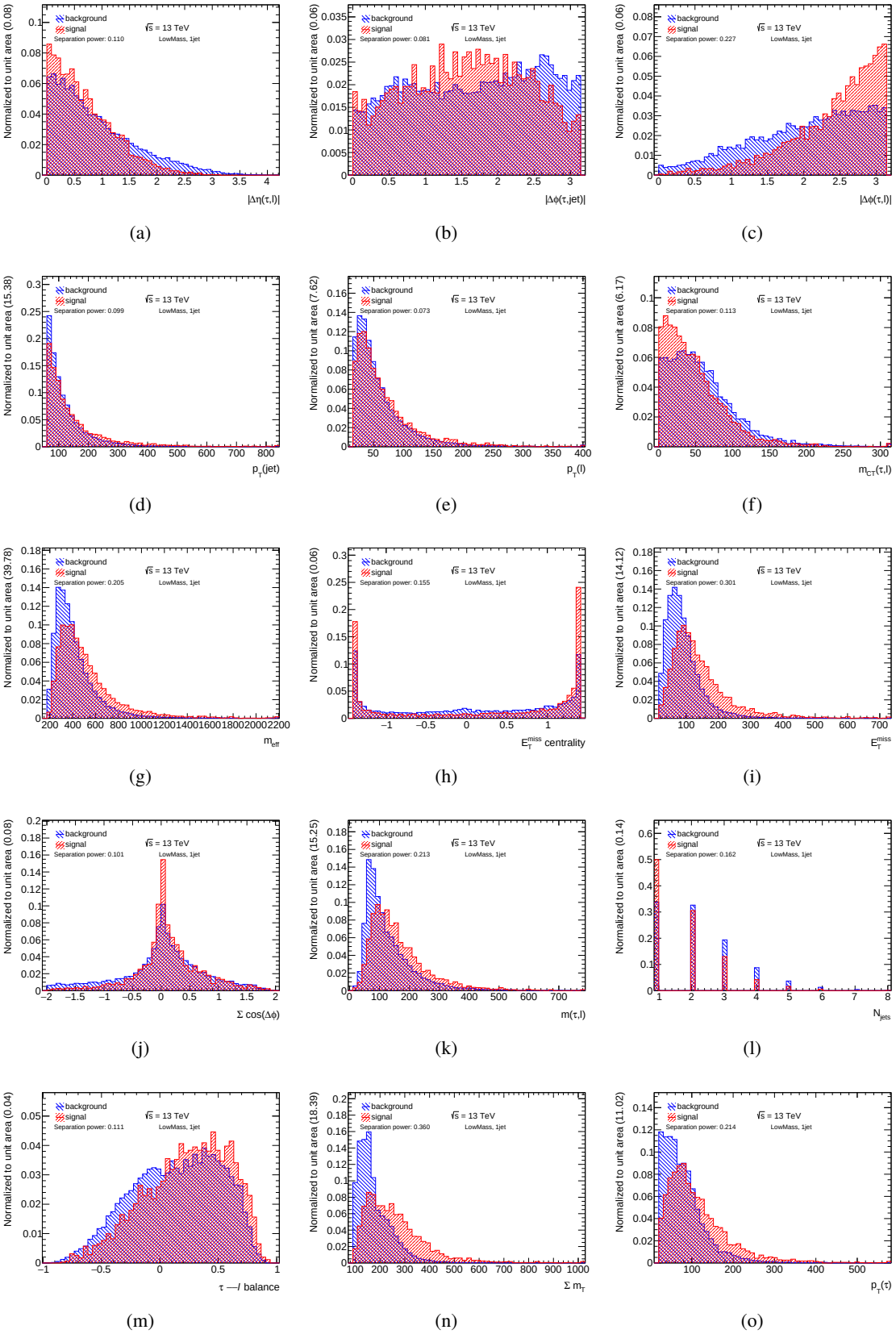

Figure C.7: Distributions of the training variables used in the LowMass 1-jet training.

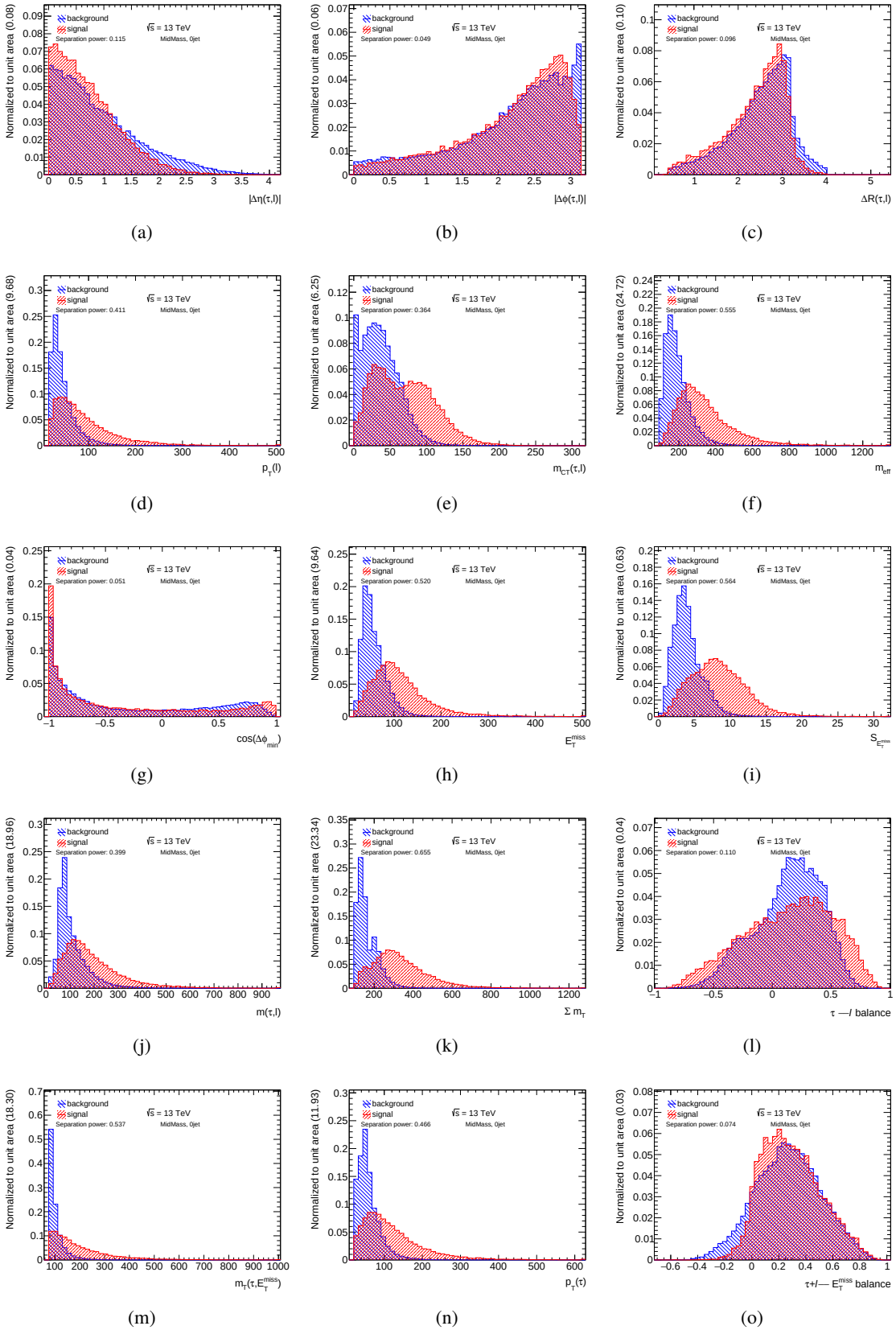

Figure C.8: Distributions of the training variables used in the MidMass 0-jet training.

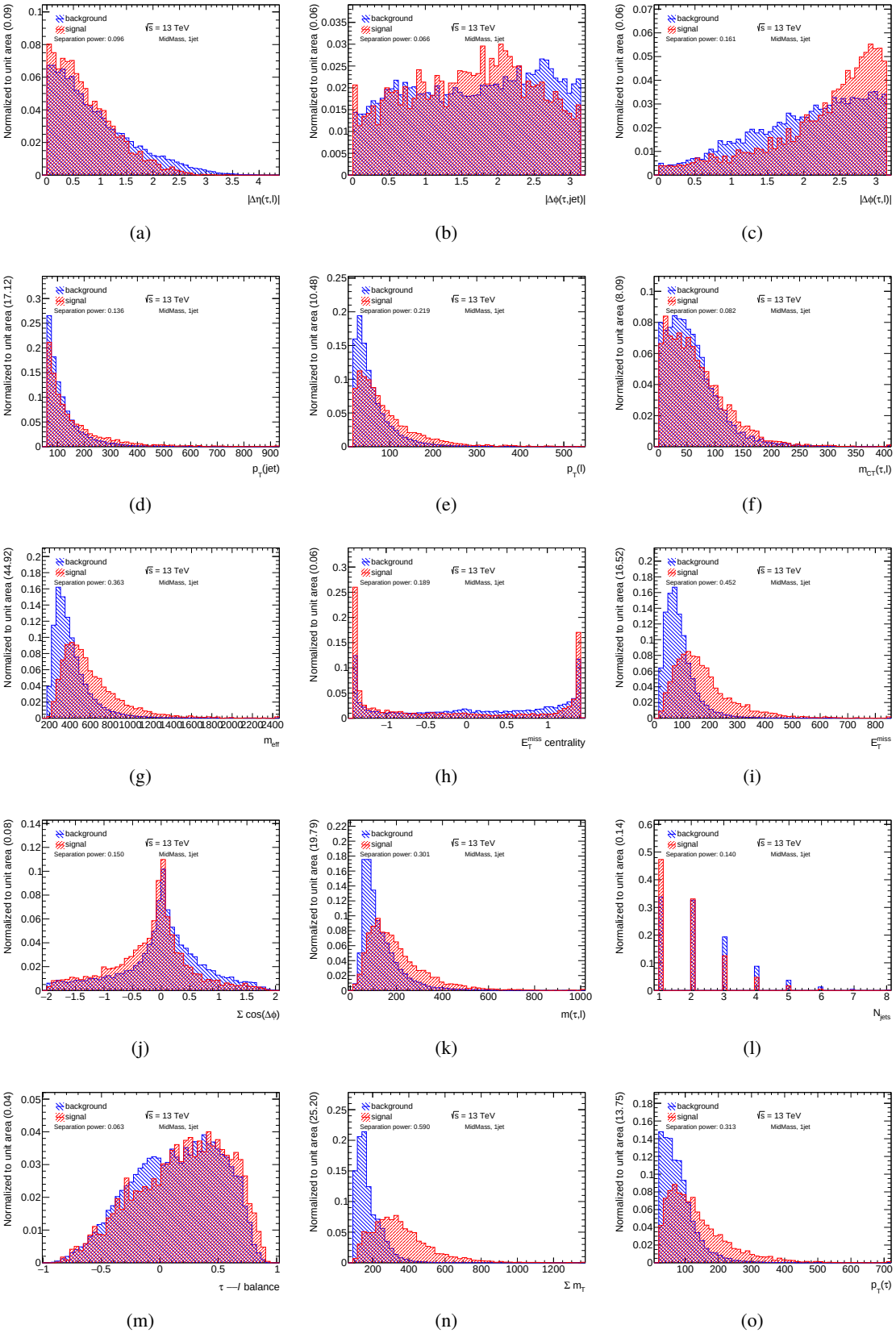

Figure C.9: Distributions of the training variables used in the MidMass 1-jet training.

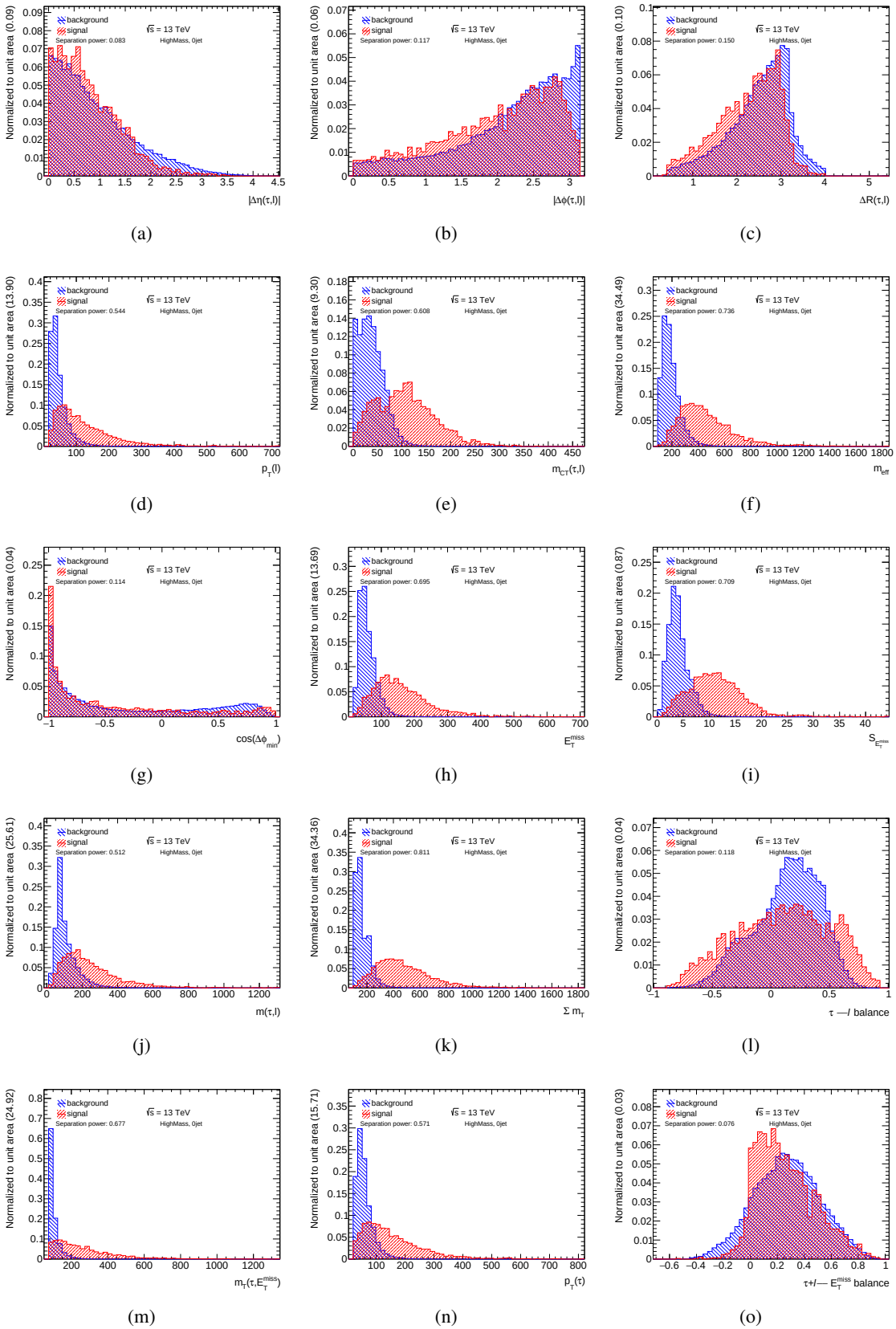

Figure C.10: Distributions of the training variables used in the HighMass 0-jet training.

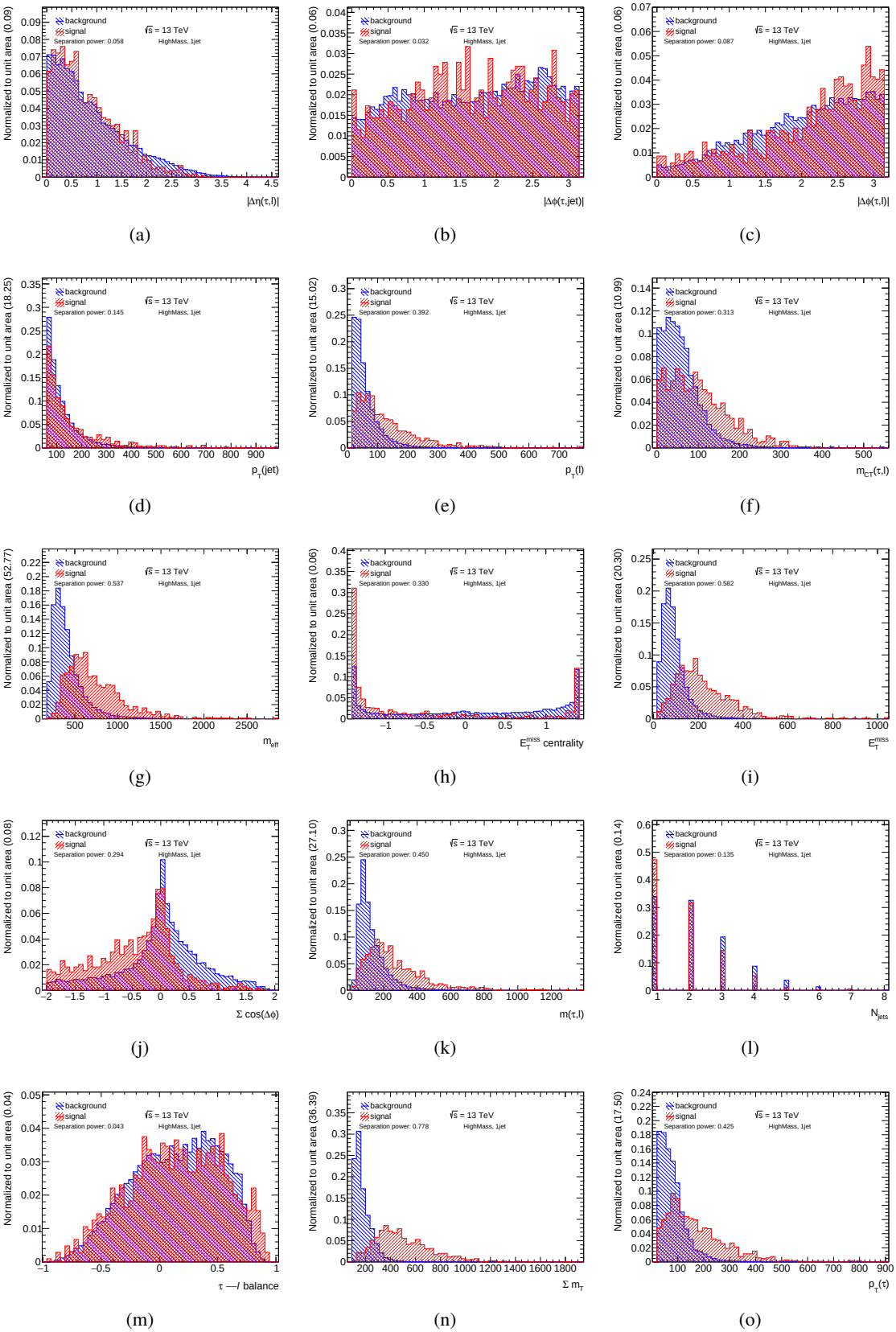

Figure C.11: Distributions of the training variables used in the HighMass 1-jet training.

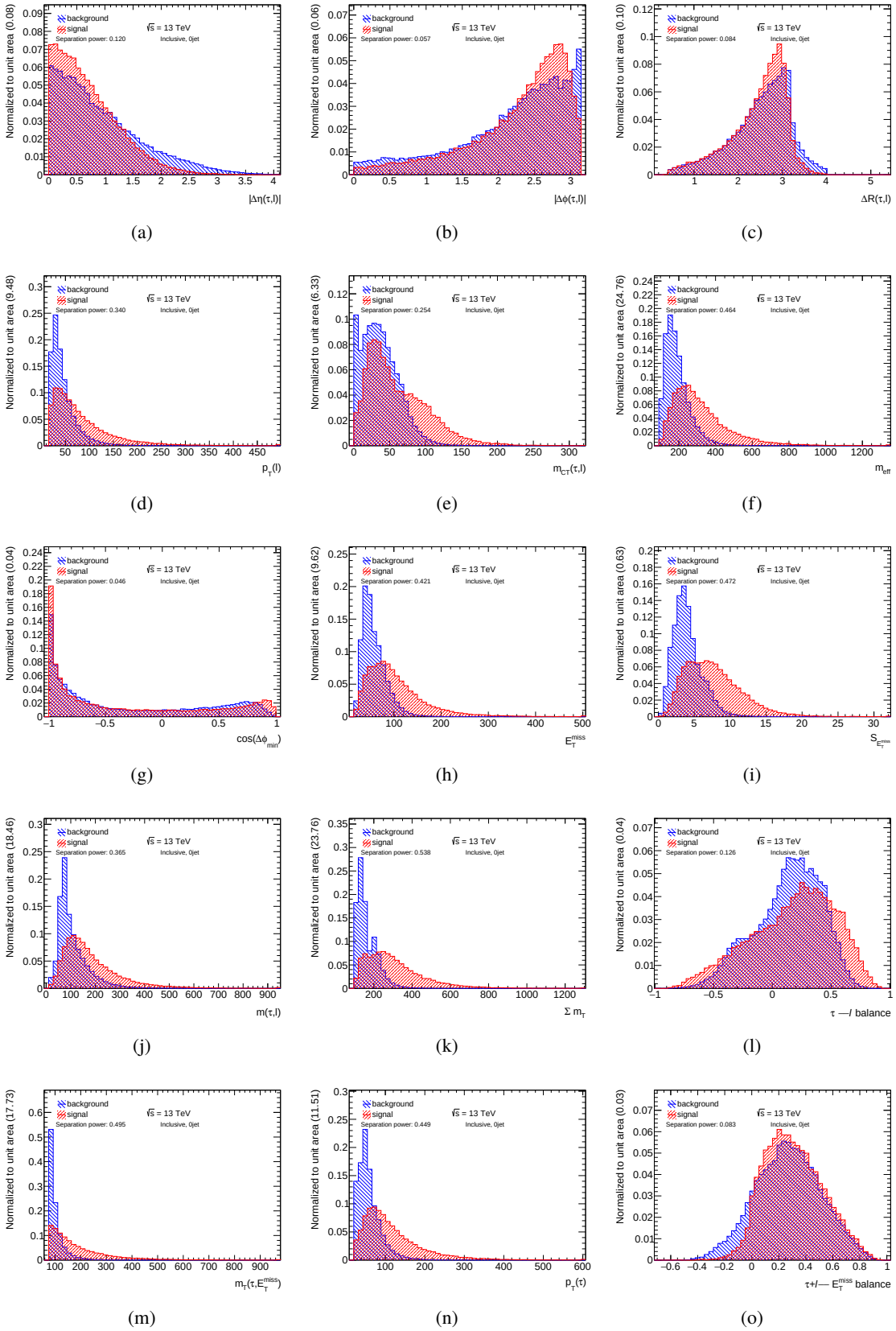

Figure C.12: Distributions of the training variables used in the Inclusive 0-jet training.

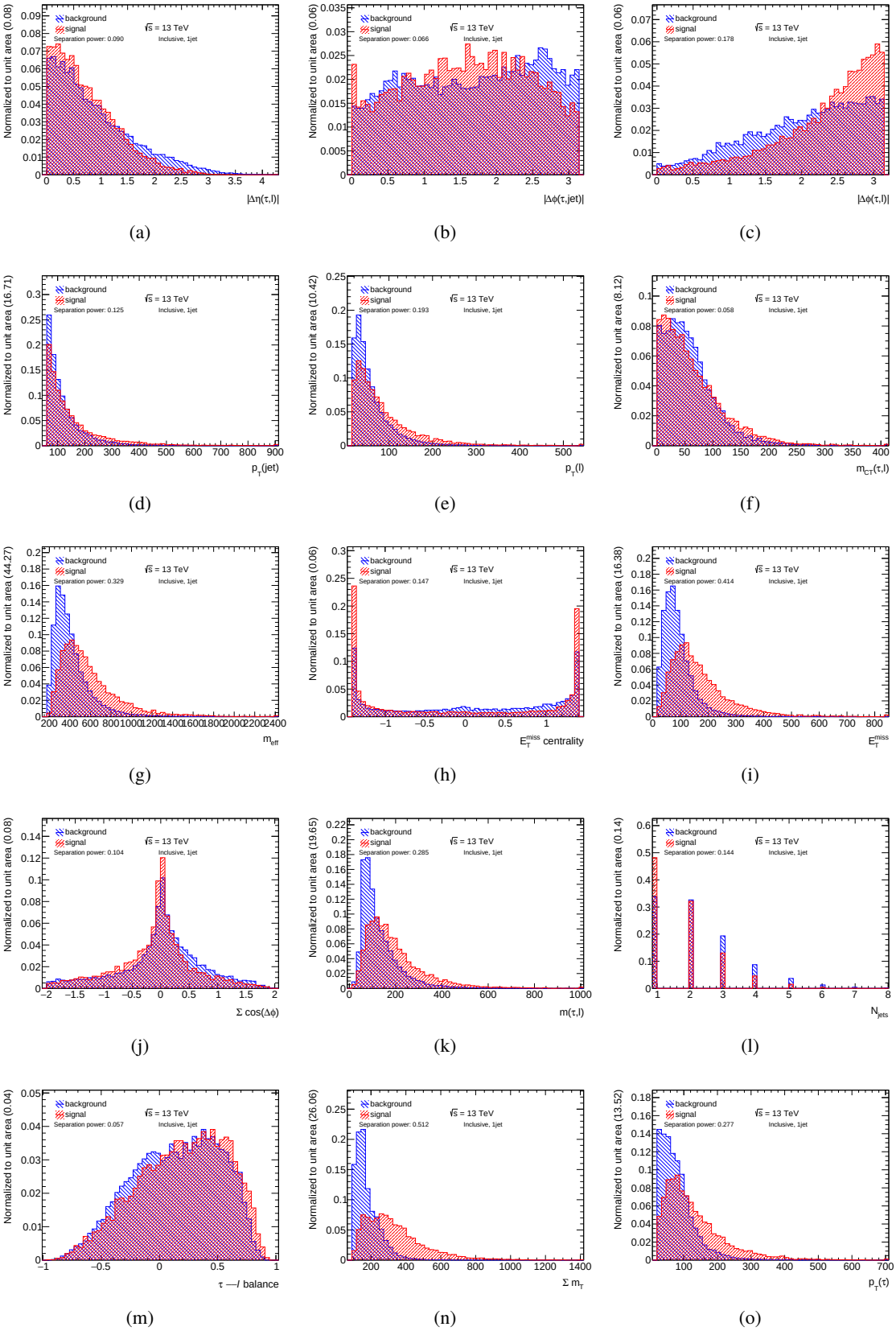

Figure C.13: Distributions of the training variables used in the Inclusive 1-jet training.

Table C.1: List of signal model points used for the multivariate analysis in the $\tau_{\text{lep}}\tau_{\text{had}}$ channel. The third column indicates in which training configuration the particular signal points have been used. For the Inclusive training all signal samples are used.

$m_{\tilde{\tau}}$ [GeV]	$m_{\tilde{\chi}_1^0}$ [GeV]	Used in
80	1	LowMass
100	1	LowMass
120	1, 40	LowMass
140	1, 40	LowMass
160	1, 40, 80	LowMass
180	1, 40	LowMass
200	1, 40, 80, 120	MidMass
220	1, 40	MidMass
240	1, 40, 80, 120, 160	MidMass
260	1, 40, 80, 120, 160	MidMass
280	1, 40, 80, 120, 160	MidMass
300	1, 40,	MidMass
320	1, 40, 80, 120, 160, 200	HighMass
340	1, 40,	HighMass
360	1, 40, 80, 120, 160, 200	HighMass
380	1	HighMass
400	1, 40, 80, 120, 160	HighMass
440	1, 40	HighMass

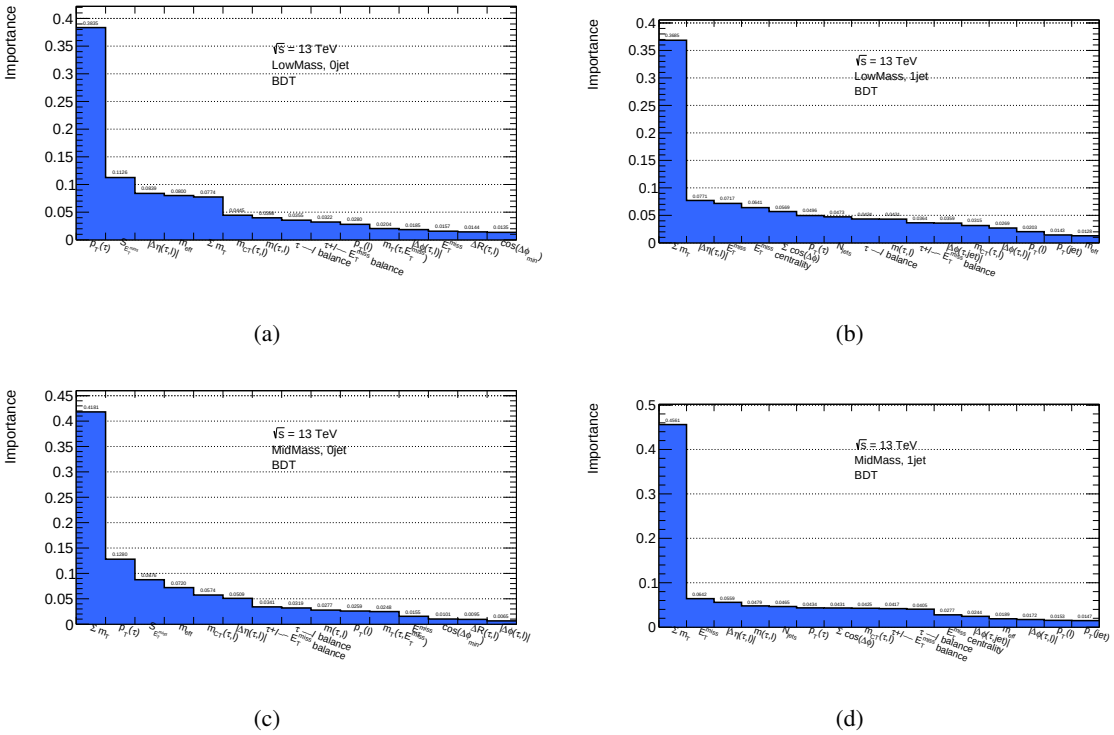

Figure C.14: Ranking of the training variables used in the LowMass (top) and MidMass (bottom) scenario for the 0 jet and 1 jet channel. The ranking is calculated from the relative fraction of nodes in which the particular variable is used.

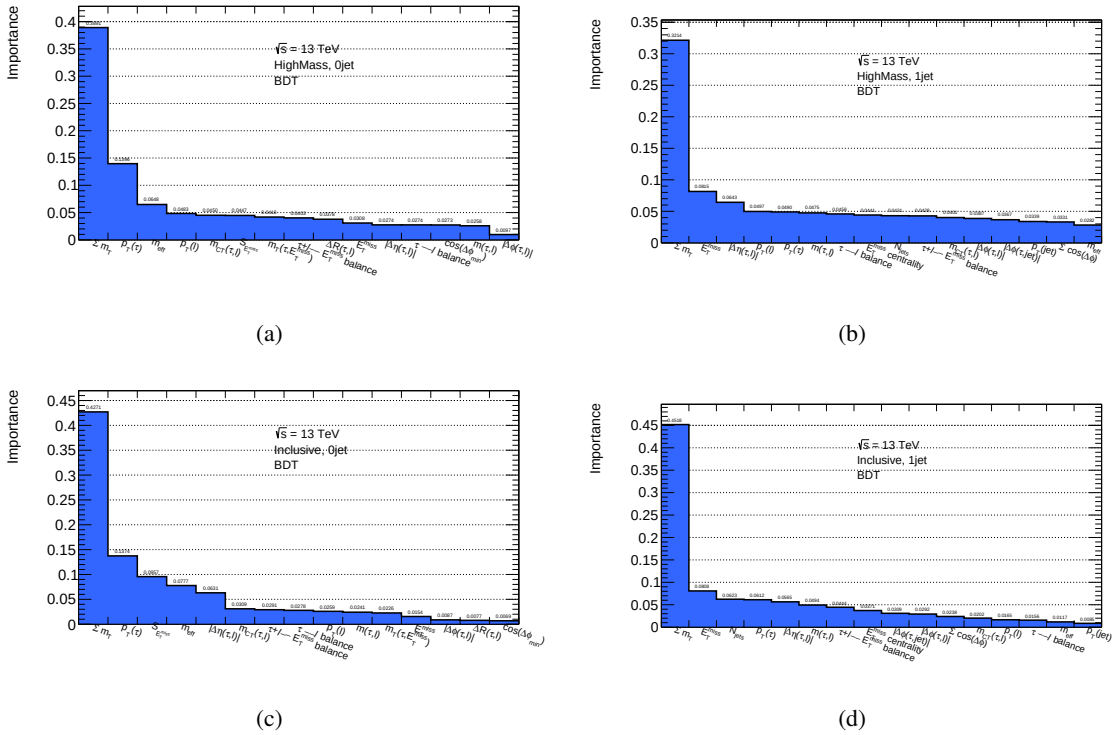

Figure C.15: Ranking of the training variables used in the HighMass (top) and Inclusive (bottom) scenario for the 0 jet and 1 jet channel. The ranking is calculated from the relative fraction of nodes in which the particular variable is used.

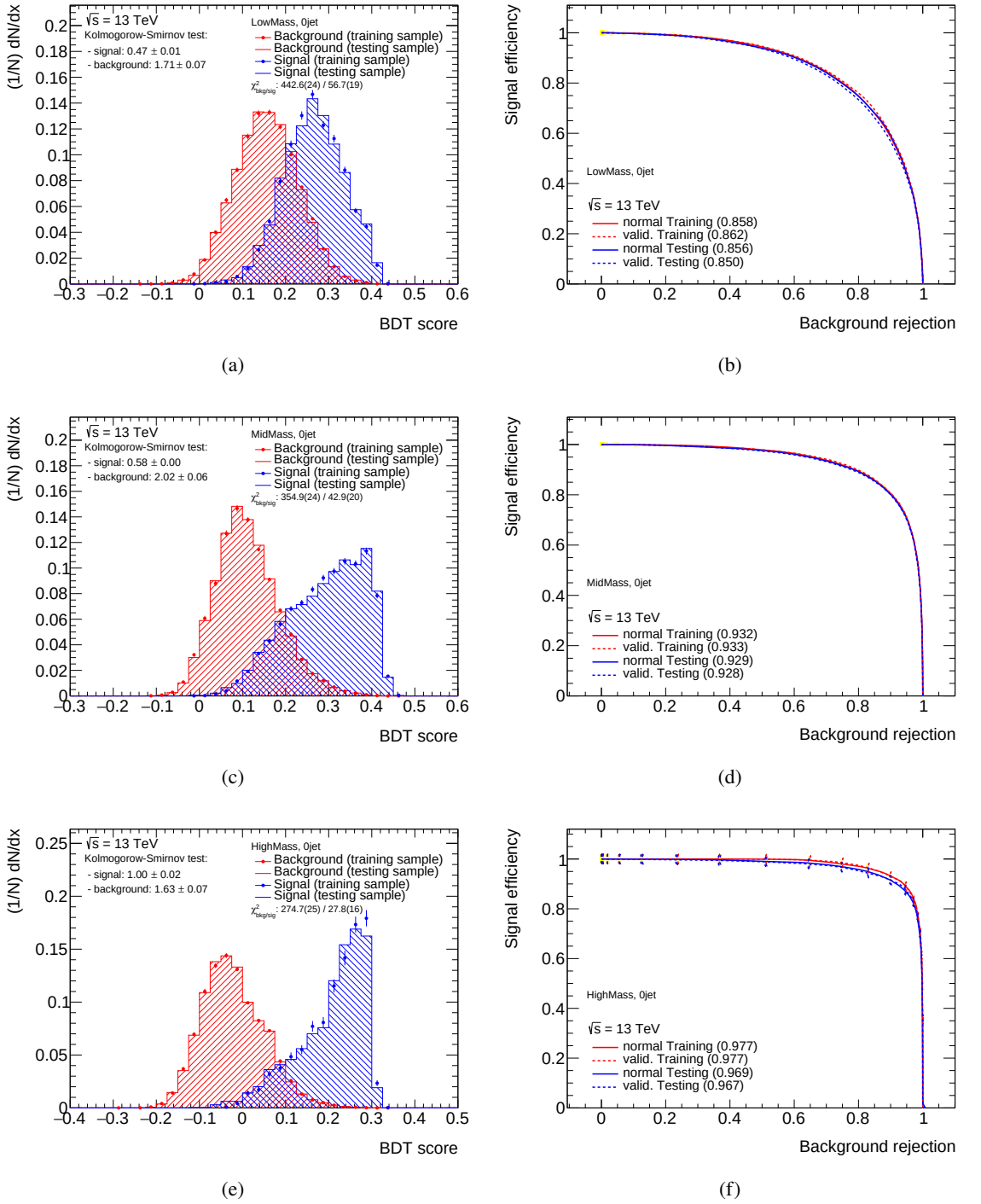

Figure C.16: stribution of the multivariate classifier scores (left)and the corresponding ROC curve (right) for a BDT trained in 0 jet events for the LowMas (top), MidMass (middle) and HighMass (bottom) scenario. In (a), the distributions of the events from the training sample for background and signal are shown as blue and red hatched areas, respectively and from the test sample as data points. The χ^2 tests are calculated from the comparison of the respective training and testing datasets. In (b), the ROC curves in the training and testing datasets are shown for the nominal (solid line) and for the cross validation (dashed line) trainings. The numbers in brackets indicate the area under the ROC curve.

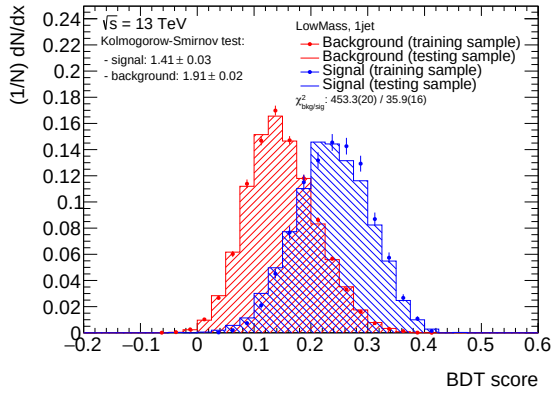

(a)

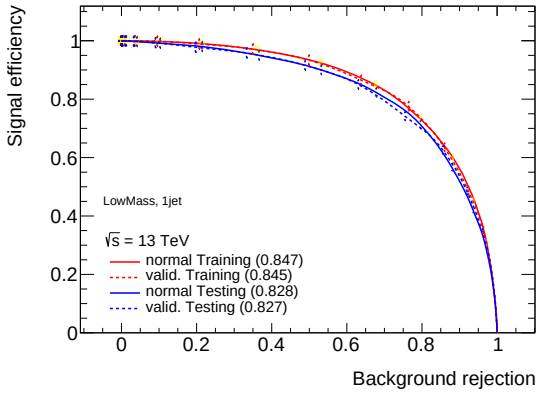

(b)

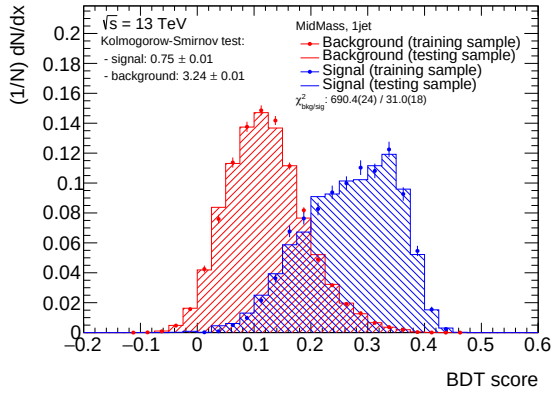

(c)

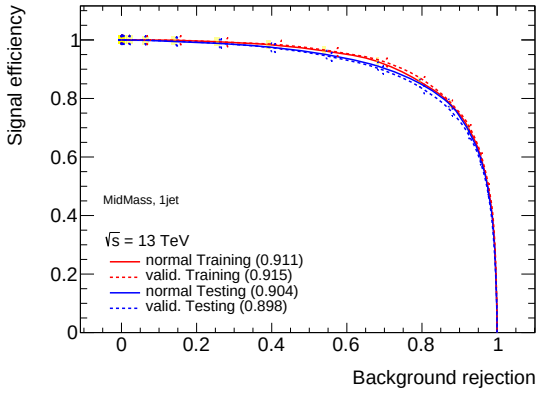

(d)

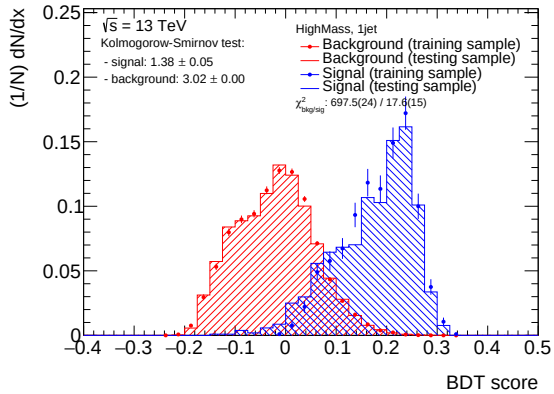

(e)

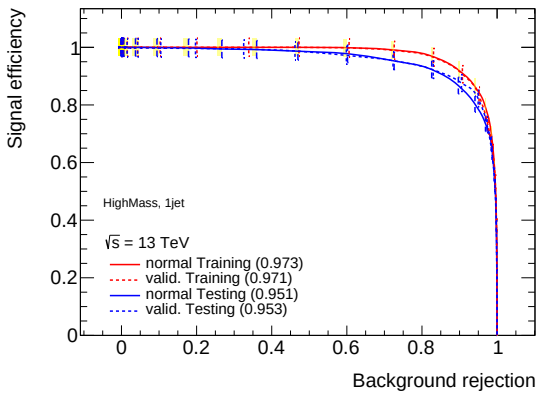

(f)

Figure C.17: stribution of the multivariate classifier scores (left)and the corresponding ROC curve (right) for a BDT trained in 1 jet events for the LowMas (top), MidMass (middle) and HighMass (bottom) scenario. In (a), the distributions of the events from the training sample for background and signal are shown as blue and red hatched areas, respectively and from the test sample as data points. The χ^2 tests are calculated from the comparison of the respective training and testing datasets. In (b), the ROC curves in the training and testing datasets are shown for the nominal (solid line) and for the cross validation (dashed line) trainings. The numbers in brackets indicate the area under the ROC curve.

BIBLIOGRAPHY

[1] A. Purcell, *Go on a particle quest at the first CERN webfest. Le premier webfest du CERN se lance à la conquête des particules*, (2012) 10.

[2] M. E. Peskin and D. V. Schroeder,
An Introduction To Quantum Field Theory (Frontiers in Physics), Westview Press, 1995, ISBN: 0201503972.

[3] M. Schwartz, *Quantum Field Theory and the Standard Model*,
Cambridge University Press, 2014, ISBN: 9781107034730.

[4] L. H. Ryder, *Quantum Field Theory 2nd ed.* Cambridge University Press, 1996, ISBN: 9780521478144.

[5] D. H. Perkins, *Introduction to High Energy Physics 4th ed.* Cambridge University Press, 2000, ISBN: 9780521621960.

[6] M. Böhm, A. Denner and H. Joos,
Gauge theories of strong and electroweak interactions; 3rd ed. B. G. Teubner, 2001.

[7] D. J. Griffiths, *Introduction to elementary particles; 2nd rev. version*, Physics textbook, Wiley, 2008.

[8] N. Agafonova et al.,
Observation of a first ν_τ candidate in the OPERA experiment in the CNGS beam,
Phys. Rev. Lett. **B691** (2010) 138, arXiv: 1006.1623 [hep-ex].

[9] S. Weinberg, *A Model of Leptons*, Phys. Rev. Lett. **19** (21 1967) 1264.

[10] S. L. Glashow, *Partial Symmetries of Weak Interactions*, Nucl. Phys. **22** (1961) 579.

[11] A. Salam, *Weak and Electromagnetic Interactions*, Conf. Proc. **C680519** (1968) 367.

[12] C. S. Wu, E. Ambler, R. W. Hayward, D. D. Hoppes and R. P. Hudson, *Experimental Test of Parity Conservation in Beta Decay*, Phys. Rev. **105** (4 1957) 1413, URL: http://link.aps.org/doi/10.1103/PhysRev.105.1413.

[13] W. Hollik, *Quantum field theory and the Standard Model*, (), arXiv: 1012.3883 [hep-ph].

[14] ATLAS Collaboration, Georges Aad, et. al, *Measurement of the W-boson mass in pp collisions at $\sqrt{s} = 7$ TeV with the ATLAS detector*, Eur. Phys. J. C **78** (2018) 110, arXiv: 1701.07240 [hep-ex], Erratum: Eur. Phys. J. C **78** (2018) 898.

[15] G. Arnison et al., *Experimental Observation of Isolated Large Transverse Energy Electrons with Associated Missing Energy at $\sqrt{s} = 540$ GeV*, Phys. Lett. **B122** (1983) 103.

[16] M. L. Perl et al., *Evidence for Anomalous Lepton Production in $e^+ - e^-$ Annihilation*, Phys. Rev. Lett. **35** (22 1975) 1489, URL: http://link.aps.org/doi/10.1103/PhysRevLett.35.1489.

[17] F. Abe et al., *Observation of top quark production in $\bar{p}p$ collisions*, Phys. Rev. Lett. **74** (1995) 2626, arXiv: hep-ex/9503002 [hep-ex].

[18] S. W. Herb et al., *Observation of a Dimuon Resonance at 9.5 GeV in 400-GeV Proton-Nucleus Collisions*, Phys. Rev. Lett. **39** (1977) 252.

[19] J. .-.-E. Augustin et al., *Discovery of a Narrow Resonance in e^+e^- Annihilation*, Phys. Rev. Lett. **33** (1974) 1406.

[20] M. Gell-Mann, *A Schematic Model of Baryons and Mesons*, Phys. Lett. **8** (1964) 214.

[21] K. G. Wilson, *Confinement of quarks*, Phys. Rev. D **10** (8 1974) 2445, URL: https://link.aps.org/doi/10.1103/PhysRevD.10.2445.

[22] *Evidence for Exotic Hadron Contributions to $\Lambda_b^0 \to J/\psi p\pi^-$ Decays*, Phys. Rev. Lett. **117** (8 2016) 082003, URL: https://link.aps.org/doi/10.1103/PhysRevLett.117.082003.

[23] *Observation of $J/\psi\phi$ Structures Consistent with Exotic States from Amplitude Analysis of $B^+ \to J/\psi\phi K^+$ Decays*, Phys. Rev. Lett. **118** (2 2017) 022003, URL: https://link.aps.org/doi/10.1103/PhysRevLett.118.022003.

[24] *Amplitude analysis of $B^+ \to J/\psi\phi K^+$ decays*, Phys. Rev. D **95** (1 2017) 012002, URL: https://link.aps.org/doi/10.1103/PhysRevD.95.012002.

[25] H. Bohr and H. Nielsen, *Hadron production from a boiling quark soup: A thermodynamical quark model predicting particle ratios in hadronic collisions*, Nuclear Physics B **128** (1977) 275, ISSN: 0550-3213.

[26] J. Goldstone, A. Salam and S. Weinberg, *Broken Symmetries*, Phys. Rev. **127** (3 1962) 965, URL: http://link.aps.org/doi/10.1103/PhysRev.127.965.

[27] F. Englert and R. Brout, *Broken Symmetry and the Mass of Gauge Vector Mesons*, Phys. Rev. Lett. **13** (9 1964) 321.

[28] P. W. Higgs, *Broken Symmetries and the Masses of Gauge Bosons*, Phys. Rev. Lett. **13** (16 1964) 508.

[29] P. W. Higgs, *Broken symmetries, massless particles and gauge fields*, Phys. Lett. **12** (1964) 132.

[30] P. W. Higgs, *Spontaneous Symmetry Breakdown without Massless Bosons*, Phys. Rev. **145** (4 1966) 1156.

[31] W. Gordon, *Der Comptoneffekt nach der Schrödingerschen Theorie*, Zeitschrift für Physik **40** (1926) 117, ISSN: 0044-3328, URL: https://doi.org/10.1007/BF01390840.

[32] ATLAS Collaboration, Georges Aad, et. al, *Observation of a new particle in the search for the Standard Model Higgs boson with the ATLAS detector at the LHC*, Phys. Lett. B **716** (2012) 1, arXiv: 1207.7214 [hep-ex].

[33] CMS Collaboration, *Observation of a new boson at a mass of 125 GeV with the CMS experiment at the LHC*, Phys. Lett. B **716** (2012) 30, arXiv: 1207.7235 [hep-ex].

[34] ATLAS Collaboration, Georges Aad, et. al, *Measurement of the Higgs boson mass in the $H \to ZZ^* \to 4\ell$ and $H \to \gamma\gamma$ channels with $\sqrt{s} = 13$ TeV pp collisions using the ATLAS detector*, Phys. Lett. B **784** (2018) 345, arXiv: 1806.00242 [hep-ex].

[35] M. Kobayashi and T. Maskawa, *CP Violation in the Renormalizable Theory of Weak Interaction*, Prog. Theor. Phys. **49** (1973) 652.

[36] N. Cabibbo, *Unitary Symmetry and Leptonic Decays*, Phys. Rev. Lett. **10** (12 1963) 531, URL: https://link.aps.org/doi/10.1103/PhysRevLett.10.531.

[37] J. H. Christenson, J. W. Cronin, V. L. Fitch and R. Turlay, *Evidence for the 2π Decay of the K_2^0 Meson*, Phys. Rev. Lett. **13** (4 1964) 138.

[38] J. Erler and M. Schott, *Electroweak Precision Tests of the Standard Model after the Discovery of the Higgs Boson*, Prog. Part. Nucl. Phys. **106** (2019) 68, arXiv: 1902.05142 [hep-ph].

[39] *Standard Model Summary Plots Summer 2019*, ATL-PHYS-PUB-2019-024, 2019, URL: http://cds.cern.ch/record/2682186.

[40] A. Einstein, *Die Grundlage der allgemeinen Relativitätstheorie*, Annalen der Physik **354** (1916) 769.

[41] S. W. Hawking and R. Penrose, *The Singularities of gravitational collapse and cosmology*, Proc. Roy. Soc. Lond. **A314** (1970) 529.

[42] L. Smolin, *What are we missing in our search for quantum gravity?*, (2017), arXiv: 1705.09208 [gr-qc].

[43] R. P. Woodard, *How Far Are We from the Quantum Theory of Gravity?*, Rept. Prog. Phys. **72** (2009) 126002, arXiv: 0907.4238 [gr-qc].

[44] F. Zwicky, *Republication of: The redshift of extragalactic nebulae*, English, General Relativity and Gravitation **41** (2009) 207, ISSN: 0001-7701.

[45] W. Tucker et al., *1e0657-56: a contender for the hottest known cluster of galaxies*, Astrophys. J. **496** (1998) L5, arXiv: astro-ph/9801120 [astro-ph].

[46] R. Massey, T. Kitching and J. Richard, *The dark matter of gravitational lensing*, Reports on Progress in Physics **73** (2010) 086901, ISSN: 1361-6633, URL: http://dx.doi.org/10.1088/0034-4885/73/8/086901.

[47] *Planck 2013 results. I. Overview of products and scientific results*, Astron. Astrophys. **571** (2014) A1, arXiv: 1303.5062 [astro-ph.CO].

[48] V. Springel et al., *Simulating the joint evolution of quasars, galaxies and their large-scale distribution*, Nature **435** (2005) 629, arXiv: astro-ph/0504097 [astro-ph].

[49] *Planck 2015 results. XIII. Cosmological parameters*, Astron. Astrophys. **594** (2016) A13, arXiv: 1502.01589 [astro-ph.CO].

[50] A. G. Riess et al., *Observational evidence from supernovae for an accelerating universe and a cosmological constant*, Astron. J. **116** (1998) 1009, arXiv: astro-ph/9805201 [astro-ph].

[51] A. Kusenko, F. Takahashi and T. T. Yanagida, *Dark Matter from Split Seesaw*, Phys. Lett. **B693** (2010) 144, arXiv: 1006.1731 [hep-ph].

[52] L. M. Krauss, S. Nasri and M. Trodden, *A Model for neutrino masses and dark matter*, Phys. Rev. **D67** (2003) 085002, arXiv: hep-ph/0210389 [hep-ph].

[53] C. Boehm and P. Fayet, *Scalar dark matter candidates*, Nucl. Phys. **B683** (2004) 219, arXiv: hep-ph/0305261 [hep-ph].

[54] S. P. Martin, *A Supersymmetry Primer*, Adv. Ser. Direct. High Energy Phys. **18** (1998) 1, arXiv: hep-ph/9709356.

[55] J. Ellis, J. Hagelin, D. V. Nanopoulos, K. A. Olive and M. Srednicki, *Supersymmetric relics from the big bang*, Nucl. Phys. B **238** (1984) 453.

[56] H. Goldberg, *Constraint on the Photino Mass from Cosmology*, Phys. Rev. Lett. **50** (1983) 1419, Erratum: Phys. Rev. Lett. **103** (2009) 099905.

[57] H. Goldberg, Phys. Rev. Lett. **103** (2009) 099905.

[58] J. M. Lindert, F. D. Steffen and M. K. Trenkel, *Direct stau production at hadron colliders in cosmologically motivated scenarios*, Journal of High Energy Physics **2011** (2011), ISSN: 1029-8479, URL: http://dx.doi.org/10.1007/JHEP08(2011)151.

[59] R. D. Peccei, *The Strong CP problem and axions*, Lect. Notes Phys. **741** (2008) 3, [,3(2006)], arXiv: hep-ph/0607268 [hep-ph].

[60] V. Anastassopoulos et al., *New CAST Limit on the Axion-Photon Interaction*, Nature Phys. **13** (2017) 584, arXiv: 1705.02290 [hep-ex].

[61] K. Agashe and G. Servant, *Warped unification, proton stability and dark matter*, Phys. Rev. Lett. **93** (2004) 231805, arXiv: hep-ph/0403143 [hep-ph].

[62] N. Arkani-Hamed, A. G. Cohen and H. Georgi, *Electroweak symmetry breaking from dimensional deconstruction*, Phys. Lett. **B513** (2001) 232, arXiv: hep-ph/0105239 [hep-ph].

[63] N. Arkani-Hamed et al., *The Minimal moose for a little Higgs*, JHEP **08** (2002) 021, arXiv: hep-ph/0206020 [hep-ph].

[64] G. W. Horndeski, *Second-Order Scalar-Tensor Field Equations in a Four-Dimensional Space*, International Journal of Theoretical Physics **10** (1974) 363.

[65] ATLAS Collaboration, Georges Aad, et. al, *Search for scalar dark energy in $t\bar{t}$ + E_T^{miss} and mono-jet final states with the ATLAS detector*, ATL-PHYS-PUB-2018-008, 2018, URL: https://cds.cern.ch/record/2627837.

[66] P. Brax, *What makes the Universe accelerate? A review on what dark energy could be and how to test it*, Reports on Progress in Physics **81** (2017) 016902, URL: https://doi.org/10.1088%2F1361-6633%2Faa8e64.

[67] A. D. Sakharov, *Violation of CP Invariance, C asymmetry, and baryon asymmetry of the universe*, Pisma Zh. Eksp. Teor. Fiz. **5** (1967) 32, [Usp. Fiz. Nauk161,no.5,61(1991)].

[68] L. Canetti, M. Drewes and M. Shaposhnikov, *Matter and Antimatter in the Universe*, New J. Phys. **14** (2012) 095012, arXiv: 1204.4186 [hep-ph].

[69] B. Ishak, *Neutrino Cosmology, by J. Lesgourgues, G. Mangano, G. Miele and S. Pastor*, Contemporary Physics **54** (2013) 178, eprint: https://doi.org/10.1080/00107514.2013.818063, URL: https://doi.org/10.1080/00107514.2013.818063.

[70] S. Gariazzo et al., *Neutrino masses and their ordering: global data, priors and models*, Journal of Cosmology and Astroparticle Physics **2018** (2018) 011, ISSN: 1475-7516, URL: http://dx.doi.org/10.1088/1475-7516/2018/03/011.

[71] Z. Maki, M. Nakagawa and S. Sakata, *Remarks on the Unified Model of Elementary Particles*, Progress of Theoretical Physics **28** (1962) 870, ISSN: 0033-068X, eprint: http://oup.prod.sis.lan/ptp/article-pdf/28/5/870/5258750/28-5-870.pdf, URL: https://doi.org/10.1143/PTP.28.870.

[72] B. Pontecorvo, *Inverse beta processes and nonconservation of lepton charge*, Sov. Phys. JETP **7** (1958) 172, [Zh. Eksp. Teor. Fiz.34,247(1957)].

[73] M. Lindner, T. Ohlsson and G. Seidl, *Seesaw mechanisms for Dirac and Majorana neutrino masses*, Phys. Rev. **D65** (2002) 053014, arXiv: hep-ph/0109264 [hep-ph].

[74] M. J. Dolinski, A. W. Poon and W. Rodejohann, *Neutrinoless Double-Beta Decay: Status and Prospects*, Annual Review of Nuclear and Particle Science **69** (2019) 219, ISSN: 1545-4134, URL: http://dx.doi.org/10.1146/annurev-nucl-101918-023407.

[75] *An improved upper limit on the neutrino mass from a direct kinematic method by KATRIN*, (2019), arXiv: 1909.06048 [hep-ex].

[76] F. Couchot et al., *Cosmological constraints on the neutrino mass including systematic uncertainties*, Astron. Astrophys. **606** (2017) A104, arXiv: 1703.10829 [astro-ph.CO].

[77] L. Susskind, *Dynamics of spontaneous symmetry breaking in the Weinberg-Salam theory*, Phys. Rev. D **20** (10 1979) 2619, URL: https://link.aps.org/doi/10.1103/PhysRevD.20.2619.

[78] S. Ferrara and B. Zumino, *Supergauge invariant Yang-Mills theories*, Nucl. Phys. B **79** (1974) 413.

[79] J. Wess and B. Zumino, *Supergauge invariant extension of quantum electrodynamics*, Nucl. Phys. B **78** (1974) 1.

[80] A. Salam and J. Strathdee, *Super-symmetry and non-Abelian gauges*, Phys. Lett. B **51** (1974) 353.

[81] J. Wess and B. Zumino, *Supergauge transformations in four dimensions*, Nucl. Phys. B **70** (1974) 39.

[82] R. Haag, J. T. Łopuszański and M. Sohnius, *All possible generators of supersymmetries of the S-matrix*, Nuclear Physics B **88** (1975) 257, ISSN: 0550-3213, URL: http://www.sciencedirect.com/science/article/pii/0550321375902795.

[83] S. Coleman and J. Mandula, *All Possible Symmetries of the S Matrix*, Phys. Rev. **159** (5 1967) 1251, URL: https://link.aps.org/doi/10.1103/PhysRev.159.1251.

[84] R. Ball, *Chiral gauge theory*, Physics Reports **182** (1989) 1, ISSN: 0370-1573, URL: http://www.sciencedirect.com/science/article/pii/0370157389900276.

[85] H. E. Haber and L. S. Haskins, *Supersymmetric Theory and Models*, Anticipating the Next Discoveries in Particle Physics (2018), URL: http://dx.doi.org/10.1142/9789813233348_0006.

[86] G. Giudice and R. Rattazzi, *Theories with gauge-mediated supersymmetry breaking*, Physics Reports **322** (1999) 419, ISSN: 0370-1573, URL: http://dx.doi.org/10.1016/S0370-1573(99)00042-3.

[87] L. Randall and R. Sundrum, *Out of this world supersymmetry breaking*, Nuclear Physics B **557** (1999) 79, ISSN: 0550-3213, URL: http://dx.doi.org/10.1016/S0550-3213(99)00359-4.

[88] A. H. Chamseddine, R. Arnowitt and P. Nath, *Locally Supersymmetric Grand Unification*, Phys. Rev. Lett. **49** (14 1982) 970, URL: https://link.aps.org/doi/10.1103/PhysRevLett.49.970.

[89] R. Barbier et al., *R-parity violating supersymmetry*, Phys. Rept. **420** (2005) 1, arXiv: hep-ph/0406039 [hep-ph].

[90] G. Jungman, M. Kamionkowski and K. Griest, *Supersymmetric dark matter*, Phys. Rept. **267** (1996) 195, arXiv: hep-ph/9506380 [hep-ph].

[91] *Search for proton decay via $p \to e^+\pi^0$ and $p \to \mu^+\pi^0$ in 0.31 megaton · years exposure of the Super-Kamiokande water Cherenkov detector*, Phys. Rev. D **95** (1 2017) 012004, URL: https://link.aps.org/doi/10.1103/PhysRevD.95.012004.

[92] H.-S. Lee, *Minimal gauge origin of baryon triality and flavorful signatures at the LHC*, Phys. Lett. **B704** (2011) 316, arXiv: 1007.1040 [hep-ph].

[93] A. D. Martin, W. J. Stirling, R. S. Thorne and G. Watt, *Parton distributions for the LHC*, The European Physical Journal C **63** (2009) 189, ISSN: 1434-6052, URL: http://dx.doi.org/10.1140/epjc/s10052-009-1072-5.

[94] J. C. Collins, D. E. Soper and G. Sterman, *Factorization of Hard Processes in QCD*, 2004, arXiv: hep-ph/0409313 [hep-ph].

[95] R. P. Feynman, 'The Behavior of Hadron Collisions at Extreme Energies', *Special Relativity and Quantum Theory: A Collection of Papers on the Poincaré Group*, ed. by M. E. Noz and Y. S. Kim, Springer Netherlands, 1988 289, ISBN: 978-94-009-3051-3, URL: https://doi.org/10.1007/978-94-009-3051-3_25.

[96] A. Buckley et al., *LHAPDF6: parton density access in the LHC precision era*, The European Physical Journal C **75** (2015), ISSN: 1434-6052, URL: http://dx.doi.org/10.1140/epjc/s10052-015-3318-8.

[97] A. D. Martin, W. J. Stirling, R. S. Thorne and G. Watt, *Uncertainties on α_S in global PDF analyses and implications for predicted hadronic cross sections*, The European Physical Journal C **64** (2009) 653, ISSN: 1434-6052, URL: http://dx.doi.org/10.1140/epjc/s10052-009-1164-2.

[98] A. D. Martin, W. J. Stirling, R. S. Thorne and G. Watt, *Heavy-quark mass dependence in global PDF analyses and 3- and 4-flavour parton distributions*, The European Physical Journal C **70** (2010) 51, ISSN: 1434-6052, URL: http://dx.doi.org/10.1140/epjc/s10052-010-1462-8.

[99] S. Dulat et al., *Higgs Boson Cross Section from CTEQ-TEA Global Analysis*, Phys. Rev. **D89** (2014) 113002, arXiv: 1310.7601 [hep-ph].

[100] H. L. Lai et al., *Global QCD analysis of parton structure of the nucleon: CTEQ5 parton distributions*, Eur. Phys. J. C **12** (2000) 375, arXiv: hep-ph/9903282.

[101] J. Butterworth et al., *PDF4LHC recommendations for LHC Run II*, J. Phys. G **43** (2016) 023001, arXiv: 1510.03865 [hep-ph].

[102] J. Pumplin et al., *New Generation of Parton Distributions with Uncertainties from Global QCD Analysis*, JHEP **07** (2002) 012, arXiv: hep-ph/0201195.

[103] H.-L. Lai et al., *New parton distributions for collider physics*, Physical Review D **82** (2010), ISSN: 1550-2368, URL: http://dx.doi.org/10.1103/PhysRevD.82.074024.

[104] R. D. Ball et al., *Parton distributions with LHC data*, Nucl. Phys. B **867** (2013) 244, arXiv: 1207.1303 [hep-ph].

[105] R. D. Ball et al., *Parton distributions for the LHC Run II*, JHEP **04** (2015) 040, arXiv: 1410.8849 [hep-ph].

[106] Y. L. Dokshitzer, *Calculation of the Structure Functions for Deep Inelastic Scattering and e+ e- Annihilation by Perturbation Theory in Quantum Chromodynamics.*, Sov. Phys. JETP **46** (1977) 641, [Zh. Eksp. Teor. Fiz.73,1216(1977)].

[107] V. N. Gribov and L. N. Lipatov, *Deep inelastic e p scattering in perturbation theory*, Sov. J. Nucl. Phys. **15** (1972) 438, [Yad. Fiz.15,781(1972)].

[108] G. Altarelli and G. Parisi, *Asymptotic freedom in parton language*, Nuclear Physics B **126** (1977) 298, ISSN: 0550-3213, URL: http://www.sciencedirect.com/science/article/pii/0550321377903844.

[109] A. D. Martin, *Proton structure, Partons, QCD, DGLAP and beyond*, 2008, arXiv: 0802.0161 [hep-ph].

[110] *Sherpa and Open Science Grid: Predicting the emergence of jets*, URL: https://sciencenode.org/feature/sherpa-and-open-science-grid-predicting-emergence-jets.php (visited on 08/11/2019).

[111] T. Gleisberg et al., *Event generation with SHERPA 1.1*, JHEP **02** (2009) 007, arXiv: 0811.4622 [hep-ph].

[112] J. Alwall et al., *The automated computation of tree-level and next-to-leading order differential cross sections, and their matching to parton shower simulations*, JHEP **07** (2014) 079, arXiv: 1405.0301 [hep-ph].

[113] S. Alioli, P. Nason, C. Oleari and E. Re, *A general framework for implementing NLO calculations in shower Monte Carlo programs: the POWHEG BOX*, JHEP **06** (2010) 043, arXiv: 1002.2581 [hep-ph].

[114] S. Frixione and B. R. Webber, *Matching NLO QCD computations and parton shower simulations*, JHEP **06** (2002) 029, arXiv: hep-ph/0204244.

[115] J. Alwall, M. Herquet, F. Maltoni, O. Mattelaer and T. Stelzer, *MadGraph 5 : Going Beyond*, JHEP **06** (2011) 128, arXiv: 1106.0522 [hep-ph].

[116] S. Frixione, F. Stoeckli, P. Torrielli and B. R. Webber, *NLO QCD corrections in Herwig++ with MC@NLO*, JHEP **01** (2011) 053, arXiv: 1010.0568 [hep-ph].

[117] J. Bellm et al., *Herwig 7.0/Herwig++ 3.0 release note*, Eur. Phys. J. C **76** (2016) 196, arXiv: 1512.01178 [hep-ph].

[118] P. Nason, *A new method for combining NLO QCD with shower Monte Carlo algorithms*, JHEP **11** (2004) 040, arXiv: hep-ph/0409146.

[119] S. Frixione, P. Nason and C. Oleari, *Matching NLO QCD computations with Parton Shower simulations: the POWHEG method*, JHEP **11** (2007) 070, arXiv: 0709.2092 [hep-ph].

[120] S. Höche, F. Krauss, S. Schumann and F. Siegert, *QCD matrix elements and truncated showers*, JHEP **05** (2009) 053, arXiv: 0903.1219 [hep-ph].

[121] F. Cascioli, P. Maierhöfer and S. Pozzorini, *Scattering Amplitudes with Open Loops*, Phys. Rev. Lett. **108** (2012) 111601, arXiv: 1111.5206 [hep-ph].

[122] N. Lavesson and L. Lönnblad, *Merging parton showers and matrix elements—back to basics*, Journal of High Energy Physics **2008** (2008) 085, ISSN: 1029-8479, URL: http://dx.doi.org/10.1088/1126-6708/2008/04/085.

[123] T. Sjöstrand et al., *An introduction to PYTHIA 8.2*, Comput. Phys. Commun. **191** (2015) 159, arXiv: 1410.3012 [hep-ph].

[124] T. Sjöstrand, S. Mrenna and P. Z. Skands, *PYTHIA 6.4 Physics and Manual*, JHEP **05** (2006) 026, arXiv: hep-ph/0603175.

[125] D. J. Lange, *The EvtGen particle decay simulation package*, Nucl. Instrum. Meth. A **462** (2001) 152.

[126] P. Artoisenet, R. Frederix, O. Mattelaer and R. Rietkerk, *Automatic spin-entangled decays of heavy resonances in Monte Carlo simulations*, JHEP **03** (2013) 015, arXiv: 1212.3460 [hep-ph].

[127] B. Andersson, G. Gustafson, G. Ingelman and T. Sjöstrand, *Parton fragmentation and string dynamics*, Physics Reports **97** (1983) 31, ISSN: 0370-1573, URL: http://www.sciencedirect.com/science/article/pii/0370157383900807.

[128] N. Davidson, T. Przedzinski and Z. Was, *PHOTOS Interface in C++: Technical and Physics Documentation*, Comput. Phys. Commun. **199** (2016) 86, arXiv: 1011.0937 [hep-ph].

[129] P. Z. Skands, *Tuning Monte Carlo generators: The Perugia tunes*, Phys. Rev. D **82** (2010) 074018, arXiv: 1005.3457 [hep-ph].

[130] P. Skands, S. Carrazza and J. Rojo, *Tuning PYTHIA 8.1: the Monash 2013 Tune*, Eur. Phys. J. C **74** (2014) 3024, arXiv: 1404.5630 [hep-ph].

[131] L. Evans and P. Bryant, *LHC Machine*, JINST **3** (2008) S08001.

[132] S. Myers, *The LEP Collider, from design to approval and commissioning*, John Adams' Lecture, Delivered at CERN, 26 Nov 1990, CERN, 1991, URL: https://cds.cern.ch/record/226776.

[133] ATLAS Collaboration, Georges Aad, et. al, *The ATLAS Experiment at the CERN Large Hadron Collider*, JINST **3** (2008) S08003.

[134] CMS Collaboration, *The CMS experiment at the CERN LHC*, JINST **3** (2008) S08004.

[135] *The LHCb Detector at the LHC*, JINST **3** (2008) S08005.

[136] *The ALICE experiment at the CERN LHC. A Large Ion Collider Experiment*, JINST **3** (2008) S08002. 259 p, Also published by CERN Geneva in 2010, URL: http://cds.cern.ch/record/1129812.

[137] E. Mobs, *The CERN accelerator complex. Complexe des accélérateurs du CERN*, (2016), General Photo, URL: https://cds.cern.ch/record/2197559.

[138] ATLAS Collaboration, Georges Aad, et. al, *Evidence for the spin-0 nature of the Higgs boson using ATLAS data*, Phys. Lett. B **726** (2013) 120, arXiv: 1307.1432 [hep-ex].

[139] CMS Collaboration, *Evidence for the direct decay of the* 125 *GeV Higgs boson to fermions*, Nature Phys. **10** (2014) 557, arXiv: 1401.6527 [hep-ex].

[140] ATLAS Collaboration, Georges Aad, et. al, *Measurements of Higgs boson production and couplings in diboson final states with the ATLAS detector at the LHC*, Phys. Lett. B **726** (2013) 88, arXiv: 1307.1427 [hep-ex], Erratum: Phys. Lett. B **734** (2014) 406.

[141] ATLAS Collaboration, Georges Aad, et. al, *Measurement of Higgs boson production in the diphoton decay channel in pp collisions at center-of-mass energies of* 7 *and* 8 *TeV with the ATLAS detector*, Phys. Rev. D **90** (2014) 112015, arXiv: 1408.7084 [hep-ex].

[142] ATLAS Collaboration, Georges Aad, et. al, *Observation and measurement of Higgs boson decays to WW^* with the ATLAS detector*, Phys. Rev. D **92** (2015) 012006, arXiv: 1412.2641 [hep-ex].

[143] ATLAS Collaboration, Georges Aad, et. al, *Measurements of the Higgs boson production and decay rates and coupling strengths using pp collision data at $\sqrt{s}$ = 7 and* 8 *TeV in the ATLAS experiment*, Eur. Phys. J. C **76** (2016) 6, arXiv: 1507.04548 [hep-ex].

[144] ATLAS Collaboration, Georges Aad, et. al, *Search for Scalar Diphoton Resonances in the Mass Range 65–600 GeV with the ATLAS Detector in pp Collision Data at $\sqrt{s}$ = 8 TeV*, Phys. Rev. Lett. **113** (2014) 171801, arXiv: 1407.6583 [hep-ex].

[145] ATLAS Collaboration, Georges Aad, et. al, *Search for a multi-Higgs-boson cascade in $W^+W^-b\bar{b}$ events with the ATLAS detector in pp collisions at $\sqrt{s}$ = 8 TeV*, Phys. Rev. D **89** (2014) 032002, arXiv: 1312.1956 [hep-ex].

[146] ATLAS Collaboration, Georges Aad, et. al, *Evidence for the Higgs-boson Yukawa coupling to tau leptons with the ATLAS detector*, JHEP **04** (2015) 117, arXiv: 1501.04943 [hep-ex].

[147] T. Taylor, *Incident at the CERN LHC: The event, the repair and lessons to drawn*, TEION KOGAKU **45** (2010) 344, URL: https://cds.cern.ch/record/1405027.

[148] M. Lamont, *Status of the LHC*, Journal of Physics: Conference Series **455** (2013) 012001, URL: https://doi.org/10.1088%2F1742-6596%2F455%2F1%2F012001.

[149] ATLAS Collaboration, Georges Aad, et. al, *ATLAS data quality operations and performance for 2015-2018 data-taking*, tech. rep. arXiv:1911.04632, CERN, 2019, URL: https://cds.cern.ch/record/2700249.

[150] ATLAS Collaboration, Georges Aad, et. al, *Reconstruction of primary vertices at the ATLAS experiment in Run 1 proton–proton collisions at the LHC*, Eur. Phys. J. C **77** (2017) 332, arXiv: 1611.10235 [hep-ex].

[151] *ATLAS Computing: technical design report*, 2005, URL: http://cds.cern.ch/record/837738.

[152] *The Worldwide LHC computing grid*, URL: http://wlcg-public.web.cern.ch/tier-centres (visited on 06/12/2019).

[153] I. Bird et al., *Update of the Computing Models of the WLCG and the LHC Experiments*, 2014, URL: https://cds.cern.ch/record/1695401.

[154] ATLAS Collaboration, Georges Aad, et. al, *ATLAS Inner Detector: Technical Design Report, 1*, ATLAS-TDR-4, 1997, URL: https://cds.cern.ch/record/331063.

[155] ATLAS Collaboration, Georges Aad, et. al, *ATLAS Inner Detector: Technical Design Report, 2*, ATLAS-TDR-5, 1997, URL: https://cds.cern.ch/record/331064.

[156] ATLAS Collaboration, Georges Aad, et. al,
ATLAS Insertable B-Layer Technical Design Report, ATLAS-TDR-19, 2010,
URL: https://cds.cern.ch/record/1291633, Addendum: ATLAS-TDR-19-ADD-1,
2012, URL: https://cds.cern.ch/record/1451888.

[157] B. Abbott et al., *Production and integration of the ATLAS Insertable B-Layer*,
JINST **13** (2018) T05008, arXiv: 1803.00844 [physics.ins-det].

[158] ATLAS Collaboration, Georges Aad, et. al, *Performance of the ATLAS Transition Radiation Tracker in Run 1 of the LHC: tracker properties*, JINST **12** (2017) P05002,
arXiv: 1702.06473 [hep-ex].

[159] ATLAS Collaboration, Georges Aad, et. al,
ATLAS Calorimeter Performance: Technical Design Report, ATLAS-TDR-1, 1996,
URL: https://cds.cern.ch/record/331059.

[160] ATLAS Collaboration, Georges Aad, et. al,
ATLAS Liquid-Argon Calorimeter: Technical Design Report, ATLAS-TDR-2, 1996,
URL: https://cds.cern.ch/record/331061.

[161] ATLAS Collaboration, Georges Aad, et. al,
ATLAS Tile Calorimeter: Technical Design Report, ATLAS-TDR-3, 1996,
URL: https://cds.cern.ch/record/331062.

[162] ATLAS Collaboration, Georges Aad, et. al,
Readiness of the ATLAS liquid argon calorimeter for LHC collisions,
Eur. Phys. J. C **70** (2010) 723, arXiv: 0912.2642 [hep-ex].

[163] ATLAS Collaboration, Georges Aad, et. al,
ATLAS Muon Spectrometer: Technical Design Report, ATLAS-TDR-10, 1997,
URL: https://cds.cern.ch/record/331068.

[164] ATLAS Collaboration, Georges Aad, et. al,
Standalone vertex finding in the ATLAS muon spectrometer, JINST **9** (2014) P02001,
arXiv: 1311.7070 [hep-ex].

[165] ATLAS Collaboration, Georges Aad, et. al,
Resolution of the ATLAS muon spectrometer monitored drift tubes in LHC Run 2,
JINST **14** (2019) P09011, arXiv: 1906.12226 [hep-ex].

[166] H. Kroha, R. Fakhrutdinov and A. Kozhin,
New High-Precision Drift-Tube Detectors for the ATLAS Muon Spectrometer. New High-Precision Drift-Tube Detectors for the ATLAS Muon Spectrometer,
JINST **12** (2017) C06007. 12 p, proceedings of INSTR17 conference, Novosibirsk, Russia,

February 2017, extended version, to be publsihed in Journal of Instrumentation, URL: https://cds.cern.ch/record/2268241.

[167] C. Ferretti and H. Kroha, *Upgrades of the ATLAS muon spectrometer with sMDT chambers*, Nuclear Instruments and Methods in Physics Research Section A: Accelerators, Spectrometers, Detectors and Associated Equipment **824** (2016) 538, ISSN: 0168-9002, URL: http://dx.doi.org/10.1016/j.nima.2015.11.043.

[168] ATLAS Collaboration, Georges Aad, et. al, *2015 start-up trigger menu and initial performance assessment of the ATLAS trigger using Run-2 data*, ATL-DAQ-PUB-2016-001, 2016, URL: https://cds.cern.ch/record/2136007.

[169] ATLAS Collaboration, Georges Aad, et. al, *Performance of electron and photon triggers in ATLAS during LHC Run 2*, Eur. Phys. J. C **80** (2020) 47, arXiv: 1909.00761 [hep-ex].

[170] ATLAS Collaboration, Georges Aad, et. al, *Performance of the ATLAS trigger system in 2015*, Eur. Phys. J. C **77** (2017) 317, arXiv: 1611.09661 [hep-ex].

[171] ATLAS Collaboration, Georges Aad, et. al, *Trigger monitoring and rate predictions using Enhanced Bias data from the ATLAS Detector at the LHC*, ATL-DAQ-PUB-2016-002, 2016, URL: https://cds.cern.ch/record/2223498.

[172] ATLAS Collaboration, Georges Aad, et. al, *Trigger Menu in 2016*, ATL-DAQ-PUB-2017-001, 2017, URL: https://cds.cern.ch/record/2242069.

[173] ATLAS Collaboration, Georges Aad, et. al, *Trigger Menu in 2017*, ATL-DAQ-PUB-2018-002, 2018, URL: https://cds.cern.ch/record/2625986.

[174] ATLAS Collaboration, Georges Aad, et. al, *The ATLAS Simulation Infrastructure*, Eur. Phys. J. C **70** (2010) 823, arXiv: 1005.4568 [physics.ins-det].

[175] S. Agostinelli et al., *GEANT4 – a simulation toolkit*, Nucl. Instrum. Meth. A **506** (2003) 250.

[176] A. Ribon et al., *Status of Geant4 hadronic physics for the simulation of LHC experiments at the start of the LHC physics program*, (2010), URL: https://lcgapp.cern.ch/project/docs/noteStatusHadronic2010.pdf.

[177] ATLAS Collaboration, Georges Aad, et. al, *The simulation principle and performance of the ATLAS fast calorimeter simulation FastCaloSim*, ATL-PHYS-PUB-2010-013, 2010, URL: https://cds.cern.ch/record/1300517.

[178] R. Brun and F. Rademakers, *ROOT – An object oriented data analysis framework*, Nucl. Instrum. Meth. A **389** (1997) 81, ISSN: 0168-9002.

[179] A. Buckley et al., *Implementation of the ATLAS Run 2 event data model*, Journal of Physics: Conference Series **664** (2015) 072045, URL: https://doi.org/10.1088%2F1742-6596%2F664%2F7%2F072045.

[180] J. Pequenao and P. Schaffner, 'How ATLAS detects particles: diagram of particle paths in the detector', 2013, URL: https://cds.cern.ch/record/1505342.

[181] ATLAS Collaboration, Georges Aad, et. al, *Performance of the ATLAS track reconstruction algorithms in dense environments in LHC Run 2*, Eur. Phys. J. C **77** (2017) 673, arXiv: 1704.07983 [hep-ex].

[182] ATLAS Collaboration, Georges Aad, et. al, *Track Reconstruction Performance of the ATLAS Inner Detector at* $\sqrt{s}$ = 13 *TeV*, ATL-PHYS-PUB-2015-018, 2015, URL: https://cds.cern.ch/record/2037683.

[183] T. Cornelissen et al., *The new ATLAS track reconstruction (NEWT)*, J. Phys.: Conf. Ser. **119** (2008) 032014, URL: https://cds.cern.ch/record/1176900.

[184] T. Cornelissen et al., *Concepts, Design and Implementation of the ATLAS New Tracking (NEWT)*, ATL-SOFT-PUB-2007-007, 2007, URL: https://cds.cern.ch/record/1020106.

[185] R. Frühwirth, *Application of Kalman filtering to track and vertex fitting*, Nuclear Instruments and Methods in Physics Research Section A: Accelerators, Spectrometers, Detectors and Associated Equipment **262** (1987) 444, ISSN: 0168-9002, URL: http://www.sciencedirect.com/science/article/pii/0168900287908874.

[186] ATLAS Collaboration, Georges Aad, et. al, *A neural network clustering algorithm for the ATLAS silicon pixel detector*, JINST **9** (2014) P09009, arXiv: 1406.7690 [hep-ex].

[187] ATLAS Collaboration, Georges Aad, et. al, *Vertex Reconstruction Performance of the ATLAS Detector at* $\sqrt{s}$ = 13 *TeV*, ATL-PHYS-PUB-2015-026, 2015, URL: https://cds.cern.ch/record/2037717.

[188] G. Piacquadio, K. Prokofiev and A. Wildauer, *Primary vertex reconstruction in the ATLAS experiment at LHC*, Journal of Physics: Conference Series **119** (2008) 032033, URL: https://doi.org/10.1088%2F1742-6596%2F119%2F3%2F032033.

[189] ATLAS Collaboration, Georges Aad, et. al, *Topological cell clustering in the ATLAS calorimeters and its performance in LHC Run 1*, Eur. Phys. J. C **77** (2017) 490, arXiv: 1603.02934 [hep-ex].

[190] ATLAS Collaboration, Georges Aad, et. al, *Electron and photon performance measurements with the ATLAS detector using the 2015–2017 LHC proton–proton collision data*, JINST **14** (2019) P12006, arXiv: 1908.00005 [hep-ex].

[191] ATLAS Collaboration, Georges Aad, et. al, *Improved electron reconstruction in ATLAS using the Gaussian Sum Filter-based model for bremsstrahlung*, ATLAS-CONF-2012-047, 2012, URL: https://cds.cern.ch/record/1449796.

[192] ATLAS Collaboration, Georges Aad, et. al, *Electron reconstruction and identification efficiency measurements with the ATLAS detector using the 2011 LHC proton–proton collision data*, Eur. Phys. J. C **74** (2014) 2941, arXiv: 1404.2240 [hep-ex].

[193] ATLAS Collaboration, Georges Aad, et. al, *Electron reconstruction and identification in the ATLAS experiment using the 2015 and 2016 LHC proton–proton collision data at* $\sqrt{s} = 13$ *TeV*, Eur. Phys. J. C **79** (2019) 639, arXiv: 1902.04655 [hep-ex].

[194] ATLAS Collaboration, Georges Aad, et. al, *Electron identification measurements in ATLAS using* $\sqrt{s} = 13$ *TeV data with* 50 *ns bunch spacing*, ATL-PHYS-PUB-2015-041, 2015, URL: https://cds.cern.ch/record/2048202.

[195] ATLAS Collaboration, Georges Aad, et. al, *Electron and photon reconstruction and performance in ATLAS using a dynamical, topological cell clustering-based approach*, ATL-PHYS-PUB-2017-022, 2017, URL: https://cds.cern.ch/record/2298955.

[196] A. Hoecker et al., *TMVA - Toolkit for Multivariate Data Analysis*, 2007, arXiv: physics/0703039 [physics.data-an].

[197] ATLAS Collaboration, Georges Aad, et. al, *Electron and photon energy calibration with the ATLAS detector using data collected in 2015 at* $\sqrt{s} = 13$ *TeV*, ATL-PHYS-PUB-2016-015, 2016, URL: https://cds.cern.ch/record/2203514.

[198] ATLAS Collaboration, Georges Aad, et. al, *Expected photon performance in the ATLAS experiment*, ATL-PHYS-PUB-2011-007, 2011, URL: https://cds.cern.ch/record/1345329.

[199] M. Cacciari, G. P. Salam and G. Soyez, *The anti-*k_t *jet clustering algorithm*, JHEP **04** (2008) 063, arXiv: 0802.1189 [hep-ph].

[200] M. Cacciari and G. P. Salam, *Pileup subtraction using jet areas*, Physics Letters B **659** (2008) 119, ISSN: 0370-2693, URL: http://www.sciencedirect.com/science/article/pii/S0370269307011094.

[201] ATLAS Collaboration, Georges Aad, et. al, *Jet energy scale measurements and their systematic uncertainties in proton–proton collisions at $\sqrt{s}$ = 13 TeV with the ATLAS detector*, Phys. Rev. D **96** (2017) 072002, arXiv: 1703.09665 [hep-ex].

[202] ATLAS Collaboration, Georges Aad, et. al, *Tagging and suppression of pileup jets with the ATLAS detector*, ATLAS-CONF-2014-018, 2014, URL: https://cds.cern.ch/record/1700870.

[203] ATLAS Collaboration, Georges Aad, et. al, *Optimisation and performance studies of the ATLAS b-tagging algorithms for the 2017-18 LHC run*, ATL-PHYS-PUB-2017-013, 2017, URL: https://cds.cern.ch/record/2273281.

[204] ATLAS Collaboration, Georges Aad, et. al, *ATLAS b-jet identification performance and efficiency measurement with $t\bar{t}$ events in pp collisions at $\sqrt{s}$ = 13 TeV*, Eur. Phys. J. C **79** (2019) 970, arXiv: 1907.05120 [hep-ex].

[205] ATLAS Collaboration, Georges Aad, et. al, *Identification of hadronic tau lepton decays using neural networks in the ATLAS experiment*, ATL-PHYS-PUB-2019-033, 2019, URL: https://cds.cern.ch/record/2688062.

[206] ATLAS Collaboration, Georges Aad, et. al, *Measurement of the tau lepton reconstruction and identification performance in the ATLAS experiment using pp collisions at $\sqrt{s}$ = 13 TeV*, ATLAS-CONF-2017-029, 2017, URL: https://cds.cern.ch/record/2261772.

[207] ATLAS Collaboration, Georges Aad, et. al, *Identification and energy calibration of hadronically decaying tau leptons with the ATLAS experiment in pp collisions at $\sqrt{s}$ = 8 TeV*, Eur. Phys. J. C **75** (2015) 303, arXiv: 1412.7086 [hep-ex].

[208] T. Barillari et al., tech. rep., 2008, URL: https://cds.cern.ch/record/1112035.

[209] ATLAS Collaboration, Georges Aad, et. al, *E_T^{miss} performance in the ATLAS detector using 2015–2016 LHC pp collisions*, ATLAS-CONF-2018-023, 2018, URL: https://cds.cern.ch/record/2625233.

[210] K. Rehermann and B. Tweedie, *Efficient identification of boosted semileptonic top quarks at the LHC*, Journal of High Energy Physics **2011** (2011), ISSN: 1029-8479, URL: http://dx.doi.org/10.1007/JHEP03(2011)059.

[211] ATLAS Collaboration, Georges Aad, et. al, *Muon reconstruction performance of the ATLAS detector in proton–proton collision data at $\sqrt{s}$ = 13 TeV*, Eur. Phys. J. C **76** (2016) 292, arXiv: 1603.05598 [hep-ex].

[212] ATLAS Collaboration, Georges Aad, et. al,
Measurement of lepton differential distributions and the top quark mass in $t\bar{t}$ production in pp collisions at $\sqrt{s}$ = 8 TeV with the ATLAS detector, Eur. Phys. J. C **77** (2017) 804,
arXiv: 1709.09407 [hep-ex].

[213] ATLAS Collaboration, Georges Aad, et. al, *Measurement of the top quark mass in the $t\bar{t} \to$ dilepton channel from $\sqrt{s}$ = 8 TeV ATLAS data*, Phys. Lett. B **761** (2016) 350,
arXiv: 1606.02179 [hep-ex].

[214] ATLAS Collaboration, Georges Aad, et. al, *Measurements of top-quark pair differential cross-sections in the $e\mu$ channel in pp collisions at $\sqrt{s}$ = 13 TeV using the ATLAS detector*, Eur. Phys. J. C **77** (2017) 292, arXiv: 1612.05220 [hep-ex].

[215] A. Collaboration, *Higgs boson production cross-section measurements and their EFT interpretation in the 4ℓ decay channel at $\sqrt{s}$ = 13 TeV with the ATLAS detector*, (2020),
arXiv: 2004.03447 [hep-ex].

[216] A. Collaboration, *Measurements of the Higgs boson inclusive and differential fiducial cross sections in the 4ℓ decay channel at $\sqrt{s}$ = 13 TeV*, 2020, arXiv: 2004.03969 [hep-ex].

[217] ATLAS Collaboration, Georges Aad, et. al, *Study of the rare decays of B_s^0 and B^0 mesons into muon pairs using data collected during 2015 and 2016 with the ATLAS detector*,
JHEP **04** (2019) 098, arXiv: 1812.03017 [hep-ex].

[218] ATLAS Collaboration, Georges Aad, et. al,
Measurement of the production cross-section of J/ψ and $\psi(2S)$ mesons at high transverse momentum in pp collisions at $\sqrt{s}$ = 13 TeV with the ATLAS detector,
ATLAS-CONF-2019-047, 2019, URL: https://cds.cern.ch/record/2693955.

[219] ATLAS Collaboration, Georges Aad, et. al, *Search for high-mass dilepton resonances using 139 fb^{-1} of pp collision data collected at $\sqrt{s}$ = 13 TeV with the ATLAS detector*,
Phys. Lett. B **796** (2019) 68, arXiv: 1903.06248 [hep-ex].

[220] A. Collaboration, *Search for a scalar partner of the top quark in the all-hadronic $t\bar{t}$ plus missing transverse momentum final state at $\sqrt{s}$=13 TeV with the ATLAS detector*, (2020),
arXiv: 2004.14060 [hep-ex].

[221] ATLAS Collaboration, Georges Aad, et. al, *Performance of missing transverse momentum reconstruction with the ATLAS detector using proton–proton collisions at $\sqrt{s}$ = 13 TeV*,
Eur. Phys. J. C **78** (2018) 903, arXiv: 1802.08168 [hep-ex].

[222] ATLAS Collaboration, Georges Aad, et. al, *Calibration of the b-tagging efficiency on charm jets using a sample of W + c events with $\sqrt{s}$ = 13 TeV ATLAS data*, ATLAS-CONF-2018-055,
2018, URL: https://cds.cern.ch/record/2652195.

[223] ATLAS Collaboration, Georges Aad, et. al, *Measurement of the muon reconstruction performance of the ATLAS detector using 2011 and 2012 LHC proton–proton collision data*, Eur. Phys. J. C **74** (2014) 3130, arXiv: 1407.3935 [hep-ex].

[224] N. Van Eldik, 'The ATLAS muon spectrometer: calibration and pattern recognition', Presented on 22 Feb 2007, 2007, URL: https://cds.cern.ch/record/1044839.

[225] Z. van Kesteren, 'Identification of muons in ATLAS', Presented on 12 Mar 2010, 2010, URL: https://cds.cern.ch/record/1255858.

[226] J. Illingworth and J. Kittler, *A survey of the hough transform*, Computer Vision, Graphics, and Image Processing **44** (1988) 87, ISSN: 0734-189X, URL: http://www.sciencedirect.com/science/article/pii/S0734189X88800331.

[227] G. Barone, J. J. Junggeburth, F. Sforza, S. Rosati and N. M. Kohler, *Muon performance results with 2018 dataset: efficiencies, scales, and resolutions.*, tech. rep. ATL-COM-PHYS-2018-661, CERN, 2018, URL: https://cds.cern.ch/record/2320120.

[228] M. Oreglia, 'A Study of the Reactions $\psi' \to \gamma\gamma\psi$', PhD thesis: SLAC, 1980, URL: http://www-public.slac.stanford.edu/sciDoc/docMeta.aspx?slacPubNumber=slac-r-236.html.

[229] J. E. Gaiser, 'Charmonium Spectroscopy From Radiative Decays of the J/ψ and ψ''', PhD thesis: SLAC, 1982, URL: http://www-public.slac.stanford.edu/sciDoc/docMeta.aspx?slacPubNumber=slac-r-255.html.

[230] ATLAS Collaboration, Georges Aad, et. al, *Validation of the muon momentum corrections for the ATLAS simulation using the $\Upsilon \to \mu\mu$ channel based on 36.5 fb^{-1} of pp collision data collected in 2015 and 2016*, ATL-PHYS-PUB-2019-018, 2019, URL: https://cds.cern.ch/record/2674152.

[231] ATLAS Collaboration, Georges Aad, et. al, *Identification of very-low transverse momentum muons in the ATLAS experiment*, ATL-PHYS-PUB-2020-002, 2020, URL: https://cds.cern.ch/record/2710574.

[232] ATLAS Collaboration, Georges Aad, et. al, *Measurement of the four-lepton invariant mass spectrum in 13 TeV proton–proton collisions with the ATLAS detector*, JHEP **04** (2019) 048, arXiv: 1902.05892 [hep-ex].

[233] ATLAS Collaboration, Georges Aad, et. al, *Simulation of top-quark production for the ATLAS experiment at $\sqrt{s}$ = 13 TeV*, ATL-PHYS-PUB-2016-004, 2016, URL: https://cds.cern.ch/record/2120417.

[234] ATLAS Collaboration, Georges Aad, et. al, *Monte Carlo Generators for the Production of a W or Z/γ^* Boson in Association with Jets at ATLAS in Run 2*, ATL-PHYS-PUB-2016-003, 2016, URL: https://cds.cern.ch/record/2120133.

[235] ATLAS Collaboration, Georges Aad, et. al, *Multi-boson simulation for* 13 *TeV ATLAS analyses*, ATL-PHYS-PUB-2016-002, 2016, URL: https://cds.cern.ch/record/2119986.

[236] ATLAS Collaboration, Georges Aad, et. al, *Modelling of the $t\bar{t}H$ and $t\bar{t}V(V = W, Z)$ processes for $\sqrt{s}$ = 13 TeV ATLAS analyses*, ATL-PHYS-PUB-2016-005, 2016, URL: https://cds.cern.ch/record/2120826.

[237] ATLAS Collaboration, Georges Aad, et. al, *Measurement of the Z/γ^* boson transverse momentum distribution in pp collisions at $\sqrt{s}$ = 7 TeV with the ATLAS detector*, JHEP **09** (2014) 145, arXiv: 1406.3660 [hep-ex].

[238] E. Bothmann et al., *Event Generation with Sherpa 2.2*, (2019), arXiv: 1905.09127 [hep-ph].

[239] T. Gleisberg and S. Höche, *Comix, a new matrix element generator*, JHEP **12** (2008) 039, arXiv: 0808.3674 [hep-ph].

[240] A. Denner, S. Dittmaier and L. Hofer, *Collier: A fortran-based complex one-loop library in extended regularizations*, Comput. Phys. Commun. **212** (2017) 220, arXiv: 1604.06792 [hep-ph].

[241] S. Schumann and F. Krauss, *A parton shower algorithm based on Catani–Seymour dipole factorisation*, JHEP **03** (2008) 038, arXiv: 0709.1027 [hep-ph].

[242] S. Höche, F. Krauss, M. Schönherr and F. Siegert, *A critical appraisal of NLO+PS matching methods*, JHEP **09** (2012) 049, arXiv: 1111.1220 [hep-ph].

[243] S. Höche, F. Krauss, M. Schönherr and F. Siegert, *QCD matrix elements + parton showers. The NLO case*, JHEP **04** (2013) 027, arXiv: 1207.5030 [hep-ph].

[244] S. Catani, F. Krauss, R. Kuhn and B. R. Webber, *QCD Matrix Elements + Parton Showers*, JHEP **11** (2001) 063, arXiv: hep-ph/0109231.

[245] ATLAS Collaboration, Georges Aad, et. al, *ATLAS Pythia 8 tunes to* 7 *TeV data*, ATL-PHYS-PUB-2014-021, 2014, URL: https://cds.cern.ch/record/1966419.

[246] W. Verkerke and D. Kirkby, *The RooFit toolkit for data modeling*, 2003, arXiv: physics/0306116 [physics.data-an].

[247] T. Aaltonen et al.,
Search for new particles decaying into dijets in proton-antiproton collisions at $\sqrt{s} = 1.96$ *TeV*,
Phys. Rev. **D79** (2009) 112002.

[248] ATLAS Collaboration, Georges Aad, et. al,
Measurements of top-quark pair differential cross-sections in the lepton+jets channel in pp collisions at $\sqrt{s} = 13$ *TeV using the ATLAS detector*, JHEP **11** (2017) 191,
arXiv: 1708.00727 [hep-ex].

[249] ATLAS Collaboration, Georges Aad, et. al, *Measurement of the* $W^{\pm}Z$ *boson pair-production cross section in pp collisions at* $\sqrt{s} = 13$ *TeV with the ATLAS Detector*,
Phys. Lett. B **762** (2016) 1, arXiv: 1606.04017 [hep-ex].

[250] ATLAS Collaboration, Georges Aad, et. al, *Measurements of the production cross section of a Z boson in association with jets in pp collisions at* $\sqrt{s} = 13$ *TeV with the ATLAS detector*,
Eur. Phys. J. C **77** (2017) 361, arXiv: 1702.05725 [hep-ex].

[251] ATLAS Collaboration, Georges Aad, et. al,
Luminosity determination in pp collisions at $\sqrt{s} = 8$ *TeV using the ATLAS detector at the LHC*,
Eur. Phys. J. C **76** (2016) 653, arXiv: 1608.03953 [hep-ex].

[252] ATLAS Collaboration, Georges Aad, et. al,
Constraints on promptly decaying supersymmetric particles with lepton-number- and R-parity-violating interactions using Run-1 ATLAS data, ATLAS-CONF-2015-018, 2015,
URL: https://cds.cern.ch/record/2017303.

[253] ATLAS Collaboration, Georges Aad, et. al,
Dark matter interpretations of ATLAS searches for the electroweak production of supersymmetric particles in $\sqrt{s} = 8$ *TeV proton–proton collisions*, JHEP **09** (2016) 175,
arXiv: 1608.00872 [hep-ex].

[254] A. Czarnecki and W. J. Marciano,
The Muon Anomalous Magnetic Moment: Standard Model Theory and Beyond, 2000,
arXiv: hep-ph/0010194 [hep-ph].

[255] T. M. g-2 Collaboration,
Final report of the E821 muon anomalous magnetic moment measurement at BNL,
Phys. Rev. D **73** (7 2006) 072003,
URL: https://link.aps.org/doi/10.1103/PhysRevD.73.072003.

[256] T. L. collaboration, *Measurement of the* $B_s^0 \to \mu^+\mu^-$ *branching fraction and effective lifetime and search for* $B^0 \to \mu^+\mu^-$ *decays*, Physical Review Letters **118** (2017), ISSN: 1079-7114,
URL: http://dx.doi.org/10.1103/PhysRevLett.118.191801.

[257] S. KHALIL, *CP Violation in supersymmetric theories*, International Journal of Modern Physics A **18** (2003) 1697, ISSN: 1793-656X, URL: http://dx.doi.org/10.1142/S0217751X03013570.

[258] R. Catena and L. Covi, *SUSY dark matter(s)*, The European Physical Journal C **74** (2014), ISSN: 1434-6052, URL: http://dx.doi.org/10.1140/epjc/s10052-013-2703-4.

[259] C. F. Berger, J. S. Gainer, J. L. Hewett and T. G. Rizzo, *Supersymmetry without prejudice*, Journal of High Energy Physics **2009** (2009) 023, ISSN: 1029-8479, URL: http://dx.doi.org/10.1088/1126-6708/2009/02/023.

[260] C. Borschensky et al., *Squark and gluino production cross sections in pp collisions at* $\sqrt{s} = 13, 14, 33$ *and* 100 *TeV*, Eur. Phys. J. C **74** (2014) 3174, arXiv: 1407.5066 [hep-ph].

[261] W. Beenakker, R. Höpker, M. Spira and P. Zerwas, *Squark and gluino production at hadron colliders*, Nucl. Phys. B **492** (1997) 51, arXiv: hep-ph/9610490.

[262] A. Kulesza and L. Motyka, *Threshold Resummation for Squark-Antisquark and Gluino-Pair Production at the LHC*, Phys. Rev. Lett. **102** (2009) 111802, arXiv: 0807.2405 [hep-ph].

[263] A. Kulesza and L. Motyka, *Soft gluon resummation for the production of gluino-gluino and squark-antisquark pairs at the LHC*, Phys. Rev. D **80** (2009) 095004, arXiv: 0905.4749 [hep-ph].

[264] W. Beenakker, C. Borschensky, M. Krämer, A. Kulesza and E. Laenen, *NNLL-fast: predictions for coloured supersymmetric particle production at the LHC with threshold and Coulomb resummation*, JHEP **12** (2016) 133, arXiv: 1607.07741 [hep-ph].

[265] M. Beneke, M. Czakon, P. Falgari, A. Mitov and C. Schwinn, *Threshold expansion of the* $gg(q\bar{q}) \to Q\bar{Q} + X$ *cross section at* $O(\alpha_s^4)$, Phys. Lett. B **690** (2010) 483, arXiv: 0911.5166 [hep-ph], Erratum: Phys. Lett. B **778** (2018) 464.

[266] W. Beenakker et al., *NNLL resummation for squark-antisquark pair production at the LHC*, JHEP **01** (2012) 076, arXiv: 1110.2446 [hep-ph].

[267] W. Beenakker et al., *Towards NNLL resummation: hard matching coefficients for squark and gluino hadroproduction*, JHEP **10** (2013) 120, arXiv: 1304.6354 [hep-ph].

[268] W. Beenakker et al., *NNLL Resummation for Squark-Antisquark and Gluino-Pair Production at the LHC*, JHEP **12** (2014) 023, arXiv: 1404.3134 [hep-ph].

[269] W. Beenakker et al.,
The Production of Charginos/Neutralinos and Sleptons at Hadron Colliders,
Phys. Rev. Lett. **83** (1999) 3780, arXiv: hep-ph/9906298,
Erratum: Phys. Rev. Lett. **100** (2008) 029901.

[270] J. Fiaschi and M. Klasen, *Neutralino-chargino pair production at NLO+NLL with resummation-improved parton density functions for LHC Run II*,
Phys. Rev. D **98** (2018) 055014, arXiv: 1805.11322 [hep-ph].

[271] B. Fuks, M. Klasen, D. R. Lamprea and M. Rothering, *Precision predictions for electroweak superpartner production at hadron colliders with Resummino*, Eur. Phys. J. C **73** (2013) 2480, arXiv: 1304.0790 [hep-ph].

[272] B. Fuks, M. Klasen, D. R. Lamprea and M. Rothering,
Gaugino production in proton-proton collisions at a center-of-mass energy of 8 *TeV*,
JHEP **10** (2012) 081, arXiv: 1207.2159 [hep-ph].

[273] J. Debove, B. Fuks and M. Klasen,
Threshold resummation for gaugino pair production at hadron colliders,
Nucl. Phys. B **842** (2011) 51, arXiv: 1005.2909 [hep-ph].

[274] B. de Carlos and J. Casas, *One-loop analysis of the electroweak breaking in supersymmetric models and the fine-tuning problem*, Phys. Lett. B **309** (1993) 320, arXiv: hep-ph/9303291.

[275] R. Barbieri and D. Pappadopulo, *S-particles at their naturalness limits*,
Journal of High Energy Physics **2009** (2009) 061, ISSN: 1029-8479,
URL: http://dx.doi.org/10.1088/1126-6708/2009/10/061.

[276] G. Bozzi, B. Fuks and M. Klasen,
Threshold Resummation for Slepton-Pair Production at Hadron Colliders,
Nucl. Phys. B **777** (2007) 157, arXiv: hep-ph/0701202 [hep-ph].

[277] B. Fuks, M. Klasen, D. R. Lamprea and M. Rothering,
Revisiting slepton pair production at the Large Hadron Collider, JHEP **01** (2014) 168,
arXiv: 1310.2621 [hep-ph].

[278] J. Fiaschi and M. Klasen, *Slepton pair production at the LHC in NLO+NLL with resummation-improved parton densities*, JHEP **03** (2018) 094,
arXiv: 1801.10357 [hep-ph].

[279] *LHC SUSY Cross Section Working Group*,
URL: https://twiki.cern.ch/twiki/bin/view/LHCPhysics/SUSYCrossSections
(visited on 10/01/2020).

[280] J. Alwall, P. Schuster and N. Toro,
Simplified models for a first characterization of new physics at the LHC,
Phys. Rev. D **79** (2009) 075020, arXiv: 0810.3921 [hep-ph].

[281] D. Alves et al., *Simplified models for LHC new physics searches*, J. Phys. G **39** (2012) 105005, arXiv: 1105.2838 [hep-ph].

[282] ATLAS Collaboration, Georges Aad, et. al, *Search for supersymmetry in events with four or more leptons in $\sqrt{s} = 8$ TeV pp collisions with the ATLAS detector*,
Phys. Rev. D **90** (2014) 052001, arXiv: 1405.5086 [hep-ex].

[283] R. Barbieri and G. Giudice, *Upper bounds on supersymmetric particle masses*,
Nucl. Phys. B **306** (1988) 63.

[284] *LEP2 SUSY Working Group Combined LEP Chargino Results, up to 208 GeV for low DM*,
URL: http://lepsusy.web.cern.ch/lepsusy/www/inoslowdmsummer02/charginolowdm_pub.html (visited on 06/12/2019).

[285] ATLAS Collaboration, Georges Aad, et. al,
Searches for electroweak production of supersymmetric particles with compressed mass spectra in $\sqrt{s} = 13$ TeV pp collisions with the ATLAS detector, ATLAS-CONF-2019-014, 2019, URL: https://cds.cern.ch/record/2675954.

[286] P. Meade, N. Seiberg and D. Shih, *General Gauge Mediation*,
Prog. Theor. Phys. Suppl. **177** (2009) 143, arXiv: 0801.3278 [hep-ph].

[287] T. A. Collaboration,
Search for scalar leptons in e^+e^- collisions at centre-of-mass energies up to 209 GeV,
Physics Letters B **526** (2002) 206, ISSN: 0370-2693,
URL: http://dx.doi.org/10.1016/S0370-2693(01)01494-0.

[288] T. D. Collaboration, *Searches for supersymmetric particles in e^+e^- collisions up to 208 GeV and interpretation of the results within the MSSM*,
The European Physical Journal C **31** (2003) 421, ISSN: 1434-6052,
URL: http://dx.doi.org/10.1140/epjc/s2003-01355-5.

[289] T. L. Collaboration, *Search for scalar leptons and scalar quarks at LEP*,
Physics Letters B **580** (2004) 37, ISSN: 0370-2693,
URL: http://dx.doi.org/10.1016/j.physletb.2003.10.010.

[290] T. O. Collaboration, *Search for anomalous production of dilepton events with missing transverse momentum in e^+e^- collisions at $\sqrt{s} = 183$ Gev to 209 GeV*,
Eur. Phys. J. **C32** (2004) 453, arXiv: hep-ex/0309014 [hep-ex].

[291] *LEP2 SUSY Working Group Combined LEP Selectron/Smuon/Stau Results, 183-208 GeV*, URL: http://lepsusy.web.cern.ch/lepsusy/www/sleptons_summer04/slep_final.html (visited on 06/12/2019).

[292] L. Breiman, J. H. Friedman, R. A. Olshen and C. J. Stone, 'Classification and Regression Trees', 1983.

[293] Y. Freund and R. E. Schapire, *A Decision-Theoretic Generalization of On-Line Learning and an Application to Boosting*, J. Comput. Syst. Sci. **55** (1997) 119, ISSN: 0022-0000, URL: https://doi.org/10.1006/jcss.1997.1504.

[294] F. Pedregosa et al., *Scikit-learn: Machine Learning in Python*, Journal of Machine Learning Research **12** (2011) 2825.

[295] J. T. Linnemann, *Measures of Significance in HEP and Astrophysics*, 2003, arXiv: physics/0312059 [physics.data-an].

[296] ATLAS Collaboration, Georges Aad, et. al, *Validation of Monte Carlo event generators in the ATLAS Collaboration for LHC Run 2*, ATL-PHYS-PUB-2016-001, 2016, URL: https://cds.cern.ch/record/2119984.

[297] H.-L. Lai, M. Guzzi, J. Huston, Z. Li, P. M. Nadolsky et al., *New parton distributions for collider physics*, Phys. Rev. D **82** (2010) 074024, arXiv: 1007.2241 [hep-ph].

[298] W. Beenakker et al., *Soft-gluon resummation for squark and gluino hadroproduction*, JHEP **12** (2009) 041, arXiv: 0909.4418 [hep-ph].

[299] W. Beenakker et al., *Squark and gluino hadroproduction*, Int. J. Mod. Phys. A **26** (2011) 2637, arXiv: 1105.1110 [hep-ph].

[300] D. de Florian et al., *Handbook of LHC Higgs Cross Sections: 4. Deciphering the Nature of the Higgs Sector*, (2016), arXiv: 1610.07922 [hep-ph].

[301] M. Czakon and A. Mitov, *NNLO corrections to top pair production at hadron colliders: the quark-gluon reaction*, JHEP **01** (2013) 080, arXiv: 1210.6832 [hep-ph].

[302] M. Czakon and A. Mitov, *NNLO corrections to top-pair production at hadron colliders: the all-fermionic scattering channels*, JHEP **12** (2012) 054, arXiv: 1207.0236 [hep-ph].

[303] E. Bothmann, M. Schönherr and S. Schumann,
Reweighting QCD matrix-element and parton-shower calculations,
Eur. Phys. J. C **76** (2016) 590, arXiv: 1606.08753 [hep-ph].

[304] S. Dulat et al.,
New parton distribution functions from a global analysis of quantum chromodynamics,
Phys. Rev. D **93** (2016) 033006, arXiv: 1506.07443 [hep-ph].

[305] L. Harland-Lang, A. Martin, P. Motylinski and R. Thorne,
Parton distributions in the LHC era: MMHT 2014 PDFs, Eur. Phys. J. C **75** (2015) 204,
arXiv: 1412.3989 [hep-ph].

[306] S. Frixione, E. Laenen, P. Motylinski and B. R. Webber, *Angular correlations of lepton pairs from vector boson and top quark decays in Monte Carlo simulations*, JHEP **04** (2007) 081,
arXiv: hep-ph/0702198.

[307] S. Frixione, P. Nason and G. Ridolfi,
A positive-weight next-to-leading-order Monte Carlo for heavy flavour hadroproduction,
JHEP **09** (2007) 126, arXiv: 0707.3088 [hep-ph].

[308] H. B. Hartanto, B. Jäger, L. Reina and D. Wackeroth,
Higgs boson production in association with top quarks in the POWHEG BOX,
Phys. Rev. D **91** (2015) 094003, arXiv: 1501.04498 [hep-ph].

[309] P. Nason and C. Oleari,
NLO Higgs boson production via vector-boson fusion matched with shower in POWHEG,
JHEP **02** (2010) 037, arXiv: 0911.5299 [hep-ph].

[310] M. Ciccolini, A. Denner and S. Dittmaier, *Strong and Electroweak Corrections to the Production of Higgs + 2 Jets via Weak Interactions at the Large Hadron Collider*,
Phys. Rev. Lett. **99** (2007) 161803, arXiv: 0707.0381 [hep-ph].

[311] M. Ciccolini, A. Denner and S. Dittmaier, *Electroweak and QCD corrections to Higgs production via vector-boson fusion at the CERN LHC*, Phys. Rev. D **77** (2008) 013002,
arXiv: 0710.4749 [hep-ph].

[312] P. Bolzoni, F. Maltoni, S.-O. Moch and M. Zaro,
Higgs Boson Production via Vector-Boson Fusion at Next-to-Next-to-Leading Order in QCD,
Phys. Rev. Lett. **105** (2010) 011801, arXiv: 1003.4451 [hep-ph].

[313] A. Djouadi, J. Kalinowski and M. Spira, *HDECAY: A program for Higgs boson decays in the Standard Model and its supersymmetric extension*, Comput. Phys. Commun. **108** (1998) 56,
arXiv: hep-ph/9704448.

[314] M. Spira, *QCD Effects in Higgs physics*, Fortsch. Phys. **46** (1998) 203, arXiv: hep-ph/9705337.

[315] A. Djouadi, M. M. Mühlleitner and M. Spira, *Decays of supersymmetric particles: The Program SUSY-HIT (SUspect-SdecaY-Hdecay-InTerface)*, Acta Phys. Polon. B **38** (2007) 635, arXiv: hep-ph/0609292.

[316] A. Bredenstein, A. Denner, S. Dittmaier and M. M. Weber, *Radiative corrections to the semileptonic and hadronic Higgs-boson decays $H \to WW/ZZ \to 4$ fermions*, JHEP **02** (2007) 080, arXiv: hep-ph/0611234.

[317] A. Bredenstein, A. Denner, S. Dittmaier and M. M. Weber, *Precise predictions for the Higgs-boson decay H —> WW/ZZ —> 4 leptons*, Phys. Rev. **D74** (2006) 013004, arXiv: hep-ph/0604011 [hep-ph].

[318] A. Bredenstein, A. Denner, S. Dittmaier and M. M. Weber, *Precision calculations for the Higgs decays H —> ZZ/WW —> 4 leptons*, Nucl. Phys. Proc. Suppl. **160** (2006) 131, [,131(2006)], arXiv: hep-ph/0607060 [hep-ph].

[319] ATLAS Collaboration, Georges Aad, et. al, *Studies on top-quark Monte Carlo modelling for Top2016*, ATL-PHYS-PUB-2016-020, 2016, URL: https://cds.cern.ch/record/2216168.

[320] P. Bärnreuther, M. Czakon and A. Mitov, *Percent-Level-Precision Physics at the Tevatron: Next-to-Next-to-Leading Order QCD Corrections to $q\bar{q} \to t\bar{t} + X$*, Phys. Rev. Lett. **109** (2012) 132001, arXiv: 1204.5201 [hep-ph].

[321] M. Czakon and A. Mitov, *Top++: A program for the calculation of the top-pair cross-section at hadron colliders*, Comput. Phys. Commun. **185** (2014) 2930, arXiv: 1112.5675 [hep-ph].

[322] T. Sjöstrand, S. Mrenna and P. Skands, *A brief introduction to PYTHIA 8.1*, Comput. Phys. Commun. **178** (2008) 852, arXiv: 0710.3820 [hep-ph].

[323] L. Lönnblad, *Correcting the Colour-Dipole Cascade Model with Fixed Order Matrix Elements*, JHEP **05** (2002) 046, arXiv: hep-ph/0112284.

[324] L. Lönnblad and S. Prestel, *Matching tree-level matrix elements with interleaved showers*, JHEP **03** (2012) 019, arXiv: 1109.4829 [hep-ph].

[325] C. Anastasiou, L. J. Dixon, K. Melnikov and F. Petriello, *High precision QCD at hadron colliders: Electroweak gauge boson rapidity distributions at NNLO*, Phys. Rev. D **69** (2004) 094008, arXiv: hep-ph/0312266.

[326] ATLAS Collaboration, Georges Aad, et. al, *Search for supersymmetry in events with four or more leptons in* $\sqrt{s} = 13$ *TeV pp collisions using* $13.3\,fb^{-1}$ *of ATLAS data.*, ATLAS-CONF-2016-075, 2016, URL: https://cds.cern.ch/record/2206245.

[327] ATLAS Collaboration, Georges Aad, et. al, *Search for supersymmetry in events with four or more leptons in* $\sqrt{s} = 13$ *TeV pp collisions with ATLAS*, Phys. Rev. D **98** (2018) 032009, arXiv: 1804.03602 [hep-ex].

[328] ATLAS Collaboration, Georges Aad, et. al, *Search for supersymmetry in events with four or more leptons in* $139\,fb^{-1}\sqrt{s} = 13$ *TeV pp collisions with the ATLAS detector*, Publication in preparation ().

[329] ATLAS Collaboration, Georges Aad, et. al, *Selection of jets produced in* 13 *TeV proton–proton collisions with the ATLAS detector*, ATLAS-CONF-2015-029, 2015, URL: https://cds.cern.ch/record/2037702.

[330] ATLAS Collaboration, Georges Aad, et. al, *The ATLAS Tau Trigger in Run 2*, ATLAS-CONF-2017-061, 2017, URL: https://cds.cern.ch/record/2274201.

[331] ATLAS Collaboration, Georges Aad, et. al, *Estimation of non-prompt and fake lepton backgrounds in final states with top quarks produced in proton–proton collisions at* $\sqrt{s} = 8$ *TeV with the ATLAS Detector*, ATLAS-CONF-2014-058, 2014, URL: https://cds.cern.ch/record/1951336.

[332] M. Baak et al., *HistFitter software framework for statistical data analysis*, Eur. Phys. J. C **75** (2015) 153, arXiv: 1410.1280 [hep-ex].

[333] G. Avoni et al., *The new LUCID-2 detector for luminosity measurement and monitoring in ATLAS*, JINST **13** (2018) P07017.

[334] ATLAS Collaboration, Georges Aad, et. al, *Luminosity determination in pp collisions at* $\sqrt{s} = 13$ *TeV using the ATLAS detector at the LHC*, ATLAS-CONF-2019-021, 2019, URL: https://cds.cern.ch/record/2677054.

[335] S. Dittmaier et al., *Handbook of LHC Higgs Cross Sections: 2. Differential Distributions*, (2012), arXiv: 1201.3084 [hep-ph].

[336] ATLAS Collaboration, Georges Aad, et. al, *Measurement of the* $t\bar{t}Z$ *and* $t\bar{t}W$ *cross sections in proton–proton collisions at* $\sqrt{s} = 13$ *TeV with the ATLAS detector*, Phys. Rev. D **99** (2019) 072009, arXiv: 1901.03584 [hep-ex].

[337] G. Ranucci, *The profile likelihood ratio and the look elsewhere effect in high energy physics*, Nuclear Instruments and Methods in Physics Research Section A: Accelerators, Spectrometers, Detectors and Associated Equipment **661** (2012) 77, ISSN: 0168-9002, URL: http://www.sciencedirect.com/science/article/pii/S0168900211018420.

[338] G. Cowan, K. Cranmer, E. Gross and O. Vitells, *Asymptotic formulae for likelihood-based tests of new physics*, Eur. Phys. J. C **71** (2011) 1554, arXiv: 1007.1727 [physics.data-an], Erratum: Eur. Phys. J. C **73** (2013) 2501.

[339] L. Moneta et al., *The RooStats Project*, 2010, arXiv: 1009.1003 [physics.data-an].

[340] A. L. Read, *Presentation of search results: The CL(s) technique*, J. Phys. G **28** (2002) 2693.

[341] ATLAS Collaboration, Georges Aad, et. al, *Search for pair production of higgsinos in final states with at least three b-tagged jets in $\sqrt{s}$ = 13 TeV pp collisions using the ATLAS detector*, Phys. Rev. D **98** (2018) 092002, arXiv: 1806.04030 [hep-ex].

[342] ATLAS Collaboration, Georges Aad, et. al, *Search for direct stau production in events with two hadronic τ-leptons in $\sqrt{s}$ = 13 TeV pp collisions with the ATLAS detector*, Phys. Rev. D **101** (2020) 032009, arXiv: 1911.06660 [hep-ex].

[343] ATLAS Collaboration, Georges Aad, et. al, *Improved description of the di-tau final state in events with associated production of a W boson and jets in the ATLAS detector using the tau-promotion method*, ATL-PHYS-PUB-2019-039, 2019, URL: https://cds.cern.ch/record/2692073.

[344] A. Samara, 'Improving the modelling of the associated production of W-bosons and jets in the ATLAS detector', MA thesis: LMU München, 2018, URL: https://www.etp.physik.uni-muenchen.de/publications/theses/download/master_asamara.pdf.

[345] C. G. Lester and D. J. Summers, *Measuring masses of semi-invisibly decaying particles pair produced at hadron colliders*, Phys. Lett. B **463** (1999) 99, arXiv: hep-ph/9906349.

[346] A. Barr, C. Lester and P. Stephens, *A variable for measuring masses at hadron colliders when missing energy is expected; m_{T2}: the truth behind the glamour*, J. Phys. G **29** (2003) 2343, arXiv: hep-ph/0304226.

[347] ATLAS Collaboration, *Search for direct stau production in events with two hadronic tau leptons in $\sqrt{s}$= 13 TeV pp collisions with the ATLAS detector*, tech. rep. ATLAS-COM-CONF-2019-037, CERN, 2019, URL: https://cds.cern.ch/record/2674914.

[348] F. Krieter,
'Search for Scalar Top Quarks in Final States with Two Hadronically Decaying Tau Leptons',
MA thesis: LMU München, 2017, URL: https://www.etp.physik.uni-muenchen.de/publications/theses/download/master_fkrieter.pdf.

[349] G. Polesello and D. Tovey,
Supersymmetric particle mass measurement with the boost-corrected contransverse mass,
JHEP **03** (2010) 030.

[350] D. Tovey, *On measuring the masses of pair-produced semi-invisibly decaying particles at hadron colliders*, JHEP **04** (2008) 034, arXiv: hep-ph/0802.2879.

[351] ATLAS Collaboration, Georges Aad, et. al,
Object-based missing transverse momentum significance in the ATLAS Detector,
ATLAS-CONF-2018-038, 2018, URL: https://cds.cern.ch/record/2630948.

[352] C. Leitgeb and A. Bertolini, Private correspondence, 2020.

[353] J. J. Junggeburth, *Muon identification and reconstruction efficiencies in full Run-2 dataset*,
tech. rep. ATL-COM-PHYS-2019-1001, CERN, 2019,
URL: https://cds.cern.ch/record/2685295.